REPORT DOCUMENTATION PAGE

Form Approved
OMB NO. 0704-0188

Public reporting burden for this collection of information is estimated to average 1 hour per response, including the time for reviewing instructions, searching existing data sources, gathering and maintaining the data needed, and completing and reviewing the collection of information. Send comment regarding this burden estimates or any other aspect of this collection of information, including suggestions for reducing this burden, to Washington Headquarters Services, Directorate for information Operations and Reports, 1215 Jefferson Davis Highway, Suite 1204, Arlington, VA 22202-4302, and to the Office of Management and Budget, Paperwork Reduction Project (0704-0188), Washington, DC 20503.

1. AGENCY USE ONLY *(Leave blank)*	2. REPORT DATE	3. REPORT TYPE AND DATES COVERED
		Final Report

4. TITLE AND SUBTITLE

Advanced Luminescent Materials and Quantum Confinement

5. FUNDING NUMBERS

DAD19-99-1-0356

6. AUTHOR(S)

Marc M. Cahay

7. PERFORMING ORGANIZATION NAMES(S) AND ADDRESS(ES)

Electrochemical Society, Inc.
10 South Main St.
Pennington, NJ 08534-2896

8. PERFORMING ORGANIZATION REPORT NUMBER

9. SPONSORING / MONITORING AGENCY NAME(S) AND ADDRESS(ES)

U.S. Army Research Office
P.O. Box 12211
Research Triangle Park, NC 27709-2211

10. SPONSORING / MONITORING AGENCY REPORT NUMBER

ARO 40392.1-EL-CF

11. SUPPLEMENTARY NOTES

The views, opinions and/or findings contained in this report are those of the author(s) and should not be construed as an official Department of the Army position, policy or decision, unless so designated by other documentation.

12a. DISTRIBUTION / AVAILABILITY STATEMENT

Approved for public release; distribution unlimited.

12 b. DISTRIBUTION CODE

13. ABSTRACT *(Maximum 200 words)*

DTIC QUALITY INSPECTED 4

14. SUBJECT TERMS

15. NUMBER IF PAGES

16. PRICE CODE

17. SECURITY CLASSIFICATION OR REPORT	18. SECURITY CLASSIFICATION OF THIS PAGE	19. SECURITY CLASSIFICATION OF ABSTRACT	20. LIMITATION OF ABSTRACT
UNCLASSIFIED	UNCLASSIFIED	UNCLASSIFIED	UL

ADVANCED LUMINESCENT MATERIALS AND QUANTUM CONFINEMENT

Proceedings of the International Symposium

Editors

M. Cahay
University of Cincinnati
Cincinnati, Ohio

S. Bandyopadhyay
University of Nebraska
Lincoln, Nebraska

D. J. Lockwood
National Research Council
Ottawa, Canada

N. Koshida
Tokyo University of Agriculture
and Technology
Tokyo, Japan

J. P. Leburton
University of Illinois
Urbana, Illinois

M. Meyyappan
NASA Ames Research Center
Moffett Field, California

T. Sakamoto
Electrotechnical Laboratory
Ibaraki, Japan





DIELECTRIC SCIENCE AND TECHNOLOGY, ELECTRONICS, AND LUMINESCENCE AND DISPLAY MATERIALS DIVISIONS

Proceedings Volume 99-22



THE ELECTROCHEMICAL SOCIETY, INC.,
10 South Main St., Pennington, NJ 08534-2896, USA

DTIC QUALITY INSPECTED 4

20000627 031

Copyright 1999 by The Electrochemical Society, Inc.
All rights reserved.

This book has been registered with Copyright Clearance Center, Inc.
For further information, please contact the Copyright Clearance Center,
Salem, Massachusetts.

Published by:

The Electrochemical Society, Inc.
10 South Main Street
Pennington, New Jersey 08534-2896, USA

Telephone 609.737.1902
Fax 609.737.2743
e-mail: ecs@electrochem.org
Web: http://www.electrochem.org

Library of Congress Catalogue Number: 99-66079

ISBN 1-56677-245-1

Printed in the United States of America

PREFACE

This book is a collection of many of the papers presented at the International Symposium on Advanced Luminescent Materials and Quantum Confinement held October 18-20 in Honolulu, Hawaii, as part of the 196th Meeting of the Electrochemical Society. This symposium was a follow-up of previous meetings held in St Louis (Spring '92), San Francisco (Spring '94), Chicago (Fall '95), Montreal (Spring '97) and Boston (Fall '98).

The symposium was sponsored by the Dielectric Science and Technology, the Electronics, and the Luminescence and Display Materials Divisions of the Electrochemical Society.

The symposium addresses recent developments in the area of nanoscale semiconductors, metallic, and organic structures, porous silicon, quantum dot structures, self-ordered nanostructures and clusters, quantum devices and circuits, and quantum well infrared photodetectors. Ten invited papers featured the main themes of the symposium.

This Proceedings Volume was prepared beforehand to be available at the symposium and includes 45 of the 50 papers presented at the meeting. The symposium was organized into oral presentations that spanned three days. Posters were also presented during an evening session. Invited papers are indicated by an asterisk in the Table of Contents.

The editors thank all the speakers and session chairpersons for their contributions to the success of the symposium. We also thank the Electrochemical Society staff for their constant support and for their help in preparing the volume for publication.

Finally, we would like to conclude by expressing our appreciation for the financial support provided by the National Science Foundation, the U.S. Army Research Office and the Electrochemical Society.

M. Cahay
S. Bandyopadhyay
D. J. Lockwood
N. Koshida
J. P. Leburton
M. Meyyappan
T. Sakamoto

TABLE OF CONTENTS

PREFACE iii

Porous Silicon

High efficiency electroluminescence from anodically oxidized porous silicon 3
Y. Show, S. Nozaki, H. Morisaki, M. Iwase, and T. Izumi

Quantum confinement in porous silicon as a function of size distribution of luminescent sites 10
G. Dalba, N. Daldosso, P. Fornasini, M. Grimaldi, R. Grisenti, and F. Rocca

Anomalous Behavior of Polarization Memory in Oxidized Porous Silicon . 21
H. Koyama and P.M. Fauchet

Enhancing Efficiency and Stability of Porous Silicon Electroluminescence Using Electrochemical Techniques 27
B. Gelloz and N. Koshida

Nonlinear Refractive Index Change in Porous Silicon Fabry-Perot Resonators 35
M. Takahashi, Y. Toriumi, T. Matsumoto, Y. Masumoto, and N. Koshida,

Si Superlattices and Photonic Crystals

Wavy SiGe/Si Superlattices: Structural and Optical Properties and Application to Near Infrared Light Detection 45
J.-M. Baribeau, A. Delage, S. Janz, H. Lafontaine, D. J. Lockwood, J. McCaffrey, S. Moisa, N. Rowell, and D.-X. Xu*

First Principle Calculations of the Optical Properties of Si Quantum Wells 62
S. Ossicini and E. Degoli

Modifications in the Light Emission from Anisotropic 3-Dimensional Photonic Crystal 78
S. Romanov, M. Muller, R. Zentel, T. Maka, and C. Sotomayor Torres

Electronic Raman Scattering from Weakly Bound Electrons in Lightly Doped n-type GaAs 96
D.J. Lockwood, M. Potemski, and M.L. Sadowski
Propagation and Localization of Vertically Polarized Plasmon-LO Phono Collective Excitations in Doped GaAs/AlAs Superlattices 105
Yu.A. Pusep, M.T.O. Silva, N.T. Moshegov, P. Basmaji, and J.C. Galzerani
Bragg reflection, superradiant coupling, and giant Rabi splitting in system with resonantly distributed quantum wells 118
D.H. Christensen
Thermalization of Hot Electrons and Thermionic Cooling of Superlattice 130
C. Zhang and R. A. Lewis
Dynamic Characteristics of Current Hyteresis in Weakly Coupled Superlattices GaAs/AlGaAs 137
G.K. Rasulova

Optics in Quantum Dots and Nanostructures

Spontaneous Emission and Lasing Characteristics of 1.3 μ Quantum Dots 149
D.G. Deppe, D.L. Huffaker, O. Shchekin, S. Csutak, and G. Park*
Phonon-Assisted Optical Transitions in Disk-Shaped Quantum Dots 160
J.T. Devreese, V.M. Fomin, S.N. Klimin, and J.-P. Leburton*
Optical properties of single quantum dot 172
*Y. Arakawa**
Carrier Relaxation in Self-organized Stressor Quantum Dots: the Effect of Doping 176
H. Lipsanen, H. Koskenvaara, J. Toivonen, M. Sopanen, and J. Ahopelto
Resonant Raman Study of the Topology of the InAs/GaAs Self-Assembled Quantum Dots 181
G. Zanelatto, Yu.A. Pusep, N.T. Moshegov, A.I. Toropov, P. Basmaji, and J.C. Galzerani

Nanoclusters, Nanoparticles and Nanotubes

Coulomb Crystals and Glasses for Self-Assembly of Nanoparticles 189
P.F. Williams, A. Belolipetski, A. Goussev, and M. E. Markes*
Scanning Photoluminescence and Electroluminescence Microscopy of Semiconductor Nanostructures and Devices 201
M. Zacharias, P. Fischer, J. Christen, H. Nakashima, K. Hiramatsu, and M. Kamp*
Electron Response to Ultrashort laser Pulses in Semiconductor and Metal Nanoparticles: Ge vs. Ga 216
A. Stella, P. Tognini, S. De Silvestri, M. Nisoli, S. Stagira, P. Cheyssac, and R. Kofman

Quantum Dots and Mesoscopic Systems

Quantum Chaotic Transport in Mesoscopic Antidot Arrays 377
T. Ando and S. Uryu*

Spin effects in artificial molecules 392
S. Nagaraja and J.-P. Leburton

Microwave Spectroscopy of a Single Quantum Dot in the Few Electron Limit 406
H. Qin, F. Simmel, A.W. Holleitner, R.H. Blick, J.P. Kotthaus, W. Wegscheider, and M. Bichler

Magnetic Properties of Self Assembled Fe Quantum Dashes 413
L. Menon, M. Zheng, H. Zeng, D.J. Sellmyer, and S. Bandyopadhyay

Quantum Well Infrared Photodetectors

Development of Simultaneous Multicolor Quantum Well Infrared Photodetector Focal Plane Arrays 425
*W. Dyer**

A Novel Quantum Well Infrared Photodetector with Digital Graded Superlattice Barrier for Long Wavelength and Broadband Detection 436
J.-H. Lee, S.S. Li, M. Tidrow, W.K. Liu, and K. Bacher

Very-Long-Wavelength Quantum Well Infrared Photodetectors 447
M. Tidrow, X. Jiang, S.S. Li, and A. Liu

Two-Color MW/LW QWIP FPA and Commercial One-Color LW QWIP FPA 459
M. Sundaram, T. Faska, M. Taylor, R. Williams, A. Reisinger, and S. Wang

The Strong Blue-Shifted Photoluminescence from Amorphous Silicon-Nitride (a-SiN_x:H)Layers prepared by PECVD method 474
Z. Pei, Y.R. Chang, H.L. Hsiao, and H.L. Hwang

Characteristics of Photovoltaic Wavelength -tunable Superlattice Infrared Photodetector 485
M. C. Hsu, C. C. Chen, S. Y. Wang, and C. H. Kuan

*** Invited Speaker**

AUTHOR INDEX 497

SUBJECT INDEX 501

FACTS ABOUT THE ELECTROCHEMICAL SOCIETY, INC.

The Electrochemical Society, Inc., is an international, nonprofit, scientific, educational organization founded for the advancement of the theory and practice of electrochemistry, electrothermics, electronics, and allied subjects. The Society was founded in Philadelphia in 1902 and incorporated in 1930. There are currently over 7,000 scientists and engineers from more than 70 countries who hold individual membership; the Society is also supported by more than 100 corporations through Contributing Memberships.

The Technical activities of the Society are carried on by Divisions and Groups. Local Sections of the Society have been organized in a number of cities and regions. Major international meetings of the Society are held in the Spring and Fall of each year. At these meetings, the Divisions and Groups hold general sessions and sponsor symposia on specialized subjects.

The Society has an active publications program which includes the following:

Journal of The Electrochemical Society - The *Journal* is a monthly publication containing technical papers covering basic research and technology of interest in the areas of concern to the Society. Papers submitted for publication are subjected to careful evaluation and review by authorities in the field before acceptance, and high standards are maintained for the technical content of the *Journal*.

Electrochemical and Solid-State Letters - *Letters* is the Society's rapid-publication, electronic journal. Papers are published as available at http://www3.electrochem.org/letters.html. This peer-reviewed journal covers the leading edge in research and development in all fields of interest to ECS. It is a joint publication of the ECS and the IEEE Electron Devices Society.

Interface - *Interface* is a quarterly publication containing news, reviews, advertisements, and articles on technical matters of interest to Society Members in a lively, casual format. Also featured in each issue are special pages dedicated to serving the interests of the Society and allowing better communication among Divisions, Groups, and Local Sections.

Meeting Abstracts *(formerly Extended Abstracts)* - Meeting Abstracts of the technical papers presented at the Spring and Fall Meetings of the Society are published in serialized softbound volumes.

Proceedings Series - Papers presented in symposia at Society and Topical Meetings are published as serialized Proceedings Volumes. These provide up-to-date views of specialized topics and frequently offer comprehensive treatment of rapidly developing areas.

Monograph Volumes - The Society sponsors the publication of hardbound Monograph Volumes, which provide authoritative accounts of specific topics in electrochemistry, solid-state science, and related disciplines.

For more information on these and other Society activities, visit the ECS Web site:

http://www.electrochem.org

Porous Silicon

HIGH EFFICIENCY ELECTROLUMINSCENCE FROM ANODICALLY OXIDIZED POROUS SILICON

Y. Show*, S. Nozaki*, H. Morisaki*,
M. Iwase** and T. Izumi**

*Dept. of Comm. and Systems,
The Univ. of Electro-comm.
1-5-1 Chofu-gaoka, Chofu. Tokyo 182-8585 JAPAN

**Fac. of Engineering, Tokai Univ.
1117 Kitakaname, Hiratsuka, Kanagawa, 259-1292 JAPAN

The electroluminescence (EL) and defect structure in the anodically oxidized porous silicon (PS) have been studied by FT-IR and ESR methods. The anodic oxidation leads to increase in the EL intensity by 9 times because of compensation of the P_b-center (emission killer center) with oxygen atoms. The external quantum efficiency (EQE) of the EL for this anodically oxidized PS has been as high as 0.5 %.

1. INTRODUCTION

Porous silicon (PS) is one of materials promising for a silicon-based light emitting device, because the PS emits strong visible light at room temperature.[1,2] The light emission from the PS, however, is unstable. The decrease in the light intensity is due to desorption of the hydrogen atoms, which compensate defects in the as-prepared PS surface.[3,4] Oxidation of the surface is one way to stabilize the light emission from the PS. Recently, it was reported[5] that the anodic oxidation stabilizes the PS surface with oxygen atoms and increases both the photoluminescence (PL) and the electroluminescence (EL) intensities.

In this paper, the correlation between EL and defects in the anodically oxidized PS has been discussed with the help of Fourier transform infrared (FT-IR) and the electron spin resonance (ESR) spectroscopy.

2. EXPERIMENTS

The porous silicon EL devices were formed by the following procedure.

1) Formation of PS layer

The PS layers were formed on (100) p-type silicon substrates with a resistivity of 17 - 22 Ω-cm. Si substrates were anodized at 1 mA/cm^2 for 60 min in 46 % HF at 40 □. The PS layer was then dried after rinsing with H_2O for 1 min.

2) Anodic oxidation of PS layer

The anodic oxidation was performed at 1 mA/cm^2 in 5 % HCl for 5 to 30 min. The anodically oxidized PS layer was dried after rinsing with H_2O for 1 min.
Oxidation of PS surface was confirmed by FT-IR spectroscopy.

3) Formation of electrode

The indium tin oxide (ITO) film with a thickness of 200 nm was deposited by sputtering method on PS surface for use as the top electrode.

The EL spectra were measured by applying the voltage of -10 V to the ITO electrode. The photoluminescence spectra were measured by Ar ion laser (488nm, 2mW) at room temperature. ESR measurements at room temperature were also carried out in order to characterize the defect structure in the PS

3. RESULT AND DISCUSSION

Fig. 1(a) and (b) show the EL and the PL spectra for the as-prepared PS, respectively. The EL spectrum exhibits a Gaussian line shape with a peak at 680 nm and a full width at half-maximum (FWHM) of 120nm. On the other hand, the PL spectrum exhibits a Gaussian line shape with a peak of 700 nm and FWHM of 120 nm. The EL spectrum from PS was almost the same as those of the PL spectrum. This result indicates that both EL and PL originate from same carrier recombination mechanism in PS.

Fig.2 shows the FT-IR transmission spectrum observed for the as-prepared PS. The PS sample shows the presence of strong Si-H_X bonds around 640, 910 and 2100 cm^{-1} and a weak Si-O_X bond around 1060 cm^{-1}. The FT-IR analysis has revealed that almost all the Si dangling bonds of the as-prepared PS surface are terminated with hydrogen atoms leaving a very few of them being terminated with oxygen atoms.

Fig. 3 shows the typical ESR signal for the as-prepared PS. The ESR signal with an asymmetrical and isotropic line ($g_{/\!/}$=2.0028, $g_{\perp}$=2.0076) has been observed in the PS sample. This ESR signal corresponds to the P_b-center, which is observed from dangling bonds between crystalline Si/SiO_2 interface.[3,4] The spin density of the P_b-center in the as-prepared PS is found to be as low as 10^{17} spins/cm^3, because the dangling bonds are

compensated with hydrogen atoms. This P_b-center is the non-radiative center.[3] Therefore, the PS with high spin density of the P_b-center does not emit strong light. It is necessary to suppress the P_b-center in order to obtain strong light emission from PS.

Fig. 4(a) shows a change on the IR absorption intensities for the Si-O_X (1060 cm^{-1}) and Si-H_X (640 cm^{-1}) bonds as a function of the anodic oxidation time. The signal intensity of the Si-O_X bond increases and that of the Si-H_X bond decreases with an increase in the anodic oxidation time. The absorption intensity of the Si-O_X bond for the anodically oxidized PS for 30 min is 2.5 times higher than that of the as-prepared one. Thus, the FT-IR result shows that the hydrogenated (as-prepared) PS surface is modified to an oxidized one by the anodic oxidation.

The thermally oxidized PS exhibits the a-center (g=2.005), which originates from silicon dangling bonds in amorphous silicon.[3] However, the anodically oxidized PSs exhibit only P_b-center. Therefore, it is considered that the PS surface is oxidized without formation of amorphous silicon region by the anodic oxidation. Fig. 4(b) and (c) show a change in the intensities of the P_b-center and the EL as a function of the anodic oxidation time, respectively. The anodic oxidation results in a decrease in the ESR intensity along with an increase in the EL intensity. The ESR intensity of the oxidized PS for 30 min is half of the value that is obtained for the as-prepared PS. On the other hand, the EL intensity of this oxidized PS is about 9 times higher than that of the as-prepared PS. The external quantum efficiency (EQE) of the EL for this anodically oxidized PS for30 min is as high as 0.5%.

We previously reported[6] that the anodic oxidation leads to an increase in the PL intensity from the PS. The PL intensity for the anodically oxidized PS for 30 min is 6 times higher than that of the as-prepared one. On the other hand, the thermal oxidation leads to a decrease in the PL intensity, because of the desorption of the hydrogen atoms compensated the PS surface and the formation of the P_b- and the a-centers (non-radiative centers) on the PS surface region.[3] These results indicated that the EL and the PL intensities from the oxidized PSs strongly depended on the oxidation condition.

The mechanism of the anodic oxidation is different from that of the thermal oxidation.[7] That is to say, the anodic oxidation selectively occurs at the low resistance region of PS surface, which is non-oxidized surface and/or has the P_b-center, because the carrier (hole) is injected from the low resistance region to electrolyte during the anodic oxidation. Therefore, the anodic oxidation compensates the P_b-center in the PS surface with oxygen atoms, in addition to confinement of the PS surface with a SiO_2 layer. The Si/SiO_2 interface with low spin density is formed in the anodically oxidized PS surface region. Consequently, the anodic oxidation reduces the leakage current flowing via nonconfined silicon and the carriers to be trapped by the non-radiative centers. The EL with a high EQE is obtained for the anodically oxidized PS, because of improvement of both the diode characteristics and radiative efficiency.

The anodic oxidation could be a simple and effective technique for the fabrication of high-efficiency light-emitting diodes (LED). The optimization of design of LED should increase the EQE to more than 0.5 % by anodic oxidation technique.

4. SUMMARY

The anodic oxidation for 30 min increases the intensity of EL from PS by 9 time due to the compensation of the P_b-center (emission killer) with oxygen atoms. The EQE of the EL for the anodically oxidized PS was as high as 0.5 %. Therefore, the anodic oxidation is a simple and effective technique for the fabrication of high-efficiency LEDs.

REFERENCES

1) L. T. Canham: Appl. Phys. Lett. 57(1990)1046

2) P. D. J. Calcott: Materials Sci. and Eng. B51(1998)132

3) M. Shimasaki, Y. Show, M. Iwase, T. Izumi, T. Ichinohe, S. Nozaki and H. Morisaki: Appl. Surf. Sci 92(1996)617

4) H. Yokomichi, H. Takakura and M. Kondo: Jap. J. Appl. Phys. 32(1993)L365

5) B. Gelloz, T. Nakagawa and N. Koshida: Appl. Phys. Lett. 73(1998)2021

6) Y. Show, S. Nozaki, H. Morisaki, M. Iwase and T. Izumi: Presented at 1998 MRS fall meeting

7) S. Billat: J. Electrochem. Soc. 143(1993)319

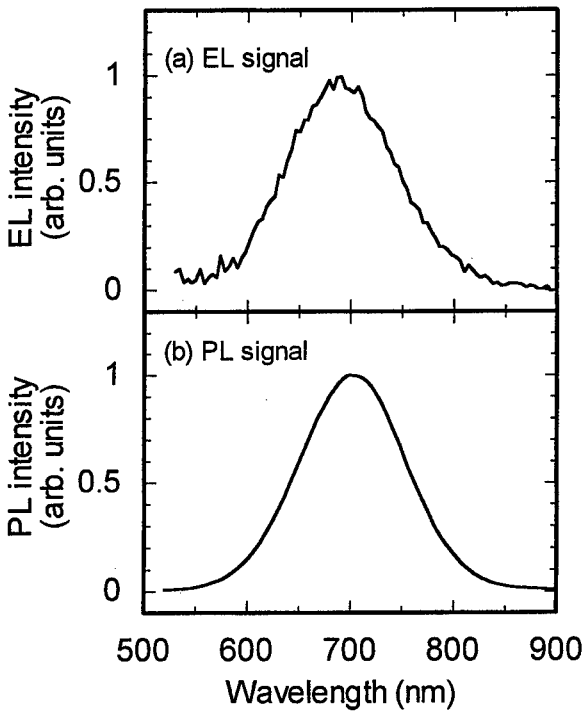


Fig. 1 Typical (a) EL and (b) PL spectrum observed for the as-prepared PS

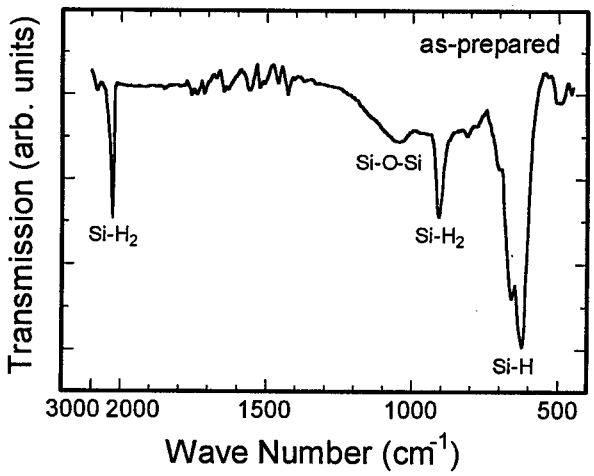


Fig.2 Typical FT-IR spectra observed for the as-prepared PS

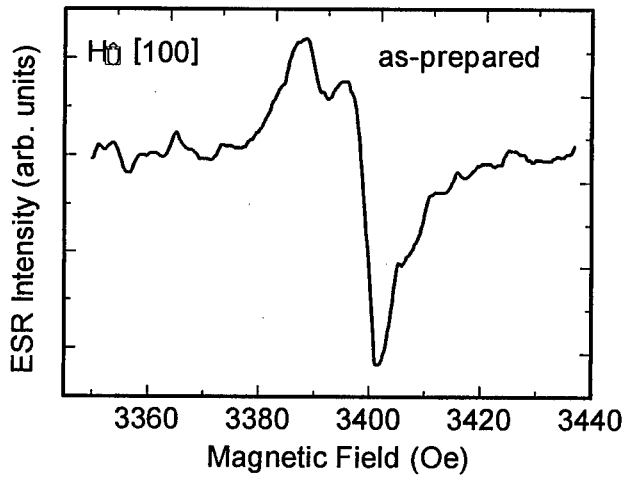


Fig. 3 Typical ESR signal observed for the as-prepard PS

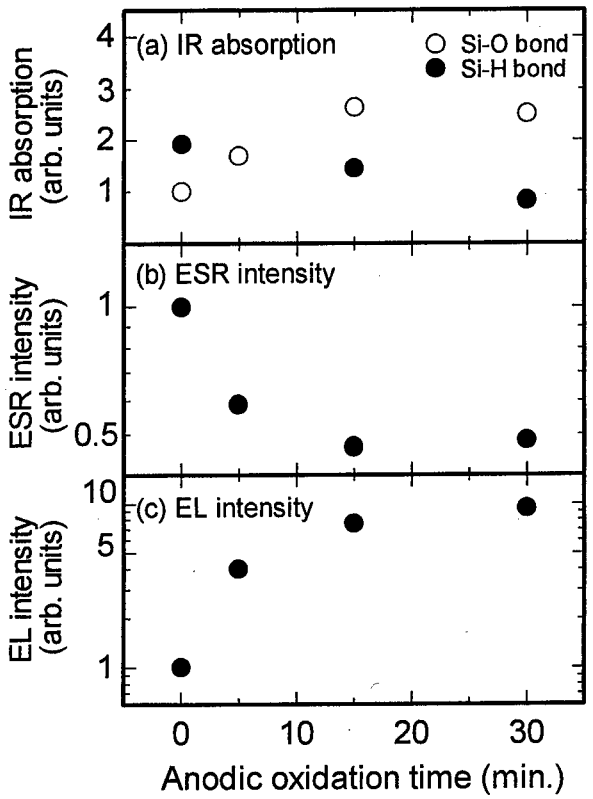


Fig. 4 The correlation between the EL and the defect in the anodically oxidized PS. (a) the IR absorption intensities of the Si-H_X bond (640 cm^{-1}) and the Si-O_X bond (1060 cm^{-1}), (b) intensity of the P_b-center and (c) intensity of the EL for the anodically oxidized PS.

QUANTUM CONFINEMENT IN POROUS SILICON AS A FUNCTION OF SIZE DISTRIBUTION OF LUMINESCENT SITES

G. Dalba, N. Daldosso, P. Fornasini, M. Grimaldi, R. Grisenti
Dipartimento di Fisica dell'Università di Trento - INFM
Via Sommarive, 14 - 38050 POVO (Trento), Italy

F. Rocca
CeFsa - Centro CNR-ITC di Fisica degli Stati Aggregati
Via Sommarive, 14 - 38050 POVO (Trento), Italy

ABSTRACT

Photo Luminescence Yield (PLY) and Total Electron Yield (TEY) techniques have been applied simultaneously to porous silicon at the Si K edge to obtain XANES and EXAFS spectra. Experimental results confirm that PLY is able to monitor only the luminescent sites, contrary to TEY, which provides average structural information on all Si sites of the porous layer. The luminescent sites are the smaller and more disordered ones.
The peculiar site sensitivity of PLY-XANES spectra obtained at different emission energy from the same X-ray excited optical luminescence band (XEOL) allows us to study the effects of the size distribution of different luminescent sites present in the same sample on the local electronic structure. The paper presents an experimental confirmation of the quantum confinement origin of the photoluminescence in p-Si, obtained for the first time by a site selection inside the same porous silicon sample.

I. INTRODUCTION

In the recent years, fundamental studies on the correlation between optical and structural properties of porous silicon have developed in parallel with applied researches [1,2,3,4].

Porous silicon is obtained from electrochemical dissolution of bulk crystalline silicon: shape and dimensions of the resulting sponge-like structures are determined by the characteristics of the wafer and by the parameters of the electrochemical process (HF content, current density, etching time, temperature) [5,6]. By varying one of these

parameters, it is possible to change the porosity or the nanostructure's dimensions and tune the wavelength of the emitted light, typically from the infrared to the green-blue.

The extremely reduced dimensions of the structures present in the porous layer (wires or dots of the order of nanometers) have been proposed as the most probable cause of the intense photoluminescence. Many experiments performed on different p-Si samples indicate that both size and chemical coverage of the porous nanostructures influence the excitation-recombination processes which determine the luminescence band parameters (intensity, peak wavelength, FWHM).

Quantum confinement is expected to enlarge the band gap, producing the observed blue shift of the photoluminescence band, and to enhance the radiative transition probability, which is quite low for an indirect band semiconductor such as c-Si.

The influence of surface states to luminescence must also be taken into account, because, as it is well known, the progressive substitution of Si-H by Si-O bonds increases the photoluminescence intensity. More recently, it has been shown that just within a few minutes after the drying of freshly prepared p-Si samples, the coverage by oxidized states of the p-Si nanostructures produces a red shift of the photoluminescence band, connected with the presence of stabilized electronic states or self trapped excitons [7].

Although it is generally recognized that a porous silicon layer contains a distribution of both luminescent and non luminescent sites, little is known about the local structural properties and their relative amount. Moreover, till now, the effect of quantum confinement has been proved only by comparing different samples, without considering size and shape distribution of luminescent sites present inside each porous Si sample [8,9,10].

Among the various techniques that have been used to characterize porous silicon, X-ray Absorption Spectroscopy (XAS) has already provided remarkable help to understanding the short-range order structure. XAS was applied in different detection modes: transmission[11], Total Electron Yield (TEY) [12,13,14] and Photoluminescence Yield (PLY) [15,16], also called XEOL (X-ray-Excited Optical Luminescence)[17].

In principle, TEY and PLY modes bring different information, because they monitor different secondary processes induced by the absorption of an x-ray photon: TEY measurements collect secondary electrons, while PLY measurements collect the visible radiation. The present authors have experimentally shown [18,19] that for porous silicon the PLY intensity monitors only the modulation of the x-ray absorption due to the atoms which are in the vicinity of the luminescent centers.

This paper presents a summary of the results obtained by the present authors using a specially developed apparatus to monitor XEOL signals from porous silicon.

The peculiar site sensitivity of PLY technique is strongly enhanced by the possibility to obtain many PLY-XANES spectra from different emission energy ranges inside the same XEOL band: this allows us to study the effects of the size distribution of different luminescent sites present in the same sample. The paper presents an experimental confirmation of the quantum confinement origin of the photoluminescence in p-Si, obtained for the first time by a site selection inside the same porous silicon sample.

II. EXPERIMENTAL

Sample preparation

The porous Si specimens were produced by electrochemical anodization [20] of (100) *p*-type boron doped c-Si wafers. Different types of Si substrates characterized by different resistivity were used: 3 Ω·cm, 10 Ω·cm and 16-20 Ω·cm. An aluminum film was sputtered and sintered at 400 °C on the back side of each wafer to form the anodic electric contact, while a platinum wire constituted the cathode of a PTFE electrochemical cell. The electrolyte was an ethylic solution of HF (10% - 25%); the entire galvanostatic process was usually carried out in the dark (recently a photoassisted etching process has been also utilized). The specimens so prepared were rinsed in pentane and dried in air. Measurements were done: 1) on samples at least one week old, 2) on the same samples washed with HF, just before XAFS measurements, in order to remove superficial oxides (fresh samples) and 3) on fresh samples prepared and immediately mounted inside the vacuum chamber of the X-ray Synchrotron beamline.

EXAFS measurements and data analysis

XAFS measurements were carried out with synchrotron radiation at the Super ACO storage ring of the LURE laboratories in Orsay-Paris, using the SA 32 beamline equipped with an InSb (111) monochromator with two independent crystals. The X-ray energy resolution was 0.7 eV at 2000 eV. The electron energy was 800 MeV with a maximum stored current of 400 mA. X-ray energy scans were made from 1800 to 2500 eV.

The absorption spectra of the K edge of Si were simultaneously recorded by the TEY and the PLY techniques. In the former case, the absorption signal was measured as a function of the incident X-ray beam energy by measuring the current required to neutralize the sample as a result of photoelectron emission. In the latter, the luminescence photons excited by X-rays were monitored. In the older sets of measurements [18,19], the main luminescence band (FWHM) was directly integrated and stored at each point of the XAFS spectrum; in the very recent experiments, we were able to store the whole luminescence band, in order to have the possibility for off-line analysis. In both TEY and PLY modes, the signal was normalized to the intensity of the X-ray beam incident on the sample.

XEOL measurements were done using a wavelength dispersive optical spectrometer. Our special XEOL apparatus consists of a system of lens and optical fibers, which collects the light emitted from the sample in the high vacuum chamber and focalises it in a dispersive spectrometer (CP200 Jobin-Yvon). An optimized back-illuminated CCD (1100PB Princeton Instrument) cooled with nitrogen is used as detector to recover in a few seconds the luminescence spectra at fixed x-ray energy.

By using this apparatus, PLY can be recorded in a wide x-ray energy range to obtain the extended x-ray absorption fine structure (EXAFS) at the Si K edge of p-Si. Many XANES and EXAFS spectra sampled at different optical wavelengths within the broad luminescence band of porous Si can be measured in a single experiment.

The specimens were mounted in high vacuum at an angle of about 35° with respect to the incident beam. The EXAFS signal, $\chi(k)$ (k is momentum wave-vector of the photo-

electron), was extracted by standard techniques [21]; the k range used in the Fourier Transform was 2-12 $Å^{-1}$. Structural parameters of the non oxidized samples were extracted from EXAFS spectra through two different data analysis procedures in order to check the independence of data processing of the final results: 1) amplitude ratio and phase-shift difference method and 2) least squares method [22]. c-Si was used as a reference compound to extract experimental phaseshift and backscattering amplitude functions. Within the reported experimental uncertainty, both analysis procedures gave consistent results.

III. RESULTS AND DISCUSSION

Comparison between TEY and PLY data.

XANES analysis. In the near edge region, the differences between PLY and TEY exclude the importance of luminescence due to of molecular-like units present at the surface and support the quantum confinement model. In fact, TEY reveals the presence of different Si sites, including those related to oxygen or to OH bonds, while PLY is not influenced by the presence of oxidized states.

Typical examples of the x-ray absorption near edge structure (XANES), recorded in TEY and in PLY mode at the Si K edge of porous silicon, are shown in figure a before and after washing it with HF for removing the surface oxygen. By exciting the sample with x-rays photons of different energy, below and above the Si K edge (1830, 1841, 1850, 2300 eV), shape and center of the luminescence band do not change; only the intensity is modified following the x-ray absorption coefficient. There is no evidence of XEOL band-shape modification at the excitation energies where the x-ray absorption coefficient presents structures characteristic of the Si-OH bond (1844 eV) or the Si-O bond (1847 eV): this is a good indication that the luminescence originates from confined c-Si sites. So the PLY-XAFS signal, that monitors the intensity modifications of the XEOL band, provides information on the Si environment of the luminescent sites.

figure aa shows that the XANES spectra recorded by TEY and PLY on the aged sample are very different in the region just above the edge, while they are similar after oxygen removal (figure ab). In particular, the peak at 1847 eV, which is a typical structure of the tetrahedral Si-O bond due to the presence of SiO_2 on the surface [13], is present only in the TEY spectrum of the aged sample (figure aa, continuous line). Such peak disappears after washing the samples in HF: the rinse removes the superficial oxides and makes the TEY and PLY spectra much more similar to each other (figure ab). The fact that the luminescence does not originate from the silicon oxide was already found by Sham et al.[15]. From all these results it is confirmed that the XEOL signal does not depend on the Si-O bonds, but is related only to Si clusters.

The absence of any positive contribution to the XEOL due to the absorption of x-ray photons by the oxidized states of the porous Si implies also that the luminescent sites are well separated from them. HF cleaning currently causes a change of the luminescence intensity and in a small shift of its center [2]. This, of course, influences the shape of PLY-XANES spectra: here we can note that, generally, the PLY-XANES of the as-prepared

samples depend both on the preparation parameters and on the history of the sample, while the HF-cleaned samples show well reproducible behavior [18,23]. We will see later from EXAFS measurements that both TEY and PLY signals contain information from the bulk: TEY at the K-edge of Si can not be considered a "surface sensitive" probe, but PLY signal is originating also from much deeper atoms inside the porous layer.

EXAFS analysis. The comparison between TEY and PLY EXAFS spectra allows us to obtain very peculiar information on the different local structures present in the porous layer.

To investigate the influence of porous silicon preparation parameters on the TEY and PLY EXAFS, many sets of samples with different wafer resistivity were prepared. For each wafer resistivity, we studied the influence on the local structure of the the preparation parameters (current density, HF content, ...).

For instance , in figure b the FTs of PLY- and TEY-EXAFS spectra (k^3-weighted) for two samples of resistivity 3 Ω·cm (prepared with 20% HF, 60 and 100 mA/cm^2, respectively) are compared (FT range: 4-9.5 Å^{-1}, 15% Hanning window). The analysis of TEY-EXAFS signals evidences the contribution of at least three coordination shells and confirms the presence of a well defined crystalline order in the porous layer. The EXAFS amplitude in porous silicon is strongly reduced in respect to c-Si: this is mainly related to the reduced dimensions of the crystalline nanostructures[12,14,18]. A quantitative analysis of the first-shell TEY-EXAFS presented in figure b leads to coordination numbers $N_{Si\text{-}Si}$ = 3.1 ± 0.1 and to the same Debye-Waller factors of the c-Si for the two samples, confirming the absence of significant static disorder. According to the model suggested by Zhang *et al.* [14] these values correspond to diameters of the nanostructures of about 15-20 Å, in the hypothesis of nanowires. Similar values were obtained by Schuppler *et al.* [12] and by the present authors on different sets of samples [18].

However, contrary to other TEY-EXAFS measurements [12,14], we have shown in Ref.18 that it is not generally possible to establish direct correlations between the structural information obtained by TEY-EXAFS and the optical properties (or the porosity) without carefully considering how the samples were prepared. For example, in figure b (bottom) the two samples, characterized by different luminescence bands, exhibit a quite similar FT.

The analysis of PLY-EXAFS presents remarkable differences. As shown in figure b, the first-shell signal is weaker in PLY- than in TEY-EXAFS. A quantitative analysis shows that this reduction is due to both the decrease of the coordination number and the increase of disorder. This result suggests that PLY-EXAFS monitors nanostructures with average dimensions reduced in comparison with those monitored by TEY-EXAFS.

Furthermore, there are evident differences between the PLY-EXAFS of samples obtained by changing the current density. figure b (top) shows that the peaks in the FT of PLY-EXAFS are weaker for the 100 mA/cm^2 sample than for the 60 A/cm^2 sample; similar results have been found for other samples with different resistivity. A comparative analysis of these PLY-EXAFS spectra shows that these differences can be mainly attributed to an increase of the Debye-Waller factor, i.e. of the disorder inside the first coordination shells of silicon atoms near the luminescent sites. In this case, contrary to TEY-EXAFS, PLY-EXAFS can be correlated with the luminescence properties: the expected blue shift obtained by increasing the current density is accompanied by a change of the EXAFS signal.

The different behavior of TEY-EXAFS and PLY-EXAFS can be interpreted as follows. The first one monitors the local structure of all Si atoms of the porous layer, independently of their contribution to luminescence: the average morphology is mainly determined by the wafer's resistivity and the HF content in the etching solution, not by the current density [18]. On the contrary, PLY-EXAFS monitors a subset of the porous layer, characterized by nanostructures whose dimensions are smaller than the average ones and are modified by changes of the current density.

The PLY-EXAFS results are consistent with the identification of red-orange luminescent sites with regions at the surface of the crystalline nanostructures present in the porous layer, characterized by a very reduced dimension and by a high static disorder.

The site sensitivity of PLY-EXAFS at the K edge of Si can be interpreted assuming the presence of a very efficient radiative recombination channel in the vicinity of a limited subset of the absorbing Si atoms, probably at the surface of the nanowires. On the basis of such assumption, the XEOL is produced only by those excitons (trapped in the c-Si superficial sites) which radiatively recombine with high efficiency just where they are created. Other photoelectrons and Auger secondary processes decay mainly outside the luminescent regions, giving rise to non radiative processes.

Comparison between different XANES-PLY spectra from a single sample.

Very recently, we have been able to detect and carefully analyze several XANES spectra from a single sample by selecting several energy ranges from the luminescence band.

Following the hypothesis that each nanoparticle constituting the porous silicon layer yields a very sharp luminescence spectrum, whose emission energy is defined by the nanoparticle size, we may expect to obtain different XANES and EXAFS spectra from PLY sampled at different energy ranges of the broad luminescence band. Moreover, since the very near edge structures above the main absorption edge carry information about the empty states in the bottom of the conduction band, we may use XANES as a very sensitive probe of small variations related to the sizes of the luminescent sites.

The analysis of many PLY-XANES spectra carried out on very different samples confirms our work hypothesis. A continuous shift towards higher energy of the X-ray absorption edge is present in all our experiments, with increasing photoluminescence energy. In figure c (bottom) we document this effect showing a selection of two PLY-XANES spectra from those obtained sampling at intervals of 0.1 eV the XEOL band shown on the top of the Figure.

The site selectivity of our technique allows us to monitor the continuous increasing of the conduction band energy as a function of the decreasing size of the luminescence sites. This is the first experiment able to measure the enlargement of the energy gap E_g due to the different dimensions of the nanostructures present in a same porous silicon sample. Previous experimental evidences were obtained only by comparison of different samples, using optical [9] or soft X-ray absorption techniques [8,10]. The quantitative analysis of the E_g shift on different samples is currently under study, together with a more comprehensive view of all the features present in the XANES spectra.

In figure c, the corresponding TEY spectrum is also shown. Different slopes of the absorption edges, and a significant shift of the maximum between PLY and TEY data can be observed. The interpretation of this effect is not simple, because it is mainly related to

the density of states of the conduction band. The high sensitivity of our technique to small changes in the electron density of states above the Fermi level allows us to detect for the first time differences inside the same sample, directly related to the site sizes.

ACKNOWLEDGMENTS

We are grateful to C. Armellini for the preparation and basic characterization of the samples and to R. Graziola for his collaboration to the development of the new XEOL apparatus. Optical measurements and sample preparation were done in cooperation with L. Pavesi, to whom authors are indebted for stimulating discussions. We thank P. Lagarde and A. M. Flank for scientific collaboration in the EXAFS measurements. We acknowledge the support by the Training and Mobility of Researchers (TMR) Programme of the European Community for measurements at the LURE Laboratories (Orsay-Paris).

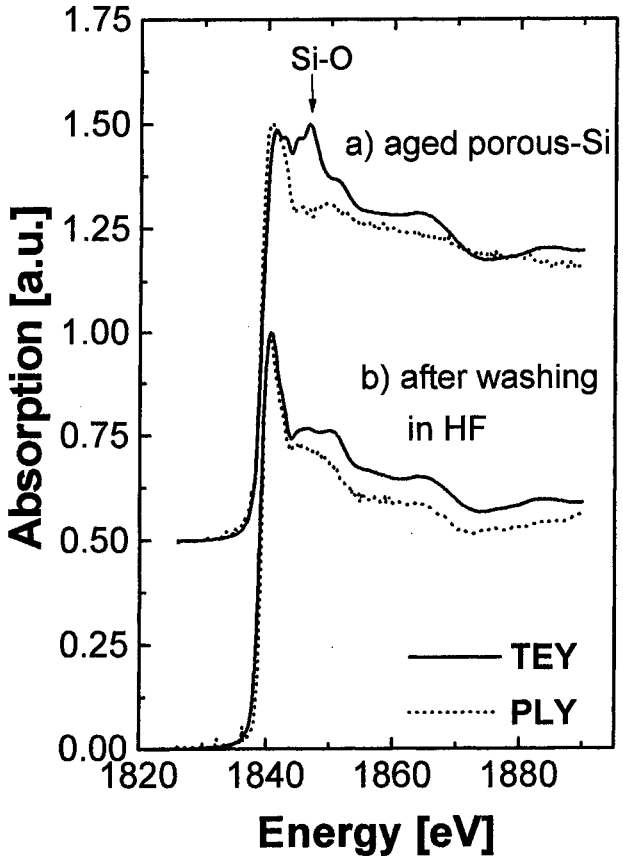


Figure A

Normalized x-ray absorption spectra near the Si K edge (XANES) for a porous-Si aged sample (a) and for the same sample washed in HF (b), obtained by TEY (continuous line) and PLY (dotted line) techniques. The arrow in the figure indicates the peak at 1847 eV, characteristic of the Si-O bonds.

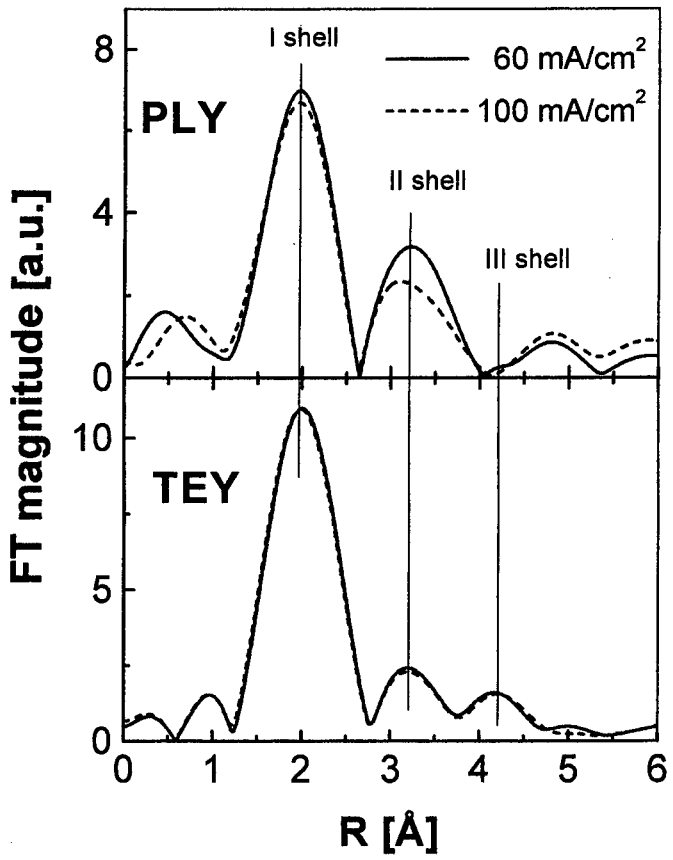


Figure B

k^3-weighted Fourier Transform of PLY and TEY EXAFS signals on two different porous silicon samples (3 Ω·cm). They differ only in the current density applied during the preparation: 60 mA/cm2 (continuos line) and 100 mA/cm2 (dashed line), and show luminescence spectra centered at ~720 nm and at ~ 680 nm, respectively.

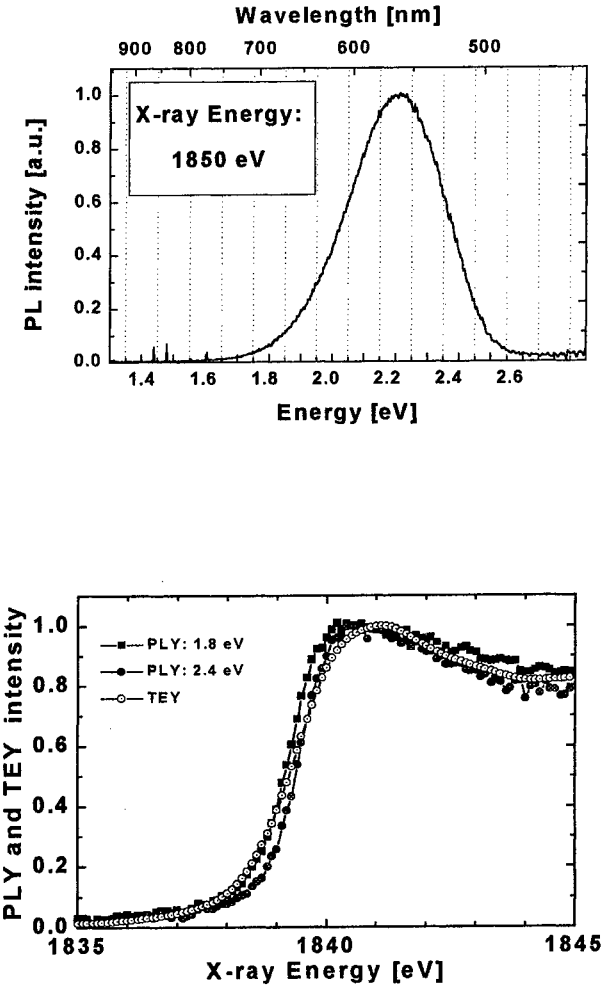


Figure C

XEOL band (top) and XANES (bottom) spectra of a porous silicon sample with luminescence band maximum centered at 2.2 eV. PLY spectra are obtained by integrating the luminescence energy (over a range of 0.1 eV) at 1.8 eV (filled squares) and 2.4 eV (filled circles). TEY spectrum is shown as empty circles.

REFERENCES

1. L. T. Canham, Appl. Phys. Lett., 57, 1046 (1990).
2. A. G. Cullis, L. T. Canham and P. D. J. Calcott, J. Appl. Phys., 82, 909 (1997).
3. L. Pavesi, La Rivista del Nuovo Cimento, 20, 1(1997).
4. L. Pavesi, Phys. St. Solidi, A 165, 91(1998).
5. V. Lehmann and U. Gösele, Appl. Phys. Lett., 58, 856 (1991).
6. R. L. Smith and S. C. Collins, J. Appl. Phys., 71, R1 (1992).
7. M.V. Wolkin, J. Jorne, P. M. Fauchet, G. Allan and C. Delerue, Phys. Rev. Letters, 82, 197 (1999).
8. T. van Buuren, Y. Gao, T. Tiedje, J. R. Dahn and B. M. Way, Appl. Phys. Letters, 60, 3013 (1992).
9 J. von Behren, T. van Buuren, M. Zacharias, E. H. Chimowitz and P. M. Fauchet, Sol. State Comm., 105, 317 (1998).
10. T. van Buuren, L. N. Dinh, L. L. Chase, W. J. Siekhaus and L. J. Terminello, Phys. Rev. Letters, 80, 3803 (1998).
11. G. Dalba, P. Fornasini, M. Grazioli, R. Grisenti, Y. Soldo and F. Rocca, Nucl. Instr. & Methods, B 97, 322 (1995).
12. S. Schuppler, S. L. Friedman, M. A. Marcus, D. L. Adler, Y. H. Xie, F. M. Ross, T. D. Harris, W. L. Brown, Y. J. Chabal, L. E. Brus and P. H. Citrin, Phys. Rev. Lett., 72, 2648 (1994).
13. J. R. Dahn, B. M. Way, E. W. Fuller, W. J. Weydanz, J. S. Tse, D. D. Klug, T. Van Buuren and T. Tiedje, J. Appl. Phys., 75, 1946 (1994).
14. Qi Zhang and S. C. Bayliss, J. Appl. Phys., 79, 1351 (1996).
15. T. K. Sham, D. T. Jiang, I. Coulthard, J. W. Lorimer, X. H. Feng, K. H. Tan, S. P. Frigo, R. A. Rosenberg, D. C. Houghton and B. Bryskiewicz, Nature, 363, 331 (1993).
16. D. T. Jiang, I. Coultard, T. K. Sham, J. W. Lorimer, S. P. Frigo, X. H. Feng and R. A. Rosenberg, J. Appl. Phys., 74, 6335 (1993).
17. R. F. Pettifer, A. Glanfield, S. Gardelis, B. Hamilton, P. Dawson and A. D. Smith, Phisica B, 208&209, 484 (1995).
18. G. Dalba, N. Daldosso, P. Fornasini, R. Graziola, R. Grisenti and F. Rocca, J. Non-Cryst. Solids, 232, 370 (1998).
19. G. Dalba, P. Fornasini, R. Grisenti, N. Daldosso and F. Rocca, Appl. Phys. Letters, 74, 1454 (1999).
20. L. Pavesi, M. Ceschini, G. Mariotto, E. Zanghellini, O. Bisi, M. Anderle, L. Calliari, M. Fedrizzi and L. Fedrizzi, J. Appl. Phys., 75, 1118 (1994).
21. G. Dalba, P. Fornasini and F. Rocca, Phys.Rev., B 47, 8502 (1993).
22. D.E. Sayers and B.A. Bunker in: X-ray Absorption, D. C. Koningsberger and R. Prins, Editors, p. 211, University of Technology, Eindhoven (1988) .
23. N. Daldosso, Thesis, University of Trento (1997).

ANOMALOUS BEHAVIOR OF POLARIZATION MEMORY IN OXIDIZED POROUS SILICON

Hideki Koyama and Philippe M. Fauchet
Department of Electrical and Computer Engineering
University of Rochester, Rochester, NY 14627

Visible photoluminescence (PL) from thermally oxidized porous silicon (PSi) has been characterized in terms of polarization memory (PM). Large and emission-energy-independent PM was observed in samples oxidized at 800 °C. In addition, this PM is significantly anisotropic and exhibits maxima when the excitation light is polarized parallel to the <100> axes of the sample. These features become less significant at higher oxidation temperatures. In particular, samples oxidized at 1000 °C exhibited an almost unpolarized emission. These experimental results are explained on the basis of two different emission components present in the PL spectra.

INTRODUCTION

Since the observation of visible photoluminescence (PL) (1) and electroluminescence (EL) (2) at room temperature, porous silicon (PSi) has attracted much attention as an active material for novel Si-based light emitting devices. PSi contains a large density of quantum-size Si nanocrystals, which are often believed to be responsible for the visible light emission (3). Because of the huge internal surface area resulting from these nanostructures, the light emission from PSi is relatively unstable in air (4). Even a weak excitation light intensity of ~ 1 mW/cm^2 can cause significant PL degradation. This PL fatigue is due to the increase in dangling bond density resulting from imperfect surface oxidation. Stabilization of the emission is thus an important issue in developing practical PSi-based devices.

Similar efficient, red-light emission is also observed in thermally oxidized PSi (5-12). Because this emission is remarkably stable, thermal oxidation has been believed to be a useful technique to overcome the instability problem of PSi. It is also compatible with the device fabrication procedures involving high-temperature processing (13). However, the origin of this red emission is still a matter of debate. In fact, several authors claim that the emission from oxidized PSi has a different origin from that of as-anodized PSi (8-10).

In this work, we have studied the red PL from thermally oxidized PSi in terms of polarization memory (PM) (14, 15). PM is a phenomenon where the linear polarization of the excitation light is partially preserved in the emitted light. This happens if the emission originates from localized electronic states with optical anisotropy. Energy migration among those localized states should decrease the degree of PM. PM of as-anodized PSi is attributed to the carrier localization in optically anisotropic Si nanocrystals. The optical anisotropy of Si nanocrystals can result from either their elongated shape or anisotropic surroundings (e.g., location of the neighboring crystallites).

We report here that the PM properties of oxidized PSi are completely different from those of as-anodized PSi. We suggest that at least two different emission mechanisms are responsible for the PL from oxidized PSi.

EXPERIMENT

PSi samples were prepared by the anodization of p-type (~10 Ωcm), (100)-oriented Si wafers in a solution of 50% HF: ethanol = 1:1 at 20 mA/cm^2 for 12.5 min. The samples were then oxidized in dry O_2 at 500-1000 °C for 10 min. Oxidized PSi shows fast, highly-polarized blue-green emission after prolonged exposure to air (16-18). In order to minimize this effect, PM measurements were performed within a few days after oxidation.

A 514.5-nm Ar^+ laser was used as the excitation source for PL. The laser beam was normally incident on the sample surface, and the emission was collected through an analyzer placed at a small angle off the normal direction. The degree of PM is defined by $P = (I_{\parallel} - I_{\perp})/(I_{\parallel} + I_{\perp})$, where $I_{\parallel}$ and $I_{\perp}$ are the intensity of the PL components polarized parallel and perpendicular, respectively, to the polarization direction of the excitation light. In order to cancel out the polarization-dependent response of the monochromator, $I_{\parallel}$ and $I_{\perp}$ were measured by changing the polarization direction of the excitation light by 90° using a half-wave plate while keeping the analyzer fixed. A Si diode array detector was used for the measurements of the degree of PM. The PL spectra were obtained without the analyzer, using a cooled Ge detector and a lock-in technique. All the PL spectra were corrected for the apparatus response.

RESULTS

Figure 1 shows the PL spectra as a function of oxidation temperature. The oxidized PSi samples display a red PL with a broad, Gaussian spectrum that resembles that of the as-anodized sample. The PL peak intensity and photon energy are plotted as a function of the oxidation temperature in Fig. 2. The PL intensity has a maximum at an oxidation temperature of ~700 °C. This behavior is qualitatively similar to the results reported before (6), although the oxidation temperature at which the PL intensity is maximum is slightly lower in our results. This difference in the oxidation temperatures may result from the difference in the oxidation time (the oxidation time used in Ref. 6 is 30 sec). As seen in Fig. 2, the peak photon energy shows a slight blueshift at 800 °C, followed by a significant redshift with increasing oxidation temperatures.

Figure 3 shows the degree of PM, P, as a function of the polarization direction of the excitation light with respect to the [010] crystalline axis of the samples. In the as-anodized sample [Fig. 3(a)], P is almost isotropic especially near the PL peak energy. At higher emission energies, P is slightly anisotropic and larger when the excitation light is polarized along the <100> axes. In contrast, the sample oxidized at 800 °C [Fig. 3(b)] shows significantly anisotropic PM with a preferential direction along the <100> axes. It should be noted that this behavior is opposite to that observed by Kovalev *et al.* (19) in their as-anodized PSi sample under resonant excitation at 1.96 eV. In their results P has maxima and minima along the <110> and <100> directions, respectively, although this is reversed at the low-energy edge of the emission spectrum. They did not observe any anisotropic PM under nonresonant excitation at 2.54 eV.

Another difference in PM between the as-anodized and oxidized samples is found in its emission energy dependence, as shown in Fig. 4. In the as-anodized sample, P decreases monotonically with decreasing emission photon energies, resulting in a very small value (~0.02) at the PL peak energy. This trend is seen in any as-anodized PSi samples including that used in the experiment by Kovalev *et al.* (19). In the sample oxidized at 800 °C, on the other hand, P is almost constant and keeps a high value even at its PL peak energy. Figure 5 shows the degree of PM at the emission photon energy of 1.5 eV as a function of oxidation temperature. A remarkable increase in P is seen in samples oxidized at temperatures up to 900 °C, beyond which P decreases sharply with increasing oxidation temperatures.

DISCUSSION

Several models have been proposed for the red PL from thermally oxidized PSi. Cullis *et al.* (7) performed a microscopic study in conjunction with luminescence experiments. They found a positive relationship between the density of Si nanocrystals and the PL intensity, and attributed the origin of the PL to Si nanocrystals as in as-anodized PSi. Takazawa *et al.* (10) have observed in their time-resolved experiments that the emission-energy dispersion in the PL decay time disappears in oxidized PSi. Based on this result,

they proposed a luminescent center model. Prokes *et al.* (8, 9) have shown that in some PSi sample the PL energy does not shift, as expected from the quantum confinement hypothesis, with either the oxidation temperature or the measurement temperature. They suggested nonbridging oxygen hole centers (NBOHCs) as the origin for their PL.

Our experimental results can not be explained satisfactory by any of the above models, if one assumes a single origin for the PL. Our results, however, can be explained if we assume two emissions with peak energies of 1.5 ~ 1.6 eV and 1.3 ~ 1.4 eV, where the former emission has a high, anisotropic *P*, while the latter exhibits almost unpolarized PL. In this case, the high-energy emission component should dominate the PL at low oxidation temperatures. The intensity of this emission decreases with increasing oxidation temperatures, and at about 1000 °C the low-energy emission becomes dominant. The presence of two different emission components in the PL of oxidized PSi has also been suggested from the analysis of its temperature dependence (12).

The high-energy, anisotropically polarized emission can be ascribed to Si nanocrystals as follows. In bulk crystalline Si, the thermal oxidation rate is slower along the <100> directions than along the <110> or <111> directions (20). If this is the case also in the PSi nanostructures, thermal oxidation enhances the structural anisotropy along the <100> axes. This may result in anisotropic PM with its maxima in the <100> directions. The large increase in the degree of PM can be attributed to the suppression of carrier hopping by the oxide layers among the crystallites. There could be significant carrier hopping in as-anodized PSi within a very short time (< 1 μs) after excitation (21), although it has been experimentally verified to be absent in the μs regime (22, 23).

A defect-related origin of the PL can also explain the behavior of the high-energy emission. In particular, the lack of emission energy dependence in *P* (Fig. 4) can be explained better by the emission from deep defects with a wide homogeneous broadening. NBOHCs are probably not the origin of this emission. The PL of NBOHCs, which is known as the red emission in damaged silica, has a peak emission energy of 1.8~1.95 eV and shows emission-energy dependent PM due to inhomogeneous broadening (24). These properties are clearly different from our experimental results. The existence of an anisotropy with respect to the crystalline axes means that the emission should occur inside or on the surface of crystallites. This is consistent with the results of Cullis *et al.* (7), where PL was observed only in the region containing Si crystallites.

The PL spectrum of the low-photon-energy emission component (i.e., PL spectrum of the sample oxidized at 1000 °C in Fig. 1) is similar to those observed by Shiba *et al*, in thermally oxidized Si quantum dots deposited on SiO_2 (25). They have ascribed this emission to Si/SiO_2 interface defects, based on the fact that there is a large Stokes shift between the absorption and emission energies. No information about polarization properties was reported.

CONCLUSION

We have reported the PM properties of the PL from thermally oxidized PSi. A large increase in polarization memory *P* is observed for oxidation temperatures up to 900 °C, together with significant anisotropy where it has maxima in the <100> directions. At higher oxidation temperatures, *P* and its anisotropy decrease rapidly with increasing oxidation temperatures. At these elevated oxidation temperatures, the PL-spectra shift also changes from a blueshift to a redshift. These experimental results can be explained by assuming two different emission components. The higher energy emission (1.5~1.6 eV) has a large, anisotropic *P* and is responsible for the behavior at oxidation temperatures below 900 °C. The lower energy emission component (1.3~1.4 eV) with low *P* dominates the PL from samples oxidized at higher temperatures. Although the microscopic origins of these emissions are left unresolved, we have demonstrated that the PL from oxidized PSi can not be explained as a simple extension of the PL from as-anodized PSi.

ACKNOWLEDGMENTS

This work was supported by the Army Research Office.

REFERENCES

1. L. T. Canham, Appl. Phys. Lett., **57**, 1046 (1990).
2. N. Koshida and H. Koyama, Appl. Phys. Lett., **60**, 347 (1992).
3. P. M. Fauchet, in Light Emission in Silicon: From Physics to Devices, D. J. Lockwood, Editor, Semiconductors and Semimetals, Vol. 49, P. 205, Academic Press, San Diego (1998).
4. M. A. Tischler, R. T. Collins, J. H. Stathis, and J. C. Tsang, Appl. Phys. Lett. 60, 639 (1992).
5. T. Ito, T. Ohta, and A. Hiraki, Jpn. J. Appl. Phys., **31**, L1 (1992).
6. V. Petrova-Koch, T. Muschik, A. Kux, B. K. Meyer, F. Koch, and V. Lehmann, Appl. Phys. Lett., **61**, 943 (1992).
7. A. G. Cullis, L. T. Canham, G. M. Williams, P. W. Smith, and O. D. Dosser, J. Appl. Phys., **75**, 493 (1994).
8. S. M. Prokes, Appl. Phys. Lett., **62**, 3244 (1993).
9. S. M. Prokes and O. J. Glembocki, Phys. Rev. B, **49**, 2238 (1994).
10. A. Takazawa, T. Tamura, and M. Yamada, J. Appl. Phys., **75**, 2489 (1994).
11. L. Tsybeskov, S. P. Duttagupta, and P. M. Fauchet, Solid State Commun., **95**, 429 (1995).
12. L. Tsybeskov, K. D. Hirschman, L. F. Moore, P. M. Fauchet, and P. D. J. Calcott, Mat. Res. Soc. Symp. Proc., **452**, 687 (1997).
13. K. D. Hirschman, L. Tsybeskov, S. P. Duttagupta, and P. M. Fauchet, Nature, **384**, 338 (1996).
14. H. Koyama and N. Koshida, Phys. Rev. B, **52**, 2649 (1995).
15. D. Kovalev, M. Ben Chorin, J. Diener, F. Koch, Al. L. Efros, M. Rosen, N. A. Gippius, and S. G. Tikhodeev, Appl. Phys. Lett., **67**, 1585 (1995).
16. A. Loni, A. J. Simons, P. D. J. Calcott, and L. T. Canham, J. Appl. Phys., **77**, 3557 (1995).
17. H. Koyama and N. Koshida, Solid State Commun., **103**, 37 (1997).
18. H. Koyama, Y. Matsushita, and N. Koshida, J. Appl. Phys., **83**, 1776 (1998).
19. D. Kovalev, M. Ben-Chorin, J. Diener, B. Averboukh, G. Polisski, and F. Koch, Phys. Rev. Lett. **79**, 119 (1997).
20. E. A. Irene, H. Z. Massoud, and E. Tierney, J. Electrochem. Soc., **133**, 1253 (1986).
21. N. Akiyama, K. Ishii, M. Ohkura, T. Kure, and H. Ohkura, Jpn. J. Appl. Phys., **34**, L1647 (1995).
22. I. Mihalcsescu, J. C. Vial, and R. Romestain, Phys. Rev. Lett., **80**, 3392 (1998).
23. S. Tanaka, H. Koyama, and N. Koshida, Appl. Phys. Lett., **73**, 2334 (1998).
24. L. Skuja, J. Non-Cryst. Solids, **179**, 51 (1994).
25. K. Shiba, K. Nakagawa, M. Ikeda, A. Kohno, S. Miyazaki, and M. Hirose, Jpn. J. Appl. Phys., **36**, L1279 (1997).

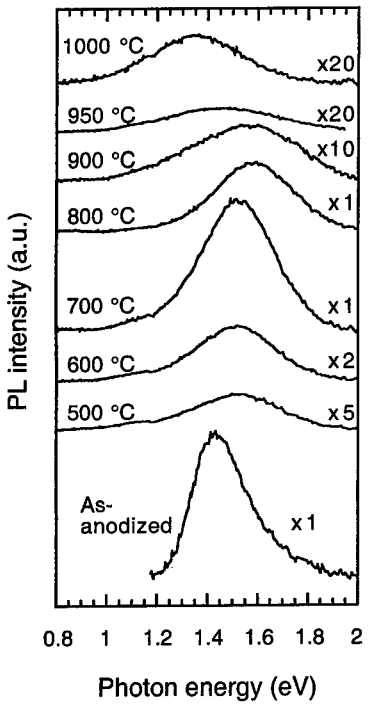


Fig. 1. PL spectra of as-anodized and oxidized PSi samples.

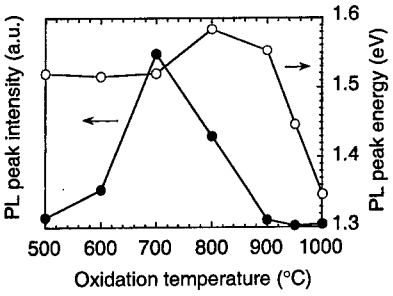


Fig. 2. PL peak intensity and peak energy as a function of oxidation temperature.

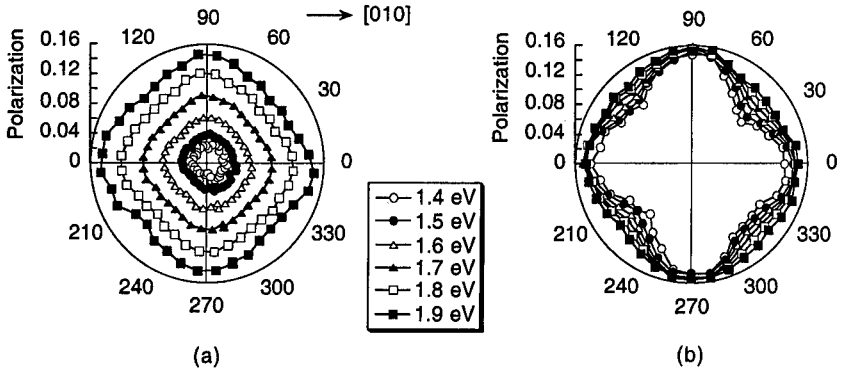


Fig. 3. Degree of PM in as-anodized (a) and oxidized (800 °C) (b) samples, plotted as a function of the angle between the [010] axis and the polarization direction of the excitation light.

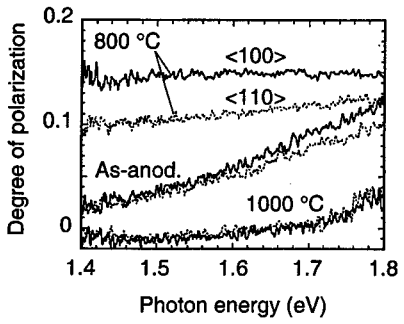


Fig. 4. Degree of PM for the as-anodized and two oxidized samples as a function of the emission photon energy. The polarization direction of the excitation light is along either the <100> (solid lines) or <110> (dotted lines) crystalline axes.

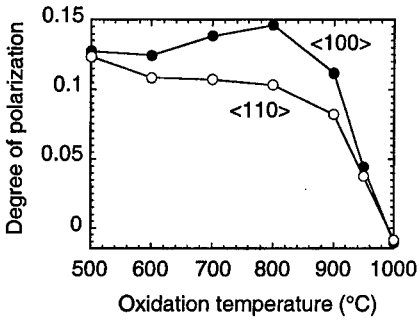


Fig. 5. Oxidation-temperature dependence of the degree of PM at the emission energy of 1.5 eV. The excitation light is polarized along the <100> or <110> crystalline axes.

ENHANCING EFFICIENCY AND STABILITY OF POROUS SILICON ELECTROLUMINESCENCE USING ELECTROCHEMICAL TECHNIQUES

B. Gelloz and N. Koshida

Tokyo University of Agriculture and Technology, Department of Electronics and Electrical Eng., Faculty of Technology, Tokyo Univ. A&T, Koganei, Tokyo 184 8588, Japan.

ABSTRACT

We present here our recent progresses aiming at enhancing the power efficiency, lowering the operating voltage below 10 V, and enhancing the stability of porous silicon based light emitting devices, in order to fit the practical requirements for display purposes. High quantum efficiencies have been attained thanks to the use of anodic oxidation of porous silicon. By using anodically oxidized thin porous layers, high electroluminescence intensity with power efficiency up to 0.2 % has been obtained below 10 V. This value of the power efficiency is the highest obtained to date. The anodic oxidation treatment enhances the stability of the devices even though oxidation during operation still occurs. The performances of the devices are very sensible on the porous silicon formation conditions, including the anodization temperature. The incorporation of a low porosity superficial layer between the optically active porous silicon and the top contact has been found necessary for stabilization and reproducibility.

INTRODUCTION

For display purposes, the power efficiency of electroluminescence (EL) should be at least 1 %, the operating voltage below 10 V, the time response below 1 ms and the stability longer than 10 000 hours. As for porous silicon (PS) based devices, the best values of the power efficiency are all below 0.1 %[1]. Operating voltages are usually larger than 20V [1]. The only parameter which seems not a problem is the EL time response. The stability of current devices is very poor, usually not exceeding 10 min [2]. We have recently shown that an electrochemical treatment (anodic oxidation) of PS allows to gain several orders of magnitude as for the external quantum efficiency (EQE) [3], and then to reach high values (EQE of 1.1 % has been obtained [1]). However, the power efficiencies associated to these devices are still below 0.1 % (max.: 0.08 %[1]), due to high applied voltages.

We present here our recent progresses, including different techniques for reducing the operating voltage, enhancing the power efficiency and the stability of PS electroluminescent devices. In order to enhance the power efficiency as well as to fit the operating voltage requirements (<10V), the anodic oxidation technique has been applied to thin PS layers. Different PS formation conditions has been investigated in order to optimize the results obtained after the application of anodic oxidation post-treatment. To enhance the stability of the devices, the effect of a superficial, low porosity, thin layer between the optically active PS and the top contact made of indium tin oxide, has been

studied. Again, different formation conditions of this layer has been investigated, with an optimization goal in mind. Furthermore, the anodization temperature has been found to be a critical factor in order to obtain reproducible results.

EXPERIMENTAL

N^+-type PS are formed from n^+ (111) (0.018Ω.cm) substrates. In order to achieve reproducible results, it has been necessary to take a special care in the cleaning of the silicon wafers. Several micrometers of silicon are removed from the surface by chemical dissolution in a solution consisting of HNO_3:HF:H_2O=1:0.5:1, just before PS formation. Also for reproducibility reasons, anodization is performed at a temperature of 0°C in some cases. The superficial low porosity layers are formed either under 3 mA/cm^2 during 20 s in HF (40 vol. %) (condition Sup.1), or under 5 mA/cm^2 during 30 s in HF (10 vol. %) (condition Sup. 2), in the dark. Optically active PS is subsequently formed under 3 mA/cm^2 during 10 min, under illumination from a 500W tungsten lamp mounted at a distance of 20 cm, in either HF (40 vol. %). Total thickness of the porous layer is about 1 μm. Some devices does not include any superficial layers.

Having been rinsed with ethanol for 2 min, and without being dried, anodic oxidation of the porous layers is achieved by anodically polarizing (3 mA/cm^2) PS in an aqueous solution containing 1M sulfuric acid (H_2SO_4). This oxidation implies hole consumption and electron injection [4]. Therefore, EL can be observed during the treatment when oxidation takes place in luminescent crystallites after a while during which oxidation occurs only in non-confined silicon. The best results for EQE are obtained when anodic oxidation is performed until the maximum of EL intensity during the treatment (3 min). Samples discussed in this paper has been oxidized in this condition. Then, the samples are rinsed with ethanol for 2 min, and dried. 200 nm of indium tin oxide (ITO) is then deposited by sputtering onto the porous layers for use as the top electrode.

Photoluminescence (PL) and EL measurements are conducted in N_2 atmosphere. PL spectra are measured using 325nm excitation beam from a He-Cd laser. Keithley source-measure unit (Model 238) is used as a voltage source and also as an ammeter of the diode current. The emitted light is detected via a monochromator (Nikon G250) and a photomultiplier tube (Hamamatsu R928) whose output current is measured using a picoammeter (Advantest TR8652). The polarity of the voltage bias is defined such that it is negative when the silicon substrate is reverse biased. All experiments are conducted under reverse CW operation in N_2 atmosphere.

EQE is calculated as the ratio of the number of photons emitted in the hemisphere by the number of charges flowing through the device. A photometer (collecting surface = 1cm^2) is used to count the emitted photons, at a distance of 4.7cm from the emitting device. The total number of photons emitted in the hemisphere is derived by assuming that the radiation profile of the output light is in accordance with Lambert's cosine law [5]. Power efficiency is calculated as the ratio of the number of photons emitted in the hemisphere by the power (voltage multiplied by current) dissipated in the device.

RESULTS AND DISCUSSION

Many different formation conditions of PS have been investigated in a view to obtain efficient devices operating at voltages below 10V. The strategy is to use thin n^+-

type porous layers. Fig. 1. shows the results obtain by using an anodically oxidized thin porous layer formed at room temperature, without superficial layer. During the first potential scan, the onset of EL is above -0.5 V, and the EL intensity shows a peak at about -2.5 V. At this point, both the EQE and the power efficiency equal about 0.03 %. Afterwards, the EL intensity decreases as a function of the voltage whereas the current density continues increasing. This results in loss of efficiency of about 3 orders of magnitude. During the second scan, the EL intensity and the current density are the same as during the return of the first scan. This shows that there happened an irreversible modification of the device during the first scan. This behavior may be a result of a not homogeneous porous layer. Indeed, getting homogeneous sub-micrometer thick porous layers is not always trivial. As this device shows quite a high efficiency at low voltages during the first scan, it would be worthwhile to find a solution to avoid the irreversible modification of the device.

With this aim in mind, the influence of a low porosity superficial layer between the optically active porous layer and the top contact made of ITO has been studied. With devices including such a superficial layer, the current-voltage and EL intensity-voltage curves show no hysteresis, and no drop of EL intensity. This implies that the interface between the top contact and the active PS may be responsible for the peculiar behavior of Fig. 1. The low porosity superficial layer should provide a better electrical contact and greater mechanical stability to the optically active PS layer. The formation conditions of the superficial layer is important since the efficiency is found much lower when the superficial layer is built using condition Sup. 1. than when using condition Sup. 2.

Even though the irreversible device modification is prevented by using a superficial layer, the reproducibility is still rather poor. In order to get good reproducibility, it has been necessary to clean the silicon wafers by removing several micrometers of silicon before anodization. Moreover, the control of the anodization temperature has also been found critical. The use of 0°C as the anodization temperature gives well reproducible results. The effect of the temperature can be understood from the fact that it greatly affects the PL and the PS structure [6]. As the temperature is lowered, the PL decreases but PS is much more homogeneous.

Fig. 2. shows the EL intensity and the current density for an efficient device whose porous layer has been formed at 0°C, and anodically oxidized. The device also includes a superficial low porosity layer formed under condition Sup. 2. The EL can be seen with naked eye in day light, for an operating voltage of -5 V. At this voltage, the EQE is 0.5 % and the power efficiency 0.2 %. This last value is the highest obtained with PS. Fig. 3. shows the EL intensity as a function of the current density for this last device and for the same device, but without the superficial layer and without the anodic oxidation treatment. It clearly shows the power of the techniques used to improve the efficiency and the EL output. Indeed, the EQE is here improved of several orders of magnitude. The effect of anodic oxidation is to considerably reduce the current density because of the preferential oxidation of the coarser part of PS [3]. Indeed, as the electrochemical oxidation is performed under constant current, holes flows via the energetically-easiest paths. During the first stages of the process, hole injection, i.e. oxidation, occurs only in non-confined silicon. The formation of oxide at the surface makes charge-exchange between silicon and the electrolyte more difficult. The potential must correspondingly be increased in order to maintain the current constant. Hole injection in more energetic levels is then achieved. There is a period when injection occurs in confined crystallites. EL can be observed at this stage. EL intensity reaches a maximum when carrier injection in confined crystallites is optimal. When oxidation is

performed up to the maximum of EL, non-confined silicon is much more oxidized than luminescent crystallites. This significantly reduces the number of carriers flowing through non-confined silicon, optimizing carrier injection into luminescent crystallites. This results in enhanced EQE. It should be noted that thermal oxidation could not lead to such an enhancement since it occurs on the whole internal surface of PS (without selecting non-confined silicon from confined silicon). Moreover, contrary to thermal oxidation, anodic oxidation does not affect both the PS structure and passivation with hydrogen [10]. It also enhances the luminescence-homogeneity. It is a known fact that this treatment improves the quantum efficiency and induces a blue shift of the PL [7]. This is also the case for the porous layer included in our device, as shown in Fig. 4. The EL spectrum acquired at –10 V with the device shown in Fig. 2. is also represented. The EL peak is red-shifted compared to the PL one. This suggests that the highest energetic levels are not accessible for carrier injection.

The stability of the efficient device has been evaluated. The voltage needed to obtain a given EL intensity increases with time. This is usually explained by oxidation of PS, during operation and upon storage in air [2]. Fig. 5. shows the EL intensity and the current density as a function of time when a constant voltage of –15 V is applied to our efficient device. The current density increases and reaches a constant value after about 3 min. The EL intensity increases during 1.5 min and then decreases. The discontinuity at 10 min is because the experiment was stopped and started again. The current density and the EL intensity rise again during about 1.5 min when the voltage is set again after 10 min. This shows that this behavior, which is still unclear, is not related to an irreversible modification of the device. After the initial increase, the current density is stable. EL intensity is divided by 2 after 15 min of operation. This should be a result of a progressive depassivation of the luminescent silicon nanocrystals during operation. The stability is improved compared to untreated devices and compared to usual devices whose EL intensity decreases of at least 1 order of magnitude within 10 min [2].

CONCLUSION

Our study aims at enhancing the efficiency and stability of EL from PS, as well as to obtain bright EL at voltages below 10 V. Optimized PS formation conditions have been found in order to get efficient devices, operating at voltages below 10 V. A superficial low porosity layer between the optically active PS and the top contact is necessary to get a good electrical contact and a good mechanical stability. Moreover, a special care in the cleaning of the wafers before anodization and in the control of the anodization temperature has been found necessary in order to get reproducible results.

The use of anodic oxidation of PS has improved the EL-EQE of our devices based on porosified n^+-type silicon by several orders of magnitude. CW power efficiency of 0.2 % has been achieved. This value is the highest reported to date for a PS based light emitting device. This dramatic enhancement can be explained by the fact that the post-treatment based on anodic oxidation considerably reduces carrier flow via non-confined silicon which has been preferably oxidized. As a result, both carrier injection and localization in luminescent crystallites is enhanced. The anodic oxidation treatment also improves the stability of the devices, even though it is still altered by oxidation during operation.

We are currently working on improving further the power efficiency. In order to enhance further the stability, we will try to prevent the oxidation by using a post-treatment of PS based on the methylation method that has been demonstrated by Dubois

et al. [11].

ACKNOWLEDGMENTS

This work has been supported by the Japanese Society for the Promotion of Science.

REFERENCES

1. B. Gelloz, T. Nakagawa and N. Koshida, Mater. Res. Soc. Symp. Proc. **536**, 15 (1998).
2. A. J. Simons, T. I. Cox, A. Loni, L. T. Canham and R. Blacker, Thin Solid Films, **297**, 281 (1997).
3. B. Gelloz, T. Nakagawa and N. Koshida, Appl. Phys. Lett. **73**, 14, 2021 (1998).
4. J. N. Chazalviel and F. Ozanam, Mater. Res. Soc. Symp. Proc. **283**, 359 (1992).
5. F. Kozlowski, M. Sauter, P. Steiner, A. Richter, H. Sandmaier and W. Lang, Thin Solid Films **222**, 196 (1992).
6. H. Ono, H. Gomyou, H. Morisaki, and S. Nozaki, J. Electrochem. Soc., **140**, No. 12, L180 (1993).
7. J. C. Vial, S. Billat, A. Bsiesy, G. Fishman, F. Gaspard, R. Herino, M. Ligeon, F. Madeore, I. Mihalcescu, F. Muller and R. Romestain, Physica B **185**, 593 (1993).
8. A. Loni, A. J. Simons, T. I. Cox, P.D.J. Calcott and L.T. Canham, Electronics Letters, **31**, 1288 (1995).
9. K. Nishimura, Y. Nagao and N. Ikeda, Jpn. J. Appl. Phys. **37**, L303 (1998).
10. M. A. Hory, R. Herino, M. Ligeon, F. Muller, F. Gaspard, I. Mihalcescu and J. C. Vial, Thin Solid Films **255**, 200 (1995).
11. T. Dubois, F. Ozanam and J. N. Chazalviel, **PV 97-7**, p. 296, International Symposium on Pits and Pores: Formation, Properties, and Significance for Advanced Luminescent Materials/1997, P. Schmuki, D.J. Lockwood, H. Isaacs and A. Bsiesy, Editors, **PV 97-7**, p. 296, The Electrochemical Society Proceedings Series, Pennington, NJ (1997).

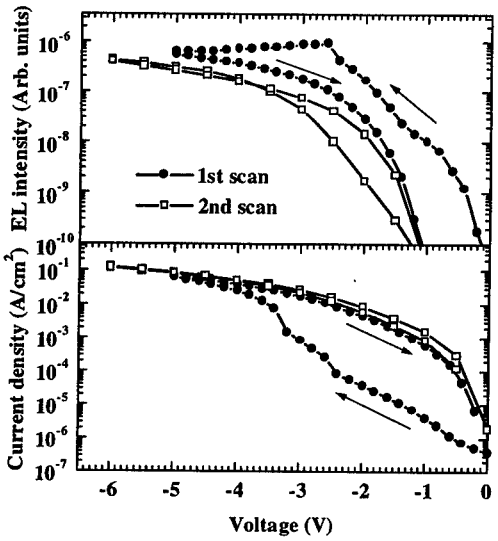


Fig. 1. EL intensity and current density versus voltage for an anodically oxidized n^+ device which includes a porous layer formed at room temperature, and no superficial low porosity layer. The Si substrate is reverse biased. The first and second voltage scans are shown. Arrows show the progress of the first scan.

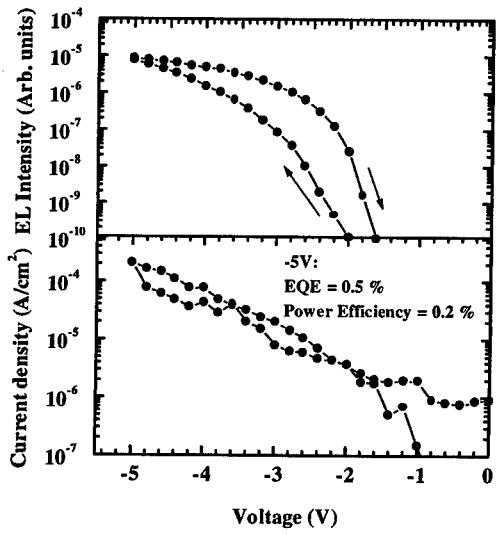


Fig. 2. EL intensity and current density versus voltage for an anodically oxidized n^+ device which includes a porous layer formed at 0°C, and a superficial low porosity layer. Arrows show the progress of the scan.

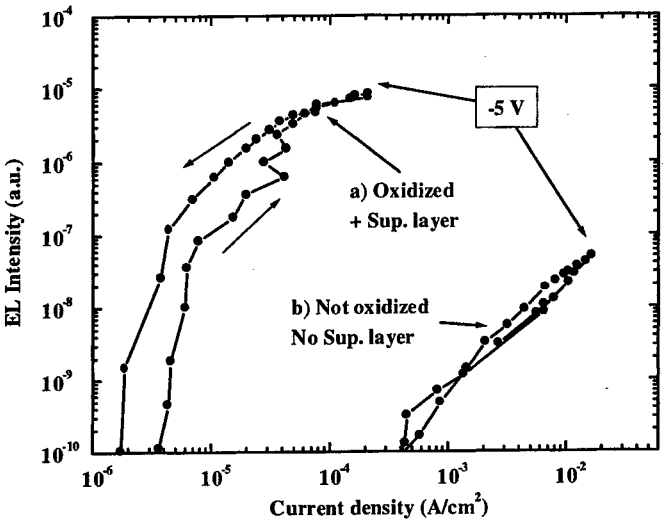


Fig. 3. EL intensity versus current density for the same device as in Fig. 2. (a), and the same device without superficial layer and not oxidized (b). Arrows show the progress of the scan.

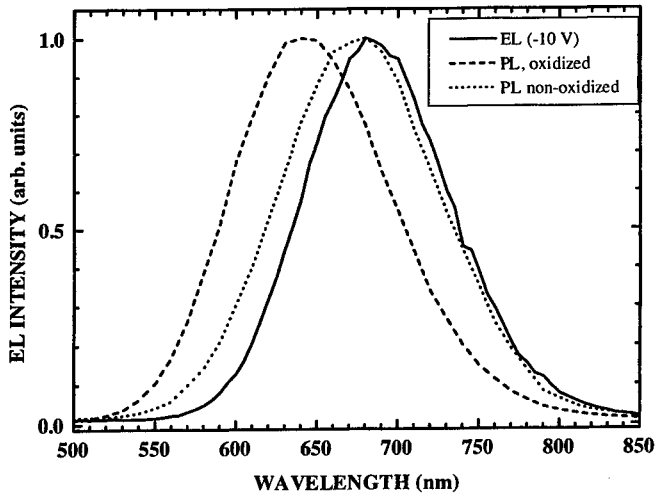


Fig. 4. Normalized EL at –10 V and PL spectra for the anodically oxidized n^+-based device also shown in Fig.2. Also represented is the PL spectrum of a non-oxidized

device.

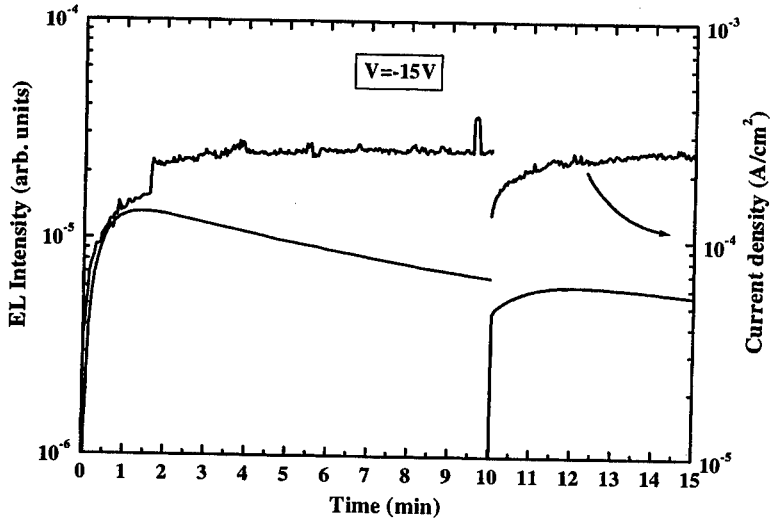


Fig. 5. EL intensity and current density at –15 V as a function of time for the anodically oxidized n^+-based device also shown in Fig.2. After 10 min, the experiment is stopped and started again.

NONLINEAR REFRACTIVE INDEX CHANGE IN POROUS SILICON FABRY-PEROT RESONATORS

Morio Takahashi*, Yuichi Toriumi*, Takahiro Matsumoto, Yasuaki Masumoto**, and Nobuyoshi Koshida*,**

**Department of Electrical and Electronic Engineering, Faculty of Technology, Tokyo University of Agriculture and Technology, Koganei, Tokyo 184, Japan*
***Single Quantum Dot Project, ERATO-JST, Tohkohdai, Tsukuba, Ibaraki 300, Japan*

ABSTRACT

Nonlinear optical behavior of porous silicon (PS) has been investigated using a Fabry-Perot resonator device at wavelengths in the near-infrared region. Different types of hysteresis were observed in the transmission-excitation curve at wavelengths around the resonance position. Based on some related experimental analyses, this nonlinear effect can be explained as a result of a nonlinear refractive index change of nanocrysrtalline silicon in PS, not of a photo-induced absorption change. The estimated quantity of the change in refractive index is 0.45%. The observed nonlinear phenomenon is potentially useful for silicon-based integrated photonic devices.

I. INTRODUCTION

Porous silicon (PS) is an attractive material for optoelectronic applications owing to its efficient visible photoluminescence [1] (PL) and electroluminescence [2] (EL) at room temperature. To date, a high EL external quantum efficiency (EQE) of 1.1% has been reported in PS light-emitting diodes [3]. This value is close to minimum requirements of EQE for applications to display devices and optical interconnection. Besides luminescent devices, operation as useful optoelectronic devices such as microcavities [4,5], nonvolatile memory [6] and optical waveguides [7–10] were demonstrated by simple monolithic PS processing.

In recent years, the nonlinear optical phenomena of nano-scale silicon crystallites have been investigated using various experimental and theoretical methods [11,12]. In these studies, the optical nonlinearity in PS has been interpreted as a large photoinduced absorption change under laser excitation with visible wavelength range. This optical phenomenon leads to the availability of PS for optical switches and optical logic gates [11]. These findings suggest further possibility of silicon-based photonic integration using PS optical devices.

In this report, it is shown that in PS-based Fabry-Perot resonators (PS-FPRs) we can observe the nonlinear optical effect due to a refractive index change at wavelengths of near infrared region. Significance of the introduction of the PS-FPR structure is also discussed by experimental and theoretical analyses.

II. EXPERIMENTAL

The device structure of PS-FPR is schematically shown in Fig. 1. The PS-FPR was prepared by anodizing *p*-type (100) Si wafers (0.1–0.5 Ωcm) in a mixture of 55wt% HF: ethanol = 1:1 at 0℃. The anodization current density was periodically modulated between 20 mA/cm^2 and 250 mA/cm^2. The refractive indices of low- and high-porosity PS layers are 2.60 and 1.54, respectively. The distributed Bragg reflector (DBR) is composed of 5 pairs of high- and low-refractive index layers with an optical thickness of $\lambda/4$, where λ is an operating wavelength of the PS-FPR. The optical thickness is expressed to nl, where n and l are refractive index and thickness of PS layer, respectively. The thickness l was controlled by the anodization current density and processing time. The DBRs were symmetrically fabricated on both sides of the active layer with an optical thickness of λ. The resonant wavelength was tuned to ~800 nm. Finally the PS-FPR layer was peeled out from the silicon substrate electrochemically, and then was bonded on a quartz glass. Transmittance spectra of the prepared PS-FPR were measured using a spectrophotometer.

To investigate the nonlinearity of PS, a change in the transmittance of PS-FPR was measured as a function of the incident Ti:Al_2O_3 laser power. Figure 2 shows the experimental arrangement employed here. A continuous wave Ti:Al_2O_3 laser beam was modulated using an acousto-optic modulator (AOM). To probe the input laser power, the modulated laser beam was split by a quartz glass. The split beam was introduced into a silicon photodiode (PD). The main laser beam was focused onto the central part of PS-FPR. The diameter of incident laser beam was about 200 μm. Optical power of incident beam at the sample surface is adjusted to 150 mW. The transmitted beam was detected using a silicon PD. The detected signals were observed by a digital oscilloscope.

III. RESULTS AND DISCUSSION

A. PS Fabry-Perot Resonators

A cross-sectional view of the device by scanning electron microscope (SEM) is shown in Fig. 3. The DBRs are completely symmetrically fabricated on both sides of the active layer as designed. The multilayered structures in upper- and lower-side mirrors are clearly observed. The designed optical length corresponds to the real thickness l~300 nm of the active layer ($l=\lambda/n$). This structure are reproducible under the same conditions.

As shown in Fig. 4, the measured peak wavelength in the transmittance spectrum of PS-FPR is 807 nm. The transmittance intensity $I_T(\lambda)$ of PS-FPR made with absorptive material is expressed by

$$I_T(\lambda) = \frac{Te^{-\alpha l}}{(1-Re^{-\alpha l})^2 + 4Re^{-\alpha l}\sin^2\left(\frac{2\pi nl}{\lambda}\right)}, \qquad (1)$$

where T and R are the transmittance and reflectivity of DBRs, respectively, and α is the absorption coefficient of active layer in PS-FPR. According to the result of fitting treatment, T and R of DBRs are 15% and 85%, respectively. The value of αl is 0.07, which is consistent with the previously-reported experimental results [13].

The finesse F, a figure of merit for Fabry-Perot resonator, is given by

$$F = \frac{\pi\sqrt{R}}{1-R} . \qquad (2)$$

The F value in the present PS-FPR is 19.3. It is expected that the optical power of incident laser beam is strongly confined into the active layer of PS-FPR, and that possible nonlinear optical effects are clearly detected.

B. Nonlinear Behavior in PS-FPR

Figure 5 shows input-output power waveformes and their hysteretic characteristics at various wavelengths. Distinctly different behavior in transmittance was observed near the resonant wavelength. The optically induced absorption causes the nonlinearity of PS-FPR at wavelengths shorter than the resonant point as shown in Fig. 5(a)(a'). A large hysteresis loop was observed in this wavelength region. This behavior is similar to previously-reported nonlinearity in silicon nanocrystallites and PS. At a resonant wavelength, opposite nonlinear phenomena as shown in Fig. 5(b)(b'). Thus the hysteresis loop is twisted in the strong-excitation region.

Apparent nonlinear phenomena in which the transmittance becomes larger with increasing incident optical power are observed at wavelengths longer than the resonant point as shown in Fig. 5(c)(c'). The measurement wavelength and the modulation frequency of AOM are 816 nm and 100 Hz, respectively. This type of nonlinear response has not been reported to date. There should be some intrinsic nonlinear optical effects rather than simple photo-induced absorption change.

To understand the nonlinear effect that the transmittance becomes larger with increasing integrated incident optical power, a nonlinear refractive index change is discussed here. When the refractive index of the active layer in PS-FPR becomes larger with increasing input optical power, the resonant point shifts to longer wavelength. Then transmittance of PS-FPR would become larger at wavelengths longer than the resonant point. At wavelengths shorter than the resonant point, the transmittance should also be decreased. From this viewpoint, the quantity of refractive index change can be estimated under the assumption that the absorption coefficient is not affected by laser excitaion. The transmittance intensity $I_{NL}(\lambda)$ of PS-FPR with the active layer of refractive index $n+\Delta n$ is derived from Eq. 1 as

$$I_{NL}(\lambda) = \frac{Te^{-\alpha l}}{(1-Re^{-\alpha l})^2 + 4Re^{-\alpha l}\sin^2\left\{\frac{2\pi l}{\lambda}(n+\Delta n)\right\}} . \qquad (3)$$

The Δn value corresponding to the refractive index change can be easily calculated from the change in transmittance I_{NL}–I_T. The initial value of transmittance in the linear region is 36% at 816 nm. As suggested from Fig. 5(c'), the transmittance is increased by a factor of 1.2 compared with the initial value at the maximum input power. Thus the estimated value of Δn is 0.0116 and $\Delta n/n$=0.45%. In the actual device, a photo-induced absorption change may also occur separately. So the value of $\Delta n/n$ should be larger than the estimated one.

C. Temperature Dependence of Transmittance Spectra

In the above experiments, a high-power laser beam was focused onto the sample surface with an optical power of 150 mW and a beam diameter of 200 μm. It looks that the temperature of PS-FPR is raised during measurements. To determine whether or not the thermal effects relate to the experimental results, the temperature dependence of transmittance spectra was investigated. The transmittance spectra were measured in the temperature range of 0℃ to 180℃ as shown in Fig. 6. The resonant wavelength of PS-FPR employed here was tuned to 740 nm. It is clear that the resonant wavelength is independent of temperature, although the absorption increases with increasing temperature. This is a strong indication that the refractive index change is not due to thermal effects but due to optically induced effects.

IV. CONCLUSIONS

The nonlinear optical behavior in a free-standing PS-FPR has been investigated by experimental and theoretical approaches. The characteristics of PS-FPR suggest that the incident optical power is strongly confined into the active PS layer. Owing to the enhanced optical activity in PS-FPR, apparent nonlinear hysteresis in transmittance was observed. Besides the photo-induced absorption change, a significant nonlinear change in the refractive index is produced at a wavelength longer than the resonant point. The relative refractive index change reaches 0.45%. These results indicate the availability of PS devices for optical switches and optical logic gates.

ACKNOWLEDGMENTS

This work was partially supported by a Grant-in-Aid from the Ministry of Education, Science, Sports and Culture of Japan, and TUAT-VBL (Tokyo Univ. of Agri. & Tech. – Venture Business Laboratory) Project.

REFERENCES

1. L. T. Canham, Appl. Phys. Lett. **57**, 1046 (1990).
2. N. Koshida and H. Koyama, Appl. Phys. Lett. **60**, 347 (1992)
3. B. Gelloz, T. Nakagawa and N. Koshida, Mater. Res. Soc. Symp. Proc. **536**, 15 (1998).
4. L. Pavesi, C. Mazzoleni, A. Tredicucci and V. Pellegrini, Appl. Phys. Lett. **67**, 3280 (1995).
5. M. Araki, H. Koyama and N. Koshida, jpn. J. Appl. Phys. **35**, 1041 (1996).
6. K. Ueno and N. Koshida, Appl. Phys. Lett. **74**, 93 (1999).
7. A. Loni, L. T. Canham, M. G. Berger, R. Arens-Fischer, H. Muender, H. Lueth, H. F. Arrand and T. M. Benson, Thin Solid Films **276**, 143 (1996).
8. H. F. Arrand, T. M. Benson, A. Loni, M. G. Krueger, M. Thoenissen and H. Lueth, Electron. Lett. **33**, 1724 (1997).
9. M. Araki, M. Takahashi, H. Koyama and N. Koshida, Mater. Res. Soc. Symp. Proc. **486**, 107 (1998).
10. M. Takahashi, M. Araki and N. Koshida, Jpn. J. Appl. Phys. **37**, L1017 (1998).

11. T. Matsumoto, M. Daimon, H. Mimura, Y. Kanemitsu and N. Koshida, J. Electrochem. Soc. **142**, 3528 (1995).
12. S. Vijayalakshmi, M. A. George and H. Grebel, Appl. Phys. Lett. **70**, 708 (1997).
13. J. von Behren and P. M. Fauchet, in *Properties of Porous Silicon*, Section 8.2, p. 229, INSPEC, London (1997).

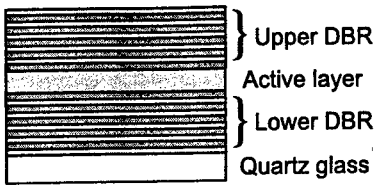


Fig. 1. A schematic device structure of PS-FPR used in the experiment. The DBR mirrors were fabricated on both sides of the active PS layer with a low-porosity (high-refractive index). The PS-FPR layer was peeled out from Si substrate electrochemically and was bonded on a quartz glass.

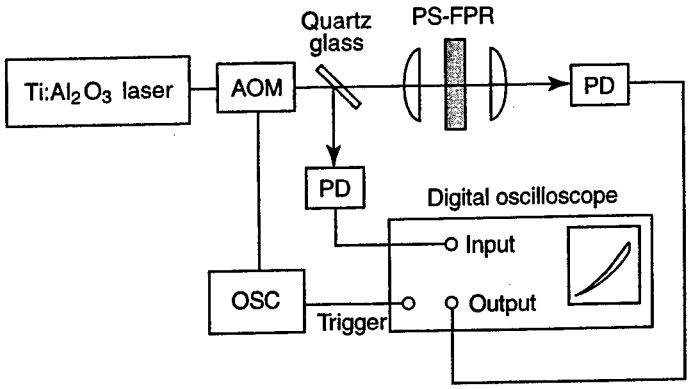


Fig. 2. An experimental setup for measurements. The AOM, OSC and PD are acousto-optic modulator, oscillator and silicon photodiode, respectively. A continuous wave Ti:Al_2O_3 laser beam is modulated by an AOM with a frequency of 100 Hz. The input optical power and transmittance of PS-FPR are detected using PDs. These detected signals are observed by a digital oscilloscope as waveformes and input-output hysteresis curves.

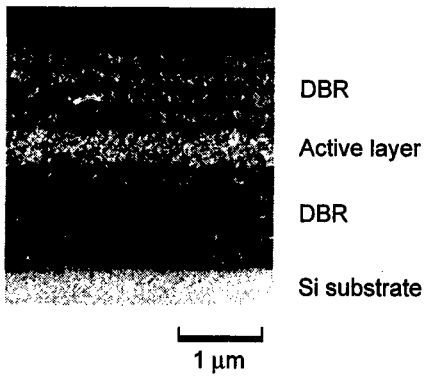


Fig. 3. A SEM cross-sectional view of a PS-FPR formed on the Si substrate. Symmetric DBRs with five pairs of layers are fabricated on both sides of the active PS layer as designed. It is observed that the multilayer structures are produced as-designed.

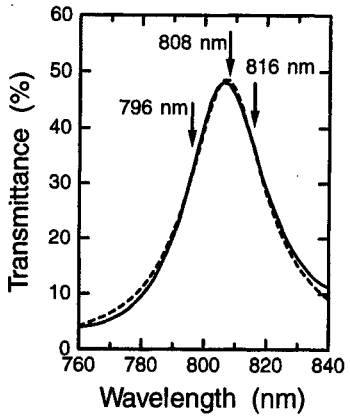


Fig. 4. A typical transmittance spectrum of a PS-FPR (solid curve). The dashed curve is a fitting spectrum calculated under the condition that the transmittance and reflectivity of DBRs are 15% and 85%, respectively, and that the absorption term αl is 0.07. The resonant wavelength is located at 807 nm which is close to the designed value. The indicated wavelengths of 796 nm, 808 nm and 816 nm are detection points described in Sec. III. B.

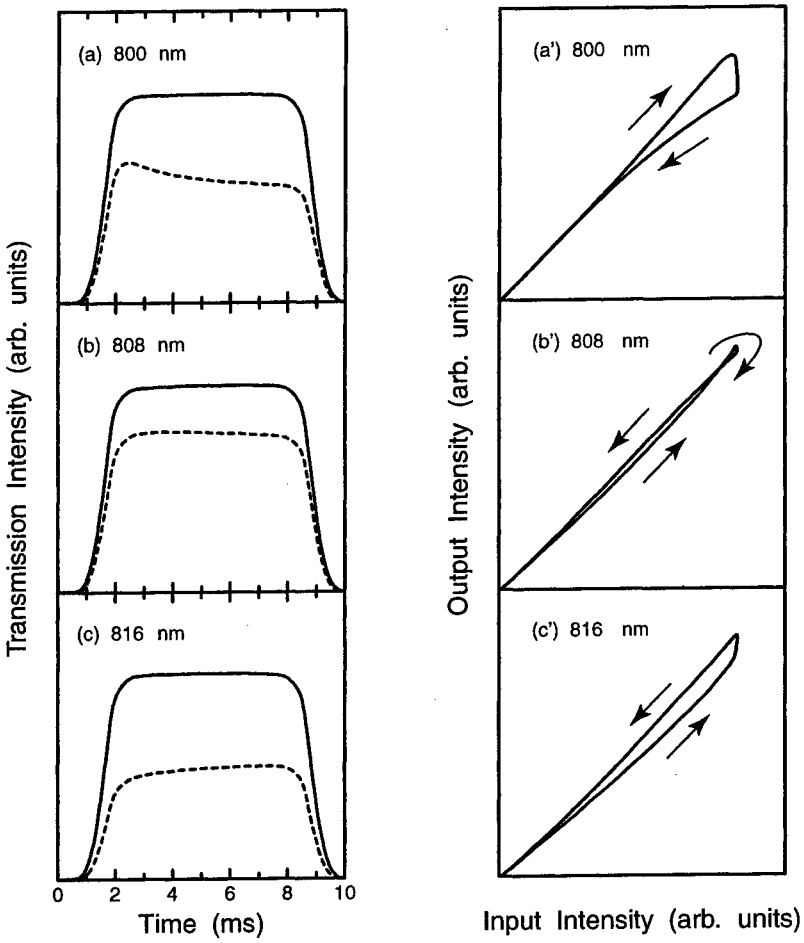


Fig. 5. The input (solid curves) and output (dotted curves) power waveforms at various wavelengths ((a), (b), and (c)) and the corresponding hysteretic input-output curves ((a'), (b'), and (c')). Different characteristics are observed in the transmittance at aroud the resonant wavelength (807 nm) of PS-FPR. The non-linear behavior at wavelengths shorter than 807 nm ((a) and (a')) is mainly due to a photoinduced absorption. In contrast, the dominant factor in nonlinearity observed at wavelengths longer than the resonant position ((c) and (c')), where the transmittance is enhanced with increasing incident optical power, should be an intrinsic change in refractive index.

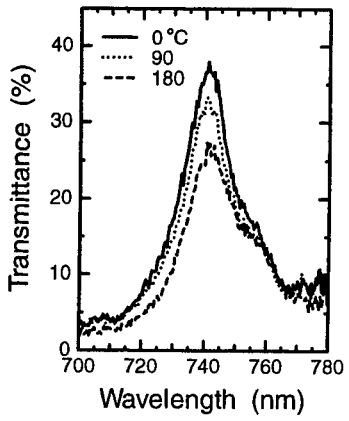


Fig. 6. Temperature dependence of transmittance spectra at 0–180℃. It should be noted that the resonant wavelength of PS-FPR is independent of temperature, although significant effects of thermal induced absorption are observed in the whole region.

Si Superlattices and Photonic Crystals

WAVY SIGE/SI SUPERLATTICES: STRUCTURAL AND OPTICAL PROPERTIES AND APPLICATION TO NEAR INFRARED LIGHT DETECTION

J.-M. Baribeau, A. Delâge, S. Janz, H. Lafontaine*, D.J. Lockwood, J.P. McCaffrey, S. Moisa, N.L. Rowell** and D.-X. Xu

Institute for Microstructural Sciences, National Research Council Canada, Ottawa, K1A 0R6, Canada

**Institute for National Measurements Standards, National Research Council Canada, Ottawa, K1A 0R6, Canada

*SiGe Microsystems Inc., 1500 Montreal Rd., Ottawa, Ontario, K1A 0R6, Canada

$Si_{1-x}Ge_x$/Si strained undulated superlattices have been prepared by both molecular beam epitaxy (MBE) and ultra high vacuum chemical vapor deposition (UHV-CVD) and their structural/optical properties studied. In these superlattices, the undulated $Si_{1-x}Ge_x$ layers are self-aligned in the growth direction and the lateral size and amplitude of the undulations can be controlled by choice of growth parameters. The interface undulations are very regular and predominantly oriented along [100] directions. Raman scattering spectroscopy and x-ray diffraction measurements exhibit features normally seen in planar superlattices and confirm the retention of strain in structures whose average Ge content exceeds the metastable limit. The low temperature photoluminescence spectra of MBE grown samples (x in the range 0.3-0.55) is dominated by a broad and strong luminescent peak around 0.8 eV. This peak shifts to lower energy with increasing Ge content and persists after a 100 s anneal at 850 °C. Photocurrent spectroscopy measurements on several samples also indicate that the room temperature optical absorption edges are situated well below 0.8 eV. These observations support the idea that the photoluminescence peaks are intrinsic to the $Si_{1-x}Ge_x$ layers and not defect mediated, and indicate the structures are thermally robust. The UHV-CVD superlattices exhibit multi-peak luminescence in the same energy range that shifts to higher energy with smaller thickness, presumably due to confinement effects. Waveguide photodetectors based on the latter coherent-wave Si/SiGe superlattices have achieved a photoresponse of 0.1 A/W at 1.55 μm.

INTRODUCTION

$Si_{1-x}Ge_x$ /Si strained layer superlattices have been considered for some time as candidates for near infrared light detection and even light emission (1). These structures are generally grown in a pseudomorphic state in which the interfaces are planar and the $Si_{1-x}Ge_x$ layers are elastically distorted to accommodate their lattice mismatch with the Si substrate and spacer layers. These structures are metastable and will relax by the introduction of structural defects if a critical thickness for the $Si_{1-x}Ge_x$ layer is exceeded,

or, alternatively, if the structure is allowed to reach equilibrium by thermal annealing. Light detection at optical communication wavelengths (1.3-1.55 μm) requires the use of $Si_{1-x}Ge_x$ alloys with a Ge fraction of 0.5 or more, which greatly restricts the thickness of the defect-free $Si_{1-x}Ge_x$ active layers, due to built-in strain. A small $Si_{1-x}Ge_x$ layer thickness not only reduces the photoresponse efficiency of the structure, but also introduces a widening of the band gap that shifts the photoresponse to shorter wavelengths due to quantum confinement. It is, however, possible to grow these $Si_{1-x}Ge_x$/Si multilayers in a regime in which the interfaces, rather than being planar, become undulated to minimize strain energy. This three-dimensional growth mode may also increase the effective Ge concentration in regions of maximum quantum well thickness and reduce the local quantum confinement at these thickness maxima. The combination of these two effects produces a significant increase in the photoresponse at larger wavelengths.

$Si_{1-x}Ge_x$ /Si strained undulated superlattices have been prepared by both molecular beam epitaxy (MBE) and ultra high vacuum chemical vapor deposition (UHV-CVD) and their structural/optical properties probed using different techniques. In superlattices, the undulated SiGe layers are self-aligned in the growth direction and the lateral size and amplitude of the undulations can be controlled by choice of growth parameters. The interface undulations are very regular and predominantly oriented along <100> directions. Raman scattering spectroscopy and x-ray diffraction measurements exhibit features normally seen in planar superlattices and confirm the retention of strain in structures whose average Ge content exceeds the metastable limit. The low temperature photoluminescence spectra of MBE grown samples (x in the range 0.3-0.55) is dominated by a broad and strong luminescent peak around 0.8 eV. This peak shifts to lower energy with increasing Ge content and persists after a 100 s anneal at 850 °C. Photocurrent spectroscopy measurements on several samples also indicate that the room temperature optical absorption edges are situated well below 0.8 eV. These observations support the idea that the photoluminescence peaks are intrinsic to the $Si_{1-x}Ge_x$ layers and not defect mediated, and indicate the structures have good resistance to thermal treatment. The UHV-CVD superlattices exhibit multi-peak luminescence in the same energy range that shifts to higher energy with smaller thickness, presumably due to confinement effects (2). Waveguide photodetectors based on the latter coherent-wave $Si_{1-x}Ge_x$/Si superlattices have achieved a photoresponse of 0.1 A/W at 1.55 μm (3).

EXPERIMENT

MBE Growth

A series of $Si_{1-x}Ge_x$/Si superlattices on Si (001) was prepared by MBE using a VG Semicon V80 deposition system. Details of the growth methodology and wafer preparation have been presented elsewhere (4,5), and only specific details from the present study are discussed here. Superlattices were grown with 10, 15 or 20 periods at typical Si and Ge deposition rates of 0.1 and 0.05 nm/s respectively. The Si layers in the structures have a nominal thickness of 1.3 nm while the $Si_{1-x}Ge_x$ layers have nominal thickness ranging from 3 to 5 nm and Ge composition x ranging from 0.3 to 0.55. Two growth temperatures were investigated, namely, 675 and 625 °C. Most of the samples were terminated at the surface by a $Si_{1-x}Ge_x$ alloy layer to enable study of the alloy

surface morphology. Some samples were also terminated with Si layer to investigate the effectiveness of a silicon cap in smoothing the surface.

UHV-CVD Growth

$Si_{0.5}Ge_{0.5}$/Si superlattices were grown on Si (001) at 525 °C in a Leybold Sirius production compatible UHV-CVD deposition system (6,7). Pure silane and diluted germane (10% in helium) were used as precursors at a pressure of 1.33 mbar. The base pressure between runs was typically 1.0×10^{-9} mbar. After a standard RCA clean and final 10 s rinse in a $HF:H_2O$ (1:10) solution, wafers were introduced into the reactor through a load lock. Growth was initiated immediately by silane injection. At this growth temperature a deposition rate of 1.2 nm/min for the Si spacer layers and of 4 nm/min for the $Si_{0.5}Ge_{0.5}$ layers was obtained. A series of 10 period $Si_{0.5}Ge_{0.5}$/Si superlattices was prepared. These had a nominal Si spacer layer of 11 nm, but differ by a different nominal alloy layer thickness, which was varied from 3 to 8 nm. All these samples were terminated by a $Si_{0.5}Ge_{0.5}$ layer at the surface.

Characterization Techniques

The various samples were examined by a variety of techniques to investigate and compare the structural and optical properties of MBE and UHV-CVD grown structures. The interface morphology was investigated by [100] and [110] cross-section transmission electron microscopy (Philips EM430), while the surface morphology was examined by atomic force microscopy (Nanoscope III). Strain and long range ordering in the superlattices were investigated by x-ray diffraction and Raman scattering spectroscopy. X-ray reciprocal lattice maps were measured on a Philips MRD and specular and diffuse x-ray scattering was collected on a Philips 1820 vertical goniometer. The Raman spectra were excited with 300 mW of Ar laser light at 457.9 nm in a quasi backscattering geometry (8) using an angle of incidence of 77.7° to the (001) surface. The incident light was polarized in the scattering plane and the scattered light (collected at 90°) was collected without polarization analysis.

Photoluminescence spectra were recorded using a Fourier transform infrared spectrometer with the samples immersed in cold helium gas (T~4.5 K).The excitation wavelength was 514 nm (Ar^+ laser) and the power density at the sample was 10-100 mW/cm^2. The luminescence was measured with an InSb detector, which has a good responsivity in the wavelength regime of interest (i.e., 1.5 μm and higher).

Photocurrent spectra were collected using several light sources. For wavelengths between λ=1180 and 1500 nm a conventional tungsten lamp/monochromator arrangement was used. The output of the monochromator was modulated using a mechanical chopper and coupled into an optical fiber, which illuminated either the input facet of the waveguide photodetector, or the surface of the other non-waveguide samples. Simple Al electrode structures were deposited on each sample. All samples were biased at 2 V and the generated photocurrent was measured using a transimpedance amplifier and lock-in amplifier referenced to the modulation frequency. Photocurrent was collected as the monochromator wavelength was scanned. Photocurrent spectra were also collected using a tunable external cavity semiconductor laser (for the λ =1480 – 1580 nm wavelength range), a colour centre laser (for λ =1480 – 1620 nm), and a YAG laser (λ=1320 nm) as light sources. In each case the laser light was coupled into a fiber, and the photocurrent was collected as described above.

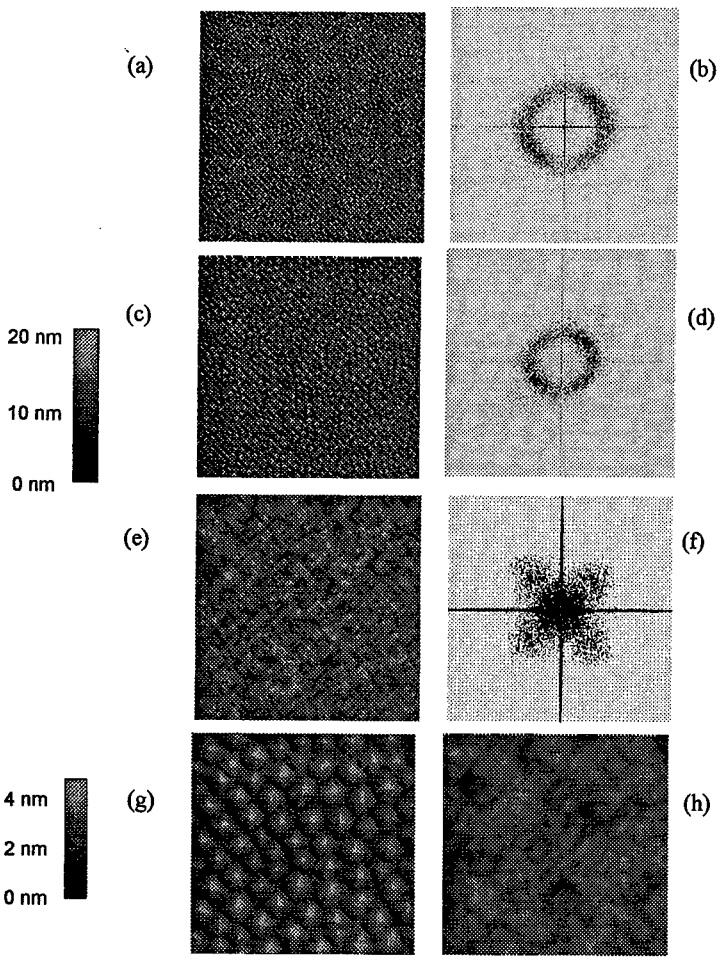


Figure 1. Atomic force microscopy images (5 μm square) from various wavy superlattices. (a) 10 period $Si/Si_{0.6}Ge_{0.4}$ superlattice with t(SiGe) = 0.31 nm grown by MBE at 675 °C and corresponding Fourier transform (power spectrum density) (b), (c) 10 period $Si/Si_{0.54}Ge_{0.46}$ superlattice with t(SiGe) = 0.34 nm grown by MBE at 625 °C and corresponding power spectrum (d), (e) 10 period $Si/Si_{0.50}Ge_{0.50}$ superlattice with t(SiGe) = 0.30 nm grown by CVD at 525 °C and corresponding power spectrum (f). (g) Magnified view (1 μm square) of (c) and (h) magnified view of a 10 period $Si/Si_{0.6}Ge_{0.4}$ superlattice grown by MBE at 625 °C.

STRUCTURAL PROPERTIES

Atomic Force and Microscopy Electron Microscopy

Figure 1 compares AFM images obtained from various samples. The MBE grown superlattices that are terminated by a $Si_{1-x}Ge_x$ alloy exhibit a very rough surface morphology with features aligned predominantly along the <100> and <010> directions (Fig. 1 (a), (c), and (g). The shape of these bumps is independent of the Ge composition in the range investigated, but their size decreases with increasing growth temperatures. The surface root mean square (RMS) roughness of MBE grown superlattice is typically 4 nm. The preferred size and orientation of the surface undulations are clearly seen in a power spectrum density of the surface topography (Fig. 1 (b) and (d)). The well defined size of the surface bumps is revealed in the power spectrum by the presence of a ring of constant length. The fourfold symmetry of the Fourier image (higher intensity along <001> directions) indicates the preferential orientation of the bump facets along these crystallographic axes. Scans over smaller areas (Fig. 1 (e)) show that the surface features have a pyramid-like shape with the side of the square base of the pyramid aligned along <100> directions. The sides of the pyramids have an angle of about 11° and thus probably consist of <105> facets. When capped with a 13 nm Si layer, the surface smoothens dramatically and only weak undulations persist.

Wavy superlattices grown by UHV-CVD exhibit a different surface morphology.

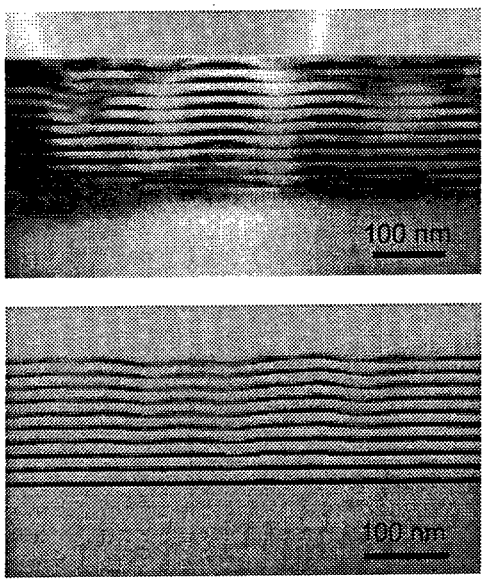


Figure 2. Cross-section transmission electron micrograph from (a) a $Si_{0.52}Ge_{0.48}$/Si superlattice on Si(001) (t(SiGe) = 3.7 nm) grown by MBE and (b) a 10 period $Si_{0.50}Ge_{0.50}$/ Si superlattice on Si(001) (t(SiGe) = 5 nm) grown by UHV-CVD.

Elongated mounds meandering along <100> directions are observed on the surface (RMS roughness of 2.5 nm). These mounds also have facets at an angle of ~10° with respect to the (001) surface. This morphology is very similar to that reported on single layer $Si_{1-x}Ge_x$ alloys grown by high temperature low pressure vapor deposition (9). The power spectrum of the AFM image exhibits a analogous fourfold symmetry with distinct lobes oriented along <100> directions. The alignment of the surface features is better defined here since no ring is seen in the power spectrum. Also, strong signal at the center of the image, corresponding to long spatial frequencies is seen for UHV-CVD grown samples. In contrast to MBE grown superlattices, the surface of the UHV-CVD samples remains highly corrugated even after deposition of a 10 nm Si cap.

The interface morphology of the wavy superlattices is illustrated in Fig. 2, which presents cross-section views from two similar samples grown by UHV-CVD and MBE. Both micrographs reveal presence of a pronounced interface waviness that extends to the bottom of the superlattice structures. The lateral wavelength and amplitude of the oscillations is similar for both samples, but there are also qualitative differences. The MBE superlattice exhibits a strong asymmetry in the roughness between the Si on $Si_{1-x}Ge_x$ and $Si_{1-x}Ge_x$ on Si interfaces, the former being very wavy, while the latter are virtually flat. The $Si_{1-x}Ge_x$ islands are also highly correlated vertically and the roughness and size of the islands do not increase significantly in the growth direction. Undulations on the UHV-CVD sample are seen at both types of interfaces, the vertical alignment is not as pronounced, and the corrugation increases along the growth direction. The deposition of a thin (10 nm) Si cap is sufficient to flatten the surface in MBE, but leaves a residual corrugation in UHV-CVD. In both cases, no dislocations can bee seen, but the layers are heavily strained as evidenced by the periodic strain contrast in the TEM micrographs.

X-ray Diffraction and Reflectometry

The various superlattices were examined by high-resolution x-ray diffraction and grazing incidence x-ray reflectivity. Details on the x-ray measuremetns can be found elsewhere (11,12). Figure 3 compares reciprocal space maps measured on representative samples. These maps were acquired using very asymmetric reflections in a low-exit angle geometry to enhance diffraction effects due to undulations in the plane of growth (10). The maps exhibit the usual satellite peaks in the vertical direction associated with the super-periodicity of the structures. The alignment of the satellite peaks in the same vertical line as the substrate peak indicates that the structures have retained their strain. In addition, secondary features are seen in the horizontal direction beside the superlattice peaks. These side lobes are associated with the lateral undulation of the interfaces. Figure 3(a) and (b) compares maps recorded on the same samples, using 404 and 113 Bragg peaks corresponding to having the scattering plane along the <010> and <110> crystallographic directions, respectively. It is apparent from the larger spacing, stronger intensity of the side lobes and presence of higher order lobes in the measurement along the <010> azimuth that the surface undulations are preferentially oriented in that direction, in agreement with the AFM analysis. The side lobes are also seen on the CVD grown samples (fig. 3 (c)), although they are generally not as intense or well defined. They also become weaker in MBE samples as the growth temperature is decreased and disappear below 600 °C.

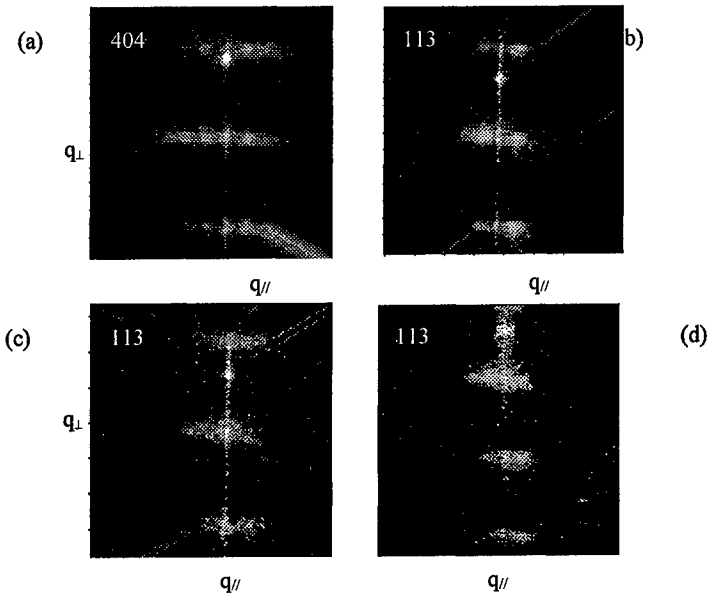


Figure 3. Reciprocal space maps from wavy superlattices. (a) and (b) 15 period $Si/Si_{0.63}Ge_{0.37}$ (t(SiGe) = 5 nm) grown by MBE at 640 °C, measured about two different Bragg reflections. (c) 10 period $Si/Si_{0.580}Ge_{0.42}$ grown by CVD at 525 °C and (d) a 15 period $Si/Si_{0.54}Ge_{0.46}$ (t(SiGe) = 3.6 nm) grown by MBE at 625 °C and terminated by a 13 nm Si layer.

Interface structure can also be probed by grazing incidence diffraction, a technique very sensitive to variations in the electron density in the direction perpendicular to the sample surface. Figure 4 (a) shows the specular reflectivity (full line) measured on a typical wavy superlattice grown by MBE. Despite the pronounced wavy nature of the interfaces, the reflectivity curve exhibits sharp superlattice reflections. These remain visible and relatively sharp even at high angles of incidence. The intensities of successive satelllite orders decay monotonically and do not display the usual modulation seen in periodic bilayer systems (12). Figure 4 (a) also displays angle of incidence rocking scans measured at the position of a strong satellite peak along both <110> and <010> azimuths. Off-specular diffuse scattering is weak and distributed in a narrow angular range centered on the specular direction. This is typical of interfaces with long (~100 nm) in-plane correlation. The diffuse scattering is anisotropic and exhibits side lobes when the scattering is along the <100> azimuth. The position of the side lobes can be associated with a length scale of ~1 μm on the surface, which is one order of magnitude larger than the wavelength of the surface undulations. Similar long wavelength undulations have been observed before on MBE grown multilayers and were correlated to the residual wafer misorientation with respect to the <001> direction (13,14).

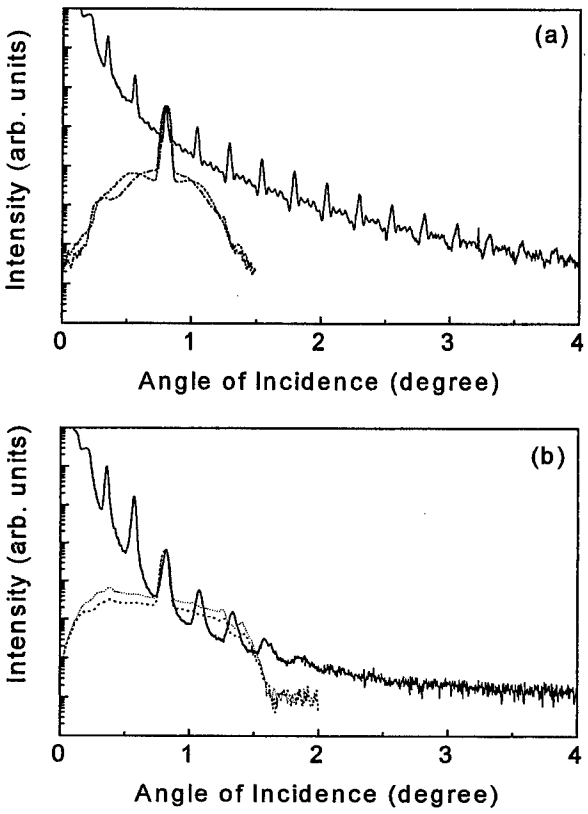


Figure 4. Specular x-ray reflectivity (full line) and angle of incidence rocking scans (dotted lines) for (a) a 10 period wavy $Si_{0.54}Ge_{0.4}$ /Si superlattice (t(SiGe) = 3.6 nm) grown by MBE and (b) a ten period $Si_{0.50}Ge_{0.50}$ /Si superlattice (t(SiGe) = 3.0 nm) grown by UHV-CVD.

In comparison, the satellite peaks on a CVD grown wavy superlattice are broader and much weaker, as shown in Fig. 4 (b). The faster decay of specular intensity with angle of incidence is due to a large surface roughness of this sample, which does not have a Si cap. The rocking scans (dotted lines) exhibit a strong and broad diffuse scattering spectra extending to the critical angle. This indicates a shorter correlation distance in the plane of growth for growth using UHV-CVD. Contrary to the MBE case, no strong anisotropy is observed as a function of azimuth direction and would indicate the absence of any long-range surface roughness correlation. This result is qualitiatively similar to that obtained on longer periodicity UHV-CVD grown superlattices and seem to be typical of that growth technique (11).

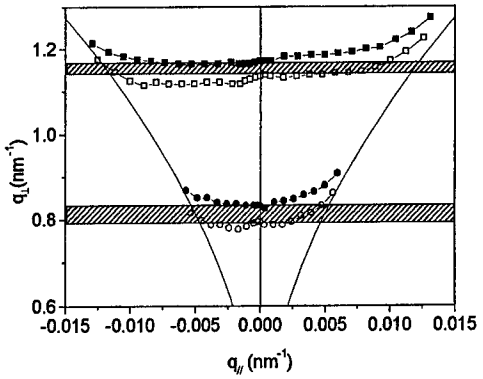


Figure 5. Intensity distribution in reciprocal space for two strong satellites from the samples of Fig. 4. The top two curves gives the position of half intensity for the third superlattice peak for the MBE sample while the bottom two curves are the half intensity of the second order satellite for the UHV-CVD sample. The cross hatched regions indicate the theoretical width of the satellite reflections taking into account the finite thickness of the superlattices.

The intensity distribution about a strong satellite peak from an MBE and a UHV-CVD grown wavy superlattice is shown in Fig. 5. In both cases, The intensity is distributed on the Bragg sheet, indicating good vertical correlation of the interface undulations. The half width of the distribution intensity is close to that expected for interfaces correlated over the whole superlattice depth (cross-hatched regions in Fig. 5).

The above x-ray results point to several interesting features for these wavy superlattices. In the MBE case, the reflectivity results are very analogous to what is found in superlattices with planar interfaces. This possibly reflects the fact that in the MBE wavy superlattices one type of interface remains atomically flat (see Figure 2(a)). Furthermore, the wavy interfaces exhibit a strong vertical correlation, which preserve a well defined vertical modulation of the layered structure, despite the strong interface corrugation. This results in a reflectivity curve with strong superlattice reflections, but in which information on the relative thickeness within a superlattice period has been loss, because this quantity is no longer well defined. In the UHV-CVD case, both types of interfaces are wavy and the vertical correlation is not as good. As is apparent in Fig. 2 (b), the periodic nature of the superlattice is not well preserved and results in a reflectivity curve characteristic of a ill- defined superlattice.

Raman Scattering Spectroscopy

Representative optic mode Raman spectra of MBE grown superlattices are given in Fig. 6. The spectra show features near 295, 415, and 505 cm^{-1} that are so-called Ge-Ge, Ge-Si, and Si-Si modes of the alloy layers and a line at 519.9 cm^{-1} that is due to the Si layers of the superlattice (for 457.9 nm excitation, the laser beam is mostly absorbed within the alloy layers before reaching the substrate in these 10 period superlattices).

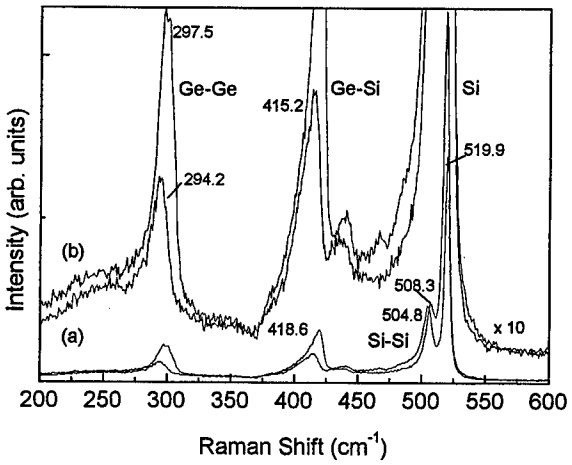


Figure 6. Room temperature Raman spectrum of (a) a 10 period $Si_{0.515}Ge_{0.485}$/Si wavy superlattice (t(SiGe = 3.7 nm) and (b) a 10 period $Si_{0.48}Ge_{0.52}$/Si flat superlattice (grown at 525 °C as a reference sample, t(SiGe = 3.7 nm) showing the optic modes. Both samples were grown by MBE.

There are noticeable frequency shifts between the optic modes of the strained flat-layer reference superlattice and those of the wavy superlattice alloy layer. The step down (Si-Si mode) or up (Ge-Ge and Ge-Si modes) in frequency with respect to the reference superlattice values indicate the "average" strain in the wavy superlattice is reduced from that in the planar case. The dependence of the optic mode frequency on alloy composition (and partly on growth temperature) is shown in Fig. 7. The Si-Si line generally decreases in frequency while the Ge-Ge and Ge-Si modes generally increase in frequency with x, as expected, but there is an overall shift in frequency from the corresponding fully strained epilayer case (as discussed above). Similar spectra were obtained from the UHV-CVD samples of composition x = 0.5. In both cases, strain relaxation was observed from a shift down in frequency of the Si layer peak when the composition/layer thickness and/or growth temperature exceeded the stable growth condition requirements.

In the low-frequency Raman spectra (see Fig. 8), folded longitudinal acoustic (FLA) modes are observed. Such FLA modes are a sensitive indicator of the superlattice layer interface sharpness (8). The FLA spectrum of the planar superlattice shows pairs of folded modes up to 6th order in the folding index m (8). Even the m = 5 modes are still very sharp (almost resolution limited) indicating excellent control of the superlattice periodicity and atomically abrupt Si/SiGe interfaces. In the MBE-grown wavy superlattices, the FLA modes are still observed up to the order m = 3, although the overall FLA intensity is reduced compared with the reference sample, and there is a more rapid decrease in FLA peak intensity with increasing m combined with a rapid increase in the FLA linewidth (see Fig. 8). These results show that the overall FLA intensity is derived mainly from the maintenance of atomic abruptness at the wavy-superlattice layer interfaces. The decrease in FLA peak intensity and increasing linewidth with increasing

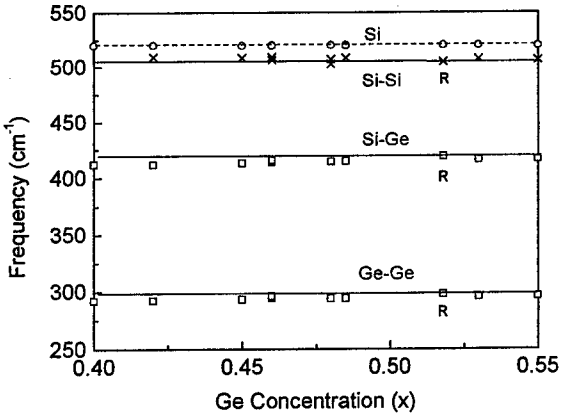


Figure 7. Alloy composition dependence of the room-temperature Raman frequencies of the optic modes in MBE grown wavy superlattices. The R designates the reference planar structure.

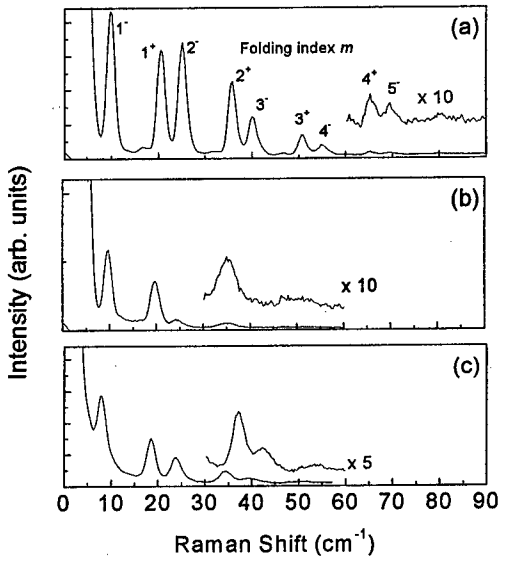


Figure 8. Low-frequency room-temperature Raman spectra showing the FLA modes of (a) a 10 period $Si_{0.48}Ge_{0.52}$/Si flat-layer reference superlattice grown by MBE, (b) a 10 period $Si_{0.515}Ge_{0.485}$/Si wavy superlattice grown by MBE, and (c) a 10 period $Si_{0.5}Ge_{0.5}$/Si wavy superlattice grown by UHV-CVD. The alloy layer thickness is comparable in all three superlattices.

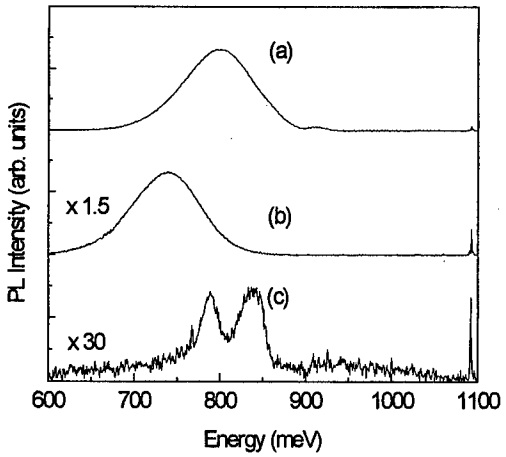


Figure 9. Low- temperature PL spectrum of (a) a 10 period $Si_{0.47}Ge_{0.53}$/Si wavy superlattice and (b) a 10 period $Si_{0.47}Ge_{0.53}$/Si wavy superlattice grown by MBE, and (c) a 10 period $Si_{0.5}Ge_{0.5}$/Si wavy superlattice grown by UHV-CVD. The samples have similar alloy layer and Si spacer layer thickness (0.35 and 0.3 nm, and 14 and 15 nm, for the MBE and UHV-CVD samples, respectively.). PL spectra were recorded at 5K with an excitation power density of 100 mW/cm^2.

index *m* can be due to composition grading along the SiGe/Si interface and/or a non-uniformity in the periodicity. As the FLA modes were observed to have similar characteristics in all the MBE-grown wavy superlattices, the compositional grading has to be the primary cause. It is indeed remarkable that FLA modes can be observed at all in these wavy superlattices given the strong interface undulation (see Fig. 2); their observation simply reflects the long wavelength nature of acoustic modes compared with the undulation modulation. The FLA peaks in the various MBE grown superlattices varied in frequency from sample to sample consistent with the period variation, but were not sensitive to strain variations. Similar FLA mode Raman spectra were obtained from UHV-CVD grown wavy superlattices (see Fig. 8), although the instrumental background due to stray light is higher, because of their rougher surfaces. The FLA modes are seen to order m = 3 indicating an interface atomic abruptness comparable to the MBE grown superlattices despite the quite different growth modes (see Fig. 2). This confirms that the overall FLA intensity is governed primarily by interface sharpness. In the UHV-CVD superlattices, where the composition was held at x = 0.5 but the alloy layer thickness was varied, the overall FLA peak intensity increased with increasing alloy layer thickness, but the higher-order (*m* = 2 and 3) FLA modes became more diffuse, indicating some variation in the superlattice period during growth. The FLA peak frequencies decreased.with increasing alloy layer thickness consistent with the increased superlattice periodicity.

Annealing the MBE-grown $Si_{0.515}Ge0_{0.485}$/Si superlattice for 100 s at temperatures from 700 to 850 °C had no observable effect on the optic and acoustic mode Raman spectrum. This indicates the wavy superlattice structure is resistant to interface atomic interdiffusion and strain relaxation under these conditions.

OPTICAL PROPERTIES

Photoluminescence

The photoluminescence (PL) data shown in Fig. 9 for MBE and UHV-CVD samples is similar to that obtained for other samples over the photon energy range from 500 to 1200 meV. Further discussion of the phonon-resolved PL from undulating $Si_{1-x}Ge_x$ layers grown by CVD is contained elsewhere (2). The upper trace in Fig. 9 is the PL of a 3.3 nm thick $Si_{0.55}Ge_{0.45}$ ten-period structure at 5 K for an excitation density of 100 mW/cm^2 at 514 nm. The PL for this and other MBE samples is contained in a broad no phonon (NP) line with no resolved phonon replicas in a manner similar to the strong, "phononless" recombination described by Fukatsu et al. (14) for $Si_{1-x}Ge_x$ quantum dots. The shape of the PL spectra for these MBE samples is also similar to that for the SiGe platelets (15). The PL peak for the MBE samples shifts to lower energy with increasing Ge-fraction (x) as can be observed between the top and middle traces of Fig. 9. The PL peaks shifted to higher energy with increased excitation density due to the fact that crests with highest Ge-fraction, which give the lower energy PL, have an exciton accommodation limit which leads to PL saturation for these crests. At higher excitation densities PL from lower Ge-fraction crests dominates. The spectra in the lower two traces were chosen such that the samples were fairly compatible in structure - one grown by MBE (t(SiGe) = 3.5 nm, x = 0.53) and the other by CVD (t(SiGe) = 3 nm, x = 0.5). As is apparent, the spectra of these two samples differ greatly. Firstly the MBE PL is to much lower energy and is of much higher intensity. The occurrence at lower energy for the MBE material suggests a greater concentration of Ge at the wave crests and/or lower strain there. Furthermore the

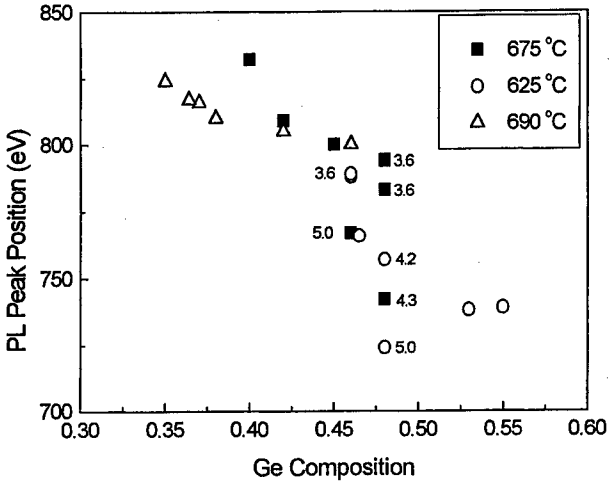


Figure 10. PL peak position as a function of composition for various wavy superlattices, grown by MBE. Numbers on the graph indicate the nominal $Si_{1-x}Ge_x$ layer thickeness in the various superlattices.

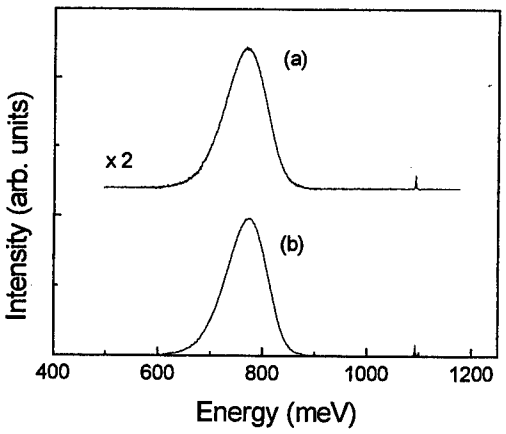


Figure 11. Low- temperature PL spectrum of a 10 period $Si_{0.47}Ge_{0.53}$/Si wavy superlattice, annealed 100 s at 850 °C (a) compared to the as-grown sample (b) PL spectra were recorded at 5K with an excitation power density of 100 mW/cm^2.

peak energy shifts to lower energy compared to planar (parallel interface) layers because of lower confinement energy shifts obtained with undulated structures (2). Secondly, the MBE PL comprises a relatively broad NP line whereas the CVD PL exhibits phonon resolved lines with the NP and TO lines roughly equivalent in intensity. The PL peak position for various MBE grown layers is displayed in Fig. 10. The peak shifts to lower energy for increasing Ge content. Furthermore, for a given composition, the shift is less pronounced in samples with a thinner alloy layer, indicating again a confinement effect.

To investigate the stability of the wavy structure under heat treatment a MBE sample was annealed at various temperatures from 700 to 850 °C for a period of 100 s. Two spectra are shown in Fig. 11 from this set of annealed samples. No significant shifting of the PL peak was observed although the intensity decreased by 50% for the highest temperature. Nonetheless the structure appears to have remained stable under annealing conditions where strain relaxation would probably occur for planar $Si_{1-x}Ge_x$ strain layers with Ge fraction above 0.3.

Photoresponse

In addition to providing information on the room temperature optical absorption, photocurrent spectroscopy is the most relevant measurement for the evaluation of Si/Si_xGe_{1-x} coherent wave and island structures for photodetectors. Figure 12 shows photocurrent spectra measured for two different samples. The first sample consisted of a ten period $Si_{0.5}Ge_{0.5}$/Si coherent wave superlattice grown by UHV-CVD on a conventional Si substrate with a thick Si cap layer to help planarize the surface. This wafer was fabricated into a waveguide MSM photodetector with a geometry to be described elsewhere. The second sample was a MBE grown $Si_{0.5}Ge_{0.5}$/Si superlattice, also grown on a conventional Si substrate. It was not possible to collect photocurrent spectra in the 1350 nm to 1480 nm range on these non-waveguide samples, since the photocur-

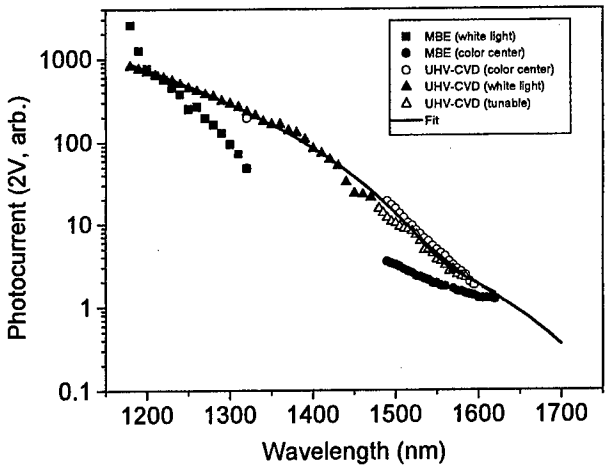


Figure 12. Photocurrent response measured at 2V bias voltage for one MBE grown island superlattice and one UHV-CVD wavy superlattice. The solid curve is a fit of the UHV-CVD sample photocurrent using Eq. (1).

rent noise floor was much larger due to the large dark current flowing in the Si substrate. This can be eliminated by growing the superlattice on a silicon-on-insulator (SOI) wafer or incorporating it into a p-i-n diode geometry.

The photocurrent spectra near an absorption edge can be modeled using a simple polynomial expression of the form

$$I(E)= C(E-E_g)^n, \qquad (1)$$

where E is the photon energy and E_g is the absorption edge energy (16,17). A summation of such terms may be used if more than one optical band edge is involved. For indirect materials the exponent n is expected to be 2, but values obtained for $Si_{1-x}Ge_x$ superlattices vary between 2 and 4 (16,17). In any case, our thickness modulated superlattices have a band edge that will vary from point to point, so the fitted value of n should be regarded as a purely empirical parameter. On the other hand, the transition energy E_g gives an unambiguous determination of the room temperature absorption edge. In Fig. 12, the CVD data is fit quite well by a sum of two expressions of the form given in Eq. (1), one with E_g=0.785 eV, and a second much weaker contribution with an effective absorption edge at E_g=0.68 eV. This is consistent with previous PL measurements on these wafers (2) which indicate a minimum band gap of 0.787 eV at 4.2 K. The photocurrent result establishes that these CVD samples have a room temperature absorption edge well below 0.8 eV. The second transition energy may correspond to local areas of very high Ge concentration in the $Si_{1-x}Ge_x$ islands, or possibly defect mediated photocurrent generation. However, no evidence of crystal defects appears in the previous TEM and PL characterization of this wafer.

The photocurrent spectrum from the MBE sample has a very different shape. A higher energy absorption edge near 0.9 eV ($\lambda \sim$ 1380 nm) is evident, followed by a strong

absorption tail at wavelengths extending past λ=1600 nm. We attribute this to the fact that, unlike the CVD superlattices, this structure clearly exhibits the island/wetting layer geometry of the Stranski-Krastanow growth mode. Our preliminary interpretation is that the low energy tail corresponds to the high Ge concentration regions near the centre of the SiGe islands, while the 0.9 eV edge corresponds to absorption in the thinner wetting layer. Finally, by measuring the optical power coupled into the waveguide metal-semiconductor-metal photodetector, the absolute photocurrent quantum efficiency was determined. At λ = 1550 nm the measured quantum efficiency for the 240 mm long waveguide detector was approximately 0.1 A/W at 1550 nm.

CONCLUSION

Wavy $Si_{1-x}Ge_x$/Si superlattices can be obtained by both MBE and UHV-CVD. In MBE, a high growth temperature (above 600 °C, for typical MBE growth rates) is required to allow morphological instabilities to take place. The resulting morphology is the formation of pyramidal shape $Si_{1-x}Ge_x$ islands, whose size decreases with increasing growth temperature. This rough morphology is suppressed by deposition of thin Si spacer layers, but is recovered after subsequent deposition of another $Si_{1-x}Ge_x$ layer. The existence of sharp $Si_{1-x}Ge_x$ to Si interfaces and the vertical alignment of the $Si_{1-x}Ge_x$ islands preserve the superlattice character of the structures which is reflected in x-ray diffraction and x-ray reflectivity. Despite the presence of wavy interfaces, the chemical abruptness is also preserved as evidenced by the observation of strong FLA modes in Raman scattering. In the UHV-CVD case, the wavy superlattices are obtained in a very different growth regime. Despite a lower growth rate, low Si adatom mobility on the surface prevents the interfaces flattening during growth of the spacer layers. The low adatom mobility would also explain the cumulative roughening observed during growth. The observation of stronger FLA modes is also consistent with a low surface mobility restricting interdiffusion at the interfaces. The Raman scattering of optic modes in the wavy superlattices differ from those seen in flat superlattices, despite the fact that the wavy superlattices do not exhibit structural defects. This is consistent with a redistribution of the strain in the wavy layers that would cause a periodic modulation of the lattice constants in the plane of growth.

The PL properties of the MBE and UHV-CVD wavy superlattices differ considerably. In MBE samples, the $Si_{1-x}Ge_x$ islands are better defined and the PL signal arises from a phononless recombination mechanism. The PL peak position is also seen at energies below the band gap energy for coherently strained $Si_{1-x}Ge_x$ alloy layers of same composition. This suggests a concentration of Ge greater in the islands than the nominal Ge concentration and is consistent with local relaxation of the strain in the alloy. Some quantum confinement shifts are also seen for wavy superlattices with small (<3 nm) $Si_{1-x}Ge_x$ nominal layer thickness. The PL spectrum from UHV-CVD samples exhibits phonon resolved lines with the NP line appearing at a lower energy than a strained flat alloy layer of the same composition, but at a higher energy than in a MBE sample of identical Ge concentration. This would suggest that less Ge migration and strain reduction occur at the $Si_{1-x}Ge_x$ crests in UHV-CVD superlattices. Both types of structures exhibit promising properties for optical absorption at 1.5 μm, but further work is required to optimize the materials properties and the design of the photodetectors operating at optical communication wavelengths.

REFERENCES

(1) R.A. Soref, Proc. IEEE, **81**, 687 (1993).

(2) H. Lafontaine, N.L. Rowell, and S. Janz, Appl. Phys. Lett. **72**, 2430 (1998).

(3) D.-X Xu, S. Janz, H. Lafontaine, and M.R.T. Pearson in *Silicon-Based Optoelectronics*, Derek C. Houghton, and Eugene A. Fitzgerald, Editors, Proceedings of the SPIE Vol. **3630**, pp.50-57 (1999).

(4) J.-M. Baribeau, T.E. Jackman, D.C. Houghton, P. Maigné, and M.W. Denhoff, *J. Appl. Phys.*, **63**, 5738 (1988).

(5) J.-M. Baribeau, D.J. Lockwood, M.W.C. Dharma-wardana, N.L. Rowell, and J.P. McCaffrey, *Thin Solid Films*, **183**, 17 (1989).

(6) H. Lafontaine, D.C. Houghton, D. Elliott, N.L. Rowell, J.-M. Baribeau, S. Laframboise, G.I. Sproule, and S.J. Rolfe, *J. Vac. Sci. Technol.*, **B 14**, 1675 (1996).

(7) H. Lafontaine, D.C. Houghton, B. Bahierathan, D.D. Perovic, and J.-M. Baribeau, *Mater. Res. Soc. Symp. Proc.*, **399**, 413 (1995).

(8) D.J. Lockwood, M.W.C. Dharma-wardana, J.-M. Baribeau, and D.C. Houghton, *Phys. Rev. B* **35**, 3243 (1987).

(9) A.G. Cullis, D.J. Robbins, S.J. Barnett, and A.J. Pidduck, *J. Vac. Sci. Technol.*, **A 12**, 1924 (1994).

(10) J.-M. Baribeau, *J. Cryst. Growth*, **157**, 52 (1995).

(11) J.-M. Baribeau and H. Lafontaine, *Thin Solid Films*, **321**, 141 (1998).

(12) J.-M. Baribeau, D.J. Lockwood, and R.W.G. Syme, *J. Appl. Phys.*, **80**, 1450 (1996).

(13) Y.H. Phang, C. Teichert, M.G. Lagally, L.J. Peticolas, J.C. Bean, and E. Kasper., *Phys. Rev. B*, **50**, 14435 (1994).

(14) S. Fukatsu, H. Sunamura, Y. Shiraki and S. Komiyama, *App. Phys. Lett.*, **71**, 258 (1997).

(15) J.-P. Noël, N.L. Rowell, and D.C. Houghton, *Appl. Phys. Lett.*, **57**, 1037 (1990).

(16) T.P. Pearsall, L. Colace, A. DiVergilio, W. Jager, D. Stenkamp, G. Theodoru, H. Presting, E. Kasper, and K. Thonke, *Phys. Rev. B*, **57**, 9128 (1998).

(17) B. L. Colace, A. DiVergilio, S. Vaidyanathan, T.P. Pearsall, H. Presting, and E. Kasper, *Appl. Surf. Sci.*, **102**, 272 (1996).

FIRST PRINCIPLE CALCULATIONS OF THE OPTICAL PROPERTIES OF SI QUANTUM WELLS

Stefano Ossicini and Elena Degoli
Istituto Nazionale per la Fisica della Materia (INFM) and
Dipartimento di Fisica, Universita` di Modena e Reggio Emilia,
via Campi 213/A, I-41100 Italy

ABSTRACT

The electronic and optical properties of Si based multiple quantum wells (QW's) are studied *ab initio* by means of the linear-muffin-tin-orbital method in order to investigate their dependence on the simmetry of the lattice and on the passivating species that saturates the Si dangling bonds. We find that the simmetry of the lattice changes the nature of the gap that is indirect in the Si-H(111) saturated QW's and becomes direct in the Si-H(001) saturated QW's. Changing the saturating species we show that they play an important role in the formation of interface states that can occupy or leave free the band gap so improving or making worse the optical properties of the material. In the case of the Si-CaF_2(111) and Si-SiO_2(001) QW's the results for the optical properties are compared with the experimental outcomes on absorption and photoluminescence for similar systems. In particular, studying the Si-SiO_2(001) superlattices we found that oxigen related defects play an important role in the determination of the optoelectronic properties of the material.

I. INTRODUCTION

The recent developments in communication systems and computer technology make increasingly attractive the substitution of electrons with photons in the transmission and elaboration of data. One of the main direction of research in the field of photonic applications is to develop efficient Si-based emitters. Such devices would enable optoelectronic circuitry to be based entirely on Si, since it has been demonstrated the feasibility of the other required Si-based devices (detectors,waveguides, modulators, etc.) [1]. Efficient Si-based emitters cannot be obtained from crystalline Si, since it is an indirect-bandgap semiconductor which emits light in the infrared and at very low efficiencies. Nevertheless the desire for the integration of optoelectronic devices with silicon microelectronics has stimulated an intense effort to search Si-based materials that emit light efficiently.

In 1990, the demonstration of efficient visible photoluminescence from porous silicon and its attribution to quantum confinement effects [2] has resulted in an enormous interest in the optoelectronic properties of confined silicon systems [3]. Si-based quantum wells are a prototype, microscopically controlled, of a quantum confined system as those present in porous silicon and actually, photoluminescence in Si-CaF_2(111) and Si-SiO_2(001) QW's has already been predicted [4] and observed [5,6,7,8,9].

In this work we investigate the physical properties of 2D low-dimensional Si systems saturated with H, CaF_2 and SiO_2, through *ab-initio* calculations of their electronic and optical properties. The self-consistent electronic structures of the QW's are calculated by means of the Linear Muffin-Tin Orbital method in the Atomic-Sphere Approximation (LMTO-ASA) within the supercell technique. Exchange and correlation effects are included within the Density Functional Theory in the Local Density Approximation (DFT-LDA). Due to the LDA we underestimate the energy gaps: in bulk Si, for example, we obtained a gap of 0.56 eV instead of the experimental value of 1.1 eV. Once the self-consistent electronic properties have been calculated, the optical functions have been computed by evaluating the dipole matrix elements that allow to obtain directly the imaginary part of the dielectric function ε_2, in the dipole approximation. The ε_2, that actually contains the various inter-band transitions weighted by the momentum optical matrix element, can give informations directly on the absorption process and indirectly about the photoluminescence processes throught its features.

All the silicon multi-quantum wells are studied to elucidate: i) the role of dimensions, using different thickness of the silicon embedded layers, ii) the role of simmetry, considering both (111) and (001) silicon surfaces passivated with hydrogen, and iii) the role of different passivating agents like CaF_2 or SiO_2 at the Si interface. The study of these superlattices is also interesting because it is possible to compare our results with recent experimental results [5,6,7,8,9], in order to evidentiate the role of calcium, of oxigen, and of oxigen related defects on the optoelectronic properties of the Si QW's.

The paper is organized as follow: in chapter 2 we present and discuss our results for the electronic and optical properties of Si-H multi-quantum wells. Chapters 3 and 4 are devoted to the optical and electronic properties of the Si-CaF_2 and the Si-SiO_2 superlattices and the last section is addressed to the conclusions.

II. THE ELECTRONIC AND OPTICAL PROPERTIES OF THE Si-H QUANTUM WELLS

We have performed calculations for the electronic properties of several ultrathin Si-H(111) [12] and Si-H(001) wells.

In order to elucidate the role of quantum confinement (QC), we have considered wells of different thickness, between 0.5 and 2.5 nm, choosing a variable number of Si double layers (DL's) in the well. A blue shift of the band gap due to the QC is evident in each system, as we can see from the gap values for the different structures collected in Table I.

Concerning the role of passivation we observed that the H-Si bond, being mostly covalent, gives rise to a large bonding-anti-bonding energy separation and pushes the interface states well inside the Si valence and conduction bands leaving the energy gap free of states and enhancing the gap opening. Contrary to this, the bonding-antibonding states in the Si/CaF_2(111) systems [4,10,11,12] were not completely removed from the gap thus reducing it with respect to the H-saturation case.

The role of simmetry has been investigated considering both (111) and (001) silicon surfaces passivated with hydrogen. The indirect gap observed in the first case [12] become direct in the second direction of growth throught the folding that shifts the conduction band minima at the Γ point. Figure 1 shows this direct band gap at the Γ point, for the Si-H(001) QW with 5 layers of Si, throught its band structure projected along 2 symmetry directions of the two-dimensional Brillouin zone of the (001) surface.

Figures 2 and 3 show the imaginary part of the dielectric function for the Si-H(111) and Si-H(001) QW's, respectively, for different thicknesses of the Si slab compared with the ε_2 calculated for bulk Si. A decreasing of the main peak due to bulk Si is evident in both cases as evident is, in Fig. 3, the presence of new structures in the energy region between 1.0 an 2.0 eV (this is the visible range if we consider the underestimation of the gap due to the local density approximation) totally absent in bulk Si and in Si-H(111) lattices too: the direct band gap of the (001) H-saturated case originates more intense transitions, in the visible range than the indirect one observed in the (111) structures. This result supports the idea that symmetry considerations can play an important role for the optical response of confined Si wells.

III. THE ELECTRONIC AND OPTICAL PROPERTIES OF THE Si-CaF_2(111) QUANTUM WELLS

In the case of Si-CaF_2(111) QW's the calculated electronic properties show that the opening of the gap due to the confinement is less effective than for the H-Si systems [4,10,11,12] (see Table II).

It should be noted that the Si-Ca bond at the interface is somewhat intermediate between the covalent Si-Si bond and the ionic Ca-F bond, therefore the bonding-antibonding interface states are not completely removed from the gap as in the case of the H-saturated structures. The H-Si bond, being mostly covalent, gives rise instead to a larger bonding-antibonding energy separation and pushes the interface states inside the Si valence band and above the conduction band minimum, thus the gap region is, in this case, free of interface states. For the Si-CaF_2 QW's, even for the thicker slab, the bulk-like situation is not recovered: an interface state appears just below the conduction band at Γ, together with an interface state in the valence band region that becomes the highest valence state in the thinner slabs (1 DL and 2 DL's). These two interface states are the bonding-antibonding states resulting from the Ca-Si bond at the interface.

These electronic properties are reflected in the optical results. In Fig. 4 we show the dependence of our calculated imaginary part of the dielectric function ε_2 on the thickness of the Si slab embedded in CaF_2. For comparison we report also our ε_2 result for bulk Si (solid line). We note a reduction of the maximum value for ε_2. This reduction follows exactly the lowering in thickness of the Si slab and it is due to the QC effect. More important for our discussion is the low energy region (between ~1 eV and ~2.5 eV). Here new features appear (which are completely absent in the case of bulk Si). If we take into account the LDA underestimation of the Si energy gap, this is the optical region of interest. In order to enucleate the transitions which play an important role in this low energy region we show in Fig. 5 (for the 2 DL's Si case) the total ε_2 (solid line) together with the contributions due to the transitions from the last valence band to the first conduction band (small dashed line) and from the last two valence bands to the first two conduction bands (long dashed line). From the figure it is evident the predominant role played by the band edges and in particular by the interface states in the optical region; we remember that for very thin Si slabs the last occupied and the first unoccupied states are mostly related to the interface states. The origin of the peaks of ε_2 in this region is related to the presence of significant matrix elements between particular states which are located at, or just below, the top of the valence band and at, or just above, the bottom of the conduction band. It is worthwhile to note that the oscillator strengths for the matrix elements between these states increase very rapidly as the thickness of the Si slabs decreases. For layers with thickness less than 2.5 nm the oscillator strengths are of the same order of magnitude as for the direct transition at Γ in bulk Si and only one order of magnitude smaller than those for GaAs. We remember that the experimentally grown Si-CaF_2 QW's show photoluminescence only for Si thickness less than 2.5 nm [5,6].

Figure 6 shows the comparison between our calculated absorption spectra and the experimental data [6]. A striking resemblance between the two results is evident. In both cases we observe a blue shift of the onset and a decrease of the optical absorption with decreasing Si thickness.

IV. THE ELECTRONIC AND OPTICAL PROPERTIES OF THE Si-SiO2(001) QUANTUM WELLS

We have also studied the Si-SiO_2 quantum wells, not only to elucidate the behaviour of this new passivating agent but also: i) to evidentiate the role of oxigen and oxigen related defect in the optoelectronic properties of this superlattice structures and ii) to compare our theoretical results with the experimental data of Lockwood [7] Novikov [8] and Mulloni [9]. For the Si-SiO_2 confined quantum wells we use the β-cristobalite model for the SiO_2 with 2 O atoms added at the two interfaces in order to saturate the dangling bonds of the Si atoms at the center of the interfaces. To study the role of the oxigen related defects we have introduced a defect in the Si/SiO_2 lattice, leaving one of the O-double bonded Si interface atoms unsaturated.

Figure 7 compares the band structure for the fully saturated (top panel) and partially saturated (bottom panel) lattice. In the first case we notice that the system is still a semiconductor with a band gap larger than in the case of bulk silicon as consequence of the confinement. A localized state, partially due to O-Si interaction, is found near the top of the valence band. In the second case we observe the appearence of a new state in the band structure at the top of the valence band, that was absent in the fully saturated lattice. This defect state produces a closing of the gap (from 0.82 eV to 0.70 eV) that is still indirect but with the top of the valence band at a different k-point in the reciprocal space. Nevertheless, the material is still a semiconductor; this situation is quite different from that of H-covered Si quantum dots and wires, where the presence of only one dangling bond destroys the optical properties of the material in the visible region [13,14,15].

Figure 8 shows the imaginary part of the dielectric function calculated for the lattice with no defect and for that without one saturating oxigen both compared with the ε_2 of bulk Si. The analysis of the optical properties both for the fully saturated structure and for the quantum wells with the inclusion of one defect evidentiates the presence of several peaks in the low energy optical region (between 1.0 and 2.2 eV) that are absent in bulk Si.

To have a better comparison with the experimental data on photoluminescence we show in Fig. 9 our calculated oscillator strength for the transitions at the Γ point (including a shift toward higher energies of 0.8 eV in order to overcome our underestimation of the gap due to the LDA) for the two lattice with (top panel) and without (bottom panel) defects. We note the presence of intense optical matrix elements whose onset is located at 1.7 and 1.85 eV for the two considered systems, thus in good agreement with the experimental observations [7,8,9]. These results seems to confirm the idea that photoluminescence peaks experimentally observed are due to two mechanisms: confinement effects and oxigen related defects.

CONCLUSIONS

We have presented and discussed theoretical results for the electronic and optical properties of 2D confined Si structures. Our calculations and the comparison with available experimental data indicate that simmetry and surface passivation are important in the determination of the optical properties.
In particular we have shown that the correct choise of the crystal simmetry and a good passivation of the Si dangling bonds at the surfaces improve the optical properties in the visible range, moreover we have shown that the oscillator strengths for the transitions at the onset of absorption increase very rapidly for Si well thickness less than 2.5 nm. In the case of Si-SiO_2 QW's we have shown that photoluminescence can arise both from quantum confinement and oxigen related defects.

ACKNOWLEDGEMENTS

This work has been carried out within the european projects ESPRIT MEL ARI n. 28741 SMILE and INCO-Copernicus n. 977037 SBLED, the italian CNR MADESS project n.97.013575.PF48, the italian MURST project n. 9702178261, and has benefited from collaborations within the Network on "Ab-initio (from electronic structure) calculation of complex processes in
materials" (contract: ERBCHRXCT930369).The calculations have been performed at CICAIA, University of Modena and at CINECA, Bologna.

REFERENCES

[1] R.A.Soref, Silicon-Based Optoelectronics, Proceedings of the IEEE, Vol. 81, N.12, Dec. 1993, p.1687-1706;
[2] L. T. Canham, Appl. Phys. Lett. 57, 1046 (1990);
[3] Optical Properties of Low Dimensional Silicon Structures, edited by D. Bensahel, L.T. Canham, and S. Ossicini, Kluwer, Dordrecht (1993);
[4] S. Ossicini, A. Fasolino and F. Bernardini, Phys. Rev. Lett. 72,1044 (1994);
[5] F. Arnaud D'Avitaya, L. Vervoort, S. Ossicini, A. Fasolino and F. Bernardini, Europhys. Lett. 31, 25 (1995);
[6] F. Bassani, I. Mihalcescu, J. C. Vial, F. Arnaud D'Avitaya, Appl. Surf. Sci. 117/118, 670 (1997);
[7] D. J. Lockwood, Z. H. Lu and J.-M. Baribeau, Phys. Rev. Letters 76, (1996) 539;
[8] S. V. Novikov, J. Sinkkonen, O. Kilpelä, S. V. Gastev, J. Vac. Sci. Technol. B 15, (1997) 1471.

[9] V. Mulloni, R. Chierchia, C. Mazzoleni, G. Pucker, L. Pavesi and P. Bellutti (submitted to Philosophical Magazine B);
[10] E. Degoli and S. Ossicini, Phys. Rev. B 57, 14776 (1998);
[11] E. Degoli and S. Ossicini, J. of Luminescence 80/1-4, 411-415 (1999);
[12] S. Ossicini, A. Fasolino and F. Bernardini, Phys. Stat. Sol. (b) 190, 117 (1995);
[13] C. Delerue, G. Allen and M. Lannoo, Phys. Rev. B 48, 11024 (1993);
[14] S. Ossicini, C. M. Bertoni, M. Biagini, A. Lugli, G. Roma, O. Bisi, Thin. Sol. Films 297, 154 (1997);
[15] S. Ossicini, Phys. Stat. Sol. (a) 170, 377 (1998).

Table I: Si layer thickness and calculated energy gaps for the different considered Si-H(111) and Si-H(001) QW's.

Si-H(111)		Si-H(001)	
Thickness (nm)	Gap (eV)	Thickness (nm)	Gap (eV)
1.95 (6 DL's)	0.86	1.28 (4.5 DL's)	0.86
1.01 (3 DL's)	1.22	0.73 (2.5 DL's)	1.07
0.70 (2 DL's)	1.78	0.46 (1.5 DL's)	1.57
0.39 (1 DL's)	2.38		

Table II: Si layer thickness and calculated energy gaps for the different considered Si-CaF_2(111) QW's.

Si-CaF_2(111)	
Thickness (nm)	Gap (eV)
2.44 (7 DL's)	0.56
1.49 (4 DL's)	0.63
0.87 (2 DL's)	1.24
0.55 (1 DL's)	0.76

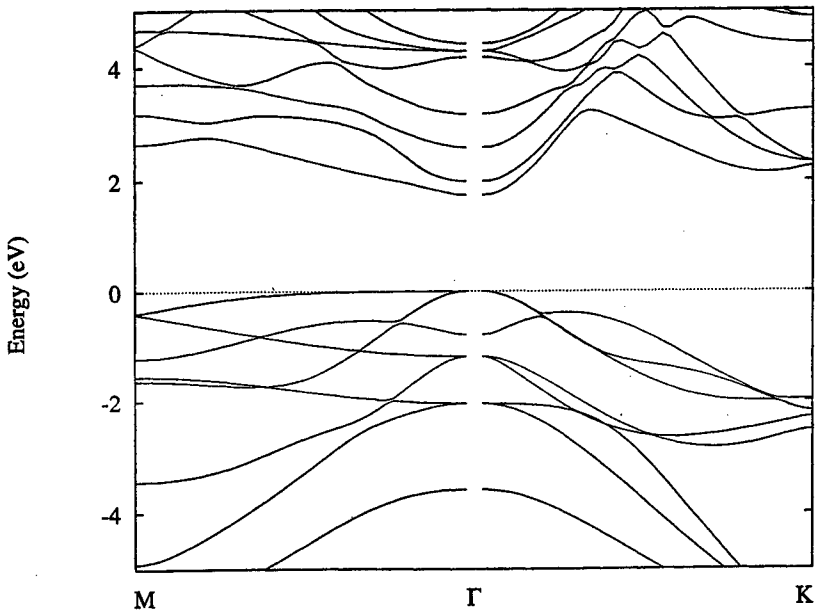


Figure 1: Band structure of the Si-H(001) lattice with 2.5 double layers of silicon projected along two simmetry directions of the two-dimensional Brillouin zone of the (001) surface. Energies (in eV) are refered to the valence band maximum.

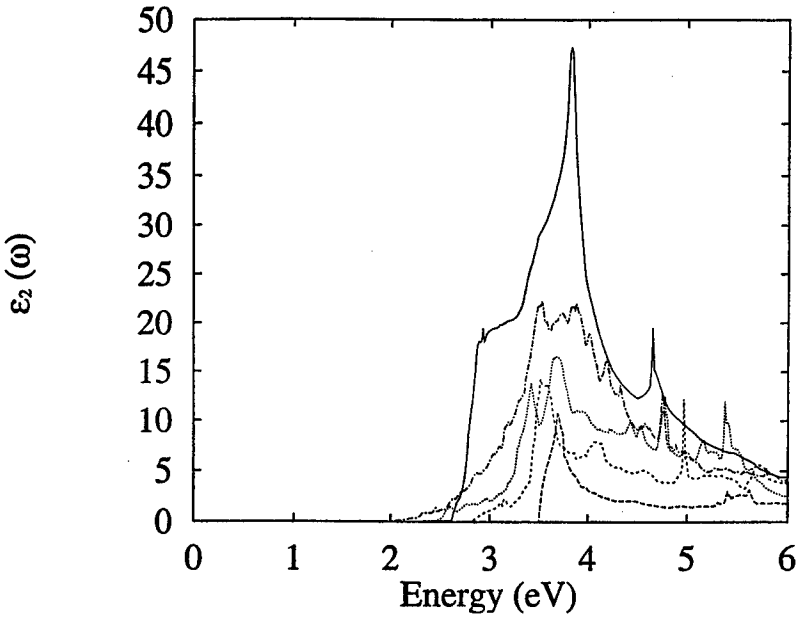


Figure 2: The imaginary part of the dielectric function ε2 for the Si-H(111) systems. Dot-dashed line: 6 Si DL's, dotted line: 3 Si DL's, small dashed line: 2 Si DL's, large dashed line: 1Si DL's. The values are compared with that of bulk Si: solid line.

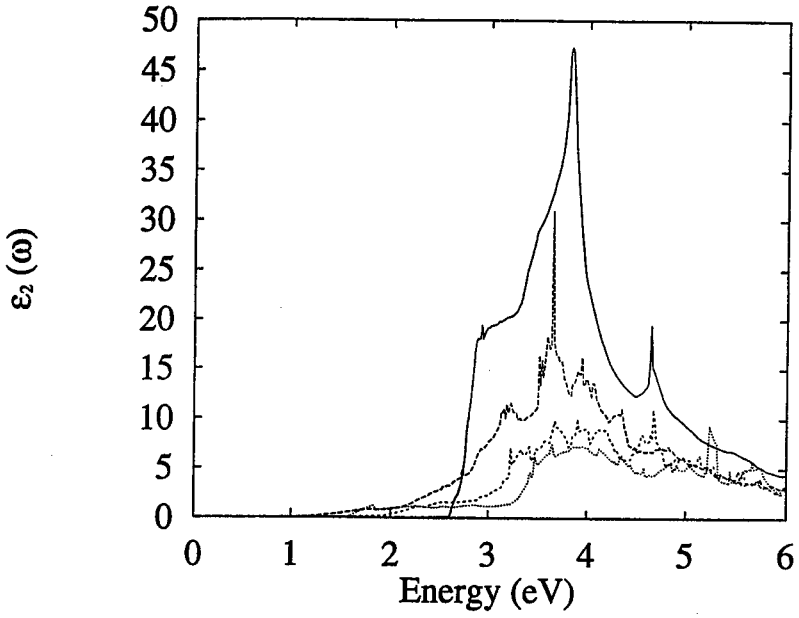


Figure 3: The imaginary part of the dielectric function ε2 for the Si-H(001) systems. Large dashed line: 4.5 Si DL's, small dashed line: 2.5 Si DL's, dotted line: 1.5 Si DL's. The values are compared with that of bulk Si: solid line.

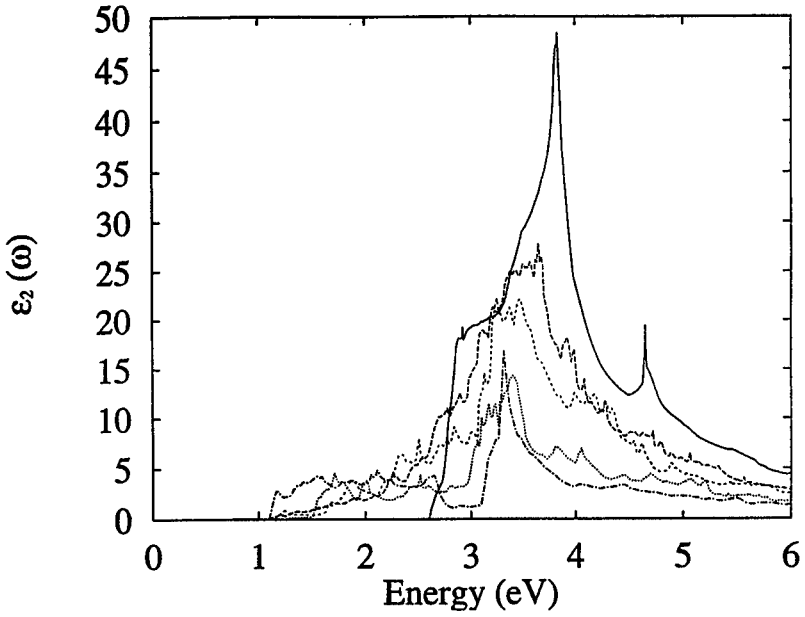


Figure 4: The imaginary part of the dielectric function ε2 for the Si-CaF_2(111) systems. Large dashed line: 7 Si DL's, small dashed line: 4 Si DL's, dotted line: 2 Si DL's, dash-dotted line: 1 DL. The values are compared with that of bulk Si: solid line.

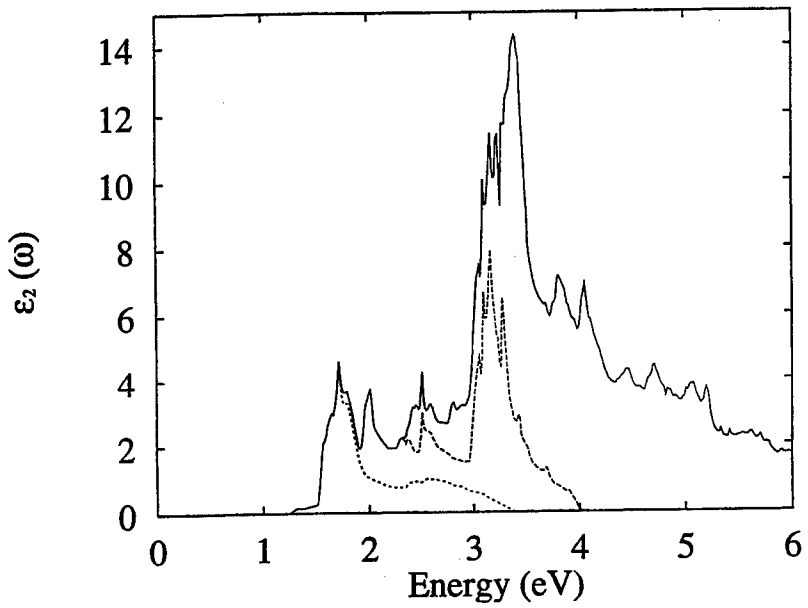


Figure 5: The most important interband contributions to ε_2 for 2 DL's Si-CaF_2 QW's. Solid line: total ε_2, small dashed line: contribution from the transitions between the last occupied state and the first unoccupied one, large dashed line: the same considering the last two occupied states and the first two empty states.

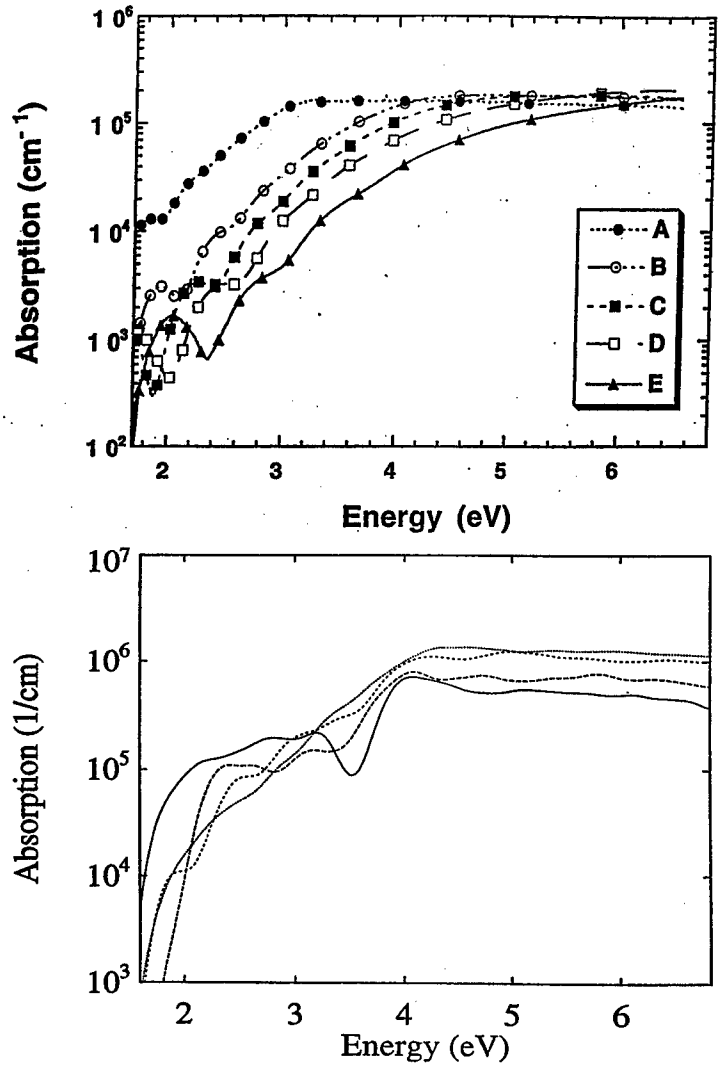


Figure 6: The absorption coefficient for the Si-CaF_2(111) systems. Top panel: experimental results from Ref. [6]; (A) Si thickness 5 nm, (B) 2 nm, (C) 1.6 nm, (D) 1.5 nm, (E) 1 nm. Bottom panel: theoretical results; large dashed line:7 Si DL's, small dashed line: 4 Si DL's, dotted line: 2 Si DL's, dash-dotted line: 1 DL.

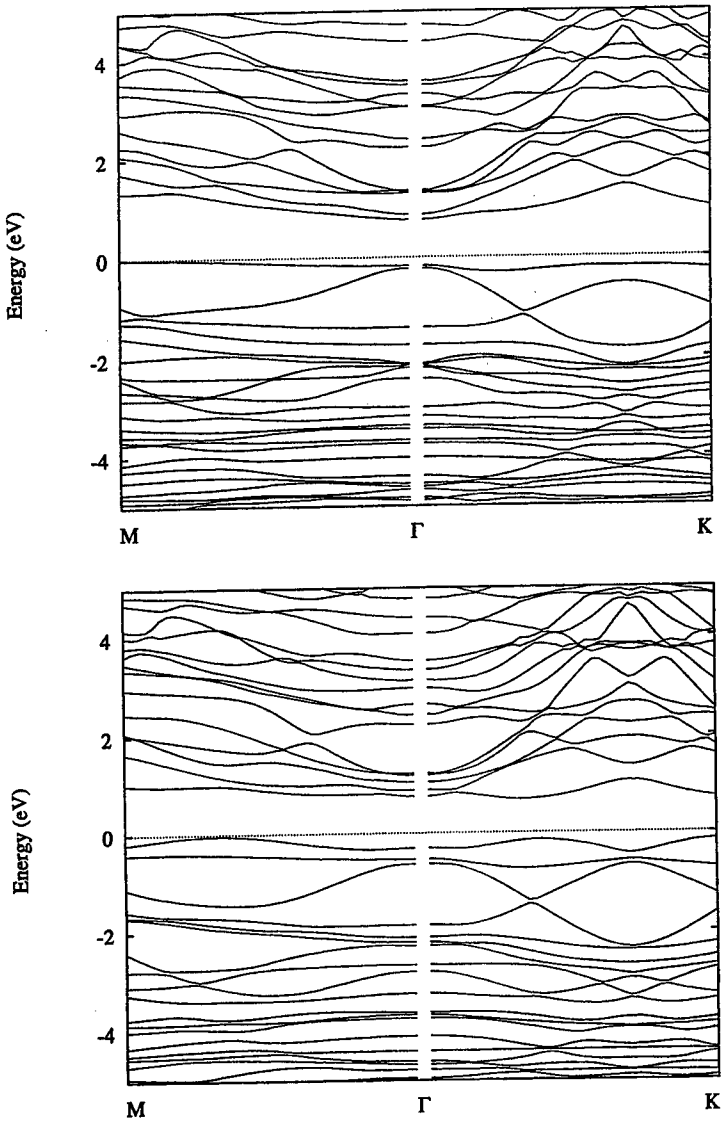


Figure 7: Band structure of the fully saturated (top panel) and partially saturated (bottom panel) Si-SiO2(001) lattice projected along two simmetry directions of the two-dimensional Brillouin zone of the (001) surface. Energies (in eV) are refered to the valence band maximum.

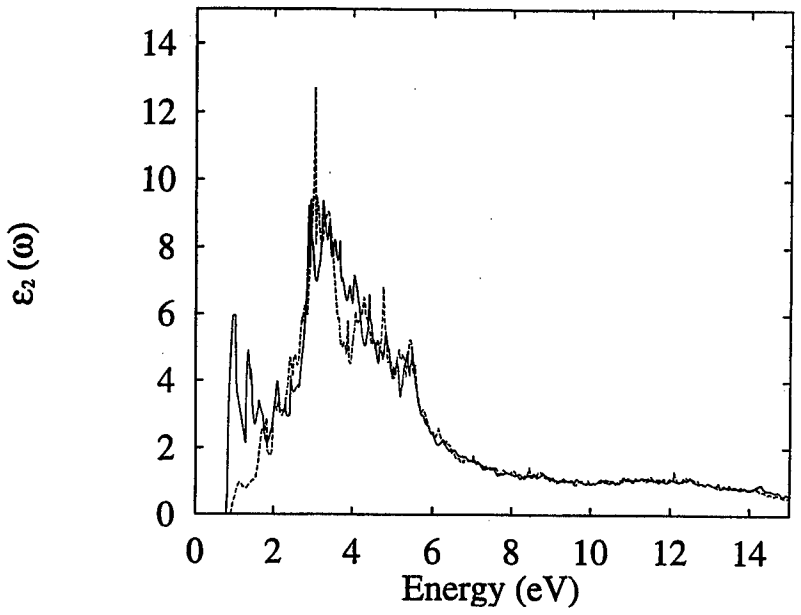


Figure 8: The imaginary part of the dielectric function ε2 for the Si- SiO_2(001) systems. Large dashed line:fully saturated lattice, solid line: partially saturated lattice.

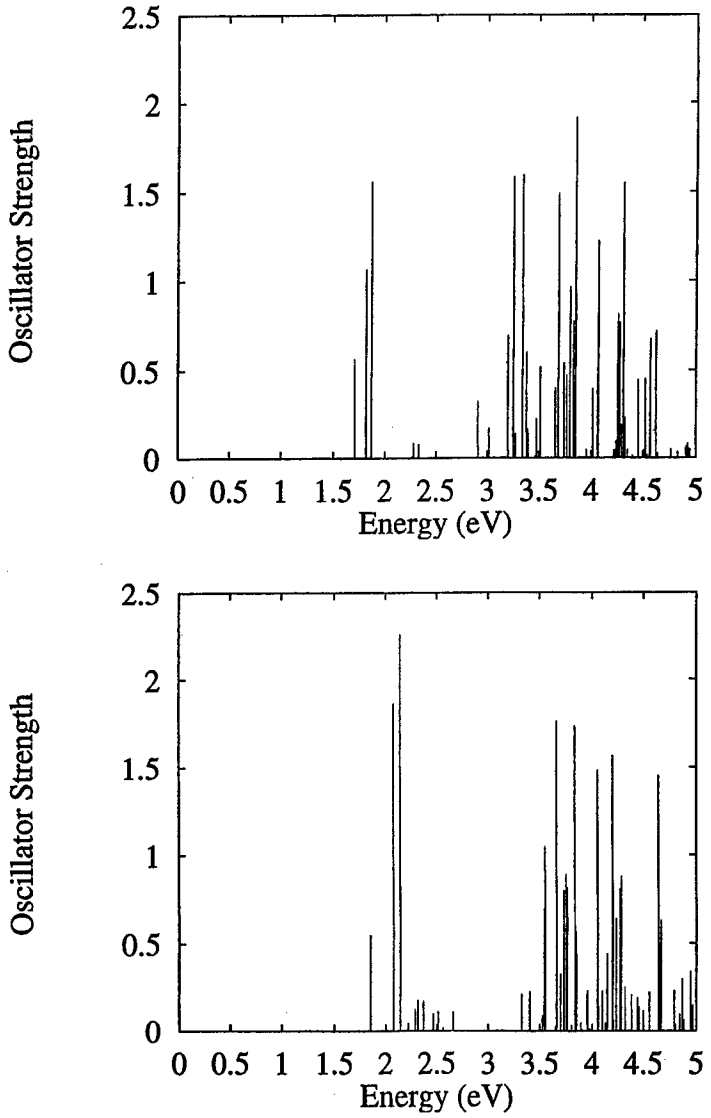


Figure 9: The oscillator strengths at the Γ point for the Si- SiO_2(001) systems. Top panel: fully saturated lattice, bottom panel: partially saturated lattice.

MODIFICATIONS OF THE LIGHT EMITTED WITHIN AN ANISOTROPIC 3-DIMENSIONAL PHOTONIC CRYSTAL

S.G. Romanov
Department of Electronics and Electrical Engineering, University of Glasgow, Glasgow, G12 8QQ, UK and
Ioffe Physical Technical Institute
194021, St.Petersburg, Russia

M. Müller and R. Zentel
Institute of Materials Science and Department of Chemistry, University of Wuppertal, 42097 Wuppertal, Germany

T. Maka and C. M. Sotomayor Torres
Institute of Materials Science and Department of Electrical Engineering, University of Wuppertal, 42097 Wuppertal, Germany

ABSTRACT

Anisotropic photonic crystals based on opals and TiO_2 coated opals have been prepared by impregnating opal matrices with dye/rare earth ion-containing polymers. The emission properties have been studied by angle resolved photoluminescence measurements. Despite the low refractive index contrast in the composites, the significant changes of the emission properties in accord with the anisotropic photonic bandgap structure of material have been observed. The spectrum of the spontaneous emission rate has been found following the local profile of the density of photonic states. Two competitive mechanisms were suggested to contribute to the spontaneous emission enhancement – the photonic bandgap structure and the localisation of photons.

INTRODUCTION

Among many approaches to improve the effectiveness of the light emitting devices the key one is to control the density of optical modes in the emission frequency range [1]. In particular, 3-dimensional photonic bandgap (PBG) crystals can be used to extend and enhance the functionality of LEDs and lasers.

In order to take advantage of PBG structures light emitting devices have to be designed as a spatially extended light source integrated with a 3-dimensional photonic crystal. The promising design implies the separation of functions of the light source and the photonic template. Accordingly, the approach under investigation here uses 3D photonic templates infilled with a light emitting material [2]. Two separate issues were

addressed. The first one is the choice of the appropriate light source. Dyes or rare-earth ions are seen as good candidates to study their performance in a PBG environment because they are the effective light emitters and the energy separation between their absorption and emission bands is large. Another issue is the design of a template. Opals, which are nearly crystalline ensembles of closely packed silica balls, were used as 3D quasi-PBG structures. Anticipating the prospects of practical applications, the PBG light sources have to be solid materials ready for mechanical shaping, contacting, etc. To ensure mechanical strength of these materials, dye/rare earth additives were dissolved in a polymer, then solutions were soaked by opals and polymerised in opal voids. However, the refractive index (RI) contrast between the silica-based opal structures ($n \approx 1.45$) with the polymer in their voids ($n \approx 1.5$) is apparently too low to modify significantly the emission rate of these light emitting species. An attempt of an increasing the RI contrast in such a composite photonic crystal was made by coating the internal surface of the opal with titanium dioxide prior to embedding with polymer.

In the low-RI contrast limit the emission properties of dye-doped opals were studied both in continuous wave and pulse regimes of the excitation [3,4,5]. The common features revealed in these experiments are the anisotropic PBG, suppression of the dye emission within the frequency range of the overlap with the stop-band and the line narrowing under the intense pulse excitation. However, the time-resolved analysis of the decay dynamics gives rise to the intensive debate whether it is possible to detect the change in the emission rate in highly anisotropic PBG environment [5,6]

The problem to be studied is how different is the response of the light emitting material in a PBG environment when emitters possess a broad or narrow emission band. It is believed that a narrowband emission spectrum, the bandwidth of which is less than the bandgap width, would be more vulnerable to the PBG environment compared with the opposite case of an emission band broader than the stop-bandwidth. However, the emission spectrum of most rare earth ions possessing radiative transitions in the visible consists of several lines and the interference of the one of these with the PBG structure may cause changes in the emission of other lines.

The aim of this paper is to discuss the change in the emission properties of dye/rare earth ion light sources caused by their embedding in an anisotropic PBG environment.

EXPERIMENTAL TECHNIQUE

The samples under study were thin platelets of opal nanocomposites with the (111) plane of the ball package facing the wider side. Bare opal is denoted thereafter as the Air-opal and filled opal – the "infill-name"-opal. The transmission and reflectance spectra were measured by illuminating the sample with monochromatic light and detecting the scattered light within a 0.0012π *sr* fraction (or about 2°) of a solid angle. The angular dispersion of the Bragg diffracted light was studied by measuring reflectance spectra at different angles θ between the (111) direction of opal and the beam axis. The similar Bragg configuration was used with photoluminescence (PL) excited by laser radiation using front, back and side window configurations, denoted as FW, BW and SW, respectively. In the FW configuration the PL was excited and collected from the same surface, whereas the BW PL was excited on the front sample surface and collected from the back surface after travelling inside the material. In SW configuration PL was excited through the front surface and collected from the cleaved edge of the sample. The angle

was varied between $\theta = 0°$ and $40°$ and PL was collected within 0.0035π *sr* solid angle formed by a collimating diaphragm placed between the sample and the spectrometer.

Changes in the light diffraction from bare and infilled opals in (111) direction in the *fcc* opal structure have been quantified using the Bragg law $\lambda_{(111)} = 2n_{eff}\,0.816D$, where n_{eff} is the effective refractive index of the composite and D the diameter of opal balls. The n_{eff} was determined using the effective medium approximation $n_{eff} = n_{Opal} f + n_{air}(1-f)$, where f_i, n_i are the volume fraction and RI of the components, respectively [7,8].

COUMARIN 6-POLYMER-OPAL

A solution of 1 wt.% of coumarin 6 and 1 wt.% of the photoinitiator diphenyl(2,4,6-trimethylbenzoyl)phosphine oxide in diehtylene glycol dimethacrylate was droped to the opal. 10 minutes later the impregnated opal was irradiated with UV light to transform the dye solution into a solid network.

Two sets of reflectance spectra of opal before and after impregnation with coumarin-polymer solution acquired with different light collection angles are shown in Fig.1 a, b. In agreement with the Bragg law the "red" shift of the diffraction maximum along the (111) direction from 535 nm in Air-opal to 561 nm in polymer-opal occurs due to the increase in the effective RIC of the composite from 1.39 to 1.46. Obviously, small additives like the coumarin dissolved in the polymer cannot change the RI of the composite. In the frame of the effective medium approximation replacement of the air by polymer in opal voids can be accounted for by the replacement of the RI of air by that of polymer $n_{pol-opal} = n_{SiO_2} f_{SiO_2} + n_{pol} f_{void} = 1.46$. Because $n_{pol} \cong 1.5$, this relation holds for $f_{void} = 0.13$.

It is known, that to some extent the angular dispersion of diffraction peaks mimics the dispersion of the stop-band in the $E-k$ space and the width of these peaks reflects the stop-band width [9]. Both, Air-opal and polymer-opal possess a highly anisotropic PBG structure where stop-bands overlap only in narrow ranges of angles or *k*-vectors. As it was discussed earlier, the extent to which opal-based photonic crystals approach the omnidirectional bandgap limit is the product of the interplay of the RI contrast, volume fraction of the high-RI component and the topology of the ensemble [10].

From a set of diffraction spectra the relative stop-band width and its change with varying the angle of incidence of the light can be estimated by plotting the angular dependence of the relative stop-bandwidth $\Delta\lambda/\lambda_0 - \theta$. Here $\Delta\lambda$ is the full width at half height (FWHH) of the diffraction peak and λ_0- is the peak centre wavelength (Fig. 1c). The dramatic decrease of the RI contrast from $n_{SiO_2}/n_{air} = 1.45$ to $n_{pol}/n_{SiO_2} = 1.03$ is not accompanied by a same decrease of the bandgap width, because the fraction of the high-RI component in polymer-opal is better than for air-opal.

The broadband emission from coumarin dissolved in the polymer matches well with the spectral range of the stop-band detected by angular resolved reflectance. As compared with the PL spectrum from coumarin-polymer reference spectrum, the coumarin-opal spectrum shows a dip in emission spectrum, the central energy of which is shifted with changing the angle of the light collection (Fig.2 a and b) [11]. Therefore, by dividing the PL spectrum of coumarin-opal on that of the reference sample, the resulting transmission

function may be thought as the estimate of the local density of the photonic states (LDOPS) taken within the solid angle of the emission collection in the direction, which is specified be the angle θ (Fig. 2 c). By integration of the LDOPS over the whole solid angle the actual DOPS can be produced, which is known as possessing the very shallow pseudogap for such a low RI contrast [12]. Nevertheless, the stop-band-related minimum in LDOPS can reach a sufficient depth to suppress strongly the emission in particular direction.

The angular dispersion of the stop-band around the [111] direction in the *fcc* polymer-opal photonic crystal was mapped as the FWHH of the Bragg diffraction resonance (Fig.3 a). Similar dependence was extracted from FWHH of the dip in the LDOSP spectra (Fig.3 b). Both dependencies look similar, however the stop-band estimate from the emission spectra exceeds the width of its counterpart estimated from reflectance spectra. Apparently, this difference comes from the poorer resolution of the stop-band in the emission spectra, where the stop-band-related change of the emission intensity is less than 50%, whereas peaks in the reflectance spectra show intensity variations over an order of magnitude.

The scattering strength is obviously higher in the coumarin-polymer-opal than in the coumarin-polymer itself because of the scattering on silica balls. Using the SW it was observed that the emission intensity decays exponentially with the distance from the point-like light source in contrast to the linear decrease in the pure polymer sample (Fig.4 a,b). The difference in the scattering strength facilitates the localisation of photons with a characteristic length of about 0.5 mm in opal composite. The localisation length l_{loc} (Fig.5), which was estimated from the exponential fit $I \sim I_0 \exp(-x/l_{loc})$ of the experimental data, appears shorter for the shorter wavelength in the wavelength range of the coumarin emission band (Fig.6). However, as Fig.6 shows, this decrease can be accommodated by the re-absorption of the light emitted at the short wavelength limit of the coumarin emission band, where the emission and absorption bands of the coumarin overlap, rather than by an increase in the scattering strength. The wavelength dependence of l_{loc} does not show any short-range variation, which could be associated with the stop-band, i.e. it represents other than the PBG mechanism of the light-to matter interaction, which is, apparently, similar to the light localisation in the randomised array of scatterers.

The rate of the spontaneous emission is known to follow the spectral profile of the density of photonic states [13]. Correspondingly, it is reasonably to suggest that the spectrum of the emission rate in the coumarin-polymer-opal correlates with the spectrum of LDOPS. In order to reveal the spectrum of the emission rate we compared PL spectra, which were collected at different intensities of the excitation. Assuming the PL signal will rise more rapidly at those wavelengths where the emission rate is higher, the ratio of PL spectra will indicate these bands. Fig.7 b and d (solid lines) gives the experimental evidence of the correlation of the spontaneous emission rate and the LDOPS spectrum (Fig.7 a and c): the ratio spectrum possesses a minimum at the centre of the stop-band and peaks at both edges of the stop-band. Remarkably, the minimum of the ratio spectrum changes its spectral position with changing the angle of the emission detection in accord with the shift of the stop-band.

The bands in the spectrum of the spontaneous emission rate can be understood as the bands of the amplified spontaneous emission (ASE). Two ASE bands were observed, at the upper (ASE1) and the lower (ASE2) edges of the stop-band, correspondingly. Note, the existence of the ASE bands at the edges of the stop-band agrees well with the theoretical prediction [14].

With further increase of the excitation intensity another ASE band was detected (Fig.7 b and c, dotted lines). This band does not shift when the angle of detection is changed, i.e., it exists irrespective of the presence of the stop-band and th localisation . We refer to this band as the analogy of the light amplification in disordered multiple-scattering gain medium [15]. Fig.8 compares the angular dispersions of the LDOPS minimum, two stop-band-related ASE band and localisation-induced ASE band. Two ASE bands follow the LDOPS dispersion, whereas the central wavelength of the third one remains almost unchanged.

We would like to emphasise, that the separation of PBG- and localisation-related ASE bands can be made only conditionally. We used this approach to demonstrate the co-existence of different mechanisms affecting the light-matter interaction in dye-polymer-opal composite. In reality, at any arbitrary level of the excitation the contributions from both mechanisms take part in the modification of the light emission properties of the dye. With further increase of the RI contrast we are expecting that PBG-related amplification will prevail as the mechanism providing a stronger emitter-to-radiation coupling.

Sm^{3+}-POLYMER-OPAL

The same opal used for coumarin impregnation was used for impregnation with a Sm^{3+}- containing polymer.

To impregnate the opal a solution of 1.5 wt.% of samarium thenoyltrifluoracetonate and 1 wt.% of the photoinitiator diphenyl(2,4,6-trimethylbenzoyl)phosphine oxide in diehtylene glycol dimethacrylate was used. After curing with UV light, the samarium chelat was incorporated to the network.

The PBG structure of Sm-doped polymer-opal is essentially the same as the PBG structure of dye-doped polymer-opal – it depends on the RI index of polymer, diameter of the opal balls and the amount of the free space available for impregnation with the polymer, but not on the sort of doping. Thus, we refer to the previous sections for the details of the anisotropic photonic bandgap of polymer-opal.

The Bragg diffraction peak in the (111) direction is shown in Fig.9 a. The PL spectrum of Sm-doped polymer-opal shows three from four available $^4G_{5/2} - {}^6H_J$ transitions in the Sm^{3+} ion. It is seen, that for this particular sample the stop-band may affect the emission at the bands centered at 562 and 598nm, whereas the band at 645nm is far away from the bandgap wavelength range (Fig.9 b). Comparison of the emission spectra collected in FW and BW configurations shows only a weak decrease of the emission intensity at two short wavelength bands. Apparently, in order to suppress the emission, the thickness of the low RI contrast photonic crystal has to be much larger than 0.3mm used in the experiment. In contrast, in the SW configuration the difference between PL spectra taken at the very edge of the sample and from light source excited at the distance more than 1 mm from the edge manifests itself as the suppression of the emission at the bands overlapping with the stop-band (Fig.9 b).

The angular variation of the PL intensity was not observed in Sm-polymer-opal spectra in contrast to the coumarin-polymer-opal case probably to the insufficient RI contrast of the photonic crystal under investigation.

An attempt to resolve the spectrum of the spontaneous emission rate has also failed in Sm-polymer-opal in both FW and BW configurations. In the SW geometry the increase of the excitation intensity resulted in no change in the PL spectra ratio if the spectra are taken at the edge of photonic crystal (Fig.9 c, upper curve). In contrast, for volume

emission the ratio spectrum shows three distinct bands, which are centered at the same wavelengths as the emission bands. It is worth to mention that the width of the bands in the spectrum of the emission rate is larger than the corresponding bands in the PL spectrum and the magnitudes of these bands are nearly the same. Assuming the absence of the saturation of electronic transitions at the level of the excitation intensity used, we suggest the localisation origin of these ASE bands and rule out the PBG origin in accord with the absence of the angular dependence of the emission intensity in these bands. Obviously, the localised photons can interact longer with excited ions thus increasing the probability of the stimulated emission [15].

Eu^{3+}-POLYMER-TiO_2-OPAL

A solution of 1.5 wt.% of europium thenoyltrifluoracetonate and1 wt.% of the photoinitiator diphenyl(2,4,6-trimethylbenzoyl)phosphine oxide in diehtylene glycol dimethacrylate was used as precursor of the network.

The TiO_2 coating was deposited by 54 times repetition of the synthesis cycle. Each cycle includes the adsorption of $TiCl_4$ on the inner surface of the void walls and then reduction the $TiCl_4$ to TiO_2 by treatment with water vapour flow [16]. The titanium dioxide thus prepared crystallises in the form of anatase, as it was confirmed by observing the intensive 148 cm^{-1} line in the Raman spectrum.

Fig.10a shows the diffraction maximum of Eu^{3+}-polymer-TiO_2-opal (D=230nm) at 590 nm in the (111) direction in opal, which is red-shifted from 501 nm in bare opal and from 553nm in TiO_2-opal. The volume fractions of SiO_2 in this opal $f_{SiO_2} = 0.755$, TiO_2 – $f_{TiO_2} = 0.068$ and polymer – $f_{pol} = 0.2$ apply. The RI contrast in this photonic crystal is much higher than in the polymer-opal system, because the RI of TiO_2 is around 2.6.

PL spectrum (Fig.10 b) shows three emission bands characteristic for the $^5D_0 \rightarrow {}^7F_J$ group of radiative transitions in Eu^{3+} ion. This spectrum is similar to the spectrum of pure solution Eu^{3+}-polymer with two differences: broader band of triplet transition at 612nm and two times weaker band of singlet transition at 579nm for TiO_2-opal embedded solution. The stop-band overlaps with the two short wavelength emission bands if the emission is collected in the (111) direction. Moreover, the stop-band is broad enough to overlap with these bands, although with the various extent, in the range of the angles of light collection between 0 and 40° (Fig. 10 a and b). This overlap is a result of the increase of the RIC and indicates the improvement of the PBG structure of the coated opal. This is the first reason why no apparent dependence of the emission probabilities at different bands upon the angle of the light detection was observed. The second reason is the worse resolution of the diffraction peaks in this sample due to the poorer crystallinity of this opal as compared with the opals discussed in previous sections. Due to this circumstances we expect the tendency for photons to be localised in the randomised array of scatterers will be as strong as the PBG effect.

The scattering strength in Eu-polymer-TiO_2-opal exceeds strongly that of Sm-polymer-opal that makes it difficult to study the emission in BW configuration. Another consequence of the increased scattering strength is the stronger photon-to-emitter coupling. Correspondingly, the intensity ratio spectrum demonstrates much stronger increase of the emission intensity with the increase of the excitation intensity as compared with Sm-polymer-opal. Similarly to the Sm-polymer-opal, the ASE bands were detected in the ratio spectrum at the positions of the emission bands of the Eu-ion and the

ASE bandwidth exceeds the bandwidth of the emission bands (Fig.10 c). Moreover, the 613nm band, being situated at the edge of the stop-band, shows the emission intensity increase, the rate of which exceeds the excitation intensity increment by four times, indicating optical gain. Thus, the stimulated emission clearly can be thought of as the significant process, which accompanies the emission in photonic crystal with a moderate refractive index contrast.

CONCLUSIONS

The scattering of photons, which appears coherent over the whole volume of the photonic crystal, produces the pseudogap in the spectrum of the density of the photon states. From the study of PL of opals impregnated with dye-doped polymers we have concluded that even an anisotropic PBG environment enhances the photon-to-emitter interaction in the stop-band frequency range and changes significantly the spectrum of emission. Changes in the emission intensity and the emission rate follow the spectrum of the density of photon states. It is reasonably to expect more pronounced PBG effect upon the emission if the photonic bandgap structure gets improved.

Simultaneously, there is the competitive process, the weak localisation of photons, which is the summation over the crystal volume of locally coherent but otherwise uncorrelated scattering events. Localisation of photons also modifies the rate of the spontaneous emission. Correspondingly, the experimentally observed alteration of the dye emission properties is the superposition of coherent and incoherent mechanisms. Further experiments are in progress with opal templates with a higher RIC, i.e., possessing a shorter localisation length and less anisotropic dispersion of the stop-band.

The ro-vibronic electronic structure of the dye molecules appears flexible in adopting the superimposed PBG structure: if the probability of a fraction of radiative transitions becomes partly blocked by the stop-band, the redistribution of the emission probabilities in favor of other allowed transitions within one and the same continuous ro-vibronic band takes place. In contrast to the dye emission, the emission from rare earth ions demonstrates another sort of response on the PBG environment because no possibility of transition probability redistribution over the energy exists in the case of highly discrete electronic levels of rare earth ions. The redistribution in the transition probability of the direction may, obviously, take place assuming the random distribution of the emitting dipoles. However, in a medium with partial disorder (e.g. defects in the opal package and inhomogeneity of filling) the scattering on these defects will mask the directionality of the emission as it was discussed elsewhere [6]. This means that the detected decrease of the emission probabilities for lines overlapped with the stop-band characterizes rather the reduction of the emission probability averaged over all directions in photonic crystal. With the increase of the RI contrast the angular range of the stop-band overlap will be much larger that causes the enhancement of the photon-to-atom interaction.

ACKNOWLEDGEMENT

The authors are grateful to the RFBR (grant 99-02-1856) and EU Esprit Project PHOBOS, No. 27731 for partial financial support.

REFERENCES

1 E. Yablonovitch, Phys. Rev. Lett, 58 2059 (1987)

2 S.G. Romanov, C.M. Sotomayor Torres, in "Handbook of Nanostructured Materials and Technology", ed. H.S. Nalwa, v.4, ch.4, pp.231-323, Acad. Press, (1999)

3 K. Yoshino, K. Tada, M.Ozaki, A.A. Zakhidov, R.H. Baughman, *Jpn. J .Appl. Phys.*, **36**, L714 (1997); K. Yoshino, S.B. Lee, S. Tatsuhara, Y. Kawagishi, M. Ozaki, A.A. Zakhidov, *Appl. Phys. Lett.*, **73**, 3506 (1998)

4 T. Yamasaki, T. Tsutsui, *Appl. Phys. Lett.*, **72**, 1957 (1998)

5 E. P. Petrov, V. N. Bogomolov, I. I. Kalosha, S. V. Gaponenko. *Phys.Rev.Lett.*, **81**, 77 (1998)

6 M. Megens, J.E.G.J. Wijnhoven, A. Lagendijk, W.L. Vos, to appear in *Phys. Rev. A* (1999)

7 W.L. Vos, R. Sprik, A. von Blaaderen, A. Imhof, A. Lagendijk and G. H. Wegdam, *Phys. Rev. B*, **53**, 16231 (1996); R. D. Pradhan, I. I .Tarhan and G. H. Watson, *Phys. Rev B*, **54**, 13721 (1996); V.N. Bogomolov, N. V. Gaponenko, A. V. Prokofiev, A. N. Ponyanina, N. I. Silvanovich, and S. M. Samoilovich, *Phys. Rev. E*, **55**, 7619 (1997)

8 C. López, H. Míguez, L. Vázquez, F. Meseguer, R. Mayoral and M. Ocaña. *Superlat. and Microstruct.* **22**, 399 (1997).

9 V. Yannopapas, N. Stefanou, A. Modinos, *J. Phys.: Cond. Matter*, **9**, 10261 (1998)

10 S.G. Romanov, A.V. Fokin, R.M. De La Rue, *J. Phys.: Cond. Matter*, **11**, 3593 (1999)

11 S.G. Romanov, T. Maka, C. M. Sotomayor Torres, M. Müller, D. Allard and R. Zentel, to appear in *Appl. Phys. Lett.*

12 K. Busch, S. John, *Phys. Rev. E*, **58**, 3896 (1998)

13 E.M. Purcell, *Phys. Rev.* **69**, 681 (1946)

14 S. John,T. Quang, *Phys. Rev. A*, **50**, 1764 (1994)

15 S. John and G. Pang, *Phys. Rev. A*, **54**, 3642 (1996)

16 S.G. Romanov, A.V.Fokin, V.Y.Butko, V.V. Tretiakov, S.M.Samoilovich, C.M.Sotomayor Torres, *Physics Solid State*, **38**, 3347 (1996)

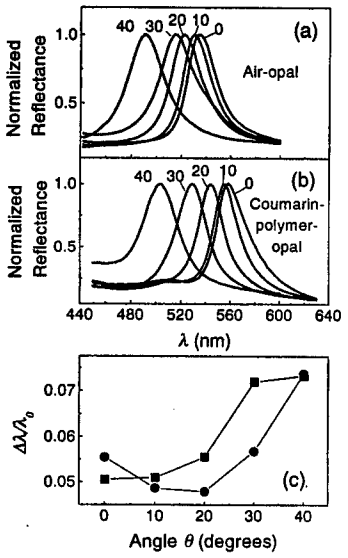


Figure 1: Reflectance spectra of Air-opal (a) and coumarin-polymer-opal (b) at different angles θ of the light incidence. Numbers indicate the angle. $\theta = 0^0$ corresponds to the (111) direction in the *fcc* lattice of opal. (c) – angular dispersion of the relative stop-bandwidth in Air- and polymer-opal, squares and circles, respectively.

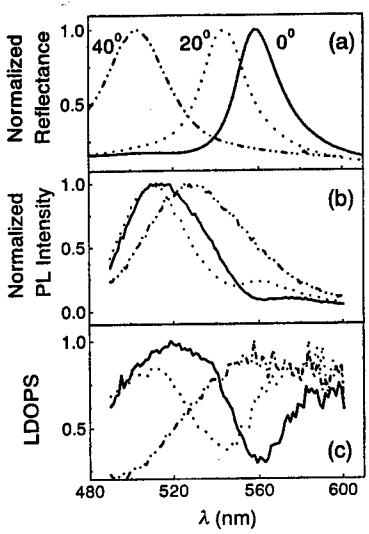


Figure 2: Reflectance (a), PL (b) and LDOPS spectra (c) of coumarin-polymer-opal at $\theta = 0°$, 20° and 40°, respectively, solid, dotted and dash-dotted lines. The LDOPS profiles were obtained by dividing the PL spectra of coumarin-polymer-opal on PL spectrum of coumarin-polymer reference sample under the assumption of the absence of interaction between coumarin molecules with silica of the opal template in the case of the low concentration of dye in the polymer.

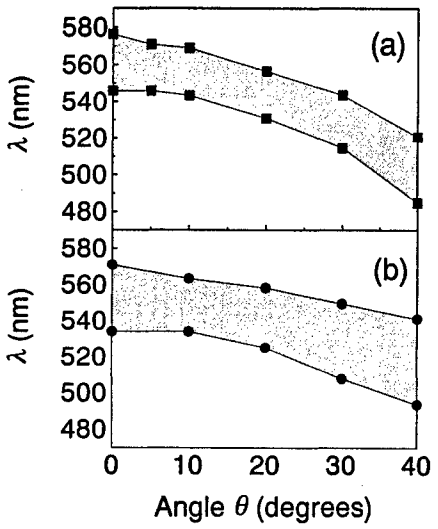


Figure 3: (a) - The stop-band dispersion for coumarin-polymer-opal obtained as the FWHH estimates of the diffraction peaks in reflectance spectra. (b) – similar plot obtained from LDOPS spectra. At $\theta > 40^0$ the PL estimate becomes unreliable because the light outgoing from the photonic crystal meet the angle of the complete internal reflection at the crystal-air boundary.

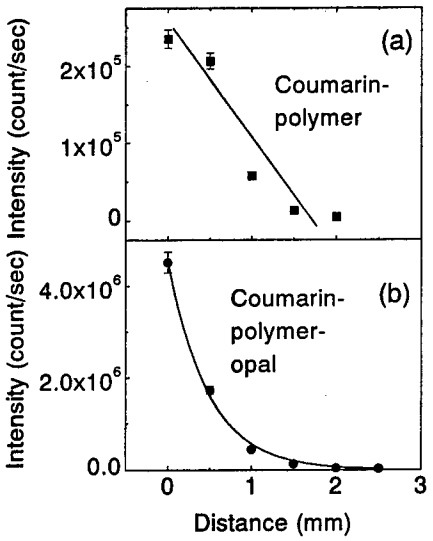


Figure 4: Decay of the intensity of the PL signal at $\lambda = 516nm$ from the point-sized light source (laser spot size ~0.1mm) in pure coumarin-polymer solution (a) and coumarin-polymer-opal (b) as they are seen at SW configuration. Dots represent experimental data and lines linear (a) and single exponential (b) fits, respectively.

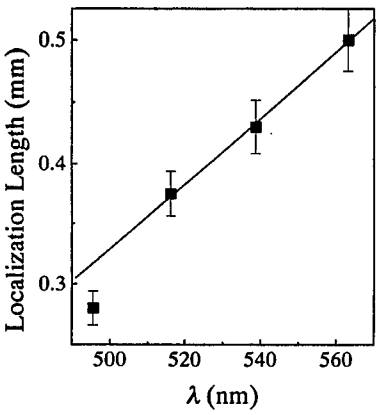


Figure 5: Wavelength dependence of the localization length in coumarin-polymer-opal.

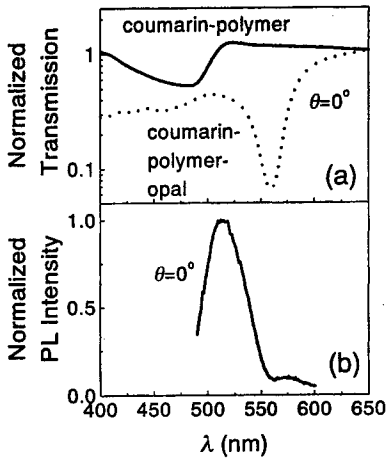


Figure 6: (a) Transmission spectra of the pure coumarin-opal solution (solid line) and coumarin-polymer-opal (dotted line) at $\theta = 0^0$. (b) Squeezing the bandwidth of coumarin emission band by the stop-band on the "red" side and by the absorption band of the coumarin on the "blue" side.

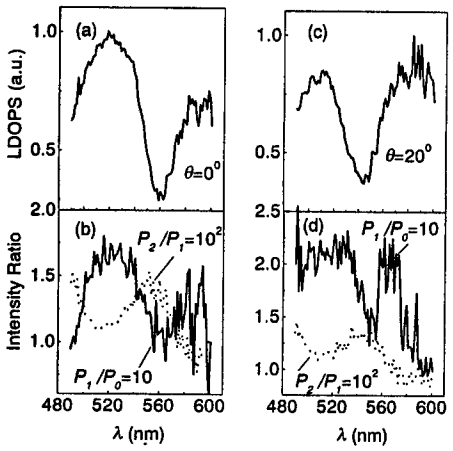


Figure 7: (a,c) LDOPS spectra for $\theta = 0^0$ *and* 20^0. Solid lines in (b, d) – the PBG-related ASE bands at low intensity pumping. Dotted lines in (b,d) – the localization-induced ASE band at high intensity pumping. Numbers indicate the increment of the excitation power increase $P_2 > P_1 > P_0$.

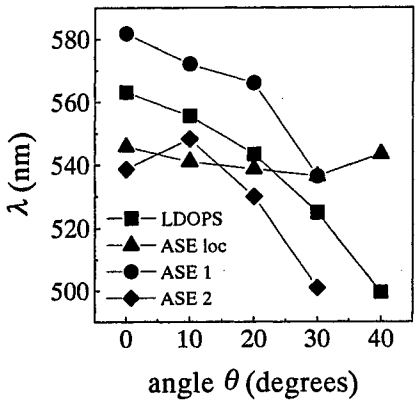


Figure 8: Angular dispersions of the LDOPS minimum (squares), PBG-ASE bands at the upper and lower edges of the stop-band (circles and diamonds) and localization-induced ASE band (triangles).

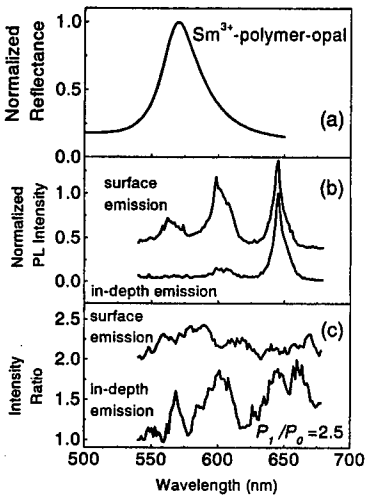


Figure 9: (a) The diffraction peak in (111) direction ($\theta = 0^0$) of Sm^{3+}-polymer-opal. (b) – SW PL spectra of this sample under 351 nm excitation: upper curve – emission without PBG effect, bottom curve – emission from PBG environment specified by spectrum panel (a). (c) Spectra of the emission rate at 2.5 increase of the excitation power; curves correspond to those of the panel (b). Curves in panels (b) and (c) are offset for clarity.

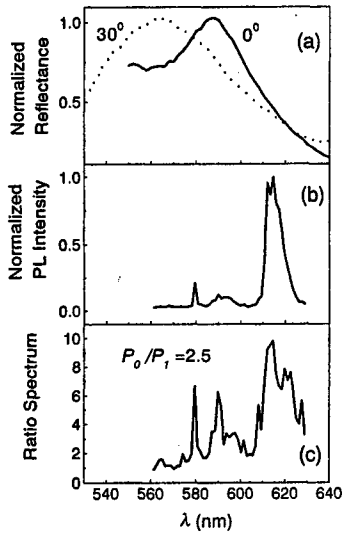


Figure 10: (a) Diffraction peaks in Eu^{3+}-polymer- TiO_2-opal reflectance at $\theta = 0°$ and 30°. (b) – SW PL spectrum, (c) – spectrum of the emission rate at 2.5 times increase of the excitation intensity.

ELECTRONIC RAMAN SCATTERING FROM WEAKLY BOUND ELECTRONS IN LIGHTLY DOPED n-TYPE GaAs

D.J. Lockwood[a], M. Potemski[b], and M.L. Sadowski[b]

[a]National Research Council of Canada, Ottawa, Ontario, Canada K1A 0R6
[b]Grenoble High Magnetic Field Laboratory, MPI/FKF & CNRS, 38042 Grenoble, France

ABSTRACT

We have examined the physical properties of donor bound electrons in a series of very lightly doped n-type GaAs samples (doped with 2×10^{14}–3×10^{15} Te atoms/cm^3) being far-infrared and inelastic light scattering measurements at low temperature. In this system there is a pronounced coupling between the spins of nuclei and donor electrons, which would be suitable for application in the quantum computer envisaged by Kane. The infrared and Raman results reveal correspondingly the 1s–2p$^{\pm}$ and 1s–2s transitions of the weakly bound donor at around 40 cm^{-1}. The Raman results are remarkable for the intensity of the scattering owing to excitonic resonance enhancement. An impurity-induced, localized phonon was observed at 271.7 cm^{-1}, again owing to strong resonance enhancement of the Raman cross section.

INTRODUCTION

Inelastic light (Raman) scattering has long been used to probe the electronic and vibrational properties of dopants in bulk semiconductors (1,2). Such experiments reveal electronic excitations, within bound donors and acceptors, single-particle excitations and collective modes of carriers such as plasmons and their interactions with bulk phonons, and the vibrational properties of the defect sites. Usually, this work is performed for systems where the dopant concentration lies in the range 10^{17}–10^{20} atoms/cm^3 where there are enough impurities for observable effects in conventional Raman scattering.

Recently, Kane has proposed a quantum-mechanical computer based on the coherent control of nuclear spins and their influence on electronic spins of arrays of donors in semiconductors (3). The development of such a computer requires a better understanding of the electronic properties of such donors, which resemble a single-electron quantum dot system with a Coulomb trapping potential.

A recent spin resonance study of weakly bound electrons donated by Te atoms in GaAs has shown the pronounced effects of coupling between spins of donor electrons and those of the nuclei. As an adjunct to this study we have used optical techniques to examine further the physical properties of donor bound electrons in the same series of lightly doped (2×10^{14}–3×10^{15} Te atoms/cm^3) n-type GaAs samples. This low doping concentration range ensures that the impurities are well spaced and are essentially isolated, but causes problems in

detecting Raman signals. By using laser excitation at energies just below the GaAs band-gap, we have been able to observe the bound electron transition not only at these very low donor electron densities but also, for the first time, in GaAs:Te.

In the next section we describe the sample and experimental details. This is followed by sections on the results and discussion of the optical measurements. The last section provides some conclusions about the nature of Raman scattering from donor impurities at very low densities.

EXPERIMENTAL DETAILS

GaAs:Te Samples

The bulk samples used in this study were from a GaAs ingot grown by Freiberger GmbH that was intentionally doped with Te. Wafers were sliced from the ingot and then polished front and back for the optical measurements. Elemental analysis of parts of the three wafers used here was performed by glow discharge mass spectroscopy. The wafers were first etched in methanol with 5% Br for 5 min and then sputtered in the vacuum system for 30 min with Ar gas to remove surface absorbed species before the analysis.

The major impurities found in the three samples are given in Table I. The presence of impurities other than the neutral Te dopant affects the number of carriers found in each sample. Generally speaking, however, the carrier concentration n increases in accord with the Te concentration of each sample (see Table I).

Optical Studies

The Raman measurements were performed in a quasibackscattering geometry (5) using Ti:sapphire laser excitation with a laser power in the 1–50 mW range. The scattered light was collected (along Y) at 90° to the incident light (along X), dispersed with a Spex 14018 double monochromator equipped with blazed master holographic gratings, and detected with a cooled RCA 31034A (GaAs) photomultiplier. The scattered light polarization was analyzed with Polaroid film before being polarization scrambled to avoid instrumental effects. For the temperature dependent study, the sample was mounted on a cold finger in the He exhange gas space of a Thor S500 continuous-flow cryostat and the sample temperature was monitored with a gold-iron/Chromel thermocouple mounted on the wafer surface. The angle of incidence of the laser beam on the wafer (001) surface was 56°. Because the excitation energies were always below the GaAs band gap, little laser heating of the sample was evident (10 or 50 mW of laser power gave the same electronic Raman spectrum).

The far-infrared measurements were performed with a Bruker 113 Fourier transform spectrometer. A mercury lamp was used as the light source. The spectrometer was connected to the liquid helium insert in the magnet by means of pumped light pipe optics. A black polyethylene filter was used to cut off shorter wavelengths. The sample was placed in a liquid helium cryostat, at the bottom of a U-turn insert. A composite Ge bolometer, operated at 2 K and placed in a separate cryostat outside the magnetic field, was used to detect

Table I. Major impurities found in the GaAs wafers used in this study. The amounts are in atomic parts per billion (ppb). All remaining elements (apart from Ga and As) of the 60 that were looked for were at the ~1 ppb level or lower (*i.e.*, at or below the detectable limit for that element). Also given is the measured carrier concentration n given as the difference between the numbers of donors (N_D) and acceptors (N_A) in units of 10^{14} cm^{-3}.

	Sample		
	1	2	3
Impurity[a]			
B	200	200	300
C	1500	1100	1100
N	100	80	95
O	600	490	490
F	<100[b]	<50	<30
Na	20	50	6
K	<200	<80	<80
Ge	<250	<300	<250
In	<100	<100	<100
Te	60	100	210
Carrier concentration			
n	2.6	6.5	27

[a]The absolute error for each element is a factor of 3.
[b]A less than (<) sign indicates this element, if present, is below the detectable limit given.

the light transmitted through the sample. The absorption of the sample, shown in Fig. 1, was taken to be proportional to minus the logarithm of the transmitted signal: $A = -\ln(T)$.

RESULTS

Infrared

The magnetic field dependence of the infrared absorption is given for sample 2 in Fig. 1. The other samples gave similar results and these will be presented in detail elsewhere. The splitting of the transition (peaked at 39 cm^{-1} at 0 T) with magnetic field and its field dependence clearly identifies it as the 1s–2p$^{\pm}$ excitation of a weakly bound donor electron. The variations in field-dependent behaviour for the different samples showed the strong

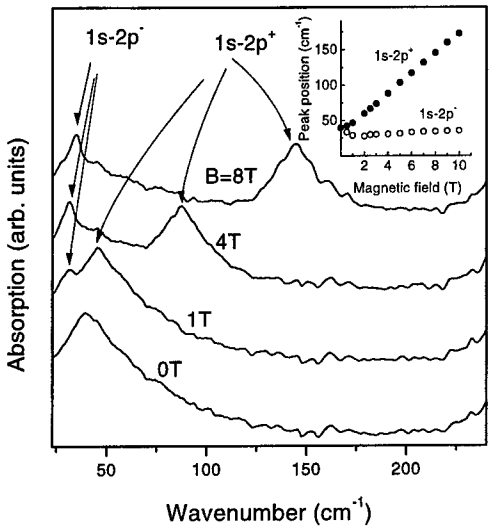


Figure 1. Representative infrared magneto-absorption spectra for sample 2 at 2 K. The inset shows the magnetic field dependence of the absorption peaks.

influence of the compensation ratio of donors to acceptors.

Raman

Sample 1 was investigated extensively by Raman scattering. Representative results as a function of excitation laser energy at low temperature are shown in Fig. 2. These excitation energies were chosen so as to be just below the GaAs band gap of 1.519 eV (12250 cm^{-1}) at low temperature, where the sample is becoming optically transparent. The spectra show a strong signature of the GaAs photoluminescence (PL) together with a phonon replica shifted by ~300 cm^{-1} to lower absolute energy. These two PL features shift to lower relative energy in the Raman plot with decreasing excitation energy, as expected for PL. The other features in the spectra remain at the same relative energy with excitation energy shift indicating that they are true Raman peaks. The broad asymmetric low-frequency peak at 42 cm^{-1} exhibits a pronounced resonant enhancement in its intensity when the excitation energy is increased, but eventually becomes lost in the much stronger PL signal. Two sharp features at 271 and 295 cm^{-1} are due to optic phonons, while a number of very weak peaks are evident near 150 cm^{-1}. The observation of the latter features varied depending on the laser beam position in sample 1 and they are believed to arise from weakly bound acceptors (including C), which give rise to transitions around this energy (1,6,7).

Figure 3 shows the polarization dependence of the Raman spectrum of sample 1 at 10 K. The other samples and other excitation energies gave similar polarization results for the Raman features. The 142 cm^{-1} band and 295.0 cm^{-1} line are predominant in X(YX)Y polarization, while the other sharp line at 270.7 cm^{-1} in X(YX)Y polarization merges with

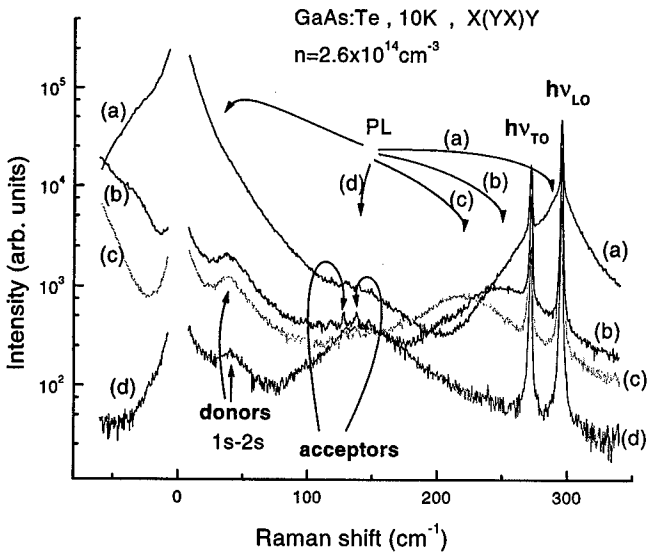


Figure 2. Raman spectrum of sample 1 at 10 K recorded in X(YX)Y polarization with 10 mW of excitation power at (a) 12000, (b) 11960, (c) 11930, and (d) 11850 cm^{-1}.

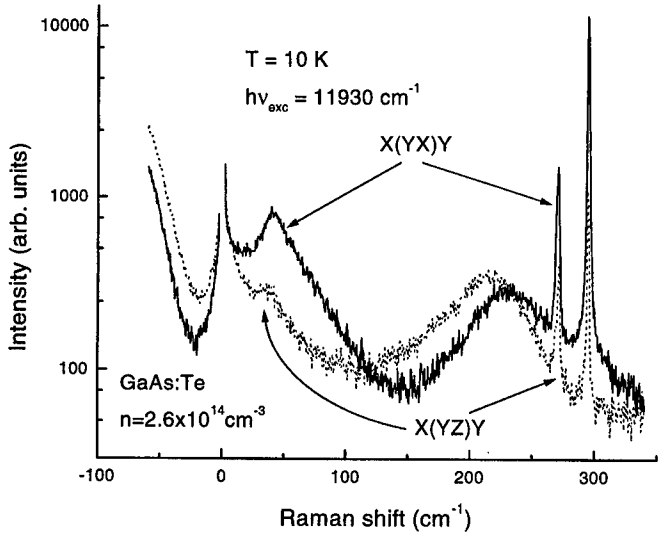


Figure 3. Polarization dependence of the Raman spectrum of sample 1 at 10 K excited with 10 mW of laser power at 11930 cm^{-1}.

another sharp line at 271.4 cm^{-1} in X(YZ)Y polarization. The quasibackscattering geometry used here implies that longitudinal optic (LO) and transverse optic (TO) modes should be strongest in the X(YX)Y and X(YZ)Y polarizations respectively; no strict selection rules apply because the sample refractive index is low at the excitation energies used here and thus the incident and scattered light directions are not close to true backscattering within the sample.

The temperature dependence of the Raman scattering from sample 1 is shown in Fig. 4. With increasing temperature the direct and phonon-assisted PL peaks decrease in intensity, as usual in GaAs, and cannot be distinguished for temperatures of 75 and 100 K. The two sharp phonon lines show relatively little variation in frequency, line width, and intensity over this low temperature range, but changing the temperature does affect the low-frequency scattering. The peak at 142 cm^{-1}, which is well evident at 4.2 K, broadens out until only a wide shoulder feature remains at 100 K. At the same time, an anti-Stokes peak (negative energy shift) emerges where none was visible at low temperatures.

Finally, in Fig. 5 we show a comparison of the low-frequency Raman peak in the three samples. The spectra were excited with 1 mW of laser power to minimize the laser heating of the sample and the number of photoexcited carriers. Under these conditions, the linewidth of the peak is slightly narrower than with 10 and 50 mW excitation. The frequency of the peak is the same (within the measuring accuracy of 1 cm^{-1}) in all samples and the intensity is much the same in samples 1 and 2 but has definitely increased for sample 3. The optical phonon behavior is similar in all three samples. The peak frequencies of the three samples versus polarization are summarized in Table II.

Table II. Peak frequencies of Raman lines in GaAs:Te samples at 10 K excited with 50 mW of laser light at 11930 cm^{-1}.

Sample	Peak 1	Peak 2		Peak 3	
	X(YX)Y	X(YX)Y	X(YZ)Y	X(YX)Y	X(YZ)Y
1	42	270.7	271.4	295.0	295.0
2	44	270.8	271.6	295.1	295.0
3	43	270.7	271.5	295.1	295.2

DISCUSSION OF RAMAN RESULTS

Low-Frequency Band

The Raman peak at ~40 cm^{-1} has an intensity that grows with Te concentration but whose frequency remains constant. The peak cannot be due to a collective excitation such as a plasmon since the frequency would shift with Te concentration and also because the frequency is too high for a plasmon at these low carrier concentrations (1). The peak polari-

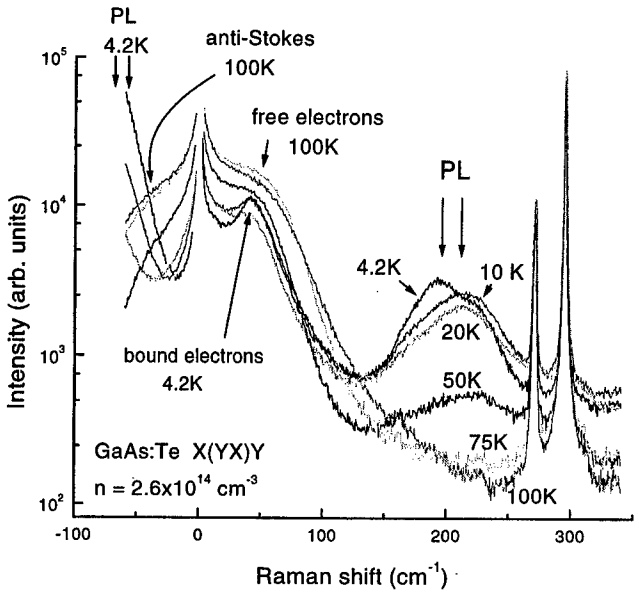


Figure 4. Temperature dependence of the Raman spectrum of sample 1 recorded in X(YX)Y polarization and excited with 50 mW of laser power at 11930 cm^{-1}.

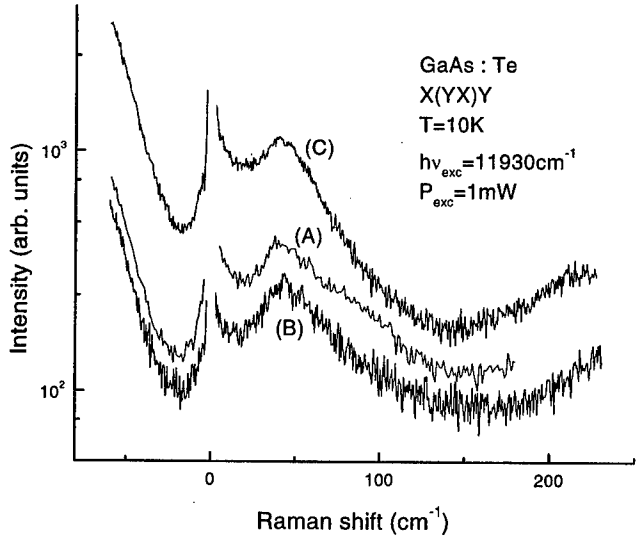


Figure 5. Low-frequency Raman spectrum of (A) sample 1, (B) sample 2, and (C) sample 3 at 10 K recorded in X(YX)Y polarization with 1 mW of laser excitation at 11930 cm^{-1}.

zation, the lack of an anti-Stokes peak (8), and the intensity behaviour are consistent with it being an electronic excitation of weakly bound electrons associated with the Te donor. The infrared absorption results are consistent with an assignment of the Raman peak to the 1s–2s transition. At higher temperatures, free carriers are created and the electronic Raman scattering is dominated by single-particle scattering (1,2), which is evidenced by the advent of a more diffuse peak in both Stokes and anti-Stokes scattering, as shown in Fig. 4.

It is remarkable that any electronic Raman scattering is seen at all from such a low concentration (~100 ppb) of Te donors. That it is seen here is a consequence of the significant enhancement factors one can obtain with Raman excitation in resonance with the associated bound and free excitons. Such enhancement (by a factor of 10) was first reported by Yu (9) for donors in CdS and, later, Ulbrich *et al.* (10) demonstrated a 10^{10} enhancement for donors in CdTe that they attributed to an exciton-polariton-mediated light scattering mechanism.

Optic Modes

The optical phonon at 295.1 cm^{-1} seen predominantly in X(YX)Y polarization is readily attributed to the bulk GaAs LO phonon, while the weaker peak appearing in X(YZ)Y polarization at 271.5 cm^{-1} is likewise the bulk GaAs TO phonon. The peak 0.8 cm^{-1} away at 270.7 cm^{-1} that is very strong in X(YX)Y polarization and can still be seen in X(YZ)Y polarization as a weak shoulder to the TO phonon is unexpected. From its polarization behavior, this phonon has LO-mode symmetry character. We attribute this "extra" Raman peak to a Te impurity vibrational mode. Its strength comes from the resonance enhancement of the incident (or scattered) light with excitons bound to the impurities. Similar huge enhancements of the Raman cross section have been observed previously for Cl impurities in CdS (11).

CONCLUSIONS

This resonance Raman study of GaAs:Te at very low doping concentrations (~10^{15} atoms/cm^3) has shown the remarkable power of the resonance Raman technique in obtaining direct information on the electronic excitations of shallow donors even at such low concentrations. The 1s–2s transition at 43 cm^{-1} was identified in this way for the first time for Te shallow donors in GaAs. In addition, an LO-like impurity vibrational mode was identified at 271.5 cm^{-1}, again owing to huge resonance Raman enhancement factors.

ACKNOWLEDGEMENTS

We thank H.J. Labbé for expert technical assistance in the Raman measurements and A. Mykytiuk and B. Methven of NRC for the glow-discharge mass spectrometry analysis. Part of this work has been performed under the CERION program of the CEC (DG III).

REFERENCES

1. M.V. Klein, in *Light Scattering in Solids,* M. Cardona, Editor, p. 147, Springer-Verlag, New York (1975).

2. G. Abstreiter, M. Cardona, and A. Pinczuk, in *Light Scattering in Solids IV,* M. Cardona and G. Günterodt, Editors, p. 5, Springer-Verlag, New York (1984).

3. B.E. Kane, *Nature*, **393**, 133 (1998).

4. M. Seck, M. Potemski, and P. Wyder, *Phys. Rev. B,* **56**, 7422 (1997).

5. D.J. Lockwood, M.W.C. Dharma-wardana, J.-M. Baribeau, and D.C. Houghton, *Phys. Rev. B,* **35**, 2243 (1987).

6. E.S. Koteles, S. Zemon, and P. Norris, *Inst. Phys. Conf. Ser.,* **79**, 259 (1986).

7. J. Wagner, M. Ramsteiner, H. Seelewind, and J. Clark, *J. Appl. Phys.,* **64**, 802 (1988).

8. Nguyen Ba An, Nguyen Van Hieu, Nguyen Toan Thang, and Nguyen Ai Viet, *Phys. Stat. Sol. (b),* **99**, 635 (1980).

9. P.Y. Yu, *Phys. Rev. B,* **20**, 5286 (1979).

10. R.G. Ulbrich, Nguyen Van Hieu, and C. Weisbuch, *Phys. Rev. Lett.,* **46**, 53 (1981).

11. P.Y. Yu, M.H. Pilkuhn, and F. Evangelisti, *Solid State Commun.,* **25**, 371 (1978).

PROPAGATION AND LOCALIZATION OF VERTICALLY POLARIZED PLASMON-LO PHONON COLLECTIVE EXCITATIONS IN DOPED GaAs/AlAs SUPERLATTICES

Yu.A.Pusep, M.T.O.Silva, N.T.Moshegov[1,2], P.Basmaji[1], J.C.Galzerani,

Universidade Federal de São Carlos, 13565-905 São Carlos, SP, Brasil

[1]*Instituto de Fisica de São Carlos, Universidade de São Paulo,*

13560-970 São Carlos, SP, Brasil

[2]*Institute of Semiconductor Physics, 630090 Novosibirsk, Russia*

The coupled plasmon-LO phonon collective excitations polarized normal to the layers were studied by Raman scattering in doped GaAs/AlAs superlattices with broad minibands. Different characteristical asymmetries of the Raman lines corresponding to the coupled modes were found in samples with different electron densities. It was shown that the observed asymmetries are caused by the dispersions of the coupled plasmon-LO phonon excitations. In accordance with the theoretical predictions, the coupled modes reveal either a plasmon or a phonon character, depending on the electron density. The transition from propagating to localized superlatice plasmons was observed with the increase of the doping concentration.

The physics of the collective plasmon and coupled plasmon-LO phonon excitations in semiconductor superlattices (SL's) attracted much attention in the last years. A rich spectrum of collective excitations has been found theoretically; among them are the quasi-two-dimensional (intrasubband) and the intersubband plasmons, both studied in [1-3], their counterparts arising due to the coupling of plasmons with optical phonons [1] and the superlattice plasmons (polarized normal to the layers), which appear in systems of strongly coupled quantum wells (superlattices) [3,4]. Experimental works were devoted to study the energy spectra of the intrasubband [5,6] and intersubband [7] plasmons, and the coupling between them [8,9]. The superlattice plasmons at the center of the Brillouin zone (BZ) have been investigated in [10]. As a result, the dispersion of the intrasubband two-dimensional plasmons has been well studied, while, to our knowledge, to date no experimental evidence of the dispersion of the superlattice plasmons was presented.

In this paper we study the influence of the dispersion of the collective excitations propagating normal to the layers which are caused by the coupling of the superlattice plasmons with the optical phonons on Raman spectra of the doped, strongly coupled GaAs/AlAs superlattices. The analysis of the shape of the Raman lines allowed us to identify the character of the coupled plasmon-LO phonon modes - we found that depending on electron density, the coupled modes reveal either phonon or plasmon character in good agreement with the theoretical predictions. This effect was well known in bulk doped ionic crystals from theoretical considerations for many years (see for instance [11]), however, so far it was not verified experimentally. Finally, we demonstrated the localization of the plasmon-LO phonon excitations caused by impurity scattering.

The samples here studied were strongly coupled $(GaAs)_{17}(AlAs)_2$ superlattices

(the numbers indicate the thicknesses of the corresponding layers expressed in monolayers) doped with Si. The total number of 20 periods was grown by molecular beam epitaxy (MBE) on (100) GaAs substrates. The calculations of the electron energy spectrum of these superlattices made by the envelope function approximation [12] revealed a broad lowest miniband (with the width about 70 meV) formed by the Γ-Γ electron transfer; the complete occupation of this miniband demands an electron density N=4.5x10^{18} cm^{-3}.

Backscattering unpolarized Raman spectra were performed at T=10 K with a Jobin-Yvon double grating spectrometer supplied with the usual photocounting system; the 5145 Å line of an Ar^+ laser was used for excitation. In this case, because of the conservation of momenta of the elementary excitations involved in the Raman process, the collective plasmon-LO phonon modes polarized normal to the layers should contribute to the Raman scattering.

As it is well known, the fluctuations of the electronic potential, which occur in doped SL's preferentially because of the impurity random potential, destroy the translational invariance giving rise to a spatial coherence length of the elementary excitations (L) and, as a consequence, cause the breakdown of the Raman selection rules leading to the broadening and asymmetry of the Raman lines [13,14]. The analysis of the shape of the spectral lines allows one to determine the coherence lengths of the elementary excitations involved in the Raman process and thus, to study their localization properties. This effect has been used to study the localization of the optical phonons in semiconductor alloys [13,14].

According to [13], the relaxation of the conservation of the crystal momentum caused by a crystal disorder can be taken into account by means of a Gaussian spatial correlation function $\exp(-\frac{4R^2}{L^2})$; then the Raman efficiency can be written as:

$$I(\omega) \sim \int f_{sc}(\vec{q}) \cdot \exp(-\frac{q^2L^2}{4}) \frac{d^3q}{[\omega - \omega(q)]^2 + (\Gamma/2)^2} \qquad (1)$$

where $f_{sc}(\vec{q}) = (\frac{4\pi}{q^2+q_{TF}^2})^2$ is the screening correlation function with the q_{TF} being a Thomas-Fermi wave vector; $\omega(q)$ is the dispersion of the relevant excitations and Γ is their damping constant.

We utilized (1) in order to calculate the intensities of the Raman lines caused by the coupled plasmon-LO phonon modes in the samples under investigation and to extract the values of the plasmon coherence lengths.

As it is expected from the theoretical considerations [15], three coupled longitudinal vibrational modes exist in the doped GaAs/AlAs superlattices: that of the low-frequency acoustic-like (ω^-) and those of the optical GaAs-like (ω_1^+) and AlAs-like (ω_2^+). All these modes can be found in the Raman spectra of the studied samples, some of which are depicted in Fig.1.

Moreover, the additional modes originated from the depletion surface layer, which correspond to the longitudinal optical (LO) phonons of the wells and those of the barriers (labeled in Fig.2 as LO(GaAs) and LO(AlAs) modes) are seen in the Raman spectra as well. The widths of the LO(GaAs) phonon lines were much narrower than those of the GaAs-like coupled mode (ω_1^+) due to the absence of an electron-electron interaction in the depletion layer. The frequency of the LO(AlAs) mode was found to be lower than the one expected for the 2 ML thick AlAs due to the confinement effect. This means the formation of an $Al_xGa_{1-x}As$ alloy in the barrier instead of the nominal AlAs, which is considered as an unavoidable process and which takes place due to segregation [16].

Taking into account the downshifts of the AlAs LO phonon caused by the confinement together with the alloying, we obtained for the barriers the average x = 0.5,

which agrees well with the data presented in [16] where we have already shown that the segregation of cations during the MBE growth of the GaAs/AlAs superlattices causes the alloying and the broadening of the ultrathin AlAs barriers - the nominal 2 ML wide AlAs barriers convert to the $Al_xGa_{1-x}As$ barriers with an average value of x $\approx$ 0.4 and with an effective thickness about 4 ML's. These parameters of the barriers were used in the calculations of the miniband structure of the samples studied here. The results of these calculations show the energy corresponding to the top of the lowest Γ miniband in good agreement with the plateau in the ω_2^+ mode predicted by the theory [17] to occur due to the finite width of the miniband when the Fermi level enters a minigap. The comparison of the obtained miniband structure with the one calculated with the nominal parameters of the barriers showed that the decrease of the barriers heights due to the alloying was almost completely compensated by the broadening of the barriers.

The frequencies of all the modes determined by Raman scattering are collected in Fig.3 together with the frequencies of the vertically polarized plasmon-LO phonon modes calculated for wavevectors at the center of the BZ according to the theory presented in [15] where the finite width of the miniband was taken into account according to [17]. The calculations were performed with the electron effective masses found in the studied superlattices by the envelope function approximation [12] and then averaged over the electron states which form the Fermi surface of the relevant superlattice. The results presented in Fig.3 show a good correspondence between the measured and calculated frequencies of the coupled collective plasmon-LO phonon excitations found for the $(GaAs)_{17}(AlAs)_2$ superlattices with different doping levels.

The Raman data obtained for the bulk doped $Al_{0.11}Ga_{0.89}As$ alloy with the contents of Al being equivalent to the SL's here studied are shown in Fig.3 as well. The same modes as in the spectrum of the collective plasmon-LO phonon excitations of the GaAs/AlAs SL's are expected in this alloy due to a two-phonon behavior [18]. The difference is expected in the dispersion of the plasma vibrations influenced by the formation of the miniband structure in SL's, which should modify the dependence of the ω_2^+ mode on electron concentration. This indeed was observed in the SL's, in good agreement with the theory, showing that the collective modes propagating normal to the layers are involved in the Raman scattering and the contributions due to the in-plane components are negligible.

As it is seen in Figs.1,2, at low electron concentrations both the ω_1^+ and ω_2^+ plasmon-LO phonon modes reveal a disorder induced asymmetry opposite to the one observed for the optical phonons in the $Al_xGa_{1-x}As$ alloys [14]; this is explained by the different dispersions of the optical phonons and of the plasmons - a negative dispersion (characterized by a negative group velocity) for the phonons and a positive one (with a positive group velocity) for the plasmons [19]. However, as the electron concentration increases, the observed asymmetry of the GaAs-like ω_1^+ coupled mode becomes less pronounced and finally changes its character at N $>10^{18}$ cm^{-3}. In the samples with such high electron concentrations the observed asymmetry of the ω_1^+ is definitely caused by the negative phonon-like dispersion. At the same time, the AlAs-like ω_2^+ mode reveals the asymmetry caused by the positive plasmon dispersion in all the samples under investigation.

The modification of the character of the ω_1^+ collective mode observed with increase of electron concentration is similar to the one predicted by the theory for the plasmon-LO phonon modes in bulk doped ionic crystals [11]. According to the theory, the electron screening effects are responsible for this modification. However, the situation is somewhat different in SL's due to their anisotropy. There no longer exist bulk phonons, but instead the confined and interface modes appear [20]. Now, in the presence of electrons the energy spectrum of the collective excitations is given by the zeros of the full dynamical dielectric function tensor of the SL. The component of this tensor related to the electric polarization normal to the layers (parallel to the growth

direction z) can be taken in the following form [11], [20]:

$$\epsilon_z(q,\omega) = \frac{d_1+d_2}{\frac{d_1}{\epsilon_1(q,\omega)}+\frac{d_1}{\epsilon_2(q,\omega)}} - v_q^{\infty}P(q,\omega) \tag{2}$$

where d_1 and d_2 are the thicknesses of the wells and of the barriers respectively; $v_q^{\infty} = \frac{4\pi e^2}{\epsilon_{\infty} q^2}$ is the potential of the electron-electron interaction, $P(q,\omega)$ is the polarization function of the electron gas.

$$\epsilon_{1,2}(q,\omega) = \epsilon_{\infty 1,2}\frac{\omega^2-\omega_{L1,2}^2(q)}{\omega^2-\omega_{T1,2}^2(q)} \tag{3}$$

where $\omega_{L1,2}(q) = \omega_{LO1,2}(1-A_{L1,2}q^2)$ and $\omega_{T1,2}(q) = \omega_{TO1,2}(1-A_{T1,2}q^2)$ are the dispersion relations for the longitudinal optical and transverse optical (TO) phonons of the wells and the barriers respectively, with ω_{LO} , ω_{TO} being the frequencies of the LO and TO vibrations taken at the center of the BZ and with the constants $A_{L1,2}$, $A_{T1,2}$ determined according to the data presented in [21].

The first term in (2) represents the lattice contribution where the bulk-like LO phonons and the interface TO vibrations, both polarized normal to the layers are included. The second term is due to the electrons.

Two limiting cases were examined. In the low-electron density limit, when $\omega_p \lessapprox \omega_{L1}, \omega_{L2}$ the electron scattering is weak. Therefore, the plasmon-LO phonon modes in a narrow interval of the wavenumbers close to the center of the BZ, which are characterized by the coherence lengths $L >> d_{SL}$ (where $d_{SL} = d_1 + d_2$), are involved in the Raman process. In this case, the electron term can be taken in the random phase approximation (RPA) in the limit of small q [11]:

$$v_q^{\infty}P(q,\omega) \approx \frac{\omega_p^2}{\omega^2}[1+\frac{3}{5}\frac{(qv_F)^2}{\omega^2}] \tag{4}$$

where $\omega_p = (\frac{4\pi e^2 N}{m_z})^{1/2}$ is the plasma frequency and v_F is the Fermi velocity.

At high electron densities, when $\omega_p > \omega_{L1}, \omega_{L2}$ but L is still larger than d_{SL} , the approximation (4) is valid and the theory predicts that the low-frequency coupled modes (ω^- and ω_1^+) should approximate the frequencies of the corresponding TO phonons, while the highest-frequency mode (ω_2^+) acquires a plasmon character. The analysis of (2) shows that in the case of the GaAs/AlAs SL, at such electron concentrations the ω^- and ω_1^+ coupled modes approximate the TO GaAs-like and AlAs-like inteface modes with vanishing parallel wavevectors.

With further increase of the doping level, when $\omega_p >> \omega_{L1}, \omega_{L2}$ an electron scattering may become so strong that $L \lessapprox d_{SL}$; as a consequence, a significant part of the states of the BZ contribute to the Raman scattering and therefore, we need to calculate the energy spectrum of the collective excitations over all the BZ, which presents a rather hard problem. However, in this case theoretical considerations show that electrons cannot screen out the LO phonons with wavevectors close to the edge of the BZ where the LO-TO splitting appears again. As a consequence, for extremely large wavevectors, beyond the screening limit, the frequencies of the ω^- and ω_1^+ modes should approximate the frequencies of the corresponding unscreened LO phonons. We do not expect that this will cause a drastic modification of the dispersion of the collective excitations in the GaAs/AlAs SL's with ultrathin barriers (when the ratio d_1/d_2 is large) where the dispersion of the LO AlAs-like phonons is located close to the dispersion of the TO AlAs-like interface modes, while the same is true for the LO phonons of the GaAs wells with wavevectors close to the edge of the BZ. The

results of the calculation of the energy spectrum of the plasmon-LO phonon modes performed with formulas (2)-(4) in the $(GaAs)_{15}(Al_{0.4}Ga_{0.6}As)_4$ SL are presented in Fig.4.

It should be mentioned that using the phonon contribution in the form presented in (2) we neglect the effect of the quantization of the optical phonons. This is certainly true in the case of thick enough layers (GaAs wells in the studied SL's). However, even in the four-monolayer thick AlGaAs layers the continuum approximation can be used because due to the alloying the energies of the phonon states are broad and the confined modes are hardly resolved [16]. Thus, indetermination of the phonon energy in thin AlGaAs layers makes the phonon spectrum a quasicontinual instead of a discrete one.

Fig.4 shows that at low electron concentrations relevant to the samples under investigation all the plasmon-LO phonon modes with small wavenumbers reveal a plasmon character. In the limit of high-electron densities free electrons screen out the long-range Coulomb part of the ion-ion interaction, which is responsible for the difference between the LO and TO frequencies and therefore, the dispersions of the ω^- and ω_1^+ modes approximate the dispersions of the TO interface modes (those the GaAs-like and AlAs-like ones respectively), while the ω_2^+ mode continues to be of the plasmon type.

The dispersions of the coupled modes obtained in this way were used in the calculations of the Raman intensities in the samples with low electron densities, which reveal the plasmon-like asymmetry of the plasmon-LO phonon modes. These calculations were done according to the formula (1) assuming an isotropic spatial correlation. At high doping levels, in agreement with the theory, the low-frequency ω^- and ω_1^+ modes reveal the phonon-like asymmetry, while the high-frequency ω_2^+ mode remains the plasmon-like; correspondingly, the dispersions of the optical phonons and of the plasmons were used to obtain the shapes of the relevant Raman lines in this case. The calculated Raman spectrum, obtained by the best fitting for one of the samples with low doping level, is shown in Fig.2 by the dotted line.

It is worth to notice, that as it is seen in Fig.1, in the SL's with high electron concentrations the observed asymmetry of the ω^- mode is similar to the asymmetry of the ω_1^+ caused by a negative phonon-like dispersion. According to the theory, in the high-electron density limit the dispersion of the GaAs TO phonons contributes to the shape of the ω^- Raman line being responsible for the observed asymmetry.

Thus, the experimental results, revealing a modification of the character of the coupled plasmon-LO phonon modes in the doped GaAs/AlAs SL's which occurs with the increase of electron density, were found in good agreement with the theory presented above..

In order to study the effects of the localization of plasmons in the doped $(GaAs)_{17}(AlAs)_2$ superlattices with different electron densities, we analyzed the forms of the Raman lines corresponding to the plasmon-LO phonon coupled modes. The obtained dependencies of the coherence lengths of the plasmon-LO phonon excitations on the electron density are depicted in Fig.5. The calculated electron energy spectrum of the superlattice is shown in the insertion to Fig.5, where the shaded area corresponds to the interval of the Fermi energies relevant to the electron concentrations in the samples studied. The different values of the coherence lengths obtained for the different modes are associated with their different localization properties.

We observed a strong decrease of the coherence lengths of the ω_1^+ and ω_2^+ coupled modes associated with a transition from a propagative regime to a localized one, which takes place when the electron density exceeds 10^{18} cm^{-3}; then L_1 and L_2 becomes comparable to or is even smaller than the superlattice period (d_{SL}), which means an evidence of the localization of plasmons inside one superlattice period. The approximate position of the mobility edge corresponding to this transition is shown by an arrow labeled by E_c.

For a comparison, the coherence lengths of the AlAs-like plasmon-LO phonon excitations obtained in the $Al_{0.11}Ga_{0.89}As$ alloy are presented in Fig.5 as well. Significant differences between the coherence lengths measured in the alloy and in the SL's were found when the Fermi level entered a minigap of the SL's (above the energy E_{max}). This shows an influence of the miniband structure of the SL's on the effect of localization of the coupled modes, which probably is caused by a "reentrant localization" characterized by a mobility gap in the electron spectrum separating electron states localized at the minband extremities [22].

In conclusion, we found that the asymmetrical form of the Raman lines corresponding to the plasmon-LO phonon modes observed in the doped GaAs/AlAs superlattices is caused by the dispersion of the relevant excitations (phonons or plasmons, depending on electron concentration). This finding was shown to serve as an indicator of the character (plasmon or phonon) of the coupled plasmon-LO phonon modes. We observed the change of the modes character with the increase of electron density in good agreement with the theoretical predictions. In addition, the effect of localization of the collective plasmon-LO phonon excitations was studied. We observed a transition from propagating to localized collective excitations which occurs with the increase of the doping concentrations.

The financial support from CNPq, FAPESP and CAPES is gratefully acknowledged. Y.A.P. appreciates discussions with Prof. S.S.Sokolov.

[1] A.C.Tselis and J.J.Quinn, Phys.Rev. B29, 3318 (1984)

[2] M.Babiker, N.C.Constantinou, and M.G.Cottam, J.Phys.C: Solid State Phys. 19, 5649 (1986)

[3] H.Ishida, J.Phys.Soc.Jap. 55, 4396 (1986)

[4] X.Zhu, X.Xia, J.J.Quinn, and P.Hawrylak, Phys.Rev. B38, 5618 (1988)

[5] D.Olego, A.Pinczuk, A.C.Gossard, and W.Wiegmann, Phys.Rev. B26, 7867 (1982)

[6] A.Pinczuk, M.G.Lamont, and A.C.Gossard, Phys.Rev.Lett. 56, 2092 (1986)

[7] A.Pinczuk, J.M.Worlock, H.L.Störmer, R,Dingle, W.Wiegmann, A.C.Gossard, Sol.St.Comm. 36, 43 (1980)

[8] G.Fasol, N.Mestres, H.P.Hughes, A.Fisher, and K.Ploog, Phys.Rev.Lett. 56, 2517 (1986)

[9] G.Fasol, R.D.King-Smith, D.Richards, U.Ekenberg, N.Mestres, and K.Ploog, Phys.Rev. B39, 12695 (1989)

[10] Yu.A.Pusep, M.T.O.Silva, J.C.Galzerani, A.G.Milekhin, N.T.Moshegov, and A.I.Toropov, J.Appl.Phys. 79, 8024 (1996)

[11] G.D.Mahan, Many-particle physics, Plenum Press, New-York, London, 1981.

[12] Yu.A.Pusep, A.G.Milekhin, and A.I.Toropov, J.Phys.Condens.Matter. 6, 93 (1994)

[13] H.Richter, Z.P.Wang, and L.Ley, Solid State Comm. 39, 625 (1981)

[14] P.Parayanthal and F.H.Pollak, Phys.Rev.Lett. 52, 1822 (1984)

[15] Yu.A.Pusep, A.G.Milekhin, and A.I.Toropov, Superlatt. and Microstruct. 13, 115

(1993)

[16] Yu.A.Pusep, S.W. da Silva, J.C.Galzerani, D.I.Lubyshev, and P.Basmaji, Phys.Rev. B51, 9891 (1995)

[17] S.-R.E.Yang and S.Das Sarma, Phys.Rev. B37, 10090 (1988)

[18] S.Baroni, S. de Gironcoli, and P.Gianozzi, Phys.Rev.Lett., 65, 84 (1990)

[19] Yu.A.Pusep, M.T.O.Silva, J.C.Galzerani, N.T.Moshegov, P.Basmaji, Phys.Rev. B58, 10683 (1998)

[20] B.Jusserand and M.Cardona, Raman spectroscopy of vibrations in superlattices, in Light-scattering in solids V, ed. by M.Cardona and G.Güntherodt, Springer-Verlag, Berlin, Heidelberg, 1989.

[21] Yu.A.Pusep, S.W. da Silva, J.C.Galzerani, A.G.Milekhin, V.V.Preobrazhenskii, B.R.Semyagin, and I.I.Marahovka, Phys.Rev. B52, 2610 (1995)

[22] H.A.Fertig and S.Das Sarma, Phys.Rev. B42, 1448 (1990)

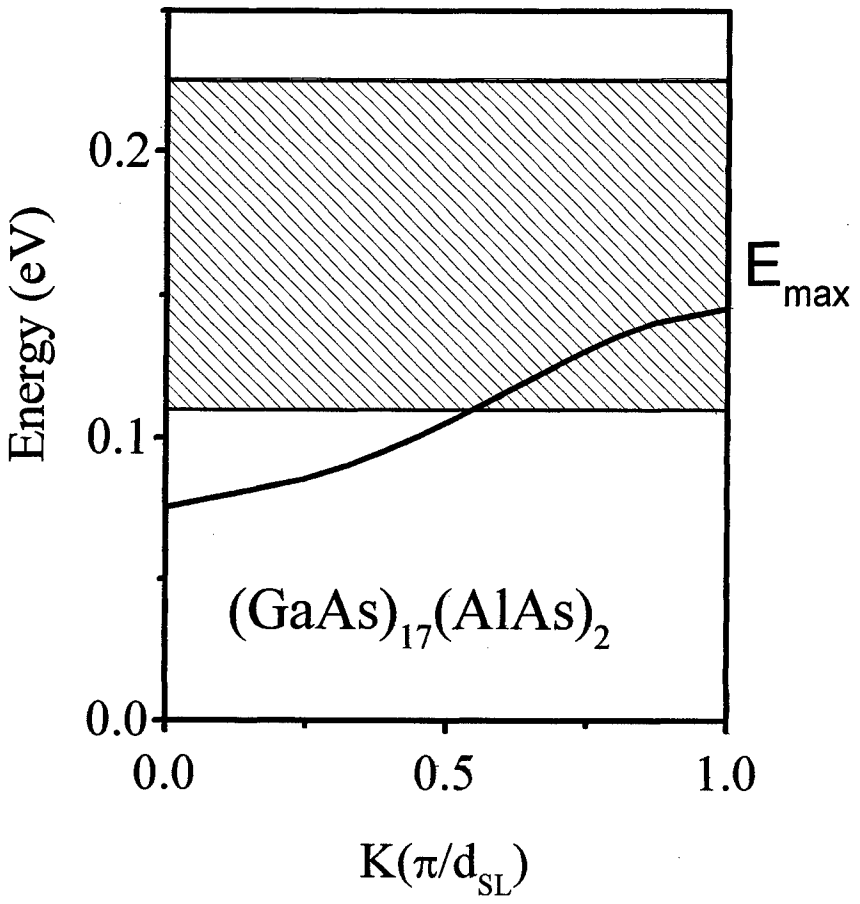


Fig.1. The calculated electron energy spectrum of the $(GaAs)_{17}(AlAs)_2$ superlattices. The lowest Γ miniband with the maximum energy E_{max} is shown); the shaded area corresponds to the interval of the Fermi energies relevant to the samples under investigation.

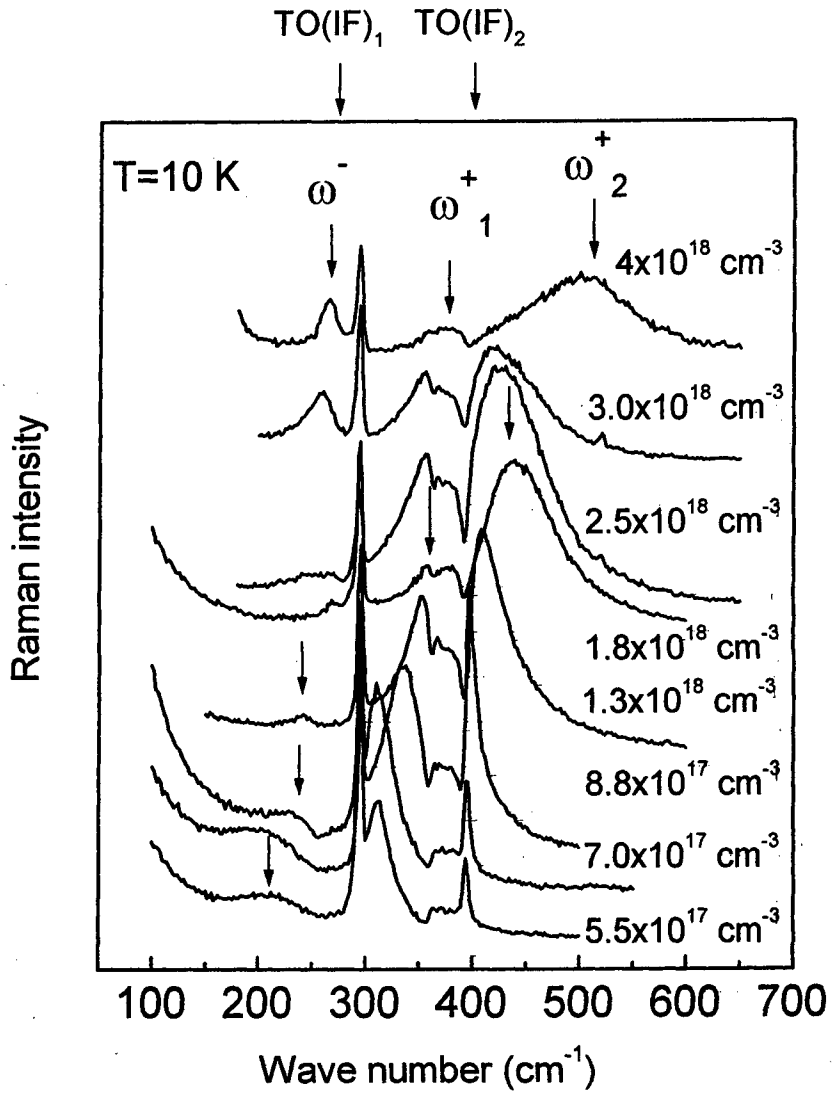


Fig.2. The Raman spectra of the doped $(GaAs)_{17}(AlAs)_2$ superlattices with different electron concentrations measured at the temperature T=10 K with the excitation energy 2.41 eV. The calculated frequencies of the TO GaAs-like and AlAs-like interface modes are shown at the top of the figure.

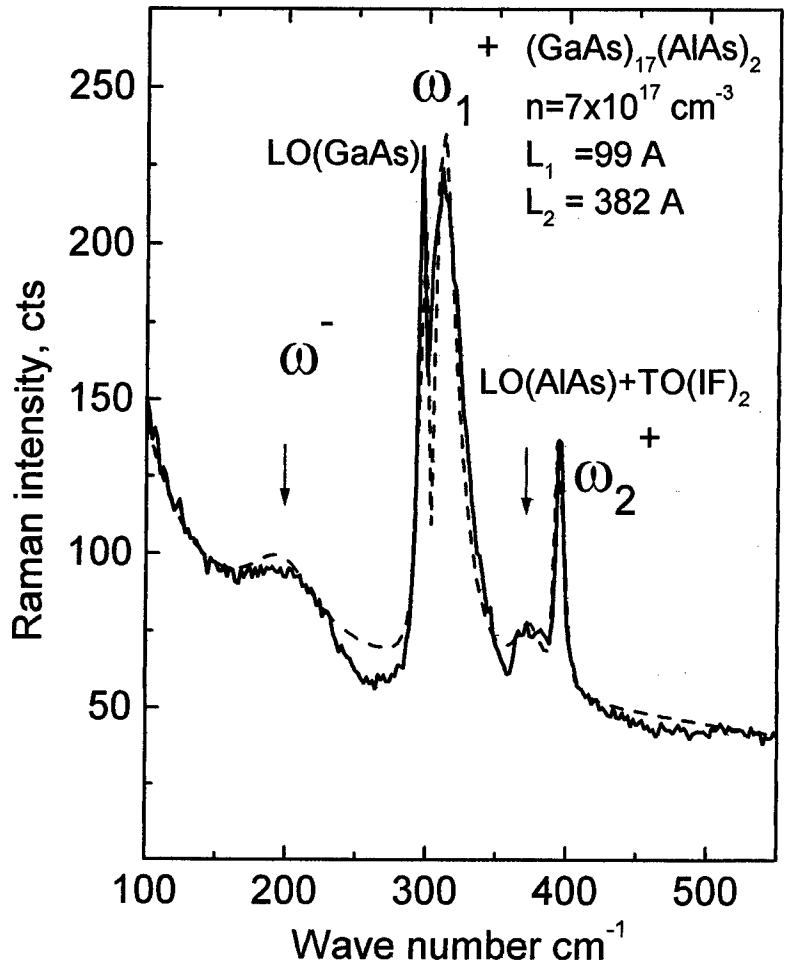


Fig.3. The Raman spectra of the doped $(GaAs)_{17}(AlAs)_2$ superlattice with $N=7x10^{17}$ cm^{-3} measured at the temperature T=10 K with the excitation energy 2.41 eV (full line) and calculated with the parameters collected in the Table 1 (dotted line).

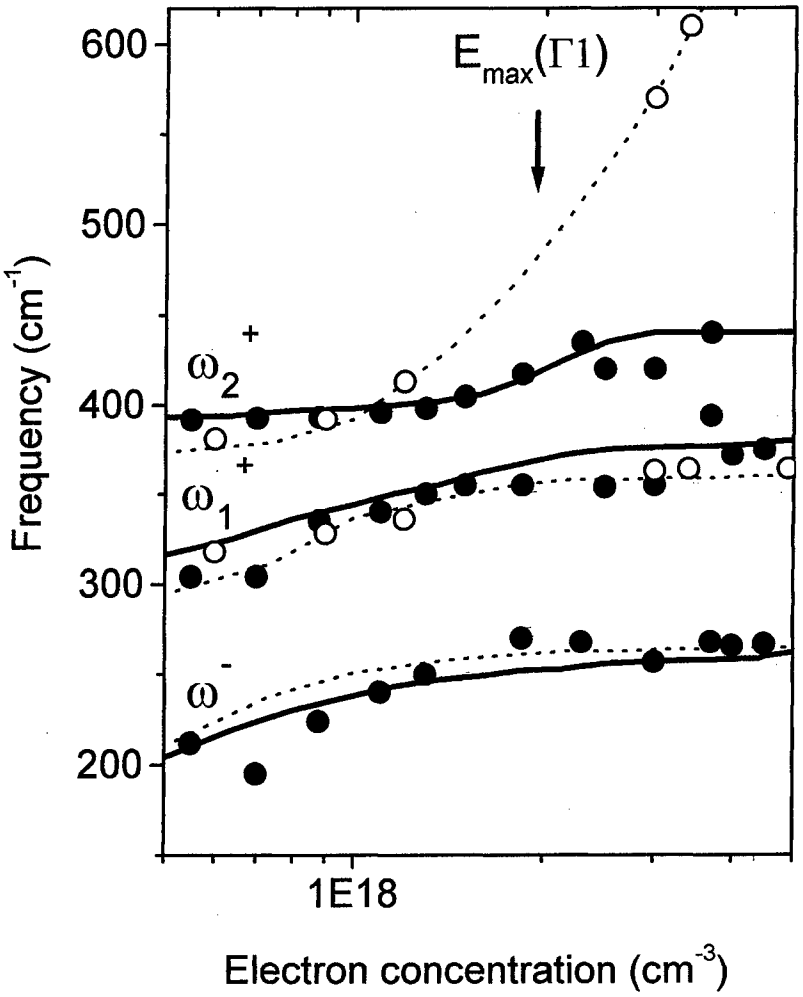


Fig.4. The frequencies of the Raman lines measured in the $(GaAs)_{17}(AlAs)_2$ superlattices (closed circles) and the frequencies of the collective vertically polarized plasmon-LO phonon modes calculated at the center of the Brillouin zone (full lines) in the $(GaAs)_{15}(Al_{0.4}Ga_{0.6}As)_4$ superlattices with different electron concentrations. The dotted lines and the open circles show the theoretical and experimental data respectively obtained for the $Al_{0.11}Ga_{0.89}As$ alloy.

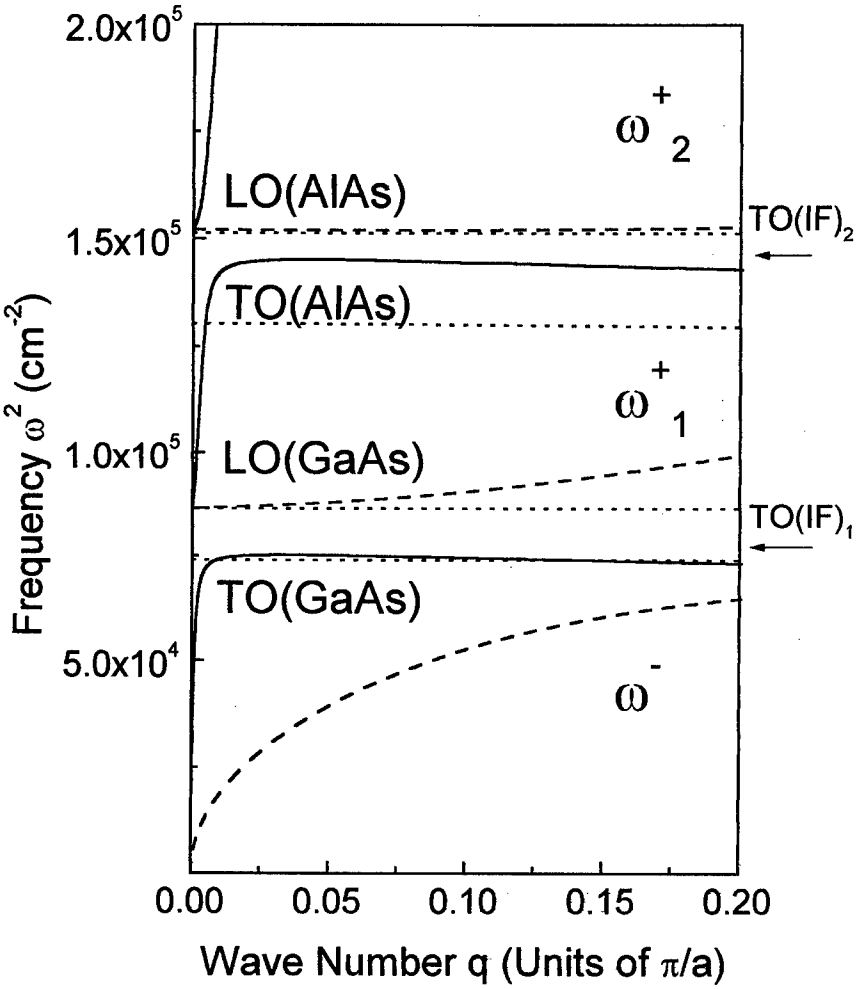


Fig.5. The dispersions of the collective plasmon-LO phonon excitations polarized normal to the layers, calculated in the $(GaAs)_{15}(Al_{0.4}Ga_{0.6}As)_4$ superlattices with different electron concentrations: the full lines correspond to the low electron density limit (ω_p=200 cm^{-1}, N = $5x10^{17}cm^{-3}$), while the broken lines were obtained in the high electron density limit (ω_p=800 cm^{-1}, N = $9x10^{18}cm^{-3}$). The dotted lines are the dispersions of the corresponding lattice optical vibrations.

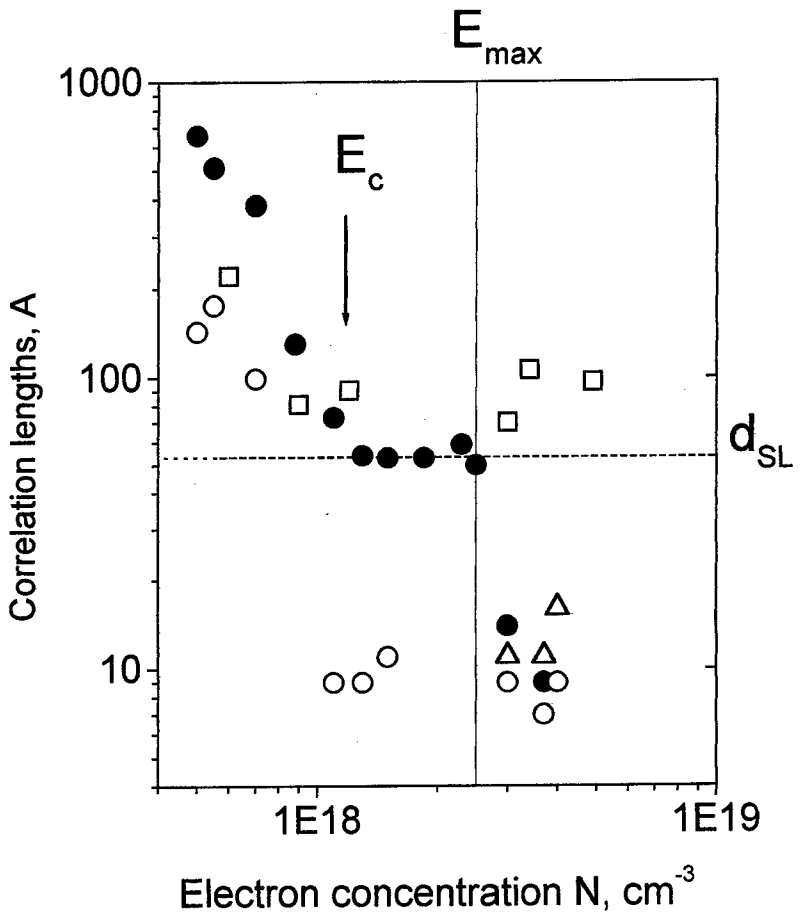


Fig.6. The coherence lengths L (open triangles), L_1 (open circles), L_2 (closed circles) of the plasmon-LO phonon excitations ω^-, ω_1^+, ω_2^+ respectively measured in the doped $(GaAs)_{17}(AlAs)_2$ superlattices with different electron concentrations. E_c is the mobility edge energy, d_{SL} is the superlattice period, while E_{max} is the top energy of the miniband. The squares present the coherence lengths obtained in the doped $Al_{0.11}Ga_{0.89}As$ alloy.

BRAGG REFLECTION, COHERENT COUPLING, RABI SPLITTING AND LASING IN SYSTEMS WITH RESONANTLY DISTRIBUTED QUANTUM WELLS

D. H. Christensen

University of Colorado
Departments of Physics and Electrical and Computer Engineering
Boulder, CO 80306

Quantum wells that are resonantly spaced by one-half of the heavy-hole exciton wavelength exhibit substantial Bragg reflection values even though the reflectance from a single quantum well is quite small. Bragg reflection and coherent coupling effects in these structures are very sensitive to the precision in spacing of the quantum wells and measurements that are in addition to optical measurements are needed. Their spacing is analyzed using x-ray diffractometry, reflectance spectroscopy, and transmission electron microscopy. Placing a resonantly spaced distribution of quantum wells in a half-wavelength microcavity such that the quantum wells are located at the interfaces of the distributed Bragg mirrors leads to strong exciton-photon coupling which is observable in the reflectance spectra at room temperature. When this cavity is excited to radiate, it operates as a distributed-feedback vertical-cavity surface-emitting laser. The periodicity of these microcavity structures is also analyzed using x-ray diffractometry, reflectance spectroscopy, and transmission electron microscopy.

RESONANTLY DISTRIBUTED QUANTUM WELLS

A set of single quantum wells which are spaced by one-half the heavy-hole exciton wavelength are distinct from a more closely spaced superlattice or typical multiple quantum well array. Half-wavelength spacing is approximately 111 nm for a 10 nm quantum well with an 850 nm, n=1, heavy-hole transition, and at that spacing, there is no overlap of the electronic wavefunctions for the individual wells, thus they are electronically uncoupled. The excitons in the wells, however, are coupled by photons and this coupling leads to collective effects which can manifest as changes in the radiative decay times, observable as superradiance and motional narrowing (1-3). The resonant spacing also leads to substantial Bragg reflection. The structure can be viewed as a typical quarter-wave stack of GaAs and $Al_{0.2}Ga_{0.8}As$ where the GaAs layer is made thinner, becoming a quantum well, while the $Al_{0.2}Ga_{0.8}As$ layer is made thicker in such a way as to maintain the half-wavelength periodicity. Reflection from a single quantum well is small since reflections from the two interfaces are completely out of phase, due to the index change at each interface, and the resultant interference is nearly completely destructive since the phase shift due to traversal through the well is small. When a number of individual wells are resonantly spaced, however, the reflections from each well constructively interfere to produce substantial Bragg reflection values. The phase relationship, general dimensions and geometry of the structure, and an equation expressing the half-wave period condition are illustrated in Fig. 1, which is a photocopy

of a transmission electron micrograph (TEM) of a portion of the structure. High quality micrographs with a resolution of a few monolayers will be presented at the meeting. In the equation, λ is the photon wavelength, n_{QW} is the refractive index of the quantum well, d_{QW} is the thickness of the quantum well, n_B is the refractive index of the barrier, and d_B is the thickness of the barrier. The product, nd, is the optical thickness of the respective layer.

The structures reported on here consist of a stack of forty individual GaAs quantum wells each with nominal thickness of 10 nm and which are nominally spaced by 111.4 nm $Al_{0.2}Ga_{0.8}As$ barriers. Actual thickness values of grown structures varied by a few percent from the nominal values, although great care was taken to produce forty identical quantum wells in a given structure. Also, some variation in the thickness of the barriers across the wafer was intentional, so as to allow a relative tuning of the spacing periodicity with respect to the fixed quantum well exciton energy. The reflectance spectrum shown in Fig. 2 demonstrates the substantial reflectance values achievable when the wells are precisely spaced, in this case the value is in excess of 80%. Outside the high reflectance zone, the structure exhibits a reflectance signature that is not much different from an epilayer of AlGaAs with an average index of the composite materials and equal total optical thickness. The modeling of the reflectance spectrum requires the complex refractive index of the quantum wells, barriers and substrate. These dispersion curves are then used in a typical transfer matrix calculation for multilayer thin film optics. The complex refractive index of the quantum wells was calculated from first principles and incorporates the requisite quantum effects, the details for the quantum well dispersion curves as well as barrier and substrate indices were reported in an earlier publication (4). A fit to a reflectance spectrum is shown in Fig.3 along with the real refractive index values of the quantum well used in the fit. Also shown in the figure, for comparison, is the refractive index of GaAs and the dispersion introduced by the quantum-confined excitons is clearly seen near 850 nm. The model based on GaAs does not at all represent the data in the 850 nm region, while the quantum well model fits the data very well. In this case, the barrier thickness is 110 nm, which is slightly less than the nominal thickness of 111.4 nm and so the peak Bragg reflection occurs at a slightly shorter wavelength than the exciton transition. The index dispersion due to the exciton transition leads to peak splitting in the reflectance spectrum, as seen in the figure. When such a dispersion characteristic is incorporated in a microcavity, on resonance, it leads to splitting of the resonance dip, also known quantum mechanically as vacuum Rabi splitting, and is discussed in the next section (5).

The exact periodicity of the structure has substantial impact on the coherent coupling effect observable in these structures, and methods, which are in addition to optical methods, for determining their periodicity are valuable. Measurement of precise periodicity can be accomplished by correlating reflectance measurements with x-ray diffractometric techniques and calibrated transmission electron microscopy. Two coherent coupling effects discussed in the literature are superradiance and motional narrowing and each is very sensitive to the precision in the growth of these structures, with perfect half-wave periodicity being the optimal condition (1-3). Optical techniques to determine the period are based on the same effects being observed, or on fitted reflectance spectra, which again are model dependent. It is therefore valuable to have a technique to independently determine the period. Double-crystal and multiple-crystal

X-ray diffractometry rocking curve analysis provides precise determination of structural periodicity in compound semiconductor epilayers, details of this technique can be found in (6). A double-crystal rocking curve was taken for the forty period distributed quantum well (DQW) array and is shown in the lower graph of Fig. 4, also shown in the figure is a fitted reflectance spectrum taken at the same position on the wafer and a schematic of the DQW structure. The rocking curve contains several satellite peaks which are indicated by –3, -2, -1, 0, +1, +2, +3, +4, and +5 in the graph. The peak labeled S is due to the substrate. The angular splitting of these satellite peaks is directly related to their periodicity (7). The rocking curve analysis for this data yields a periodic spacing of 127.0 nm. The modeled fit to the reflectance spectrum shown in the upper graph of the figure was achieved using a spacing of 125.8 nm. Additionally, precisely calibrated transmission electron microscopy measurements yielded a spacing of 125.6 nm. These independent measurements made with probes having very different radiation energies are well correlated and give confidence to the precision in the characterization. In this case, the spacing is thicker than the nominal 111.4 nm value and it can be seen that the Bragg peak in the reflectance is shifted to a wavelength which is longer than 850 nm.

DISTRIBUTED QUANTUM WELLS IN A MICROCAVITY

The resonant distribution discussed in the prior section did not involve any microcavity structure or conventional quarter-wave distributed Bragg mirrors. When quantum wells are placed in the center of a one-wavelength microcavity structure, the excitons in the quantum well become coupled to the cavity resonance, the so-called exciton-cavity or exciton-cavity polariton coupling (8). This structure is also a microcavity laser structure and has been named the vertical-cavity surface-emitting laser (VCSEL)(9). The exciton-photon coupling leads to a splitting of the cavity resonance, called vacuum Rabi splitting. The magnitude of the splitting has been shown to increase with the number of "atoms", in our case excitons, in the cavity (10,11). The excitons, however, must be positioned in such a way as to maintain overlap with the cavity-field distribution. Thus, to overcome the limitation of number that can be placed at the cavity center, one can distribute the quantum wells resonantly throughout the cavity, and hence increase the magnitude of the splitting. A basic geometry for such a structure is illustrated in Fig. 5. The upper drawing is the conventional case where a single quantum well is located at the center of a one-wavelength cavity, and the lower drawing is the case where the quantum wells are distributed throughout a half-wavelength cavity. When these structures are pumped hard enough, they lase, and the distributed quantum well structure is really a distributed feedback (DFB) laser, in contrast to the conventional distributed Bragg reflector (DBR) laser. It has been shown by Zhu *et al* that the vacuum Rabi splitting can be described with a completely classical model based on linear absorption and dispersion of the "atom", in this case quantum-well exciton, as applied in a traditional multibeam interference calculation (5). The results presented in the prior section and those presented in this section are based on just that, a linear dispersion and absorption model for the quantum well. Additionally, a more accurate treatment is presented in this paper since a full transfer matrix calculation is used for the multilayer optics and also includes reflections at the interfaces of the quantum well. When there are so many quantum wells in the structure, it is absolutely necessary to include these

reflections; indeed, the results of the prior section demonstrate just how substantial these reflections can be when constructively summed.

A structure containing quantum wells at all the DBR interfaces was grown and measured. The quantum wells are nominally 10 nm thick and are surrounded by AlAs and $Al_{0.2}Ga_{0.8}As$ barriers which also are the quarter wave layers of the DBR. The barrier/DBR layers were adjusted to be slightly thinner than those of a conventional DBR since the quantum well introduces additional optical path length. The upper mirror stack has 18.5 mirror pairs, the lower stack has 18 mirror pairs and the central half-wavelength cavity layer is composed of AlAs. Additionally, the entire structure was grown on a pump reflector stack consisting of 8 mirror pairs tuned to 761 nm. This pump reflector leads to a much more uniform pump field distribution than achieved without it and ensures more uniform low-intensity excitation of the quantum wells as well as improved pumping efficiency for laser operation. The room temperature reflectance spectrum for this structure is shown in Fig. 6. The influence of the quantum well linear absorption and dispersion on the resonance structure is clearly seen, even at room temperature, as a broadening and splitting in the resonance. When the linear dispersion model for the quantum well is applied in the multilayer optics calculation, an excellent fit to the reflectance data is achieved, as seen in the upper graph of Fig. 7. Also shown in the lower graph of Fig. 7 is a measured X-ray rocking curve and a schematic for this structure. The careful periodicity analysis based on correlation of reflectance, X-ray, and transmission electron microscopy measurements of this structure was also performed. In Fig. 7, lower graph, the rocking-curve satellite peaks labeled –5, -4, -3, -2, -1, 0, +1, +2, +3, +4, and +5 are due to the periodicity of the DFB portion of the microcavity and their splitting indicates a period of 129.3 nm. The satellite peaks with reduced intensity, labeled as –2', -1', 0', and +4', have a larger splitting than those for the DFB, are due to the pump mirror stack, and indicate a period of 113.8 nm. The reflectance fit shown in the upper graph of Fig. 7 was obtained using a DFB period of 129.1 nm and a pump mirror period of 115.4 nm. Calibrated transmission electron microscopy measurements on this structure yielded periods of 129 nm for the DFB portion and 116 nm for the pump mirror portion. These measurements are in very good agreement and provide confidence in the precision obtained in the use of reflectance and X-ray diffractometry as a nondestructive metrology tool.

Optically excited emission from the device was also studied at room temperature. High-intensity excitation was performed to see if lasing could be achieved in these devices. The devices were pumped at room temperature using a CW Ti:Sapphire laser tuned near 770 nm. The beam passed through a variable attenuator and a beamsplitter, and then into a 60X microscope objective which is focused, or slightly defocused, onto the sample. The emission was monitored by coupling the light from the beamsplitter into an optical fiber that is coupled into an optical spectrum analyzer with 0.1 nm spectral resolution. The linewidth of the quantum well luminescence at a pumping level just below threshold was approximately 2.0 nm, indicating superluminescent emission, as shown in Fig. 8(a). As the optical pump intensity was increased, a threshold was observed where the emission shows further significant spectral narrowing to less than 0.3 nm. This narrowing was accompanied by a large increase, > 25 dB, of the emission intensity, indicating lasing, as shown in Fig. 8(b). The 770 nm pump line, the GaAs substrate emission near 900 nm, and the buffer superlattice emission near 800 nm are also seen in the figure. The minimum threshold pump intensity was approximately 70 mW

total power incident on the wafer and the maximum absorbed power is estimated to be less than 56 mW. The average optical output power of the laser was measured by introducing a long-pass filter to block the pump beam. At approximately 1.4 times threshold, the devices emitted approximately 1 mW, neglecting coupling loss into the optical fiber. Other regions of the wafer had thresholds as low as 32 mW absorbed pump power and lasing wavelengths ranged from 835 nm to 851 nm across the wafer. The lasing linewidth is the narrowest ever reported for a DFB VCSEL.

Low-intensity optical excitation was also performed at room temperature. The 770 nm pump was not focused and had a spot diameter of approximately 2 mm and less than 1 mW of total power. Photoluminescence spectra were taken from both the normal incidence direction, which includes the microcavity influence, and from the cross-sectional direction, which does not include the cavity influence. The cross-sectional measurements show typical quantum well emission spectra with a broad peak due to the heavy-hole, n=1 exciton, and further broadening on the high energy side of this peak which is due to the broadened light-hole exciton line. The individual lines are so broadened that they merge to form a spectrum that has one peak that appears to be asymmetrically broadened on the high-energy side, typical for room temperature spectra. Emission from the direction normal to the surface, however, is strongly influenced by the cavity effects. The emission in this direction has two peaks whose locations precisely correspond to the resonance minima at 848 and 842 nm seen in Fig. 6. This peak splitting in the low-excitation intensity photoluminescence spectrum is the result of the cavity resonance splitting.

SUMMARY

In summary, precise fitting of the reflectance spectra from quantum well Bragg reflectors is accomplished by using appropriate index dispersion models. These structures can exhibit substantial Bragg peaks with reflectances greater than 80% even though the reflection from a single quantum well is small. The linear dispersion model of the refractive index leads to peak splitting in the reflectance signature. X-ray rocking curve measurements provide a precise and nondestructive means for determining the periodicity of the structures and when correlated with the nondestructive technique of reflectance spectroscopy one obtains a precise characterization. These metrological techniques are valuable in that they provide a means of independently verifying the precise spacing of the wells.

A novel type of vertical-cavity device has also been demonstrated. The introduction of quantum wells distributed entirely throughout the cavity and the distributed Bragg reflectors leads to strong coupling of the quantum well exciton transitions to the cavity resonance mode. This is observable as resonance splitting in the reflectance spectrum and the influence of the quantum well linear absorption and dispersion interacting with the cavity mode is clearly seen even at room temperature. Precise fitting to the reflectance spectra is accomplished by using the appropriate index dispersion models. X-ray rocking curve measurements provide a precise and non-destructive means for determining the periodicity of the DFB portion of these structures as well as the pump reflector region that is buried beneath the DFB portion. The periodicity measurements

were further analyzed by calibrated TEM measurements and all these results were correlated to enable a precise characterization of these structures. When excited to radiate, the low-excitation-intensity photoluminescence spectra show unique peak splitting features that are directly related to the resonance splitting seen in reflectance. High-intensity excitation produces lasing with the narrowest emission linewidths and lowest thresholds ever reported for a DFB VCSEL.

ACKNOWLEDGEMENTS

The author gratefully acknowledges the prior collaborative interaction with Robert Hickernell, Jin Wang, Jean-Pierre Leburton, and Joseph Pellegrino to develop dispersion models for the quantum well indices (4). The author also gratefully acknowledges James Hill for his contribution to some of the X-ray work, Raghaw Rai for the transmission electron microscopy measurements, and Craig Parsons for photoluminescence measurements.

REFERENCES

1. T. Stroucken, A. Knorr, P. Thomas, and S. W. Koch, Phys. Rev. B, 53, 2026 (1996).
2. M. H□bner, J. Kuhl, T. Stroucken, A. Knorr, S. W. Koch, R. Hey, and K. Ploog, Phys. Rev. Lett., 76, 4199 (1996).
3. A. V. Kavokin and J. J. Baumberg, Phys. Rev. B, 57, R12697 (1998).
4. R. K. Hickernell, D. H. Christensen, J. G. Pellegrino, J. Wang, and J.-P. Leburton, J. Appl. Phys., 75, 3056 (1994).
5. Y. Zhu, D. J. Gauthier, S. E. Morin, Q. Wu, H. J. Carmichael, and T.W. Mossberg, Phys. Rev. Lett., 64, 2499 (1990).
6. D. H. Christensen, J. R. Hill, R. K. Hickernell, K. Matney, and M. S. Goorsky, Mater. Sci. Eng. B, 44, 113 (1997).
7. D. H. Christensen, J. G. Pellegrino, R. K. Hickernell, S. M. Crochiere, C. A. Parsons, and R. S. Rai, J. Appl. Phys., 72, 5982 (1992).
8. C. Weisbuch, M. Nishioka, A. Ishikawa, and Y. Arakawa, Phys. Rev. Lett., 69, 3314 (1992).
9. D. H. Christensen and F. S. Barnes, in Topical Meeting on Semiconductor Lasers, Technical Digest, V. 6, p. 99, Optical Society of America, Washington, D.C. (1987).
10. G. S. Agarwal, Phys. Rev. Lett., 51, 1732 (1983).
11. G. S. Agarwal, J. Opt. Soc. Am. B, 2, 480 (1985).

Fig.1 (Right) Geometry and dimensions of the DQW array.

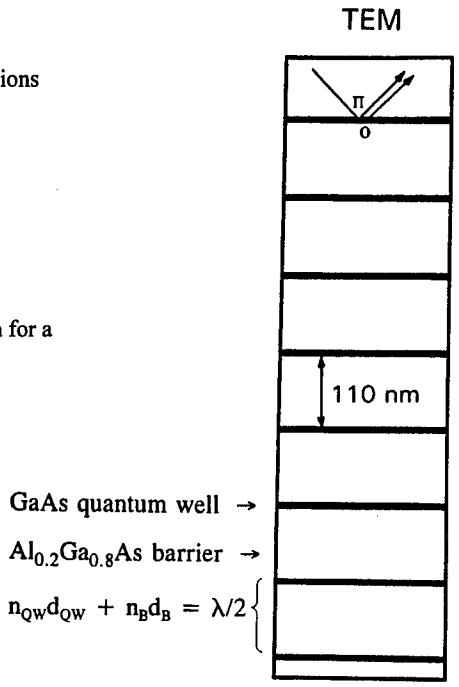
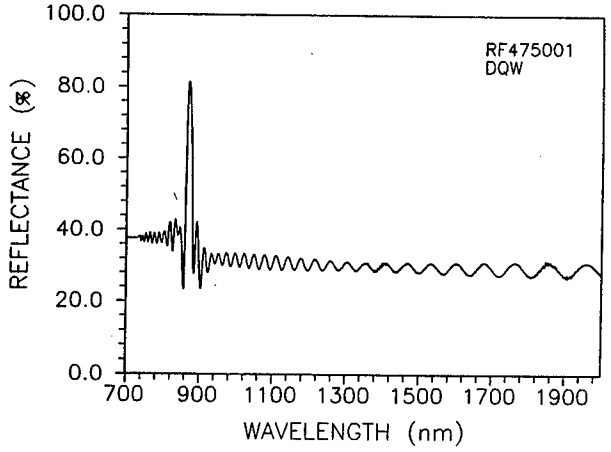


Fig. 2 (Below) Reflectance spectrum for a DQW array.



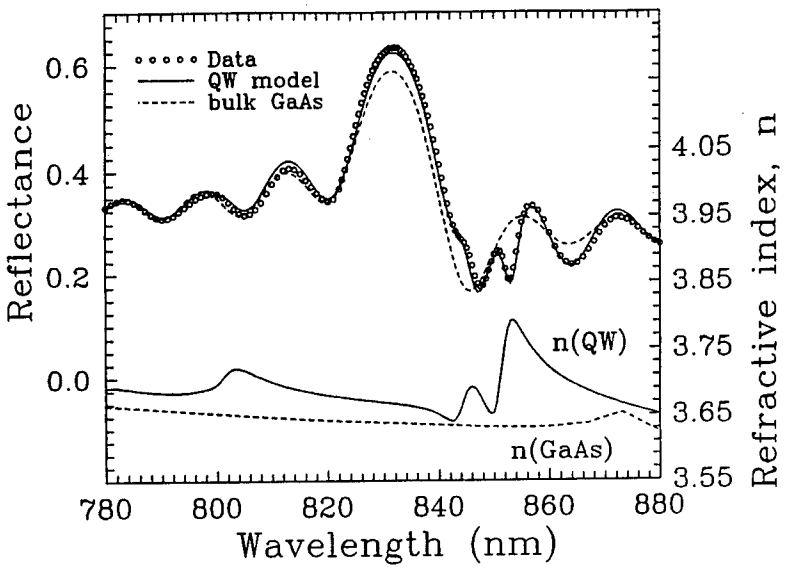


Fig. 3 Reflectance data and fits to the data using the quantum well index model and the bulk GaAs index model. The lower curves are the dispersion curves for the quantum well and GaAs index of refraction.

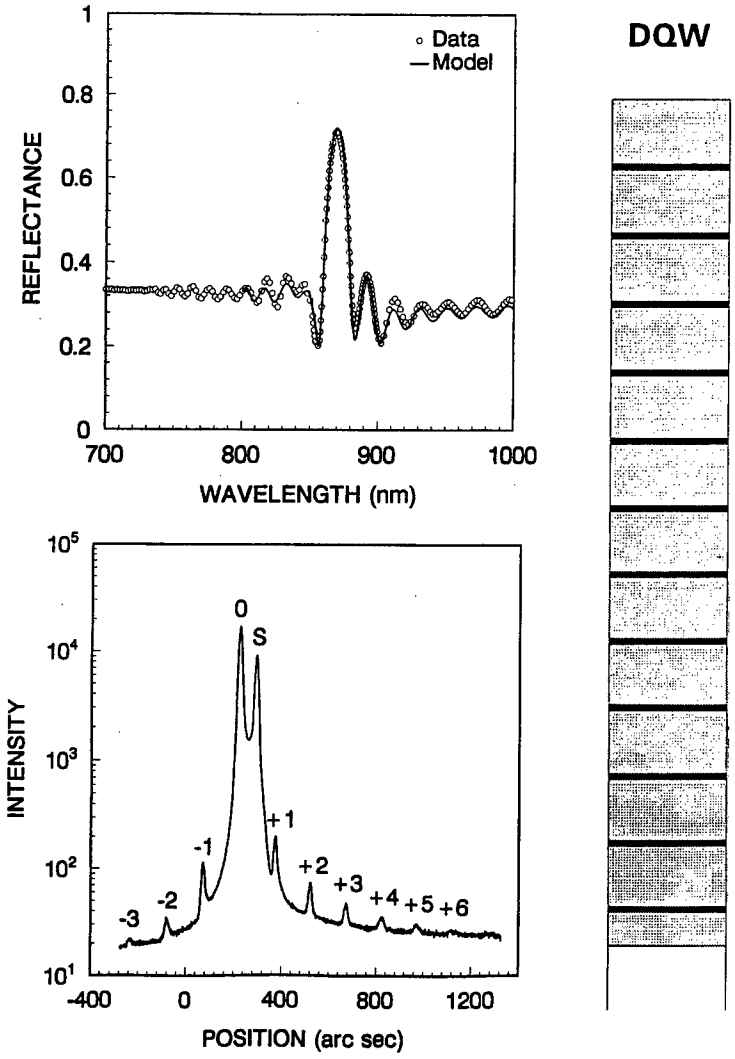


Fig. 4 The upper graph is a modeled fit to the reflectance data for the DQW array. The lower graph is the measured X-ray rocking curve for the DQW array.

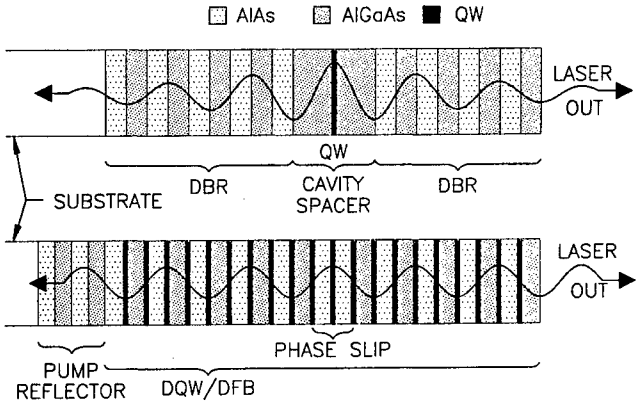


Fig. 5 Schematic illustrating the situations when a single quantum well is located at the center of the cavity (upper) and when many quantum wells are distributed throughout the cavity and DBRs.

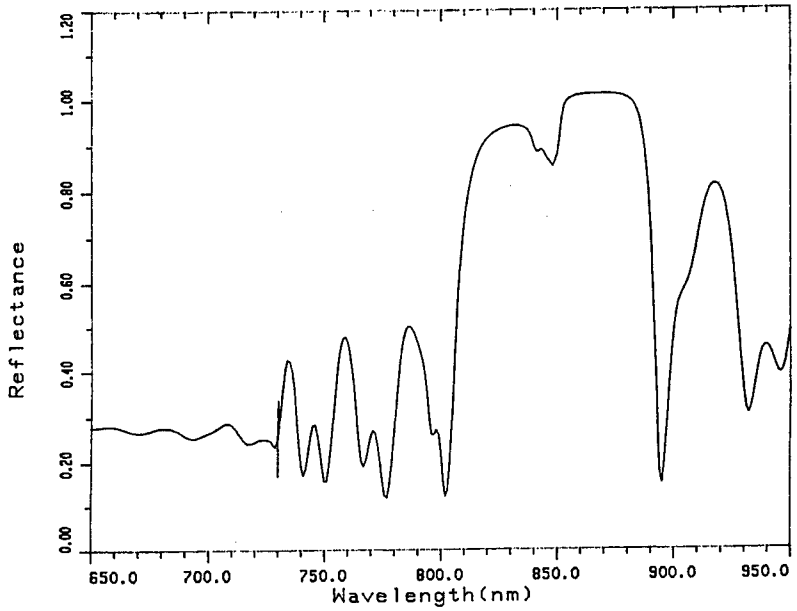


Fig. 6 The reflectance spectrum shows a broadening and a splitting of the cavity resonance near 850 nm.

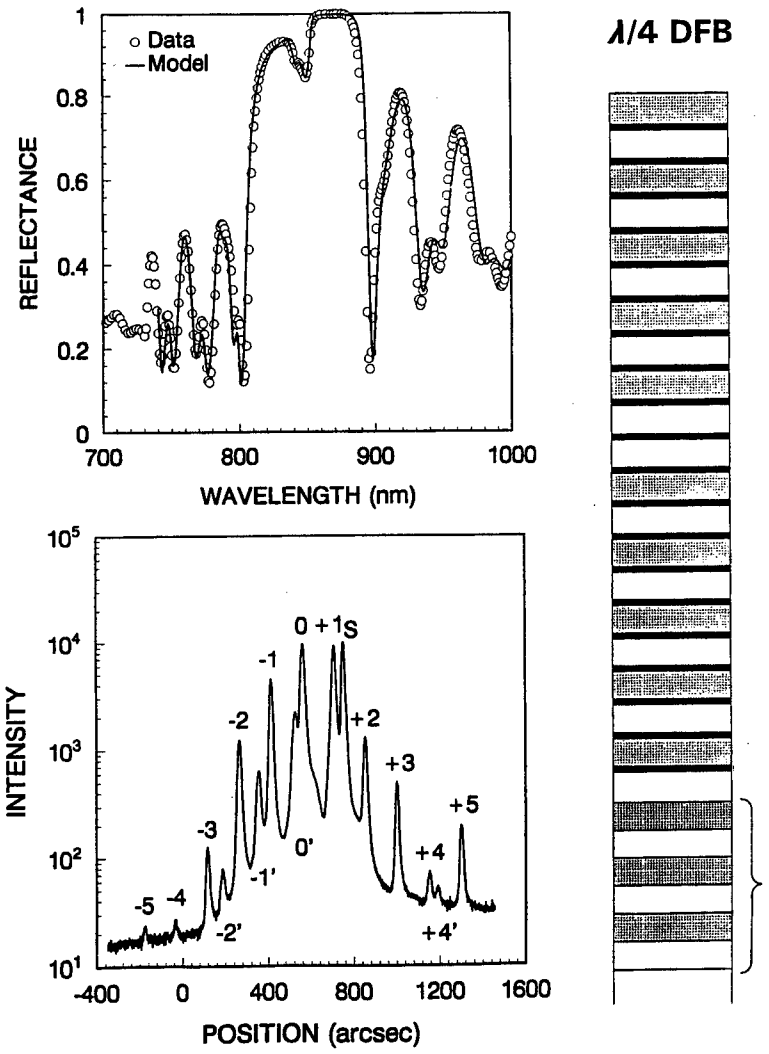


Fig. 7 The upper graph is a modeled fit to the reflectance data for the DQWs in a microcavity. The lower graph is the measured X-ray rocking curve.

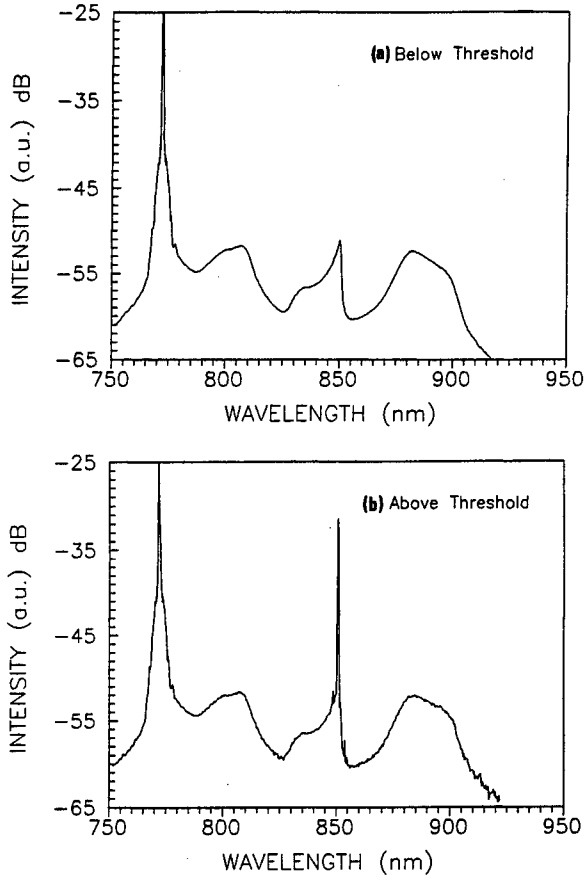


Fig. 8 The upper graph shows the emission just below threshold. The lower graph shows the emission just above threshold.

THERMALISATION OF HOT ELECTRONS AND THERMIONIC COOLING IN A SINGLE BARRIER STRUCTURE

C. Zhang and R. A. Lewis

Department of Engineering Physics, University of Wollongong, New South Wales 2522, Australia

One of the important problems in multilayer thermionics is related to the thermalisation of hot electrons in the electrodes and in the barrier region. Thermalisation may occur directly via the electron-phonon interaction, or indirectly via the electron-electron interaction. In semiconductor heterostructures at room temperature, the LO phonon plays a crucial role in thermalising electrons. In this work we study the thermalisation of electrons in a single barrier structure by taking into account the electron-phonon interaction. The relaxation is dependent on the lattice temperature of each electrode. Because the rate of thermalisation increases with the temperature exponentially and thermalisation in the barrier region only affects the emission current from the hot electrode, the reduction of thermionic emission for the hot electrode is greater than that for the cold electrode. As a result, we find that the theoretical thermal efficiency can increase due to thermalisation.

I. INTRODUCTION

Thermionics was discovered by Thomas Edison in 1883. Interest in the subject was recently revived by Mahan et al.[1-5] and Shakouri et al.[6,7]. A simple thermionic device comprises two parallel metal plates separated by a small distance. One plate is hot and the other is cold. The two plates can have equal or unequal work functions. If unequal, the hot side can have either the small or large work function. Here we consider the case of unequal work functions, where the large work function is on the hot side.

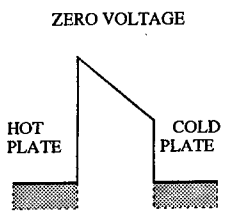


FIGURE 1

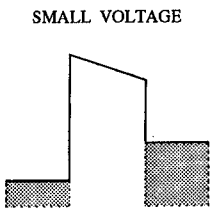


FIGURE 2

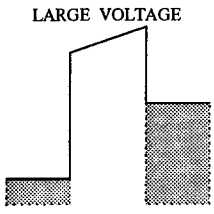


FIGURE 3

Figure 1 shows a potential energy diagram for an electron between two metal surfaces with different work functions: ϕ_L on the left which is hot with temperature T_L, and ϕ_R on the right which is cold with temperature $T_R<T_L$. Since the electron charge $e<0$ and $e\phi_{L,R}$ are positive, $\phi_{L,R}<0$. The space between the surfaces is vacuum or filled with a dilute gas. Here the electric field is constant. The two horizontal lines represent the chemical potentials for the two metal plates, which serve as electrodes.

An electron can jump between the two metal plates over the potential barrier due to thermal excitation. Since the left-hand plate has the higher temperature, there is a net electron flow from the left side to the right side. By connecting the two metal plates to an external load, a thermionic power generator is made.

By applying an increasing positive voltage V, the potential diagram will be changed sucessively from the situation shown in Figure 1 to Figure 2, and to Figure 3. Under the situation of large positive voltage, as shown in Figure 3, an electron in the right-hand electrode needs only an energy $e\phi_R$ to jump to the left-hand side, but the required energy, $e(\phi_R\text{-}V)$, for an electron in the left-hand metal to jump to the right-hand is much larger. The difference between these two *activation energies* increases with the applied voltage. Therefore, for a large enough voltage, the net flow of electrons is *from the cold metal plate to the hot metal plate.* This is the physics

of thermionic cooling, which is a Peltier effect. Depending on the value of $T_{L,R}$ and $\phi_{L,R}$, the change of operation between thermionic power generation and thermionic refrigeration may occur at a somewhat smaller voltage, as shown in Figure 2.

II. THERMIONIC EMISSION AND THERMALISATION

All thermionic devices are based on Richardson's equation for the current per unit area J emitted by a surface with work function ϕ at a temperature T,

$$J_R(\phi, T) = AT^2 \exp(-e\phi/k_B T), \tag{1}$$

where

$$A = (emk_B^2)/(2\pi^2\hbar^3) \simeq 120 \text{ A/cm}^2\text{K}^2. \tag{2}$$

For simplicity we consider the case $\phi_L = \phi_R$. The electrical current under an applied bias V is given as

$$J = J_R(\phi, T_c) - J_R(\phi, T_h)e^{-eV/k_B T_h}, \tag{3}$$

and the energy current is given as

$$eJ_Q = [e\phi + 2k_B T_c]J_R(\phi, T_c) - [e\phi + 2k_B T_h]J_R(\phi, T_h)e^{-eV/k_B T_h} - \frac{T_h - T_c}{R_{th}} \tag{4}$$

where R_{th} is the thermal resistance of the barrier. The thermal efficiency (or coefficient of performance of the thermionic refrigerator) is defined as

$$\eta = \frac{J_Q}{JV} \tag{5}$$

For thermionic cooling to work in a real device, several conditions must be met. (i) Thermionic emission is only the correct model if the barrier thickness is greater than the tunneling length $L_t = \hbar\sqrt{e\phi/m}/2k_B T$; (ii) the electron mean-free path λ should be greater than the barrier width in order for the cross-barrier motion to be ballistic; (iii) the temperature gradient in the barrier should be small so the thermal conduction is also small. Mahan has proposed to use a multilayer structure to minimise thermal conduction and to achieve thermionic cooling with thermal efficiency about twice of that of a thermoelectric device. However, in Mahan's simple development many important factors are neglected. Here we consider the influence of electron thermalisation.

In semiconductor heterostructures and metal-semiconductor multilayers at room temperature, electron thermalisation in the electrodes and in the barrier region will affect the efficiency of thermionic cooling. One can always make the barrier region

sufficiently small to avoid scattering of ballistically traveling electrons. However, the electron thermalisation due to electron-phonon and electron-electron scattering in the electrodes cannot so easily be eliminated. Here we show that the finite scattering by LO phonons in the electrodes and in the barrier region can sometimes improve the efficiency of a thermionic refrigerator.

The rate of energy loss due to electron-phonon interaction can be written as [8],

$$\frac{d\epsilon}{dt} = \frac{2\alpha\hbar\omega_o}{\sqrt{2m\epsilon}}\left[N_q \sinh^{-1}\left(\frac{\epsilon}{\hbar\omega_o}\right)^{1/2} - (N_q+1)\sinh^{-1}\left(\frac{\epsilon}{\hbar\omega_o}-1\right)^{1/2}\right] \quad (6)$$

where ϵ is the energy of the ballistic electrons, ω_o is the phonon frequency and $N_q = [\exp(\hbar\omega_o/k_BT) - 1]^{-1}$ is the phonon distribution function. The electron-LO-phonon coupling constant α is

$$\alpha = \frac{me^2\omega_o}{\hbar}\left(\frac{1}{K_\infty} - \frac{1}{K_0}\right). \quad (7)$$

Here K_∞ and K_0 are the optical and static dielectric constants of the host materials. The fractional energy loss per unit distance L_e can be written as

$$\frac{1}{L_e} = \frac{1}{\epsilon}\frac{d\epsilon}{dx} = \frac{\sqrt{m}}{\sqrt{2}}\frac{1}{\epsilon^{3/2}}\frac{d\epsilon}{dt}. \quad (8)$$

The energy loss rate in a thermionic refrigerator depends on temperature in two ways: (i) as temperature increases, the phonon number increases exponentially and therefore thermalisation increases; (ii) the energy of hot electrons involved in thermionic emission increases with temperature and this will in general lead to a reduced scattering rate. Since the net heat current across the barrier from the cold electrode to the hot electrode is the difference of the current emitted from the cold side and that emitted from the hot side, the reduction of thermal current due to effect (i) is larger for $J_R(T_h)$ than that for $J_R(T_c)$. On the other hand the reduction of the thermal current due to effect (ii) is larger for $J_R(T_c)$. The interplay of these two effects may result in and overall increase or decrease of the net heat current flowing from the cold side to the hot side. Under certain conditions, the thermal efficiency can be enhanced.

Thermalisation in the barrier region will also affect the performance of the thermionic refrigerator. In fact, if electrons are scattered mainly by phonons, thermalisation in the barrier region is as important as that in the electrodes. If the emission takes place very close to the interface, the thermalisation in the barrier region is more dominant. Under an applied bias, the barrier has a triangular shape with highest point attached to the cold electrode (Figure 3). With such a barrier

profile, thermalisation of electrons in the barrier region will mainly affect $J_R(T_h)$. The electrons emitted from the cold electrode will continue travelling towards the hot electrode once they are in the barrier region. If these electrons lose energy to the lattice they can easily move towards the hot electrode while their only way back to the cold electrode is through tunneling. The situation is the opposite for electrons emitted from the hot electrode. Any loss of energy for these electrons in the barrier region will prevent them from travelling further towards the cold electrode. The energy loss in the barrier region is given by the a result similar to equations (6) and (8). However the relavent energy of the electron is smaller by a fraction of the barrier height. Furthermore the energy loss is position dependent because energy is position dependent

$$\left(\frac{d\epsilon}{dt}\right)_{barrier} = \frac{2\alpha\hbar\omega_o}{\sqrt{2m\epsilon(x)}}\left[N_q \sinh^{-1}\left(\frac{\epsilon(x)}{\hbar\omega_o}\right)^{1/2} - (N_q+1)\sinh^{-1}\left(\frac{\epsilon(x)}{\hbar\omega_o}-1\right)^{1/2}\right]. \tag{9}$$

The amount of energy lost in the barrier region will eventually be dissipated in the two electrodes. For a symmetric system, the assumption used in the usual thermoelectric theory is that heat is dissipated equally in the two electrodes. In the present case, the energy loss is very small near the clod plate and electron can lose large amounts of energy close to the hot plate. Therefore a large proportion of the energy lost in the barrier region will be dissipated in the hot electrode. The net effect of thermalisation in the barrier region is thus to improve the thermal efficiency.

The net electrical and heat current in the presence of energy loss due to phonon scattering can now be written as

$$J = J_R(\phi, T_c)e^{-L/L_e(T_c)}B_c - J_R(\phi, T_h)e^{-eV/k_BT_h}e^{-L/L_e(T_h)B_h}, \tag{10}$$

and

$$\begin{aligned} eJ_Q &= [e\phi + 2k_BT_c]J_R(\phi, T_c)e^{-L/L_e(T_c)}B_c \\ &-[e\phi + 2k_BT_h]J_R(\phi, T_h)e^{-eV/k_BT_h}e^{-(L-L_B)/L_e(T_h)}B_h - \frac{T_h - T_c}{R_{th}} \\ &- \int_0^a dx\left(1-\frac{2x}{a}\right)\left\{J_R(T_c)\left[\frac{d\epsilon(T_c)}{dx}\right]_{barrier} + J_R(T_h)\left[\frac{d\epsilon(T_h)}{dx}\right]_{barrier}\right\}. \end{aligned} \tag{11}$$

Here L is the average distance an electron travels in the electrode. B_c and B_h represent the scattering terms in the barrier region,

$$B_{c,h} = \exp\left(-\int_0^a dx/L_B(x, T_{c,h})\right), \tag{12}$$

where a is the barrier width and L_B is the fractional energy loss per unit distance in the barrier region. The energy loss in the barrier region dissipated in both electrodes. If the amount of energy loss at x (measured from the interface at cold plate) is δE, the proportion that goes to the cold electrode is $1 - x/a$. The last term in eq.(11) represents this effect.

III. RESULTS AND DISCUSSION

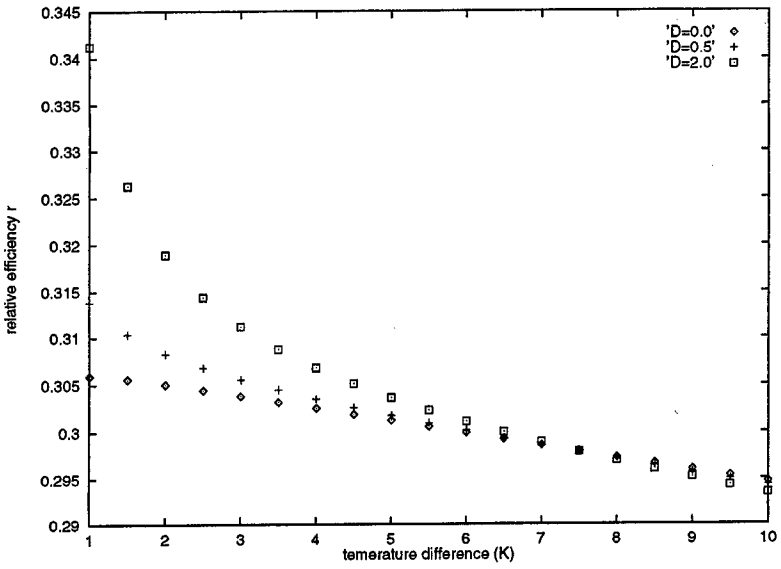


Figure 4. The relative thermal efficiency of a single barrier structure as a function of temperature difference between the electrodes.

The thermal efficiency for a single-layer structure is calculated based on equations (9-12) as a function of temperature difference $T_h - T_c$. For every temperature difference, we use the optimal bias such that the thermal efficiency is maximum. The parameters used here are those for a GaAs/Al_xGa_{1-x}As/GaAs structure: $m = 0.067m_o$, $K_\infty = 10.8$, $K_0 = 12.5$. The barrier height depends on the value of Al fraction. In our calculation we choose $\phi = 100$ meV. The phonon frequency is $\omega_o = 36$ meV. The temperature of the cold electrode is fixed at 260 K. The dimensionless quantity $Z = ek_B/(R_{th}A(k_BT_c)^2) = T_R^2/T_c^2$ is set by $T_R = 200$. In Figure 4, we plot the ratio of calculated thermal efficiency to the Carnot efficiency, $r = \eta/\eta_c$

where $\eta_c = T_c/(T_h - T_c)$ is the Carnot efficiency. For fixed temperature, thermalisation varies with the mean distance L. Since the emission is occuring very close to the interface we choose $k_F L$=0.01 Several different values of the dimensionless quantity $D = k_F a$ are used in our calculation. It is interesting to see that the efficiency is slightly higher for systems with finite electron phonon scattering than for a system with perfectly ballistic electrons. This is due to the fact that the reduction of emission current from the hot electrode is larger than that from the cold electrode.

In conclusion, we have studied the effect of electron thermalisation due to the electron-phonon interaction of a thermionic cooling device. It is found that the energy loss is larger for electrons emitted from the hot electrode than for electrons emitted from the cold electrode and thus thermalisation increases the device efficiency. However, one would expect that the situation will be reversed if the scattering is due to other defects whose distribution is temperature independent, for example, impurities and surface roughness. These effects will be studied elsewhere.

References

[1] G. D. Mahan and H. B. Lyon, Jr, J. Appl. Phys. **76**, 1899 (1994)

[2] J. O. Sofo and G. D. Mahan, Appl. Phys. Lett. **65**, 2690 (1994)

[3] G. D. Mahan and L. M. Woods, Phys. Rev. Lett. **80**, 4016 (1998)

[4] G. D. Mahan, J. O. Sofo, and M. Bartkowiak, J. Appl. Phys. **83**, 4683 (1998)

[5] G. D. Mahan, J. Appl. Phys. **76**, 4362 (1994)

[6] A. Shakouri et al., Appl. Phys. Lett. **74**, 88 (1999)

[7] A. Shakouri and J. E. Bowers, Appl. Phys. Lett. **71**, 1234 (1997)

[8] C. J. Hearn, Proc. Roy. Soc. (London) **86**, 881 (1965)

DYNAMIC CHARACTERISTICS OF CURRENT HYSTERESIS IN WEAKLY COUPLED SUPERLATTICES GaAs/AlGaAs

G.K.Rasulova
P.N.Lebedev Physical Institute of Russian Academy of Sciences

Leninskii prosp. 53, 117924 Moscow, Russia

ABSTRACT

The dynamic characteristics of weakly coupled superlattices are experimentally studied by both the investigation of the transient current responses and the oscilloscopic study of the hysteresis loop. The observed transient current responses are classified into two categories: the switching current responses with different levels of the initial and final current, and the transient current responses that retain the same value of the initial and final current. The study of the oscilloscope images of the I–V characteristics produced by different types of an external sweep allowed us to reproduce the current traces for the closed cycle current oscillations. The damped current oscillations with a frequency of 83 kHz have been observed.

I. INTRODUCTION

Recently, weakly coupled semiconductor superlattices (SL's) have attracted much attention due to the potential for application as tunable high frequency generators can operate from 50 kHz up to 10 GHz [1-5]. Theoretical study [6-9] has shown that current oscillations originate due to the spatiotemporal oscillations of the domain boundary along the SL axis. The domain boundary is formed by a charge accumulation layer which provides a voltage drop at the region of the domain boundary necessary for resonant coupling between different subbands in adjacent quantum wells (QW's). A negative differential conductance (NDC) in I–V characteristics of weakly coupled SL's is a result of the electric field domain formation. Current instabilities are inherent for NDC region and can be exhibited as current oscillations and switching.

Our interest is the low doped SL structures with a large current hysteresis in I–V characteristics. It has been supposed that the domain boundary expansion is a cause of the current hysteresis [10,11]. A magnitude of the current hysteresis is a measure of the domain boundary expansion. Current instability has been exhibited in our experiments as the switching between high- and low-current states of hysteresis loop [10]. The switching time for the current jump from high- to low-current state is about

0.1 μs, whereas the time for reverse switching is about 1 μs.

The purpose of the present paper is to obtain further insight into the dynamic properties of the domain boundary formation by means of the investigation of the transient switching current responses by applying the single square pulses with different polarity, duration and amplitudes at fixed voltages within the hysteresis loop. These measurements were produced in conjunction with the oscilloscopic study of hysteresis loop using different types of an external sweep.

II. EXPERIMENTAL RESULTS

The samples were grown by molecular beam epitaxy. The investigated sample consists of a 30-period weakly coupled SL with 390 $\AA$ $GaAs$ wells and 110 $\AA$ $Al_{0.3}Ga_{0.7}As$ barriers. The SL region was uniformly doped with silicon to a doping level of $1{\cdot}10^{16}$ cm^{-3}. The SL was sandwiched between two 50 $\AA$ $Al_{0.3}Ga_{0.7}As$ barriers. The bottom and the top of the SL were a highly doped n^+ –GaAs emitter and collector electrodes (doping level is 10^{18} cm^{-3} with thicknesses of 0.5 μm and 100 $\AA$, respectively. The devices were fabricated by etching mesas of 600 μm diameter and had ohmic $AuGe/Ni$ contacts on both sides of the structure.

The I–V characteristics were measured by standard technique. The square pulses are generated with a G5-75 pulse generator. The real time transient current responses were recorded with a digital oscilloscope. It has to be noted that our experimenal results were limited by temporal resolution of the digital oscilloscope (of about 100 ns).

a). Transient current response

The fragment of static I–V characteristic of an investigated sample at 4.2 K is shown in Fig. 1 (thick line for up-sweep, thin line for down-sweep directions). The type of high-field domains is marked by arrows at the points of their initiation.

In our previous measurements the switching traces were detected as vertical lines connecting upper- and lower-current states [10]. It was reported that by applying a positive single pulse the current is switched from high- to low-current state, by negative pulsing the reverse down-to-up current jump is done. In these experiments the initial and final switching current states were detected. In order to obtain the direct information about the switching times and to define the actual route of the switching current, the real time transient current responses have studied. In Fig. 2 the enlarged fragment of the hysteresis loop with the measured current branches is presented. The single square pulses with a width of 10 μs and an amplitude of 0.3 V were applied at fixed dc bias of 4.75 V (is marked by dashed line in Fig. 2) at high- (point (a)) and low-current (point (b)) states of the I–V characteristic. The recorded transient current responses are performed in Fig. 3. The onset of the voltage step is defined by 0 μs. In both Fig.s 2, 3 the initial and final stable current states are denoted by points (a) and (b), respectively. The points (a') and (b') are the waiting points during the applied pulse time. The two pronounced switching current responses with different levels of the initial (a) and final (b) current are displayed at the left of Fig.

3 (I, III). It was surprising to detect the transient responses by applying the positive square pulses at low-current state (Fig. 3 (II)) and negative pulses at high-current state (Fig. 3 (IV)). As shown in Fig. 3 (II, IV) the initial and final stabilized current values of the transient current responses are the same. The shapes of the observed transient current responses are typical for other fixed dc biases within the hysteresis loop.

A comparison of the stabilized current values obtained from the transient switching current responses with the current values from the static I–V characteristic made it possible to reproduce the current traces for the switching process. The main feature of the observed switching current responses (Fig. (I), (III)) that the switching is realized by trailing edge of the applied single square pulse. The switching is completed via the current branch. In Fig. 2 the switching current traces for both pulse polarity are shown by arrows. Fig. 3 (I) shows that the leading edge of the switching pulse reflects the leading edge of an applied pulse. The current reaches the stable value in a rising edge time. This time is less than 100 ns. The relaxation time of the switching process at final stabilized low-current state (point (b)) is about 1 μs. For the reverse transition (Fig. 3 (III)), when the total voltage is reduced under the leading edge of the negative single pulse, the time constant is about 1 μs (waiting point (b')). The time constant at the final high-current stable state (point (a)) is less than 1 μs. Unfortunately, due to the deficiency in resolution of our digital oscilloscope we cannot get the adequate values of the relaxation times.

b). Oscilloscopic study of the hysteresis loop

To understand the origin of the transient current response in which the current is recovered to its initial state the oscilloscopic investigation of the hysteresis loop was carried out. It was made by applying to the horizontal plates of the oscilliscope an external sweep of different shape in frequency range from 10 to 10^3 Hz. The bipolar and unipolar (negative and positive) sawtooth-shaped wave sweep has used. Both type of the sweep are presented in circular insets of Fig. 4. Three oscilloscope images of the I–V characteristic produced with a variety of sawtooth-shaped sweep at frequency of 10^3 Hz are displayed in Fig. 4. The two images measured with delayed in half a period sawtooth wave sweep of both polarity are superposed on the oscilloscope image of the I–V characteristic (dashed line) produced by bipolar sawtooth wave sweep with a peak-to-peak amplitude of 0.2 V. The dashed image clearly reproduces all the current branches at working frequency.

Let us consider the oscilloscope image of the I–V characteristic depicted at the left of Fig. 4 for negative sawtooth wave sweep. The waiting point (bright point on the oscilloscope screen) on the high-current state indicates the starting point of the sweep. The current in a prolonged front time decreases along current branch (bright line) to a low-current state. By trailing abrupt edge of the sweep the current turns back to its initial state (thin lines). The current traces for the positive sweep are shown at the right of Fig. 4. The starting point is at the low-current state. The current route is represented by arrows. In our experiments the damped oscillations with a frequency of 83 kHz at the voltage of 4.38 V have observed (Fig. 5). These findings led us to conclusion that the current traces have observed by the oscilloscopic

study of the hysteresis loop can be attributed to the current traces in the process of the closed cycle current oscillations.

III. DISCUSSION

We now continue to discuss the left-hand image of the I–V characteristic (Fig. 4), when the total bias is lowered under the negative sawtooth-shaped wave sweep. According to the simple method of evaluation a value of the domain boundary expansion [10], the expanded domain boundary manifests itself as a relative voltage shift of the same number NDC peaks on high- and low-current state of the hysteresis loop. From the closed triangle of the current traces it is clearly visible that the domain boundary expands over the three SL periods. We assume that the domain boundary propagate from the cathode (1st well) to the anode (30th well). The position of the starting point of the sweep (black point on the high-current curve) shows that in the 7th quantum well (QW) the resonant tunneling conditions are fulfilled and the domain boundary locates at the 8th QW. The corresponding electric field profile is plotted in Fig. 6 by solid line. When the electric field (F) is lowered on a value $eFd > \Delta$ (where Δ is a miniband width, d is a SL period) the miniband conduction in a high-field domain region is disrupted. At the moment of subbands decoupling the carriers with insufficient energy due to energy dissipation effects, gives rise to the spatially distributed charge tail. Hence, the low-current state is controlled by the expanded domain boundary. The electric field profile for the expanded over three SL periods domain boundary is shown in Fig. 6 by dashed line. Under the trailing edge of the sweep the total voltage is increased the electrons enters from the cathode adding a required amount of the charge to restore the resonant tunneling conditions. In this regime we observe the compression of the spatially distributed domain boundary. The process is completed when electric field distribution is recovered to its original state (Fig. 6 (solid line)).

Thus, by means of the study of the dynamic characteristics of the hysteresis loop, the current traces for the switching and for the closed cycle current oscillations have been defined. The SL biased in NDC region is inherently unstable, a fluctuation of carrier density tends to produce an instantaneous space charge leads to the rearrangement of the electric field configuration along the SL axis.

ACKNOWLEDGMENT

I would like to thank Prof. G.N.Galkin and Dr. E.A.Bobrova for the help on the initial stage of the experiments.

References

[1] J. Kastrup, R. Klann, H. T. Grahn, K. Ploog, L. L. Bonilla, J. Galan, M. Kindelan, M. Moscoso and R. Merlin, Phys. Rev. B, 52, 1371 (1995).

[2] H. T. Grahn, J. Kastrup, K. Ploog, L. L. Bonilla, J. Galan, M. Kindelan, and M. Moscoso, Jap. J. Appl. Phys. 34, 4526 (1995).

[3] J. Kastrup, R. Hey, K. H. Ploog, H. T. Grahn, L. L. Bonilla, M. Kindelan, M. Moscoso, A. Wacker and J. Galan, Phys. Rev. B, 55, 2476 (1997).

[4] Y. Zhang, R. Klann, K.H. Ploog, H. T. Grahn, Appl. Phys. Lett. 70, 2825 (1997).

[5] K. J. Luo, H. T. Grahn, K. H. Ploog, and L. L. Bonilla, Phys. Rev. Lett. 81, 1290 (1998).

[6] L. L. Bonilla, J. Galan, J.A. Cuesta, F. C. Martinez, and J. M. Molera, Phys. Rev. B, 50, 8644 (1994).

[7] A. Wacker, F. Prengel, and E. Schöll, in Proceedings of the 22nd International Conference on the Physics of Semiconductors, edited by D. J. Lockwood, (World Scientific, Singapore, 1995) vol.2, p.1075.

[8] A. Wacker, G. Schwarz, F. Prengel, E. Schöll, J. Kastrup, and H. T. Grahn, Phys. Rev. B, 52, 13788 (1995).

[9] A. Wacker, M. Moscoso, M. Kindelan, and L. L. Bonilla, Phys. Rev. B, 55, 2466 (1997).

[10] G. K. Rasulova, Yu. A. Efimov, and V. N. Murzin, J. Appl. Phys. 82, 3381 (1997).

[11] G. K. Rasulova, M. V. Yakimov, V. I. Kadushkin, Superlattices and Microstructures, 24, 313 (1998).

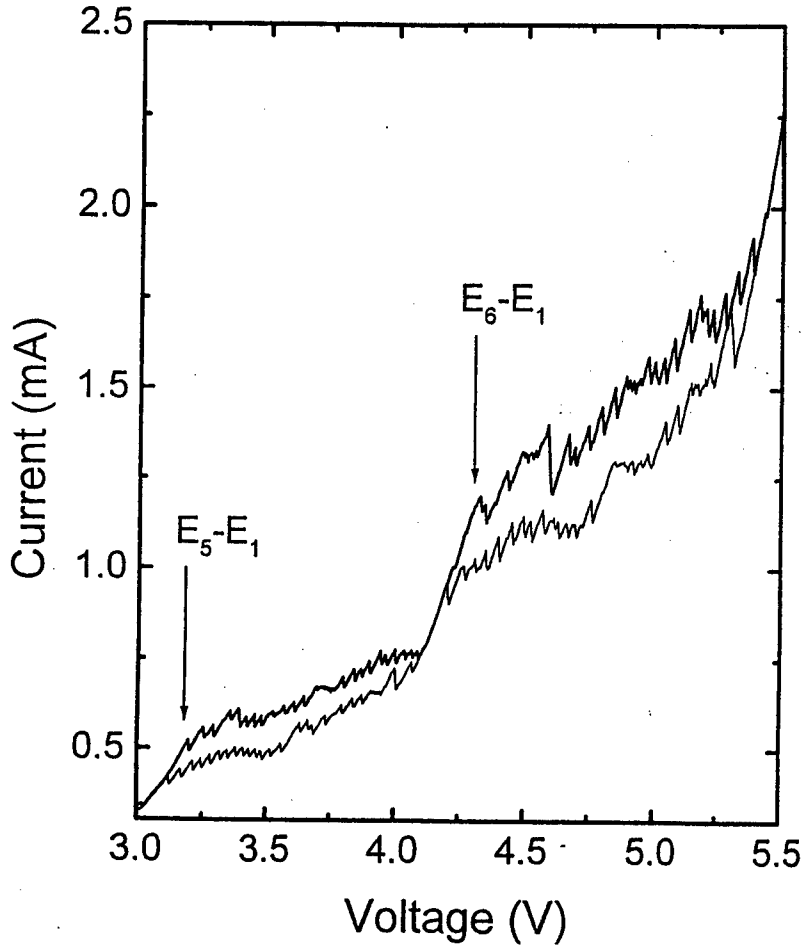


Fig1. Measured current-voltage characteristic of GaAs/$Al_{0.3}Ga_{0.7}$As superlattice at 4.2 K (thick line for up-sweep, thin line for down-sweep directions). The type of high-field domain is marked by arrows.

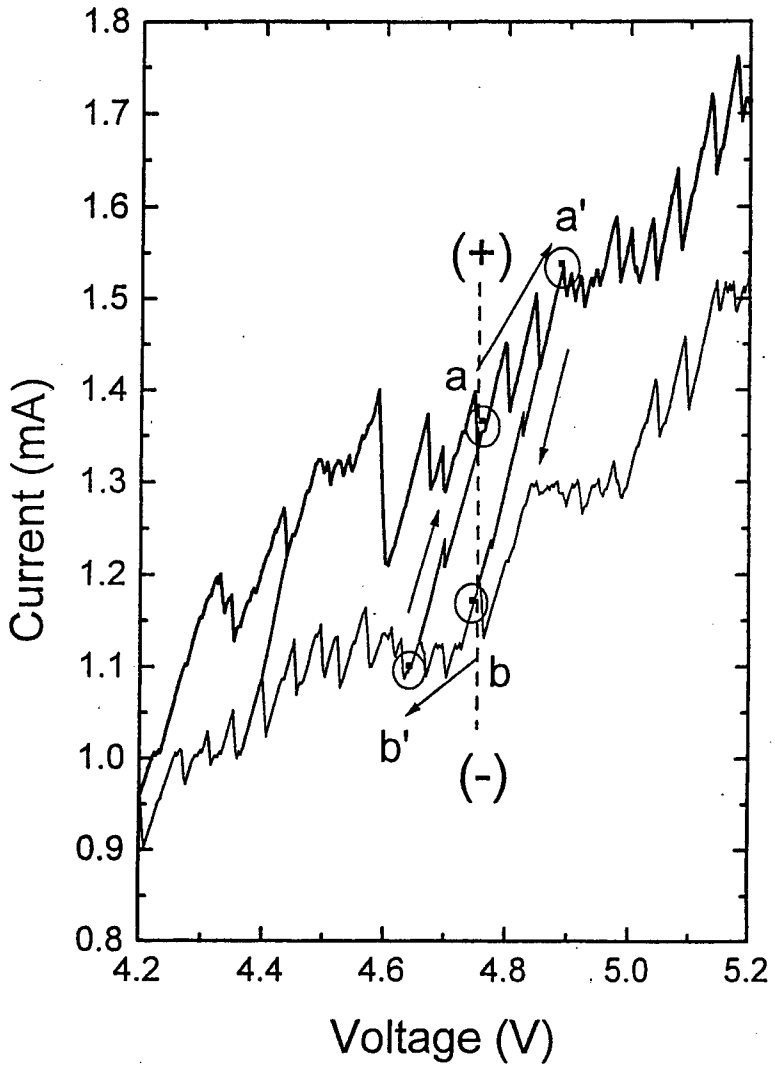


Fig.2. The enlarged fragment of I–V characteristic for $E_6 - E_1$ high-field domain propagation. The vertical dashed line indicates the voltage bias at which the single square pulses were applied. The applied pulse polarity are shown in brackets. The current traces for the switching are represented by arrows. The labels (a) and (b) indicate the initial and final current states for up-to-down switching, or the final and initial current state for down-to-up switching.

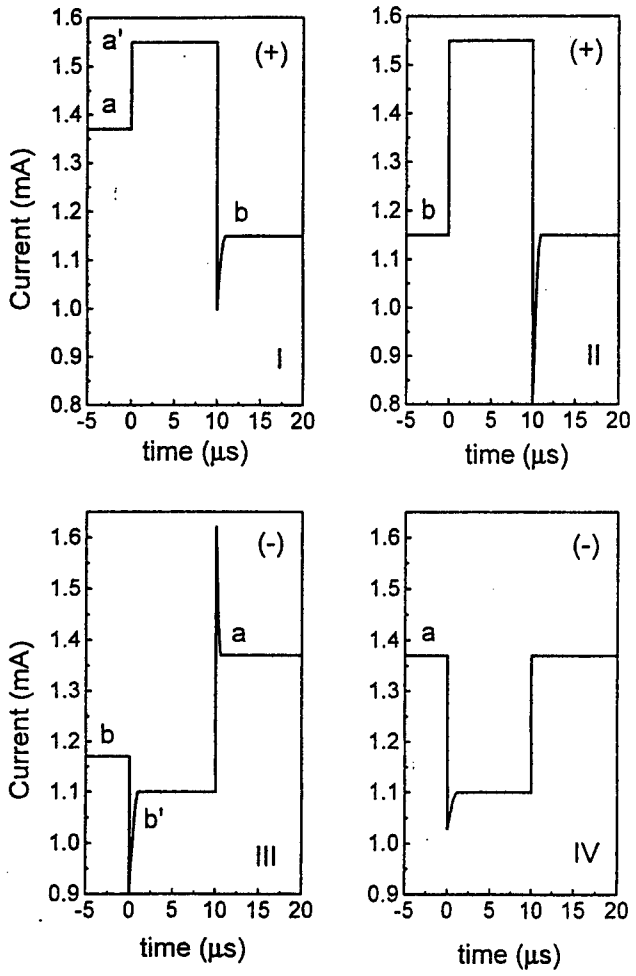


Fig.3. The transient current responses to applied single pulses of 0.3 V amplitude and of 10 μs width. At the left (I, III) the switching current responses are presented. At the right (II, IV) the time-resolved transient current responses are shown. The applied pulse polarity is denoted in brackets. The labels (a) and (b) indicate the initial or final current level of the transient response with respect to the pulse polarity. The labels (a') and (b') indicate the current level at the waiting points during a pulse time.

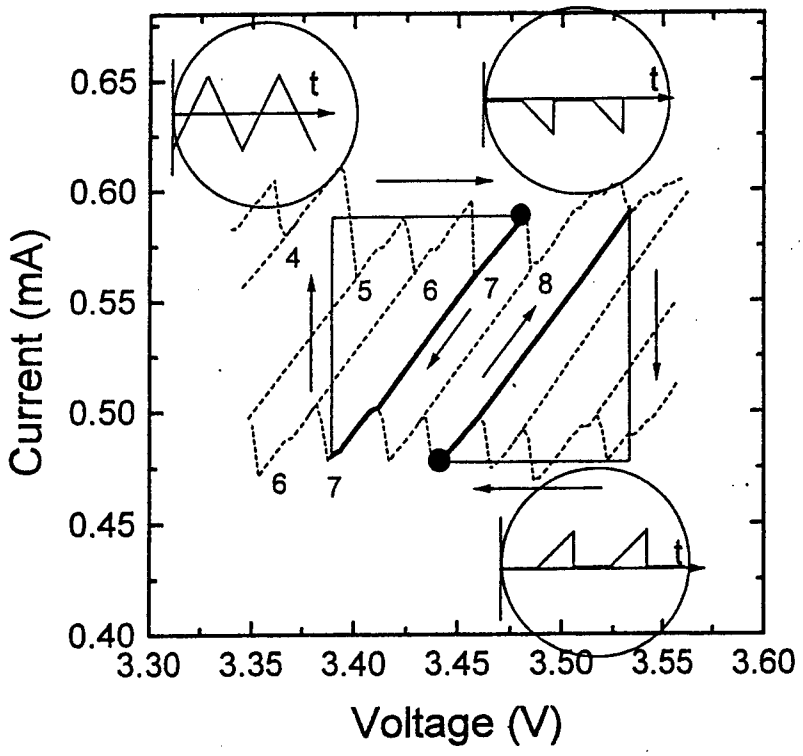


Fig. 4. The oscilloscope images of I-V characteristic produced with three types of an external sawtooth-shaped sweep at a frequency of 10^3 Hz. The shapes of sweep are shown in circular insets. Two images produced by unipolar delayed in half of a period sweep of both polarity (solid lines) are superposed onto the image produced by bipolar symmetric sweep of 0.2 V peak-to-peak amplitude (dashed line).

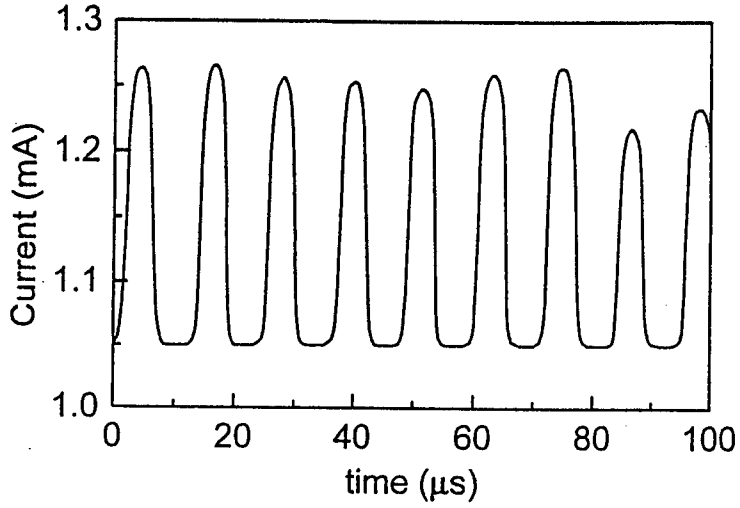


Fig.5. The damped current oscillations recorded at voltage bias of 4.38 V.

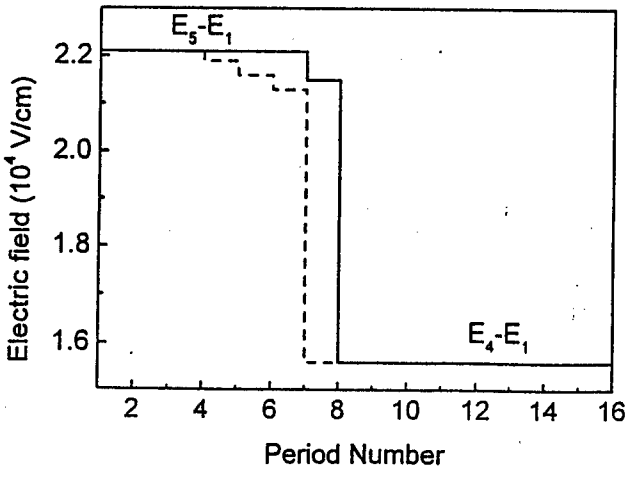


Fig. 6. The schematic representation of the electric-field profiles: for high-current state (solid line), for low-current state (dashed line).

Optics in Quantum Dots and Nanostructures

SPONTANEOUS EMISSION AND LASING CHARACTERISTICS OF GaAs-BASED 1.3 μm QUANTUM DOT LASERS

D.G. Deppe, D.L. Huffaker, O. Shchekin, S. Csutak, and G. Park
Microelectronics Research Center
University of Texas at Austin
10100 Burnet Rd., Bldg. 160, M.S. R9900
Austin, TX 78758

The recent advances in fabricating 1.3 μm wavelength, GaAs-based quantum dot lasers are described. We discuss the epitaxial crystal growth, quantum dot efficiency, and lasing characteristics in edge-emitting devices. The low dot density and deep confinement potentials for the 1.3 μm quantum dots result in low threshold current density and low threshold room temperature operation in the continuous wave mode even for p-up mounted lasers.

INTRODUCTION

Semiconductor quantum dots (QDs) exhibit many features desirable for lasers including spectrally sharp radiative transitions, low transparency current, and a very small sensitivity of the spontaneous linewidth to temperature that leads to a temperature insensitive lasing threshold. An important application of InGaAs QDs is to GaAs-based lasers that can operate at the 1.3 μm wavelength needed for high speed medium fiber optic communication. Recently it was demonstrated that InGaAs/GaAs QDs can have high spontaneous efficiency [1] and operate as room temperature laser diodes [2], [3]. Even more recently continuous-wave operation at 1.3 μm was demonstrated through stacking the QDs to increase the modal gain in an edge-emitting laser [4]. The stacking of separate QD layers is useful to overcome the small optical gain associated with a low density QD ensemble [5].

In this paper we review the status of the 1.3 μm QD GaAs-based QD laser. Besides its practical importance for fiber optics, the 1.3 μm QDs are interesting for laser diodes because the deep confinement potentials reduce the thermal escape problem of QD-confined carriers to the two-dimensional electronic states of the InGaAs wetting layer that usually leads to nonradiative recombination [5], and also lead to a number of well-resolved radiative transitions from QD confined levels. The radiative transitions take on the interesting feature of having the level degeneracies of a two-dimensional harmonic oscillator type of confinement (two-dimensional parabolic potential [6].) These well-defined radiative transitions allow gain models to be developed based on the inhomogenously broadened QD ensemble [7]. Also important are

the nonradiative transitions, and these can (and do) limit the lasing threshold current and performance of room temperature devices. Despite the nonradiative transitions, though, we show below that the 1.3 μm QD lasers are capable of low threshold current density and low threshold current even for room temperature, continuous-wave operation. Threshold current densities as low as 43 A/cm^2, and threshold currents as low as 4.1 mA are reported below for single stack QD operation continuous-wave at room temperature. At cryogenic temperature the QD lasers operate with a threshold current density as low as 6 A/cm^2.

ELECTRONIC CONFINEMENT MODEL

Experimentally, we find six radiative transitions corresponding to confined energy levels in the 1.3 μm QDs, and these are separated by nearly constant energies of ~66 meV. We also find that the saturated intensity from each higher energy transition increases with a uniform step-like intensity [8]. This experimental behavior is phenomenologically modeled by the energy levels of a 2-dimensional harmonic oscillator. The reason that the energy levels appear to be set by a parabolic potential remains unclear, and we also point out that it could well be that within the inhomogeneously broadened linewidth there also exists more finely spaced energy levels due to the individual QDs. We believe, however, that the strain-driven formation of the larger 1.3 μm QDs may lead to a minimization of that strain energy through inducing a gradient in the In composition, and that the increased In content at the QD center may generate the parabolic confinement potential. Grading in the In composition may also be due to dissolution and inter diffusion during the QD growth. However, these speculations need experimental verification through more detailed studies of the structural characteristics of the 1.3 μm QDs, and the experimental result is that the well-resolved energy levels are described by the parabolic two-dimensional confinement potential.

Figure 1 shows an illustration of the model and the assumed allowed transitions, given equal electron and hole energy level separations and equal effective masses. Ignoring the electron-hole Coulomb interaction whose energy is ~20 meV and much less than the confinement potential, the Hamiltonian for each QD can be written for an eigenfrequency ω_m as

$$\hbar\omega_m = \hbar\omega_g + \frac{p_{x,e}^2 + p_{y,e}^2}{2m_e} + \frac{p_{x,h}^2 + p_{y,h}^2}{2m_h} + \frac{1}{2}m_e\omega_e^2(x_e^2 + y_e^2) + \frac{1}{2}m_h\omega_h^2(x_h^2 + y_h^2) \quad (1)$$

where $\hbar$ is Planck's constant, q is the electronic charge, ε is the dielectric constant, m_e is the electron mass, m_h is the hole effective mass, p_e is the electron momentum, p_h is the hole momentum, and $\frac{1}{2}m_e\omega_e^2(x_e^2 + y_e^2)$ and $\frac{1}{2}m_h\omega_h^2(x_h^2 + y_h^2)$ describe the electron and hole confinement potential energies.

Equation (1) gives separately the electron and hole contributions to $\hbar\omega_m$ that come from the well-known wavefunctions of a 2-dimensional harmonic oscillator. The integer $m = m_x + m_y$ labels the collections of degenerate energy eigenstates, given by energy levels of $E_m = \hbar\omega_o(m+1) = E_{m_x,m_y} = \hbar\omega_o(m_x + m_y + 1)$ for either the conduction or valence bands, where $\hbar\omega_o = \hbar\omega_e + \hbar\omega_h$. The relative spatial extents of the electron and hole wavefunctions are set by the dimensionless parameters of $\sqrt{\omega_e m_e/\hbar}$ and $\sqrt{\omega_h m_h/\hbar}$, respectively. We expect selection rules to hold for m_x and m_y for electron-hole radiative transitions when $\sqrt{(\omega_e m_e)/(\omega_h m_h)} \sim 1$, and assume this. For such a case, an electron in an energy level with a given m_x and m_y can recombine with a hole only in the corresponding energy level with the same m_x and m_y, as illustrated in Fig. 1 (a). On the other hand, we do not expect these selection rules to hold for nonradiative transitions that occur due to point defects. For nonradiative transitions we expect that an electron in any of the QD levels can recombine with a hole in any QD level, as also illustrated in Fig. 1 (b). For nonradiative transitions, therefore, the nonradiative recombination rate increases as more electrons and holes are added to the QDs, since for an electron the number of recombination paths depends directly on the number of holes in the QD and vice-versa.

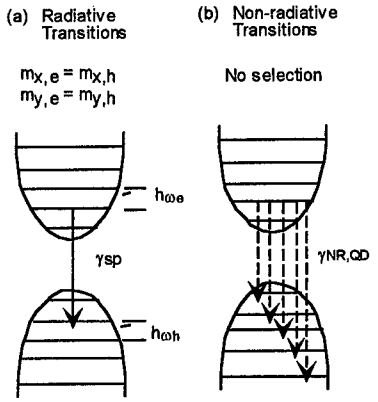


Fig. 1 Schematic illustration of the transitions between QD energy levels. (a) shows the proposed allowed electron-hole radiative transitions that follow selection rules. (b) shows some of the proposed nonradiative transitions, presumably through deep levels, that recombination between any electron-hole energy levels.

The harmonic oscillator model is used to derive a reduced density of states for the energy levels of the QD ensemble. Taking into account the inhomogeneous broadening in the QD ensemble, this density of states is then given by [9]

$$\rho_{red}(\omega) = 4\sqrt{\frac{\ln(2)}{\pi}}\frac{n_{QD}}{\Delta\omega}\sum_{m=0}^{M}(m+1)e^{-\ln(2)\frac{(\omega_g+m\omega_o-\omega)^2}{(\Delta\omega/2)^2}} \quad (2)$$

where n_{QD} is the QD density per unit area, $\Delta\omega$ is the Gaussian spectral width of a sub level, ω_g is the average ground state emission frequency, and ω_o is the frequency separation between radiative transitions. This density of states can then be used to evaluate the QD gain characteristics, and predict the drive levels necessary to achieve lasing threshold for an edge-emitting laser. Using subscripts to explicitly account for occupation by either electrons or holes, threshold is given as [7], [9]

$$\frac{\omega_o}{Q} = v_g[\frac{1}{L}\ln(\frac{1}{R}) + \alpha] = \gamma_{sp,o}\frac{\pi^2 c^3 \Gamma(n_{c,0} - n_{v,0})}{\Delta z n^3 \omega_o^2}\rho_{red}(\omega_o) \quad (3)$$

where ω_c/Q is the cavity loss rate,, $\gamma_{sp,o}$ is the spontaneous emission rate, $n_{c,0}$ is the probability of occupancy of the QD ground state by the electron with the subscript $m = 0$, $n_{v,0}$ is the probability of occupancy of the ground state with a hole, n is the refractive index, c is the speed of light in open space, v_g is the optical group velocity in the laser cavity, L is the cavity length, the mirror reflectivity is R, ω_c is the cavity resonance, α is the waveguide loss, and $\Gamma/\Delta z$ is the waveguide confinement factor normalized by the active region thickness. The magnitude squared of the dipole moment is directly related to the spontaneous emission rate, $\gamma_{sp,o}$. $\Gamma/\Delta z$ also sets the spontaneous emission rate into the lasing mode.

The temperature dependence of threshold is due to the spontaneous and nonradiative currents required to maintain a given population inversion $n_{c,0} - n_{v,0}$ in (3) for different temperatures.

EPITAXIAL GROWTH AND DEVICE FABRICATION

The QD heterostructures are grown on n-type GaAs substrates using molecular beam epitaxy. The QDs are typically grown within a waveguide clad by lightly doped p and n Al_XGa_XAs layers with x~0.75 to 0.85. The QDs are grown at 510 °C and are formed from 10 to 12 total deposited monolayers using the alternating sub-monolayer depositions described in [1]. Atomic force microscope images of QDs grown under similar conditions show a density of n_{QD}~1 to 2 x10^{10} cm^{-2} with lateral sizes before overgrowth of ~500 Å. An atomic force microscope image of the crystal surface with the growth halted immediately after deposition and formation of the QDs is shown in Ref. [1]. We believe that some dissolution of the QDs occurs when the GaAs overgrowth is carried out, and grading of the In content in the QDs may occur due to inter diffusion. The QDs emit at room temperature with a ground state transition corresponding to slightly longer than 1.3 μm wavelength, and spectral width of

the ground state emission that ranges from ~26 to 40 meV. A schematic illustration of the ridge stripe laser geometry is shown in Fig. 2. Cavities with either uncoated or coated facets are studied, with cavity lengths ranging from ~1 to 6 mm. The lasing from different energy transitions is found to depend on the cavity length. The ridge waveguide widths are varied from 60 μm to 9 μm. Ground-state continuous-wave lasing is obtained at room temperature for ~5 mm long cavities with uncoated facets, or for shorter cavities of ~1 mm length with high reflectivity (HR) coatings. Continuous-wave operation at room-temperature even for p-up mounting is obtained for HR coated lasers with ~1 mm length and 9 μm stripe width. Shorter, uncoated cavities (L = 1.1 mm) for which lasing is inhibited are studied in spontaneous emission.

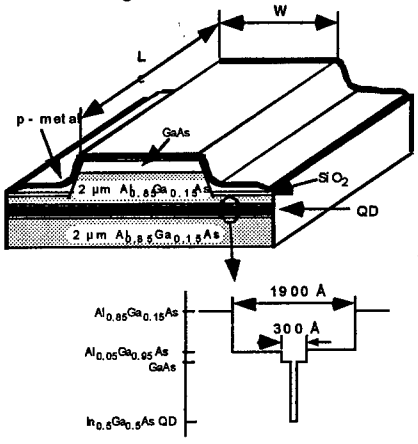


Fig. 2 Schematic illustration of the ridge-waveguide stripe laser. Also shown schematically are the III-V compositions that make up the waveguide.

SPONTANEOUS EMISSION CHARACTERISTICS

Figure 3 shows spontaneous emission spectra from a 1.3 μm QD p-n heterostructure at 300 K measured for current densities of 60 A/cm^2, 200 A/cm^2, 400 A/cm^2, and 1 kA/cm^2. The 300 K spontaneous emission characteristics are similar to that for the 80 K temperature except for a red-shift

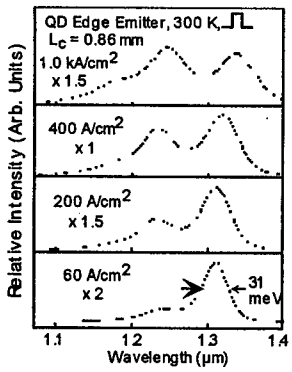


Fig. 3 Spontaneous emission spectra measured from a 1.3 μm QD ensemble for different current densities. The energy separation between the different transitions is ~60 meV. The room temperature energy spread for the ground state is 31 meV.

due to temperature dependent energy gap shrinkage. At 300 K the ground state emission peak is at 1.31 μm with a 31 meV linewidth. The higher energy transitions are peaked at 1.23 μm, 1.16 μm, and 1.09 μm. At 80 K six radiative transitions due to the QD confined states are found. The radiative transitions have nearly equal energy separations consistent with parabolic confinement, and intensity saturations from the levels that follow a two-dimensional degeneracy.

In order to assess the electroluminescence efficiency dependence of excitation level, the optical output power is measured versus current and converted to efficiency versus current density for different temperatures. The results are shown in Fig. 4 for the same cavity used for Fig. 3. Because

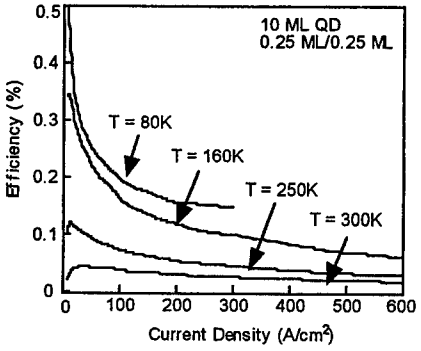


Fig. 4 Relative spontaneous efficiency versus current density measured for different temperatures. The vertical axis is not adjusted for the collection efficiency, and we estimate that 0.5% represents approaches 100% internal quantum efficiency.

of various unknowns, we have not adjusted the scale in Fig. 5 for the collection efficiency, but instead give the absolute measured efficiency. At 80 K, the peak efficiency is ~0.50% at 5 A/cm^2 for mainly ground state emission, and we believe that based on the estimated collection efficiency the internal quantum

efficiency is well over 50%. As the current density is increased the efficiency continually drops, however, and falls to ~0.20 % at 100 A/cm^2 (spectra in Fig. 3). Consistent with the lasing behavior, this decrease in efficiency associated with state filling suggests that carriers in higher energy levels nonradiatively recombine at a higher rate. This is further explained in the model described below. Figure 5 also shows that at 160 K the peak efficiency decreases to ~0.34% at 5 A/cm^2, and again decreases smoothly with increasing current density. At 250 K and 300 K, the peak efficiencies are 0.11 % and 0.04 % at 10 A/cm^2 and 40 A/cm^2, respectively. The drop in the peak efficiency at low current density as the temperature is increased indicates that temperature dependent nonradiative recombination centers are present in the QDs. As also reported in other studies [10], [19], nonradiative recombination due to the wetting layer occurs for high current densities.

Nonradiative recombination in the 1.3 μm QDs therefore manifests itself in two ways. At all temperatures, as the excitation level for each QD increases the nonradiative recombination increases. This bias dependent nonradiative recombination can be explained as caused by selection rules that hold for radiative transitions between different electron and hole energy levels, but that are absent for nonradiative electron-hole recombination. As more electrons and holes are added to each QD, the possible nonradiative recombination paths between an electron and multiple holes (or vice versa) increase. On the other hand, for radiative transitions each electron level is coupled to only one hole level. In addition, though, the nonradiative transition rate is sensitive to temperature, and increases for increasing temperature. Since the QD laser threshold current density tends to increase with increasing temperature, both effects are important. Therefore, it's important that QD lasers operate with a low threshold current density and low carrier density to reduce these nonradiative recombination effects.

LASING CHARACTERISTICS

The laser heterostructure consists of a single layer QD active region within a waveguide clad by p and n $Al_{0.85}Ga_{0.15}As$ layers. The undoped waveguide consists of $Al_{0.05}Ga_{0.95}As$ and is 0.194 mm thick, with short period superlattices grown at the interfaces between the waveguide and cladding layers. Figure 5 shows the room temperature lasing characteristics of an edge-emitting laser with a stripe width of 9 μm and cavity length of 1020 μm. Both end facets are HR coated with 5 pairs of $ZnSe/MgF_2$. With p-up mounting the threshold current is 4.1 mA, and to our knowledge is the lowest value yet reported for continuous-wave room-temperature operation of a QD laser. The inset show the ground state lasing wavelength of 1.32 μm just above the threshold. Elsewhere we have concluded that the room temperature operation

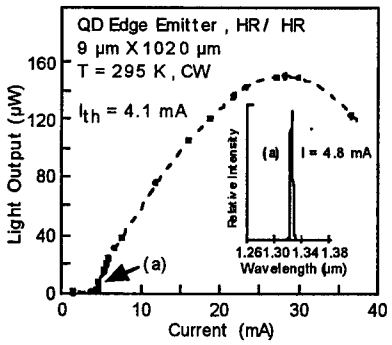


Fig. 5 Light versus current under room-temperature, continuous-wave operation. The inset shows the lasing spectra peaked at 1.32 μm.

of similar 1.3 μm QD lasers were limited by nonradiative recombination, and that the threshold current density could be quite low by eliminating this parasitic current path [3]. This is born out by the low threshold current density operation of 45 A/cm^2 for the device shown in Fig. 5. However, heating and nonradiative recombination still impact the laser operation. For the laser operation shown in Fig. 2, the differential slope efficiency just above threshold is only ~2.5%, and continually decreases for increasing drive currents. While the slope efficiency is low in part due to internal waveguide loss, the decreasing slope efficiency with increasing drive current shows that heating limits the laser performance as well. The decreasing slope efficiency for increasing drive current can be explained by a strongly temperature sensitive threshold.

Figure 6 shows the dependence of the room temperature threshold current density on the stripe width for a cavity length of 0.34 mm and different end losses. The threshold current density increases with increasing stripe width, again indicating that the threshold is sensitive to heating even for pulsed operation. The lowest threshold current density is ~25 A/cm^2 for a stripe width of 14 μm. For this cavity length, the lasing transition for the as-cleaved lasers (solid circles) is from the first excited states with a lasing wavelength of ~1.25 μm (spectrum not shown). With one facet HR coated (4 pairs of ZnSe/MgF_2), lasing shifts to the ground state with a large drop in the threshold current density from ~200 A/cm^2 to ~60 A/cm^2. With HR coatings deposited on both facets the threshold current density decreases to its minimum of 25 A/cm^2 for the 14 μm wide stripe laser. Waveguide scattering loss apparently increases the threshold current density for stripes smaller than 14 μm. Therefore, narrow stripe QD laser performance can greatly benefit through incorporation of a low loss lateral waveguide.

Figure 7 shows the temperature dependence of the threshold current density for a device with a stripe width of 29 μm and cavity length of 5.04 mm (uncoated facets). A remarkably low threshold current density of 6 A/cm^2 is

obtained at 4 K. In general, the threshold current density increases for increasing temperatures. However, at ~150 K the threshold increases less steeply. This is the temperature for which thermal QD coupling through the wetting layer occurs [8]. Above ~250 K the threshold increases more steeply due to increasing nonradiative recombination that accompanies significant population of the QD upper energy levels, and wetting layer [5], [7].

We previously suggested that the room temperature performance of the 1.3 μm QD lasers has been limited by nonradiative recombination, and the present results confirm this. In Ref. [8] we estimate that the room temperature threshold current density can be in the range of 10 to 20 A/cm^2, despite some thermal population of the upper energy levels. However, the nonradiative recombination rate is quite sensitive to the current density, and can result in thermal runaway of threshold. Therefore, an added benefit of decreasing the cavity loss through application of HR coatings is that the low threshold current density decreases the nonradiative recombination rate. This reveals the potential for these lasers to operate at low current and current density.

The remarkably low threshold current density of 6 A/cm^2 at 4 K (Fig. 7) for the 5.04 mm cavity length shows that the transparency current of this single layer QD ensemble is small. At 4 K and low excitation we can assume that nonradiative recombination is negligible and arrive at a gain estimate for the QD ensemble. For the QD density of 2x10^{10} cm^{-2}, a degeneracy of two for the ground state levels, and a spontaneous lifetime that we estimate to be ~640 psec, the transparency current is $J_{trans} = qn_{QD} / \tau_{rec} \approx$ 5 A/cm^2. The maximum ground state gain is obtained for twice the transparency current density, which is 10 A/cm^2 (in the absence of gain clamping due to stimulated emission.) For our waveguide we calculate $\Gamma/\Delta z$ = 3.57x10^6 m^{-1}. The maximum modal gain from the QD ensemble ground state is then estimated from Eq. (3) to be ~23 cm^{-1}. The threshold gain of 6 A/cm^2 would correspond to a modal gain of ~5 cm^{-1}, so that the end loss of $\frac{1}{L}\ln(\frac{1}{R}) \approx 2.5$ cm^{-1} would require that $\alpha \approx 2.5$ cm^{-1} as well. With HR coatings of □0.98 reflectivity, the end loss is readily made negligible as compared to the internal waveguide loss. Along with heating, this leads to the low external differential slope efficiency shown in Fig. 5.

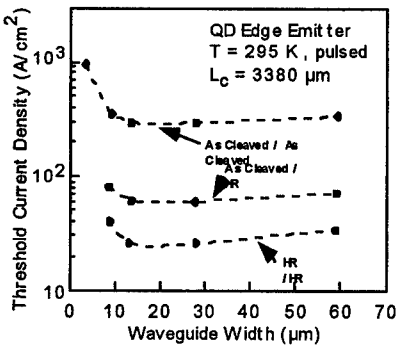


Fig. 6 Threshold current density versus the stripe width for different facet reflectivities.

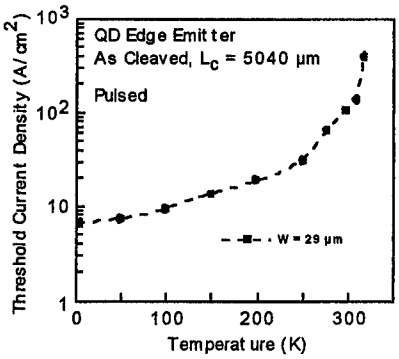


Fig. 7 Threshold current density versus temperature under pulsed operation.

SUMMARY

The spontaneous emission and lasing characteristics of 1.3 μm QD lasers are reviewed. The low QD density allow low threshold current for room temperature, continuous wave operation of 4.1 mA and 45 A/cm2, while cryogenic operation shows threshold current densities as low as 6 A/cm2. Despite these low values, the 1.3 μm QD laser performance is still limited by nonradiative recombination. As the material properties are further optimized, this system will offer the possibility for fabricating novel low threshold 1.3 μm lasers using GaAs substrates.

ACKNOWLEDGMENTS

This work is supported by the Texas Advanced Research Program, the National Science Foundation under grant ECS-9734829, and the DARPA University of New Mexico OptoCenter.

REFERENCES

[1] D.L. Huffaker and D.G. Deppe, Appl. Phys. Lett. **73**, 520 (1998).
[2] D.L. Huffaker, G. Park, Z. Zou, O.B. Shchekin, and D.G. Deppe, Appl. Phys. Lett. **73**, 2564 (1998).
[3] G. Park, D.L. Huffaker, Z. Zou, O.B. Shchekin, and D.G. Deppe, IEEE Phot. Tech. Lett. **11**, 301 (1999).
[4] K. Mukai, et al., Conference on Lasers and Electro-Optics, May 23-28, 1999, Baltimore, MD, Post-Deadline Paper.

[5] N.N. Ledentsov, V.A. Shchukin, M. Grundmann, N. Kirstaedter, J. Bohrer, O. Schmidt, D. Bimberg, V.M. Ustinov, A.Y. Egorov, A.E. Zhukov, P.S. Kop'ev, S.V. Zaitsev, N. Yu. Gordeev, Zh. I. Alferov, A.I. Borovkov, A.O. Kosogov, S.S. Ruvimov, P. Werner, U. Gosele, and J. Heydenreich, Phys. Rev. B **54**, 8743 (1996), and references therein.
[6] K. Mukai, N. Ohtsuka, H. Shoji, and M. Sugawara, Appl. Phys. Lett. **68**, 3013 (1996).
[7] D.G. Deppe, D.L. Huffaker, S. Csutak, Z. Zou, G. Park, and O.B. Shchekin, IEEE J. Quant. Electron. **35**, MS #10450 (August, 1999).
[8] G. Park, O.B. Shchekin, D.L. Huffaker, and D.G. Deppe, Appl. Phys. Lett. **73**, 3351 (1998).
[9] Z. Zou, O.B. Shchekin, G. Park, D.L. Huffaker, and D.G. Deppe, IEEE Phot. Tech. Lett. **10**, 1673 (1998).

PHONON-ASSISTED OPTICAL TRANSITIONS IN DISK-SHAPED QUANTUM DOTS

J. T. Devreese [1], V.M. Fomin [1,2], S.N. Klimin [1,2], and J.-P. Leburton [3]
[1] Theoretische Fysica van de Vaste Stof, Universiteit Antwerpen (U.I.A.), B-2610 Antwerpen, Belgium
[2] Departamentul de Fizica Teoretica, Universitatea de Stat din Moldova MD-2009 Chisinau, Republica Moldova
[3] Department of Electrical and Computer Engineering and Beckman Institute, University of Illinois at Urbana-Champaign, Urbana, IL 61801

ABSTRACT

Phonon-assisted photoluminescence and Raman scattering have been theoretically studied in nanosize InAs/GaAs disks, which represent a model for self-assembled quantum dots. Optical phonons are considered within a multimode dielectric model taking into account a finite number of vibrational modes in a quantum dot. The dependence of the Raman and the photoluminescence spectra on the size of the quantum dots is analysed. For excitation of quantum dots with radii smaller than the average radius for the statistical ensemble of quantum dots, the ratio of the intensities of the one-phonon to zero-phonon peaks in the photoluminescence spectrum increases.

I. INTRODUCTION AND APPROACH

In nanosize semiconductor systems (in particular, in quantum dots), both the electron and phonon spectra are drastically different from those in the bulk. This difference is manifested in Raman scattering and photoluminescence.

In Refs. [1, 2], it has been shown that under a strong confinement, the Jahn-Teller effect plays a key role in phonon-assisted optical transitions and strongly influences the shape of the photoluminescence and Raman spectra. The non-adiabaticity of the exciton-phonon system leads to a substantial difference of the calculated optical spectra from the Franck-Condon progression which is specific for the adiabatic theory. In the present work, we study photoluminescence and Raman scattering in InAs/GaAs

disk-shaped quantum dots due to the electron intraband transitions. These disk-shaped nanostructures are a model for the self-assembled quantum dots. Because the average diameter $\langle d \rangle$ of the structures under consideration is of the order of 10 nm, there occurs a strong size quantization of the electrons. Namely, the Franck-Condon transition frequencies are much larger as compared to the phonon frequencies. Under this condition, we can neglect non-adiabatic effects.

The *dielectric continuum model* (DCM) for the optical phonons [3, 4, 5] involves electrostatic boundary conditions only. The electron scattering probability calculated within DCM is close to results of the microscopic approach [8], but the polarization dependence of the Raman spectra, predicted by DCM, contradicts the experimental data [6]. The *hydrodynamic model* (HDM) (see Ref. [7]) takes into account only mechanical boundary conditions. The polarization dependence of the Raman spectra obtained in this approach is in agreement with the experiment [6]. On the other hand, the electron scattering probability obtained within HDM differs from that calculated within the microscopic model [8]. Various improvements of the dielectric continuum model [9, 10, 11] have been made. In Refs. [12, 13, 14], a continuum model is developed which accounts for the spatial dispersion and both electrostatic and mechanical boundary conditions. In the paper [15], optical phonon eigenmodes and the Hamiltonian of the electron-phonon interaction are obtained within the *multimode dielectric model.* In [15], dispersive optical phonons in spatially confined systems are derived subject to electrostatic boundary conditions. A finite-dimensional basis is chosen for the ionic displacement vector $\mathbf{u}_k(\mathbf{r}, t)$ (where the index k numbers different media), which satisfies the relevant mechanical boundary conditions.

The dynamics of the optical phonons in the long-wave region is determined by the Born-Huang equation generalized to the dispersive case (cf. [12]). In the Fourier representation, this equation is

$$\left(\omega_{k,\mathrm{TO}}^2 - \omega^2\right) \mathbf{u}_k(\mathbf{r}, \omega) + \left(v_{k,\mathrm{LO}}^2 - v_{k,\mathrm{TO}}^2\right) \operatorname{grad} \operatorname{div} \mathbf{u}_k(\mathbf{r}, \omega)$$
$$+ v_{k,\mathrm{TO}}^2 \Delta \mathbf{u}_k(\mathbf{r}, \omega) = \frac{V_{0k} \omega_{k,\mathrm{TO}}^2 \varepsilon_0 \left[\varepsilon_k(0) - \varepsilon_k(\infty)\right]}{e_k^*} \mathbf{E}_k(\mathbf{r}, \omega), \qquad (1)$$

where ω is the frequency, e_k^* is the effective charge of an ion, $\omega_{k,\mathrm{TO}}$ is the frequency of the transverse optical phonon at the Brillouin zone center, V_{0k} is the volume of the lattice cell, $\varepsilon_k(\infty)$ and $\varepsilon_k(0)$ are the high-frequency and static dielectric constants, respectively; ε_0 is the permittivity of the vacuum, $k = 1$ for the quantum dot, $k = 2$ outside the quantum dot. The dispersion of bulk LO and TO phonons in the long-wave region is characterized by the parameters $v_{k,\mathrm{LO}}$ and $v_{k,\mathrm{TO}}$, respectively. The right-hand side of Eq. (1) describes the long-range force expressed in terms of the macroscopic electric field $\mathbf{E}_k(\mathbf{r}, \omega)$ induced by the ionic displacement vector $\mathbf{u}_k(\mathbf{r}, \omega)$.

A specific choice of mechanical boundary conditions strongly depends on the characteristics of neighboring materials. In particular, simple models of those conditions are proposed in [13, 14, 15] for the case when optical phonon frequencies in contacting media differ from each other sufficiently strongly, so that the regions between LO and TO frequencies ($\omega_{1,\mathrm{TO}} \leq \omega \leq \omega_{1,\mathrm{LO}}$ and $\omega_{2,\mathrm{TO}} \leq \omega \leq \omega_{2,\mathrm{LO}}$) do not overlap. In this case, phonons cannot propagate from each medium into a neighboring substance.

Hence, a phonon amplitude in a nanostructure can be described with good accuracy by a superposition of standing waves. For the system under consideration, we choose the mechanical boundary conditions as in Refs. [13, 15]: the normal (tangential) component of the ionic displacement vector is zero (extremum) at the interface. Such a choice of the mechanical boundary conditions leads to a good agreement of the phonon spectra derived in [15] with those obtained in the microscopic treatment [8]. Note that the results of Ref. [13] compare well with experimental Raman scattering data [16].

After the mechanical boundary conditions are imposed, the optical phonon dynamics is determined by Eq. (1) together with the Maxwell equations with electrostatic boundary conditions. Using them, we obtain the dispersion equations for the eigenfrequencies in a disk-shaped quantum dot with $h < 2R$:

$$\begin{cases} \varepsilon_1^s(q_\perp,\omega)\tanh\left(\frac{\zeta}{2}\right)+\varepsilon_2(\omega)=0, & \text{for even modes,} \\ \varepsilon_1^a(q_\perp,\omega)\coth\left(\frac{\zeta}{2}\right)+\varepsilon_2(\omega)=0, & \text{for odd modes,} \end{cases} \tag{2}$$

where $q_\perp \equiv b_{|m|,r}/R$, $\zeta \equiv q_\perp h$, $b_{|m|,r}$ is the r-th zero of the derivative of the Bessel function $J_{|m|}(z)$, and $\varepsilon_2(\omega)$ is the dielectric function of the outer medium. The effective (multimode) dielectric function of a quantum dot is

$$\varepsilon_1^j(q_\perp,\omega)=\varepsilon_1(\infty)\left[1-\sum_{n=0}^{n_{\max}}\frac{\left(\omega_{1,\mathrm{LO}}^2-\omega_{1,TO}^2\right)u_{j,n}(q_\perp)}{\omega_{1,\mathrm{LO}}^2-v_{1,\mathrm{LO}}^2Q_{j,n}^2-\omega^2}\right]^{-1}, \tag{3}$$

with

$$Q_{j,n}^2 \equiv \begin{cases} q_\perp^2+\left(\frac{2n\pi}{h}\right)^2, & j=s \\ q_\perp^2+\left[\frac{(2n+1)\pi}{h}\right]^2, & j=a \end{cases}. \tag{4}$$

The coefficients $\chi_{j,n}(q_\perp)$ determine the oscillator strength,

$$\chi_{s,n}(q_\perp)=\frac{2(2-\delta_{n,0})q_\perp}{hQ_{s,n}^2}\tanh\left(\frac{\zeta}{2}\right), \qquad \chi_{s,n}(q_\perp)=\frac{4q_\perp}{hQ_{a,n}^2}\coth\left(\frac{\zeta}{2}\right). \tag{5}$$

The summation over n in Eq. (3) is cut off by the upper limit $n_0 \sim \frac{h}{2a_0}$. This limitation expresses the fact that the wavelength of an optical phonon cannot be smaller than twice the lattice constant.

Fig. 1 (panel *a*) illustrates graphically the solution of the dispersion equation (2) for the phonon eigenfrequencies in a disk-shaped InAs/GaAs quantum dot. The solid lines represent the left-hand side ($\varepsilon_1^{s(a)}(m,r,\omega)\tanh\frac{\zeta}{2}$) while dashed lines represent the right-hand side ($-\varepsilon_2(\omega)$) of this equation. In this figure, the branch of even phonon modes with $m = 0$, $r = 1$ is considered. The intersections of the solid and the dashed curves determine the eigenfrequencies of hybrid phonon modes. For comparison, the graphic solution of the dispersion equation for interface phonons in the same quantum dot within the dielectric continuum model (DCM) is shown on panel *b*. In this panel, solid lines are related to $\varepsilon_1(\omega)\tanh\frac{\zeta}{2}$, where $\varepsilon_1(\omega) =$

$\varepsilon_1(\infty)\frac{\omega^2-\omega_{LO}^2}{\omega^2-\omega_{TO}^2}$ is the dielectric function of InAs in the single-mode approximation. On panel *a*, there is a group of roots of Eq. (2) with frequencies $\omega < 240$ cm^{-1}, which occur between the LO and the TO InAs frequencies. It is natural to interpret them as eigenfrequencies of hybrid phonon modes related to InAs. The split-off root (with $\omega \approx 285$ cm^{-1}) has the same frequency as the GaAs-like interface phonon mode of the dielectric continuum model (see the panel *b*).

The solution of the dispersion equation allows one to calculate numerically the basis vectors of phonon eigenmodes and the amplitudes of the electron-phonon interaction. Fig. 2 illustrates the dependence of the hybrid (solid lines) and the DCM bulk-like (dashed lines) phonon amplitudes $\mathbf{u}_{mrn}^{s(a)}(\mathbf{r})$ with $m = 0$, $r = 1$, $n = 1$ (the example of weak mixing of bulk-like and interface vibrations) and with $m = 0$, $r = 1$, $n = 3$ (the example of strong mixing). The normal components of the hybrid phonon amplitudes (shown at the right-hand side panels) become zero at the interfaces according to the mechanical boundary conditions. The normal components of the bulk-like amplitudes acquire an extremum at these points.

Note that the basis vectors of the *multimode dielectric model* behave similarly as those obtained in the microscopic model [8]. The analysis of the spatial dependence of the basis vectors allows one to estimate the relative contributions of bulk-like and interface vibrations in the resulting hybrid eigenmode. When the relative contribution of the interface vibrations is small, the basis vectors $\mathbf{u}_{mrn}^{j}(\mathbf{r})$ appear to be similar to those obtained in Refs. [9, 10]. One can see that in the vicinity of the interface, for the basis vector $\mathbf{u}_{011}^{s}(\mathbf{r})$, the modulus of both the tangential and the normal components decreases as a function of $|z|$. Hence, bulk-like modes give a major contribution to this hybrid mode (the admixing of interface vibrations is comparatively weak). For the basis vector $\mathbf{u}_{011}^{a}(\mathbf{r})$, the tangential component does not strongly decrease at the boundary, because the contribution of the interface mode in $\mathbf{u}_{011}^{a}(\mathbf{r})$ is larger than in $\mathbf{u}_{011}^{s}(\mathbf{r})$. The case of strongly mixed vibrations is presented by the basis vectors $\mathbf{u}_{013}^{s}(\mathbf{r})$ and $\mathbf{u}_{013}^{a}(\mathbf{r})$. Interface vibrations give a large contribution in these amplitudes, because their tangential components take the extremal values at the boundaries.

Using the obtained amplitudes, we have calculated the Raman scattering and the photoluminescence spectra of disk-shaped quantum dots.

II. DISCUSSION OF RESULTS

For Raman scattering, the transition probability is represented as a perturbation series in the amplitudes of the electron-phonon interaction. The K-phonon scattering amplitude is written as [17]:

$$F_K^{(\pm)}(\nu_1,...,\nu_K) = \sum_{\mu_0...\mu_K} \frac{d_{0,\mu_0}^{I}\left(d_{0,\mu_K}^{S}\right)^*}{\tilde{\Omega}_{0,\mu_0} - \Omega_I + i\tilde{\Gamma}_{\mu_0}}$$

$$\times \prod_{j=1}^{K} \frac{\left\langle \mu_j \left| \hat{\beta}_{\nu_j} \right| \mu_{j-1} \right\rangle}{\tilde{\Omega}_{0,\mu_j} - \Omega_I \pm \sum_{k=1}^{j} (\omega_{\nu_k} \pm i\Gamma_{\nu_k}) + i\tilde{\Gamma}_{\mu_j}}, \tag{6}$$

where ν_i is the index numbering phonon modes [$\nu = (j, m, r, n)$], ω_ν is the phonon frequency of the ν-th phonon mode, $\hat{\beta}_\nu$ is the amplitude of the electron-phonon interaction with the ν-th phonon mode, Ω_I is the frequency of the incoming light, $\tilde{\Omega}_{0,\mu_j}$ are the Franck-Condon transition frequencies for electron transitions between the ground state $|0\rangle$ and the excited states $|\mu_j\rangle$, $\tilde{\Gamma}_{\mu_j}$ is the linewidth of these states, Γ_{ν_k} is the linewidth of phonon states, d^I_{0,μ_0} and d^S_{0,μ_K} are the transition dipole matrix elements for the incoming (I) and the scattered (S) light, respectively.

The fundamental band of the Raman scattering spectrum contains only peaks assigned to vibrational modes of even parity, while for multiphonon bands (participated by $K \geq 2$ phonons), vibrational modes of both even and odd parity are active. It is shown that when radius R and height h of a quantum dot strongly differ from each other: $R \ll h$ or $R \gg h$, Raman scattering peaks due to interface phonons dominate, while at $R/h \sim 1$, bulk-like phonons give a key contribution to Raman scattering processes.

Photoluminescence spectra of an ensemble of quantum dots with the Gaussian distribution over sizes

$$\mathcal{N}(R,h) = \frac{1}{(2\pi)^{3/2} V \sigma^3} \exp\left\{ -\frac{1}{2\sigma^2} \left[\frac{(R - \langle R \rangle)^2}{\langle R \rangle} + \frac{(h - \langle h \rangle)^2}{\langle h \rangle} \right] \right\}, \tag{7}$$

where σ is the half-width of the Gaussian, are treated for the regime of monochromatic size-selective excitation. In this regime, the radiation of the frequency Ω_{exc} can excite quantum dots of different sizes which obey the equation [1]

$$\tilde{\Omega}_{0,\mu_j}(R,h) + \sum_\nu K_\nu \omega_\nu - \Omega_{exc} = 0, \tag{8}$$

where K_ν are integers satisfying the condition $\sum_\nu K_\nu = K$. As a result, the K-phonon photoluminescence band contains peaks provided by various combinations of transitions with the light absorption participated by $N \leq K$ phonons, followed by the light emission assisted by $(K - N)$ phonons. In particular, the one-phonon peaks in the photoluminescence spectrum occur due to (i) the one-phonon light absorption with the zero-phonon light emission and (ii) the zero-phonon light absorption with the one-phonon light emission.

In the particular case $R \gg h$, when the photoluminescence is provided by intraband transition between the two lowest size-quantized states, the Franck-Condon transition frequency $\tilde{\Omega}_{0,\mu}$ is a function of R only. The equations (8) lead to two equations for the quantum dot radii $R_0(\Omega_{exc})$ (for the zero-phonon excitation, as mentioned above) and $R_{1,\nu}(\Omega_{exc})$ for the one-phonon excitation,

$$\tilde{\Omega}_{0,\mu}(R_0) - \Omega_{exc} = 0, \qquad \tilde{\Omega}_{0,\mu}(R_{1,\nu}) + \omega_\nu - \Omega_{exc} = 0. \tag{9}$$

Since the zero-phonon transition frequency is a decreasing function of the size of a quantum dot, the process described by the first of equations (9) involves quantum

dots with larger sizes than the process described by the second of these equations. This effect allows one to control the ratios between intensities of different peaks. For example, the excitation frequency can be adjusted in such a way that the zero-phonon line is suppressed, while the phonon peaks are clearly seen. For larger average radii in an ensemble of quantum dots, the ratio of the one-phonon to the zero-phonon peak intensity is more sensitive to the variation of the excitation frequency, than for smaller sizes.

In Fig. 3, one-phonon (fundamental, panel *a*) and two-phonon (1-st overtone, panel *b*) Raman scattering bands are plotted for three different sizes of a quantum dot. The spectral intensities are measured in arbitrary units (identical for all plots). The linewidth of the phonon states (which is responsible for the broadening of the Raman peaks) is taken to be 1 cm^{-1}. In the fundamental band, peaks assigned to InAs-like hybrid phonon modes occur near 220 through 240 cm^{-1} while interface-like peaks assigned to GaAs-like modes are found near 285 cm^{-1}. In Table 1, we show the frequencies of the long-wave hybrid eigenmodes which give a main contribution to the Raman spectra. Also the frequencies of the corresponding phonon modes calculated within DCM are displayed. All frequencies are given in cm^{-1}.

Table 1. Frequencies of the phonon eigenmodes in InAs/GaAs disk-shaped quantum dots

Phonon modes	$R = 5$ nm, $h = 5$ nm	$R = 5$ nm, $h = 2.5$ nm	$R = 3$ nm, $h = 2.5$ nm
Hybrid (related to InAs)	239	231	233
DCM bulk-like (related to InAs)	241	238	237
DCM interface (related to InAs)	231	229	231
Hybrid (related to GaAs)	285	287	285
DCM interface (related to GaAs)	285	287	285

For a comparatively large quantum dot ($R = 5$ nm, $h = 5$ nm), the frequency of the hybrid phonon mode related to InAs is close to the bulk-like DCM InAs mode. Hence, bulk-like vibrations give the main contribution to the phonon modes in this case. When decreasing the height of a quantum dot keeping the radius constant ($R = 5$ nm, $h = 2.5$ nm), the frequency of the hybrid eigenmode approaches the

frequency of the interface InAs-like DCM mode. For the third quantum dot under consideration (R = 3 nm, h = 2.5 nm), the hybrid phonon frequency is also closer to the interface InAs-like DCM mode than to the bulk-like mode. Comparing with each other the spectra for two quantum dots with the same radius but with different heights, we see that *for decreasing height of a quantum dot, the relative contribution of the interface vibrations to the Raman scattering spectra increases.* For a larger quantum dot, the Raman spectra contain more peaks than for smaller dots, since the total number of phonon modes is an increasing function of the quantum dot sizes.

In the 1-st overtone Raman scattering band, there are two types of combinatorial peaks: (i) the peaks related to $2\omega_\nu$, (ii) combinations between frequencies of different modes. The above-mentioned behavior of ratios between peaks, assigned to different phonon modes, takes place for this case too. When decreasing the quantum dot sizes, the ratio of the total intensity of the 1-st overtone band I_2 to the total intensity of the fundamental band I_1 increases.

In Fig. 4, we present the results of the calculation of photoluminescence spectra in Gaussian ensembles of disk-shaped InAs/GaAs quantum dots. The relative size dispersion $\Delta = 2\sigma$ is taken to be 5%. The average sizes of the quantum dots are the same as those for Raman scattering. The spectral intensities are measured here in units of the height of the zero-phonon line (ZPL). The homogeneous linewidth of the excited electron states is taken as 10 cm^{-1}. The one-phonon photoluminescence band consists of two peaks which are related to the hybrid InAs-like modes (with frequencies near 240 cm^{-1}) and to the hybrid GaAs-like modes (with frequencies near 285 cm^{-1}). The ratio of the GaAs-like peak intensity to that of the InAs-like peak increases when the height of a quantum dot diminishes. The same dependence is characteristic also for Raman scattering. *When the excitation frequency Ω_{exc} varies in such a way that the radius R_0 of the quantum dots, which are excited by photons of this frequency, becomes less than the average radius $\langle R \rangle$ for the ensemble, the ratio of the one-phonon peak intensity I_1 to the zero-phonon peak intensity I_0 increases.* Fig. 4 demonstrates that *the ratio I_1/I_0 for a larger average radius of the ensemble of quantum dots is more sensitive to the excitation frequency than that for a smaller average radius.*

The results obtained in the present work demonstrate the possibility to efficiently control and study the vibrational states and the parameters of the electron-phonon interaction with different phonon modes in quantum dots by means of varying the shape and the size of a quantum dot.

ACKNOWLEDGEMENT

We thank P.M. Koenraad, J.H. Wolter, E.P. Pokatilov, V.N. Gladilin and S.N. Balaban for useful discussions. This work is supported by Interuniversitaire Attractiepolen — Belgische Staat, Diensten van de Eerste Minister — Wetenschappelijke, technische en culturele Aangelegenheden, FWO-V project No. G.0287.95 and WO.025.99N (Belgium) and by the PHANTOMS Network.

References

[1] V. M. Fomin, V. N. Gladilin, J. T. Devreese, E. P. Pokatilov, S. N. Balaban and S. N. Klimin, Phys. Rev. B **57**, 2415 (1998).

[2] V. M. Fomin, E. P. Pokatilov, J. T. Devreese, S. N. Klimin, V. N. Gladilin, and S. N. Balaban, Solid State Electronics **42**, 1309 (1998).

[3] R. Fuchs and K. L. Kliewer, Phys. Rev. **140** A, 2076 (1965).

[4] N. Mori and T. Ando, Phys. Rev. B **44**, 9002 (1991).

[5] R. Ruppin and R. Englmann, J. Phys. C **1**, 614 (1968).

[6] M. Cardona, Superlatt. and Microstruct. **5**, 27 (1989).

[7] M. Babiker, J. Phys. C **19**, 683 (1986).

[8] H. Rucker, E. Molinari, and P. Lugli, Phys. Rev. B **45**, 6747 (1992).

[9] K. Huang and B. Zhu, Phys. Rev. B **38**, 13377 (1988).

[10] C. D. Chen, Solid State Commun. **81**, 785 (1992).

[11] R. Enderlein, Phys. Rev. B **43**, 14513 (1991).

[12] M. P. Chamberlain, M. Cardona, and B. K. Ridley, Phys. Rev. B **48**, 14356 (1993).

[13] N. C. Constantinou and B. K. Ridley, Phys. Rev. B **49**, 17065 (1994).

[14] C. Trallero-Giner, R. Pérez-Alvarez, and F. Garcia-Moliner, *Long-wave polar modes in semiconductor heterostructures*, Pergamon, 1998.

[15] S. N. Klimin, E. P. Pokatilov, and V. M. Fomin, Phys. Stat. Sol. (b) **190**, 441 (1995).

[16] M. Haines and G. Scamarcio, in *Phonons in Semiconductor Nanostructures, NATO Advanced Study Institute, series E: Applied Sciences*, edited by J. P. Leburton *et al.* (Kluwer Academic, Holland, 1993), Vol. 236, p. 93.

[17] V. M. Fomin, E. P. Pokatilov, J. T. Devreese, S. N. Klimin, S. N. Balaban, and V. N. Gladilin, in: *Proceedings of the 23-rd International Conference on the Physics of Semiconductors*, edited by M. Scheffler and R. Zimmermann (World Scientific, Singapore, 1996), p. 1461.

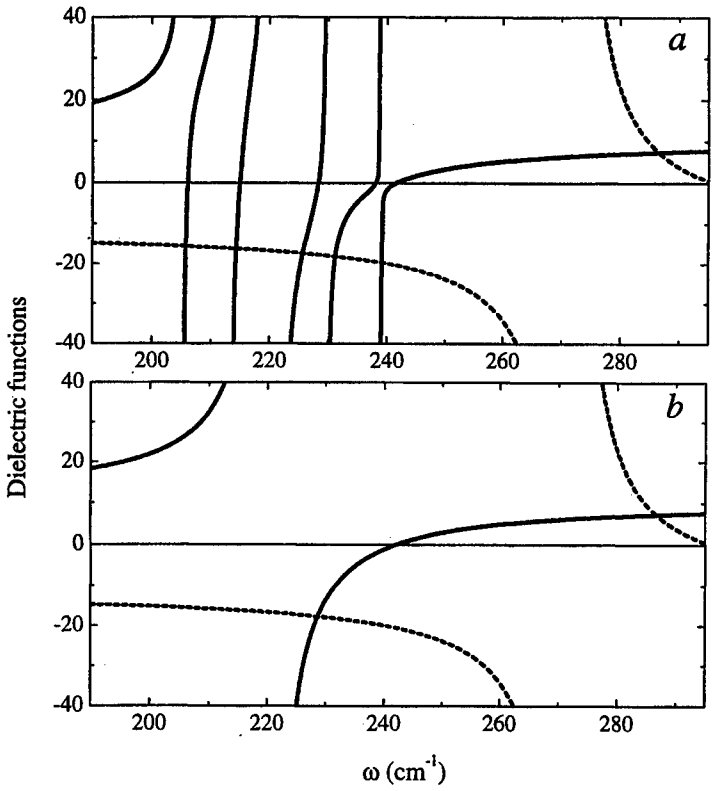


Fig. 1. Solution of the dispersion equation for hybrid phonon modes (panel *a*) and for interface DCM modes (panel *b*) in a disk-shaped InAs/GaAs QD with R=5 nm, h=5 nm.

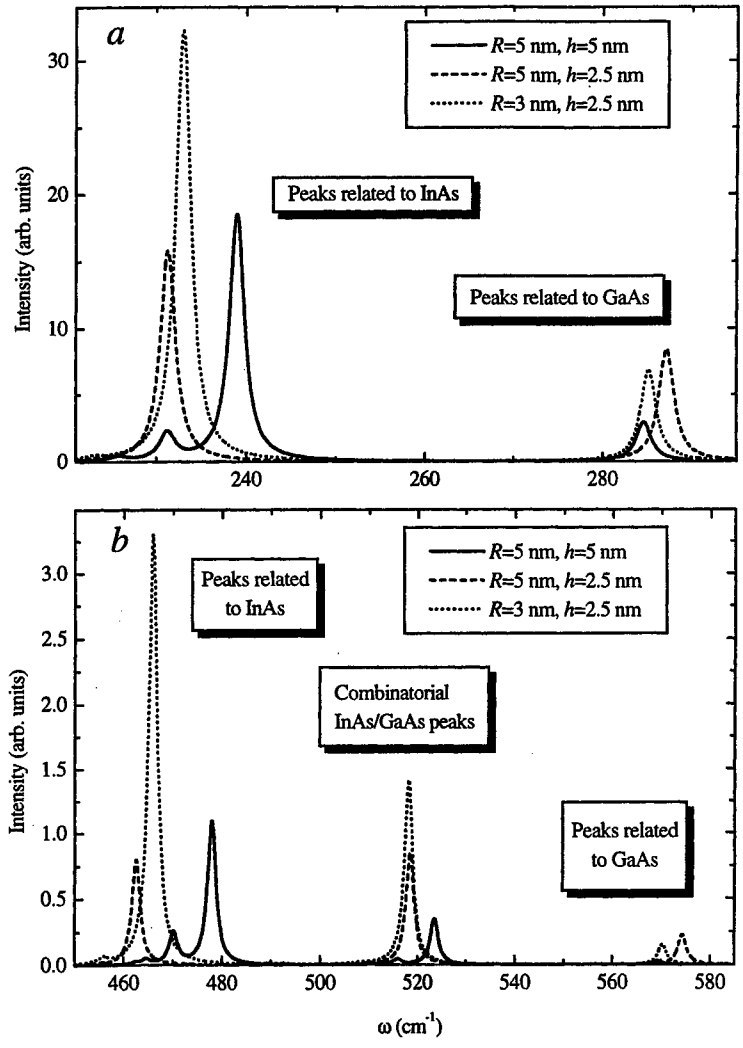


Fig. 3. Fundamental (panel *a*) and first overtone (panel *b*) Raman scattering bands of disk-shaped InAs/GaAs quantum dots.

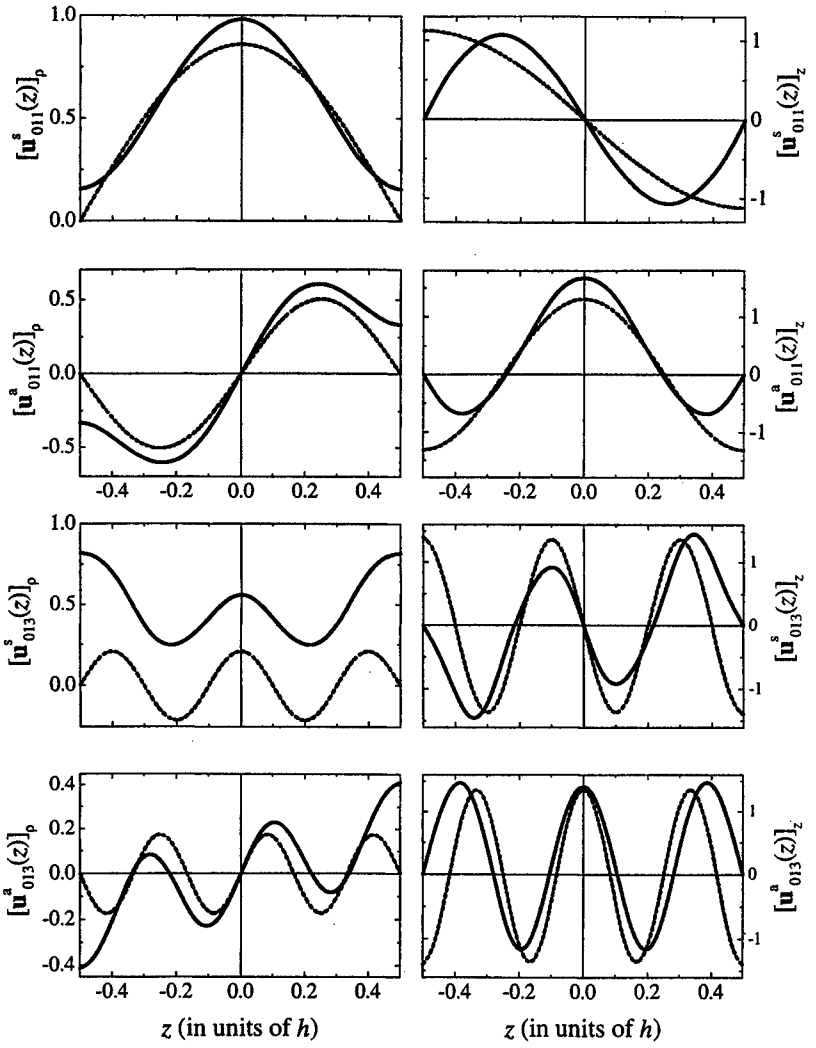


Fig. 2. Dependence of components of the basis vectors of phonon eigenmodes on the coordinate z in the InAs/GaAs disk-shaped quantum dot with $R = 5$ nm, $h = 5$ nm. Solid lines are related to hybrid modes, dashed lines are related to DCM bulk-like modes.

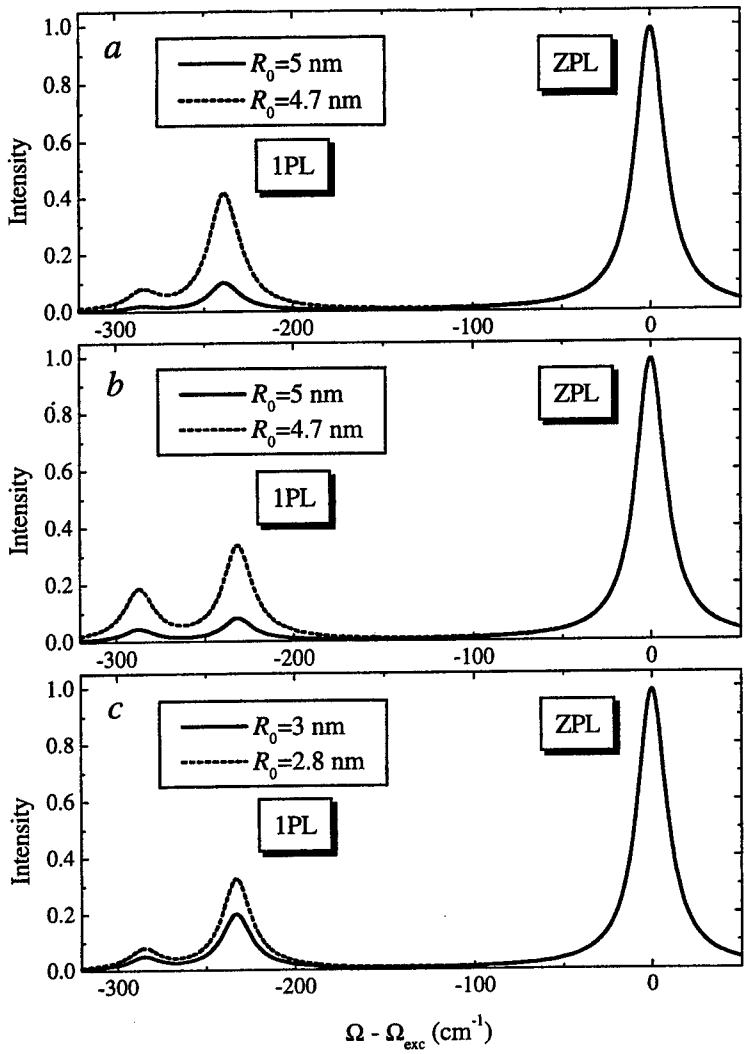


Fig. 4. Photoluminescence spectra of the Gaussian ensemble of disk-shaped InAs/GaAs quantum dots: (*a*) with $\langle R \rangle = \langle h \rangle = 5$ nm, (*b*) with $\langle R \rangle = 5$ nm, $\langle h \rangle = 2.5$ nm, (*c*) with $\langle R \rangle$ 3 nm, $\langle h \rangle = 2.5$ nm. The relative size dispersion $\Delta = 0.05$.

FABRICATION AND OPTICAL PROPERTIES OF QUANTUM DOTS FOR OPTOELECTRONICS APPLICATION

Yasuhiko Arakawa
RCAST, University of Tokyo
Roppongi, Minato-ku, Tokyo 106-8558 Japan
arakawa@is.u-tokyo.ac.jp

1. INTRODUCTION

A reduction of dimensionality of the electron motions in quantum dots (QDs) brings new phenomena in semiconductor physics. Moreover, it allows new device concept to be considered and permits improvements in performance of the transistors and lasers. Particularly, the quantum dot laser which was proposed in 1982 by Arakawa and Sakaki[1] is one of the most promising devices for practical applications. Photon can be controlled by photonic crystal or microcavities. Both the electronic and photonic nanostructures should play an important role in the optoelectronics in the 21st century. In this paper, we address the current state of the art of fabrication and optical properties of the quantum dots for future optoelectronics.

2. NITRIDR-BASED QUANTUM DOTS AND VCELS

GaN and related materials have attracted much attention, especially because of optical devices emitting from an ultraviolet to a visible region. Short-wavelength lasers with InGaN multiple quantum wells as the active layer have been demonstrated under continuous-wave and pulsed operation. In addition, the lasers with a lifetime of more than 10,000 hours have been reported . A laser with quantum dots in the active layer is expected to have a lower threshold current and other superior performance. Therefore some methods for fabricating QD structures in nitride semiconductors have been reported. We have demonstrated the growth of InGaN self-assembled QDs on a GaN buffer layer without any surfactants using atmospheric-pressure metalorganic chemical vapor deposition (MOCVD) [2]

Here, we discuss our recent successful work on lasing operation from an InGaN self-assembled QD laser at room temperature. We have also achieved the *first* lasing emission from a semiconductor laser with stacked $In_{0.2}Ga_{0.8}N$ QDs embedded in the active layer at room temperature under optical excitation. A clear threshold at a pump energy of 6.0 mJ/cm^2. The structure is schematically shown in Figure 1(a). The growth conditions of InGaN QDs are described in Ref. [3]. As the active layer, 10 periods of $In_{0.2}Ga_{0.8}N$ QDs and 5-nm-thick $In_{0.02}Ga_{0.98}N$ spacers were grown. Figure 1(b) shows an atomic force microscope (AFM) image of 3-layer stacked $In_{0.2}Ga_{0.8}N$ QDs under the same growth conditions for a reference. From Fig. 1(b), the average diameter and height of the QDs is 19.5 nm and 4.5 nm, respectively. The QD density is $6x10^9$ cm^{-2} per layer. The cavity was fabricated by low damage electron cyclotron reactive ion etching (RIE) with Ar/Cl_2 gases. Scanning electron microscopy shows the good morphology of the cavity facet. The cavity facet was not coated. The length and width of the cavity are 540 μm and 10 μm, respectively. Figure 1(c) shows the polarized emission intensity as a function of the excitation energy per pulse. The emission intensities were accumulated over 15 pulses. A clear threshold can be seen in the relation between the excitation energy and TE polarized intensity in Fig. 2. The threshold excitation energy is 6.0

mJ/cm^2. Emission spectra with various excitation intensity demonstrates very narrow linewidth which is determined by the resolution limit.

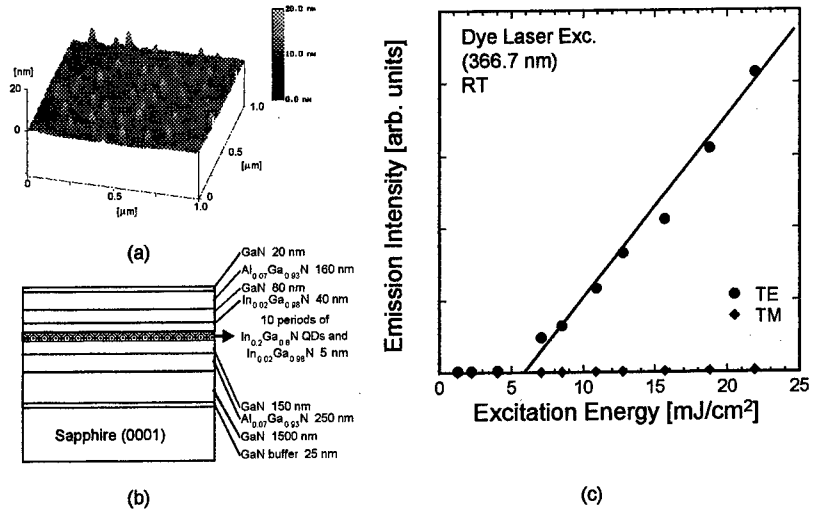


Fig. 1: (a) The laser structure with 10-layer stacked $In_{0.2}Ga_{0.8}N$ QDs embedded in the active layer is schematically shown. (b) AFM image of 3-layer stacked $In_{0.2}Ga_{0.8}N$ QDs for a reference sample. (c) dependence of the polarized emission intensity on the excitation energy, excited by the dye laser (366.7 nm). Photoluminescence was measured at room temperature.

Moreover, we have obtained room temperature operation of InGaN vertical cavity surface emitting quantum well lasers[4,5]. Post-type VCSELs with diameter 18 μm are arrayed in a two-dimensional matrix with 22 μm interval. A GaN-based multi-layer structure was grown on a (0001) sapphire substrate by atmospheric-pressure metal organic chemical vapor deposition. First, we grew a nitride DBR consisting of 43 pairs of GaN layers and $Al_{0.34}Ga_{0.66}N$ layers. Then, a 2.5λ cavity comprising 26 periods of $In_{0.1}Ga_{0.9}N$ quantum well layers was grown on the nitride DBR. Finally, a reflector consisting of 15 periods of ZrO_2/SiO_2 multi-layer (oxide DBR) was evaporated on the top of the GaN-based multi-layer to form a vertical cavity. The reflectivities of the nitride and oxide DBRs were 98% and 99.5 %, respectively.

Emission spectra from the single post-type VCSEL were measured at room temperature with an excitation source of a dye laser (367 nm) pumped by a nitrogen laser with a repetition rate of 3 Hz. The laser beam was focused on to the backside of the sapphire substrate at normal incidence. We measured emission intensities accumulated for 180 pulses as a function of excitation energy per one pulse. A clear threshold was observed at a pump energy of E_{th}=10 nJ/cm^2, which corresponds to the sheet carrier density 2-4X10^{12} cm^{-2} at the threshold. With increasing excitation powers, emission spectra showed a drastic transition from the 0.9 nm width spontaneous emission peaks spectrally filtered by the microcavity below threshold to very sharp emission peaks above threshold. Note that the linewidth of these sharp peaks is less than 0.1 nm, which is the resolution limit of our experimental setup. Such a drastic spectral narrowing is direct evidence of lasing action. TypeII GaSb/GaAs quantum dots will be also discussed[6]

3. NEARF-IELD SPECTROSCOPY OF SINGLE QUANTUM DOT

We developed a low-temperature NSOM system for single quantum dot spectroscopy. The whole scanning set-up is installed in a helium gas-flow cryostat within a sample chamber, which is paced in a closed cycle superconducting magnet. The PL measurement were carried out with the illumination-collection mode where both the excitation and collected luminescence light go through the same fiber. We observed spatially and spectrally resolved Zeeman spin splitting of the individual self assembling InAs/GaAs quantum dots in a magnetic filed up to 10 T. Fine spectral features indicated the different splitting in the individual s as well as the spatially resolved images of different spin components[7]. Moreover, circularly polarized photoluminescence successfully resolved each pair of spin up and down, discussing the spin-flip effect inside individual quantum dots[8]. PLE spectrum of a single quantum dots revealed localized LO-phonon lines as well as continuum in the density of states[9].

Scanning tunneling luminescence form single quantum dots was also investigated. The system includes a Ultra-High-Vacuum STM and the optics system. We succeeded in obtaining a STL images from a single quantum dot for the first time. Owing to lateral diffusion of injected minority carriers, the measured spatial resolution was ~10nm[10].

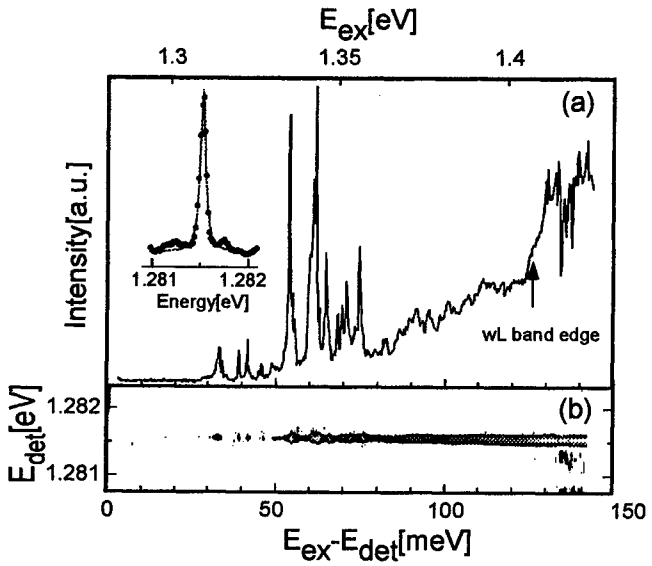


Fig. 2: PLE spectrum of an InAs single quantum dot structures. Continuum was observed in the density of states below the wetting layer energy. In addition, many localized phonons were detected.

ACKNOWLEDGMENTS

I would like to thank Dr. Someya and Dr. Toda for their intensive collaborations. This work is supported by the Future Program of the Japan Society for the Promotion of

Science (Project No. JSPS-RFTF96P00201) and Grant in-aid of Priority Area by Ministry of Education, Science and Culture.

REFERENCES

[1] Y. Arakawa and H. Sakaki, Appl. Phys. Lett. , 40, 939 (1982)
[2] K. Tachibana, T. Someya, and Y. Arakawa, Appl. Phys. Lett. 74, 383 (1998)
[3] K. Tachibana, T. Someya, and Y. Arakawa, to be published in Appl. Phys. Lett. (1998)
[4] T. Someya, K. Tachibana, Y. Arakawa, C. Li, and T. Kamiya, Jpn. J. of Appl. Phys., Expres Lett. 37, L1424 (1998)
[5] T. Someya, K. Tachibana, Y. Arakawa, CLEO'99 CPD2 (1999)
[6] K. Suzuki, R. Hogg, K. Tachibana, and Y. Arakawa, Jpn. J. of Appl. Phys. 37, L203 (1998)
[7] Y. Toda, S. Shinomori, K. Suzuki and Y. Arakawa, Appl. Phys. Lett. 73 517 (1998)
[8] Y. Toda, S. Shinomori, K. Suzuki and Y. Arakawa, to be published in Phys. Rev. B (1998)
[9] Y. Toda, T. Moriwaki, K. Suzuki, and Y. Arakawa, Phys. Rev. Lett., in press (1999)
[10] K. Yamanaka, K. Suzuki, S. Ishida and Y. Arakawa, Appl. Phys. Lett. 73 1460(1998)

CARRIER RELAXATION IN SELF-ORGANIZED STRESSOR QUANTUM DOTS: THE EFFECT OF DOPING

H. Lipsanen, H. Koskenvaara, J. Toivonen, M. Sopanen,
Optoelectronics Laboratory, Helsinki University of Technology, FIN-02150 Espoo, Finland,
and J. Ahopelto,
VTT Microelectronics, FIN-02150 Espoo, Finland.

ABSTRACT

We have studied experimentally the carrier relaxation processes in quantum dots based on self-organized stressors. The relaxation and recombination time are obtained from time-resolved photoluminescence of the quantum dot transitions yield when a high or an intermediate density of photogenerated carriers are present. A qualitative view of the relaxation behavior at very low excitation is obtained from cw luminescence as a function of the excitation intensity. The background carrier concentration in the quantum dots was modified by inserting a doped layer into the structure. The results from the n-type sample show that the electron-electron scattering is efficient, whereas slower relaxation is observed for the sample with excess holes.

I INTRODUCTION

The thermalization of carriers in zero-dimensional quantum dots (QD's) has been studied intensively during the last few years. Due to the discrete energy levels in QD's, carrier scattering by LO phonons is no more efficient as in bulk and quantum well (QW) structures. LA phonon scattering is also very slow if the energy level separation exceeds few meV's [1]. Various other scattering mechanisms have been proposed, such as Coulomb scattering [2], multiphonon processes [3] and Auger scattering between electrons and holes [4]. Most work has concentrated on self-organized QD's grown via Stranski-Krastanow mode. Another QD structure based on self-organized stressors offers an attractive approach to study these phenomena due to low inhomogeneous broadening and high luminescence efficiency [5]. The energy level separation of electrons can be tuned between 5 and 20 meV by modifying the stressor structure. In this work, we have studied carrier relaxation in the stressor QD's with four discrete energy levels which exhibit clear state-filling due to Pauli blocking.

II EXPERIMENTAL

The samples were grown by metalorganic vapor phase epitaxy. The details of the growth have been reported previously [5,6]. A schematic cross section of the QD samples is shown in Fig. 1a. The structure consists of a 8 nm thick $In_{0.20}Ga_{0.80}As/GaAs$ quantum well (QW) at depth of 10 nm from the surface. The layers were nominally undoped. Background doping was obtained by adding a 20 nm thick, either n- or p-type GaAs layer 40 nm below the QW. The carrier concentration was about 10^{18} cm^{-3} in the doped layers.

The self-organized InP islands acting as stressors were grown on the surface by depositing nominally 3 monolayers of InP at T=650 °C [6]. The typical island height is 22 nm and the density is about $1x10^9$ cm^{-2}. Fig. 1b shows a 1x1 μm^2 area of the sample surface measured by atomic force microscopy. The islands are uniform in size and show well-developed facets.

Time-resolved luminescence spectra were obtained by pumping with 200 fs pulses from a 76 MHz mode-locked titanium-sapphire laser operating at 800 nm. The luminescence was dispersed with a 0.5 m monochromator and detected by cooled multichannel plate photomultiplier and a time-correlated photon counting technique. The time resolution was 35 ps. The cw spectra were measured by excitation with a 488 nm line from an Ar ion laser and detected by a 77 K Ge p-i-n detector. The spot diameter on the surface of the sample was about 200 μm.

III RESULTS AND DISCUSSION

The electronic levels of the stressor QD's have been calculated in a theoretical paper [7]. The QD potential induced locally into the QW by the stressors is almost parabolic having a level separation of about 12 meV for the electrons and 3 meV for the holes. The selection rules require the same hole and electron level for allowed optical transitions. Due to small level separation, LA phonon scattering is expected to yield a fast relaxation channel for the holes, in contrast to electrons. The temporal behavior of the stressor QD transitions has been reported previously for the samples with the smaller In concentration of 0.10. The dominant relaxation mechanism at high excitation was attributed to fast initial Coulomb scattering [8] and to an Auger-like process involving holes at later stages [9].

A typical PL spectrum of the undoped QD sample is shown in Fig. 2a. The QW transition is seen at 950 nm and the ground state QD transition QD0 at 1040 nm. The excited QD states arise between the QD0 and QW transitions due to state-filling in QD's already with moderate excitation intensity of 30 W/cm^2 used here. The temporal behavior of the transitions are shown in Fig. 2b. After excitation, all QD states are rapidly filled and the excess carriers are collected into the QW. At later stages after about 3 ns, the carrier feed from the QW and upper QD states down to the lowest QD states starts to quench. A rate-equation analysis gives a relaxation time of 0.9 ns and a recombination time of 1.6 ns by assuming that the carrier dynamics is limited by the relaxation of electrons. This result is qualitatively in agreement with the previous work [8] but both relaxation and recombination time are here 50% longer, possibly due to the larger In concentration of 0.20 used here. However, the application of the time-resolved measurements is limited to reasonably high excitation intensities due to increasing noise in the spectra at low excitation intensities.

The doped samples were used in the further study of the scattering processes. Excess carriers, either electrons or holes, are generated into the QD's by adding an n- or p-type layer, respectively, to the structure. It is difficult to estimate the background carrier concentration in the QD's at low temperature, but the QD's are assumed to become at least partly filled with excess carriers due to doping. Nevertheless, the differences in the characteristics of the doped samples can be attributed to the type of the excess carriers. PL from the doped QD samples was also compared to that from a similar,

but undoped sample. At high and intermediate excitation intensities all samples show similar behavior showing state-filling of the QD states. Fig. 3 shows the PL spectra of the doped structures. The ground state QD transition is still visible at very low excitation of 1.3 μW (about 4 mW/cm^2) in the n-type structure. This corresponds to about 0.1 photogenerated carriers in a QD. However, the excited states and not seen if the excitation intensity is 1.4 mW or less. Thus, the relaxation of holes is very rapid down to the ground state. In the p-type sample the ground state transition quenches rapidly as the excitation intensity is decreased. A narrow fwhm of 9 meV and 5 meV is obtained at low excitation for the ground state transition of the n-type and p-type sample, respectively. The intensity and linewidth of the undoped sample behaves intermediately between the two doped cases. Also the QW transition vanishes rapidly in the p-type sample as the excitation power is decreased, whereas it remains strong in the n-type sample down to the lowest excitation levels. It is possible that a part of the mobile photogenerated electrons recombine nonradiatively, e.g. due to the surface states or in the InP island.

The intensity of the ground state PL transition from the samples is shown as a function of the excitation density in Fig. 4. The intensity of all samples is almost linear from intermediate up to high excitation where saturation of the transition occurs due to state-filling. In contrast to the n-type sample, a very rapid variation in the intensity of the p-type sample occurs at about 0.1 mW where the average occupation in a QD is estimated to be few electrons. The undoped sample exhibits mixed behavior between the doped samples. The large difference in the behavior of the samples having excess electrons or holes suggests that the electron relaxation is not dominated by LA-phonon scattering but by Coulomb scattering. Also, the low excitation results from the sample with excess holes show that the Auger-like process between electrons and holes plays a minor role.

IV CONCLUSION

The carrier relaxation in QD's was studied by using both time-resolved and cw measurements at low temperatures. The effect of excess carriers to the carrier relaxation was investigated with doped samples. The observed behavior at very low excitation intensities can be explained by efficient Coulomb scattering, i.e., electron-electron scattering and LA phonon scattering is an efficient process for holes.

ACKNOWLEDGMENTS

This work was supported by the Academy of Finland under grant #43991. The authors would like to thank J. Tulkki for helpful discussions.

REFERENCES

[1] U. Bockelmann and G. Bastard, Phys. Rev. B **42**, 8947 (1990).
[2] U. Bockelmann and T. Egeler, Phys. Rev. B **46**, 15574 (1992).
[3] T. Inoshita and H. Sakaki, Phys. Rev. B **46**, 7260 (1992).
[4] A.L. Efros, V.A. Karchenko, and M. Rosen, Solid State Commun. **93**, 281 (1995).
[5] H. Lipsanen, M. Sopanen and J. Ahopelto, Physical Review B **51**, R13868 (1995).
[6] M. Sopanen, H. Lipsanen, and J. Ahopelto, Appl. Phys. Lett. **66**, 2364 (1995).
[7] J. Tulkki and A. Heinämäki, Phys. Rev. B **52**, 8239 (1995).

[8] S. Grosse, J. Sandmann, G. von Plessen, J. Feldmann, H. Lipsanen, M. Sopanen, J. Tulkki and J. Ahopelto, Phys. Rev. B **55**, 4473 (1997).
[9] M. Braskén, M. Lindberg, M. Sopanen, H. Lipsanen and J. Tulkki, Phys. Rev. B **58**, 15993 (1998).

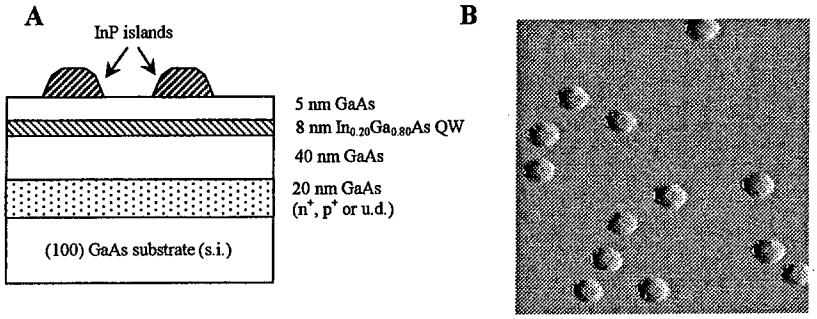


Fig. 1. a) Structure of the stressor quantum dot samples. b) Self-organized InP islands on top of the structure measured by atomic force microscopy. The scan size is 1x1 μm^2.

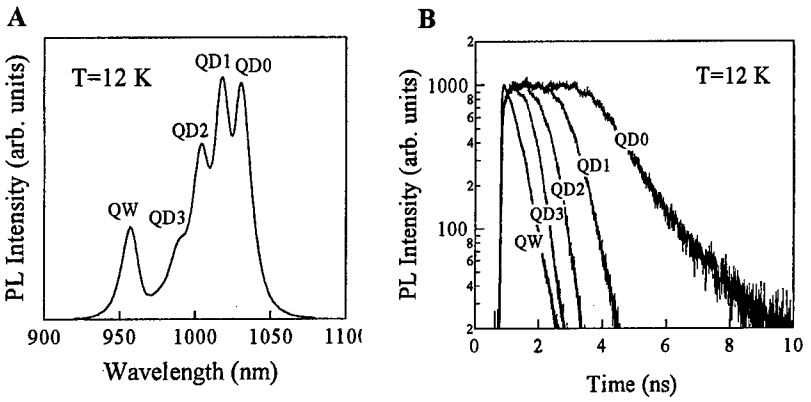


Fig. 2. a) Photoluminescence spectrum of the undoped quantum dot sample at T= 12 K. QD0, QD*n* and QW show the ground state quantum dot transition, the *n*th excited state transition and the quantum well transition, respectively. b) Time-resolved photoluminescence curves of the transitions.

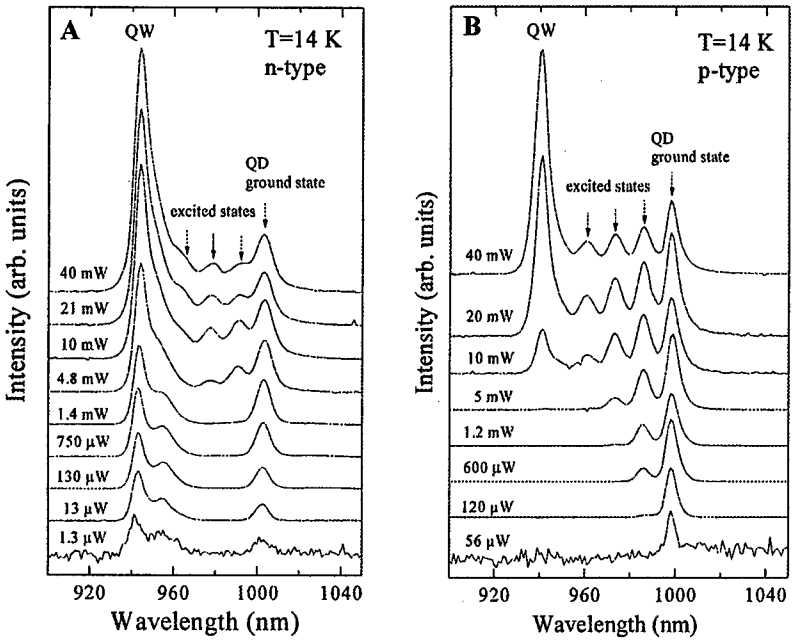


Fig. 3. Low-temperature PL spectra of the a) n- and b) p-type stressor QD samples as a function of excitation power.

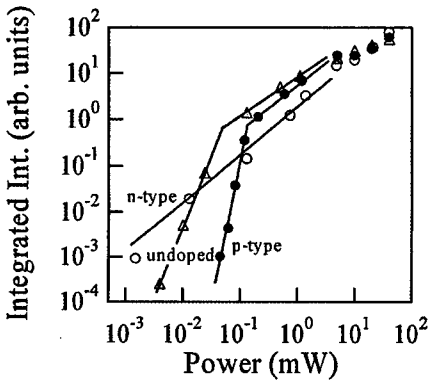


Fig. 4. Integrated intensity of the ground state PL transition of the undoped (triangles), n-type (open circles) and p- type (full circles) stressor QD samples as a function of excitation power.

RESONANT RAMAN STUDY OF THE InAs/GaAs SELF-ASSEMBLED QUANTUM DOTS

G.Zanelatto, Yu.A.Pusep, N.T.Moshegov[1,2], A.I.Toropov[2], P.Basmaji[1], J.C.Galzerani

Universidade Federal de São Carlos, 13565-905 São Carlos, SP,Brasil
[1]Instituto de Fisica de São Carlos, Universidade de São Paulo, 13560-970 São Carlos, SP, Brasil
[2]Institute of Semiconductor Physics, 630090 Novosibirsk, Russia

The topology of self-assembled InAs/GaAs quantum dots was studied by resonant Raman scattering caused by the interface modes localized near the edges of the dots. Evidences were found that on both sides of the InAs layer containing the dots, their topologies show some resemblances. In addition, in the multilayered systems the evidence of the coalescence of the dots (which form vertical columns) in neighbor layers separated by the distance smaller than 25 monolayers was obtained.

The self-assembled InAs/GaAs quantum dots which are formed during the 3D overgrowth of highly mismatched materials have been extensively studied over last years because of their promising device potentialities. Nevertheless, the process of formation of the self-assembled quantum dots is not yet well understood although it evidently influences their electronic characteristics. The widely accepted point of view is that pyramidal InAs dots are formed on a thin (1.5 ML thick) InAs wetting layer (see [1] and references herein). However, recent studies using cross-sectional tunneling microscopy [2,3] and scanning transmission electron microscopy [4,5] presented direct evidences that due to the segregation the InAs dots in forms of lenses or disks are rather embedded within the wetting layer and not on it. Moreover, as it has been shown in [4], the process of the capping of the InAs dots with GaAs changes their volume due to the redistribution of InAs from the dots to the GaAs capping layer. Obtaining information about the formation of the quantum dots in this case is very difficult. Therefore, any application of spectroscopic methods, which are simple to use, to study the topology of the self-assembled quantum dots is indispensable.

In this paper we present the Raman spectra of the InAs/GaAs self-assembled quantum dots showing that the topologies of the dots are somewhat similar on both sides of the InAs layer where they are formed. This implies in a difference between the material of the dots and the one of the wetting layer, which can be caused by a strong modification of the wetting layer between the dots due to the segregation, as it has been established in [2]-[5].

In order to study the topology of the InAs/GaAs quantum dots we measured the Raman scattering of the interface vibrational modes localized near the edges of the dots. The contribution of these modes to the Raman scattering, being proportional to the density of the dots, has been shown to appear at the resonance with electron excitations confined in the InAs dots [6]. Thus, the Raman lines associated with such interface modes can serve as indicators of the presence of the quantum dots.

The InAs/GaAs heterostructures containing the self-assembled InAs quantum dots were grown on (001)-oriented GaAs substrates by molecular beam epitaxy via Stranski-

Krastanov growth. Structures with and without 500 Å thick cap GaAs layers were grown under the same growth conditions; the last ones were characterized by an atomic force microscope (AFM) Digital Instruments Nanoscope IIIa using the tapping mode. Samples both with a single InAs layer containing quantum dots and with multilayers separated by different GaAs spacers were investigated.

The single layer dots were grown with the nominal thicknesses of InAs 2, 2.5, and 3 ML's at the temperature T=500 °C and the As_4 background pressure $P_{As} = 8x10^{-6}$ Pa. The multilayered dot structures were grown as following: after the growth of a GaAs/AlAs superlattice and a GaAs buffer, the temperature of the substrate was reduced to 450-470 °C and the InAs layer with the nominal thickness 3 ML's was deposited. The process of the formation of the dots was controlled by reflection high-energy electron diffraction (RHEED) oscillations. A transition from streaked to spotty RHEED pattern indicating a formation of the 3D islands was observed after the deposition of an effective thickness of InAs equal to 1.8 ML. The growth was interrupted for 30 sec. after the deposition of the nominal thickness of InAs; then the GaAs spacer of the corresponding thickness was grown and the process was repeated in order to obtain the multilayered structure. During the growth the fluxes of InAs and GaAs were fixed at 0.1 and 0.35 ML/s respectively, while $P_{As} = 2x10^{-6}$ Pa. Finally, the structure was capped with 500 Å of GaAs.

The Raman scattering was performed at T=8 K with a Jobin-Yvon U-1000 double-grating spectrometer supplied with a conventional photon counting system. A Ti-sapphire tuned laser pumped with an Ar^+ ion laser was used for excitation near the $E_0+\Delta_0$ resonance of the InAs quantum dots. The cross-polarized Raman spectra were measured in order to avoid photoluminescence.

In order to obtain information about the InAs dots and the GaAs substrate we compared the Raman spectra of the samples grown with and without the GaAs capping layer. We expect that in the case of a plane interface between the dots and the substrate, the interface vibrations associated with the edges of the dots would contribute to the Raman spectra in the capped samples and would not in the samples without capping layers.

As it has been shown in [6], the interface modes associated with the InAs quantum dots are seen in Raman scattering in resonance with the $E_0+\Delta_0$ electron excitations confined in the dots ($E_{ex} \approx 1.72$ eV, as measured in [7]). At such a resonance excitation the GaAs bulk phonons are week and they are detected as a shoulder at the high frequency side of the Raman line corresponding to the first interface mode [6]. The obtained Raman spectra are plotted in Fig.1. In all the samples grown with the capping layer the Raman lines caused by the GaAs-like interface modes were observed. The first interface modes located at 293 cm^{-1} reveal larger intensities as compared to the high-index ones. Although with smaller intensities, identical lines were found in all the uncapped samples. This result testifies to the formation of the edges between the dots and the underlying GaAs (similar to those between the dots and the capping layer), which can appear due to the modification of the InAs wetting layer between the dots. As it has been shown in [2-5], the segregation strongly alters the contents of the wetting layer between the dots; as a consequence, the InAs dots become effectively embedded within the InGaAs wetting layer giving rise to the relevant interface modes. Actually, in this case the interface modes are localized at the edges formed by the boundary between the dots and the InGaAs wetting layer. Analyzing the ratios of the Raman line intensities measured in the uncapped quantum dots to the capped ones, we can conclude that the

larger this ratio, the sharper the edges corresponding to the top of the dots relative to the edges of their bases embedded in the wetting layer.

It is worth mentioning, that the InAs-like interface modes were also found in the Raman spectra of the samples under investigation. However, due to their relatively weak intensity we could not include them in the analysis.

In addition, we studied the interface modes in the multilayered systems containing self-assembled quantum dots. The Raman spectra measured in the samples with different thicknesses of the spacers between the quantum dot layers are depicted in Fig.2. As it is seen, for thicknesses of the spacers smaller than 25 ML's, the intensities of the interface modes decrease with the decrease of the spacer thicknesses. This occurs because at small thicknesses of the spacers the InAs dots in vertical columns formed by aligned growth of neighbor layers coalesce (or they are close to coalescence), thus decreasing the density of the tips responsible for the relevant interface modes. At the spacer thicknesses equal to 15 ML's a significant number of dots coalesce resulting in very weak intensities of the interface modes. Thus, this shows that Raman spectroscopy can serve as a tool to characterize the separation of the quantum dots in multilayer systems.

To summarize, by Raman spectroscopy of the interface modes localized near the edges of the InAs/GaAs self-assembled quantum dots we found an evidence of the similar topologies of the quantum dots on both sides of the layer where they are formed. We showed that the Raman scattering is a tool sensitive enough to analyze the separation between the quantum dots in multilayered systems.

The financial support from CNPq, FAPESP, and CAPES is gratefully acknowledged.

1. M.Grundmann, O.Stier, and D.Bimberg, Phys.Rev. B52, 11969 (1995)
2. W.Wu, J.R.Tucker, G.S.Solomon, and J.S.Harris, Jr., Appl.Phys.Lett. 71, 1083 (1997)
3. B.Legrand, B.Grandidier, J.P.Nys, D.Stievenard, J.M.Gerard, and V.Thierry-Mieg, Appl.Phys.Lett., 73, 96 (1998)
4. P.D.Siverns, S.Malik, G.McPherson, D.Childs, C.Roberts, R.Murray, B.A.Joyce, and H.Davock, Phys.Rev. B58, 10127 (1998)
5. P.B.Joyce, T.J.Krzyzewski, G.R.Bell, B.A.Joyce, T.S.Jones, Phys.Rev. B58, R15981 (1998)
6. Yu.A.Pusep, G.Zanelatto, S.W. da Silva, J.C.Galzerani, P.P.Gonzalez-Borrero, A.I.Toropov, P.Basmaji, Phys.Rev. B58, R1770 (1998)
7. S.W. da Silva, Yu.A.Pusep, J.C.Galzerani, D.I.Lubyshev, P.P.Gonzalez-Borrero, and P.Basmaji, J.Phys.Condens.Matter 9, L13 (1997)

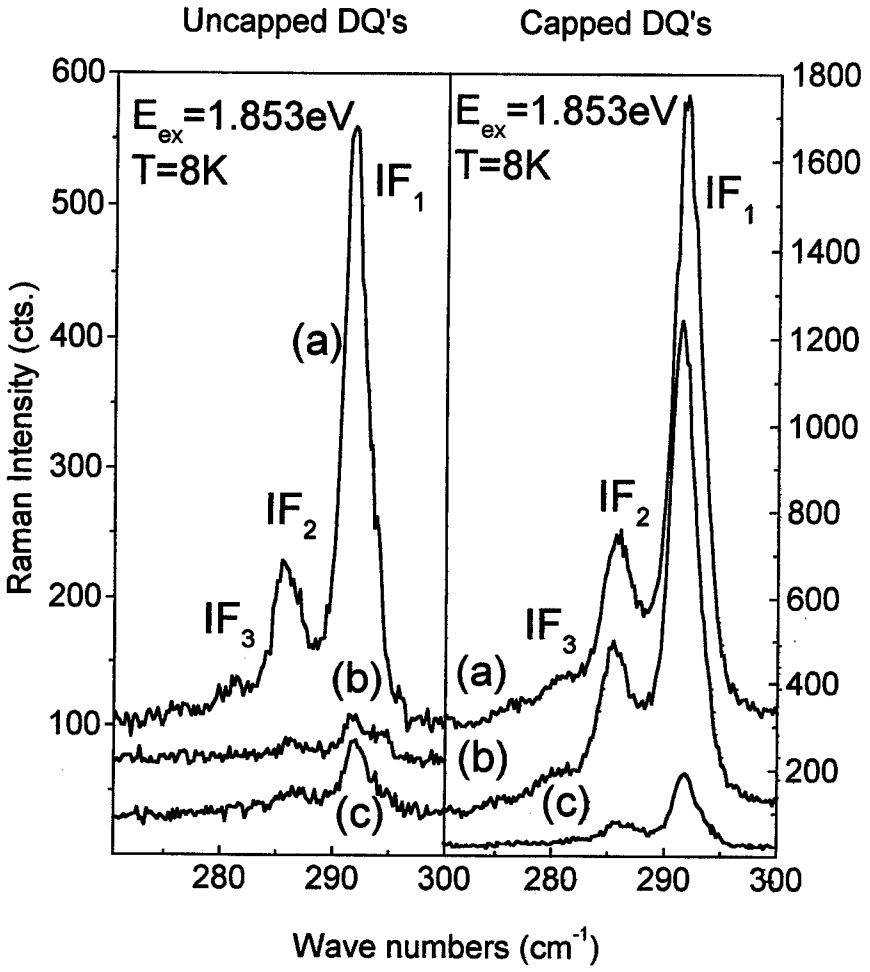


Fig.1.The GaAs-like interface modes measured in the single layer InAs/GaAs heterostructures containing self-assembled quantum dots grown with nominal thicknesses of InAs: (a) 2ML's,(b) 2.5ML's,(c) 3ML's.

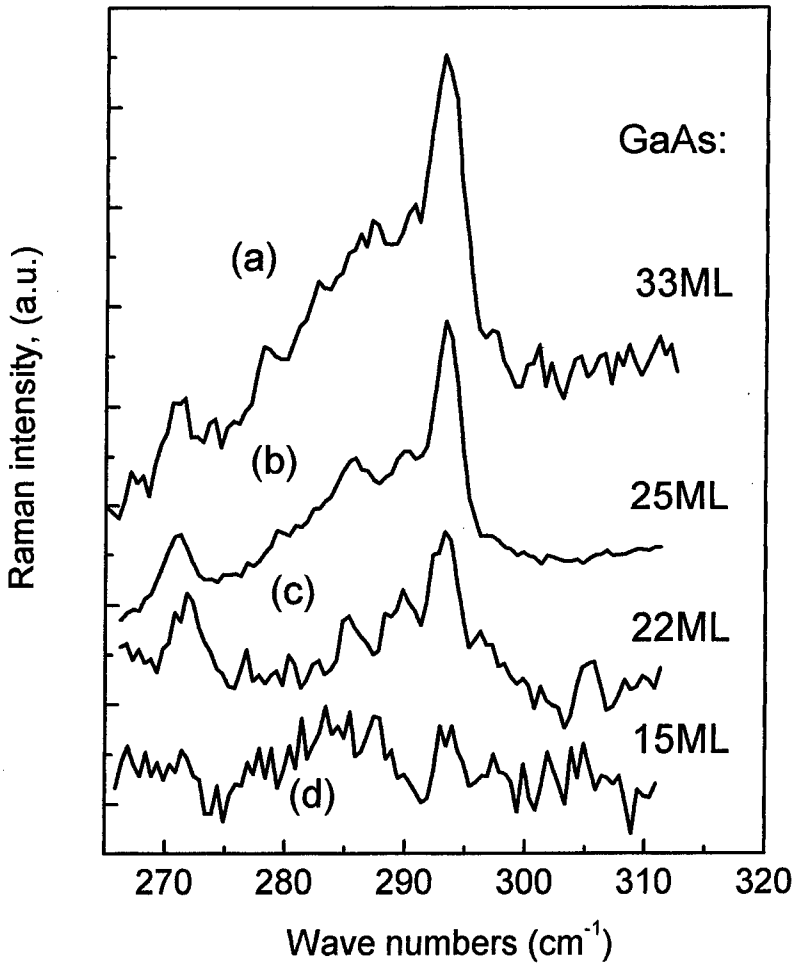


Fig.2. The GaAs-like interface modes measured at T=8 K in the multilayered InAs/GaAs heterostructures with the 2 ML's thick InAs layers separated by GaAs spacers with different thicknesses: (a) 33 ML's (Eex = 1.75 eV), (b) 25 ML's (Eex = 1.78 eV), (c) 22 ML's (Eex = 1.78 eV), (d) 15 ML's (Eex = 1.77 eV); the numbers of periods are: 15, 10, 7, and 7 respectively.

Nanoclusters, Nanoparticles and Nanotubes

COULOMB CRYSTALS AND GLASSES FOR SELF-ASSEMBLY OF NANOPARTICLES

P.F. Williams, A. Belolipetski, and A. Goussev
Department of Electrical Engineering
University of Nebraska-Lincoln
Lincoln, NE 68588-0511

M.E. Markes
Department of Physics
University of Nebraska-Kearney
Kearney, NE 68849

Abstract

Under proper conditions, small particles may be suspended in a regularly-spaced array called a Coulomb crystal. In this paper we discuss the application of this phenomenon to the self-assembly of nanoparticles in a lattice-like array on a substrate. Issues associated with depositing the particles, and the size and lattice spacing of the particles are discussed.

1 INTRODUCTION

There is interest in developing efficient and reliable technologies for synthesizing ordered arrays of ultrasmall structures such as quantum dots. These systems are potential vehicles for implementing a number of high performance electronic, magnetic and optical devices[1]. Dots small enough to host a single or few conduction electrons can be used for ultradense electronic or optical memory[2, 3, 4]. Cylindrical quantum dots of ferromagnetic materials have exhibited several-fold increase in magnetic coercivity accruing from shape anisotropy[5]. These dots could be used to create extremely high density magnetic storage disks. Recently, we have synthesized superconducting quantum dots of high T_C materials that have exhibited enhanced transition temperatures. Quantum dots of chemical catalysts are superior to their bulk counterparts since the surface-to-volume ratio increases dramatically. Additionally, self-assembled metallic dots can be utilized to fashion extremely powerful computing architectures[6] and they may have possible applications in such new and emerging areas as quantum computing[7]. In this paper, we will discuss a new technique for producing ordered or non-agglomerated arrays of small particles on a substrate.

It is well known that small particles in a plasma quickly acquire a negative charge. These particles can be levitated in a thin layer above electrodes and other surfaces exposed

to the plasma. Further, under proper conditions, these particles arrange themselves into a regularly-spaced array—a "Coulomb crystal." This phenomenon can be used to produce a regimented distribution of these small particles which can be transferred to a substrate, resulting in self-assembly. Although the spatial coherence of these "crystals" can be good, generally spatial correlation falls off rapidly after several "lattice constants." In this case, the structure might be better termed a "Coulomb glass."

2 Use of Coulomb Crystals for Nano-Fabrication

The Coulomb crystal approach has a number of potential advantages over more established self-assembly techniques. First, it is much less expensive than Stranski-Krastanow growth which requires the use of an MBE apparatus or an equivalent facility. Second, unlike electrochemical self-assembly, it is a "dry" technique and hence compatible with hydrophobic materials. The material purity may not be as good as in the case of Stranski-Krastanow growth, but it is better than what is obtained in chemical self-assembly. Unlike S-K growth or electrochemical self-assembly, this technique has an advantage in that it offers the promise of continuously varying the period or pitch of the array by varying the plasma density. Finally, it is compatible with almost any type of substrate, and is more compatible with conventional IC fabrication technology than are other self-assembly techniques.

To self-assemble a two-dimensional ordered array of nanoparticles of a desired material on a chosen substrate, we follow a sequence of steps. First, the material must be formed into a fine powder. This can be accomplished by simply grinding it. While grinding damages the particles, for many applications the crystalline quality of the material is not of paramount importance. In many cases, the particles can be annealed or otherwise processed later to reduce the damage. Alternately, nanoparticles can be produced by gentler techniques such as sol-gel reactions or laser pyrolysis[8]. In fact, we have been investigating superconducting nanoparticles of high T_C materials produced by sol-gel reactions.

To arrange the nanoparticles on a substrate as a quasi-periodic array, we use an apparatus such as that shown schematically in Fig. 1. We first introduce them into an RF plasma by means of a "salt shaker", which consists of a container with a porous membrane in the bottom. The container is shaken to sieve the particles into the plasma. This process provides a degree of particle size selection. The plasma occurs in an inert gas such as argon at a pressure typically of about 1 Torr. The R.F generator supplies about 10 W of power at 13.56 MHz through a standard matching network.

Once the particles are introduced into the plasma, they become negatively charged. The charged particles levitate in a quasi two-dimensional layer over the driven electrode in the plasma chamber because of Coulomb repulsion (the electrode is also negatively charged). Under proper conditions, the electrostatic interaction between the charged particles leads to the formation of a more-or-less regularly-spaced array of particles, a "Coulomb crystal" or "Coulomb glass.". The array is then transferred to the substrate by simply turning the plasma off and allowing the particles to fall freely under gravity onto the substrate. We have found that spatial order is maintained reasonably well in this process. Several techniques can be used to stick the fallen particles to the substrate.

Considerable care is required to obtain good spatial coherence. Under many conditions, the particles form an array that would be better called a glass than a crystal. Even though

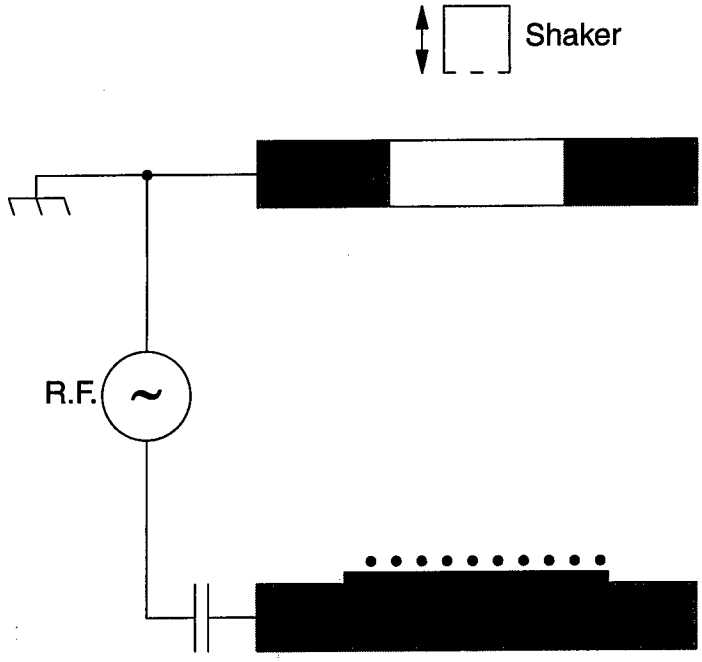


Figure 1: Schematic drawing of the cell used for deposition of regimented nanoparticle arrays.

they are not perfectly ordered, the particles in the glass are well-separated from each other and non-agglomerated. Such arrangements still exhibit interesting properties accruing from size quantization. For example, as discussed in a later section, we have recently synthesized Coulomb glasses of high T_C superconductors and found that they exhibit a somewhat enhanced transition temperature.

3 Physics of Coulomb Crystal Formation

It has been observed that small particles suspended in an R.F.-driven plasma will under the proper conditions collect in a quasi-two-dimensional layer just above the driven electrode, and arrange themselves into a regularly-spaced array—a so-called "Coulomb crystal."[9] Similar structures have been seen in the positive column of glow discharges[10], thermal plasmas[11], ion traps[12], and even (originally) in colloidal suspensions[13]. It has been proposed that a Coulomb crystal could be produced by using photoionization to charge the particles[14], but to our knowledge, such a structure has not been demonstrated in the laboratory. The Coulomb crystal phenomenon has attracted considerable interest because of the insight it may lend into the formation and dynamics of conventional crystals, and because of possible technological applications.

Fig. 2 shows BCC and HCP crystals produced by Chu and I in a low pressure plasma[15]. These crystals are suspended in the plasma. The particle size is too large (several μm) for

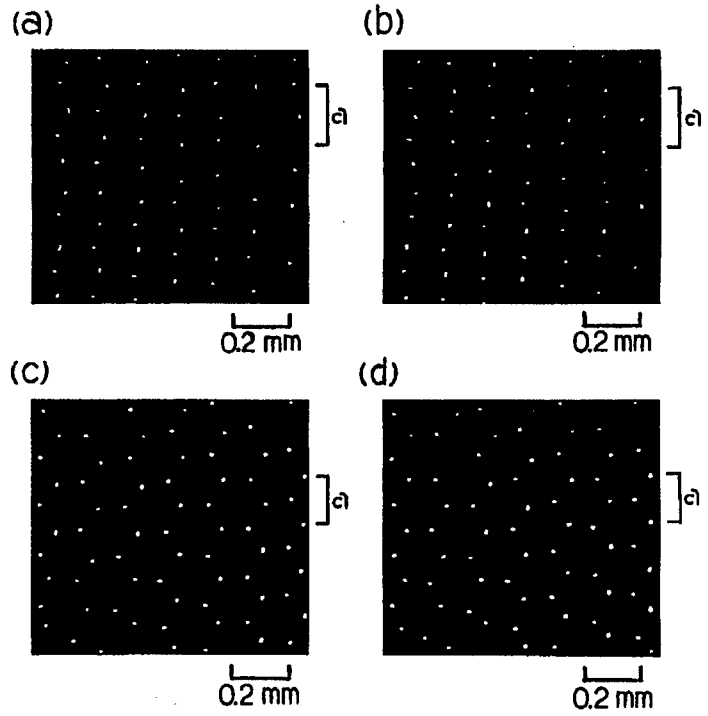


Figure 2: Micrographs of BCC (a and b) and HCP (c and d) Coulomb lattices from Ref. [15].

them to qualify as "quantum dots," and the interparticle spacing is about 100 μm. The particle diameter must be reduced by about two orders of magnitude, and it would be desirable to make a similar reduction in the interparticle spacing if this technique is to be useful for nanodevice applications. It appears that it is possible to reduce the particle diameter by the required amount, but substantial reduction of the interparticle spacing will be more difficult.

In most experiments (including ours), a low-pressure, parallel-plate, R.F. glow, two-component (free electrons and positive ions) plasma was used. Because the average speed of the electrons is much greater than that of the positive ions in the plasma, a particle in the plasma charges negatively. In steady state, the negative charge is adjusted so that the electron and positive ion currents balance. For a similar reason, the driven electrode of the plasma cell also charges negatively, causing a levitating force on particles in the vicinity. The combined effects of gravity, the ion wind, and this electric repulsion conspire to confine the particles to a thin sheet just above the electrode.

3.1 "Crystal" Bonding

According to the most common theory of Coulomb crystals, the particles levitated just above the driven electrode must be confined horizontally as well as vertically. The like-charged particles repel each other, and the lowest energy configuration is one with crystalline order. Thermal agitation of the particles acts to disrupt this order, and the system undergoes a phase transition similar to melting as this agitation is increased. The critical temperature depends on the parameter, Γ, defined as the ratio of the electrostatic energy of the particles at the equilibrium "lattice" position to the thermal translational energy of the particles. Values of Γ larger than about 170 are expected to result in formation of a regular lattice[16].

The interaction between the particles is complicated by the presence of the plasma. The negative charge on the particle repels the free electrons and attracts the positive ions, resulting in a halo of uncompensated ions around the particle. One effect of the halo is to shield the plasma from the field of the central particle. This effect is conventionally treated using a linearization of the Boltzmann distribution, resulting in Debye-Hückel shielding[17]. A second effect of the positive cloud is that it alters the effective force on a "dressed" particle when placed in a given electric field (such as that from a neighboring "dressed" particle). The net force is the vector sum of the force from the bare particle and the distorted positive cloud. The situation is roughly analogous to a classical diatomic molecule, and, over a range of particle separations, the net force between two "dressed" particles can be attractive, rather than repulsive. A rigorous calculation is difficult, however.

As a preliminary step in studying the process, we have calculated the net potential energy of a simplified two-"dressed" particle system as a function of particle separation. A principal simplification is that the force is treated as if the positive charge were rigidly attached to the negative particle. Thus, the net force on a particle is calculated as the sum of the force on the negative particle and the positive ion cloud. A second simplification relates to the electron and ion densities in the vicinity of the two particles. We have investigated several different approximations for this purpose. For all the situations we investigated, we found a net attraction between these "dressed" particles.

3.2 A Linear Model

The Debye-Hückel approximation for the electron and ion densities around a charged particle is obtained by 1) assuming thermodynamic equilibrium, so that the local densities are related to the local potential by a Boltzmann exponential, and 2) expanding the exponentials in a Taylor series and keeping only the linear terms. The result is that the local charge density, $\rho(\vec{r})$, is linearly related to the local potential, $\Phi(\vec{r})$, by

$$\rho(\vec{r}) = -\varepsilon_0 \alpha^2 \Phi(\vec{r}) \tag{1}$$

where α has the dimensions of an inverse length, and is usually defined to be the reciprocal of the linearized Debye length, λ_D,

$$\alpha = \frac{1}{\lambda_D} = \sqrt{\frac{n_0 q_e^2}{\varepsilon_0}\left(\frac{1}{kT_i} + \frac{1}{kT_e}\right)} \tag{2}$$

Here, n_0 is the bulk plasma density, k the Boltzmann constant, and T_i and T_e are the ion and electron temperatures respectively, and q_e is the (unsigned) charge on an electron. Solving Poisson's equation for the case of an isolated particle of charge $-Zq_e$ gives

$$\Phi(\vec{r}) = \frac{-Zq_e}{\varepsilon_0}\frac{e^{-\alpha r}}{r}$$

The case of two charged particles is handled relatively simply within this approximation. Because Eq. (1) is linear, the potential of two particles, one at the origin, and the other at $\vec{R}$, is simply the superposition of the potentials of the isolated particles.

The interaction energy may be evaluated as

$$U = \frac{1}{2}\int \rho(\vec{r})\Phi(\vec{r})d^3r. \tag{3}$$

Eq. (3) can be evaluated exactly for the case of two particles separated by a distance, R, giving

$$U(R) = U_0\left(\frac{\lambda_D}{R} - \frac{1}{2}\right)e^{-R/\lambda_D} \tag{4}$$

where $U_0 = Z^2q_e^2/4\pi\varepsilon_0\lambda_D$ is the energy of two unshielded particles separated a distance λ_D. Fig. (3) shows a plot of $U(R)/U_0$ vs. R/λ_D. There is a potential well of depth $0.00872U_0$, located at $R = (1+\sqrt{3})\lambda_D \approx 2.73\lambda_D$.

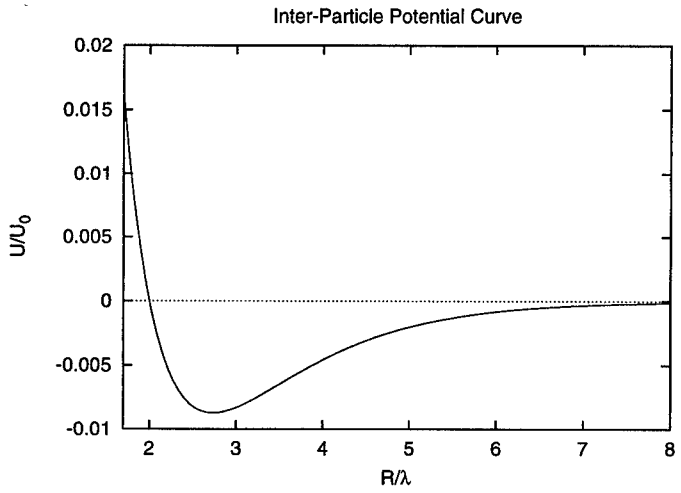


Figure 3: Inter-particle potential energy curve. The units of energy are $Z^2q_e^2/4\pi\varepsilon_0\lambda_D$, the energy of two unshielded particles separated a distance λ_D.

The assumption that the ion density is given by a linearized Maxwellian distribution is questionable in this application. Because of recombination at the dust particles, the ions are not in thermodynamic equilibrium, and even if equilibrium prevailed the exclusion of second order and higher terms in the expansion of the Maxwellian is typically not justified. Daugherty *et al.*[18], however, have shown that a linear relation such as that in Eq. (1) provides a remarkably good approximation to the results they obtain from a presumably more accurate theory similar to that conventionally used to analyze spherical Langmuir probes. Perhaps the Debye-Hückel-like approximation works as well as it does because the two errors (non-equilibrium, and linearization) partly cancel.

3.3 A Collisionless Model

A rather different model is also tractable. In this model, the electron density around the particle is assumed to be given by a Boltzmann distribution, and the positive ion density is determined by tracking ion trajectories as they pass by the particle, assuming that there are no collisions. The ion density, $n_+(\vec{r})$, at a point inside the sheath is given by

$$n_+(\vec{r}) = \int f_+(\vec{r},\vec{v})d^3v \tag{5}$$

where $f_+(\vec{r},\vec{v})$ is the ion distribution function. Watson showed that for a collisionless ensemble[19, 20]

$$f(\vec{r},\vec{v}) = f(\vec{r}_0,\vec{v}_0) \tag{6}$$

where $(\vec{r}_0,\vec{v}_0)$ is any point which is on the same trajectory as the point $(\vec{r},\vec{v})$.

We assume that the particles are located within a collisionless sheath of radius r_0, outside of which the ions are in local thermodynamic equilibrium. Then f_+ is a Maxwellian distribution on the surface of the sheath region. Other treatments assume monoenergetic ions at the sheath edge[18]. The assumption apparently is made for convenience, but the results are not significantly simpler than those we obtain. Eqs. (5) and (6) may be combined to obtain

$$n_+(\vec{r}) = n_0\left[\frac{2}{\pi}\sqrt{-q_e\Phi(\vec{r})/kT} + \mathrm{erfc}\left(\sqrt{-q_e\Phi(\vec{r})/KT}\right)e^{-q_e\Phi(\vec{r})/KT}\right] \tag{7}$$

In deriving these results, closed orbits and ion collisions with the particle are neglected.

This result can be used in Poisson's equation to determine Φ. Doing so produces a non-linear differential equation that can be solved numerically. The inter-particle potential can then be calculated numerically from Eq. (3) using this result for Φ along with n_+ from Eq. (7), and n_e from a Boltzmann distribution. Fig. (4) shows the results obtained for 2 μm diameter particles, $Z = 1000$, $n_0 = 10^9$ cm^{-3}, and $T_e = 1$ and $T_i = 0.026$ eV. Also shown for comparison are the results of the linearized Debye-Hückel model under the same conditions.

In these calculations, the charge density was taken to be the superposition of the densities of the isolated particles. Since the relationship between charge density and potential is not linear, this procedure is an approximation. The positive ion clouds will surely distort as the two "dressed" particles are brought together—an effect that we have tacitly neglected in the Langmuir-like model, and absent in the linearized model. The important point here is that such a distortion will cause the ion distribution to relax to a *lower-energy* configuration than that of the fixed configuration we used. Thus, we will have under-estimated the attractive force, and a more sophisticated treatment would find a stronger attraction than we find. The qualitative conclusion that the net force is attractive is still correct.

3.4 Empirical Evidence

The existence of an attractive force has been verified experimentally by Chen *et al.*[21] They present photographs of dust particles in a parallel-plate RF discharge showing "molecules" of six particles in hexagonal and square configurations. They also show a photograph which seems to show several "diatomic" and "triatomic" molecules, but the interpretation of these data is complicated by the possibility that the photo may be showing two or more

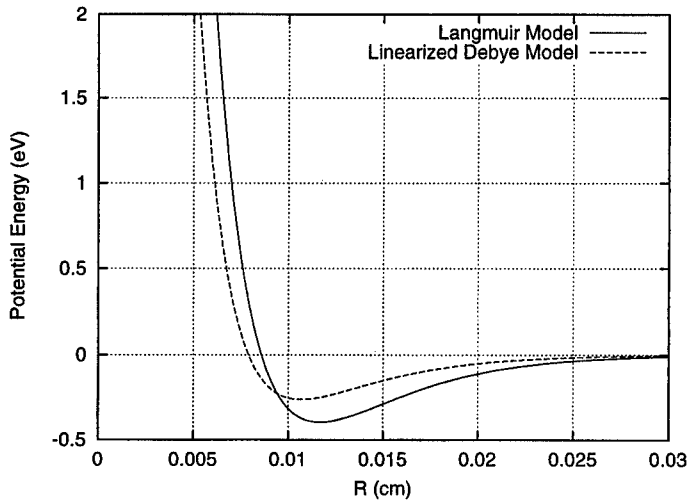


Figure 4: Comparison of the inter-particle potential energy obtained from the Langmuir-like and Debye-Hückel models. The assumed particle diameter was 2 μm, $Z = 1000$, $n_0 = 10^9$ cm^{-3}, $T_e = 1$ eV, and $T_i = 0.026$ eV.

layers of a Coulomb crystal. The existence of isolated "molecules" provides substantial empirical support for the claim that the inter-particle force is attractive. Additionally, several workers report that the individual particles in adjacent layers line up so that a particle in one layer is directly above the corresponding particle in the layer just below[22, 23]. This observation also supports the attractive force contention.

4 ISSUES FOR NANOFABRICATION

Several problems should be solved in order that this technique be considered viable for nanofabrication applications. Among these are

1. Transfer of the particle array from plasma to substrate.
2. Reduction in particle size to "nano" dimensions.
3. Reduction in inter-particle spacing values less than 1 μm.

Of these the first two are the most important, and, fortunately, these seem well in hand. Although the third problem will be more difficult to solve, an adequate solution is required only for some applications.

4.1 Deposition on the Substrate

After the Coulomb crystal has formed, it must be transferred to a substrate without excessively disturbing the long range order. Transfer can be accomplished in the standard

configuration by simply turning off the plasma and letting the particles fall to the surface. If the particles do not adhere adequately to the surface, they can be "glued" to the surface by coating the surface with a viscous material, or by depositing a suitable thin film over them. Deposited particles can also be used as a mask for a sputtering or reactive-ion etching process carried out *in situ* to create mesa-etched or buried quantum dots in a suitable substrate. For example, Lim *et al.* have demonstrated the creation of 9 nm pillars in silicon using Au clusters as an etching mask[24]. Alternately, if the composition of the particles allows it, the surface can be heated to make the particles react chemically with or diffuse into the surface. Doing so will undoubtedly degrade the size control, but it may still be within tolerable limits for many applications.

We have produced non-agglomerated arrays of particles on a substrate by using a "glue." The construction of the cell (see Fig. 1) is such that the driven electrode is near the bottom, and that the plasma forms above it. The substrate is coated with a suitable sticky substance (partially cured G.E. varnish seems to work well for this purpose) and placed on top of the driven electrode. When the R.F. power is abruptly turned off the particles fall 1–2 mm onto the substrate. The "glue" holds them in place sufficiently well that the substrate can be removed from the chamber, and a more robust fixing method applied to permanently fix them in place.

Besides disorder introduced as the particles fall onto the substrate, the existence of multiple layers in the Coulomb crystal introduces another potential problem. Typically, there are several layers each containing a regimented array, and each layer will fall onto the substrate. If the layers are not well correlated, this will be a second source of disorder in the deposited array. It is found that the layers tend to align themselves such that particles in one layer are directly above the corresponding particle in the layer just below[22, 23]. Because we have looked mostly at Coulomb glasses, we do not have very good information about the effect of multiple layers on the ordering of the deposited particles. Certainly, for good order it would be desirable to employ a technique producing only one layer.

4.2 Particle Size

For most applications particle diameter is a critical parameter. Particle spacing is also relevant, but in many cases it is not critical. In published experiments, particle diameters have typically been 1 to 10 μm. In order for this technique to be applicable to nanoscale structures, the particle diameter must be reduced by more than an order of magnitude, to $\approx$ 100 nm. It appears that the required reduction in particle size should not be difficult. With no special effort, we have formed Coulomb glasses of 300 nm diameter alumina particles, and Boufendi *et al.* report observing strongly coupled particles of about 250 nm diameter in a processing plasma[25].

4.3 Particle Spacing

For many applications, it is desirable to reduce the spacing between particles to a value less than 1 μm. This goal may be more difficult to achieve. The interparticle forces responsible for the bonding of particles to form crystalline structures is not well understood. In most theories, the interparticle spacing is closely related to the Debye length in the plasma,

$$\lambda_D = \left[\frac{q_e^2 n_0}{k\varepsilon_0}\left(\frac{1}{T_e}+\frac{1}{T_i}\right)\right]^{-1/2}$$

where T_e and T_i are the electron and ion temperatures, and n_0 is the plasma density. For a typical, low-power, parallel-plate, R.F. discharge, $n_0 \approx 10^9$ cm^{-3}, $T_e \approx 2$ eV, and $T_i \approx 0.025$ eV, leading to $\lambda_D \approx 40$ μm. The inter-particle spacing in the Coulomb crystals described to date are typically a few times this value.

According to the standard theory of Coulomb crystals, crystallization depends on the parameter Γ, defined as the ratio of the electrostatic energy (Φ) to the thermal translational energy of the particles ($k_B T$). Values of Γ larger than roughly 170 are expected to result in formation of a regular lattice[16]. For a given set of parameters, Φ would be expected to decrease with particle diameter because of reduced charge, and to increase with decreasing lattice constant because of reduced inter-particle separation.

The principal conclusion from our models is that there is a potential minimum. The lattice constant of a Coulomb crystal would be determined by the location of this minimum, and is predicted to be a few times the Debye length. This prediction is consistent with the lattice spacing observed empirically. Theories based on electrostatic repulsion between trapped, charged particles make a similar prediction. The Debye length, λ_D, in turn, is inversely proportional to the square root of the plasma density. For typical parameters in a parallel-plate, capacitive R.F. discharge, the plasma density is 10^9 cm^{-3}, and $\lambda_D \approx 40\mu$m. To obtain smaller lattice constants higher plasma densities are required. We find qualitative verification of this prediction in our experiments. As we increase the R.F. power the particle separation decreases, and *vice versa.* Quantitative measurements are difficult, however, because the relation between R.F. power and plasma density is not simple, and increasing the power also changes other plasma parameters, such as electron temperature.

Continuing along these lines, it appears that to obtain a lattice constant of 1 μm, a plasma density of about 10^{12} cm^{-3} will be required. The upper limit for plasma density in parallel plate reactors is probably about 10^{10} cm^{-3}. Fortunately, there exist other configurations capable of producing densities up to about 10^{13} cm^{-3}. Inductively-coupled plasmas such as barrel and TCP reactors routinely produce densities of 10^{12} cm^{-3}[26], and wave-heated discharges such as ECR and helicon discharges can produce plasma densities up to 10^{14} cm^{-3}[27]. Surface wave discharges routinely produce plasma densities above 10^{11} cm^{-3}, and 10^{15} cm^{-3} has been reported[28]. The neutral density in these high-plasma-density discharges is typically lower (10 mTorr vs. 1 Torr) than in parallel-plate reactors and the neutral temperature is higher (100°–200° vs. 30° C). The higher temperature and lower neutral density may lead to more disordered lattices, but on the other hand the potential energy minimum becomes narrower and deeper as the plasma density increases, which would lead to a more ordered array. Thus, it is not clear *a priori* whether these high-density plasmas will be conducive or detrimental to better ordering.

Kunhardt has reported achieving electron densities of the order of 10^{12} cm^{-3} in an atmospheric-pressure helium discharge[29]. In these discharges a relatively high plasma density is achieved while maintaining a neutral temperature near room temperature. Schoenbach *et al.*[30] and Frame *et al.*[31], also report glow-like discharges in near-atmospheric pressure gases using a somewhat different configuration, but do not report plasma density or neutral temperature. These high-neutral-density discharges appear promising for production of Coulomb crystals. The low neutral temperature, coupled with the high pressure should provide good cooling of the particles, while the high plasma density should provide reduced lattice constant.

5 AN APPLICATION—T_C ENHANCEMENT

The critical temperature, T_C, of a superconductor depends on the electronic density of states. In nanoparticles this density of states can be modified substantially over the bulk form because of wavefunction confinement, with the density becoming peaked around discrete energy values. One effect of this change should be an increase in T_C, relative to bulk material.

In order to test this hypothesis, we have synthesized Coulomb glasses of YBCO with particle diameter less than about 300 nm and transferred them to a silicon substrate. GE varnish was used as the "glue" to stick the particles to the substrate. To our knowledge, this is the first time that a Coulomb glass (or crystal) of a high T_C superconductor has been produced and transferred intact to a substrate. SQUID measurements were carried out to determine the transition temperature T_C in these YBCO quantum dots. The T_C of samples was increased by up to 4–6 K.

6 ACKNOWLEDGEMENTS

We thank J. Betanabhatla for providing us with the YBCO starting material for the T_C experiments, and L. Menon and S. Bandyopadhyay for making the measurements of T_C. We acknowledge helpful conversations with S. Bandyodadhyay, E.E. Kunhardt, and M.J. Kushner. The work was supported by the Nebraska Research Initiative.

References

[1] D. S. Chemla, D. A. B. Miller, and P. W. Smith, in R. Dingle, ed., *Semiconductors and Semimetals* (Academic Press, 1987), pp. 279–318.

[2] A. J. Shields, M. O'Sullivan, I. Farrer, D. Ritchie, K. Cooper, C. Foden, and M. Pepper, Appl. Phys. Lett. **74**, 735 (1999).

[3] S. Tiwari, F. Rana, H. Hanafi, A. Hartstein, E. F. Crabbè, and K. Chan, Appl. Phys. Lett. **68**, 1377 (1996).

[4] L. Zhuang, L. Guo, and S. Y. Chou, Appl. Phys. Lett. **72**, 1205 (1998).

[5] S. Bandyopadhyay, L. Menon, N. Kouklin, H. Zheng, and D. J. Sellmyer, J. Elec. Mat.: Special Issue on Quantum Dots In Press.

[6] V. P. Roychowdhury, D. B. Janes, and S. Bandyopadhyay, Proc. IEEE **85**, 574 (1997), and references therein.

[7] S. Bandyopadhyay, A. Balandin, V. Roychowdhury, and F. Vatan, Superlat. Mictrostruct. **23**, 445 (1998).

[8] E. Barsella, S. Botti, M. Cremona, S. Martelli, R. Montereali, and A. Nesterenko, J. Mat. Sci. Lett. **16**, 221 (1997).

[9] G. Morfill and H. Thomas, J. Vac. Sci. Technol. A **14**, 490 (1996).

[10] V. Fortov, A. Nefedov, V. Torchinskii, V. Molotkov, A. Khrapak, O. Petrov, and K. Volykhin, JETP Lett. **64**, 92 (1996), [Pis'ma Zh. Èksp. Teor. Fiz. **64**, 86-91 (1996)].

[11] V. Fortov, A. Nefedov, O. Petrov, A. Samarian, A. CHernyschev, and A. Lipaev, JETP Lett. **63**, 187 (1996), [Pis'ma Zh. Èksp. Teor. Fiz. **63**, 176-180 (1996)].

[12] I. Waki, S. Kassner, G. Birkl, and H. Walther, Phys. Rev. Lett. **68**, 2007 (1992).

[13] C. Murray and D. V. Winkle, Phys. Rev. Lett. **58**, 1200 (1987).

[14] M. Rosenberg and D. Mendis, IEEE Trans. Plasma Sci. **23**, 177 (1995).

[15] J. Chu and L. I, Physica A **205**, 183 (1994).

[16] H. Ikezi, Phys. Fluids **29**, 1764 (1986).

[17] M. Lieberman and A. Lichtenberg, *Principles of Plasma Discharges and Materials Processing* (Wiley, 1994), pp. 40–42.

[18] J. Daugherty, R. Porteous, M. Kilgore, and D. Graves, J. Appl. Phys. **72**, 3934 (1992).

[19] K. Watson, Phys. Rev **102**, 12 (1956).

[20] K. Brueckner and K. Watson, Phys. Rev. **102**, 19 (1956).

[21] Y.-P. Chen, H. Luo, M.-F. Ye, and M. Yu, Phys. of Plasmas **6**, 699 (1999).

[22] Y. Hayashi and K. Tachibana, Jpn. J. Appl. Phys. **33**, L804 (1994).

[23] J. Pieper, J. Goree, and R. Quinn, J. Vac. Sci. Technol. A **14**, 519 (1996).

[24] S. Lim, Y. Shimogaki, Y. Nakano, K. Tada, and H. Komiyama, Appl. Phys. Lett. **68**, 832 (1996).

[25] L. Boufendi, A. Bouchoule, R. Porteous, J. P. Blondeau, A. Plain, and C. Laure, J. Appl. Phys. **73**, 2160 (1993).

[26] M. Lieberman and A. Lichtenberg, *Principles of Plasma Discharges and Materials Processing* (Wiley, 1994), p. 388.

[27] M. Lieberman and A. Lichtenberg, *Principles of Plasma Discharges and Materials Processing* (Wiley, 1994), p. 434.

[28] J. Margot and M. Moisan, in P. Williams, ed., *Plasma Processing of Semiconductors* (Kluwer, 1996), pp. 187–210.

[29] E. Kunhardt, Unpublished (1998).

[30] K. Schoenbach, R. Verhappen, T. Tessnow, F. Peterkin, and W. Byszewski, Appl. Phys. Lett. **68**, 13 (1996).

[31] J. Frame, D. Wheeler, T. DeTemple, and J. Eden, Appl. Phys. Lett. **71**, 1165 (1997).

SCANNING PHOTOLUMINESCENCE AND ELECTROLUMINESCENCE MICROSCOPY OF SEMICONDUCTOR NANO- AND MICROSTRUCTURES AND DEVICES

M. Zacharias, P. Fischer, J. Christen

Institute of Experimental Physics, Otto- v.- Guericke University, Magdeburg, Germany

H. Nakashima[1], K. Hiramatsu[2], M. Kamp[3]

[1] ISIR, Osaka University, 8-1 Mihogaoka, Ibaraki, Osaka 567, Japan

[2] Dep. of Electrical and Electronic Engineering, Mie University, Mie 514-8507, Japan

[3] Dep. of Optoelectronics, University of Ulm, 89069 Ulm, Germany

ABSTRACT

Highly spatially resolved photoluminescence and electroluminescence imaging experiments are presented. Lateral arrays of selforganized GaAs quantum wires , a cross section prepared thick GaN heteroepitaxial layer and an InGaN/GaN light emitting diode structure are investigated. Wavelength fluctuations along single quantum wires as well as from wire to wire are monitored. Using different excitation wavelengths the carrier transfer and capture processes into the quantum wire are investigated. The second example under investigation is a highly strained GaN layer on sapphire substrate. The thickness dependent influence of strain and defects on the optical properties in heteroepitaxial GaN is discussed. Different recombination channels are monitored by selective PL wavelength imaging. The spatially resolved spectral emission characteristic of an InGaN/GaN UV LED is directly imaged by scanning electroluminescence microscopy as a function of the injected current densities. We will prove that this provides direct access to the optical quality of the device. While for low injection current densities the electroluminescence is dominated by the emission from the p-GaN area, the emission from the InGaN active layer is dominating for higher injection conditions showing a strongly spatial localized characteristic.

INTRODUCTION

Luminescence techniques belong to the most sensitive, non-destructive methods analyzing semiconductor properties. Generally, a luminescence material converts certain types of energy into electromagnetic radiation. Such luminescence process can be exited by many types of energy. Photoluminescence is excited by electromagnetic radiation, cathodoluminescence by an electron beam, electroluminescence by a current through the device structure, X-ray luminescence by X- rays, and so on. For semiconductor materials the luminescence is related to the characteristic band gap and represents either an intrinsic recombination or a recombination involving impurity states. It should be noted that not all recombination results in light emission. Various and efficient non-radiative recombination paths may exist in addition. High efficient luminescence materials are used for a variety of optoelectronic devices, e.g., light emitting diodes (LED) and injected laser diodes.

Conventional photoluminescence (PL) or electroluminescence (EL) spectroscopy uses the excitation of large sample volumes and therefore averages the properties over this volume. This is insignificant for macroscopic homogeneous semiconductor, since the properties observed are the same over the length scale probed. However, the properties vary over a length scale of some μm down to some nm for inhomogeneous semiconductors, low dimensional structures like quantum dots and quantum wires, or device structures. During the last decades there has been a clear trend towards new luminescence materials and *nm* or *μm* sized structures. It is obvious that alternative methods to the conventional, macroscopic way of investigation are required with a sub-μm spatial resolution. In addition it is important to characterize light emitting electronic devices in a non-destructive way under working conditions.

Scanning photoluminescence (PL) and electroluminescence (EL) microscopy allows the direct assignment of morphological and optical properties at the same sample position. A wide range of excitation energies is necessary for different materials and for selective excitation of carriers. The investigation on selected semiconductor

nanostructures and LED devices presented here demonstrate the power of the scanning photoluminescence and electroluminescence microscopy.

A self organized GaAs quantum wire structure grown by gas source molecular beam epitaxy is presented. Although the homogeneity is very high, there are still fluctuations from wire to wire as well as along each single quantum wire. The intensity and wavelength mapping of the GaAs quantum wire sample as well as a sequence of single spot micro- PL spectra are shown. Selective excitation is used to investigate carrier generation and carrier transport.

In addition the cross section investigation of an undoped, 220μm thick hexagonal GaN layer is presented. The GaN layer and sapphire substrate are highly strained. Spatial resolved photoluminescence is used for monitoring the thickness dependent influence of strain and defects on the optical properties in the heteroepitaxial GaN. The strong dependence of the luminescence properties on the distance to the substrate is shown.

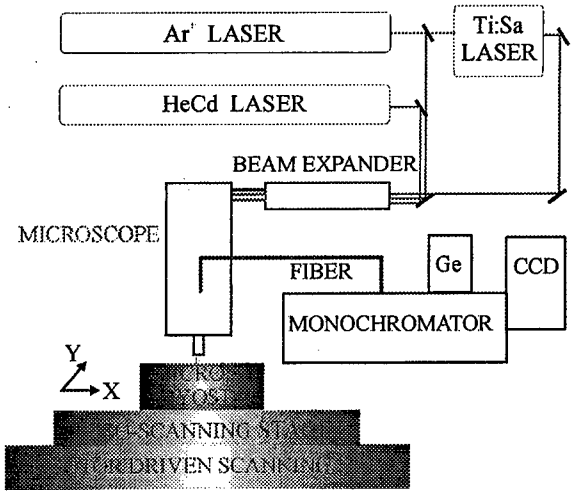


Fig. 1: Experimental setup of the μ-PL/EL system demonstrates the excitation and detection path. Different lasers and detectors are used.

An InGaN/GaN light emitting diode is characterized by scanning electroluminescence microscopy. Lateral inhomogeneities of the LED are directly visualized via micro-

electroluminescence. Fluctuations in intensity and wavelength are imaged as a function of the injected current. The combination of micro-PL and micro-EL probe the relevant properties of the optical active device region under operation and without bias. All deficiencies from either epitaxial growth or device processing are revealed and will be discussed.

EXPERIMENTAL DETAILS

The scanning photo- and electroluminescence system is based on a modified optical microscope using long distance lenses transparent to UV light. The schema of our measurement system can be seen in Fig. 1. The samples are investigated at room temperature or cooled down in a miniaturized continuous flow He cryostat (3.5-325 K). Either the micro cryostat or the room temperature sample holder are mounted on the scanning unit. A high resolution piezo stage is used with a step resolution of 1 nm. In addition, a dc-motor driven scanning stage with a resolution of 250 nm allows the scanning investigation of areas larger than 10 mm x 10 mm. A HeCd laser, an Ar ion laser and a Ti: sapphire laser are used for selective excitation. An overall spatial resolution below 600nm and 1μm is obtained for micro-PL and micro- EL, respectively, under optimized conditions. A complete spectrum is recorded at each sample position (x,y) and stored during the scan over the 128 x 100 spot positions. The luminescence is dispersed using a 0.5 m spectrometer and detected by a liquid nitrogen cooled CCD camera. Fig. 2 demonstrates the different measurement modes of our scanning EL/PL microscopic system. A 3-dimensional data tensor $I(\lambda, x, y)$ is obtained after completing the scan. All types of data cross sections through this tensor subsequently can be generated. Typical examples of such EL or PL data extraction are local spot spectra $I_{EL,PL}(\lambda, x_i, y_i)$ (see Fig. 2 (a, b)), mappings of local

(a) spot mode: $I_{PL}(\lambda)$ ***(b) local spectrum***

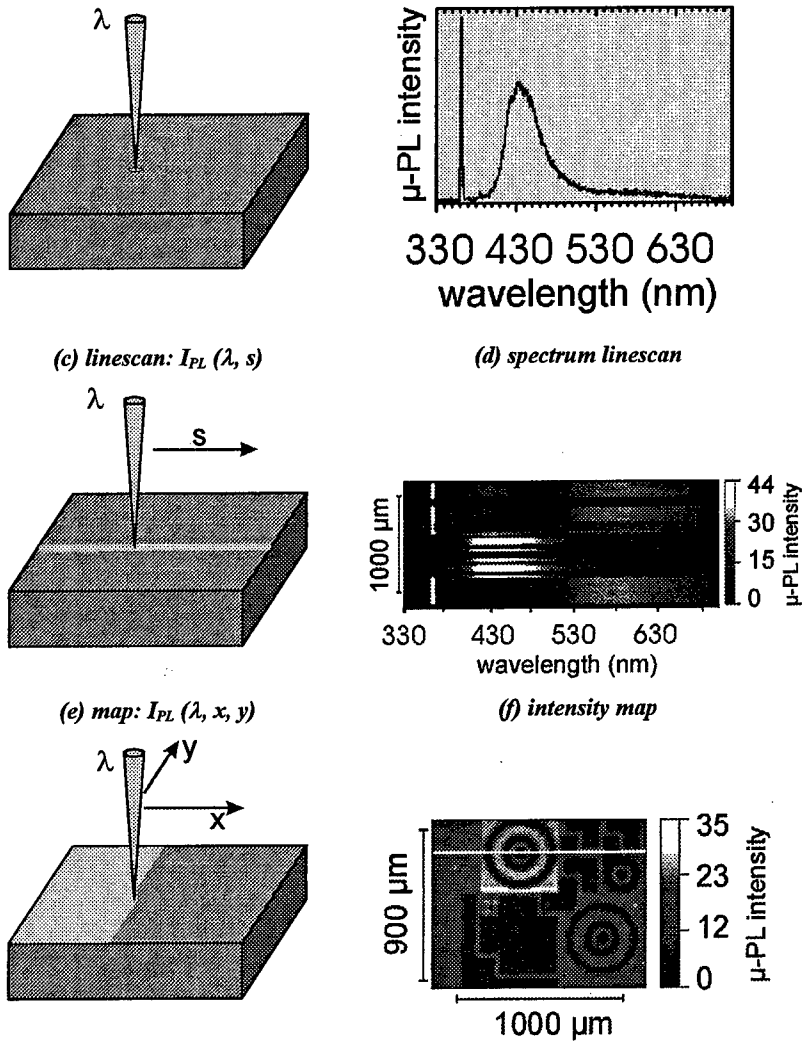


Fig. 2: The different measurement modes of our scanning EL/PL microscopy system

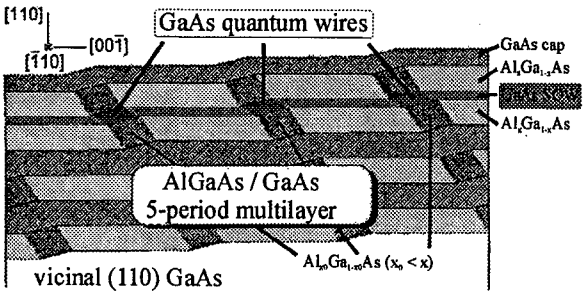
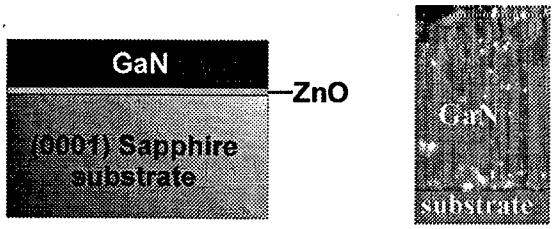
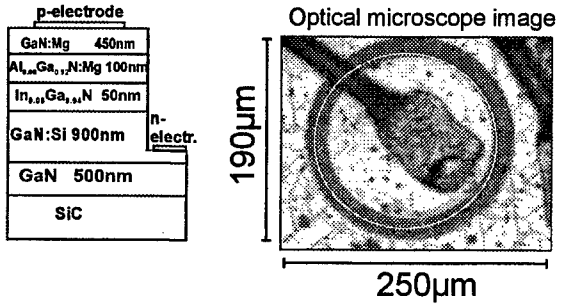


Fig. 2:
(a) Schematic cross section through the GaAs quantum wire sample,



(b) schematic sample structure and optical microscope image of the GaN sample in cross section view,



(c) device structure of the InGaN/GaN UV-LED, and the microscope image of the scanning area.

emission peak wavelength $\lambda_{peak}(x, y)$, spectrum line scans (Fig. 2 (c, d)), and intensity mappings (Fig. 2 (e, f)) etc.

The first sample presented is a self organized GaAs quantum wire structure grown by gas source molecular beam epitaxy on vicinal (110) GaAs tilted 3° towards (111). The

average distance between two adjacent quantum wires is 250 nm. Although the homogeneity is very high and the steps are nearly equidistant, there are still fluctuations from wire to wire as well as along each single quantum wire which are investigated by scanning PL microscopy. For more details about sample growth see [1]. Fig. 3 (a) shows a schematic cross section through the GaAs quantum wire sample.

The second sample is an undoped, 220μm thick hexagonal GaN layer prepared for cross section investigation. A GaN layer is grown on a (0001) sapphire substrate using hydride vapor phase epitaxy with a ZnO buffer layer. Details of the sample growth can be found in [2]. The sample structure and the optical microscope image of the cross section view are demonstrated in Fig. 3 (b).

The third sample selected here is an InGaN/GaN near UV-LED which is grown by low pressure MOVPE in a horizontal reactor on a SiC substrate. The sample structure can be seen in Fig. 3 (c). The mesa structure is defined by photolithography using a conventional photoresist mask and chemical assisted ion-beam etching (CAIBE). A second lithographic step defines the n- and p- contact area. The structure consists of 500 nm GaN, and 900 nm Si- doped GaN followed by an active region of 50 nm InGaN, 100 nm Mg-doped AlGaN with a nominal Al content of ~4 %, and finally covered by 450 nm p-doped GaN. The InGaN layer with an In mole fraction of ~6 % is nominal undoped, the hole concentration of the Mg-doped GaN is ~$2x10^{17}$ cm^{-3}, and the doping concentration of the n-type GaN is approximately $1x10^{18}$ cm^{-3} [3].

RESULTS AND DISCUSSION

The integrated photoluminescence spectrum (Fig. 4) of the GaAs quantum wire sample integrated over the whole scan area (12.8μm x 10μm) shows as well the luminescence of the GaAs layers in the AlGaAs/GaAs multi quantum well at 820 nm as the quantum wire luminescence at 730 nm. In addition, higher energetic peaks are seen around 680 nm. Different excitations are used to investigate the carrier transfer and

carrier capture processes into the quantum wires. The quantum wire luminescence could not be excited with a laser wavelength of 700 nm. Decreasing the excitation wavelength to 620 nm and below (i.e. into the $Al_{0.5}Ga_{0.5}As$ region) results in an increase of the wire luminescence. This gives a direct evidence that most of the carriers are not generated in the quantum wires themselves and in the single quantum well but in the AlGaAs barriers [1].

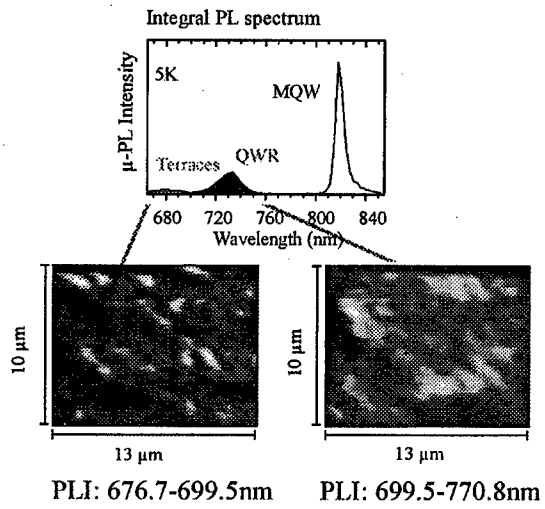


Fig. 4: The upper spectrum presents the integrated photoluminescence spectrum of the scanned area. Below, PL intensity mapping of selective wavelength ranges is shown.

Photoluminescence intensity mapping in selected wavelength regions (quantum wire, higher energetic peaks) is demonstrated in Fig. 4. The quantum wires are self organized during the growth and run from the upper left to the lower right corner of the mapping images. Comparing the images, complementary bright and dark areas are found. If the luminescence intensity in the wavelength range of the quantum wire is high, the PL

intensity in the higher energy peak is low, and vice versa. Obviously, a non zero fraction of the generated carriers recombines at the terraces and is not able to move into the quantum wires. In addition, mapping of the peak wavelength in the chosen wavelength window shows wavelength fluctuations in the quantum wire direction as well as in the perpendicular direction which gives a quantitative mapping of the lateral confinement potential [1]. Local spot spectra were taken at positions of high and low quantum wire PL intensity. The changes in peaks, peak wavelength, and peak intensity from spot to spot are clearly observed. Thickness fluctuations of the quantum wires result in wavelength fluctuations, for more details see [1].

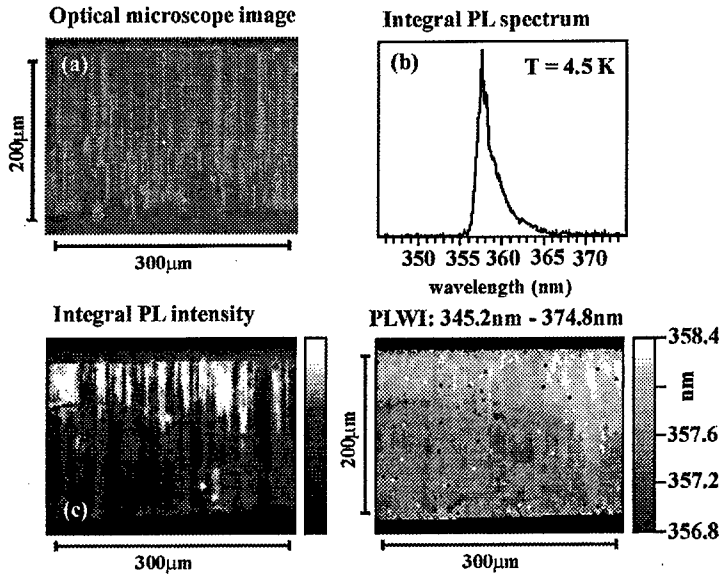


Fig. 5: (a) Optical microscope image of the GaN layer, (b) integral PL spectrum, (c) integral photoluminescence intensity image (PLI), and (d) wavelength image (PLWI).

The cross section investigation of an undoped, 220μm thick hexagonal GaN layer grown on (0001) sapphire with a ZnO buffer layer is presented as second example. GaN

layers on sapphire substrates are highly strained because of the large mismatch of the lattice constants and the differences in thermal expansion. We will focus here on the thickness dependent influence of strain and defects on the optical properties in heteroepitaxial GaN using spatial resolved photoluminescence.

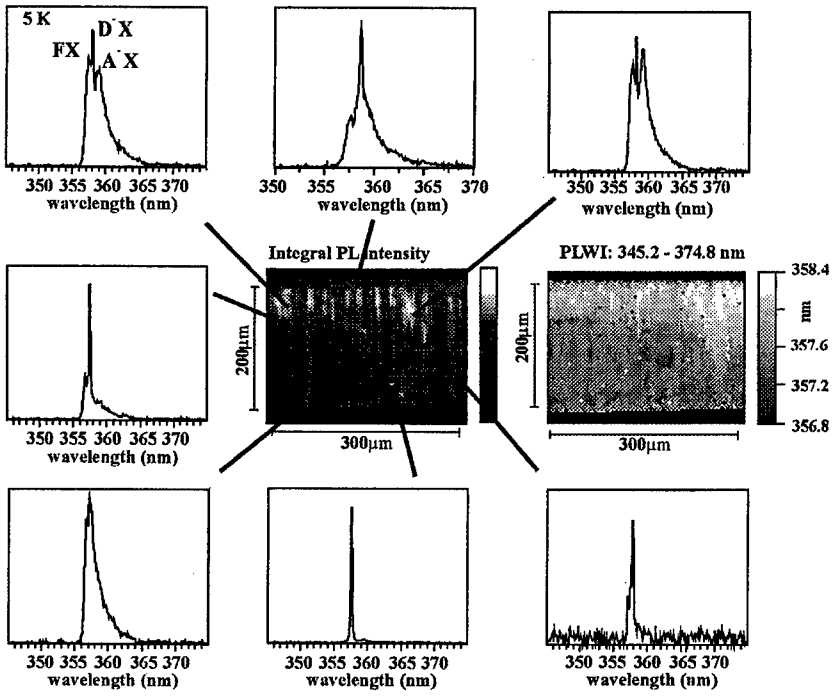


Fig. 6: Local spot spectra are taken at different position of the sample.

Fig. 5 compares the optical microscope image (a) and the integral PL spectrum of the scanned area (b), with the integral photoluminescence intensity mapping and the wavelength mapping. The dark area at the upper border represents the sapphire substrate. Typical recombination channels can be seen in our µ-PL investigations: the free- exciton emission (FX) at 356.5 nm (3.478 eV), the neutral-donor bond exciton

($D^{\circ}X$) at 357.1 nm (3.472 eV), and a weak emission at 359 nm (3.454 eV) due to excitons bond to neutral shallow acceptors ($A^{\circ}X$). The integral PLI (c) shows intensity fluctuations correlated with the columnar microscopic image of the sample. The wavelength image (d) clearly monitors a blue shift of the ($D^{\circ}X$) emission by scanning toward the substrate interface.

Fig. 6 presents single spot spectra taken at various distance from the substrate interface in combination with integral PL intensity mapping and mapping of the peak wavelength. $D^{\circ}X$ and $A^{\circ}X$ dominated spectra are demonstrated. We assume an increased enrichment of impurity into columnar paths leading to the observed luminescence patterns.

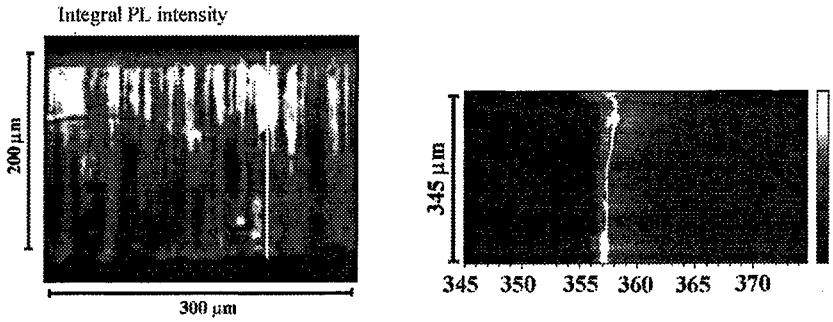


Fig. 7: (a) Integral PL intensity. The white line marks the PL spectrum linescan. (b) PL linescan extracted from the data.

Starting from the sample surface the PL spectrum linescan (Fig. 7 (a, b)) shows a red shift observed for both the free- exciton emission and the neutral- donor bond exciton. Therefore, a change in excitonic recombination, e.g. a exciton bond to a different donor, can be excluded for explanation of the red shift. A possible explanation for the red shift of the excitonic luminescence can be the inhomogeneous free- carrier distribution in the film. Micro- Raman measurements revealed that the free- carrier concentration increases monotonously from some 10^{18} to 10^{19} cm^{-3} [4]. Thus, band gap renormalization induced

by the strong gradient of free- carrier concentration can explain the gradual decrease of band gap [4]. In the vicinity of the substrate interface (last 40 μm) the red shift is compensated by a strong blue shift as result of the increasing compressive strain when approaching the substrate. On the other hand, the concentration of impurity atoms diffused from the ZnO buffer layer into the growing GaN layer decreases with increasing distance to the substrate.

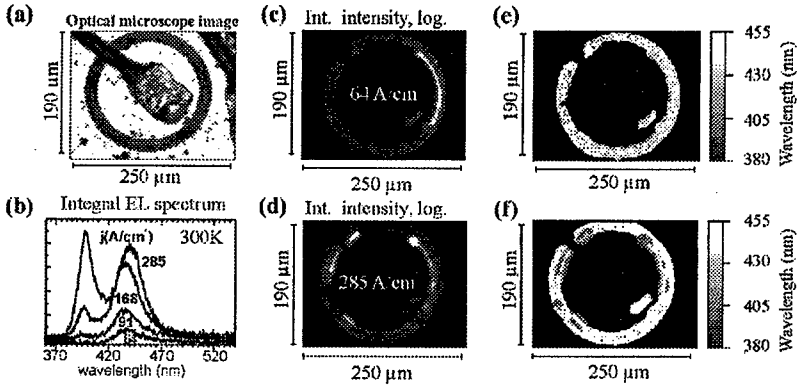


Fig. 8: (a) Microscope image of the scanned area, (b) integrated EL spectra over the whole area as a function of current density, (c) and (d) EL intensity mapping for 64 and 285 A/cm^2, (e) and (f) peak wavelength mapping for the injected current densities of 64 and 285 A/cm^2, respectively.

Finally, the spatial and spectral emission characteristic of an InGaN/GaN double heterostructure light emitting diode (LED) is investigated under operation as a function of the injected current density using electroluminescence microscopy. The optical microscope image of the investigated area is shown in Fig. 8 (a). Fig. 8 (b) compares the integrated EL spectra of different injected current densities. For the low current density of 64 A/cm^2 the electroluminescence of the p- GaN layer at 440 nm dominates the spectrum which represents the typical DAP recombination for this level of Mg doping.

We assume an insufficient carrier confinement in the active region being the reason of the observed 440 nm emission. Both a small In content in the active region and an insufficient Al content in the electron barrier (being lower than nominal designed) may be responsible. With increase of the current density the 400 nm emission from the InGaN active region improves and dominates the spectrum at high current densities. The 400 nm emission is assigned to an In mole fraction of the InGaN layer of around 0.06, in perfect agreement to X-ray diffraction measurements. Increasing the current density from 64 to 91 A/cm^2 a blue shift of around 20 meV is observed related to band filling effects. However, the red shift of the spectra for higher current densities (Fig. 8 (b)) is explained by thermal effects [5].

The intensity distribution becomes more uniform with increasing current densities which is monitored by our logarithmically scaled EL intensity mappings (Fig. 8 (c, d)). We conclude that this is due to the saturation of spatially distributed non- radiative recombination centers. The EL wavelength images are seen in Fig. 8 (e, f). The emission around 420 nm is homogeneously distributed. However, a slight red shift of 20 meV is found due to heating at high current densities. In addition, the InGaN peak at 400 nm emerges with the increased current and shows a localized distribution.

To control the quality of the device it is necessary to separate and identify the recombination channels involved. This can be done by intensity and wavelength mapping of a chosen wavelength interval corresponding to the typical emission range of the channel. Therefore, in Fig. 9 we present the separated EL intensity and wavelength images within the 380-420 nm (InGaN) and the 420-470 nm (p- GaN) range. The inhomogeneity of the typical InGaN EL intensity is visible in Fig. 9 (c). The wavelength image in Fig. 9 (e) directly monitors the In mole fraction fluctuations in the InGaN layer. The observed emission fluctuates in the range of 390 to 410 nm. Assuming band to band recombination and a bowing parameter of 3.2 eV, this corresponds fairly good to In fluctuations from 0.06 to 0.09.

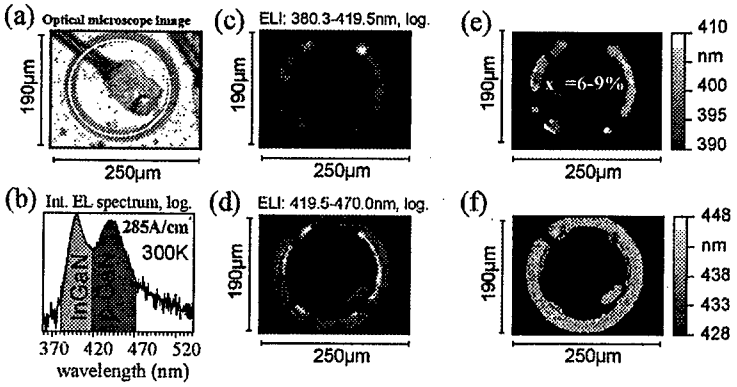


Fig. 9: (a) Microscope image of the investigated area, (b) integral EL spectrum of the LED. (c) and (e) EL intensity and emission wavelength distribution of the InGaN layer, (d) and (f) EL intensity and emission wavelength distribution of the p-GaN layer.

The EL intensity for the p-GaN is inhomogeneous distributed as well (Fig. 9 (d)). However, the emission wavelength of the p-GaN layer is homogeneously distributed over a wide region as can be seen in Fig. 9 (f). It clearly turns out that the inhomogeneity of the InGaN layer quality (rather than the fluctuation in In content) is the limiting parameter of the device quality.

CONCLUSION

In conclusion, the advantages of the scanning photoluminescence and electroluminescence microscopy are demonstrated using investigations on semiconductor nanostructures, microstructures and light emitting devices. The different modes of the investigation are demonstrated. The comprehensive investigation of self-organized GaAs quantum wires , a cross section prepared thick GaN heteroepitaxial layer and an InGaN/GaN light emitting diode structure is presented and discussed.

ACKNOWLEDGEMENTS

Financial support by the Kultusministerium Sachsen- Anhalt and the Deutsche Forschung Gemeinschaft (DFG) are gratefully acknowledged.

REFERENCES

1. P. Fischer, J. Christen, M. Zacharias, H. Nakashima, K. Hiramatsu, Solid state Phenomena 63, 151 (1998).
2. T. Detchprohm, K. Hiramatsu, H. Amano, I. Akasaki, Appl. Phys. Lett. 61, 2688 (1992)
3. P. Fischer, J. Christen, M. Zacharias, V. Schwengler, Ch. Kirchner, M. Kamp, submitted.
4. H. Siegle, A. Hoffmann, L. Eckey, C. Thomsen, J. Christen, F. Bertram, M. Schmidt, D. Rudloff, K. Hiramatsu, Appl. Phys. Lett. 71, 2490 (1997).
5. A. Link, K. Bitzer, W. Limmer, R. Sauer, K. Kirchner, V. Schwengler, M. Kamp, D. Ebeling, submitted.

ELECTRON RESPONSE TO ULTRASHORT LASER PULSES IN SEMICONDUCTOR AND METAL NANOPARTICLES: Ge vs. Ga

A. Stella, P. Tognini
INFM - Dipartimento di Fisica "A. Volta", Università di Pavia,
Via Bassi 6, I-27100 Pavia, Italy

S. De Silvestri, M. Nisoli, S. Stagira
INFM - Centro di Elettronica Quantistica e Strumentazione Elettronica - CNR,
Dipartimento di Fisica, Politecnico, Milano, Italy

P. Cheyssac, R. Kofman
Laboratoire de Physique de la Matière Condensée, UMR 6622,
Université de Nice-Sophia Antipolis, 06108 Nice Cedex 2, France

We present a study of the electron dynamics in metallic Ga and semiconducting Ge nanoparticles embedded in amorphous dielectric matrix. The particles are grown by an evaporation-condensation self organisation technique, with a low spatial dispersion and a large available size range. Ga has been selected for its low melting point, that allows the investigation of the crystalline solid with no appreciable perturbation on the samples. Ge presents interesting aspects related to the small effective mass of the carriers and the presence of direct and indirect transitions in the optical interval. For what concerns ultrafast optical response on both materials, our interest has been focused on the electron relaxation after the pump pulse, in a timescale between ~1 and ~100 ps. In the case of Ga nanoclusters, the electron relaxation is essentially related to the scattering of the electrons with the phonons and it is very sensitive to the interface metal/dielectric; the ultrafast investigation in Ge quantum dots, through a wide energy range above the gap, appears to be essentially intrinsic and related to the decay paths of the electrons inside the Brillouin zone

INTRODUCTION

Semiconducting and metallic clusters in the nm size range are currently the object of both experimental and theoretical work, motivated by the possibility of tailoring their physical behavior, to a considerable extent, on the basis of size. In this paper the attention will be confined to the study of the electron dynamics in semiconducting Ge and metallic Ga nanoparticles embedded in dielectric matrices.

The samples were prepared by an evaporation condensation self organisation technique (1). Ga or Ge vapor was condensed on a previously evaporated amorphous Al_2O_3 film, and the growth occurred in the liquid state. The nanoparticles were subsequently covered and protected by an additional alumina layer. This technique allows to obtain nanocrystals in a wide size range, a gaussian size dispersion ($\sigma/R<20\%$) and shape of truncated spheres, since Ga and Ge only partially wet alumina. The phase of the Ga nanoparticles has been demonstrated to be β (but also δ, ε may occur) (2). The structural characteristics of the samples investigated are reported in table I. The average size and size distribution of the particles inside the samples have been obtained by means of transmission electron microscopy investigation.

LINEAR SPECTRA

Transmission measurements were performed using a spectrophotometer Varian Cary 5. Concerning Ga, The linear optical spectra of the nanoparticles investigated are reported in fig. 1. The dominant feature is represented by the surface plasmon peak, which is expected to be positioned at about $\frac{\omega_P}{\sqrt{1+2\varepsilon_m}}$ (ω_P is the bulk plasma frequency and ε_m the dielectric constant of the matrix) (3), and has been previously studied (4). Here we show the transmission curves corresponding to the solid phase. From the data reported in fig. 2a and 2b we can see that:

i) there is evidence of a progressive blueshift of the resonance peak position, which becomes relevant for small sizes, i.e. 0.4 eV in the size range 7-30 nm;

ii) the width appears to be considerably large and roughly constant.

Concerning Ge, the dominant features are the absorption peaks corresponding to the E_1, $E_1+\Delta_1$ and E_2 transitions (fig. 3). The former ones are originated from transitions among nearly-parallel bands along the Λ direction in the Brillouin zone (BZ), and are considered to have a partially excitonic origin; the latter one originates in a well defined portion of the BZ around the Chadi-Cohen special point (5).

ULTRAFAST ELECTRON DYNAMICS

Transient transmittivity and reflectivity measurements were performed by using a conventionl pump-probe configuration. The laser system consists of a Ti:sapphire laser with chirped-pulse amplification, which provides pulses of 150-fs duration at 780 nm with energy up to 750 μJ at 1-kHz repetition rate. The experiments were performed at pump and probe wavelength of 390 and 780 nm respectively. The 390-nm pump beam, was obtained by frequency doubling a fraction of the laser beam in a LiB3O5 crystal of 1-mm length. The excitation pulse duration was 180 fs and the energy used in the experiment was 37 nJ. The pump and probe beams were focused onto the sample to focal spots with diameter of ~240 and 100 μm, respectively.

Gallium

The transient transmission changes in the Ga samples at 77K (i.e. when the particles are in the solid phase) are shown in fig. 4 for pump and probe wavelengths at 390 and 780 nm respectively, as a function of probe time delay, for nanoparticles having radii between 5 and 9 nm. The deduced scattering time constants are reported in table II. During the pump pulse a change is induced in the electron energy distribution due to the formation of a low-density nonthermalized highly energetic electron population. The acquired energy is redistributed inside the nanoparticles by electron-electron and electron-phonon (e-p) collisions. The excess thermal energy is then removed by thermal diffusion toward the matrix.

The fact that the ultrafast response shows a similar size dependence, can be ascribed primarily to electron-surface interactions and electron mean free path limitations, which in the physical systems here examined become more important than the electron-phonon coupling mechanism, which is typical of bulk crystals.

The electron relaxation dynamics, which in bulk metal is usually described by electron-phonon coupling models (6), is substantially different in very small metallic nanoparticles. In fact, if the radius R of the nanoparticle is comparable or smaller than the bulk electron mean free path, scattering of the electrons from the surface of the nanoparticle becomes relevant and the electrons oscillate inside the spherical potential well of the particle with a frequency $\nu = v_F/R$ (7), where v_F is the Fermi velocity. In this case the electrons dissipate the excess energy through generation of surface oscillations. In the case of gallium the mean free path at 77 K is of the order of 160 Å (8), i.e. larger than the maximum size of the nanoparticles studied in the present work. Interaction between electrons and surface thus plays a relevant role in the electron relaxation dynamics.

As demonstrated in ref. (9), the electron-surface phonon (*e-sp*) coupling constant α, which allows to calculate the time evolution of the electron and lattice temperatures, in small metallic particles can be derived in the framework of a quantum-kinetic treatment (10).

By using the calculated values of α it is possible to calculate the time evolution of the effective electron and lattice temperatures after laser excitation. The obtained values of

the time constant τ_{th} of the T-evolution (i.e. time over which the normalized transient trasmittivity curve decays to 1/e of its initial value) are reported in Tab.II. Such time constants turn out to be in very good agreement with the measured ones. It is worth pointing out that the size-dependence of the electron relaxation time constant is entirely to be ascribed to the size-dependence of the *e-sp* coupling constant. In fact the calculated variations in the time constant values caused by the different energy absorbed by the three samples are negligible. The results of such a comparison between experimental data and theoretical predictions represent a clear indication that in small metallic nanoparticles the interaction between electrons and surface modes is the dominant effect in electron-lattice energy exchange.

Germanium

The $\Delta T/T$ spectra of the two Ge samples at room temperature are shown in Fig. 5 for different pump-probe delays τ_D. The spectra at τ_D=0 are dominated by a prominent bleaching ($\Delta T>0$) with a maximum at ~480 and ~490 nm in Ge4 and Ge16 respectively, which corresponds to the position of the $E_1 + \Delta_1$ spectral structure. In both samples the bleaching band completely disappears in about 1 ps. At longer delays the spectra of both samples are dominated by a broad photoinduced absorption (PA) band with a maximum at ~610 nm. The formation of the PA band is nearly completed at τ_D=4 ps. A similar time evolution was observed for Ge16 at the same probe wavelength as well.

The dominant absorption mechanism is given by single-photon interband transitions near the Γ point of the Brillouin zone. The electrons initially created in the Γ valley scatter into the L valley in about a hundred fs (11) and thermalize with the lattice (12). The temporal evolution of the spectra in Fig. 5 can be separated in a faster and a slower regime (13). The faster regime, associated to the bleaching, is caused by the electron population created by the pump pulse which partially fills the conduction band along the Λ direction during its decay towards the L minimum. When the electrons reach the bottom of the band a large part of the conduction states is empty and the transition probability recovers its unperturbed-like character. The slower regime, characterized by a minimum at about 600 nm in the $\Delta T/T$ curves vs. wavelength, decays in some hundreds of ps. The mechanism which produces such a spectral feature is given by the population-induced band gap renormalization (BGR) (13,14). BGR, in our case, is caused by the electronic population of the conduction band in the Λ direction and is conserved after the relaxation towards the minimum since it depends on the density of carriers rather than on their position in the band.

In order to evaluate the transmittance changes related to these effects, we have calculated their influence on the dielectric function of the "effective medium" composed by Ge nanoparticles + matrix. The bleaching has been evaluated from the variation of the electron population in the conduction band (CB) (curve reported as open squares in Fig. 6). The population induced BGR ΔE (15) has been calculated to be of the order of few meV. Its influence on the dielectric function can be evaluated using the expression $\Delta\varepsilon_{1,2} = \frac{\partial\varepsilon_{1,2}}{\partial E}\Delta E$ (16). The change in the dielectric function of Ge has been introduced in

the effective medium formulation to obtain the variation in the dielectric function of the composite medium, and consequently the $\Delta T/T$ reported in Fig. 6 (triangles). The composition of the two effects is the continuous line in the same figure. The spectral behavior presents a good agreement with the experiment reported in Fig. 5.

CONCLUSIONS

For what concerns Ga, the experimental data have been interpreted in terms of an electron-surface interaction model, with no need of introducing additional effects of any kind from the matrix on the thermalization processes. These results bring new information on the role of the energy exchange with surface-phonons in the electronic thermalization process occuring in confined metallic structures.

The investigation of ultrafast carrier dynamics in Ge nanoparticles has given evidence of two regimes of the response, both amenable to the electronic energy level distribution in the conduction band. Both bleaching and band gap renormalization are attributed to the dynamics of a population of carriers in the conduction band along the Λ direction. The response is clearly intrinsic and related to a bulk-like band structure, where quantum confinement effects in the ultrafast response can be deduced from the blueshift of the $E_1 + \Delta_1$ spectral structure.

REFERENCES

1. E. Sondergard, R. Kofman, P. Cheyssac, A. Stella, Surf. Sci. 364, 467 (1996).
2. A. Di Cicco, Phys. Rev. Lett. 81, 2942 (1998).
3. The experimental peak positions have been found at energies lower than those calculated using this simple formula, since the matrix is not completely transparent. See ref. (4).
4. P. Tognini, A. Stella, P. Cheyssac and R. Kofman, Journal of Non-Crystalline Solids (in press, 1999).
5. M.L. Cohen, J.R. Chelikowsky, Electronic Structure and Optical Properties of Semiconductors (Springer-Verlag, Berlin, 1988).
6. H. E. Elsayed-Ali, T. B. Norris, M. A. Pessot, and G. A. Mourou, Phys. Rev. Lett. 58, 1212 (1987).
7. U. Kreibig and C. V. Fragstein, Z. Physik 224, 307 (1969).
8. N. W. Ashcroft and N. D. Mermin, Solid State Physics (Holt-Saunders, Orlando, 1976).
9. M. Nisoli, S. Stagira, S. De Silvestri, A. Stella, P. Tognini, P. Cheyssac, R. Kofman, Phys. Rev. Lett. 78, 3575 (1997).
10. E. D. Belotskii and P.M. Tomchuk, Int. J. Electronics 73, 955 (1992).
11. S. Zollner, K.D. Myers, K.G. Jensen, J.M. Dolan, D.W. Bailey, C.J. Stanton, Sol. St. Comm. 104, 51 (1997).
12. A. Othonos, H.M. van Driel, J.F. Young, P.J. Kelly, Phys. Rev. B 43, 6682 (1991).
13. P. Tognini, A. Stella, S. De Silvestri, M. Nisoli, S. Stagira, P. Cheyssac, R. Kofman, Appl. Phys. Lett. (in press, 1999).

14. R. Haight, M. Baeumler, Phys. Rev. B 46, 1543 (1992).
15. R. Zimmermann, Phys. Stat. Sol. (b) 146, 371 (1988).
16. H.R. Choo, X.F. Hu, M.C. Downer, V.P. Kesan, Appl. Phys. Lett. 63, 1507 (1993).

TABLES

Table I: structural characteristics of the samples investigated (substrate: sapphire 1 mm thick). Equivalent thickness: the thickness of a film containing the same volume of material.

Sample	Equivalent layer thickness (nm)	Average radius (nm)
Ga2	2	5
Ga3	3	7
Ga4	4	9
Ga5	5	13
Ga10	10	21.5
Ga15	15	30.5
Ge4	1.7	4
Ge16	8	16

Table II: values of the time constants τ obtained from the fitting of transient transmittivity measurements in the investigated Ga samples and corresponding values τ_{th} evaluated by the model described.

Sample	t (fs)	t_{th} (fs)
Ga2	650±30	630
Ga3	1000±50	1030
Ga4	1500±70	1450

FIGURES

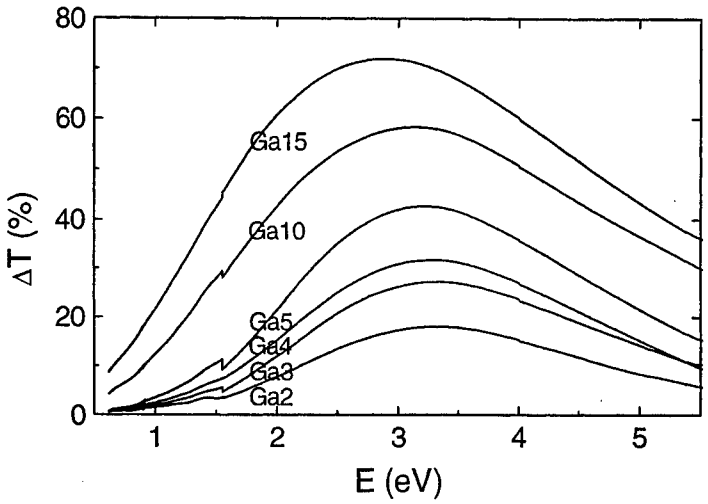


Figure 1: Transmittance difference between a sample without nanoparticles and the samples investigated.

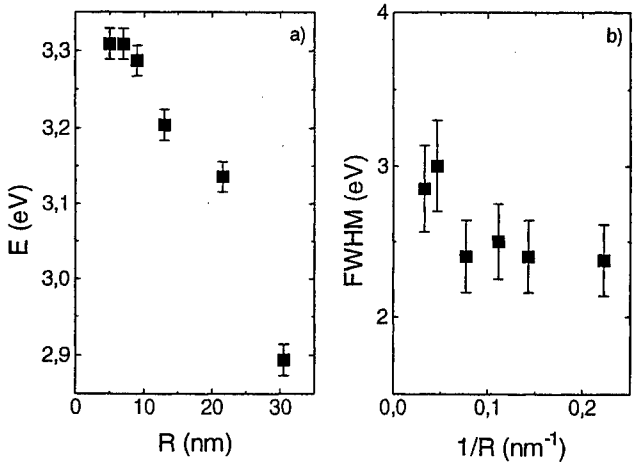


Figure 2: a) Energy peak position and b) full width half maximum (FWHM) of the plasma resonances reported in fig. 1

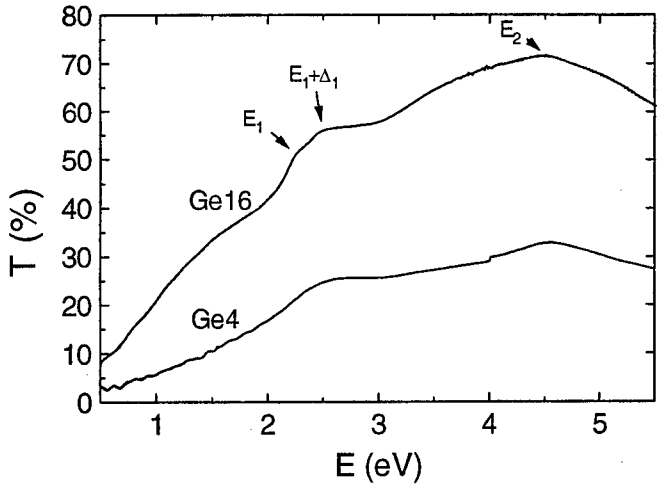


Figure 3: Transmittance difference between a sample without nanoparticles and the samples investigated.

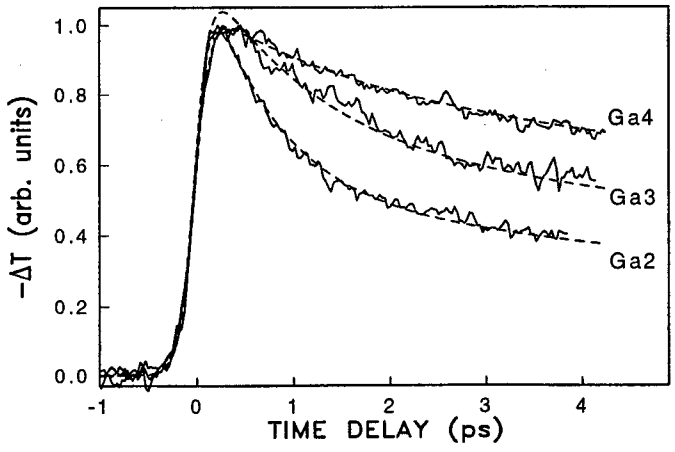


Figure 4: Transient transmittivity changes in Ga nanoparticles in the solid phase, as a function of the probe time delay. The dashed lines are the fitting curves.

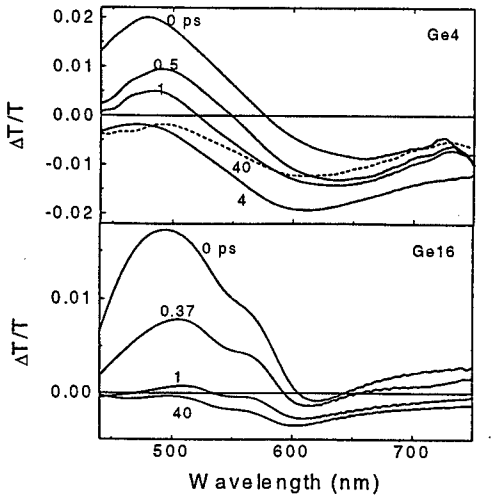


Figure 5: Differential transmission spectra of Ge4 and Ge16 for various pump-probe delays.

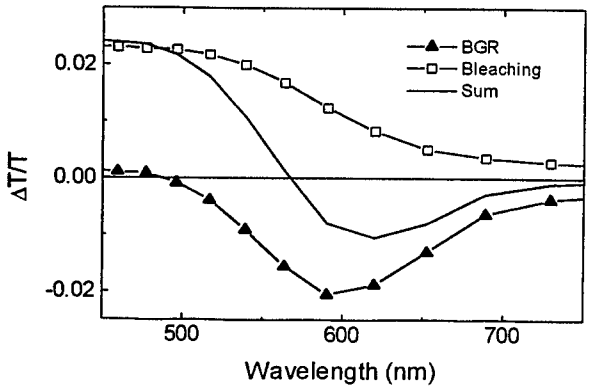


Figure 6: Open squares: contribution of the conduction band filling along the Λ direction to the ΔT/T; triangles: contribution of the BGR; continuous line: sum of the two effects.

ABSORBANCE AND PHOTOLUMINESENCE OF Si, Ge, AND MoS_2 NANOPARTICLES STUDIED BY LIQUID CHROMATOGRAPHY.

J.P. Wilcoxon, G.A. Samara, and P.P. Provencio
Nanostructures and Advanced Materials Chemistry, Dept 1152
Sandia National Laboratories
Albuquerque, NM 87185-1421
USA

ABSTRACT

We have successfully synthesized highly crystalline, size-selected indirect band-gap nanocrystals (NC) of Si, Ge and MoS_2 in the size range 2-10 nm in inverse micelles and studied their optical absorption and photoluminescence (PL) properties using liquid chromatography. Room temperature, visible PL from these nanocrystals was demonstrated in the range 700-350 nm (1.8 - 3.5 eV). Our experimental results are interpreted in terms of the corresponding electronic structure of the bulk materials and it is demonstrated that these nanocrystals retain bulk-like electronic character to sizes as small as 2 nm, but the absorbance energies are strongly blue-shifted by quantum confinement. Our experimental results on Si-NCs are also compared to earlier work on Si clusters grown by other techniques and to the predictions of various model calculations. Currently, the wide variations in the theoretical predictions of the various models along with considerable uncertainties in experimental size determination for clusters less than 3-4 nm, make it difficult to select the best model.

INTRODUCTION AND MOTIVATION

Silicon (Si) possesses many outstanding properties and for numerous reasons is the semiconductor of choice for the microelectronics industry. These properties include silicon's simple elemental nature, high purity, high mechanical strength, and ease and control of oxidation, doping and processability. Along with advances in microminiaturization, these properties are responsible for the high level of functional integration and cost reduction of microelectronic chips. Despite its almost exclusive position in microelectronics today, however, Si has a major drawback as a semiconductor: its inability to emit light efficiently, and, furthermore, its weak emission is in the near IR. This limitation poses a serious obstacle to the next major phase of large-scale integration, namely optoelectronic/micro-electronic integration, and excludes Si from a broad range of optoelectronic applications.

Silicon's inability to emit light efficiently derives from the fact that it is an indirect bandgap semiconductor, and its luminescence is thus electron dipole forbidden. This is an intrinsic feature related to silicon's crystal structure and the bonding/antibonding character and hybridization of its electronic orbitals. There is presently a very large research effort aimed at exploring physical and chemical means to break silicon's lattice symmetry and mix different momentum (k) states in order to induce a useful level of luminescence and optical gain. The approaches include:[1] (1) impurity-induced luminescence (e.g., S, B, Be, Er), (2) alloy-induced luminescence (e.g., Si-Ge-C), (3) porous silicon, and (4) quantum wires and dots (or nano-size clusters). The first two of these approaches are plagued by, among other things, relatively low luminescence intensity at low temperature which becomes vanishingly weak at room temperature, whereas the last two, which may be mechanistically related via quantum confinement, have considerable potential but have remained largely uncontrolled and poorly understood. Success in this endeavor is obviously a major challenge to materials science, one that could have profound implications for optoelectronics and many other potential applications.

Because visible photoluminescence (PL) has been observed from Si nanoclusters[2], these clusters and their potential are a subject of great current interest. Si nanoclusters have

been produced by aerosol techniques, spark ablation, and grown in glass matrices by a variety of approaches including ion implantation followed by high temperature annealing; however, all of these techniques produce a large distribution of cluster sizes resulting in very broad optical absorption and PL features which limit usefulness and make definitive interpretation in terms of quantum confinement and other mechanisms very difficult.
Germanium (Ge) is another important indirect gap semiconductor whose energy gap is considerably smaller than that of Si (~ 0.7 vs. 1.1 eV). Ge clusters can be expected to have very interesting and useful optical properties in the visible and near IR. There is evidence for visible light emission from Ge clusters grown in glass matrices and other media, but even less is known about these clusters than about Si clusters, and the few available results are plagued by a broad distribution of cluster sizes.

To understand the origin of visible PL in Si and Ge nanoclusters, it is necessary to study size-selected nanoclusters and to assess the role of surface recombination. Definitive experimental results will be key to future progress and practical utilization of these exciting materials. From a physics perspective such studies should lead to a better understanding of quantum confinement of electrons and holes in indirect bandgap semiconductors. Quantum confinement in direct gap semiconductors such as GaAs and CdSe is fairly well understood, but little is known about confinement in indirect gap materials.[2] The bulk excitonic radius for Si is ~ 4 nm and that for Ge is ~ 11 nm which suggests that quantum confinement effects should be observed for nanocrystals smaller than these sizes.

MoS_2 is an indirect gap material with a graphite-like layered structure which enbues it with outstanding stability against oxidation. Its principal uses are as a fuel refining hydrodesulfurization catalyst and a high temperature solid phase lubricant. It is also a near-IR absorbing indirect bandgap semiconductor and our interest in this material is as a photocatalyst for photo-redox reactions to oxidize organic chemicals (i.e. solar detoxification).[7] Nanosize clusters of MoS_2 possess size-dependent optical and electronic properties which allow one to adjust its light absorbance and the efficiency of hole-electron pair (exciton) creation. The large surface area of nanoclusters facilitates efficient electron transfer to a molecule in solution (reduction) and/or hole oxidation of another species also in solution. For efficient electron and/or hole transfer, the valence and conduction band levels must match those of the target molecules in solution. This is a formidable task if one has only bulk materials to work with. For example, TiO_2 has the ability to oxidize and reduce a wide range of molecules because of its wide bandgap, but its ability to absorb sunlight is also very small. An additional problem is that, for typical powders of TiO_2, bulk recombination of the hole-electron pair and light emission is vastly favored over the transport of the hole and the electron to the surface where they can be transferred to a solution species.

We have developed and patented a synthesis method based on using inverse micelles as reaction vessels[3] to produce useful quantities of size-selected clusters and have used this method to synthesize a variety of metal and compound semiconductor clusters.[4-6] The overall objective of the present work was to apply our inverse micellar synthesis method to produce nearly monodisperse Si, Ge, and MoS_2 nanoclusters, and to study and under

Synthesis and Characterization

A. Synthesis

Size-selected nanosize Si, Ge, and MoS_2 clusters were grown by a generic process which is described in detail elsewhere.[3-5,8] Controlled nucleation and growth of the nanoclusters occurs in the interior of nanosize surfactant aggregates called inverse micelles. In our process an anhyrous ionic salt (e.g., MX_4, where M=Si, Ge, or Mo X = Cl, Br, or I) is dissolved in the hydrophilic interior of a solution of micelles. The basic idea is that since the ionic salts used are completely insoluble in the continuous oil medium used (e.g. octane), nucleation and growth of Si is restricted to the micelle interior. The interior

volume of micelles can be varied over the range of 1-10 nm. We emphasize that the anhydrous salt is dissolved to form a transparent ionic solution but with a complete absence of water; in a sense the salt is "hydrated" by the micelle. The absence of water prevents simple hydrolysis to form MO_2, which is why this synthesis must be performed in water-free oils like octane or decane, and using a controlled atmosphere glove box. Once the metal halide salts are solubilized in the inverse micelles, the formerly clear inverse micelle solution takes on the color of the salt (clear for the Cl salts, light yellow for the Br and I types). This transparent precursor solution has distinct absorbance peaks much as do charge transfer complexes of other metal salts (e.g. $CoCl_2$) in water.

We next reduce M(IV) to M(0) using an anhydrous metal hydride, (usually 1M $LiAlH_4$ in THF). The reduction is rapid with vigorous bubbling as H_2 gas is released, electrons are transferred to the M(IV) and the light yellow solution turns clear (for d=1.5 nm) to dark yellow-brown (d=8-10 nm). To make molybdenum disulfide, H_2S is introduced into the reactor. One can determine the correct stoichiometry of the reaction by following the disappearance of the M(IV) absorbance peaks from the precursor solution. Generally we find that for complete reduction we need to use a 2-fold excess of the $LiAlH_4$ reducing agent. Alternatively, it is possible to effect a 4-electron transfer reaction to M(IV) using alkaline N_2H_4, but there is a possibility of competing hydrolysis to MO_2, because of the presence of water. Our experience is that this hydrolysis is actually slower than the reduction, however, so either reducing agent is acceptable.

Since there is no source of oxygen in the reaction mixture, and anhydrous metal hydrides are used as reducing agents, it is possible that the Si or Ge cluster surface is terminated by hydrogen from the metal hydride, although we currently have no direct proof of this. When kept in the glove box under Ar, there appears to be no long term (i.e. 6 month to 1 year) degradation of the Si or Ge nanoclusters. However, upon exposure to oxygen, a yellowing of the solution occurs which, sometimes over a period of weeks, leads to an observable precipitate. It is possible that oxidation of the surface renders the nanocluster surface hydrophilic, and since the clusters are in a solution of very hydrophobic oils, they simply lose their solubility. A hydrogen terminated Si surface, on the other hand, is hydrophobic and likely more stable in the oil.

B. Chromatography

HPLC separation and elution peak spectral data were obtained using two apparatii; (1) a HP model 1050 HPLC system, with automated fraction collection, complete solvent purging, and three sequential detectors, a photodiode array spectrometer (for absorbance measurements between 180 and 600 nm), a PL detector (with selectable excitation wavelength and full scanning capability between 200 and 800 nm), and a refractive index detector; (2) a Waters HPLC system with a photodiode array spectrometer with a range of 190-800 nm, a conductance detector, and a refractive index detector. The fraction collector developed by us allowed fractions to be collected without exposure to air or moisture. It consists of a programmable microvalve and small teflon solvent lines which are filled with Ar-purged solvent up to a needle which penetrates a septum on a collection vial filled with Ar. Under computer control, the valve switches from the waste position to the sample position (up to six fractions are possible), at the time interval corresponding to the elution of the desired nanocluster fraction. Since the sample is extracted from sealed, crimp-type, sampling vials filled in the glove box, the complete HPLC operation and/or fraction collection can be both moisture- and air-free. In additon, the versatility of our fraction collection scheme allows samples to be collected in septum-sealed quartz cuvettes filled with Argon and subsequently studied with conventional fluoresence and UV-visible spectrophotometers.

Previous HPLC experiments on Si/SiO_2 nanoclusters synthesized in the gas phase showed a broad range of elution times[2,10] which is in contrast with our results where the Si peak is of comparable width to that from the other molecular constituents of the solution. Figure 1 shows an example of using chemical affinity chromatography to separate nanosize Si from other chemicals in the reaction bath. The clusters were stabilized with octylamine.

The excess (i.e. unbound) octylamine separates from the clusters as do the surfactant and solvent used in the synthesis, leaving the clusters dispersed in anhydrous acetonitrile (ACN). The complete absorbance spectrum of the clusters and the PL could also be collected during the chromatography and will be shown later. We note that the elution peak width of these Si nanoclusters (size = 2.2 nm) is comparable to the completely monodisperse chemical octylamine, showing very little size dispersion.

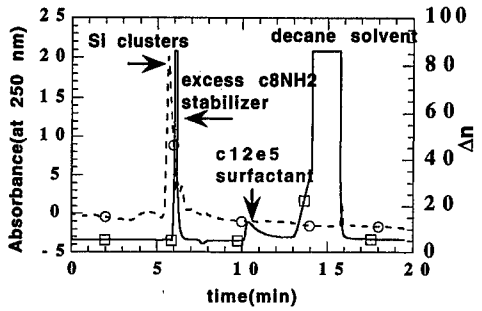


Figure 1. Coplot of the absorbance at 250 nm (dashed curve/open circles) and the refractive index Δn (solid curve/open squares) vs. elution time for Si nanoclusters.

There are three valuable features of HPLC which helped us determine optimal synthesis conditions. 1) Any unreacted salt elutes as a separate peak (usually at the same time as the surfactant), 2) any charged species (e.g. salt, ionic surfactants) can be identified by using an on-line conductivity meter, and 3) nanoclusters of different sizes can be separated and their optical properties determined on-line, without exposure to oxygen. The second feature of HPLC analysis is illustrated in Fig. 2 by the separation of Si clusters made using a charged cationic surfactant. We observed that the ionic byproducts of the reaction and the ionic surfactant are separated in time from the small neutral Si nanoclusters.[6]

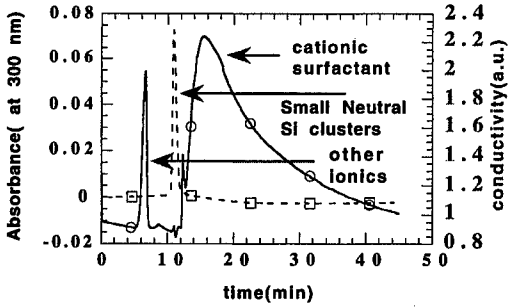


Figure 2. Coplot of the Absorbance (dashed curve/open squares) at 300 nm and the Conductivity (solid curve,open circles) of Si nanoclusters vs. elution time.

Finally, we illustrate separation of two sizes of Si nanoclusters in Fig 3. Using the PL detector we can identify which size of cluster has significant room temperature PL, and also make sure that no impurity organic chemicals could be giving rise to the PL signal. In both cases only the absorbance peak corresponding to the more numerous population of small, 2.0 nm clusters coincides with a strong visible PL signal. We also obtained the complete absorbance and PL wavelength dependences for each size Si nanoclusters as will be shown in Sec. III. Inductively coupled plasma/mass spectoscopy (ICP-MS) of the collected Si fractions showed that nearly 80% of the total Si was recovered by HPLC, and

the only inorganic detected was Si. Gas chromatography/mass spectroscopy (GC/MS) showed the only significant organic chemical in the collected fractions was the mobile phase solvent (i.e. the fractions had been chemically purified as desired). In particular, no surfactant was detected.

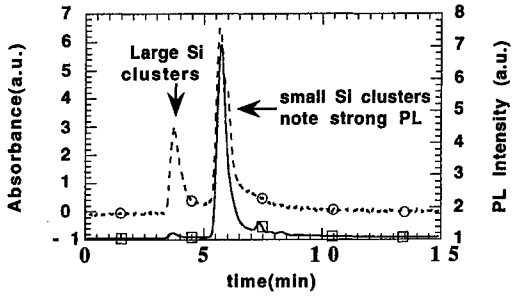


Figure 3. Coplot of the Absorbance at 300 nm (dashed curve) and PL Intensity at 450 nm (solid curve), vs. elution time for a sample with two sizes of Si nanoclusters.

C. Other Characterization

In addition to the on-line HPLC optical and size characterization discussed above, we used x-ray diffraction (XRD), selected area electron diffraction (SAD), and high-resolution transmission electron microscopy (HRTEM) to examine the Si nanoclusters. HRTEM lattice fringe images of d=2 nm and d=8-10 nm Si clusters shown in Fig. 4 reveal the high crystalline quality of these clusters. Since the contrast between the Si and the amorphous holey carbon grid on which the clusters are deposited from solution is low, there is ~10% uncertainty in determining the edges (size) of the clusters (this is only one lattice plane in the case of the smallest clusters).

The largest clusters (d=8-10 nm) were collected as a powder after HPLC purification and subjected to XRD analysis. The diffraction lines are identical to those of bulk Si . Interestingly, no oxide diffraction peaks were observed, though it was not possible to exclude air during the XRD measurement. The SAD reflections shown in figure 4 on these clusters were also the same as the bulk, though broadened by the finite crystallite size.

Although the above presentation on chromatography and other characterization has emphasized results on Si, similar results have been obtained on Ge and MoS_2.

Si RESULTS AND DISCUSSION

1. Optical Absorption

In order to better understand the optical absorption spectra of Si clusters, it is instructive to review briefly the main features of the spectrum of bulk Si.[9] These features, reflect the details of the band structure' The long absorption tail between 1.2 and ~ 3 eV reflects the indirect nature of the bandgap. The sharp rise in absorption with increasing photon energy starting around 3.2 eV (380 nm) is associated with the direct transition at the , Γ point [$\Gamma_{25} \rightarrow \Gamma_{15}$] whose energy is 3.4 eV (365 nm), and the second sharp rise starting around 4 eV (320 nm) is associated with a second direct transition, most likely the Γ_{25} - $\Gamma_{2'}$ transition whose energy is 4.2 eV (295 nm).

2. Nanocrystal Spectra

The measured optical response (or extinction) of nanocrystals reflects the sum of the scattering and absorption. The scattering needs to be taken into consideration in comparing cluster spectra to that of bulk Si.

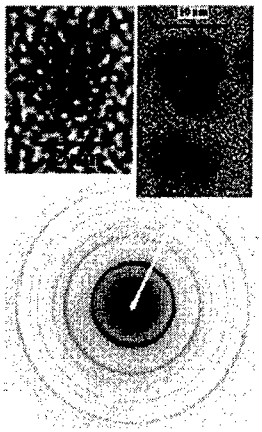


Figure 4. HRTEM of d=2.0 nm, d=8-10 nm, and SAD from a field of d=8.0 nm Si nanoclusters.

Figure 5 shows the extinction spectrum of relatively large (d=10 nm) Si clusters calculated[2,10] from Mie theory and compares it to absorption spectrum of bulk Si. The two spectra are normalized around the absorption shoulder corresponding to the $\Gamma_{25} \rightarrow \Gamma_{15}$ direct transition. One of the obvious differences in the two spectra is the significantly enhanced extinction of the clusters which is due to scattering. Shown also in Fig. 5 are three cluster spectra (also normalized at about the shoulder of the $\Gamma_{25} \rightarrow \Gamma_{15}$ transition), two (d = 10 and 1.8 nm) from the present work and the third (d = 3.7 nm) from Kanemitsu's work.[10] Our d = 10 nm spectrum is from one of our earliest samples that was not purified and size-separated by HPLC, and thus we suspect that it had a relatively broad size distribution. Because of uncertainties in the absolute values of the measured extinction coefficients, the normalization of the nanocrystal spectra in Figure 5 is only approximate and is merely intended to reveal the shape and influence of scattering, leaving the discussion of the details of the cluster spectra until later.

Some of our Si nanocrystal samples exhibited considerable structure in their absorption spectra while others had less structured spectra. The difference is undoubtedly related to the details and subtleties of the synthesis, but the reason is not known at present. Broad distributions of nanocrystal sizes can, of course, smear out spectral features, and impurities and unreacted precursors can be responsible for extrinsic spectral effects. Our HPLC separation procedures should rule out both effects, and, as will be shown, most of the observed features appear to be intrinsic to Si nanocrystals.

Some of our smaller size nanocrystal samples exhibited highly structured absorption spectra. An example is shown in Fig. 6 for a sample with d = 2.0 nm. The figure also shows the bulk Si spectrum for comparison. The two spectra are remarkably similar with that of the nanoclusters shifted to shorter (higher) wavelength (energy). The long absorption tail associated with the indirect bandgap and the two direct transitions ($\Gamma_{25} \rightarrow \Gamma_{15}$ and $\Gamma_{25} \rightarrow \Gamma_{2'}$) are very well defined in the nanocrystal spectrum. The data in Fig. 6 show clear evidence for quantum confinement; specifically, both the $\Gamma_{25} \rightarrow \Gamma_{15}$ and $\Gamma_{25} \rightarrow \Gamma_{2'}$ direct transitions of the nanocrystals are blue-shifted by about 0.4 eV compared

to the bulk. As we shall see below this is a smaller quantum confinement effect than is found for the indirect gap, but it is larger than is predicted by model calculations.

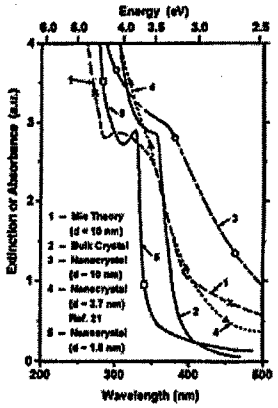


Figure 5. The extinction spectra of several Si nanocrystal samples compared with the absorption spectrum of bulk Si and a Mie theory calculation for d = 10 nm Si taken from the literature.

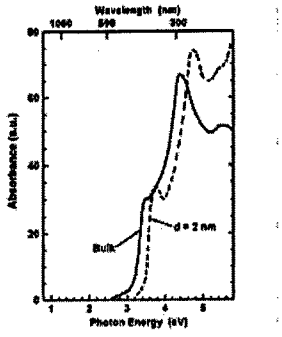


Figure 6. Linear absorbance vs wavelength plots for a d=2 nm Si nanocrystal and bulk Si crystal, showing the similarities of the two spectra.

While substantial, this ~ 0.4 eV blue shift from the bulk for these small Si nanocrystals is considerably smaller than the ~1 eV blue shifts (for about the same size) observed for direct bandgap transitions in II-VI semiconductors, e.g. CdSe. It has been noted[2b] that in CdSe, the quantized s-type conduction-band levels shift monotonically to higher energy with decreasing size because the effective mass is positive in all k-space directions. In Si, on the other hand, the $\Gamma_{25} \rightarrow \Gamma_{15}$ transition is to a p-type conduction band point which is a saddle point in k-space (i.e., it has the opposite curvature from that in CdSe). This transition in Si might then be expected to broaden rather than to shift to higher energy with decreasing size.[2b] In our data we do not see definitive evidence for broadening, but do find a relatively small (compared to CdSe) shift to higher energy.

There is another aspect of the results in Fig. 6 that deserves attention. The Si conduction band at Γ involves two overlapping bands of $p\sigma^*$ states, one with positive and the other with negative dispersion. Quantum size confinement can be expected to influence these

two bands differently resulting in their splitting which in turn might be reflected in the shape of the $\Gamma_{25} \rightarrow \Gamma_{15}$ absorption. While model calculations[12] do indeed predict such splitting, our cluster results in Fig. 6 and for other samples do not show any evidence for this splitting.[8] However, calculations[13] and other experiments[14] on Ge nanocrystals do show evidence for such splitting.

We should also note here that the top of the valence band at Γ is also made up of two $p\sigma^*$ bands which are split by spin-orbit coupling. Model calculations[12] predict an increase in this splitting by quantum confinement, but there is no discernible experimental manifestation of this splitting in the present absorption data.

The absorption data in Figs. 5 and 6 suggest a blue shift of the indirect absorption tail with decreasing nanocrystal size, and the gap appears to remain indirect. The small absorbance values in the tail region along with some uncertainty due to correcting the data for the scattering contribution make detailed analysis of the data in this wavelength region uncertain. However, the quality of the data on several of our samples was sufficiently good to allow meaningful analysis. For an indirect transition the absorption data in the region of the band edge can be described by[18]

$$\alpha h\nu = C(h\nu - E_g)^2, \qquad (1)$$

where α is the absorption coefficient, h is the photon energy, C is a constant and E_g is the bandgap energy. Absorption data on bulk Si can be fit by this relationship,and the intercept of the linear response with the x-axis is the indirect bandgap. Our experiments yield E_g =2.2 eV for 1.8 nm Si nanocrystals.[8] While the uncertainty in this value of E_g may be as large as $\pm$(0.2-0.3) eV because of the afore-mentioned weak absorption of the cluster solutions in the tail region as well as some inaccuracies introduced in correcting for scattering, the result clearly demonstrates a significant quantum confinement effect for the indirect gap of Si. Our result is in close agreement with a recent study by Brus et al[2b] on SiO_2-capped Si nanocrystals. From photoluminescence excitation (PLE) and photoluminescence (PL) measurements on nanoclusters estimated to have a Si core diameter in the range 1-2 nm, these authors deduced a bandgap of 2.06 eV.

1. Si Photoluminesence

The fate of photogenerated electron-hole pairs in a semiconductor is determined by traps and recombination processes. As noted earlier, weak light emission, or photoluminescence (PL), from phonon-assisted, indirect bandgap, *e* - *h* recombination in bulk Si has been observed.[15] At room temperature, this PL peaks in the near IR at 1130 nm (= 1.1 eV), and at low temperatures (e.g., 77K) there is also emission from, or to, shallow impurity levels. In the present work on Si nanocrystals we have observed room temperature emission at various wavelengths in the range 700-350 nm (~ 1.8 - 3.5 eV), i.e., across the visible range. All our data were obtained at room temperature (295K) and the solvent was in almost all cases acetonitrile.

In small nanocrystals, a large number of the atoms are at or near the surface leading to a preponderance of dangling bonds and defects which result in surface states. Adsorbed impurities can produce additional surface states, and all of these states can act as traps or recombination sites. Consequently, light emission from nanostructures, be they nanocrystals or porous Si, can be quite complex with considerable uncertainties about the origin of the observed PL. In solution-grown nanocrystals such as our own, there is the added concern that surfactants and reaction products can lead to some luminescence which can interfere with that due to the Si clusters. In this regard, chromatographic separation/purification has led to significant improvement in the quality of the observed PL spectra. Even so, it is difficult to definitively rule out the role of contaminants in the measured PL spectra of nanoclusters in colloidal solutions.

2. Results on Si Nanocrystals

Results on a d = 2 nm size-selected, purified sample are shown in Fig. 7. The absorption spectrum was discussed earlier (Figure 6). The first absorption peak at 325 nm (3.81 eV) is attributed to the $\Gamma_{25} - \Gamma_{15}$ direct gap, but blue shifted by ~ 0.4 eV due to quantum confinement. Excitation at 245 nm yields the PL spectrum shown. The major peak is centered at 365 nm (= 3.40 eV). We attribute this peak to direct e - h recombination at Γ. It is red shifted from the absorption peak by 0.4 eV largely due to the strong exciton binding energy for very small clusters. Takagahara and Takeda[16] find $E_B > 0.25$ eV for the indirect gap of Si clusters with $d \leq 2$ nm. Tagaki et al[17] deduced a value of $E_B = 0.32$ eV for $d \approx 3.3$ nm Si clusters. As appears to be typical for Si nanostructures, this 365 nm PL peak is fairly broad, its width at half max being 1 eV. This sample also exhibits weaker and quite broad emission at wavelengths longer than 500 nm as shown. The data in Fig. 7 originate from a very monodisperse sample as suggested by its sharp absorption features and narrow elution width.

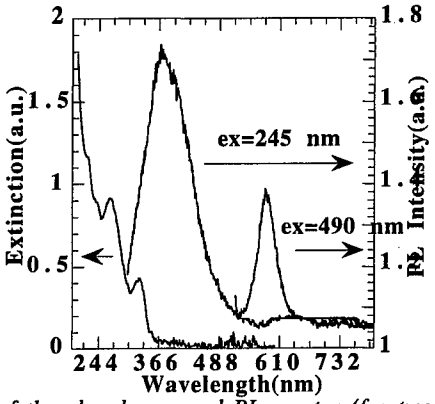


Figure 7. Co-plot of the abosrbance and PL spectra (for two indicated excitation wavelengths (ex)) for a d = 2 nm Si nanocrystal sample.

Figure 7 also shows the PL spectrum for a similar sample excited at 490 nm (2.53 eV) i.e., just above the indirect gap for this nanocrystal size. This PL peak is centered at 580 nm (2.14 eV), and it is tempting to attribute it to indirect bandgap recombination. However, we note that this luminescence is identical to that observed on much larger ($d \cong$ 8-10 nm) nanocrystals.[8] We are thus led to conjecture that this PL is due to surface or defect recombination.

Figure 8 shows the absorption and PL spectra of a nanocrystal sample (d = 4 nm) with structured absorption [peaks at 355 nm (3.48 eV) and 280 nm (4.40 eV) which we believe are associated with the quantum confinement-shifted two direct transitions at Γ] exhibited a PL peak centered at 540 nm (2.30 eV) for excitation at 470 nm (2.64 eV), i.e., well below the first direct transition at Γ. The fact that this sample has a shorter PL peak wavelength than the peaks in Figure 7 is somewhat surprising and indicates an extrinsic origin of this PL. The PL spectrum in Fig. 8 also has a secondary peak at ~ 700 nm (~ 1.8 eV) which is most likely due to recombination at the indirect bandgap.

3. Photoluminescence Quantum Efficiency

To estimate the quantum efficiency (Q.E.) of various solutions of Si nanoclusters, we measured the total area under the PL curve and normalized this by the absorbance of the sample at the excitation wavelength. We performed identical measurements on a laser dye, Coumarin 500, known to be close to 100% efficient at light emission. We take the ratio of the dye emission PL area to the cluster solution PL area under identical excitation conditions, lamp energy, and spectrometer bandpass as a measure of the efficiency of light emission of the nanoclusters. The largest room temperature Q.E. achieved was 3.9% for

2.0 nm Si nanocrystals in acetonitrile with no special treatment of the cluster surface, or annealing.

In a similar study on Ge nanocrystals[13] we examined the influence of the polarity of the solvent on the Q.E. Extensive data on d=2 nm Ge nanocrystals revealed a gradual decrease in PL efficiency with decreasing solvent polarity (ethylene glycol >acetonitrile > toluene > ortho-xylene). The same trend is expected for Si.

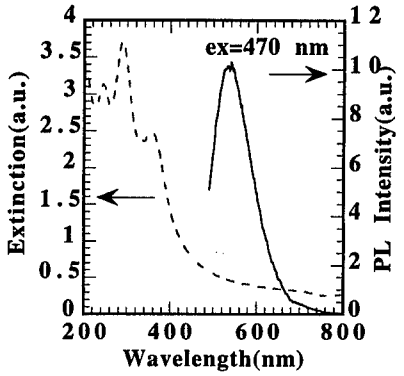


Figure 8. Coplot of the extinction and PL spectra for a d=4.0 nm Si nanocrystal sample.

GERMANIUM NANOCRYSTALS

1. Bulk Properties and Comparison to Silicon

Before presenting our results on Ge nanocrystals, it is helpful to compare and contrast the electronic structure and properties of bulk Si and Ge and review the optical absorption of bulk Ge. The valence bands are similar and for both crystals are derived from $p_{3/2}$ and $p_{1/2}$ states of the free atoms. The $p_{3/2}$ states are higher in energy than the $p_{1/2}$ states, the difference in energy being equal to the spin-orbit interaction shown. The lowest conduction bands of the two crystals, however, are different. For Si this band is made up of antibonding p states, i.e. $p\sigma*$, states, whereas for Ge it is made up of antibonding s, or $s\sigma*$, states. The ordering of these two sets of states is reversed in the two crystals. The smallest gap for Ge is the indirect gap from the top of the valence band at k = 0 to the bottom of the conduction band at k = $\frac{2\pi}{a}\left(\frac{1}{2},\frac{1}{2},\frac{1}{2}\right)$, i.e., the L point, with Eg = 0.66 eV at 300K. Interestingly the energy of the direct $\Gamma_{25}-\Gamma_{15}$ transition (3.4 eV), which corresponds to $p_\sigma \rightarrow p_{\sigma*}$, is the same for both crystals. Similarly, the corresponding, i.e., $p_\sigma \rightarrow p_{\sigma*}$ direct transition at X and L have nearly the same energies for the two crystals.

The Ge absorption samples a variety of transitions across the Brillouin zone. Starting at low energies there is first the indirect gap $\Gamma \rightarrow L$ absorption followed by the first direct $\Gamma_{25}-\Gamma_{2'}$ absorption at 0.8 eV, followed by a long indirect tail and a shoulder at ~ 2.4 eV (which may correspond to the first direct transition at L), and then finally cusps at ~ 4.3 eV and 6 eV. The cusp at ~ 4.3 eV is also observed in bulk Si as shown, and in both cases it is associated with the direct transitions at X.

Compared with Si, bulk Ge has a larger dielectric constant (15.4 vs. 11.4) and smaller electron and hole effective masses leading to a much larger excitonic, Bohr radius,

a_B, (11.5 vs. 4 nm). This means that quantum confinement effects should become observable at much larger cluster sizes in Ge than in Si. This fact along with the variety of direct and indirect transitions make Ge a scientifically interesting material to study in nanocrystal form.

2. Nanocrystal Spectra

As was true for Si, some of our Ge nanocrystal samples exhibited highly structured optical extinction while other samples had less structure. The differences are undoubtedly related to subtleties in the synthesis and possibly to size dispersion as well as impurity/solvent effects. In this latter regard, HPLC separation and on-line spectroscopy were extremely helpful.

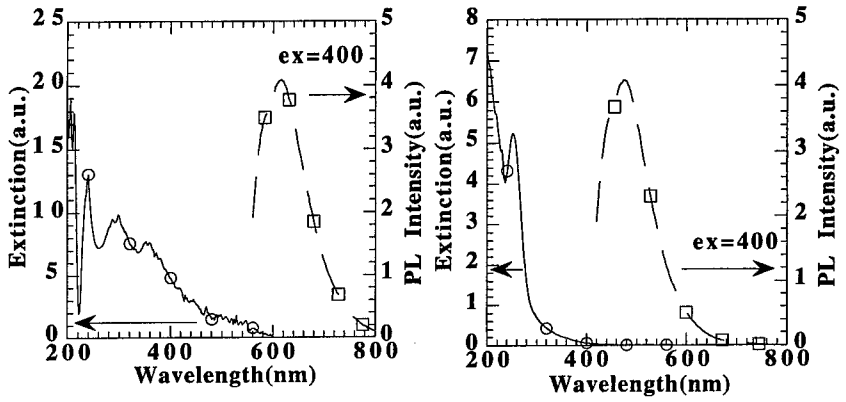


Figure 9: Extinction and PL spectra of Ge nanocrystal samples with (a) d = 4.0 nm and (b) d = 2.2 nm.

Figure 9 shows the extinction spectra for two Ge nanocrystal samples, from the same parent solution eluted at two distinct times during HPLC separation. The major, smaller size (d = 2.2 nm) population eluted at 5.8 minutes and a minor, larger size (d = 4.0 nm) population eluted at 3.8 minutes. The sharpness of the elution peaks suggests a narrow size distribution for each population. The extinction of the larger size population, Fig. 9(a) is highly structured, and, as we shall see below, the various spectral features can be understood in terms of the electronic structure of bulk Ge. The extinction of the smaller size population, on the other hand, is featureless for wavelengths > 260 nm (< 4.8 eV), but exhibits a sharp peak at 252 nm (4.9 eV) and other less well-defined features at shorter wavelengths. As will be discussed below, we believe that the 252 nm peak is most likely associated with $\Gamma_{25} - \Gamma_{15}$ transitions, blue-shifted by quantum confinement and modified by the expected splitting of the bands at Γ_{15} .

The main features in our d = 4.0 nm nanocrystal spectrum (fig 9a) are a well-defined shoulder at ~ 550 nm (2.25 eV) which is essentially unshifted from its counterpart in the bulk spectrum. The lack of influence of quantum confinement on this feature reflects the flatness of the conduction and valence bands at L. Other features are peaks at 355 nm (3.5 eV) and 300 nm (4.03 eV), a shoulder at ~ 280 nm (4.42 eV), and finally a sharp rise in extinction below ~ 250 nm (~5 eV). We believe that the 355 and 300 nm peaks represent direct transitions from Γ_{25} to the quantum confinement-split-off conduction bands at Γ_{15}. As was discussed for Si, there are two overlapping $p\sigma^*$ bands at Γ_{15} which are expected, and shown by calculations to split by quantum confinement. The upper of these two bands for Ge has stronger dispersion than the lower band and is

expected to show the larger shift with quantum confinement. Our results are consistent with this expectation. Similar findings have been reported by Heath et al[14] as discussed below.

The fact that the Γ_{25} - Γ_{15} transition is so clearly seen in solution-grown Ge nanocrystals (ours and those of Heath et al.) and not in bulk Ge is interesting. It is tempting to suggest that its emergence in the spectrum of the nanocrystals is a consequence of zone folding which enhances the oscillator strength for the transition. In bulk Ge the Γ_{25} - Γ_{15} gap is 3.4 eV. The split-off transitions for our nanocrystals at 3.5 eV and 4.03 eV demonstrate a relatively weak (~ 0.1 eV) quantum confinement effect on the lower and a stronger (~ 0.6 eV) effect on the higher transition, as expected. Here we should note that both the top of the valence band at Γ_{25} and the conduction bands at Γ_{15} are affected by quantum confinement as predicted by theoretical calculations for Si. Thus, conceivably, and most likely, the lower of the split-off bands at Γ_{15} can actually decrease in absolute energy, but the Γ_{25} is expected to decrease more leading to the small (0.1 eV) observed blue shift of this Γ_{25} - Γ_{15} transition compared to the bulk transition. It is also of interest to note here that although we did not observe clear evidence in our Si nanocrystal spectra for the expected splitting of the Γ_{15} bands, we observed a 0.4 eV blue shift for the Γ_{25} - Γ_{15} transition for our small (d = 2 nm) clusters. This is of the same magnitude, but a smaller, quantum confinement shift than the 0.6 eV shift for the transition to the upper split-off Γ_{15} band we see for Ge, also as expected.

As for the shoulder at ~ 280 nm in our spectrum in Fig. 9a, it occurs at about the same energy as the cusp in the bulk sample and is probably also associated with the direct transition at X. The fact that it exhibits only a very week (~ 0.1 eV) quantum confinement shift for our d = 4.0 nm clusters is consistent with the weak dispersion in the bands at X. The situation here is akin to that of the 550 nm transition at L. The close similarity of our cluster spectrum to that of the bulk with respect to both the 550 nm and 280 nm transitions is quite remarkable, indicating that scattering plays a minor role in the extinction spectrum of our small clusters.

Heath et al.[14] synthesized Ge nanocrystals via the ultrasonic-mediated reduction of mixtures of chlorogermanes and organochlorogermanes by a colloidal sodium/potassium alloy in heptane. This solution synthesis approach comes closest to our micellar approach of any of the methods to produce Ge nanocrystals, and Heath et al.'s spectrum for their d = 5-6 nm sample is quite similar to ours. Specifically, their spectrum exhibits a peak at ~ 360 nm, a shoulder at ~ 300 nm and a second peak at ~ 285 nm, which correspond closely to the features in our spectrum at 355, 300 and 280 nm, respectively. One difference between our results and those of Heath et al is that they apparently do not see as clear evidence for the transition at 550 nm as we do.

Figure 9b shows the extinction spectrum for our d = 2 nm nanocrystals. This is the population that eluted at t = 5.8 minutes. There is a sharp increase in extinction below ~ 280 nm leading to a peak at 252 nm (4.9 eV) and more subtle absorption features at ~ 230 nm (5.4 eV) and ~ 220 nm (5.65 eV). Compared with the results in Figs. 9a the feature due to the direct transition at L (at ~ 550 nm) is missing for the small nanocrystal size. As for the peak at 252 nm, there are two possible interpretations.

Our first conjecture is that it is associated with the upper split-off Γ_{15} band at Γ. If this is indeed the case, then there is a large (~ 1.5 eV) blue shift of this transition from its bulk value. This is a considerably larger shift than is indicated by our data on Si for the same transition and for comparable nanocrystal size -- a feature possibly related to the expected larger quantum size effect for Ge. In this hypothesis, one has to explain the disappearance of the transition to the lower split-off band as well as the transition at L (~ 550 nm). As for the lower $\Gamma_{25}-\Gamma_{15}$ transition, its disappearance for very small sizes would most likely be due to the change in curvature of the lower Γ_{15} band with decreasing

size. For very small nanoclusters, there are no bound states associated with this band. The increased sharpness of the 252 nm transition compared to that for the larger nanocrystals would most likely be due to the increased effect of zone folding and the resulting increase in oscillator strength. This zone-folding effect could also explain the disappearance of the transition at L.

MoS_2 NANOCLUSTERS

Our investigations of the optical, electronic, and catalytic properties of this layered transition metal material have been described elsewhere[5,19,20] and we simply summarize our observations here.

Highly crystalline nanoclusters of hexagonal (2H-polytype) MoS_2 and several of its isomorphous Mo and W chalcogenides have been synthesized with excellent control over cluster size down to ~2 nm. These clusters exhibit highly structured, band-like optical absorption and photoluminescence spectra which can be understood in terms of the band-structures for the bulk crystals. Key results of our work include: (1) strong quantum confinement effects with blue shifts in some of the absorption features relative to bulk crystals as large as 4 eV for clusters ~2.5 nm in size, thereby allowing great tailorability of the optical properties; (2) the quasiparticle (or excitonic) nature of the optical response is preserved down to clusters ~2.5 nm in size which are only two unit cells thick; (3) the demonstration of the strong influence of dimensionality on the magnitude of the quantum confinement. Specifically, three-dimensional confinement of the carriers produces energy shifts which are over an order of magnitude larger than those due to one-dimensional (perpendicular to the layer planes) confinement emphasizing the two-dimensional nature of the structure and bonding; (4) the observation of large increases in the splittings at the top of the valence band at the K and M points of the Brillouin zone with decreasing cluster size, a feature that reflects quantum confinement as well as possible changes in the degree of hybridization of the electronic orbitals which make up the states at these points; and (5) the observation of photoluminescence due to both direct and surface recombination. Several of these features bode well for the potential of these materials for solar photocatalysis.

1. Photoluminescence of MoS_2 Nanoclusters

In our earlier work on unpurified MoS_2 clusters[5], the observed photoluminescence (PL) was generally observed at considerably longer λ's than any of the absorption thresholds and was thus dominated by surface recombination. Chromatographic purification has led to significant improvement in the quality of the PL spectra and to the observation of both band edge (direct) as well as surface e-h recombination. Of course, essentially no PL is expected or is observed at the smallest, or indirect, gap of MoS_2.

Figure 10(a) shows the room temperature absorption and PL spectra (excited at two different λ's) of a 3.0 nm cluster sample. For excitation at λ=450 nm, which is seen to be a slightly longer λ than the first absorption threshold at ~420 nm, a single PL peak centered at 520 nm is observed. Clearly this PL is associated with surface recombination. Excitation at 348 nm however, leads to a PL spectrum consisting of two overlapping peaks. The more intense peak is centered at 420 nm which is seen to be the first absorption threshold for these clusters. We attribute this peak to direct band (K) edge recombination. Decomposition of the PL spectrum into its two components reveals the second peak which is centered at ~520 nm. This much less intense peak is at the same λ as the PL observed for 450 nm excitation, again pointing to its surface states recombination character. Early PL measurements on unpurified samples yielded intense luminescence due largely to surface recombination.

Figure 10(b) shows the room temperature absorption and PL spectra of a chromatographically purified 4.5 nm cluster sample. As in the case of the 3.0 nm clusters, excitation of this sample at 348 nm produces a PL peak near the first absorption threshold (~560 nm), i.e., direct recombination.

In an earlier collaboration,[19] we studied the PL emission kinetics of as-prepared (i.e., not chromatographically purified) ~3.0 nm and ~4.5 nm clusters. These samples exhibited weak PL peaks close to the first excitonic λ threshold. The PL decay times were nonexponential having components with time constants ranging from <100 ps to >10 ns. The small values of these time constants are consistent with direct e-h recombination as found in our data on purified samples.

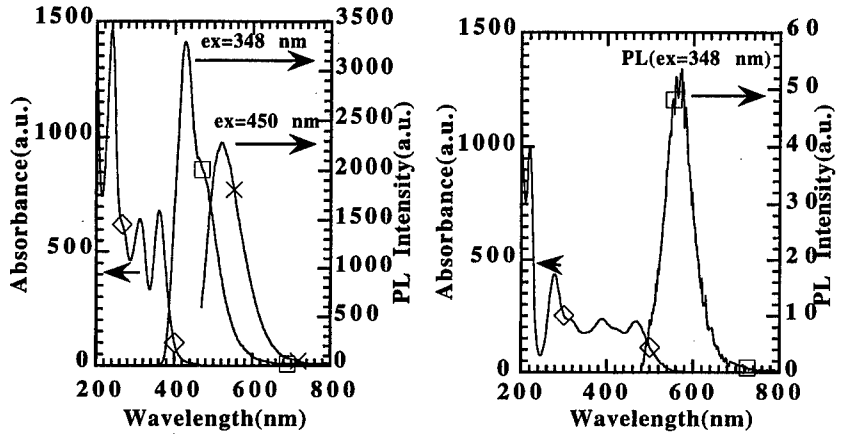


Figure 10. Absorbance and PL of MoS_2 nanocrystals of size (a)3.0 nm, and (b)4.5 nm.

SUMMARY AND CONCLUSIONS

We have successfully grown size-selected Si,Ge and MoS_2 nanocrystals in the size range 1.8 to 10 nm. High resolution TEM fringe images show that these nanocrystals are of high crystalline quality, and electron diffraction results show that they retain their bulk structure down to about 4-5 nm diameter. Optical absorption data suggest that these nanocrystals retain their bulk-like properties and structure down to the smallest sizes produced (e.g. ~1.8 nm diamter containing about 150 Si atoms).

High pressure liquid chromatography (HPLC) techniques with on-line optical and electrical diagnostics capabilities were developed to purify and separate the clusters into chemcially pure, monodisperse populations. These techniques proved to be crucial to obtaining background-free absorbance and PL spectra which allowed assignments of the observed optical transitions based on band theory calculations and estimates of the energy shifts associated with quantum confinement effects.

The work presented here represents our first attempts to understand the relationship between Si, Ge and MoS_2 nanocluster size, structure, surface chemistry and the resulting optical properties. We have identified features in the optical absorption and PL of nanosize these materials that deserve more detailed study in order to understand the effect of size and surface termination on the optical and electronic properties. Especially with the smallest sized clusters studied, many of the concepts of, for example, band structure, derived from assumptions of translational symmetry of the lattice may seem inappropriate, and the nature of the bonding at the cluster surface should play a significant role in the optical and electronic properties. However, it is surprising how well the optical features of nanoclusters of these indirect materials as small as 2 nm can be identified with bulk optical properties. Since experimental methods of studying the surface characteristics and bonding arrangement of nanosize clusters are nearly non-existent it may be some time before

experimental observations and the predictions of modern theoretical models of quantum confinement can be more quantitative. We assert that HPLC, which is very sensitive to small changes in surface characteristics, may play an important role in elucidating the role of surface structure on the optical properties of nanoclusters.

REFERENCES

1. See, e.g., S. S. Iyer and Y. H. Xie, Science 260, 40 (1993) and references therein.
2. (a) K. A. Littau, P. J. Szajowski, A. J. Muller, A. R. Kortan and L. E. Brus, J. Phys. Chem. 97, 1224 (1993);. (b) L. E. Brus et al, J. Am. Chem. Soc. 117, 2915 (1995) and references therein;
3. J. P. Wilcoxon, U.S. Patent #5,147, 841, issued September 15, 1992
4. J. P. Wilcoxon, R. L. Williamson and R. J. Baughman, J. Chem. Phys., 98, 9933 (1993).
5. J. P. Wilcoxon and G. A. Samara, Phys. Rev. B51, 7299 (1995); see also J. P. Wilcoxon, P. P. Newcomer and G. A. Samara, Sol. State Commun. 98, 581 (1996)
6. J.P. Wilcoxon and S.A. Craft, in NanoStructured Materials, Vol. 9, 85-88, Elsevier Science Ltd., (1997).
7. T.R. Thurston and J.P. Wilcoxon, J. Phys. Chem. B, 103, 11, (1999).
8. J.P. Wilcoxon, G.A. Samara, and P.N. Provencio. to appear in Phys. Rev. B, (1999).
9. See, e.g., S.M. Sze, Physics of Semiconductor Devices, Wiley-Inferscience (New York, 1969) Chapt. 2 and references therein.
10. Y. Kanemitsu, Phys. Rev. B 49, 16845 (1994).
11. N. Binggeli and J. R. Chelikowsky, Phys. Rev. Lett. 75, 493 (1995).
12. M. V. Rama Krishna and R. A. Friesner, J. Chem. Phys. 96, 873 (1992).
13. J. P. Wilcoxon and G.A. Samara, to be published.
14. J. R. Heath, J. J. Shiang and A. P. Alivisatos, J. Chem. Phys. 101, 1607 (1994).
15. J. R. Haynes and W. C. Westphal, Phys. Rev. 101, 1676 (1956).
16. T. Takagahara and K. Takeda, Phys. Rev. 3 46, 15578 (1992).
17. H. Takagi, H. Ogawa, Y. Yamazaki, A. Ishizaki and T. Nakagiri, Appl. Phys. Lett. 56, 2379 (1990).
18. See, e.g., J. I. Pankove, Optical Processes in Semiconductors (Dover, New York, 1975), Chapt. 2.
19. F. Parsapour, D.F. Kelley, S. Craft, and J.P. Wilcoxon, J. Chem. Phys., 104, 1, (1996).
20. T.R. Thurston and J.P. Wilcoxon, J. Phys. Chem., 103, 11, (1998).

ACKNOWLEDGMENT

This work was supported by the Division of Materials Sciences, Office of Basic Energy Sciences, U.S. Department of Energy and by a Laboratory Directed R&D project under Contract DE-AC04-AL8500. Sandia is a multiprogram Laboratory operated by Sandia Corporation, a Lockheed Martin Company for the Department of Energy.

IMPROVEMENT OF RED LIGHT EMISSION IN H_2 TREATED SILICON NANOCRYSTAL

K. Sato*, Y. Sugiyama*, T. Izumi*, M. Iwase**,
Y. Show***, S. Nozaki*** and H. Morisaki***

*Department of Electronics, Faculty of Engineering, Tokai University
1117 Kitakaname, Hiratsuka-shi, Kanagawa, 259-1292, JAPAN

**Department of Electrical Engineering, Faculty of Engineering, Tokai University
1117 Kitakaname, Hiratsuka-shi, Kanagawa, 259-1292, JAPAN

***Department of Communications and Systems,
The University of Electro-Communications
1-5-1 Chofugaoka, Chofu-shi, Tokyo, 182-0021, JAPAN

ABSTRACT

Correlation between defect structures and light emission in H_2 treated Si-nanocrystal have been studied using electron spin resonance (ESR) and photoluminescence (PL) methods. The ESR analysis revealed the presence of three kinds of ESR centers in both the film after annealing at 1100 °C in argon (Ar) atmosphere and pressurized water boiling treated film, i.e. ① Si dangling bond in amorphous Si cluster (a-center: g=2.006), ② Si dangling bond in Si-nanocrystal/SiO_2 interface (P_b-center: g=2.003) and ③ localized electrons in Si nanocrystal (P_{ce}-center: g=1.998). Moreover, visible light emission (780 nm) was observed in these samples from the PL measurement. For the HF treated sample, a- and P_b-centers disappeared, and only the P_{ce}-center was observed. The PL spectrum of the sample exhibited a peak at 670 nm. The both signal intensities of PL and P_{ce}-center were increased by the HF treatment. These results indicate that the P_{ce}-center is associated with the emission center.

INTRODUCTION

Since the discovery of strong visible light emission from porous silicon (Si)[1] and Si nanocrystal[2-5], the mechanism of the light emission and the application to light emitting devices have been extensively investigated. On the visible light emission from the porous Si, the emission intensity decrease when the P_b-center, which originates from Si dangling bond at the interface between Si nanocrystal and SiO_2, is formed in the

surface of the porous Si[6-8]. It is well known that the P_b-center is associated with the formation of the non-luminescent center (emission killer center)[8]. Therefore, the decrease of this emission intensity is due to the existence of the P_b-center. In the case of Si nanocrystal, it is necessary to decrease the P_b-center which works as a non-luminescent center so that the emission intensity from the Si nanocrystal may increase.

In this paper, we will report the improvement of visible light emission from the H_2 treated Si nanocrystal. Moreover, we also discuss the correlation between the defect structures and the light emission in the H_2 treated Si nanocrystal, using ESR, fourier transformed infrared (FT-IR) and PL methods.

EXPERIMENTAL

The SiO_2 films containing Si-nanocrystal were deposited on p-type Si (100) substrates by co-sputtering of p-type Si (100) and SiO_2. The scheme of the RF sputtering apparatus is shown in Fig.1. The typical deposition conditions are listed in Table I. A sputtering target was consisted of 5 X 5 mm^2 Si chips placed on a SiO_2 substrate with a diameter of 100 mm, and the number of Si chips were 16. The target was sputtered in Ar gas at a pressure of 0.1 Torr at a constant RF power of 110W and the sputtering time of 2 hours.

The as-deposited sample was annealed at 1100 °C in Ar atmosphere for 1 hour. Subsequent the annealed samples were carried out pressurized water boiling (2 atm., 120 °C) and hydrofluoric (46 wt. % HF) treatments, respectively.

We have confirmed that the surface of the Si nanocrystal is terminated with the hydrogen atoms by FT-IR spectroscopy.

The paramagnetic defects in the H_2 treated Si nanocrystal were investigated by the ESR method. The ESR measurements were performed using X-band spectrometer at room temperature. The g-value, the line width (ΔH_{pp}) and the spin density were determined using the signals of Mn^{2+} and 1,1-dipheny1-2-picry1-hydrazy1 (DPPH) as the calibration references.

The PL spectra were measured using Ar ion laser (488 nm, 2 mW) at room temperature.

RESULTS AND DISCUSSION

Fig. 2(a), (b) and (c) shows the FT-IR spectra for different H_2 treated Si nanocrystal. From the sample annealed at 1100 °C, the IR spectrum which was originated from the Si-O_x bonds (around 460, 810 and 1050 cm^{-1}) was observed as shown in Fig. 2(a). The Si-O_x bonds decreased when the samples were treated with pressurized water boiling and in HF,

and the new absorption peaks which was originated from Si-H_x bonds (around 640, 900 and 2100 cm^{-1}) were observed as shown in Fig. 2(b) and (c). The FT-IR analysis revealed that the surfaces of both the pressurized water boiling and the HF treated Si nanocrystal are terminated with hydrogen atoms.

Fig. 3 shows the typical PL spectra for the samples used in Fig. 2. The visible PL spectra for both the annealed and the pressurized water boiling treated samples were observed at a peak position of 780 nm[9]. On the other hand, the PL spectrum of the HF treated sample exhibited a peak position at 670 nm. The PL intensity of the sample was very strong, and the red light emission was able to be observed even in the naked eye.

Fig. 4(a), (b) and (c) show the typical ESR spectra for the samples used in Fig. 2. The ESR signals for both the annealed and the pressurized water boiling treated samples were composed of three kinds of ESR centers as shown in Fig. 4(a) and (b)[9]. That is, (1) the a-center with g-value of 2.006, which originated from Si dangling bond in amorphous Si cluster[10], (2) the P_b-center with g-value of 2.003, which originated from Si dangling bond at the interface between Si nanocrystal and SiO_2[8,11] and (3) the P_{ce}-center with g-value of 1.998, which is due to the localized electrons trapped at a shallow level center close to the conduction band edge in the Si nanocrystal[12,13]. When the annealed sample was treated with HF, both the a-, and the P_b-centers disappeared, and only the P_{ce}-center was observed as shown in Fig. 4(c). FT-IR and ESR studies show that the P_b-center is compensated with the hydrogen atoms by the HF treatment.

Fig. 5 shows the change of PL intensity and the ESR signal intensities (including the P_b-, and the P_{ce}-centers) versus different H_2 treatment. The signal intensity of the P_{ce}-center in the HF treated sample increased to about 7.5 times higher than that of the annealed sample. On the other hand, the PL intensity increased to about 20 times higher than that of the annealed sample by the HF treatment. The increase of the PL intensity is due to the hydrogen atoms terminating the Si nanocrystal surface, which compensates the P_b-center existing in the surface of the Si nanocrystal. This implies that the P_b-center works as a non-radiative center (emission killer center)[8]. Consequently, it is reasonably conclude that the P_{ce}-center is strongly associated with the emission center.

CONCLUSIONS

Correlation between the defect structures and the light emission in the H_2 treated Si nanocrystal have been investigated by ESR, FT-IR and PL methods. The signal intensity of the P_{ce}-center (g=1.998) in the HF treated sample increased to about 7.5 times higher than that of the annealed sample. The both signal intensities of the PL and the P_{ce}-center increased by terminating P_b-center with the hydrogen atoms. It seems reasonable to conclude the P_{ce}-center is strongly associated with the emission center.

REFERENCES

1. L. T. Canham, Appl. Phys. Lett., 57, 1046 (1990).
2. H. Morisaki, F. W. Ping, H.Ono and K. Yazawa, J. Appl. Phys., 70, 1869 (1991).
3. H. Morisaki, Nanotechnology, 3, 196 (1992).
4. S. Furukawa and T. Miyasato, Jpn. J. Appl. Phys., 27, 2207 (1988).
5. S. Nozaki, H. Nakamura, H. Ono, H. Morisaki and N. Ito, Jpn. J. Appl. Phys., 34, Suppl. 34-1, 122 (1995).
6. H. J. von Bardeleben, M. Chamarro, A. Grosman, V. Morazzani, C. Ortega, J. Siejka and S. Rigo, J. Lumin., 57, 39 (1993).
7. H. Yokomichi, H. Takakura and M. Kondo, Jpn. J. Appl. Phys., 32, 365 (1993).
8. M. Shimasaki, Y. Show, M. Iwase, T. Izumi, T. Ichinohe, S. Nozaki and H. Morisaki, Appl. Surf. Sci., 92, 617 (1996).
9. K. Sato, Y. Sugiyama, M. Iwase, T. Izumi, Y. Show, S. Nozaki, and H. Morisaki, Mat. Res. Soc. Sympo. Proc., 536, 57 (1999).
10. B. L. Crowder, R. S. Title, M. H. Brodsky and G. D. Pettit, Appl. Phys. Lett., 16, 205 (1970).
11. Y. Nishi, Jpn. J.Appl. Phys., 10, 52 (1971).
12. F. Finger, C. Malten, P. Hapke, R. Carius, R. Flückiger and H. Wagner, Phil. Mag. Lett., 70, 247 (1994).
13. M. Kondo, T. Nishimiya, K. Saito and A.Matsuda, J. Non-Cryst. Solids., 227, 1031 (1998).

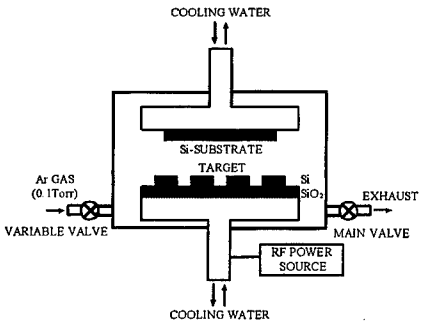


Fig. 1. Schematic diagram of the RF sputtering apparatus.

Table I. Deposition conditions.

Substrate	p-type Si (100)
Target	Si chips on SiO_2 glass
Number of Si chips	16
RF power	110 W
Sputtering gas	Ar
Gas pressure	0.1 Torr
Sputtering time	2 hours

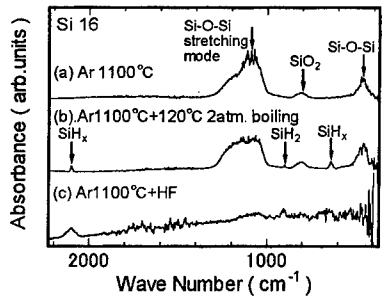


Fig. 2. FT-IR spectra for (a) annealed at 1100 °C, (b) pressurized water boiling treatment, (c) hydrofluoric treatment.

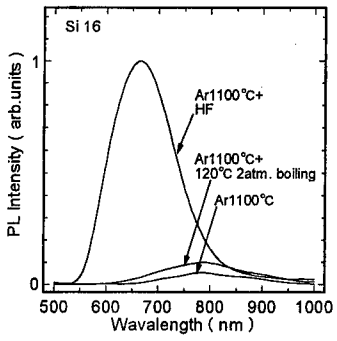


Fig. 3. PL spectra for various treated Si nanocrystal.

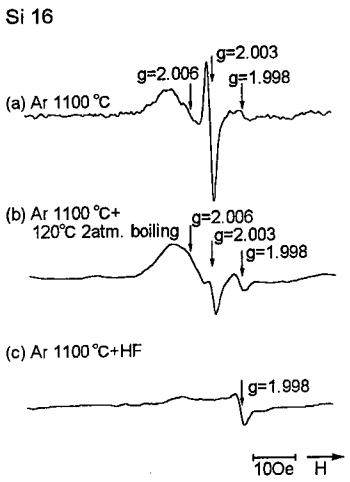


Fig. 4. ESR spectra for (a) annealed at 1100 °C, (b) pressurized water boiling treatment, (c) hydrofluoric treatment.

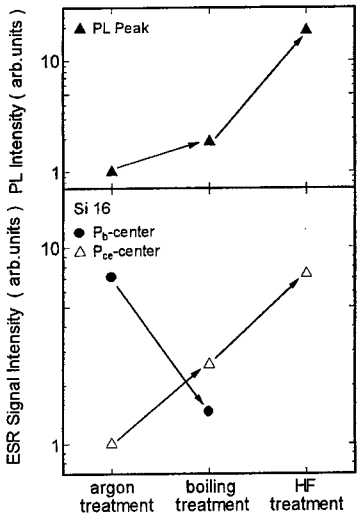


Fig. 5. Change of PL intensity and the ESR signal intensities (● P_b-center: Si dangling bond at the Si-nanocrystal/SiO_2 interface, △ P_{ce}-center: conduction electrons in Si-nanocrystal) versus various H_2 treatment.

MAGNETOEXCITONS ON THE SURFACE OF NANOTUBES

A.V.Chaplik and L.I.Magarill
Institute of Semiconductor Physics, Russian Academy of Sciences
prospekt Lavrent'eva 13, Novosibirsk, 630090, Russia

ABSTRACT

The energy spectrum of excitons attached to the surface of a hollow cylinder is considered. The curvature of the surface results in lifting both specifically Coulomb degeneracy and the degeneracy connected with the sign of the azimuthal momentum. In the magnetic field parallel to the axis of nanotube the exciton binding energy oscillates as a function of magnetic flux with the fundamental period $\Phi_0 = 2\pi\hbar c/e$.

I. INTRODUCTION

Investigations of the Wannnier-Mott excitons in a magnetic field have a rather long history (see [1]-[5]). It has been shown that the exciton binding energy, as well as all the other parameters (effective mass, dipole moment, dispersion law), are strongly magnetic field dependent. A very strong magnetic field ($l_B \ll a_0$, where l_B and a_0 are the magnetic length and effective Bohr radius, respectively) makes the 3D exciton effectively 1D with logarithmically deep ground state and with cigar-like wave function stretched along the direction of magnetic field **B**. 2D planar exciton in a strong perpendicular magnetic field has the ground state energy still stronger depending on B, namely $|E_0| \sim e^2/l_B$ (see [5]).

Recent successes in fabrication of low dimensional objects stimulate interest to the excitons in nanostructures of various geometries (for quantum dots see [6] and for quantum wires see [7]-[9]). Nanotubes (mainly carbon ones and more recently semiconductor structures [10]) are of great interest in many respects. The present paper is aimed to the problem of 2D excitons placed on the surface of a hollow cylinder. We investigate the influence of the surface curvature on the energy spectrum of excitons and the role of an external magnetic field. A specific topological feature of the system will be considered.

II. WANNIER-MOTT EXCITON ON A CURVED SURFACE

The transformation of a quantum problem from 3D to 2D on a curved surface is not quite trivial procedure. Actually we deal with curved waveguides one of characteristic sizes of which decreases resulting in the ultraquantum limit for the particle motion in appropriate direction. Such a limit transition in general case leads to origin of a specific potential energy of purely geometric nature. In other words, not only the kinetic energy operator changes because of transformation of Laplasian in curvilinear coordinates, but an additional potential arises. The only exception is the case of surfaces of constant curvature (circular cylinder, sphere). Here the mentioned above geometrical potential is just a constant and the transition to 2D is quite simple. On the cylindrical nanotube we have 2D particles with the kinetic energy operator

$$-\frac{\hbar^2}{2m}\left(\frac{\partial^2}{\partial z^2}+\frac{1}{R^2}\frac{\partial^2}{\partial\varphi^2}\right), \tag{1}$$

where m^* is the effective mass, R is the radius of nanotube z and φ are cylindrical coordinates: $-\infty < z < \infty$, $0 < \varphi \leq 2\pi$. However the Coulomb energy of the electron-hole interaction is now not simply $1/s$-law, where

$$s = \sqrt{(z_e - z_h)^2 + R^2(\varphi_e - \varphi_h)^2} \tag{2}$$

is the interparticle separation along the surface. The interaction takes the form (ε is the effective dielectric constant)

$$U = -\frac{e^2}{\varepsilon}\left[4R^2\sin^2\left(\frac{\varphi_e-\varphi_h}{2}\right)+(z_e-z_h)^2\right]^{-1/2} \tag{3}$$

and an analytical solution of even this "hydrogen-like" problem becomes impossible.

Non-Coulomb character of the potential U, Eq.(3), results in lifting of the "hydrogen" degeneracy of the exciton levels. In the case $R \gg a_0$ shifts and splittings of the energy levels can be found perturbatively. The zeroth approximation is the planar 2D exciton while the leading term in perturbation has the form:

$$V = -\frac{e^2}{\varepsilon}\left(\frac{1}{\sqrt{R^2(\vartheta^2-\vartheta^4/12)+z^2}}-\frac{1}{\sqrt{R^2\vartheta^2+z^2}}\right)\approx -\frac{e^2}{24\varepsilon}\frac{R^2\vartheta^4}{\rho^3}, \tag{4}$$

where designations ϑ, z stand for relative coordinates: $\vartheta = \varphi_e - \varphi_h$, $z = z_e - z_h$ of electron and hole and $\rho = \sqrt{(R\vartheta)^2 + z^2}$ is the radial coordinate of the corresponding planar exciton (zeroth approximation). Thus, in terms of the planar

problem in cylindrical coordinates ρ and
psi we have $R\vartheta = \rho\cos\psi$ and the perturbation reads

$$V = -\frac{e^2}{24\epsilon}\frac{\rho}{R^2}\cos^4\psi, \quad V \leq 0 \tag{5}$$

The exciton ground state shifts downwards due to perturbation V but the shift has very small numerical coefficient:

$$\Delta E_1 = -\frac{Ry^*}{128}(\frac{a_0}{R})^2 \tag{6}$$

where Ry^* is the effective Rydberg energy $\mu^* e^4/\epsilon^2$ (μ is the reduced mass of electron and hole). The first excited (triplet) level of the exciton is split in three components

$$\Delta E_2^{(1,2,3)} = -\lambda_{1,2,3} Ry^*(\frac{a_0}{R})^2, \quad \lambda_1 = \frac{7}{128}, \ \lambda_2 = \frac{1}{64}, \ \lambda_3 = \frac{5}{64} \tag{7}$$

We see that the level with principal quantum number equal to 2 (states $n_\rho = 0, m = \pm 1$ and $n_\rho = 1, m = 0$) is fully split due to angular dependence of the perturbation V, Eq.(5). The exciton on the surface of nanotube is an anisotropic system.

III. NANOTUBE IN A LONGITUDINAL MAGNETIC FIELD

Consider now electron and hole on the surface of a circular cylinder placed in an external magnetic field parallel to its axis. We take the gauge of the vector potential in the form $A_\varphi = BR/2$: this is constant on the surface where both particles reside. The Hamiltonian of the problem reads:

$$\hat{H} = \frac{\hbar^2}{2m_e R^2}(-i\frac{\partial}{\partial\varphi_e} + \lambda)^2 + \frac{\hbar^2}{2m_h R^2}(-i\frac{\partial}{\partial\varphi_h} - \lambda)^2 + \hat{H}_0(z_e, z_h) + U(\varphi_e - \varphi_h, z_e - z_h) \tag{8}$$

Here $\hat{H}_0(z_e, z_h)$ is Hamiltonian of free motion along z-axis, $\lambda = \Phi/\Phi_0, \Phi$ is the magnetic flux through the nanotube ($\Phi = \pi R^2 B$), Φ_0 is the flux quantum, U is given by Eq.(3). To separate the internal motion in the exciton from that of center-of-mass one needs to go over to the variables ($M = m_e + m_h$):

$$\varphi = \frac{m_e\varphi_e + \mu_h\varphi_h}{M}, \ \vartheta = \varphi_e - \varphi_h, \ Z = \frac{m_e z_e + \mu_h z_h}{M}, \ z = z_e - z_h \tag{9}$$

Then we have for the Hamiltonian

$$\hat{H} = -K\frac{\partial^2}{\partial\varphi^2} + \beta(-i\frac{\partial}{\partial\vartheta} + \lambda)^2 - \frac{\hbar^2}{2M}\frac{\partial^2}{\partial Z^2} + \frac{\hbar^2}{2\mu}\frac{\partial^2}{\partial z^2} + U(\vartheta, z), \qquad (10)$$

where $K = \hbar^2/2MR^2$, $\beta = \hbar^2/2\mu R^2$ The total wave function may be written as

$$\Psi = \exp(iJ\varphi - i\lambda\vartheta + iPZ)\chi(\vartheta, z), \qquad (11)$$

where J and P are real constant and $\chi(\vartheta, z)$ obeys the equation

$$-\beta\frac{\partial^2\chi}{\partial\vartheta^2} - \frac{\hbar^2}{2\mu}\frac{\partial^2\chi}{\partial z^2} + U(\vartheta, z)\chi = (E - KJ^2 - \frac{P^2}{2M})\chi \equiv W\chi \qquad (12)$$

Here E is the total energy of the exciton and W is its internal energy.

It is evident that P is arbitrary real number but to determine J and allowed solutions of Eq.(12) we have to make the total wave function independently periodic in φ_e and φ_h with period 2π. On the other hand Eq.(12) has, formally, the Bloch-type solutions

$$\chi = e^{iq\vartheta}v(\vartheta), \quad -\frac{1}{2} < q \leq \frac{1}{2}, \qquad (13)$$

where v is a periodic function of ϑ with the period 2π because this is period of the potential $U(\vartheta, z)$. By adding 2π to φ_e and φ_h independently we come to the relations

$$J\frac{m_e}{M} - \lambda + q = N_e, \quad J\frac{m_h}{M} + \lambda - q = N_h, \qquad (14)$$

where N_e, N_h are arbitrary integers. It follows from Eq.(14) that $J = N_e + N_h$, thus J is integer - the rotational quantum number of the exciton as a whole.

In small vicinities of the points $z = 0, \vartheta = 0; z = 0, \vartheta = \pm 2\pi; z = 0, \vartheta = \pm 2\pi$ and so on Eq.(12) describes a 2D particle with the mass μ moving in the field of Coulomb center of charge $e/\sqrt{\varepsilon}$. Hence We have a chain of 2D hydrogen atoms disposed equidistantly along the axis ϑ in the z, ϑ-plane. The eigenvalues of such problem form energy bands and the energy in each band is a periodic function of q with period 1. For example, in the case $2\pi R \gg a_0$ the tight binding approximation is applicable and we get

$$W = E_n - \Delta_n \cos(2\pi q), \quad n = 1, 2, ..., \quad \Delta_n > 0, \qquad (15)$$

where E_n are the energy levels of an isolated hydrogen atoms, Δ_n is the halfwidth of the n-th band determined by the probability of tunneling along the chain. The allowed values of quasimomentum q should be found from Eq.(14):

$$q = -J\frac{m_e}{M} + \lambda + N_e, \quad \text{or} \quad q = J\frac{m_h}{M} + \lambda - N_h, \qquad (16)$$

Then for the total energy of the exciton we obtain

$$E(P,J,n) = \frac{P^2}{2M} + KJ^2 + E_n - \Delta_n \cos\left(2\pi(\Phi/\Phi_0 - Jm_e/M)\right)$$
$$= \frac{P^2}{2M} + KJ^2 + E_n - \Delta_n \cos\left(2\pi(\Phi/\Phi_0 + Jm_h/M)\right)$$

(17)

Both forms of $E(P,J,n)$ are equivalent because the phase difference of the cosine arguments equals to $2\pi\times$ integer. Thus, the binding energy of the excitons in nanotubes oscillates as a function of magnetic flux with the fundamental period Φ_0. This statement has a general character and is not connected with the tight binding approximation used. The physical mechanism of such periodicity is the tunneling of electron (hole) to hole (electron) around the nanotube. Note that here we deal with purely topological effect. The magnetic field parallel to the surface on which the particles move has no effect on their orbital motion. However in the case of hollow cylinder with a magnetic flux inside electrons "see" not $\mathbf{B}$ but Φ: trajectories embracing the magnetic flux result in a phase shift of the wave function and, hence, the shift of energy levels.

To conclude, we have shown that energy levels of the exciton in nanotubes are split and shifted as compared with the planar 2D exciton. The shift and splitting of the first two levels are found. In the magnetic field parallel to the axis of nanotube the binding energy of the exciton oscillates as a function of magnetic flux.

ACKNOWLEDGEMENT

We acknowledge the financial support of RFBR (Grant 99-02-17127) and the State Program "Physics of Solid State Nanostructures."

References

[1] R.J.Elliot and R.Loudon, J.Phys.Chem.Solids, Vol. 15, p. 196 (1960).

[2] H.Hasegawa and R.E.Howard, ibid., Vol. 21, p. 179 (1961).

[3] W.A.Lamb, Phys.Rev., Vol. 85, p. 259 (1952).

[4] L.P.Gor'kov and I.A.Dzyaloshinsky, Sov.Phys.-JETP., Vol. 26, p. 449 (1968).

[5] I.V.Lerner and Yu Lozobik, ibid., Vol. 51, p. 588 (1980).

[6] A.O.Govorov and A.V.Chaplik, ibid., Vol. 72, p. 1037 (1991).

[7] S.Glutsch, D.S.Chempla and F.Bechstedt, Phys.Rev. B, Vol. 51, p. 16885 (1995).

[8] M.Graf, P.Vogl and A.B.Dzubenko, Annual report of Walter Schottky Institute, TU Muenchen, p. 14 (1995).

[9] A.V.Chaplik, Phys.Low-Dim.Struct., Vol. 9/10, p. 1 (1996).

[10] V.Ya.Prinz et al, Microelectronic Engineering, Vol. 30, p. 439 (1996).

Nanocrystalline n-TiO_2 Thin Films for Efficient Photoelectrochemical Splitting of Water

Shahed U.M. Khan, James C. Worthington and Mofarey Al-Shahry
Department of Chemistry and Biochemistry
Duquesne University
Pittsburgh, PA 15282

ABSTRACT

The high surface area nanocryatalline n-TiO_2 thin films were synthesized pyrolytically on both smooth and grooved Ti-metal surfaces at a flame temperature of 850 ° C. Optimum current densities of 2.5 mA cm^{-2} and 2.7 mA cm^{-2} were observed at a minimum applied potential of -0.7 volt/SCE (= 0.41 volt/NHE at pH = 0) at smooth and grooved surfaces respectively. An onset potential of - 1.14 volt/SCE (= 0.03 volt/NHE at pH = 0) was found for grooved thin films which is much less than that reported (10) earlier (-0.88 volt/SCE). The highest quantum efficiency was found to be 74 % which is much higher than 60 % reported earlier (10). The bandgap energy of 2.77 eV was obtained for the grooved film which is lower than 2.85 eV reported earlier (10). The maximum total conversion efficiency of photon and electrical energy to chemical energy was found to be 8.25 % whereas the corresponding photoconversion efficiency of photon to chemical energy found was 5.5 % at the grooved n-TiO_2 thin films which is half-way to the threshold efficiency of 10 % needed for a practical device.

I. INTRODUCTION

Many studies focused on photoelectrochemical splitting of water using various semiconductor materials after its discovery by Fujishima and Honda in 1972 (1) who used single crystal n-TiO_2 under externally applied potential. Efficiencies of such systems were found < 1.0. A number of approaches were attempted to overcome the need for the external applied potential for direct photoelectrochemical splitting of water. It was shown earlier on the basis of a theoretical analysis (2, 3) that a proper combination of both n-type and p-type semiconductors will yield efficient photosplitting of water without the use of any external bias potential. Kainthla, Zelenay and Bockris (4) demonstrated 8.2% conversion efficiency for photoelectrochemical splitting of water using the combination of single crystals of n-GaAs and p-InP. Multiple-junction amorphous silicon devices were also reported (5, 6). Recently, Khaseleve and Turner (7) reported an important advance in photoelectrochemical splitting of water in a self-

driven cell with 12.4% efficiency where p/n/p solar cell was used as the photocathode and Pt as an anode. The important aspect of this device is that the required potential for the photoelectrochemical splitting of water was provided internally by its built-in photovoltaic (p/n/p) component. An externally biased 12 % efficient photoelectrochemical water-splitting system involving a single crystal p-InP photoelectrode and a Pt counter electrode was reported by Heller (8, 9), However, such systems involve complex fabrication and high cost single crystal materials which are not very stable.

Recently, an externally biased nanocrystalline n-TiO_2 system was found to photo-split water with maximum 2.94 % photoconversion efficiency (10, 11) at a minimal external bias potential of 0.41 volt/NHE. Studies on n-TiO_2 is important because of its high oxidative power, stability and nontoxicity. Pyrolytically synthesized nanocrystalline n-TiO_2 films showed phonon-assisted indirect band gap energy of 2.85 eV in an earlier study (10) which is lower than that of its single crystal (3.2 eV). Furthermore, n-TiO_2 has near ideal band position to photo-split water with minimum external potential. The important aspects of such nanocrystalline n-TiO_2 systems are their high surface area, stability, low cost and simplicity in fabrication.

However, no studies were carried out earlier on photoresponse of pyrolytically synthesised nanocrystalline n-TiO_2 thin films under optimum oxygen pressure on grooved Ti metal surfaces. In this article we report both smooth and grooved nanocrystalline n-TiO_2 thin film surfaces for efficient photoelectrochemical splitting of water with the use of minimum external bias potential.

II. EXPERIMENTAL

Pyrolytic Synthesis of n-TiO_2 Films:

Titanium metal sheet (Aldrich Co) of 0.25 mm thickness was heated uniformly by a blast burner in presence of oxygen gas at a flow rate of 350 mL min^{-1}. The temperature of the flame was maintained at approximately 850 ° C to form a dark grey colored nanocrystalline titanium oxide thin film. To synthesize the grooved thin film the surface of 0.25 mm thick Ti metal sheet (Aldrich) was cut to 0.1 mm deep in the form of net and then oxidized pyrolytically to titanium oxide layer. The time of heating (5 to 15 min) was optimized for the best photoresponse for both flat and the grooved titanium oxide surfaces.

Photoelectrochemical Measurements:

Phoelectrochemical measurements were carried out using titanium oxide thin films as the working photoanodes, a Pt wire as the counter electrode and a saturated calomel electrode (SCE) as the reference electrode. The titanium oxide film was electrically connected by using a copper clip. The electrolyte solution was 5.0 M KOH. Photocurrents for the water-splitting reaction were measured using a scanning potentiostat (EG & G Model 362) as a function of applied potential and recorded in an X-Y recorder (EG & G Model RE 0092). The TiO_2 electrode was illuminated by a 150 W Xe arc lamp (Hanovia Co.) with a Kratos power supply (LPS 251 HR). The light intensity was measured by a photometer (International Light Inc. Model IL 1350) and was adjusted to 40 mW cm^{-2} through the glass window at the distance where the TiO_2 thin film electrode was placed. The photocurrent – wavelength dependences were measured using a monochromator (Kratos, Model GM 100-1).

III. RESULTS AND DISCUSSION

Photocurrent Density-Potential Dependence:

The photocurrent density, j_p (which is the measure of the rate of the photosplitting of water) as a function applied potential is given in Fig.1 both for smooth and grooved surfaces where the later shows higher photoresponse due to its high effective surface area.

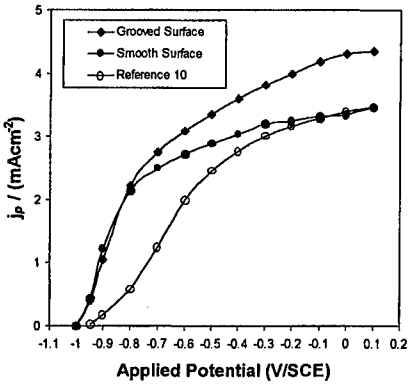


Fig. 1: Photocurrent density - applied potential dependences for grooved, smooth and also that of earlier reported (10) n-TiO_2 thin film samples.

The smooth and the grooved surfaces were pyrolysed for 6 and 8 minutes respectively at a flame temperature of 850 °C for the optimum photoresponse. Fig. 1 also shows the results of photocurrent density reported in refernce 10 which is much less than the present result. This may be due to difference in the oxygen flow rate and time of pyrolysis used during the synthesis of the TiO_2 film.

Onset Potential, E_{onset}:

The onset potential, E_{onset} can be determined from the intercept of the straight line obtained from the plot of j_p^2 versus applied potential, E_{app} according to following modified relation for the photoelectrode solution interface (12),

$$E_{app} - E_{onset} = (j_p/\alpha W_o e_o I_o)^2 \qquad (1)$$

where α is the absorption coefficient of light, W_o is the width of the depletion layer per volt of band bending having dimension m $V^{-1/2}$, e_o is the electronic charge, and I_o is the photon flux.

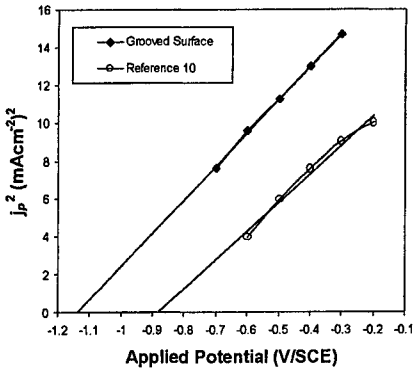


Fig. 2: Onset potential determination from j_p^2 - applied potential dependence for grooved and earlier reported (10) n-TiO_2 thin film samples.

The intercepts of the straight lines in Fig. 2 show the onset potentials of - 1.14 volt/SCE and 0.88 volt/SCE for the grooved TiO_2 surface and that of reference 10 respectively. It is observed that the onset potential at grooved TiO_2 surface is much lower than that reported earlier(10).

Quantum Efficiency:

The quantum efficiency under monochromatic light illumination, $\eta(\lambda)$ was calculated using the following relation (13),

$$\eta(\lambda) = j_p(\lambda) / e_o I_o(\lambda) \qquad (2)$$

where $j_p(\lambda)$ is monochromatic photocurrent density, e_o is the electronic charge, and $I_o(\lambda)$ is the flux of incident photon at wavelength, λ.

The quantum efficiency of n-TiO_2 films was calculated using Eq. (2), and the results are shown in Fig. 3.

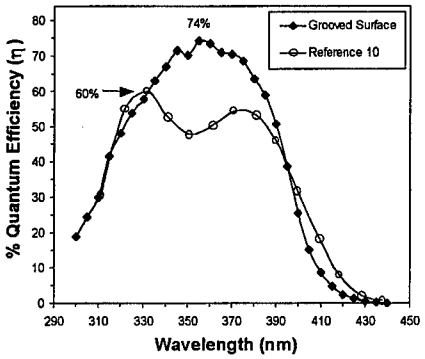


Fig. 3: The dependence of Quantum efficiency, η versus wavelength for grooved, smooth and also that of earlier reported (10) n-TiO_2 thin film samples.

The quantum efficiency starts to increase near 300 nm for both grooved and earlier reported (10) smooth TiO_2 films. The maximum quantum efficiency of 74 % was obtained at 355 nm for the grooved film. This high value of quantum efficiency indicates enhanced rate of photo-splitting of water at grooved nanocrystalline n-TiO_2 films. Fig. 3 also shows that this maximum quantum efficiency is much higher than the 60 % reported earlier (10) at 330 nm.

Bandgap Energy:

The bandgap of semiconducting TiO_2 films can be determined using the following equation (14, 15),

$$\eta(\lambda)h\nu = A(h\nu - E_g)^n \qquad (3)$$

where A is a constant, n equals either 0.5 for allowed direct transition or 2 for allowed indirect transitions. The allowed direct transition of an electron from the valence band to the conduction band by light energy, hν is not phonon assisted since such a transition does not need any change in momentum (momentum is conserved). For the indirect bandgap the transition of an electron is phonon assisted since such a transition involves change in both energy and momentum. In the case of the indirect transition, momentum is conserved via a phonon interaction, because light photons cannot provide a change in momentum (14). Furthermore, Eq. (3) is most appropriate to use when the applied potential is far from the flatband potential, so that the transport of photogenerated carriers inside the semiconductor becomes the rate determining step (16).

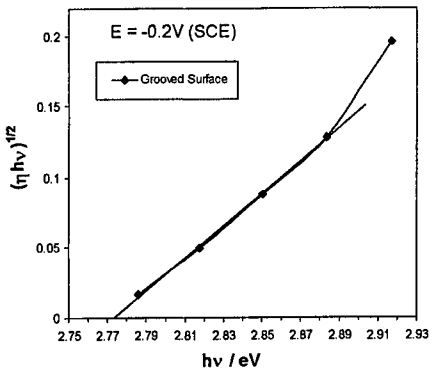


Fig. 4: Bandgap determination for grooved n-TiO_2 thin film from the intercept of straight line obtained from the plots of $(\eta h\nu)^{1/2}$ versus light energy, hν.

Fig. 4 shows the plot of $(\eta h\nu)^{1/2}$ versus hν. A straight line was observed and an intercept was obtained at 2.77 eV which corresponds to the indirect bandgap energy of the grooved n-TiO_2 films. This bandgap energy for the grooved film is smaller than that of 2.85 eV for an earlier reported (10) smooth n-TiO_2 film. These values of bandgap energy are much smaller than that of the single crystal n-TiO_2 (3.2 eV) This indicates that the

optimization of parameters of pyrolytic synthesis such as flame temperature, pyrolysis time and oxygen pressure can modify the indirect band gap of the nanocrystalline n-TiO_2 film.

Conversion Efficiency

The **total conversion efficiency** of light and electrical energy to chemical energy at a semiconductor photoelectrode in the presence of an external applied potential under illumination can be expressed as (17-20),

$$\% \varepsilon_{eff}(\text{total}) = [(\text{power output}) / (\text{power input})] \times 100$$

$$= [(j_p E^{\circ}_{rev})/I_o] \times 100 \qquad (4)$$

j_p is the total photocurrent density, E°_{rev} is the standard reversible potential which is 1.23 V/NHE for the water splitting reaction at pH = 0, I_o is the light intensity of xenon lamp in mW cm^{-2} and E_{app} is the appplied potential at the semiconducting n-TiO_2 electrode. Using I_o = 40 mW cm^{-2} and j_p = 2.7 mA cm^{-2} and E_{app} = 0.41V/NHE at pH = 0 (which is equivalent to - 0.7 volt/SCE at pH = 14.7) in Eq. 4 the conversion efficiency was found to be 8.25 % for the grooved film. For the smooth film this value becomes 7.7 % for the current density of 2.5 mA cm^{-2} at the same applied potential of –0.7 volt/SCE.

However, the **photoconversion efficiency** of light energy to chemical energy in the presence of an applied potential can be expressed as (17-20),

$$\% \varepsilon_{eff}(\text{photo}) = [(\text{power output} - \text{electrical power input})/ (\text{power input})] \times 100$$

$$= [j_p(E^{\circ}_{rev} - E_{app}l)/I_o] \times 100 \qquad (5)$$

The maximum photoconverision efficiency under xenon lamp illumination of 40.0 mW cm^{-2} was found to be 5.5 % and 5.0 % for the observed photocurrent density of 2.7 mA cm^{-2} and 2.5 mA cm^{-2} at an applied potential 0.41 V/NHE using Eq.5 for the grooved and the smooth n-TiO_2 thin films respectively (Fig. 5)[1]. However, the maximum photoconversion of 2.94 % is shown in Fig. 5 for the earlier reported (10) results at applied potential of –0.5 volt/SCE at pH = 14.7 (= 0.61 volt/NHE at pH = 0).

[1] Note that in Eq. 5 the applied potential, E_{app} must be expressed with respect to normal hydrogen electrode (NHE) corresponding to pH = 0 since E°_{rev} = 1.23 volt is with respect to NHE at pH = 0.

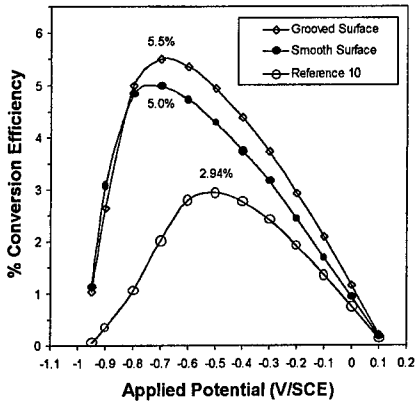


Fig. 5 The results of photoconversion efficiency versus applied potential from Eq.5 dependences for grooved, smooth and also that of earlier reported (10) n-TiO_2 thin film samples.

Such high photoconversion efficiencies at n-TiO_2 nanocrystalline grooved film are due to its high effective surface area and the lower bandgap energy of less than 3.0 eV that allows it to absorb more visible light.

In conclusion, it should be pointed out that the pyrolytically synthesized nanocrystalline n-TiO_2 thin films of optimum thickness, crystal structure on high surface area grooved surface can serve as an inexpensive and stable photoanodes for the efficient photoelectrochemical splitting of water.

IV. ACKNOWLEDGEMENTS

We are grateful for the partial support of this work by an ALCOA foundation grant.

V. REFERENCES

1. A. Fujishima and Honda, *Nature*, **283,** 37 (1972).
2. S. U. M. Khan and J. O' M. Bockris, J. Phys. Chem., **88,** 2504 (1984)
3. R. C. Kainthla, S. U. M. Khan and J. O'M. Bockris, Intl. J. Hydrogen Energy, **12,** 381 (1987).

4. R. C. Kainthla, B. Zelenay and J. O'M. Bockris, J. Electrochem. Soc., **134,** 841 (1987).
5. Y. Sakai et al., Can. J. Chem., **66,** 1853 (1988).
6. G. Lin et al., Appl. Phys. Lett., **55,** 386 (1989).
7. O. Khaselev and J.A. Turner, Science, **280,** 425 (1998).
8. A. Heller, Science, **223,** 1141 (1984).
9. E. Aharon-Shalom and A. Heller, J. Electrochem. Soc., **129,** 2865 (1982).
10. S. U. M. Khan and J. Akikusa, J. Electrochem. Soc., **145,** 89 (1998).
11. S. U. M. Khan and J. Akikusa, In Quantum Conefinement IV, Cahay et al Ed., Electrochem Soc., Pennington, NJ 1998.
12 M. A. Butler, J. Appl. Phys., **48,** 1014 (1977).
13. J. O'M. Bockris, M. Szklarczyk, A. Q. Contractor and S.U.M. Khan, *Int. J. Hydrogen Energy*, **9**, 741 (1984).
14. P. C. Searson and R.M. Latanision, *J. Electrochem. Soc.*, **135**, 1358 (1988)
15. J. I. Pankove, Optical Processes in Semiconductor, Dover Pub., Chapter 3, New York, 1971.
16. J. O'M. Bockris and S. U. M. Khan, Surface Electrochemistry, Chapter 5, Plenum Press, New York, 1993.
17. J. O'M. Bockris and O. J. Murphy, *Appl. Phys. Comm.*, **2**, 203 (1983)
18. S. U. M. Khan and S. A. Majumder, *Int. J. Hydrogen Energy*, **14**, 653 (1989)
19. S. A. Majumder and S. U. M. Khan, *Int. J. Hydrogen Energy*, **14**, 653 (1994)
20. S.U.M. Khan, and J. Akikusa, J. Phys. Chem. B, in press, 1999.

X-ray Absorption Study of Ge-Nanocluster Films

C. Bostedt[1,2], T. van Buuren[2], N. Franco[2], M. Balooch[2], T. Möller[3], L.J. Terminello[2]

[1]Universität Hamburg, Germany
[2]Lawrence Livermore National Laboratory, Livermore CA, 94550
[3]Hasylab at DESY, Hamburg, Germany

Abstract

X-ray absorption measurements at the L-edge in Germanium nanoclusters show a blue shift and broadening of the conduction band edge consistent with a distribution of quantum confinement energies. We find the magnitude of the conduction band shift is larger in the Germanium clusters when compared to silicon clusters of the same size.

Introduction

Clusters and nanocrystals show a wide variety of novel electronic, magnetic and optical properties. Germanium clusters are of particular interest, since they display a strong blue luminescence [1]. However, it is not clear, if this is due to surface species, oxide layers or quantum confinement. Quantum confinement theory predicts that the bandgap in a semiconductor cluster or nanocrystal widens compared to the bulk, with decreasing cluster size. The presented experiment focuses on probing the electronic structure of Germanium clusters deposited on a Silicon substrate. The clusters have been synthesized with a narrow size distribution in an ultra-clean environment, to unambiguously identify quantum confinement effects in these nanostructures.

Experimental

The clusters are prepared in a modification of a gas aggregation source *in situ* at the beamline. Germanium is heated up well over its melting point and the Germanium vapor is cooled down in an Argon-atmosphere. Out of the supersaturated vapor clusters condense out and are subsequently deposited on a Silicon substrate located one inch above the evaporator. The cluster size can be controlled with two parameters, the crucible temperature and the Argon pressure. Higher crucible temperatures and higher Argon pressures, respectively, force larger clusters to form. The crucible temperature is kept constant, in order to eliminate one parameter for the cluster size. The background pressure in the cluster preparation chamber is in the order of 10^{-9}-10^{-10}mTorr, to avoid contamination of the clusters.

The size of the clusters is determined with an atomic force microscope (AFM) in a non-contact (tapping) mode. Therefore witness depositions on highly orientated pyrolytic graphite (HOPG), an almost atomically flat substrate, are made. Due to the poor lateral resolution of an AFM, the clusters are assumed to be spherical and their height over the baseline is measured. The electronic structure of the clusters is probed with X-ray absorption spectroscopy (XAS) in total electron yield (TEY) mode. The experiments are performed at the Undulator Beamline 8 at the Advanced Light Source in Berkeley. In XAS a Ge2p-core electron is excited into the empty states of the conduction band. If the

conduction band of the clusters moves to higher energies by an ΔE due to quantum confinement, the absorption threshold will also shift by an ΔE to higher energies. As reference the absorption of clean bulk-Ge and GeO_2 powder is measured in addition to the cluster absorption as shown in figure 2. The experimental resolution of the absorption measurements at the Ge L-edge is approximately 0.3 eV.

Results

The AFM-pictures show that clusters in the nm-range can be produced and the cluster size clearly depends on the Argon-pressure. The cluster sizes are distributed within a relatively narrow size distribution with an average size that ranges from 2-4 nm . It is interesting to note that the clusters have a high mobility on the HOPG-substrates and they gather at step edges and defects in snowflake-like structures as shown in figure 1. This high mobility of clusters on HOPG has been observed with various types of clusters such as silicon, and antimony [2].

The XAS-spectra of bulk-Ge show in high resolution a variety of DOS features labeled a-d in the absorption edge as described in the literature [3,4]. The absorption threshold of GeO_2 is moved by approximately 5eV to higher energies compared to bulk-Ge, is different in shape and shows a strong excitonic feature below the absorption onset. The cluster absorption scans have all been energy-calibrated on a bulk absorption scan taken right before or after the cluster scan. The absorption onsets of the clusters shown in Fig. 3 are blue shifted by 0.2eV to 0.4eV compared to the bulk. The energy of the L-edge is obtained by extrapolating the linear part of the absorption edge just above the threshold to its intersection with the baseline formed by the linear extrapolation of the pre-edge part of the spectrum as shown in Fig. 3. In this case the shift of the band edge is defined as the difference between this extrapolation for the Ge nanocrystals and that for the bulk-Ge. The shift scales with the aggregation pressure and particle size, respectively. The absorption edge of the clusters is broadened compared to bulk-Ge and the DOS-features are washed out. It is interesting to note that the measured edge shift at the inflection point of the absorption edge onset is much larger. In this case the edge shift scales from 0.8eV to 1.2eV as shown in figure 4. The inflection point is located approximately at the half height of the edge jump at absorption edge onset.

Discussion

From the shape of the cluster absorption edge it can be concluded, that the clusters are crystalline and that there is no alloying with the substrate since no features due to Si-Ge bonding are observed in any of the cluster spectra [4]. We concluded that the shift in the absorption edge is not due to surface oxide since the shift of the conduction band in the Germanium clusters scales with particle size. In addition none of the cluster samples show evidence of the strong exciton peak at 1212.5 eV found in GeO_2 . Preliminary photoemission experiments show no trace of germanium oxides. Photoemission is more sensitive to surface oxygen than the absorption measurements. The broadening of the absorption onset in the cluster scans can be explained with a size distribution of the clusters, each having a different quantum shift. Yet homogeneous broadening of the edge cannot completely explain the different value of the shifts measured at the absorption onset

compared to the inflection point of the edge. One explanation is that the onset of cluster L-edge broadens due to an inherent change in the shape of the density of states. This may be due to confinement effects or a change in the cluster structure. It should be noted that structural phase transitions from the cubic to a tetragonal phase in Germanium clusters have been reported in recent publication [7]. Supplementing experiments like X-ray diffraction have to be done to determine if this is an effect in the absorption experiments.

If the observed conduction band shift is due to quantum confinement one would expect the size of the band shifts to increase as the particle size of the nanocrystalline Ge is decreased. This observed effect is shown in Fig. 4 and 5 where we plot the shift in the conduction band edge for Ge nanocluster samples with different average sizes. The conduction band shift extrapolation from the pre-edge part of the L-edge spectrum for Germanium clusters is compared to earlier measurements done at the Silicon L-edge in Silicon clusters [8]. The error bars in the energy axis of Fig. 5 indicate the measurement accuracy in determining the CB minimum. The horizontal error bars represent the full width at half maximum of the size distribution of the silicon nanoclusters. We find that the shifts in the conduction band of the Germanium clusters are much bigger. This can be explained with the lower effective mass m^* of the electrons in Germanium. Calculations, in which an electron with an effective mass m^* of Germanium and Silicon, respectively is put into a potential well with the dimensions of the corresponding cluster crystal show the same trend. However, the calculated shift of the conduction band is much larger than the measured one, because for the calculations the bulk value of the effective mass is used. This overestimates the shift, as the effective mass is expected to be bigger in clusters.

To get a complete picture of the band gap in the Germanium cluster the shift in the valence band edge as a function of cluster size is needed. Since we do not have this information yet, we can estimate a band gap assuming that the valence band shift in the Ge clusters is twice the conduction band edge shifts as observed in silicon clusters [8]. Then band gap of the 2nm Germanium clusters would be approximately 2.0 eV not large enough to produce the reported blue luminescence [1].

Summary

We were able to produce clean oxide free Germanium clusters in the nm-range and for the first time X-ray absorption data of these structures is taken. The X-ray absorption data taken from clusters in the range of 2-4nm shows a conduction band shift of 0.2-0.4eV. Comparison of the conduction band data of Germanium clusters to Silicon clusters show, that the shift in Germanium clusters is much larger. This can be explained with the lower effective mass m^* in Germanium and simple effective mass calculations of Germanium and Silicon clusters confirm this effect.

Acknowledgements

C. Bostedt acknowledges a fellowship from the German Academic Exchange Service DAAD in the HSP-III program. The work is supported by the US-DOE, BES Material Sciences under contract W-7405-ENG-48, LLNL. The ALS is supported by the US-DOE, BES Material Sciences under contract DE-AC03-76SF00098 at LBL.

References

[1] M. Zachariaf, P.M. Fauchet, Apl. Phys. Lett., **71**, 380, 1997.
[2] L. Bardotti, P. Jensen, A. Hoareau, M. Trilleux, B. Cabaud, Phys. Rev. Lett.,**74**, 4694, 1995.
[3] D.A. Papaconstantopoulus, Phys. Rev. B, **27**, 2569, 1983.
[4] P. Castrucci, R. Gunnella, M. De Crescenzi, M. Sacchi, G. Dufour, F. Rochet, J. Vac. Sci. Technol. B, **16**, 1616, 1998.
[5] J.J. Yeh and I. Lindau, Atomic Data and Nuclear Data Tables, **32**, 52, 1995.
[6] A. Goldoni, A. Santoni, M. Sancrotti, V.R. Dhanak, Surface Science, **382**, 336, 1997
[7] S. Sato, S. Nozaki, H. Morisaki, M. Iwase, Appl. Phys. Lett., **66**, 3176, 1995
[8] T. van Buuren, L.N. Dinh, L.L. Chase, W.J. Siekhaus, L. Terminello, Phys. Rev. Lett., **80**, 3803, 1998

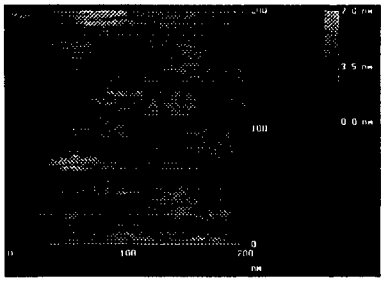


Fig. 1: Atomic force microscope picture of clusters on an HOPG-substrate. The clusters have a high mobility and gather at defects in snowflake-like structures.

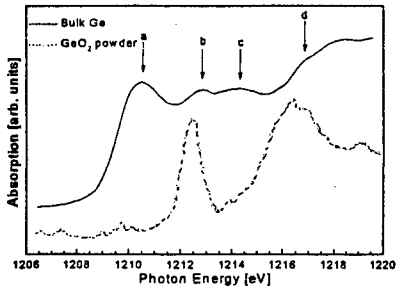


Fig. 2: Absorption spectra at the Ge2p-edge of bulk-Ge (top) and GeO_2 (bottom). Bulk-Ge shows a variety of DOS features a-d. The absorption threshold of GeO_2 is moved by 5eV to higher energies and it shows a strong excitonic feature below the absorption edge.

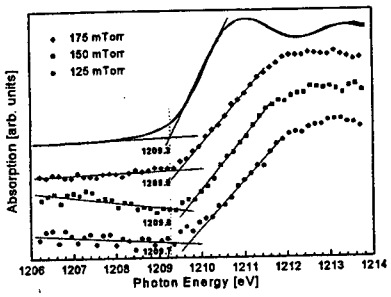


Fig. 3: Absorption data at the Ge2p-edge of bulk-Ge (top) and Ge-clusters with decreasing aggregation pressure and cluster size, respectively. The absorption onsets of the clusters are blueshifted by 0.2-0.4eV, scaling with the cluster size.

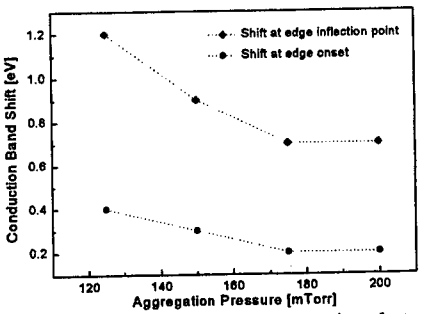


Fig. 4: Conduction band shifts in Germanium clusters as function of Ar-pressure. The shift measured at the inflection point of the absorption edge is much larger than at the absorption onset.

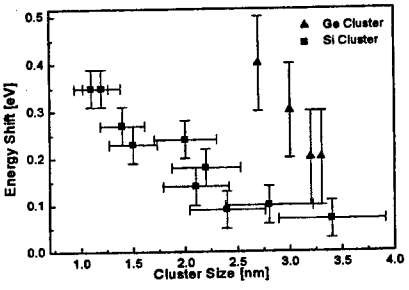


Fig. 5: Comparison of measured conduction band shifts in Silicon (bottom) and Germanium (top) clusters.

ATOMISTIC SIMULATION OF SEMICONDUCTOR NANOSTRUCTURES BY O(N) TBMD METHOD

K. Masuda-Jindo [1], M. Menon [2], K. R. Subbaswamy [2] and R. Kikuchi[3]

[1] *Department of Materials Science and Engineering, Tokyo Institute of Technology Nagatsuta, Midori-ku, Yokohama 226-8501, Japan*

[2] *Department of Physics and Astronomy, University of Kentucky, Lexington, Kentucky 40506, USA*

[3] *Materials Science and Mineral Engineering, UC, Berkeley, CA 94720-1760, USA*

The atomistic properties of nano-scale semiconductors, are studied using the tight-binding molecular-dynamics (TBMD) method. We focus our attention on the atomic reconstruction and the defects in the nano-scale crystallites and investigate their influences on the properties of the nanostructure materials. This TB theory, with only three adjustable parameters gives values of the energies and bonding distances which are in excellent agreement with the ab initio results for small semiconductor clusters. We apply the TBMD scheme for the calculations of lattice defects (dislocations) and γ-surface in the small semiconductor crystallites with the size of $N \leq 1000$. We have found that there are marked differences in the properties of lattice defects between those in the bulk and those in the nano-scale semiconductor crystallites. The similar calculations are also also performed for the nano-scale metallic systems, and qualitatively different behaviors, compared to those of the semiconductor crystallites, have been found.

1. Introduction

Recently, there has been a great interest in the study of nano-scale materials since they provide us a wide variety of academic problems as well as the technological applications [1-3]. In particular, the important experimental findings in this field are the discovery of carbon nanotubes and the discovery of superconductivity in the alkali-metal doped C_{60} system. The properties of clusters and fine particles are generally quite different from those of the bulk materials, e.g., in magnetism, catalytic activities, elastic properties and optical properties.

It is the purpose of the present study to investigate the atomistic properties of nano-scale semiconductor clusters by using the TB type of electronic theory. We

calculate the atomic configurations and electronic states of C and Si clusters including extended detects (dislocations) using the TB molecular dynamics method [4-7]. Summarizing the calculated results of the atomic and electronic structures, we discuss the physical (electrical and mechanical) properties of the clusters with or without extended defects. It is shown that the mechanical properties of the nono-scale crystallites are significantly different from those of bulk materials.

2. Principle of Calculations

The total energy of the system is assumed to be given by the sum of two terms [5,6]

$$U = U_{el} + U_{rep} = \sum_k \varepsilon_k + (1/2)\sum_{ij} \phi(r_{ij}), \quad (1)$$

where U_{el} is the sum of the one-electron energies ε_k for the occupied states, and U_{rep} represents the remaining repulsive energy contribution. Here r_{ij} is the separation of atoms i and j. The repulsive potential $\phi(r)$ is taken to be short ranged and varies exponentially with the interatomic distance. To fix absolute energies either a constant or a coordination dependent energy term is added to eq.(1).

In the nonorthogonal TB scheme the characteristic equation is written, in matrix form, as

$$(\mathbf{H} - E_n\mathbf{S})\mathbf{C}^n = 0, \quad (2)$$

where $\mathbf{C}^n$ is a column vector or LCAO coefficients. $\mathbf{H}$ is the Hamiltonian matrix and $\mathbf{S}$ the overlap matrix of the LCAO basis set.

The Hellmann-Feynman theorem for obtaining the electronic part of the force can be obtained from

$$\partial E_n / \partial x = \mathbf{C}_n^{*}[\partial\mathbf{H}/\partial x - E_n \partial\mathbf{S}/\partial x]\mathbf{C}^n / \mathbf{C}^{n*}\mathbf{S}\mathbf{C}^n, \quad (3)$$

where $\mathbf{C}^n$ vectors are normalized so that

$$\mathbf{C}^{*}\mathbf{S}\mathbf{C} = 1. \quad (4)$$

In the conventional TB (orthogonal) approach, the basis set is presumed to be an orthogonal set $S_{ij}=\delta_{ij}$. In the Slater-Koster scheme the Hamiltonian matrix elements are given in the two-center forms, which are assumed to decrease exponentially with the

interatomic distance r_{ij}.

The eigenvalues of a system with nonorthogonal basis set can then be obtained from

$$\det | H_{ij} - ES_{ij} | = 0. \qquad (5)$$

Evaluation of (5) is expedited by the use of the well known Cholesky factorization in which **S** is factored into $\mathbf{S} = \mathbf{BB}^{+}$. This factorization is always possible provided **S** is positive definite.

The above mentioned TB theory [5,6] involves six parameters, atomic energy terms E_s and E_p, the covalent radius (d_0), the interaction falloff rate α, the nonorthogonality constant K and the repulsive coefficient χ_0. Of these, E_s, E_p, d_0, and two center integrals $V_{\lambda\lambda'\mu}$ are set a priori from Harrison's universal TB scheme. Thus, in the present TB scheme, there are only three adjustable parameters, α, K and χ_0. These parameters can quite simply be fitted to the related experimental values. We use this type of non-orthogonal TB scheme for treating clusters of $N \leq 200$.

For treating larger atomic clusters of $N \geq 200$, we use the density matrix (DM) method by LNV [8,9]. To check the dependence of the calculated results on the TB scheme, we will use both orthogonal and non-orthogonal TB schemes.

The density matrix (DM) methods have been proposed by Li et al[8,9], and Daw[10], through from different arguments. In terms of the density matrix $\hat{\rho}$, the number of electrons in the system, the band energy for $k_BT=0$ and the corresponding contribution to the forces from the band energy can be given by

$$N_e = 2Tr[\hat{\rho}] \qquad (6)$$

$$U = 2Tr[\hat{\rho}\hat{H}] \qquad (7)$$

$$\vec{F}_i = -2Tr[\hat{\rho}\frac{\partial \hat{H}}{\partial \vec{R}_i}], \qquad (8)$$

where *Tr* indicates taking the trace of a matrix. The ground state energy for $k_BT=0$ can be found by minimizing U with respect to ρ subject to two constraints: idempotency of the density matrix ($\hat{\rho}^2 = \hat{\rho}$, which is equivalent to $\hat{\rho}$ having eigenvalues of 0 and 1) and constant number of particles (N_e = constant). To impose idempotency on the density matrix, it is replaced with the result of the McWeeney tranformation of a trial density matrix,

$$\tilde{\rho} = 3\hat{\rho}^2 - 2\hat{\rho}^3, \qquad (9)$$

where $\hat{\rho}$ is identified as the trial density matrix and $\tilde{\rho}$ is the physical density matrix, such that the expectation value of an operator $\hat{A}$ is given by $Tr[\tilde{\rho}\hat{A}]$.

We will use the orthogonal TBTE parameters of Kwon *et al.*, [11] which describe well the acoustic-phonon modes and elastic constants of Si, thus being adequate to to describe the strain fields associated with the dislocation cores and related defects. Owing to its good transferability between different crystal structures, ranging from diamond to fcc, this Hamiltonian is also expected to give a good description of the coordination defects in the present study. For the density matrix, we work at a real-space cutoff R_c = 6.2Å.

The DM method can be also used in a non orthogonal basis by defining the two quantities,

$$\begin{aligned} \overline{X} &= S^{-1}XS^{-1}, \\ \overline{\rho} &= 3\overline{X}S\overline{X} - 2\overline{X}S\overline{X}S\overline{X}, \end{aligned} \tag{10}$$

as alternative representation[8,9] for the trial and physical density matrices, respectively. We observe that $\overline{X}$ is a more natural representation of the density operator, in the sense that Eq. (9) still holds, i.e., $\overline{X}_{ij} = \sum_n c_{ni}^* c_{nj}$, whereas $X_{ij} = \sum_n \sum_{kl} S_{ik} c_{nk}^* c_{nl} S_{lj}$. Furthermore, the expectation value of any operator is given by $\langle \hat{A} \rangle = tr[\overline{X}A]$, where $A_{ij} = \langle \phi_i | \hat{A} | \phi_j \rangle$.

In terms of $\overline{X}$ *and* $\overline{\rho}$ the particle number becomes

$$N_e = tr\left[(3\overline{X}S\overline{X} - 2\overline{X}S\overline{X}S\overline{X})S\right], \tag{11}$$

and the energy functional is written

$$\Omega = tr\left[(3\overline{X}S\overline{X} - 2\overline{X}S\overline{X}S\overline{X})H'\right]. \tag{12}$$

To apply the nonorthogonal DM method, we use the above mentioned TB parameterization by Menon et al. [5,6].

3. Results and Discussions

a) Carbon Cluster

The discovery of carbon nanotubes with unusual geometric and electronic properties has generated considerable interest [3]. These tubes can be visualized as graphitic sheets rolled up into cylinders giving rise to quasi-one dimensional structures. Firstly, we briefly summarize the MD calculatious for carbon-related materials [5,6].

There are two kinds of carbon nanotubes, with type *A* and type *B* structures. The tube of type *A* is constructed by taking two layers of carbon atoms forming the equatorial belt structure resulting in a hollow tube. The ends of the tube are then terminated by placing the polar caps of C_{70}, resulting in a D_{5h} structure. Tube B can be obtained by rotating the hexagons forming the hollow of tube A by 90 ° and terminating the ends by placing a polar cap with threefold rotation symmetry, resulting in a D_{3h} structure. In this tube there are a series of carbon-carbon bonds parallel to the tube axis.

Tube A showed no appreciable Jahn-Teller distortions on relaxation using the TB molecular dynamics method. The relaxed structure was found to be metallic with no gap between the highest occupied molecular orbital (LUMO). Tube *B*, however, showed considerable symmetry lowering Jahn-Teller distortions. The relaxed structure was found to be semiconducting, with a gap of 0.7 eV. Furthermore, tube *B*, was found to be slightly more stable than tube *A* (by 0.5 eV).

We next consider the graphite sheet. Graphite is a prototype sp^2 covalent solid, with two atoms in the unit cell, with nearest-neighbor bond length less than the sum of the covalent radii of the carbon atoms. We obtain a nearest-neighbor bond length of 1.42 Å. The computed band structure is in good agreement with accepted band structure calculations. The dynamical matrix for graphite is calculated by special point averaging in the irreducible two-dimensional zone, to be 1588 cm^{-1} for the E_{2g} mode, in excellent agreement with the experimental value of 1582 cm^{-1}. For the A_{2u} mode, we calculate a value of 695 cm^{-1}, in reasonable agreement with the experimental value of 868 cm^{-1}.

We now turn to the discussions of structural defects in nano-scale materials [12-17]. In Fig. 1, we present the calculated atomic configurations of edge dislocation in two-dimensional (2D) planar C_{92}, C_{147} and C_{196} clusters. The core structure of the edge dislocation is characterized by the five- and seven-memvered rings in the 2D carbon clusters. The excess energies due to introduction of the edge dislocation are also estimated by comparing the energies of carbon clusters with and without the edge dislocations. In Fig. 2, we show the relative stability (excess energies) of the carbon clusters, as a function of the size of the clusters N (number of atoms). The energy is given in unit of eV/atom, relative to that of C_{142} cluster without edge dislocations. One can see in Fig.2 that there are no marked differences in the stability between the clusters with and without edge dislocations. We have also checked that this tendency is also true when we use the orthogonal TBMD scheme by Kwon et al. [11].

This indicates that the self-energy of the edge dislocation is very small and may become even negative for the certain clusters. Then, we come to the conclusion that the dislocation can be generated spontaneously without sizeable activation energy in the

small semiconductor clusters. In other words, the semiconductor clusters such as the 2D graphite-like clusters, can be mechanically deformed more easily compared to the corresponding bulk materials. The continuum elasticity theory also predicts that the elastic distortion energy of lattice defects depends on the exsistence of the free surfaces due to the so-called image effect [12-14], compared to those in the infinite crystals. However, the above mentioned cluster size dependence of the self-energy of the dislocation can not be explained within the continuum elasticity theory.

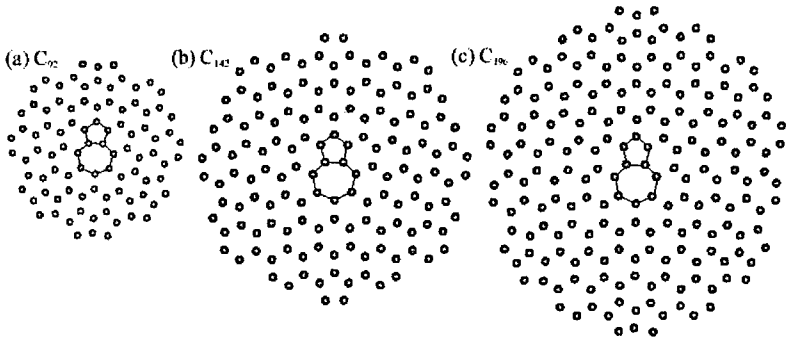


Fig.1 Atomic configurations of edge dislocations in C_{92}, C_{142} and C_{196} clusters.

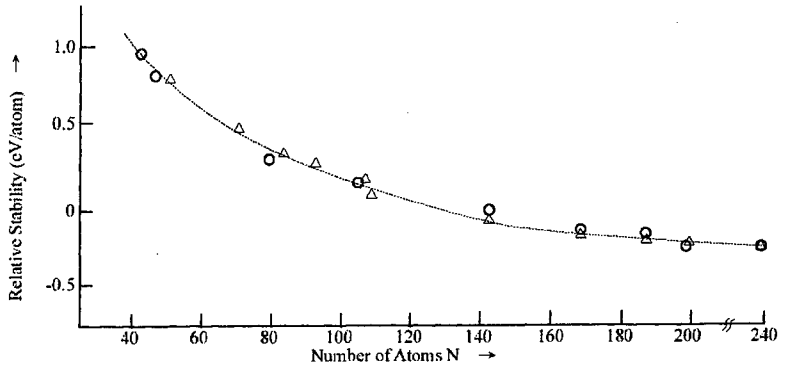


Fig.2 Relative stabilities of carbon clusters with and without edge dislocations are shown by symbols Δ and O, respectively. The energy is given in unit of eV/atom, and the origin is taken to be that of C_{142} cluster without edge dislocation.

The more detailed information on the glide behavior of the edge dislocation of graphite or 2D carbon clusters can be obtained from the γ-surface calculations [17]. In Fig.3, we present some of the atomic configurations which are formed during the rigid

body translation between the upper- and lower-half crystallites, both for (11) and (10) planes. The γ-surface calculations have been performed for larger carbon clusters $\sim C_{200}$ and the results of energy barriers as a function of the rigid body translation R_{sh} are shown in Fig.4.

Due to the geometry of the clusters, the period of the potential barriers on the (11) and (10) planes are different, and they are $\sqrt{3}/2$ and 3.0, respectively, in unit of the nearest-neighbour distance d_0. One can see in Fig.4 that the rigid body translation on (11) plane occurs more easily compared to that on (10) plane, indicating the easy (11) glide plane.

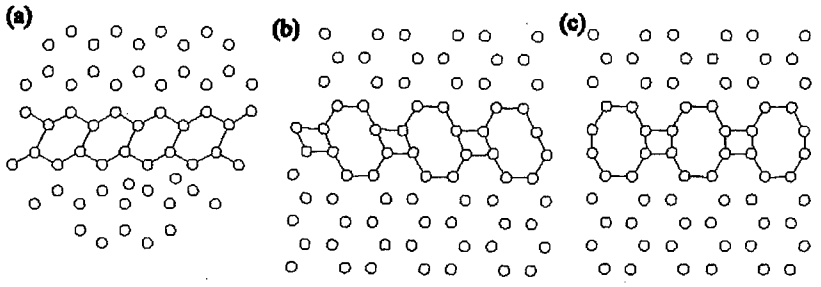


Fig. 3 Atomic configurations formed during the rigid body translation: (a) is for (11) plane, while (b) and (c) for (10) plane.

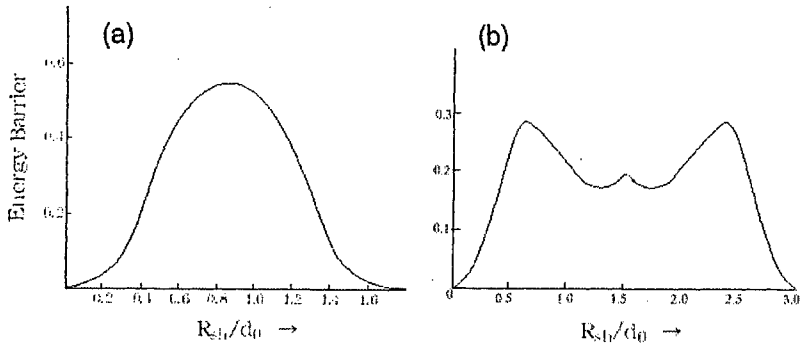


Fig. 4 Energy barriers (arbitrary unit) for the rigid body translation on (11) and (10) planes in 2D planar carbon clusters.

We now discuss the properties of dislocations in Si clusters, in comparison with the lattice dislocation in diamond cubic Si crystal. In a diamond cubic crystal, the important dislocations are the 60°, screw and 90° (edge) perfect dislocations [12-16]. The

first one dissociates into a 30° and 90° partial dislocations while the others splits into a pair of 30° and 60° partial dislocations, respectively. All the partials are separated by intrinsic stacking faults. These partials, which have line directions along <110> are believed to be reconstructed into a structure with no dangling bonds.

The atomic configurations of 30° partial dislocations in Si_{150} and in bulk Si crystal are shown in Figs. 5a and 5b, respectively. In Fig.5a, the reconstruction defects "solitons" can be seen near the center of the crystallite. These point singuralities "solitons" in the small crystallites are formed by the atomic reconstruction, which is initiated at the surfaces and then propagate into the interior region of the crystallite. Therefore, depending on the size of the cluster, e.g., for odd number of core atoms, there remains isolated single point singularity "soliton". In contrast, for the clusters with even number of core atoms, there arises no point singularity along the dislocation line.

The core structure of the dislocation in bulk crystal is calculated as follows: In order to save computational CPU time for the simulation of dislocations in the bulk crystal, the initial atomic configuration is chosen to be the artificial reconstructed structure. Therefore, in the calculation of dislocations in bulk crystals, no point singularities appear spontaneously in the process of the computer MD simulations. It is noted that in real crystals such point-like singularities do exist as thermodynamical defects, like vacancies in the crystals at finite temperatures. In this respect, the appearance of the soliton in the dislocation line is different in nature from that in the small crystallite.

The kink on the dislocation line can be modelled by breaking and forming bond in such a way that the stacking fault is advanced to the next Peierls valley [18]. The jugs A and B as ahown in Fig.5 (b), are formed by the side-wide motion of the indivisual kinks after the smallest double kink formation: This type of the double kink nucleation occure as a thermally acctivated process and can not be simulated by the computer experiments.

Figure5(b) shows the kink pair structure along the 30° partial dislocation in the bulk Si crystal. It is noted that there are two types of kinks along the 30° partial. Two five-membered rings are placed through the formation of the double kink by a four-and six-membered ring at A and by a five-and six-membered ring at B. The kinks along the 90° partial have identical structures and can be described as a trasfer of two six-membered rengs to a five-and a seven-membered ring. The kinks are fully coordinated and have the same local geometry for trailing and leading partials. We have found that no gap states associated with the kinks appear in the core of 30° 90° partial dislocations.

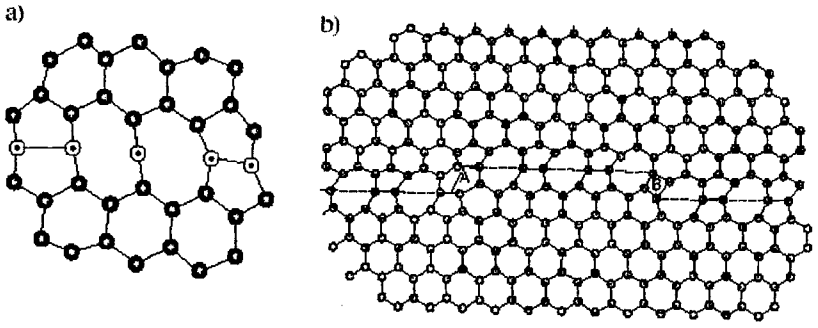


Fig. 5 Core structure of 30° partial dislocations in Si cluster (a) and in bulk Si crystal (b). Soliton like defect can be seen in a) and double kink A and B in b). In figure a), "core atoms" are shown by symbols ⊙.

b) Dislocations in Metallic Clusters

We now investigute the dislocation properties of the metallic clusters. Firstly, we briefly review the dislocation properties of bulk fcc metals.

Without applied stress, a spontaneous dissociation of the perfect edge dislocation (burgers vector b_1 and b_2) occurs: $\frac{1}{2}[1\bar{1}0] \rightarrow \frac{1}{6}[1\bar{2}1] + \frac{1}{6}[2\bar{1}\,\bar{1}]$. The resulting deformation profile exhibits two peaks, each identifying the position of the partials[19]. Recently, Aslanides and Pontikis, using the N-body phenomenological potentials, found a dissociation distance, d = 9.1Å while the elastic theory predicts d = 7.7Å, a result that is obtained by using calculated values of the shear modulus C_{44} and stacking fault energy, γ, at T = 0 K. Both values are in good agreement with experimental observations suggesting the dissociation distance to be smaller than 8Å. It has been found that the narrow ribbon fault separating the two partials is very different from the perfect stacking fault considered in the elastic approach. Moreover, the limited extension of the simulation box in the $[1\bar{1}0]$ direction and the associated free surface boundary condition implies that image forces are far from being negligible. These increase the dissociation width but their influence is still limited as is shown from the small difference existing between the two evaluations, elastic or atomistic, of the dissociation distance[19]. Due to a low stacking fault energy in copper, the equilibrium dissociation distance is larger than that in aluminium (d = 52.4 Å).

We have also employed many body potentials as used in Ref. 19, and studied the dislocation properties, separation of the partials and self-energies, in the (Cu and Au)

metallic clusters. We have found no marked differences in the properties of dislocations of the clusters compared to those of the bulk metals.

c) Electronic Structure of Semiconductor (Si) Clusters

Semiconductor nanoclusters are crystallites of semiconductor material with diameters between 10 and 100Å. Their atomic structure is similar to that of bulk semiconductor as shown by x-ray studies and electron microscopy. The optical and electronic properties differ markedly from the bulk and are strongly size-dependent [20-22]. The size-dependence is evident in the increase in the fundamental band gap and first absorption energy as the cluster size is decreased. The electronic and optical properties of nanoclusters are explained qualitatively by assuming that the electrons and holes are confined within the nanocluster, known as "quantum size" effect.

It is known that the optical properties of the semiconductor clusters are affected strongly by the degree of crystallinity [23]. A cluster riddled with defects will have a large number of trap sites which may, e.g., give rise to broadening of the exciton spectrum. While the structure of these clusters has been assumed to be identical to that of an infinite crystal, little is actually known about the atomic arrangement inside the clusters[23]. In general, there are experimental difficulties in the structural characterization.

Although Si has an *indirect* band gap (1.13 eV), pristine Si has poor optical radiative efficiency at threshold, recent experimental observations on porous Si have shown that Si quantum wires exhibit strong visible photoluminescence (PL) around 4.6 to 2.5 eV at room temperature with a size-dependent peak position. These obserrations have stimulated intense experimental and theoretical studies on the semiconductor nanostructures. Calculation of nanocluster properties is complicated by the fact that they contain too many atoms to use the *ab initio* techniques like quantum chemistry. However, effective mass approximation (EMA) is not accurate for calculating electronic states away from the Γ point, or for treating indirect band gap semiconductors. In the present study, we will investigate the properties of the semiconductor clusters including defects like lattice dislocations, because this type of lattice defects is to exist in the semiconductor nanostructures. Forthermore, it is noted that amorphous phase can be modelled by array of the lattice dislocations [24-26]. One can regard an amorphous structure as a crystal containing many dislocations in it.

We have performed atomic and electronic structure calculations of the silicon clusters, both with and without dislocations. We have confined the atomic relaxation within the first four surface layers of the clusters. Therefore, for small Si clusters like Sis,

only breathing mode relaxations are allowed to get minimum energy configuration.

For simplicity, we do not include hydrogen atoms during the atomic relaxation process of the silicon clusters. After relaxation calculation of the cluster structure, hydrogen atoms are bonded to the surface atoms to eliminate the surface dangling bonds.

We introduce a shuffle-set screw dislocation in Si clusters with N≥200. There are both compressed and stretched bonds in the core region of the dislocations, and one-dimensional symmetry along the dislocation line is preserved. One can expect that the effects of compressed and stretched bonds in the dislocation core almost cancel and important effects comes from the volume relaxation, as shown below.

The model of hydrogenarated Si clusters in the present study is identical to that used by Ren and Dow [27]. It is assumed that the H-saturated dangling bonds on the surface of the cluster have the natural H-Si bond length of d=1.48Å. We use the sp^3s^*-basis TB scheme for the electronic structure calculations which yields accurate valence bands and good conduction bands near the fundamental gap for bulk Si . There are five basis orbitals per Si site for the Hamiltonian , i,e., s, p_x, p_y, p_z and an exited s state, s*. Only on-site and nearest-neighbor matrix elements are taken into account. Each H has only a single s orbital whose free-atom energy level, taken to be the same as that of Si. The nearest-neighbor matrix-elements between the host Si and H atoms are estimated by using the Harrison's universal raw.

To calculate the electronic density of states (DOS) of Si clusters, we use the Chebychev moment method introduced in [28]. Consider the calculation of the DOS of an N x N Hamiltonian H, with eigenenergies ε_n. The first step is to put lower, ε_l and upper, ε_u, bounds on the energies in the DOS. A scaled Hamiltonian matrix, X, is defined by H = aX + b, where $a \equiv (\varepsilon_u - \varepsilon_l)/2$ and $b \equiv (\varepsilon_u + \varepsilon_l)/2$. Eigenvalues of X satisfy $-1 \leqq x_n \leqq +1$. The scaled DOS can be represented by a polynomial expansion,

$$D(x) = \frac{1}{N}\sum_{n=1}^{N}\delta(x - x_n) = \frac{1}{\pi\sqrt{1-x^2}}[\mu_0 + 2\sum_{m=1}^{\infty}\mu_m T_m(x)]. \quad (13)$$

The $T_m(x)$ are Chebyshev polynomials of the first kind defined by recurrence relations,

$$T_0(x) = 1,\ T_1(x) = x, \quad (14\text{-a})$$

$$T_{m+1}(x) = 2xT_m(x) - T_{m-1}(x). \quad (14\text{-b})$$

Chebyshev polynomial approximations are an efficient and numerically stable way to calculate properties of the very large Hamiltonians important in computational condensed matter physics. For tight binding Hamiltonians of Si, high precision and rapid convergence of the cohesive energy and density of states are obtained.

In the present study, we calculate a finite number of moments, M, and we focus on how best to use them. Abrupt truncation of eq. (13) would result in unwanted Gibbs oscillations. The kernel polynomial method (KPM) considers instead smooth truncation of the form

$$D_K(x) = \frac{1}{\pi\sqrt{1-x^2}}[\mu_0 g_0 + 2\sum_{m=1}^{M} \mu_m g_m T_m(x)]. \qquad (15)$$

The g_m are Gibbs damping factors which depend implicitly on M. The relation of this estimate to the true DOS is

$$D_K(x) = \int_{-1}^{1} K(x, x_0) D(x_0) dx_0, \qquad (16)$$

where the kernel polynomial is

$$K(x, x_0) = \frac{1}{\pi\sqrt{1-x^2}}[g_0 + 2\sum_{m=1}^{M} g_m T_m(x) T_m(x_0)]. \qquad (17)$$

To obtain the electronic DOS of Si clusters with defects, we have calculated the Chebycherv moments up to 100 levels.

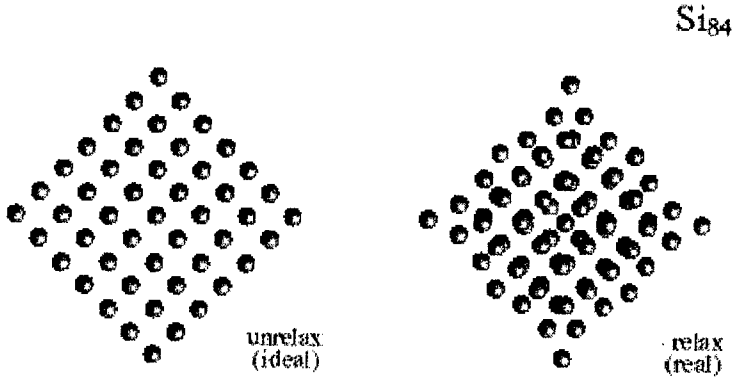


Fig.6 Atomic configurations of Si_{84} cluster (quantum dot)

In the present calculation, we take the semiconductor clusters of spherical shape as well as box or wires with square cross sections; e. g., a wire along(001) with free surfaces $(110)\times(1\bar{1}0)$. In this case, there are danagling bonds on the wire surface, leading to surface states in the band gap. The surface states are discarded bacause we are interested in transitions between bulk like states in the quantum nanostructures.

Figure 6 shows an atomic configuration of Si_{84} cluster (with (111) surface), calculated by the present TBMD method. One can see that the cluster volume is decreased strongly, and there are heavily compressed bonds in the clusters. We have found that this tendency of volume shrinkage is seen more strongly for smaller crystallite. Figure 7 shows the atomic geometry of a Si_{1390} cluster including a shuffle-set screw dislocation. In general, one can expect that the compressed bonds play a dominant role in determining the electrical properties (band gap width) of the semiconductor clusters. We have obtained a similar tendency of the energy gap of the Si clusters as reported by Ren and Dow[27], but systematically wider separations between the highest occupied valence states and lowest unoccupied conduction state, due to the exsistence of the heavily distorted (compressed) bonds.

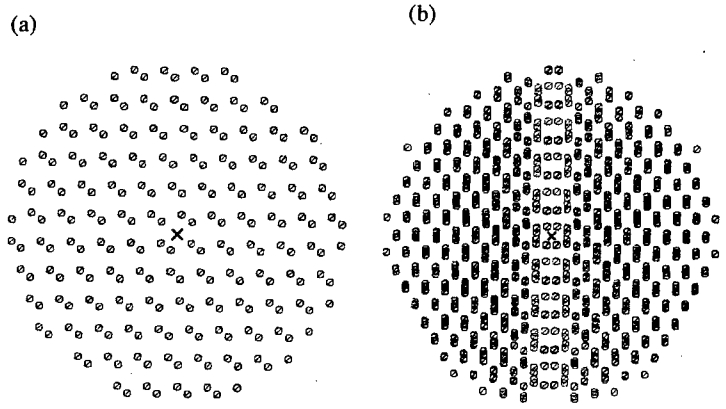


Fig.7 Atomic geometry of Si_{1390} containing a shuffle-set screw dislocation: (a) [110], and (b) [111] view. x simbols in the figure represent the center of screw dislocation.

6. Summary

We have employed a minimal parameter generalized tight-binding molecular dynamics scheme for the calculations of the semiconductor clusters with extended defects like deslocations. It has been shown that inclusion of nonorthogonality in tight-binding theory in conjunction with a judicious choice of parameters can provide results in good agreement with experiment. The scheme is considerably faster than *ab initio* or LDA methods. This has been achieved by incorporationg very few parameters and a simple scaling with distance of the parameters.

In the present study, we have focused on the atomic structures of semiconductor clusters including the extended defects and investigate the influence of the distorted bonds on the electrical and optical properties of the clusters. It has been shown that there are marked differences in the properties of lattice defects in the clusters and those in the bulk crystals. The excess energies of dislocations in the small clusters are very small and often take negative values. The core reconstruction of the dislocation in the small crystallites occurs in a different manner compared to those in the bulk crystals. These theoretical findings can suggest that the deformation behavior and mechanical properties of the small clusters depend strongly on the size of the clusters and are quite different from those of the bulk materials.

We have obtained slightly different tendency, i. e., systematically larger band gap, for the size dependence of the band gap of the Si clusters. This tendency comes from the fact that the effect of compressed bonds is stronger than that of the stretched bonds in the core of the dislocations.

References

[1] H.W. Kroto, J.R. Heath, S'.C. O' Brien, R.F. Curl and R.E. Smally, Nature **318**, 162 (1985).

[2] W. Kratschmer, L.D. Lamb, K. Fostiropoulos and D.R. Huffman, Nature **347**, 354 (1990).

[3] S.Iijima, Nature **354**, 56 (1991).

[4] K.Laasoneu and R.M. Nieminen, J. Phys: Condens. Mater. **2**, 1509 (1990).

[5] M. Menon, and K. R. Subbaswamy, Phys. Rev. **B50**, 11577 (1994).

[6] M. Menon, E. Richerter and K. R. Subbaswamy, J. Chem. Phys. **104**, 5875 (1996).

[7] M. Aoki, Phys. Rev. Lett., **71**, 3842 (1993).

[8] X. P. Li, R. W. Nunes and D. Vanderbilt, Phys. Rev. **B47**, 10891 (1993).

[9] R. W. Nuned and D. Vanderbilt, Phys. Rev. **B50**, 17611 (1994).

[10] M. S. Daw, Phys, Rev. **B47**, 10895 (1993).

[11] I. Kwon et al., Phys. Rev. B49, 7242 (1994).
[12] J.P. Hirth and J. Lothe, "Theory of Dislocations", (McGraw Hill, New York, 1968).
[13] V Vitek, Cryst. Lattice Defects **5**, (1975) 1; Prog-Mater. Sci. **36**, 1 (1992).
[14] H. Alexander and H. Teichler, Mater. Sci. and Tech. **4**, 249 (1991).
[15] K. Masuda-Jindo, Solid State Phenomena, **37-38**, 125 (1994).
[16] K. Masuda-Jindo, Superlattices and Microstructures **16**, 359 (1994); ibid., **20**, 117 (1996).
[17] K. Masuda-Jindo, M. Menon, K. R. Subbaswamy and M. Aoki, Comp. Mat. Sci., **14**, 203 (1999).
[18] R. W. Nunes, J. Bennetto and D. Vanderbilt, Phys. Rev. Lett., **77**, 1516 (1996).
[19] A. Aslanides and V. Pontikis, Comp. Mat. Sci., **10**, 401 (1998).
[20] A. Zunger and Lin-Wang Wang, Appl. Surf. Sci. **102**, 350 (1996).
[21] Chin-Yu Yeh, S. B. Zhang, and A. Zunger, Phys. Rev. B**50**, 14405 (1994).
[22] M.G. Bawendi, A.R. Kortan, M.L. Steigerwald and L.E. Brus, J. Chem. Phys. **91**, 7282 (1989).
[23] J. J. Gilman, J. Appl. Phys. **44**, 675 (1973).
[24] J. C. M. Li, Distinguished Lectures in Materials Science (Masrcel-Decken, NewYork, 1974).
[25] H. Koizumi and T. Ninomiya, J. Phys. Soc. Jap., **44**, 898 (1978).
[26] S. Y. Ren and J. D. Dow, Phys. Rev. B**45**, 6492 (1992).
[27] A. F. Voter, J. D. Kress and R. N. Silver, Phys. Rev. B**53**, 12733 (1996).
[28] M. Lannoo, C. Delerue, and G.Allan, Phys. Rev. Lett. **74**, 3415 (1995).

Novel Nanoscale Devices

PRECISE NANOELECTRONICS WITH ADATOM CHAINS

Toshishige Yamada*
MRJ, NASA Ames Research Center, M/S T27A-1, Moffett Field, California 94035-1000

ABSTRACT

Adatom chains on an atomically regulated substrate will be building components in future precise nanoelectronics. Adatoms need to be secured with chemical bonding, but then electronic isolation between the adatom and substrate systems is not guaranteed. A one-dimensional model shows that good isolation with existence of surface states is expected on an s-p crossing substrate such as Si, Ge, or GaAs, reflecting the *bulk* nature of the substrate. Isolation is better if adatoms are electronically similar to the substrate atoms, and can be manipulated by hydrogenation. Chain structures with group IV adatoms with two chemical bonds, or group III adatoms with one chemical bond, are semiconducting, reflecting the *surface* nature of the substrate. These structures are unintentionally doped due to the charge transfer across the chemical bonds. Physical properties of adatom chains have to be determined for the unified adatom-substrate system.

I. INTRODUCTION

When the gate length is reduced to 0.07 μm in a field-effect-transistor, the number of dopant atoms in the active region is no longer macroscopic, typically less than a hundred [1-3]. The spatial distribution of these dopant atoms fluctuates statistically from device to device even though each device is identically designed and fabricated, and this places a serious limitation on integration density. If device fabrication with atomic-scale accuracy [3] is required to overcome this problem, then it would be logical to create the entire electronics with components that are atomically precise, ordered, and preferably simple. This can be called precise nanoelectronics. Atomic chains, which are precise structures of adatoms created on an atomically regulated surface using atom manipulation technology [4], would become constituent components in future electronics. All the adatoms are placed at designated positions on a substrate, and all the device structures are precise, free from any statistical deviations. It was predicted using a tight-binding method with universal parameters [5, 6] that Si chains were metallic and Mg chains were semiconducting regardless of the lattice spacing [7], and a possible doping scheme was also proposed [8], when all the influences of the substrate were neglected for mathematical simplicity.

In practice, the substrate is quite influential on adatom chain properties, since the substrate must serve as a template for mounting the adatoms so that they are confined with a reasonable strength, and yet it must be electronically isolated from the adatom system. There are two possible physical mechanisms to secure adatoms at designated positions: Van der Waals bonding and chemical bonding. To evaluate the former strength, an *ab initio* study has been performed for a Mg adatom on the hydrogenated Si (111) surface [9] using a cluster model of $Si_{13}H_{22}$. It turns out that the Mg adatom will not be confined satisfactorily even at liquid-helium temperatures, with a Van der Waals potential as small as

0.39 meV [10]. The situation may not improve drastically for other kinds of substrates. Thus, we need to rely on the chemical bonding scheme. The main concern with this scheme is electronic isolation: the adatom wave function penetrates deep into the substrate through chemical bonds, and independent adatom structures couple, leading to unwanted cross talk. This problem is closely related to surface localization or how the wave function decays into the substrate. We use a chain model and clarify the existence conditions for surface states. H atoms can manipulate the surface states in a complementary manner on two distinct types of substrates. A method for obtaining semiconducting adatom chains is described with special requirements for the number of chemical bonds.

II. SURFACE LOCALIZATION AND ELECTRONIC ISOLATION

Edge (or end) states, zero-dimensional counterparts of higher-dimensional surface states, will be studied by using a chain model to represent a substrate. Surface states are supported by many atomic planes parallel to the surface as we will see later. Besides the difficulty in multi-dimensional modeling with many layers, the physics we are interested in is essentially one-dimensional, so the chain model suffices for a qualitative study. In fact, the wave function decays vertically since a reflection from each atomic plane interferes more destructively at a deeper point. This destructive interference is the origin of the surface states, and is one-dimensional in nature. In application of the edge state results to surface states, we can rely on a perturbation picture. When infinitely separated chains are brought together side by side in an array to form a finite substrate so that chain edges will form substrate surfaces, the energy levels corresponding to the edge states start widening. Since the bulk valence and conduction bands are widening, the bulk band gap is narrowing. As long as chains are distant, the adatom band widths are narrow and the entire adatom bands are located inside the bulk band gap. In this situation, the existence conditions for the edge states are equivalent to those for the surface states. When chains are brought closer, the adatom bands may overlap with the bulk bands, but the valence band maximum and conduction band minimum that are most important for electronics applications edge to remain inside the bulk band gap. Thus, the behavior of the edge states will survive in this limit. In the following, energy levels for a finite chain with edge adatoms are calculated as a function of lattice spacing d. Such plots show how surface states originate from atomic levels of constituent atoms as d is reduced and the crystal is formed [11, 12].

We might think intuitively that unsaturated (dangling-bond) states always localize at the surface, but this is not the case. Figure 1 shows electronic states of a Si atomic chain with an s-orbital and a p-orbital (representing symmetric and antisymmetric bases) as a function of atomic spacing d, calculated with the tight-binding theory with universal parameters [5, 6]: (a) energy levels and (b) edge population for states with thick line in unsaturated chain of 24 Si atoms; (c) and (d) are the same set of plots for a hydrogenated chain of 22 Si atoms. These results are essentially the same if the number of atoms is greater than 16. In both unsaturated and hydrogenated cases, the majority of levels, bulk-penetrating modes, behave similarly. When d is large, we see 3s and 3p bands in principle. Band widths increase as d is reduced. At $d \sim 2.7$ Å, both bands meet. This is an s-p crossing point and the spacing is denoted by d_{spc}. For $d < d_{spc}$, a band gap reopens.

In the unsaturated case, edge states appear for $d < d_{spc}$ as shown in Fig. 1(b). They are significant mixtures of s- and p-states and there is no apparent correlation for isolated atomic states. There are two edge states, one from the valence band and the other from the conduction band as is obvious by examining the number of states, and they constitute

symmetric and antisymmetric modes for the chain center. Twenty-four states will be filled if all the atoms, including adatoms, are assumed to create two chemical bonds to the neighboring chains, and thus the edge states are half-filled. Since the filling can be changed by changing the number of adatom chemical bonds, we can eventually design metallic or semiconducting structures using this property as will be discussed in Sec. III.

In the hydrogenated case, edge states appear for $d > d_{spc}$. They are mostly s-like as in Fig. 1(d), and are identified as isolated 1s states in H. For $d < d_{spc}$, edge states disappear. Thus, the edge states in the hydrogenated case behave in a complementary manner to those in the unsaturated case. Counting an electron from each H atom, twenty-three states are filled, and edge states are again half-filled if the substrate atoms create two chemical bonds to the neighboring chains.

The physical mechanism for this complementary behavior can be intuitively understood as follows. Figure 2 schematically shows the envelope of a wave function ϕ at the vacuum boundary. For $d < d_{spc}$ in the unsaturated case, ϕ can connect smoothly into the vacuum and there exist edge states. A H atom provides a symmetric 1s-like wave function (no p-orbitals involved) in the cell, and flips $d\phi/dx$ without changing the value ϕ at the vacuum boundary. Therefore, once hydrogenated, ϕ cannot connect smoothly without having a notch, and edge states are eliminated. For $d > d_{spc}$ in the unsaturated case, ϕ has a notch and edge states are forbidden. When hydrogenated, the smooth connection is now possible because of the flip of $d\phi/dx$, and edge states appear.

When a crystal has a natural d such that $d < d_{spc}$, it is called s-p crossing, and when $d > d_{spc}$, s-p uncrossing. Examples of s-p crossing crystals are semiconductors such as Si, Ge, or GaAs and many metals, and those of s-p uncrossing crystals are alkali halides, such as LiF or KCl [11]. Practically, semiconductor substrates may be better since they are widely used in the current device technologies, can easily have an atomically regulated surface, and are s-p crossing, supporting surface states at dangling bonds.

Edge states are quite robust. In his original work [11], Shockley assumed geometrical symmetry for the chain center, but it turns out that this assumption is not essential for the existence of edge states as he had predicted. In order to see it, we have studied an unsaturated a chain asymmetric with respect to the central atom. Edge states still appear in the main band gap for $d < d_{spc}$, in the same way as they do in the symmetric cases. Different adatoms having both s- and p-orbitals (thus excluding H) can also create edge states for $d < d_{spc}$, but localization is better for electronically similar adatoms for $d < d_{spc}$. This is more important in a realistic three-dimensional case, where the band gaps are narrower.

We need to examine practical effects on the existence of the surface states. First, an adatom may not sit directly on a substrate atom in many situations, but the above localization results are insensitive to the detail of the position. Second, there are many different surfaces for a given crystal, but the results are again independent of the surface orientation. As long as the substrate is s-p crossing, the surface states exist on all the substrate surfaces: the substrate *bulk* properties determine the existence of the surface states. However, all the quantitative results such as the decay length of the wave function or the edge state energies do sensitively depend on the adatom positions, the adatom species, or the substrate surface orientation.

III. SEMICONDUCTING CHAINS WITH Ge ADATOMS ON Si (100)

Semiconducting adatom chains are obtained by either group IV adatoms with two chemical bonds each, or group III adatoms with one chemical bond each, to substrate

atoms. A tight-binding view explains this in Fig. 3: (a) group IV and (b) group III adatoms, respectively. In Fig. 3(a), an adatom forms four sp^3-hybrid orbitals and is ready for chemical bonding to substrate atoms. When two sp^3-orbitals meet, they form bonding and antibonding orbitals separated by double the covalent energy [5], typically on the order of several eV. The remaining two dangling sp^3-orbitals will rehybridize and form an sp-orbital and a p-orbital [5, 13]. If these adatoms are arranged periodically, they form adatom bands. The sp-orbital forms a valence band and the p-orbital forms a conduction band. Since two additional electrons are provided from substrate atoms, we accommodate six electrons in total per unit cell. Thus, two bonding orbitals are filled and create two chemical (covalent) bonds, and the adatom valence band is fully filled, resulting in a semiconducting adatom structure.

In Fig. 3(b), the discussion runs parallel to the above. The difference is that in rehybridization, we now have two sp-orbitals and two p-orbitals, and one of two sp-orbitals is used for chemical bonding to a substrate atom. Two p-orbitals form two conduction bands corresponding to σ- and π-configurations, while the other sp-orbital forms a valence band. Including an electron from the substrate atom, we now have four electrons per unit cell and they fully occupy the adatom valence band as well as a bonding orbital (covalent bond), resulting again in a semiconductor.

Ge adatom structures on the Si (100) unreconstructed surface with two dangling bonds in an inset of Fig. 4 are a good example for a semiconducting chain achieving electronic isolation. Unused Si dangling bonds are hydrogenated to eliminate unwanted surface states. The ideal tetrahedral angles are assumed everywhere. There are two types of adatom chains with the same lattice spacing of 3.84 Å, σ- and π-chains, depending on the dangling sp^3-orbitals arrangement. No rehybridization is assumed for dangling bonds in the figure for clarity, but in fact resultant adatom bands are not influenced by whether dangling bonds are rehybridized or not, or mathematically the choice of the bases.

Taking into account the charge transfer effects among atoms up to the second nearest neighbors [13] as detailed in Appendix, we obtain adatom band structures in Fig. 4. The σ-chain has a conduction band minimum and a valence band maximum both at X, typical to one-dimensional s-p bands, while the π-chain has a conduction band minimum at Γ and a valence band maximum at X, because of two independent π-bands involved. The band widths are much wider than the Si bulk band gap (1.1 eV), and we expect that there would be a significant overlap between adatom and bulk Si bands. The situation is more serious in the π-chain since the adatom band gap is as wide as 4 eV, so that at least either the conduction band or the valence band will have an entire overlap with the bulk bands.

The overlap does not immediately mean poor isolation. Surface and bulk states may be able to exist independently. This is at least not contradictory to the experimental findings. In fact, a Si (111) substrate was studied using scanning tunneling microscopy, and a normalized-conductance plot as a function of voltage, known to correspond to the density of states, showed five peaks, four attributed to surface states and one to bulk states [14]. These peak positions were consistent with those of uncoupled, unperturbed surface and bulk states [14]. We may argue that the coupling between these states was so weak that no significant modulation in peak positions occurred, although the experiment did not directly detect electronic isolation in the context of device applications.

Adatoms are slightly depleted (z_0) in Fig. 4 by -0.0124e and -0.00626e (e the unit charge) and the entire adatom bands are shifted by -0.754 eV and -0.0552 eV in the σ- and π-chains, respectively. Both chains are positively charged, and the Fermi energy is slightly below the valence band maximum, resulting in unintentional p-doping. This simply reflects that the 4p levels in Ge are slightly shallower than the 3p levels in Si (the same

relation for the sp^3-hybrid levels), so that electrons tend to flow from the Ge adatoms to the Si substrate atoms. In fact in the π-chain, the first and second nearest neighbors (both Si) are accumulated slightly. In the σ-chain, the first neighbors (Si) are depleted, while the second neighbors (H) are accumulated. This is because the 1s level in H is deeper than the relevant p-levels in Si or Ge so that H atoms tend to absorb electrons from neighbors more efficiently. Since the 2p levels in C are deeper than the 3p levels in Si, the electron flow is opposite, from the Si substrate atoms to the C adatoms. Thus, C adatom chains will be unintentionally n-doped. When the conditions for a semiconductor are not satisfied, adatom structures are expected to be metallic, as long as the Peierls transition or Mott transition [15] are irrelevant. For different adatoms, these transitions are not likely to occur since adatom structures are unintentionally doped through charge transfer as discussed above, and the electron filling is always different from exact one-half, one-third, etc.

The tight-binding view developed here is insensitive to the details of the adatom positions. The crucial information is how many adatoms and dangling bonds there are per unit cell. As long as these numbers do not change, the electron filling remains the same in the adatom bands and the same criteria apply to judge whether a given adatom chain is semiconducting or not. Since different substrate surfaces have generally a different number of dangling bonds per unit cell, the *surface* changes the electronic properties of adatom chains, in sharp contrast to the above existence conditions. The details of the adatom bands as well as other quantitative results do depend on the exact adatom positions.

IV. SUMMARY

For the developement of precise nanoelectronics, electronic isolation between the adatom and substrate systems is shown to be achieved through the creation of localized adatom surface states with chemical bonds. The surface states exist at the dangling bonds on an s-p crossing substrate such as Si, Ge, or GaAs. The isolation is better if the adatoms are electronically similar to the substrate atoms. We can eliminate such surface states by hydrogenation on s-p crossing substrates. Group IV adatoms with two chemical bonds each, or group III adatoms with one chemical bond each, can form semiconducting structures. As an example for a semiconducting adatom chain with electronic isolation, σ- and π- Ge adatom chains on Si (100) were studied, and unintentional p-doping was pointed out. In the chemical bonding scheme, we cannot define intrinsic properties of an adatom chain. The existence of the surface modes depends on the bulk properties of the substrate, and the electron filling of the adatom bands depends on the surface properties of the substrate. Adatom properties have to be considered within a unified adatom-substrate system.

ACKNOWLEDGEMENTS

The author gratefully acknowledges Dr. M. Meyyappan for fruitful discussions and continuous encouragement during the course of this work. He is grateful to Dr. C. W. Bauschlicher, Jr., Dr. H. Partridge, and Dr. B. A. Biegel for many helpful discussions, and to Dr. T. R. Govindan for advice and encouragement.

APPENDIX: SELF-CONSISTENT TIGHT-BINDING METHOD

We discuss the charge transfer in the σ-chain as an example. An adatom (Ge) is 0, two nearest neighbors (Si) are 1, and two second nearest neighbors (H) are 2, where last two neighbors belong to the substrate. Charges are assumed to be distributed up to these second nearest neighbors, and therefore charge neutrality holds within this range. Charge z_i indicates the amount of excess electrons on atom i, and reflects the wave function amplitudes. Thus, z_i's are determined by the tight-binding parameters, diagonal elements ε_i's, and off-diagonal elements V's. In turn, these tight-binding parameters are functions of charge amounts z_i's through the Coulomb interaction, and have to be determined self-consistently [13]. As usual, the Coulomb interaction is assumed to change diagonals from ε_i^{orig}'s, equivalent to atomic term values [5, 6], to ε_i's, but not off-diagonals V's. Using a bond-orbital approximation introducing the simplest off-diagonal parametrization and appropriate linearization [13], we express this self-consistency by the following six equations for six unknowns ε_0, ε_1, ε_2, z_0, z_1, and z_2:

$$z_0 = (\varepsilon_1 - \varepsilon_0)/V_{01} \ , \tag{1}$$
$$z_1 = (\varepsilon_0 - \varepsilon_1)/2V_{01} + (\varepsilon_2 - \varepsilon_1)/2V_{12} \ , \tag{2}$$
$$z_2 = (\varepsilon_1 - \varepsilon_2)/2V_{12} \ , \tag{3}$$
$$\varepsilon_i = \varepsilon_i^{orig} + c_{i0}z_0 + c_{i1}z_1 + c_{i2}z_2 \ , \quad (i = 0, 1, \& \ 2) \ , \tag{4}$$

where V_{01} is an off-diagonal element, the covalent energy for atoms 0 and 1, and V_{12} is the same for atoms 1 and 2. Equations (1) - (3) show how the tight-binding parameters determine the charges (wave functions). A charge conservation relation of $z_0 + 2z_1 + 2z_2 = 0$ automatically holds in this formalism. Equations (4) show how the charges modify the diagonal tight-binding parameters. c_{ij} stands for a coefficient of the Coulomb interaction for atom i due to charge z_j. Coulomb interaction is due to intra-atomic (self-charging) repulsion, inter-atomic repulsion from the same unit cell, and Madelung interaction from the other unit cells. The Madelung energies are evaluated numerically, expressed as a function of z_1 and z_2 using the charge conservation relation, and normalized to $W = e^2/3.84$. Each c_{ij} is given by

$$\begin{aligned}
c_{00} &= U_0 \ , \\
c_{01} &= 2e^2/2.35 - 0.732W \ , \\
c_{02} &= 2e^2/3.17 - 1.17W \ , \\
c_{10} &= e^2/2.35 \ , \\
c_{11} &= U_1 + e^2/3.84 - 0.00644W \ , \\
c_{12} &= e^2/5.12 + e^2/1.48 - 1.05W \ , \\
c_{20} &= e^2/3.17 \ , \\
c_{21} &= e^2/5.12 + e^2/1.48 - 0.177W \ , \\
c_{22} &= U_2 + e^2/6.26 - 0.382W \ ,
\end{aligned} \tag{5}$$

where U_i is a self-charging energy for atom i. For example, c_{00} corresponds to a Coulomb energy shift for atom 0 due to its own charge z_0, represented by the intra-atomic repulsion U_0. c_{01} corresponds to the shift for atom 0 due to neighboring charges z_1's that are 2.35 Å apart from atom 0 in the same unit cell (interatomic repulsion $2e^2/2.35$) and due to charges z_1's in the other unit cells (Madelung energy $-0.732W$). Other coefficients are derived similarly. Necessary tight-binding parameters are taken from [13] and [16]. Once all the constants are determined, numerical solution is easy after a routine matrix inversion. A

similar procedure applied to the π-chain case.

It should be noted that in the present formalism, we do not have any quantity corresponding to a chemical potential. In fact, electrons do flow from a higher-occupied-level atom to a lower-occupied-level atom, but the flow stops before the diagonal elements become equal. This is clearly seen in Eqs. (1) - (3), where the difference in ε_i's supports nonzero charges. After charges are calculated, it is straightforward to evaluate the band structures.

REFERENCES

*Electronic address: yamada@nas.nasa.gov

[1] H.-S. Wong and Y. Taur, Tech. Dig., Int. Electron Devices Meeting, 705 (1993).

[2] J. -R. Zhou and D. K. Ferry, IEEE Comp. Sci. Engr. **2**, 30 (1995).

[3] J. R. Tucker and T.-C. Shen, Solid-State Electronics **42**, 1061 (1998).

[4] For example: D. M. Eigler and E. K. Schweizer, Nature (London) **344**, 524 (1990); I.-W. Lyo and Ph. Avouris, Science **253**, 173 (1991); H. J. Hamin, S. Chiang, H. Birk, P. H. Guenther, and D. Ruger, J. Vac. Sci. Technol. B **9**, 1398 (1991); M. F. Crommie, C. P. Lutz, and D. M. Eigler, Science **262**, 218 (1993); Ph. Ebert, M. G. Lagally, and K. Urban, Phys. Rev. Lett. **70**, 1473 (1993); Ph. Avouris, I.-W. Lyo, and Y. Hasegawa, J. Vac. Sci. Technol. A **11**, 1725 (1993); H. Uchida, D. Huang, F. Grey, and M. Aono, Phys. Rev. Lett. **70**, 1437 (1993); C. T. Salling and M. G. Lagally, Surf. Sci. **265**, 502 (1994); A. Yazdani, D. M. Eigler, and N. D. Lang, Science **272**, 1921 (1996).

[5] W. A. Harrison, *Electronic Structure and Properties of Solids* (Freeman, San Francisco, 1980).

[6] W. A. Harrison, Surf. Sci. **299/300**, 298 (1994); W. A. Harrison, Phys. Rev. B **24**, 5835 (1981).

[7] T. Yamada, J. Vac. Sci. Technol. B **15**, 1019 (1997); T. Yamada, Y. Yamamoto, and W. A. Harrison, J. Vac. Sci. Technol. B **14**, 1243 (1996).

[8] T. Yamada, J. Vac. Sci. Technol. A. **16**, 1403 (1998).

[9] J. W. Lyding, T.-C. Shen, J. S. Hubacek, J. R. Tucker, and G. C. Albeln, Appl. Phys. Lett., **64**, 2010 (1994); T.-C. Shen, C. Wang, G. C. Abeln, J. R. Tucker, J. W. Lyding, Ph. Avouris, and R. E. Walkup, Science, **268**, 1590 (1995).

[10] T. Yamada, C. W. Bauschlicher, Jr., and H. Partridge, to be published in the June 15th issue of Phys. Rev. B **59**, 1999.

[11] W. Shockley, Phys. Rev. **56**, 317 (1939).

[12] W. Shockley, *Electrons and Holes in Semiconductors* (Van Nostrand, Princeton, 1950).

[13] W. A. Harrison and J. E. Klepeis, Phys. Rev. B **37**, 864 (1988); J. E. Klepeis and W. A. Harrison, J. Vac. Sci. Technol. B **6**, 1315 (1988); J. E. Klepeis and W. A. Harrison, Phys. Rev. B **40**, 5810 (1989).

[14] J. A. Stroscio, R. M. Feenstra, and A. P. Fein, Phys. Rev. Lett. **57**, 2579 (1987).

[15] R. Peierls, *Quantum Theory of Solids*, (Oxford, Oxford, 1955); N. F. Mott and E. A. Davis, *Electronic Processes in Non-crystalline Materials*, (Clarendon, Oxford, 1979).

[16] D. Allen and E. J. Mele, Phys. Rev. B **31**, 5565 (1985).

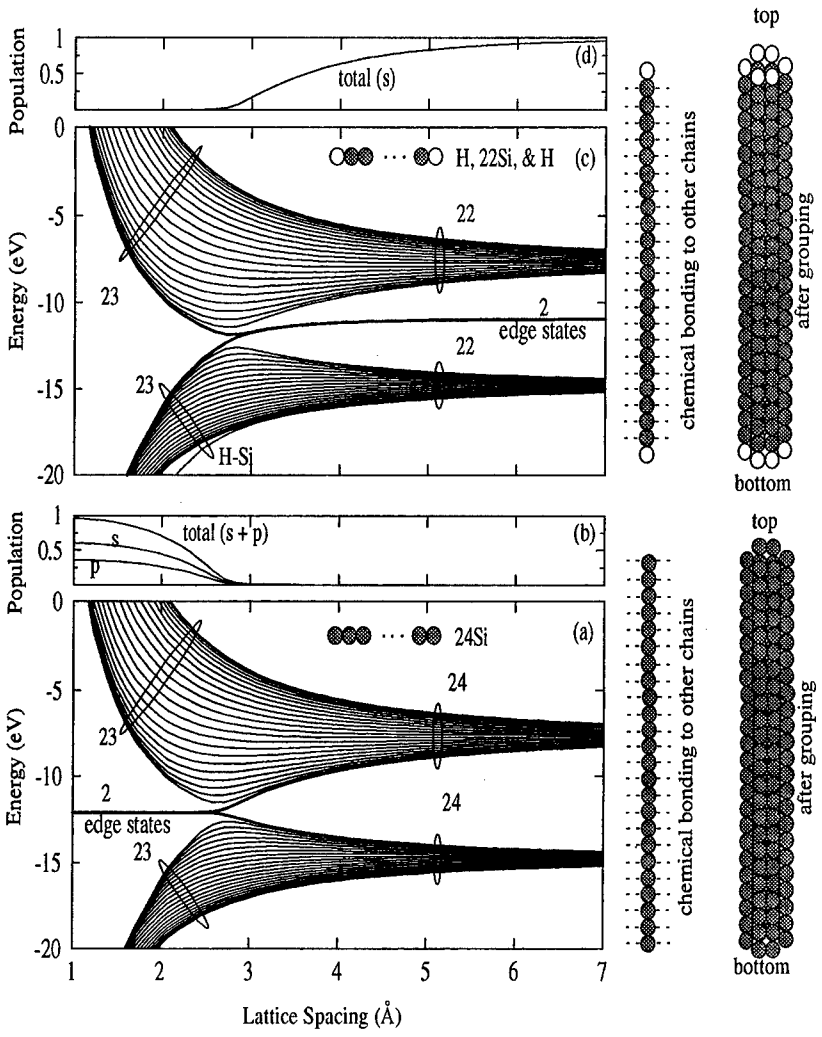


FIG. 1. Electronic states as a function of lattice spacing: (a) energy levels and (b) edge population for states with thick line in 24 Si chain; (c) and (d) the same plots in 22 Si chain with two edge H adatoms.

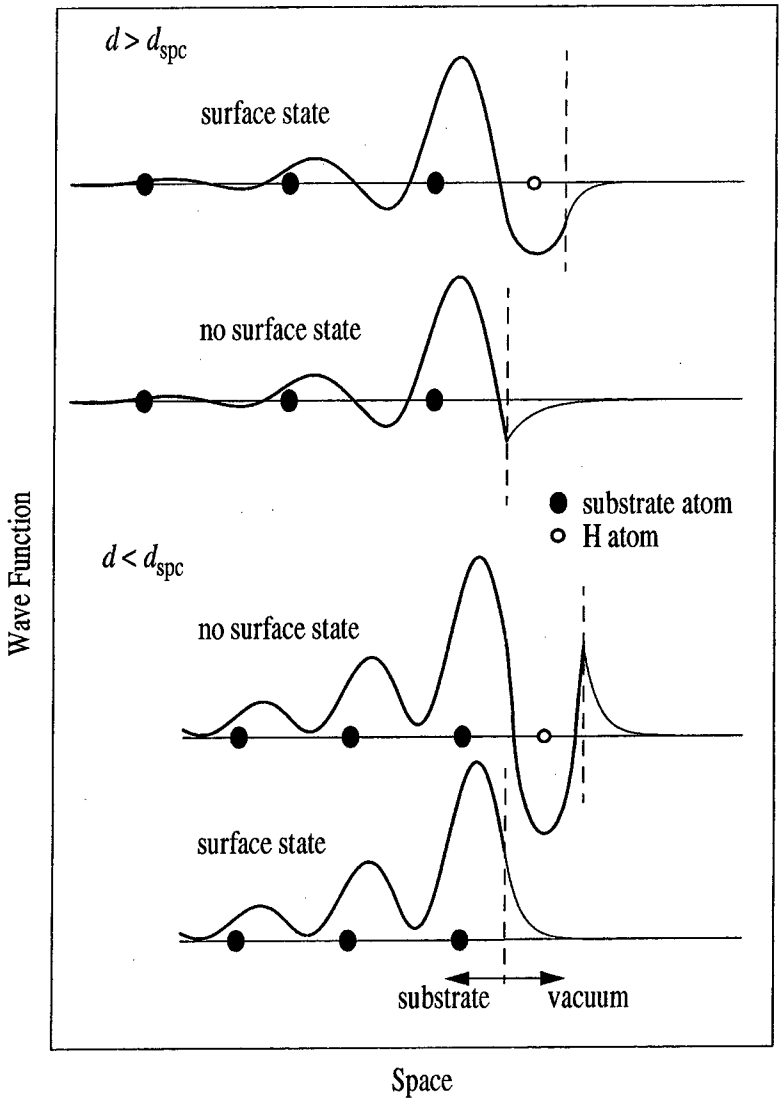


FIG. 2. Schematic plots of wave functions for unsaturated and hydrogenated cases at the vacuum boundary for $d < d_{spc}$ (lower two) and $d > d_{spc}$ (upper two).

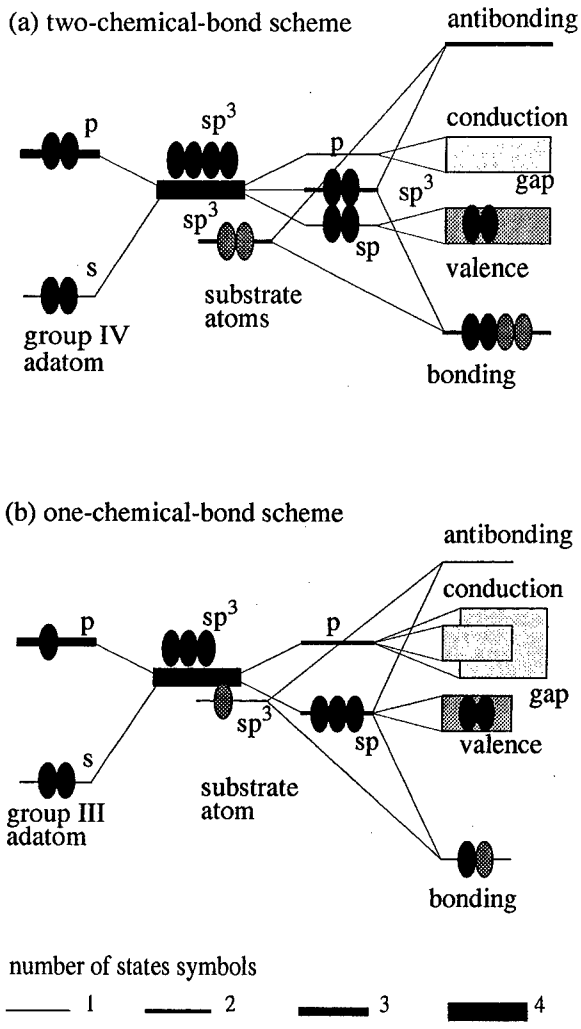


FIG. 3. Tight-binding view for semiconducting adatom chains in the chemical-bonding scheme: (a) group IV adatom with two chemical bonds and (b) group III adatom with one chemical bond.

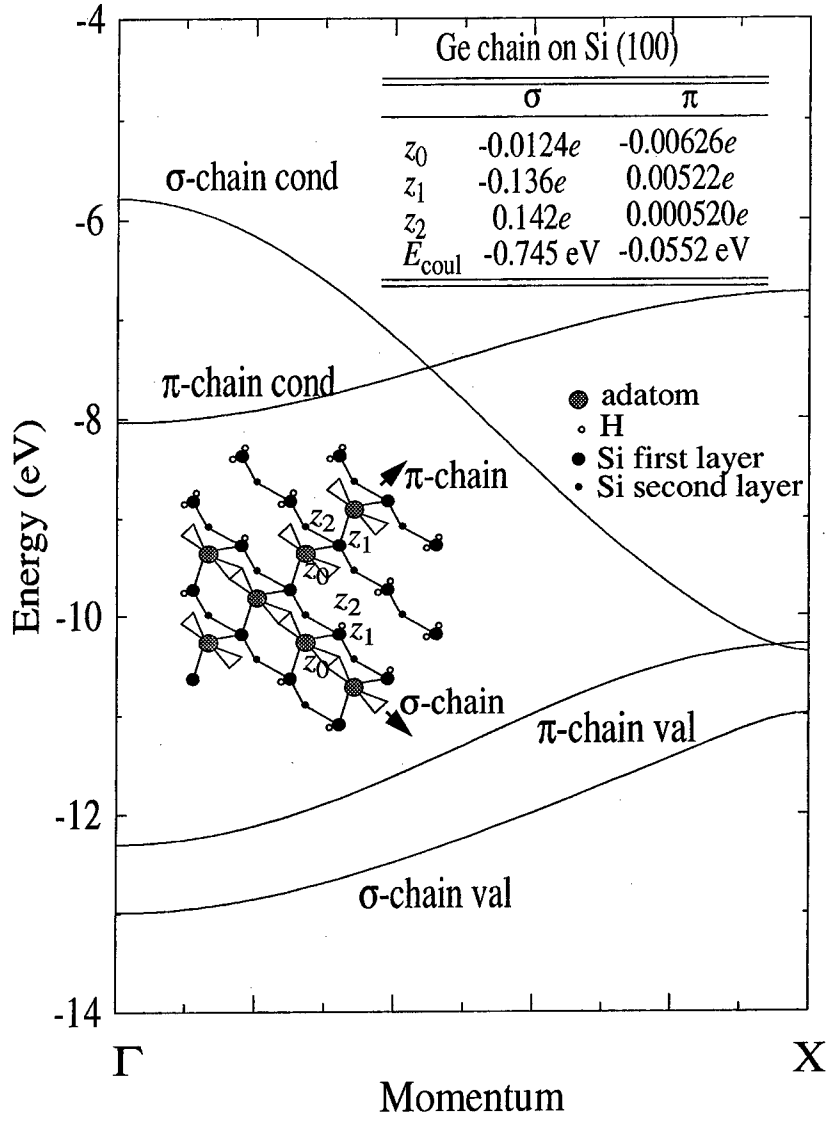


FIG. 4. Band structures for σ- and π-chains with Ge adatoms on hydrogenated Si(100) surface and transferred charges.

A New Type of Superlattice:Semiconductor-Atomic – Superlattice

R. Tsu,[a] K. Dovidenko,[b] and C. Lofgren[c]

[a] Department of Electrical and Computer Engineering, University of North Carolina at Charlotte, Charlotte NC 28223

[b] NYS Center for Advances Thin Film Technology, SUNY at Albany, Albany NY 12203

[c] NanoDynamics Inc., New York NY 10021

ABSTRACT

A new type of superlattice, replacing the heterojunction formed by adjacent semiconductors with semiconductor layers separated by adsorbed species such as oxygen atoms; and CO, molecules; shows promising results. This new type of superlattice, SAS, semiconductor-atomic-superlattice, may be formed epitaxially, enriching the present class of heterojunction superlattices and quantum wells for quantum devices. The Si growth beyond the adsorbed monolayer of oxygen is epitaxial having fairly low defect density, below 10^9 / cm^2, consisting of stacking faults and dislocations. At present, such a structure shows stable electroluminescence and insulating behavior, useful for optoelectronic and SOI applications. Molecular species such as CO forms SMS, semiconductor-molecular-superlattice, which also shows luminescence in the visible. SAS may form the basis of future all silicon ICs with both photons and electrons.

INTRODUCTION

Without a suitable heterojunction barrier, silicon has not played a significant role in quantum devices. Silicon dioxide with a barrier height of 3.2 eV in the conduction band of silicon is amorphous, preventing the building of a quantum well structure on top of the a-SiO_2 barrier. Several years ago, it was proposed that the oxides of one or two monolayers might allow the continuation of epitaxy. [1] After several failed attempts to realize the SLB (Superlattice Barrier) with thin silicon layers separated by thin oxides, a new method involving the exposure of oxygen followed by epitaxial growth of silicon using the in-situ RHEED (reflection high energy electron diffraction) for monitoring epitaxy, was introduced.[2] In fact, whenever oxygen and silicon were both present during the growth, epitaxy can still be continued, however, with horrendous amount of defects, similar to results reported by Meakin et al.[3] Our growth beyond a barrier structure consisting of 1 or 2nm of silicon sandwiched between adjacent layers of adsorbed oxygen up to 100 Langmuir (1L is defined as an exposure of 100 seconds in 10^{-8} Torr) of exposure for each layer is epitaxial and low in stacking faults as determined

in high resolution X-TEM. In this work, we present new high resolution TEM in both cross-section and plane-view. Electrical measurements show that up to 0.5eV of barrier height [4] is possible with several repeats of the double-barrier structure, Si/O/Si/O...Using an assumption that in the SAS structure, the amount of electron transfer from the Si to O is only half as much as SiO_2 , the maximum barrier height is estimated at 1.6eV instead of 3.2eV.[5] The lower value in the measured barrier height is presumably due to the difficulty in measurement using an activated process which depends on the barrier width to some degree.

SAS shows stable electroluminescence in the visible spectrum.[6] With partially transparent Au electrode, the emitted light is green. The spectrum peak is at 2.2eV extending well into the blue region of the visible spectrum. It is frequently suggested that the visible light from nanoscale structures is mostly from the interface regions. It has been shown that in the case of amorphous silicon superlattices or a-Si:H followed by crystallization [7,8], the origin of visible light emission is quantum confinement. The mechanism of SAS, with extremely thin barriers resulting in unavoidable defects such as strains, dangling bonds, etc. at the interfaces which in turn may degrade the degree of quantum confinement, is more complicated. These concerns involving damping in a quantum system, have been treated by using the quantum mechanical Langevin's equation, or by introducing a relaxation time as summarized in Ref.5. Results of these studies,[5] indicates that quantum confinement effects may be easier to manifest than the usual rule that the mean free path must be greater than the well width, or $k\ell \geq n\pi$, however, there is an up-shift somewhat complicates the simple confinement shift.

As the structure is reduced to the point that an appreciable fraction of the atoms is at the interface, the important question is whether control can be maintained and fabrication can be reproducible. In fact the SAS is really quite different from the conventional superlattices [9] or even the strain-layer superlattice [10]. Here, the dominant states are determined by the hybridization of the oxygen – silicon atoms, rather than the usual quantum confinement effected by the band-edge offset. What we are really saying is that the observed spectra originate from both quantum confinement in silicon as well as states at the interface. Probably a significant portion of the spectrum, particularly at higher energy, comes from the interface states. We need to recognize that in traditional solid state and semiconductor physics, contribution from regions other than the "bulk" are consider undesirable. In SAS, if we chose to discard the interface states, we would have thrown away the best part! The use of surface adsorption to limit the oxygen atoms to, at most one monolayer seems to be the main ingredient of the continuation of epitaxy with low stacking fault defects, although the precise mechanism is yet to be established.

Electroluminescence and Photo Luminescence

Figure 1 shows the comparison of photoluminescence of a 9-period Si/CO superlattice [11] with a 9-period Si/O superlattice. Note that the former has narrower spectrum. Incidentally, CO was chosen simply because CO molecules stick well to silicon. Figure 2. Shows the electroluminescence of a 9-period Si/O with partially

transparent gold electrode. We have life-tested a diode for more than one year of continuous operation. The spectra in the inset of Fig.3 show that the EL intensity has actually increased after the first 30 days of operation. Recently, we have found that the minimum reverse bias required for EL has decreased from –10V to –7V, indicating that some defects have been annealed away during life-test.

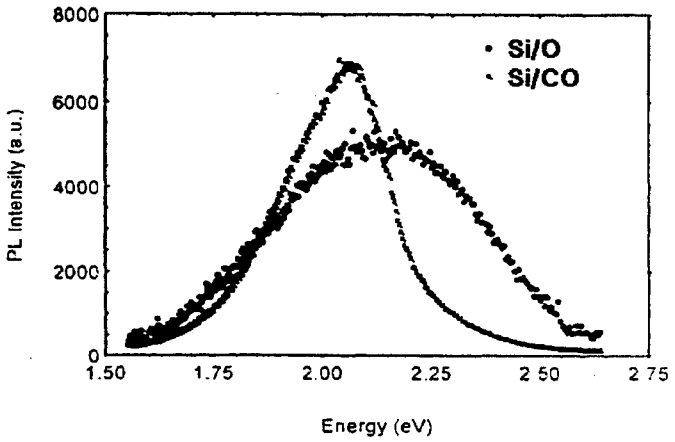


Fig. 1. Comparison of photoluminescence of Si/O with Si/CO superlattices excited by 2.7eV Ar laser.



Fig. 2 EL of a 9-period Si/O with partial transparent Au for electrode, 0.5 × 1.2mm. The dark area is caused by the contact wire vignetting part of the Au electrode.

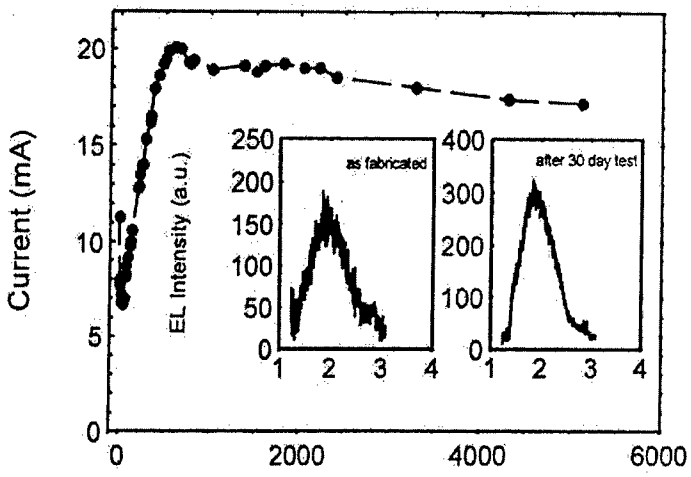


Fig.3 EL spectra and life-test under –10.4V reverse bias

Epitaxy Beyond the Adsorbed Monolayer of oxygen

We have found that the epitaxy beyond the adsorbed oxygen is low in defect density.[2] Fig.4 shows the high resolution cross-section TEM of a sample with Si (buffer) / (O-Si (1.1nm)-O-Si (1.1nm)-O) / Si on Si(100). The "whitish" part of the figure may indicate where the oxygen cluster is located. Epitaxy is continued beyond this "whitish" region. This result is consistent with Distler's assertion [12] that it is rather difficult to wipe out effects of epitaxy short of amorphizing by ion bombardment. We have also succeeded the SAS with Si (111). The structure is slightly more defective than Si (100). As pointed out before [13], discontinued clusters can serve as a barrier because electrons, as de Broglie waves, cannot pass through region of space smaller than the wavelength. This is a good place to emphasize that there are two mechanisms – step in energy, and/or step in geometrical shape can give rise to an effective barrier for electrons.

Figure 5 gives the plane-view TEM of the same sample in Fig.4. The defect density is below 10^9 /cm^2. We have lowered the defects by almost two orders of magnitude during the past couple of years. Thus we are optimistic that further reduction should be possible. Note that the defect density in Si-oxide interface is generally much higher.

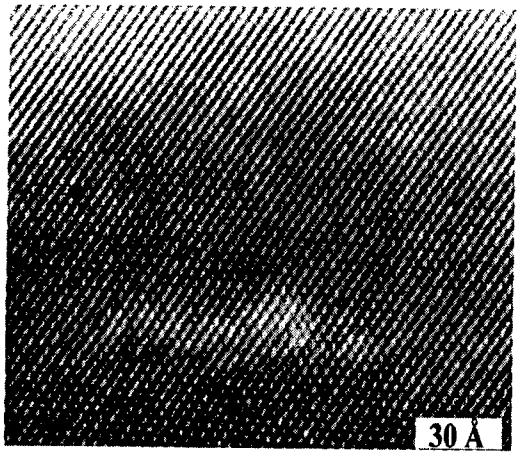


Fig.4 From bottom of figure towards the top showing Si (buffer) / (O-Si (2.2nm)-O) / Si high resolution cross-section TEM on Si(100).

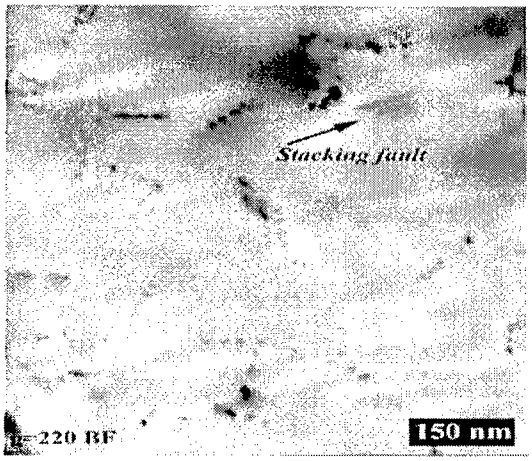


Fig. 5. Plane-view TEM of above sample showing defect densities of below $10^9/cm^2$.

Highly Defective Si growth beyond an SiO_x Layer

As pointed out previously that whenever oxygen leak valve is left on during the silicon deposition, horrendous amount of defects are generated, although the 3-D diffraction pattern still persists. Figure 6 shows a typical case of 20nm of SiO_x on Si (100). The defects persist even after 200nm of Si deposition on top of the SiO_x layer. Therefore our results are similar to what is generally known that it is impossible to grow good Si epitaxially on an oxide layer.

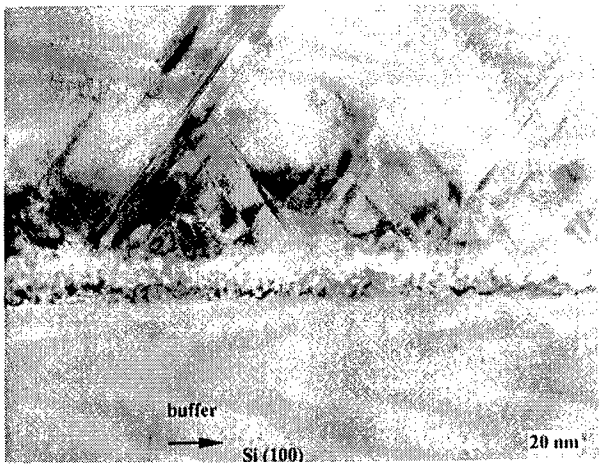


Fig. 6 Highly defective Si growth beyond 20nm of SiO_x

Possibility of Silicon Epitaxial Insulator

We have deposited a multiple Si/O-superlattice as a barrier serving to replace SOI, silicon-on-insulator. The epitaxial Si deposited on top of the Si/O-superlattice is low in defects. Preliminary mobility measurements showed that the mobility of Si beyond the

Si/O Epi-SOI is three times higher than silicon deposited on a commercial SOI substrate at room temperature. Thus the Si/O Epi – SOI may form the basis of high speed and high efficiency FETs.

Other Possible Systems

As discussed in the introduction, other system on silicon should be possible. Nitrogen forms three planar bonds which should be very interesting. Thus SAS with Si/N may improve the 2D aspect of the superlattice. Since Si_3N_4 has a bandgap of $\cong$ 5eV, it should be possible to form Si/N-superlattice with an effective gap of at least 1eV. We have observed interesting photoluminescence with Si/CO, although we have not pursued further with this system in terms of TEM studies, nor have we measured the barrier height. Si/C-superlattice is another system worthy of attention. Due to the constraint, C may be forced into 4-fold coordination. It is important to note the difference between our scheme and ALE, atomic-layer-epitaxy. In ALE, the lack of enough constraint to force the system into an epitaxial arrangement results in an alloy system. Our SAS is severely constrained – the monolayer of adsorbed species must accommodate the bonding on both sides. In other words, it is the constraint present in the scheme that forces the epitaxy.

CONCLUSION

The semiconductor-atomic-superlattice may have opened the door to the fabrication of a wide variety of electronic and optoelectronic structures. Si/O-superlattice, most probably forming SiO rather than SiO_2, is the key to allow the continuation of epitaxial growth. The observation of electroluminescence is technologically very exciting because of its potential application in a photonic chip. The possibility of an epitaxial SOI may lead to a new generation of high efficient and high frequency FETs.

ACKNOWLEDGMENTS

The authors would like to express their gratitude for the support of this work by ARO, and NanoDynamics, Inc., as well as previously by ONR. The sample with Si/CO prepared by J. Dinkler for his MS thesis, and the contributions by A. Filios, and Q. Zhang are gratefully acknowledged.

REFERENCES

1. R.Tsu, *Nature,* **364**, 19 (1993).

2. R. Tsu, A. Filios, C. Lofgren, K.Dovidenko and C.G. Wang, *Electrochem and Solid State Lett.*, **1** (2) 80 (1998).

3. D.Meakin, M.Stobbs, J.Stoemenos and N.A.Economou, *Appl. Phys. Lett.* **52**, 1053 (1988)

4. J.Ding and R. Tsu, *Appl. Phys. Lett.* **71**, 2124 (1997).

5. R. Tsu, *ECS Proc.* **98-19**, 3 (1999)

6. R.Tsu, Q.Zhang, and A. Filios, *SPIE* **3220**, 246 (1998).

7. Z.H.Lu,D.J .Lockwood and J.M.Barlbeau, *Nature*,**378**, 825(1995)

8. L.Tsybeskov,K.D.Hirschman,S.P.Duttagupta,P.M.Fauchet,M.Zacharias,P.Kohlert,J.P.McC affrey and D.J. Lockwood, *ECS Proc.* **97-11**,134 (1997)

9. L. Esaki and R. Tsu, *IBM J. Research and Develop.* **14**, 61 (1970)

10. J. Matthews and A. E. Blakeslee, *J. Crystal Growth*, **32**, 265 (1976)

11. MS Thesis by J. Dinkler, Deaprtment of ECE, UNC-Charlotte, Dec. 1998.

12. G.I.Distler, B.B. Zvyagin, *Nature*, **212**, 807 (1966).

13. R. Tsu, A.Filios, and Q. Zhang, 'Perspectives of Light Emitters in Nanoscale Silicon' Advances in Science and Technology, **27**, Innovative Light Emitting Materials, editors, P. Vincenzini and G.C.Righini, (Techna Srl. 1999) p.55Paper-ECS.Honolulu99.doc

NOVEL FABRICATION TECHNIQUES FOR SILICON SINGLE-ELECTRON DEVICES

Yasuo Takahashi, Yukinori Ono, Akira Fujiwara, Kenji Yamazaki,
Masao Nagase, Hideo Namatsu, Kenji Kurihara, and Katsumi Murase
NTT Basic Research Laboratories
3-1, Morinosato Wakamiya, Atsugi-shi, 243-0198 Japan
Email: ytaka@aecl.ntt.co.jp

ABSTRACT

We have developed a special method, called pattern-dependent oxidation (PADOX), for fabricating Si single-electron transistors (SETs). This method exploits special phenomena that occur when a laterally modulated Si layer on SiO_2 is oxidized. With the method, a one-dimensional Si wire can be converted into a small Si island with a tunneling barrier at each end. Since the size of the resultant Si island is about 10 nm, we can observe the conductance oscillations in the SET even at room temperature. The controllability and reproducibility of this method are excellent, reflecting the stability of the thermal oxidation process. We have been applying this method to the integration of single-electron devices (SEDs) to create sophisticated functions. Several kinds of devices, such as memory and logic devices, have been fabricated and their fundamental operations have been confirmed. We have also found that another type of Si pattern that can be converted into SETs. A thin Si layer under a trench of a Si wire can be converted into two SET islands which are embedded in both edges of the Si layer parallel with the wire. We have demonstrated that the two small Si islands can be operated as individual SETs. Since this method uses a vertically modulated initial pattern, we call it V-PADOX. PADOX and V-PADOX have great flexibility for fabricating various types of SEDs.

I. INTRODUCTION

A single-electron transistor (SET) is expected to be a key device for future extremely large-scale-integrated circuits because of its ultrtalow power consumption and small size. Although recent advances in deep-submicron CMOS technologies have made it possible to load a Si chip with an enormous number of devices, this can cause the power consumption in the chip to exceed its cooling limit. SETs have a great potential for overcoming this problem and hence for furthering the multimedia society.

The SET has to have a small conductive island to exploit the Coulomb blockade for manipulating electrons by means of one-by-one transfer. Any conductive material can be used as a base material for SETs. Although metals or III-V compound semiconductors so

far have been used from the physical point of view, silicon is the most promising for the LSI application because SETs made from Si have possibilities of combinational usage with conventional CMOS circuits. In addition, advanced fabrication technologies, which have already been developed for sub-quarter-micron CMOS LSIs, can be used to make small Si structures. We tried to exploit these features in order to fabricate SETs that have nanometer-scale Si islands, which enables the devices to operate at high temperatures of 300 K.

The most difficult aspect of fabricating SETs is to make a nanometer-scale island sandwiched between two small tunnel capacitors. We have already developed a method, called PADOX (PAttern-Dependent OXidation) [1], for doing this. In this method, a one-dimensional (1D) Si wire can be converted into a small Si island with a tunneling barrier at each end. We use the special phenomena that occur when a laterally modulated thin Si layer on SiO_2 is oxidized. Since the Si-island size is about 10 nm, we can observe conductance oscillations of the SET even at room temperature. This method has great flexibility for fabricating various types of single-electron devices (SEDs).

In addition, we have also found that a thin Si layer under a trench of a Si wire can be converted into twin SET islands which are embedded in both edges of the Si layer parallel with the wire. Since this uses a vertically modulated initial pattern, we call it V-PADOX (Vertical PAttern-Dependent OXidation) [2]. Due to it having almost the same mechanism as PADOX, the two islands can operate as individual SETs.

II. PADOX (PATTERN-DEPENDENT OXIDATION)

Oxidation of Si produces a very stable insulator: SiO_2. Owing to the simplicity of the formation of SiO_2, ultralarge-scale integrated circuits have been achieved on Si wafers. However, it is well known that complicated oxidation occurs in a nanometer-scale Si structure since the oxidation rate depends on the mechanical stress that builds up in the newly-formed oxide due to volume expansion [3-4]. We found that a small Si pattern can be converted into a small SET in a self-aligned manner because the amount of oxidation at particular point can be modulated depending on the initial pattern. This is the reason we call this method pattern-dependent oxidation (PADOX) [1, 5]. The structure fabricated on a thin SOI (Silicon On Insulator) wafer contains a narrow and short Si wire as shown in Fig. 1. PADOX converts the wire into a small island with a small tunnel capacitor at each end. The basic mechanism of this conversion is that the oxidation in the middle of the wire is suppressed due to stress accumulated during thermal oxidation while that at the ends of the wire is enhanced due to both the supply of oxygen from the back and less accumulation of stress. The constrictions formed at both ends of the wire function as tunnel barriers. The device shown in Fig. 1(a) acts as a SET. The equivalent circuit is shown in Fig. 1(b). The great advantages of this method are that an island smaller than the initially defined size can be made and tunnel barriers are formed automatically at both ends of the wire. The characteristics of a SET fabricated by PADOX shown in Fig. 2 indicate that the total capacitance of the SET island is as small as 1 aF [5-7]. In addition, relatively low tunnel resistance from several-hundred kΩ to several MΩ was achieved [5]. This is advantageous for high-speed operation. Another

advantage is that the fabrication process is very stable and reproducible [6, 7] because it is almost the same as the conventional Si process. This is encouraging for the use of SETs in combination with MOSFETs [8, 9].

Using this method, we have been investigating the integration of SEDs to create progressive functions. Several kinds of devices, such as memory and logic devices, have been fabricated and their fundamental operations have been confirmed. Fabrication of these devices was performed by applying PADOX to specially designed patterns. We also apply ultrafine poly-crystalline Si gates to some of them by using electron-beam lithography.

Memory Devices

The most fundamental application of transistors is a memory device. One example fabricated by using PADOX is a novel memory device that operates with a small number of electrons [8, 9]. Fig. 3(a) shows a SEM image of the device fabricated on a thin SOI wafer. The equivalent circuit is shown in Fig. 3(b). The device has a small Si memory node at the tip of the 1D wire. A fine gate electrode overlaid on the wire forms a small MOSFET, which controls the flow of electrons into and out of the memory island. The other 1D wire and the source and the drain electrodes construct a SET, which detects the small number of electrons stored in the memory node. Figure 4 shows hysteresis characteristics of the memory device during "write" and "store" operations measured at 40 K. The gate voltage V_{lg} was initially set to a low voltage of -2.7 V, at which the channel of the 1D MOSFET was closed. Side-electrode voltage V_{se} was changed from 0 to -1 V, and the gate voltage V_{lg} was scanned up to -2.1 V, and then back down. The rapid fall in the SET current around V_{lg} = -2.3 V, at which the MOSFET turned on, indicates a flow of electrons into the memory node. After the downward scan, the SET current does not return to the initial level because the memory node already contains excess electrons. The number of stored electrons is about 100. Since the SET has high sensitivity even to small charge, this memory device operates with a small number of electrons. This result clearly shows that PADOX is actually suited for combinational usage with conventional MOSFETs.

Another memory device fabricated by applying PADOX to specially designed Si wires is a single-electron memory which can operate by memorizing only one electron. When the Si wire region is designed to form a cross shaped Si wire between the wide Si layers as shown in Fig. 5(a), satellite islands are formed in addition to Si islands for the SET. PADOX converts each branch of the cross shaped wire into a Si island because the branching point is oxidized more due to less accumulation of the stress. These satellite islands act as single-electron memory cells [10]. The simplified equivalent circuit of the device is illustrated in Fig. 5(b). The device shows different conductance oscillation curves depending on the number of electrons in the satellite island, because the extra electrons in the island shift the curve to the higher gate-voltage direction. The inset of Fig. 6 shows the hysteresis characteristics of the conductance measured at 40 K. The gate voltage was scanned several times forward and then backward and the data were plotted on the same graph. The conductance curves are split into three oscillation curves. In addition, there are some jumps in the conductance from one curve to another. The time-resolved measurement of the jumps shown in Fig. 6 clearly indicates the abrupt

transition in the conductance, which suggests the single-electron tunneling between the SET island and satellite islands. These phenomena can be exploited for a memory device operating with a single electron.

Logic Devices

One of the most prominent features of SETs is low power operation. This strongly suggests that the devices should be used in logic circuits. Several circuit applications where SETs are used instead of MOSFETs have been proposed [11, 12]. However, they do not use the special advantages of SETs and need the same number of transistors used in a CMOS logic circuit. SETs have completely different characteristics from those of conventional MOSFETs. One is that a SET can inherently have multiple gates while a MOSFET can not. Another feature is that the SET exhibits an oscillatory conductance as a function of the gate voltages. These remarkable features can be exploited for fabricating a new functional device which acts as an exclusive-OR (XOR) gate [13]. A SEM image of the fabricated device is shown in Figs. 7(a) and (b). A small 1D Si wire fabricated on a SOI wafer (Fig. 7(a)) was converted into a small SET by means of PADOX. Then, using an electron-beam exposure system with a high overlay accuracy, two ultrafine poly-Si gate electrodes were attached so as to cover a part of this island as shown in Fig. 7(b). The equivalent circuit is shown in Fig. 7(c), where the gate capacitances C_{g1} and C_{g2} are almost equal due to the symmetric structure of the gates. Figure 8 shows the drain current switching measured at 40 K in response to the switching of the two input-gate voltages between 0 and 0.2 V. Low current levels were obtained only when both input voltages were high or low. This demonstrates an XOR-gate operation [14]. An XOR gate using conventional CMOS logic circuits needs 16 transistors, whereas this function can be implemented with just one SET.

The ultimate low-power operation can be achieved by the use of a logic represented by a single electron. Such kinds of logic circuits will consist of multiple-island structures. We tried to fabricate a SED with two islands by applying PADOX to a T-shaped wire structure on a thin SOI wafer (Fig. 9(a)) [15]. Each branch of the "T" was converted into a Si island because the branching point is oxidized more due to less accumulation of stress. The ultrafine gate electrodes were attached to the islands as shown in Fig. 9(b). Then a SiO_2 interlayer and an upper poly-Si gate that covers the entire region shown in Fig. 9(b) were successively formed. Figure 10 illustrates the schematic island structure and the simplified equivalent circuit of the device, where the island at the branch T_3 just acts as a lead because it is too large to operate as a Coulomb-blockade island at about 30 K. Therefore, this is a double-island device in which the two islands are capacitively coupled with each other. Figure 11 shows the upper-gate voltage dependence of the current, where currents I_1 and I_2 exhibit Coulomb-blockade oscillations. The parameter is lower-gate voltage V_{lg2}, and it was changed from 0 to -0.24 V. V_{lg2} shifts only the peaks of I_2. It is striking that the peaks of I_2 are split when they approach the peaks of I_1. This indicates that the two islands are capacitively coupled. By using the device, the so-called single-electron pump, which enables us to transfer electrons one by one, can be achieved [16]. Moreover, upon the fabrication of three capacitively-coupled islands in our T-shaped wire device, a directional switch for single-electron transfer will be realized [15, 17]. Our new device will be promising for logic circuits using single-electron transfer.

III. V-PADOX (VERTICAL-PATTERN-DEPENDENT OXIDATION)

We have developed another method where thermal oxidation is employed to form *twin* SET islands. The initial structure contains a fine trench formed in the middle of a Si wire as shown in Fig. 12(a). The oxidation converts a thin Si layer under the trench into two small islands with almost the same size, and the islands are embedded in both edges of the Si layer parallel with the wire. Figures 13(a) and (b) show cross-sectional TEM images of a thick and a thin Si wire, respectively. At both edges of the thin Si layer, small Si islands are formed in a self-aligned manner and the rest of the thin region under the trench is converted into SiO_2. This is because less oxidation occurs around the edges due to stress accumulation, which allows us to produce two tiny Si islands without the need for lithographic definition of the islands themselves. As a result, the two small islands can operate as individual SETs. Since the starting pattern of Si is vertically modulated, we call this V-PADOX [2]. The equivalent circuit of the device is shown in Fig. 12(b). Figure 14 shows the gate voltage dependence of the conductance, measured at 40 K with a drain voltage of 10 mV, for a twin-island SET with a trench length L of 30 nm and a wire width W of 80 nm. The measured conductance oscillation can be deconvoluted into two oscillations, denoted as A and B. It was demonstrated that each oscillation was independently controlled by the voltage applied to the side gates (not shown in Fig. 12), which were placed at each side of the trench. This fact indicates that each SET operates individually. This method can provide two small SETs at the same time in a tiny area, which is a great advantage for the construction of integrated logic circuits [2].

IV. CONCLUSION

We have developed two special methods for fabricating Si SEDs: PADOX and V-PADOX. Both methods utilize a special oxidation phenomenon occurring when a very small Si structure is thermally oxidized, and enable us to fabricate small SEDs in a self-aligned manner. We actually fabricated some memory and logic devices. The results demonstrate that PADOX and V-PADOX have great flexibility for fabricating various types of single-electron devices and will be very useful for the future development of single-electron LSIs.

ACKNOWLEDGMENT

The authors wish to thank Drs. Katsutoshi Izumi, Takahiro Makino and Takaaki Mukai for their continued encouragement and Drs. Michiharu Tabe, Seiji Horiguchi, Yasuyuki Nakajima, Kazumi Iwadate, and Toru Yamaguch for valuable discussions and their support for the experiments.

References

[1] Y. Takahashi, M. Nagase, H. Namatsu, K. Kurihara, K. Iwadate, Y. Nakajima, S. Horiguchi, K. Murase, and M. Tabe, Electron. Lett., **31**, 136 (1995).

[2] Y. Ono, Y. Takahashi, K. Yamazaki, M. Nagase, H. Namatsu, K. Kurihara, and K. Murase, IEDM Technical Digest, p. 123 (1998).

[3] D. Kao, J. P. McVittie, W. D. Nix, and, K. C. Saraswat, IEEE Trans. Electron Device, **35**, 25 (1988).

[4] M. Nagase, A. Fujiwara, K. Yamazaki, Y. Takahashi, K. Murase, and K. Kurihara, Microelectronic Engineering, **41/42**, 527 (1998).

[5] Y. Takahashi, A. Fujiwara, M. Nagase, H. Namatsu, K. Kurihara, K. Iwadate, and K. Murase, Int. J. Electronics, **86**, 549 (1999).

[6] Y. Takahashi, H. Namatsu, K. Kurihara, K. Iwadate, M. Nagase, and K. Murase, IEEE Trans. Electron Device, **43**, 1213 (1996).

[7] Y. Takahashi, A. Fujiwara, M. Nagase, H. Namatsu, K. Kurihara, K. Iwadate, and K. Murase, IEICE Trans. Electron., **E79-C**, 1503 (1996).

[8] Y. Takahashi, A. Fujiwara, K. Yamazaki, H. Namatsu, K. Kurihara, and K. Murase, Electron. Lett., **34**, 45 (1998).

[9] Y. Takahashi, A. Fujiwara, K. Yamazaki, H. Namatsu, K. Kurihara, and K. Murase, Jpn. J. Appl. Phys., **37**, to be published (1999).

[10] A. Fujiwara, Y. Takahashi, K. Murase, and M. Tabe, Appl. Phys. Lett., **67**, 2957 (1995).

[11] K. K. Likharev, IEEE Trans. Magn., **Mag-23**, 1142 (1987).

[12] J. R. Tucker, J. Appl. Phys., **72**, 4399 (1992).

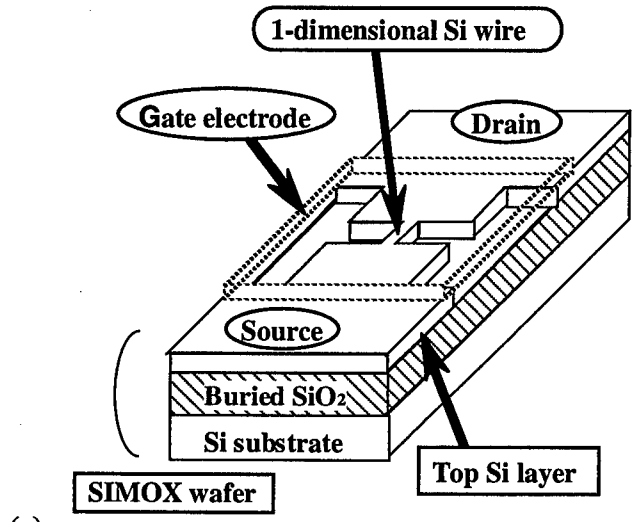
[13] R. H. Chen, A. N. Korotkov, and K. K. Likharev, Appl. Phys. Lett., **68**, 1954 (1996).

[14] Y, Takahashi, A. Fujiwara, K. Yamazaki, H. Namatsu, K. Kurihara, and K. Murase, IEDM Technical Digest, p. 127 (1998).

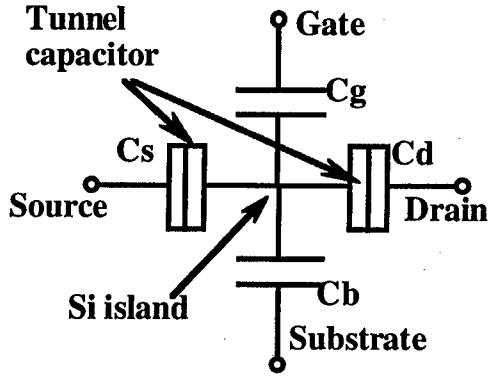
[15] A. Fujiwara, Y, Takahashi, K. Yamazaki, H. Namatsu, K. Kurihara, and K. Murase, IEEE Trans. Electron Device, **46**, 954 (1999).

[16] H. Pothier, P. Lafarge, R. F. Orfila, C. Urbina, D. Esteve, and M. H. Devoret, Physica B, **169** (1991).

[17] N. Asahi, M. Akazawa, and Y. Amemiya, IEEE Trans. Electron Device, **42**, 1999 (1995).



(a)



(b)

Fig. 1. Device structure (a) and equivalent circuit of the SET (b). We used a SIMOX (Separation by IMplanted OXygen) wafer, which is a type of SOI wafer. The Si island is surrounded by the gate electrode, substrate Si, and source and drain electrodes.

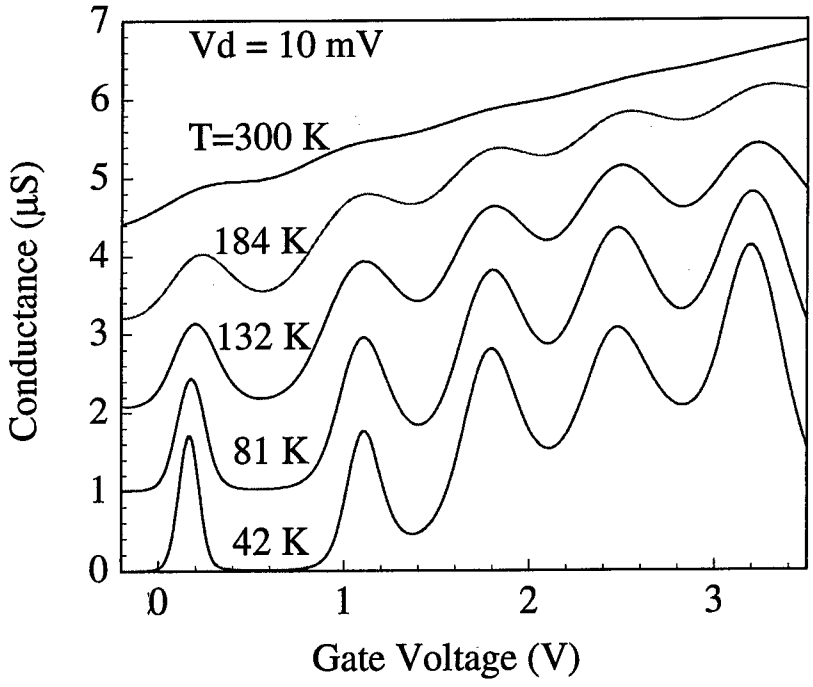


Fig. 2. Conductance oscillations as a function of the gate voltage measured at 40 K with the drain voltage of 10 mV. Initial wire width and height were both 30 nm, and initial length was 50 nm.

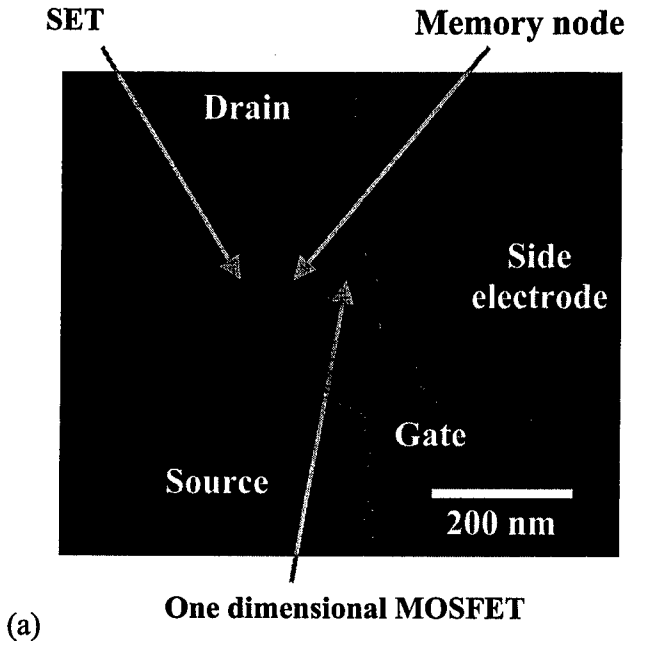


Fig. 3. SEM image of a fabricated memory device (a) and its simplified equivalent circuit (b).

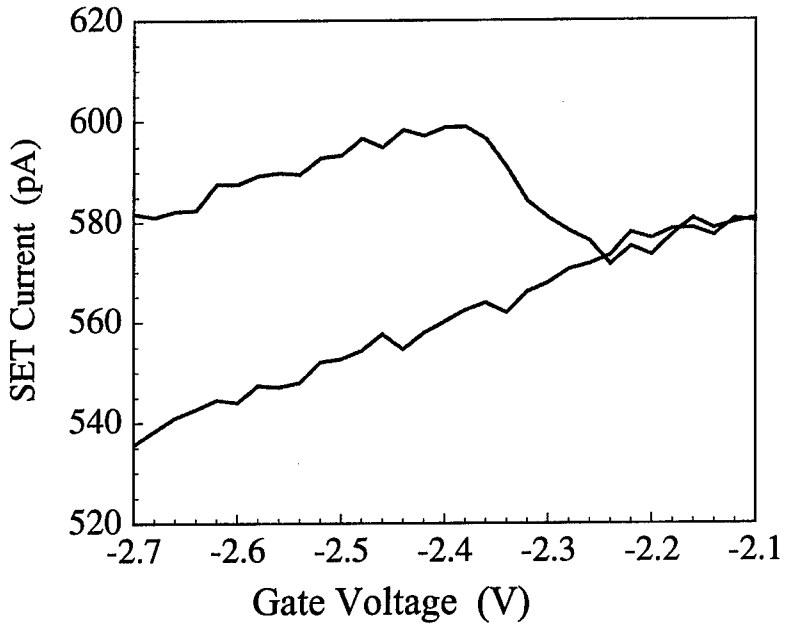
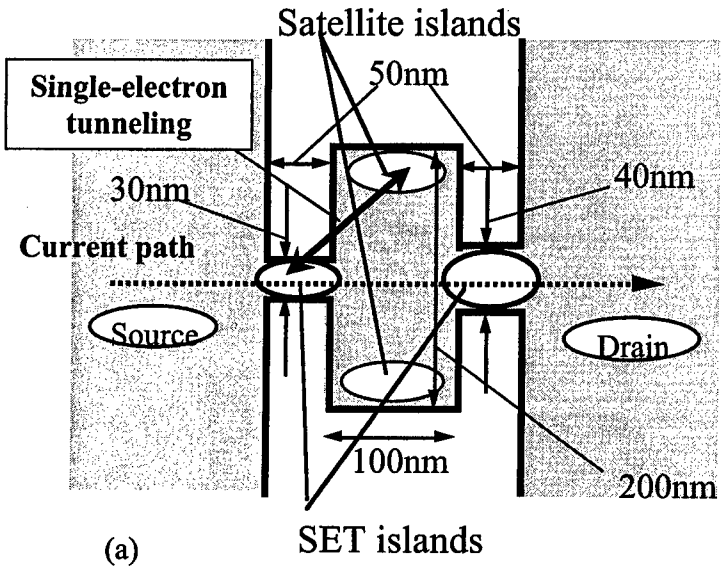


Fig. 4. Hysteresis characteristics of SET current representing "write" and "storage" actions measured at 40 K. The gate voltage V_{lg} scan started just after the V_{se}, initially 0 V, was set at -1 V.



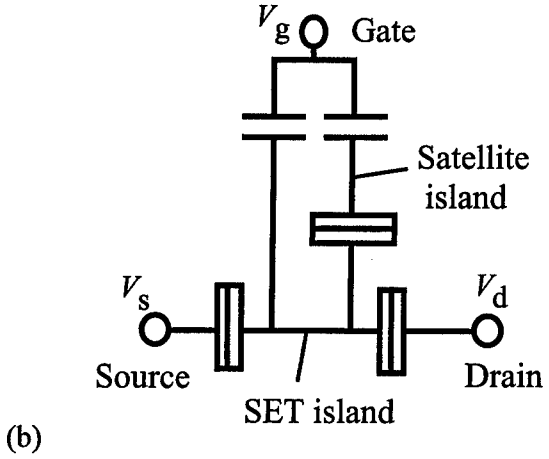


Fig. 5. Schematic structure of cross-shaped wire region (a) and simplified equivalent circuit (b). After PADOX, Si islands shown as ovals are formed.

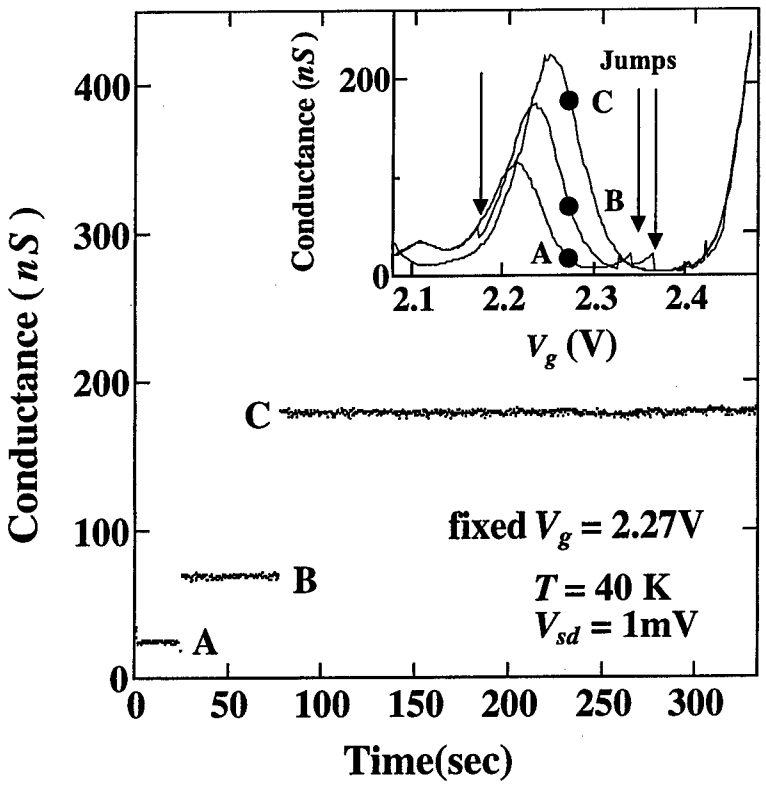


Fig. 6. Conductance as a function of time measured at 40 K with the drain voltage of 1 mV after the gate voltage is applied at 2.27 V. The inset shows three conductance curves reflecting the single-electron memory effect measured by scanning the gate voltage forward and backward for several imes. Arrows indicate the jumps in the conductance from one curve to another.

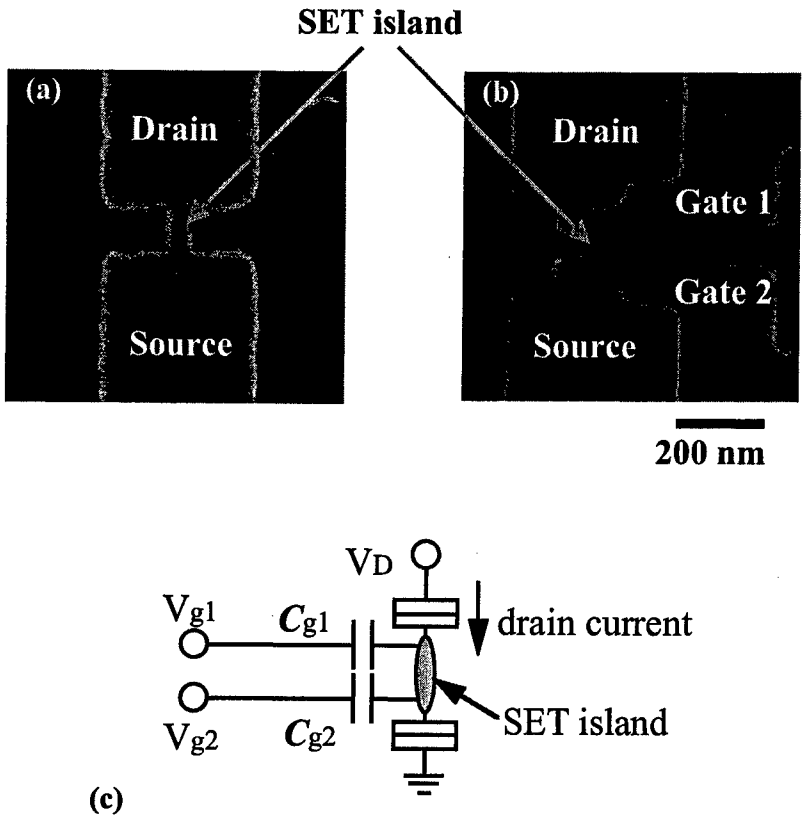


Fig. 7. SEM image of a Si wire before PADOX (a), the image after formation of two ultrafine gate electrodes (b), and its equivalent circuit (c). The wire length is 150 nm. The width of the fine gate is 60 nm. The active area of the XOR gate is within 200x200 nm^2.

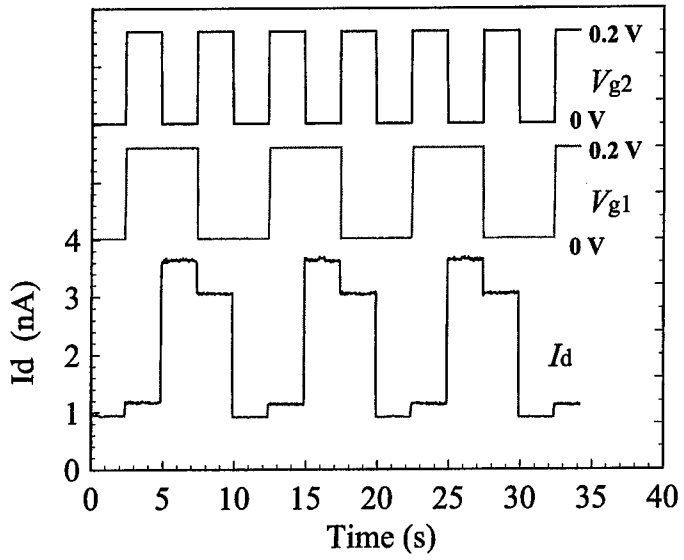


Fig. 8. Current switching characteristics of a dual-gate SET. Current levels are low only when both input voltages, V_{g1} and V_{g2}, are low or high. In contrast, current levels are high when one of the input voltages is high and the other is low.

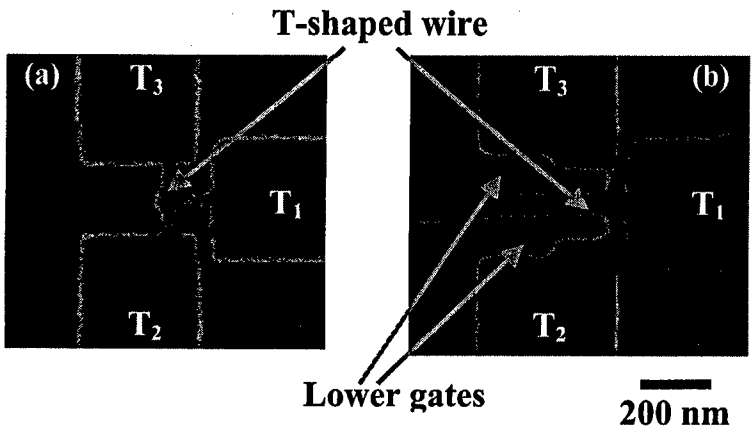
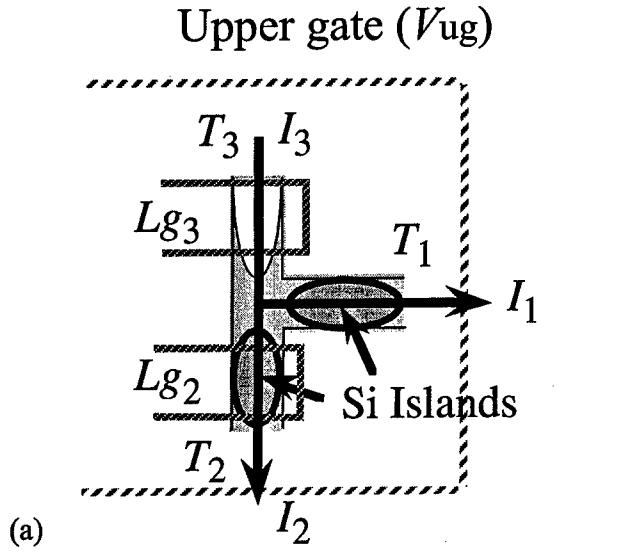


Fig. 9. SEM image of a T-shaped Si wire before PADOX (a) and the image after formation of two ultrafine gate electrodes on it (b). The width of the lower fine gate is 60 nm.



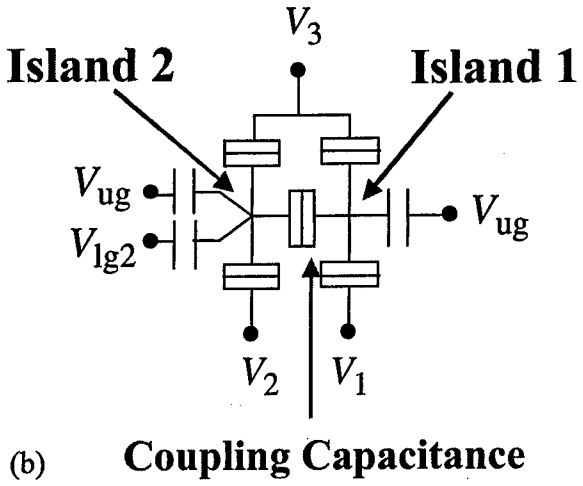


Fig. 10 Schematic structure of the T-shaped wire after PADOX (a) and the simplified equivalent circuit of the device (b). The biggest island, which is in branch T_3, just act as a lead. The wide upper gate covers over the wire region. The island in branch T_1 is controlled by the upper gate voltage (V_{ug}). The island in branch T_2 is controlled both by the lower gate voltage (V_{lg2}) and the upper one (V_{ug}).

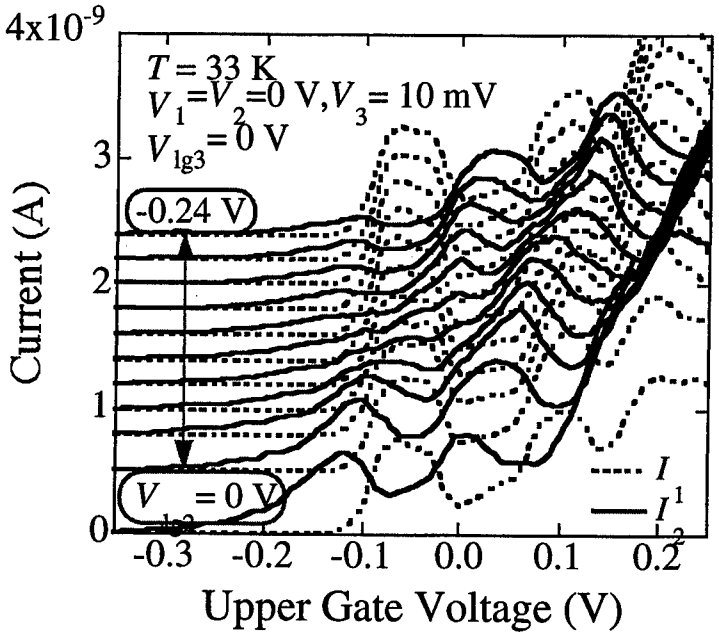
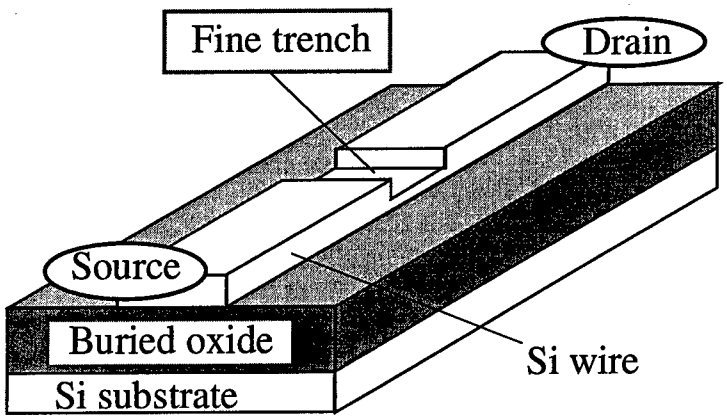
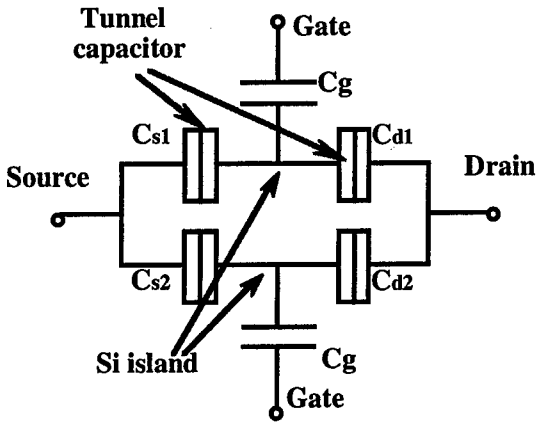


Fig. 11. Current vs. gate voltage characteristics of the T-shaped wire device measured at 33 K. The lower gate voltage V_{lg2} only affects the current I_2. Curves for different V_{lg2} are vertically offset for clarity.



(a)



(b)

Fig. 12. Initial structure of the twin SETs before V-PADOX (a) and the equivalent circuit of the device (b). *W*, *L*, *d* represent the designed wire width, trench length, and trench depth, respectively.

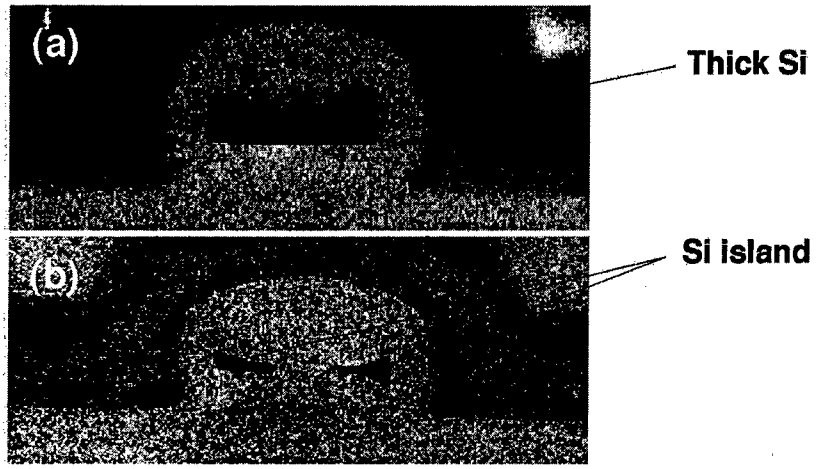


Fig. 13. Cross-sectional TEM image of the Si wire after V-PADOX. Initial thickness of the wire were 22 nm (a) and 14 nm (b). Wire width is 60 nm. Small Si islands are formed only at both edges of the thin Si wire.

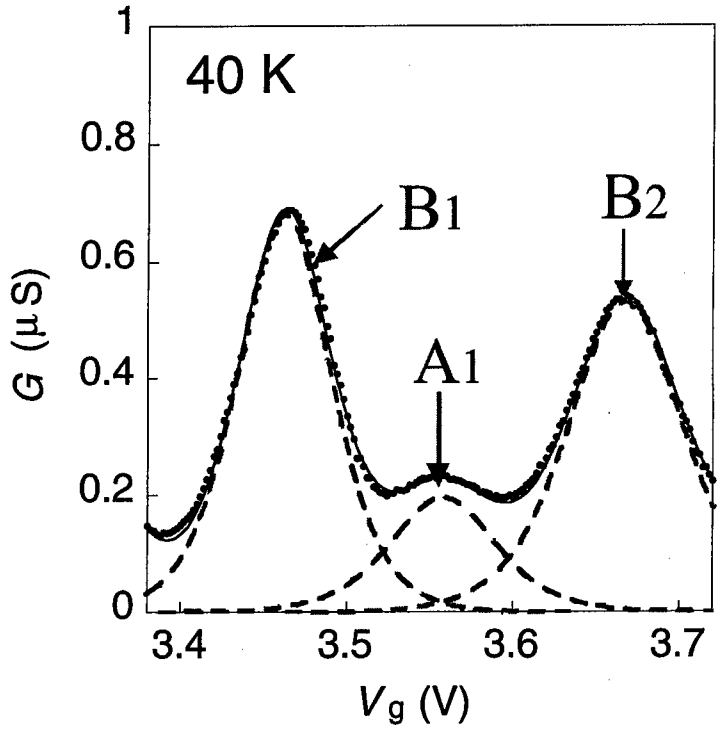


Fig. 14. Conductance oscillations of a twin-island SET as a function of the gate voltage measured at 40 K with the drain voltage of 10 mV. Dots are measured data while the solid line is the curve derived from fitting analyses. The broken lines, A and B, indicate the individual conductance from each SET.

Quantum Confined Electronics

"PIEZO-DOPED" LOW-NOISE *GaN* HETEROSTRUCTURE FIELD EFFECT TRANSISTORS

Alexander A. Balandin
Department of Electrical Engineering
University of California – Riverside
Riverside, CA 92521

Kang L. Wang
Device Research Laboratory
Electrical Engineering Department
University of California - Los Angeles
Los Angeles, CA 90095

ABSTRACT

We examined low-frequency noise in two types of specially designed $GaN/Al_xGa_{1-x}N$ heterostructure field effect transistors (HFET) grown on *SiC* substrate. Transistors of the first type were externally doped and had a low piezoelectrically induced charge density due to the small *Al* content in the barrier layer. Transistors of the second type were not doped externally, but had a higher piezoelectrically induced charge density in the interface channel due to the high *Al* content in the barrier layer. As a result, a stronger "piezo doping" in these transistors approximately compensated for the absence of the regular doping. Our results indicate that the noise spectral density in the "piezo doped" HFETs is two orders of magnitude smaller than that in the regularly doped HFETs of comparable electric characteristics. This noise reduction is important for microwave applications and may lead to novel device concepts utilizing piezoelectric effects in combination with quantum confinement in a two-dimensional channel.

I. INTRODUCTION

Development of high performance microwave technology requires detailed knowledge of the noise behavior of the semiconductor devices. It is important to know the value of the low-frequency noise, e.g. 1/f noise, since this type of noise is the limiting phase-noise factor for all kinds of HEMTs and MOSFETs, particularly when these devices are used as oscillators or mixers.

Recent advances in *GaN*-related compound materials and heterojunction field effect

transistors (HFET) have led to demonstration of high power density microwave operation of these devices. HFETs made on the basis of wide band gap materials like *GaN* offer several inherent advantages, such as higher breakdown voltage, higher thermal conductivity, comparable carrier mobility, and high saturation velocity. At the same time, first measurements of the low-frequency noise in GaN heterostructure field effect transistors (HFET) demonstrated very high levels of 1/f noise. For example, in Ref. [1] and [2], the authors reported values of the Hooge parameter higher than 10^{-2}. Fortunately enough, further improvements in *GaN* material and device processing have brought some good news. We have recently investigated a number of *GaN* HFETs with submicron gates, and extracted the Hooge parameter on the order of 10^{-5}-10^{-4} at rather high values of the drain bias V_{DS}=5 V [3]. In this paper, we describe a device structure, in which a strong piezoelectric effect at $GaN/Al_xGa_{1-x}N$ interface is utilized in order to achieve low-noise level at a relatively high carrier concentration.

It is well known that *GaN* is strong piezoelectric. In a proper designed heterostructure, the lattice constant mismatch between *GaN* and $Al_xGa_{1-x}N$ layers is accommodated by the internal strain rather than by the formation of the misfit dislocations. Because of the piezoelectric effect, this strain induces an electric field and significantly changes carrier distribution near the interface [4-6]. The piezoelectric polarization P_z along the growth direction z associated with the effect is given by a simple formula

$$P_z=2d_{31}(c_{11}+c_{12}-(c_{13})^2/c_{33})\varepsilon_{xx}, \quad (1)$$

where c_{lm} are the elastic stiffness coefficients, d_{31} is a piezoelectric tensor component, and ε_{xx} is the strain in the x direction. Here we assumed the (0001) growth direction, so that only one component of the piezoelectric tensor (d_{31}) is important. The piezo-induced electric charge density at the interface between *GaN* and $Al_xGa_{1-x}N$ is given by

$$Q_z^{piezo}=\text{div } \mathbf{P}=qN_z, \quad (2)$$

where q is the charge of an electron, and N_z is the charge density at the interface. The latter leads to an increase in the change density in the two-dimensional (2D) channel, and manifests itself as an additional "piezo doping." The device channel or barrier regions can also be externally doped to increase the total number of carriers.

In this work we investigate how the type of doping (external vs. "piezo") affects the low-frequency noise characteristics of GaN HFETs. The rest of the paper is organized as follows. In the next section we describe the device structure. Section III presents the results of the noise measurements followed by the discussion. We give our conclusions in section IV.

II. DEVICE STRUCTURE

Using Eqs. (1-2) and material parameters of *GaN* and *AlN* of Ref. [4], we have estimated that the change of the *Al* mole fraction from about 15% to about 30% would be

significant enough in order to provide approximately a 10^{13} cm^{-2} additional piezo-induced carrier density at the interface of our $GaN/Al_xGa_{1-x}N$ heterostructures. Having these considerations in mind, we have designed two HEMT-type structures on the basis of $GaN/Al_xGa_{1-x}N$ material system grown on *SiC* substrate, in which approximately the same sheet carrier density in the 2D channel was attained by the different means. The structure **A** was externally doped to N_d=2 x 10^{18} cm^{-3} and had a low piezoelectrically induced charge density due to the small *Al* content in the barrier layer and, as a result, a small strain ε_{xx} ($\varepsilon_{xx} \sim x$, where x is the *Al* mole fraction). The structure **B** was not doped externally, but had a higher piezoelectrically induced charge density due to the high *Al* content (more than two times) in the barrier layer. As a result, a stronger "piezo doping" in the structure **B** approximately compensated for the absence of the regular external doping. The external doping of the barrier and channel regions, the presence of unavoidable background charges, and the "piezo doping" resulted in a sheet electron concentration of (1.1-1.2) x 10^{13} cm^{-2} for both device structures. The doping type was the only major difference for structures **A** and **B**. The structure and layer thickness for both of them are shown schematically in Fig.1.

III. RESULTS OF THE NOISE MEASUREMENTS

We have examined a large number of devices with the gate width W=50 μm, gate length L_G=1.0 μm and a different source - drain separation distances of L_{SD}=2 μm – 4 μm. The devices were fabricated on the *SiC* substrate. For these devices we obtained experimental dependences of the equivalent input referred noise power spectrum on frequency, gate and drain voltages. The measurements were carried out for both the linear region of device operation corresponding to low drain-source voltage, V_{DS}, and the onset of the saturation region of operation (subsaturation) corresponding to V_{DS} = 5V. Typical DC current - voltage characteristic of *GaN* HFET is presented in Fig. 2 (the gate bias V_{GS} was used as a parameter and it was varied from 0 V with a step of -1 V).

As we pointed out the devices of type **A** and type **B** had approximately an equal carrier density in the 2D channel. At the same time, the mobility was very different for these devices. Electron Hall mobility at room temperature was determined to be 616 cm^2/Vs for external doped HFETs, and 1339 cm^2/Vs for "piezo-doped" HFETs. This significant difference is expected because the regular external channel doping introduces additional scattering centers in the channel, which deteriorate electron mobility. Despite this difference, both types of the devices had rather similar electrical characteristics (breakdown voltage V_{ds}>70V, threshold voltage V_{th}=-5.5V, and transconductance g_m=160-180 mS/mm).

The low frequency noise measurement system consists of a low-noise amplifier (three stages), a dynamic signal analyzer and bias power supplies. The HP4142B modular source and monitor were used for current-voltage measurements. The amplifier is made from commercially available IC op amps and has an equivalent noise voltage on the order of 3 $nV/Hz^{1/2}$ and an equivalent noise current of 2 $pA/Hz^{1/2}$. A detailed description of the amplifier used for these measurements can be found in Ref. [7,8]. The amplifier and *GaN*

HFETs were enclosed in a shielded box during the measurements in order to prevent pick up of environmental noise.

The measurements of the low-frequency noise (1/f noise) in these devices revealed a significant and important difference in the noise level in externally doped HFETs and "piezo-doped" HFETs (see Fig. 3). The experimental results indicate a *two-orders-of-magnitude reduction* in the input-referred noise spectral density of the predominantly "piezo-doped" (structure **B**) device with respect to the noise density of the predominantly externally doped channel devices (structure **A**). The threshold voltages are V_T=-4.5 V and V_T=-5.5 V for type **A** and type **B** devices, respectively. The measurements presented in Fig. 3 were carried out in the linear regime (V_{DS}=0.5 V). The difference in the low-frequency noise level is particularly significant in view of the fact that these devices have comparable characteristics, e.g., total sheet carrier concentration, g_m, and V_T.

In the subsaturation region of operation (V_{DS}=5 V), the noise spectral density for the "piezo-doped" channel device is again significantly smaller than that for the externally doped channel device (Fig. 4) with the same carrier density. The slope γ of the $1/f^{\gamma}$ dependence in all noise power density spectra is close to 1, although the noise power varies for different devices and gate bias values. We can also observe a trace of the generation-recombination (*g-r*) bulges in the noise spectra of the doped channel devices. It is important that the noise reduction in "piezo-doped" devices is observed in the subsaturation region, since GaN HFETs usually operate at high V_{DS}.

IV. CONCLUSIONS

We have shown that using the strong piezoelectric effect in *GaN* and quantum confinement of carriers at the *GaN/AlGaN* interface, one can construct a HEMT-type device with a significant number of carriers without external barrier or channel doping. The variation of the *Al* content in the device barrier region ("piezo doping") can lead to the controlled carrier density in the channel comparable to the that induced by the regular external doping. Our experimental investigation of the low-frequency noise reveals a two-orders-of-magnitude reduction in the input-referred noise spectral density for the "piezo-doped" channel devices with respect to the noise density in the externally doped devices with otherwise comparable electric characteristics. This significant reduction of the low-frequency noise is important for anticipated application of *GaN* HFETs for microwave communications, and may lead to the novel device concepts using "piezo doping" in combination with quantum confinement effects in 2D channels.

ACKNOWLEDGEMENT

The work in UCLA was supported by the DoD MURI-ARO program on Low Noise Electronics. The authors thank Dr. R. Li, Dr. S. Cai, Dr. Morozov, Mr. G. Wijeratne, and Prof. C.R. Viswanathan for the help in device manufacturing and measurements.

References

[1]. M.E. Levinshtein, F. Pascal, S. Contreras, W. Knap, S.L. Rumyantsev, R. Gaska, J.W. Yang, M.S. Shur, Appl. Phys. Lett., 72, 3053 (1998).

[2]. D.V. Kuksenkov, H. Temkin, R. Gaska, and J.W. Yang, IEEE Electron. Device Lett., 19, 222 (1998).

[3]. A. Balandin, S. Cai, R. Li, K.L. Wang, V. R. Rao, and C.R. Viswanathan, IEEE Electron. Device Lett., **19**, 475 (1998).

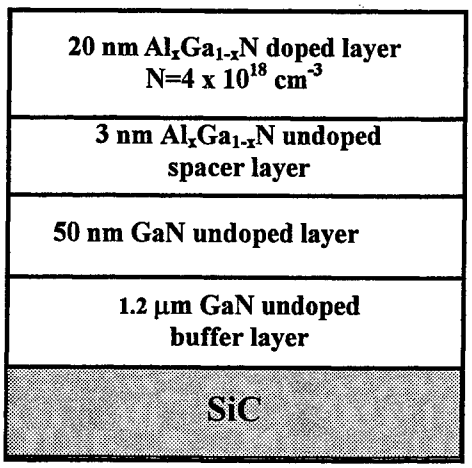
[4]. A. Bykhovski, B. Gelmont, M. Shur, J. Appl. Phys., 74, 6734 (1993).

[5]. A. Bykhovski, B. Gelmont, M. Shur, J. Appl. Phys., 81, 6332 (1997).

[6]. P.M. Asbeck, E.T. Yu, S.S. Lau, G.J. Sullivan, J. Van Hove, J. Redwing, Electron. Lett., 33, 1230 (1997).

[7]. J. Chang, A.A. Abidi, C.R. Viswanathan, IEEE Trans. Elec. Dev., 41, 1965 (1994).

[8]. A. Balandin, S. Morozov, S. Cai, R. Li, J. Li, K.L. Wang, G. Wijeratne, C.R. Viswanathan, IEEE Trans. Microwave Theory and Technique, (to appear in August, 1999).



STRUCTURE A: X ~ 14%
STRUCTURE B: X ~ 33%

Figure 1. Geometry of the GaN HFET structure.

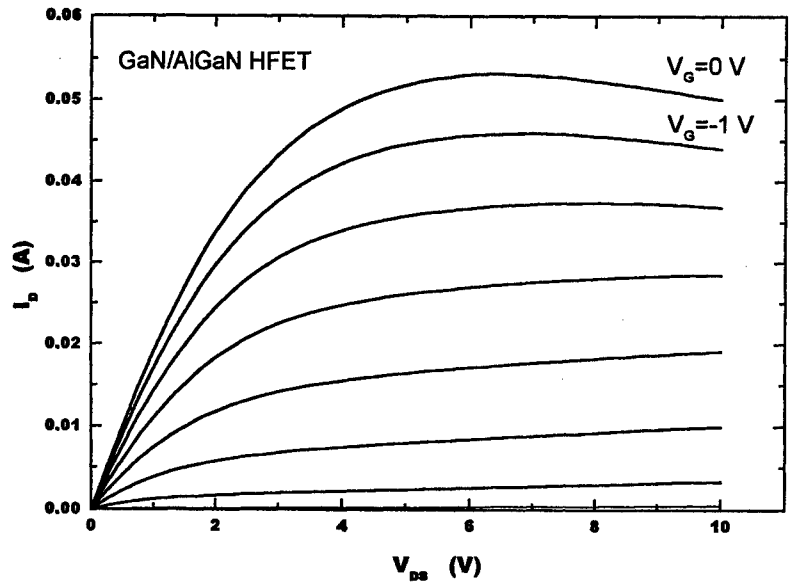


Figure 2. Typical DC current-voltage characteristics of GaN HFETs. The gate bias V_{GS} is used as a parameter and it is varied from 0 V (top curve) with the step of −1 V.

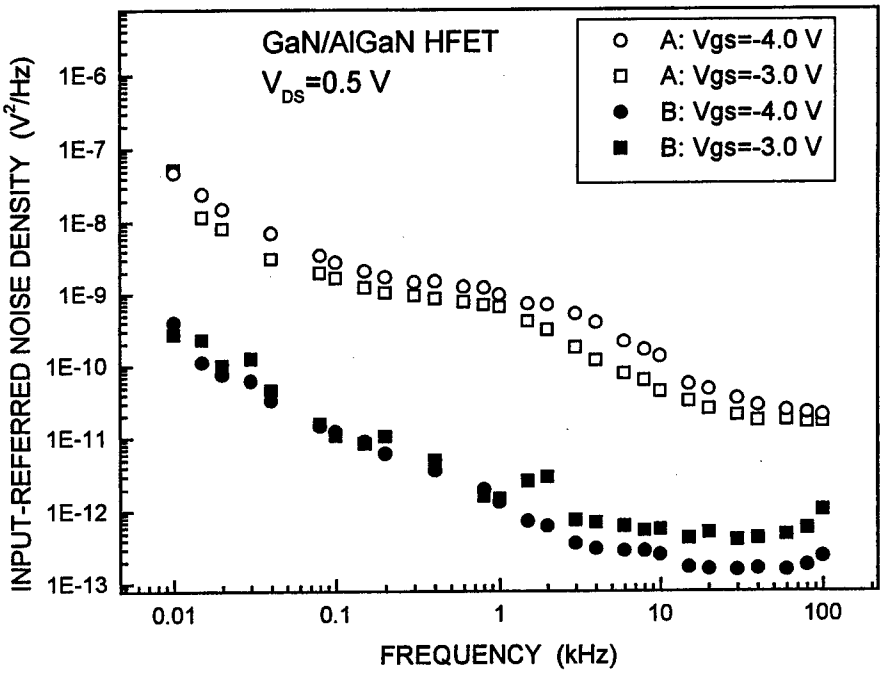


Figure 3. Input referred noise spectral density for the "regularly" doped channel device (empty squares and circles) and "piezo-doped" channel device (filled squares and circles). Data are shown for the linear regime of operation. Significant difference in the noise density was observed for all values of the gate bias (shown for two gate biases).

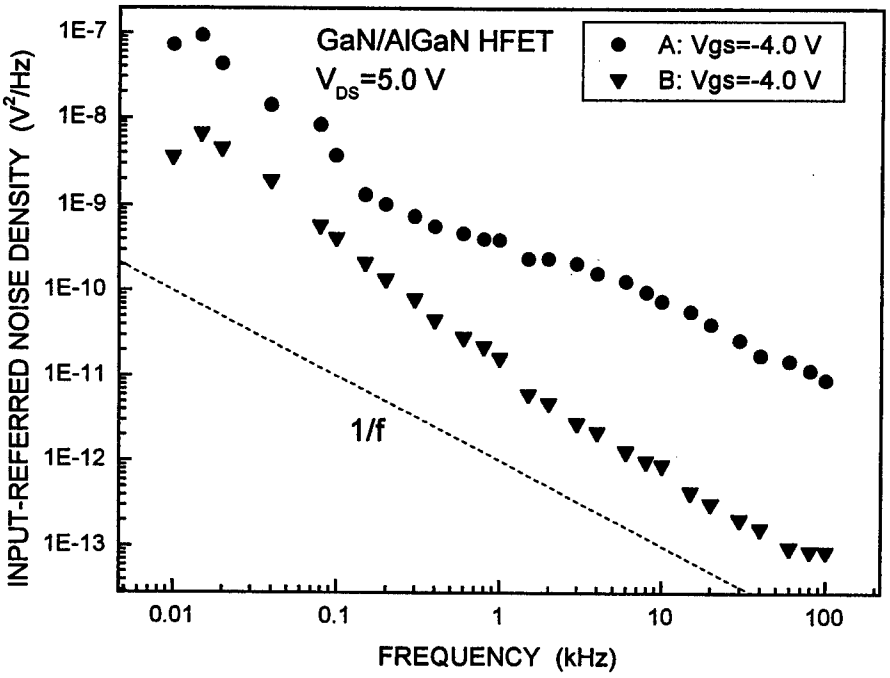


Figure 4. Input referred noise spectral density for the "regularly" doped channel device (red circles) and "piezo-doped" channel device (blue rectangles). Data are shown for the subsaturation regime of operation. Significant difference in the noise density was observed for all values of the gate bias (shown for the gate bias V_{GS}=-4 V).

TUNNELING PROPERTIES OF HOLES ACROSS LATTICE-MATCHED InP/InGaAs AND AlGaAs/GaAs HETEROINTERFACES IN THE BURT-FOREMAN FORMALISM

S. Ekbote, M. Cahay, and K. Roenker
Department of Electrical Engineering
University of Cincinnati, Cincinnati, Ohio 45221

ABSTRACT

We use Burt's envelope function formalism to analyze the tunneling properties of holes across abrupt $InP/In_{0.53}Ga_{0.47}As$ and $Al_{0.3}Ga_{0.7}As/GaAs$ heterostructures. We compare the results using the 6X6 and 4x4 Burt Hamiltonians and show that in the case of an $Al_{0.3}Ga_{0.7}As/GaAs$ heterostructure the two approaches give similar results for the transmission coefficients of holes. For the $InP/In_{0.53}Ga_{0.47}As$ system, the difference between the 4x4 and 6x6 is more pronounced. This is due to the fact that for the $InP/In_{0.53}Ga_{0.47}As$ heterostructure the spin-orbit split-off energy in the transmitted region ($In_{0.53}Ga_{0.47}As$) is smaller than the valence band discontinuity at the interface.

I. INTRODUCTION

In the past, the effective-mass approximation has been widely used to study the electrical and optical properties of bulk semiconductors [1]. Recently, Burt has extended the effective-mass theory to heterostructures using a rigorous envelope-function formalism [2]. Soon after, Foreman [3] has shown that Burt's multiband effective-mass theory leads to an unambiguous formulation of the boundary conditions to be satisfied by the envelope function components at an interface. In ref.[3], Foreman derived the explicit form of the valence-band effective mass Hamiltonian and corresponding rigorous boundary conditions at an interface while taking into account the coupling between the heavy-, light-, and split-off bands.

Recently, Meney et al. [4] calculated the valence-band structure in quantum wells starting with the Burt 4X4 and 6X6 Hamiltonians and Foreman's boundary conditions. They have shown that the warping of the highest valence band is markedly different at both intermediate and large values of the transverse wavevectors when the

spin-split-off band is included. This additional warping influences the hole band structure at even smaller transverse wavevectors in quantum wells made of materials with a spin-orbit split-off energy of the order of 100 meV (such in phosphide-base alloys like $Ga_{1-x}In_xP$). Finally, Meney et al. have shown that the valence band structure obtained using the Burt-Foreman formalism is quite different than the one derived using the typical symmetrization procedure of the Luttinger-Kohn Hamiltonian to derive the envelope wavefunction boundary conditions [5, 6].

Recently, we have used the Burt-Foreman formalism to analyze the tunneling properties of holes across an abrupt $InP/In_{0.53}Ga_{0.47}As$ heterojunction [7]. We have shown that, for large values of the transverse wavevector, the energy dependence of the hole tunneling coefficients is quite different from that calculated with the symmetrization procedure. Additionally, we have found that for lower values of the transverse wavevector, the difference between the two approaches can still be observed at low value of the incident energy. Furthermore, the tunneling coefficients of holes are found to be quite sensitive to the orientation of the hole wavevector parallel to the heterointerface. This sensitivity is particularly noticeable for large values of the hole transverse wavevector.

In this paper, we support the conclusions reached by Meney et al. by comparing the use of the 4X4 and 6X6 Burt Hamiltonians to calculate the tunneling properties of holes across abrupt $InP/In_{0.53}Ga_{0.47}As$ and $Al_{0.3}Ga_{0.7}As/GaAs$ heterostructures. An important difference exists between the two heterojunctions as shown in Fig.1. For the $Al_{0.3}Ga_{0.7}As/GaAs$ system, the valence band discontinuity is much smaller than the spin-orbit split-off energy. Holes incident from the left need a kinetic energy around 200 meV before being able to reach the threshold energy for free propagation in the SO-band in the transmitted region. On the other hand, tunneling through the $InP/In_{0.53}Ga_{0.47}As$ will be very sensitive to presence of the SO-band because the spin-orbit split-off energy in the transmitted region ($In_{0.53}Ga_{0.47}As$) is smaller than the valence band discontinuity ($\Delta E_v = 386meV$). Furthermore, the spin-orbit split-off energy in the left region (InP) is quite small (100 meV) and the dispersion relation for heavy- and light-holes in this region will be strongly affected by the SO-band even for holes with low incident kinetic energy. We therefore expect the difference between the hole tunneling coefficients calculated using the 4X4 and 6X6 Burt Hamiltonians to be more pronounced for an $InP/In_{0.53}Ga_{0.47}As$ interface than for an $Al_{0.3}Ga_{0.7}As/GaAs$ heterojunction.

In section II, the Burt 6x6 Hamiltonian and associated boundary conditions are explicitly written for the sake of completeness. The 4x4 Burt Hamiltonian and corresponding boundary conditions are readily derived from the 6X6 expressions by neglecting coupling to the SO-band. Starting with the 4X4 and 6X6 Burt-Foreman formalisms, the transmission coefficients of holes across an abrupt interface can be obtained using the technique described in [7]. Section III contains our results for the transmission coefficients of both heavy- and light-hole across abrupt $InP/In_{0.53}Ga_{0.47}As$ and $Al_{0.3}Ga_{0.7}As/GaAs$ heterostructures. Finally, section V contains our conclusions.

II. APPROACH

In the exact envelope-function theory of Burt [2], the Hamiltonian describing the interaction of the heavy-, light-, and SO-bands near the top of the valence band is given by [3]

$$H = \begin{bmatrix} P+Q & 0 & -S_- & R & (1/\sqrt{2})S_- & \sqrt{2}R \\ 0 & P+Q & -R^\dagger & -S_+ & -\sqrt{2}R^\dagger & (1/\sqrt{2})S_+ \\ -S_-{}^\dagger & -R & P-Q & C & \sqrt{2}Q & \sqrt{\frac{3}{2}}\Sigma_- \\ R^\dagger & -S_+{}^\dagger & C^\dagger & P-Q & -\sqrt{\frac{3}{2}}\Sigma_+ & \sqrt{2}Q \\ (1/\sqrt{2})S_-{}^\dagger & -\sqrt{2}R & \sqrt{2}Q & -\sqrt{\frac{3}{2}}\Sigma_+{}^\dagger & P+\Delta & -C \\ \sqrt{2}R^\dagger & (1/\sqrt{2})S_+{}^\dagger & \sqrt{\frac{3}{2}}\Sigma_-{}^\dagger & \sqrt{2}Q & -C^\dagger & P+\Delta \end{bmatrix} \begin{matrix} |\frac{3}{2},\frac{3}{2}\rangle \\ |\frac{3}{2},-\frac{3}{2}\rangle \\ |\frac{3}{2},\frac{1}{2}\rangle \\ |\frac{3}{2},-\frac{1}{2}\rangle \\ |\frac{1}{2},\frac{1}{2}\rangle \\ |\frac{1}{2},-\frac{1}{2}\rangle \end{matrix} \tag{1}$$

where, following Foreman, we have used atomic units ($\hbar = m_0 = 1$). In Eq.(1), the following notations are used

$$P = V_h(z) + \frac{1}{2}(\gamma_1 k_\rho^2 + k_z \gamma_1 k_z), \tag{2}$$

$$Q = \frac{1}{2}(\gamma_2 k_\rho^2 - 2k_z \gamma_2 k_z), \tag{3}$$

$$R = -\left(\frac{\sqrt{3}}{2}\right)\overline{\gamma} k_-^2 + \left(\frac{\sqrt{3}}{2}\right)\mu k_+^2, \tag{4}$$

$$S_\pm = \sqrt{3}k_\pm[(\sigma - \delta)k_z + k_z \pi], \tag{5}$$

$$\Sigma_\pm = \sqrt{3}k_\pm\{[\frac{1}{3}(\sigma - \delta) + \frac{2}{3}\pi]k_z + k_z[\frac{2}{3}(\sigma - \delta) + \frac{1}{3}\pi]\}, \tag{6}$$

$$C = k_-[k_z(\sigma - \delta - \pi) - (\sigma - \delta - \pi)k_z], \tag{7}$$

$$k_\rho^2 = k_x^2 + k_y^2, \quad k_\pm = k_x \pm i k_y, \quad k_z = -i\frac{d}{dz}. \tag{8}$$

and the following quantities are introduced

$$\tilde{\gamma} = \frac{1}{2}(\gamma_3 + \gamma_2), \tag{9}$$

$$\mu = \frac{1}{2}(\gamma_3 - \gamma_2), \tag{10}$$

$$\delta = \frac{1}{9}(1 + \gamma_1 + \gamma_2 - 3\gamma_3), \tag{11}$$

$$\sigma = \tilde{\gamma} - \frac{1}{2}\delta, \tag{12}$$

$$\pi = \mu + \frac{3}{2}\delta. \tag{13}$$

In Eq.(1), Δ is the spin-orbit split-off energy and the γ_i are the Luttinger parameters. Hereafter, hole energies are measured as positive moving into the valence-band. In Eq.(2), $V_h(z)$ is the valence band energy profile. We consider the case of a simple potential step hereafter.

The Hamiltonian in Eq.(1) is a 6X6 matrix in the basis composed of the $(|\frac{3}{2}, \pm\frac{3}{2}\rangle)$ heavy-hole, the $(|\frac{3}{2}, \pm\frac{1}{2}\rangle)$ light-hole, and the $(|\frac{1}{2}, \pm\frac{1}{2}\rangle)$ split-off Bloch wave functions at the center of the Brillouin zone. These functions are eigenfunctions of the total angular momentum and diagonalize the spin-orbit interaction. In Burt's theory, these functions are required to be the same throughout the heterostructure [2]. When written for a bulk sample (i.e, assuming the γ_i's are constant), Burt's Hamiltonian reduces to the 6X6 Luttinger-Kohn Hamiltonian [8].

As shown by Foreman [3], the 6X6 Effective-mass Hamiltonian in Eq.(1) can be block diagonalized using a unitary transformation [3, 9]:

$$H_{\pm} = \begin{bmatrix} P+Q & R \mp iS & \sqrt{2}R \pm \frac{i}{\sqrt{2}}S \\ R \pm iS^{\dagger} & P-Q \mp iC & \sqrt{2}Q \mp i\sqrt{3/2}\Sigma \\ \sqrt{2}R \mp \frac{i}{\sqrt{2}}S^{\dagger} & \sqrt{2}Q \pm i\sqrt{3/2}\Sigma^{\dagger} & P+\Delta \pm iC \end{bmatrix} \tag{14}$$

In the Hamiltonians $H_{\pm}$, the P, Q, and C terms are as defined earlier. The rest of the terms are defined as follows [3]

$$R = -\frac{\sqrt{3}}{2}\gamma_{\phi}k_{\rho}^2, \tag{15}$$

$$\gamma_\phi = \sqrt{\tilde{\gamma}^2 + \mu^2 - 2\tilde{\gamma}\mu cos(4\phi)}, \tag{16}$$

$$S = \sqrt{3}k_\rho[(\sigma - \delta)k_z + k_z\pi], \tag{17}$$

$$\Sigma = \sqrt{3}k_\rho\{[\frac{1}{3}(\sigma - \delta) + \frac{2}{3}\pi]k_z + k_z[\frac{2}{3}(\sigma - \delta) + \frac{1}{3}\pi]\}, \tag{18}$$

where $k_\rho^2 = k_x^2 + k_y^2$ and (k_x, k_y) are the components of the transverse wavevector. Furthermore, ϕ is the azimuthal angle ($\phi = arctan(k_y/k_x)$).

Across an interface, we require the three components of the envelope function to be continuous. If we take the z axis as the direction of growth of the heterostructure and interpret the wave vector $\vec{k} = (k_x, k_y, k_z)$ as a differential operator $-i\vec{\nabla}$, the boundary conditions can be obtained be a simple integration of the effective-mass equation with the Hamiltonian in Eq.(1) across the interface. This procedure requires that the three component vectors $B\vec{F}$ must be continuous, where $\vec{F}$ are the hole envelope wave functions solutions of the effective mass equation with Hamiltonian (14) and $B\pm$ is given by [3, 10]

$$B\pm = \begin{bmatrix} (\gamma_1 - 2\gamma_2)\frac{d}{d_z} & \pm 2\sqrt{3}\pi k_\rho & \mp\sqrt{6}k_\rho\pi \\ \mp 2\sqrt{3}(\sigma - \delta)k_\rho & (\gamma_1 + 2\gamma_2)\frac{d}{d_z} \pm 2k_\rho(\sigma - \delta - \pi) & -2\sqrt{2}\gamma_2\frac{d}{d_z} \pm \sqrt{2}k_\rho(2\sigma - 2\delta + \pi) \\ \pm\sqrt{6}k_\rho(\sigma - \delta) & -2\sqrt{2}\gamma_2\frac{d}{d_z} \mp \sqrt{2}k_\rho(\sigma - \delta + 2\pi) & \gamma_1\frac{d}{d_z} \mp 2k_\rho(\sigma - \delta - \pi) \end{bmatrix} \tag{19}$$

where $B_+(B_-)$ is associated with the Hamiltonian $H_+(H_-)$, respectively.

If the coupling to the SO-band is neglected, the Burt Hamiltonian reduced to the upper left 4X4 in the Hamiltonian (1). The resulting Hamiltonian can still be block-diagonalized using a 4x4 version of the unitary transformation described above, leading to upper and lower 2x2 Hamiltonians equal to the upper left 2x2 blocks of the Hamiltonians in Eq.(14). In that case, the enveloppe function has only two components which must be continuous across an interface. Simultaneously, the two component vectors $B\vec{F}$ must be continuous, where $\vec{F}$ are the two-component hole envelope wavefunctions solutions of the upper and lower 2x2 Hamiltonians and B are the upper left 2x2 matrices extracted from the matrices in Eq.(19).

Starting with either the 6X6 and 4X4 Burt-Foreman formalisms, the calculation of the transmission coefficients of holes incident from the left on the abrupt interfaces shown in Fig. 1 can then be solved using the technique described in details in ref. [7]. Hereafter, we compute the average of the transmission coefficients obtained with the upper and lower Hamiltonians. These averages are the quantities of interest since

they are needed for the calculation of the current densities of holes across interfaces, as discussed in [10].

III. RESULTS

First, we illustrate the energy dispersion of holes by considering an $Al_{0.3}Ga_{0.7}As$ region latticed-matched to $GaAs$. We plot in Fig.2 the real parts ($Realk_z$) of the z-component of the wavevectors for the heavy, light, and SO-bands as a function of the incident energy for a magnitude of the transverse wavevector $k_\rho = 0.04\text{X}(2\pi/a)$, where a = 5.6533 $\AA$ is the lattice constant of $GaAs$. In Fig.1, the azimuthal angle of the transverse wavevector is set equal to 45°. The full and dotted lines are the results obtained starting with the 6X6 and 4X4 Burt Hamiltonians, respectively. The results for the heavy-hole band are virtually indentical in the two approaches, but are more pronounced for the light-hole especially for energy approaching the location of the spin-orbit split-off band. Similar features were found when repeating the simulations for the $GaAs$ region.

In Fig.2, we indicate the threshold energies (E_h^-, E_1, E_{SO}) for free propagation in the heavy-, light-, and SO-bands, respectively (the latter is not defined when starting with the 4X4 Burt Hamiltonian). These threshold energies are a function of the transverse wavevector as illustrated in Fig.3. In that figure, the curves showing the threshold energies in the $AlGaAs$ region are shifted upward in energy by an amount equal to the valence band discontinuity ΔE_v (115 meV) at the $AlGaAs/GaAs$ interface. Figure 3 shows that the threshold energies obtained with the 4X4 and 6X6 Burt Hamiltonians have nearly the same dependence on the hole transverse wavevector.

We used the energy dispersion relationships discussed above to calculate the transmission of both heavy- and light-holes incident from the left across the $AlGaAs/GaAs$ interface shown in Fig.2. The results are shown in Figures 4 and 5 for the heavy- and light-hole, respectively. These figures show that the results of the 4X4 and 6X6 Hamiltonians virtually agree over all range of incident energy, except of course for energy above the energy threshold for free propagation in the SO-band. In an analysis based on the 6X6 Hamiltonian, there is a finite probability for both heavy- and light-holes to transmit in the SO-band in the $GaAs$ region around 225 meV. There is also a probability for holes to be reflected in the SO-band in the $AlGaAs$ region, which is not shown here because it occurs at the energy of the energy scale used in Figures 4 and 5. Even though not shown here, the close agreement between the transmission coefficients of heavy- and light-holes was also observed for lower values of the transverse wavevector.

We repeated the calculations described above for a $InP/In_{0.53}Ga_{0.47}As$ interface. Figures 5 and 6 are plots of the transmission coefficients of heavy- and light-holes for holes incident from the left of the structure shown in Fig.1. In the simulations, we use $k_\rho = 0.04\text{X}(2\pi/a)$, where a = 5.83 $\AA$ is the lattice constant of InP. Furthermore, the azimuthal angle of the transverse wavevector is set equal to 45°. Figures 5 and

6 show a large difference between the transmission coefficients calculated using the 4X4 or 6X6 Burt Hamiltonians. As illustrated in Fig.1, this is due partly to the low value of the spin-orbit split-off energy on the InP. As a result, the z-component of the wavevectors of the heavy- and light-holes are strongly affected by the proximity of the SO-band. Furthermore, the spin-orbit split-off band on the $InGaAs$ side lies below the height of the valence band step at the interface. As a result, the strong coupling to the SO-band in this region cannot be neglected.

IV. CONCLUSIONS

We have used the envelope function Hamiltonian derived by Burt [2] to study the effects of band mixing between heavy-, light- and SO-bands on the transmission coefficients of holes across $Al_{0.3}Ga_{0.7}As/GaAs$ and $InP/In_{0.53}Ga_{0.47}As$ abrupt interface. At the heterointerface, we have applied the rigorous boundary conditions derived by Foreman [3] while neglecting the interface band mixing effects described in [11]. In this paper, we have compared the transmission coefficients of heavy- and light-holes in Burt-Foreman formalism starting with the 4X4 and 6X6 Burt Hamiltonians. We have shown that the difference between the two formalisms is small for the $Al_{0.3}Ga_{0.7}As/GaAs$ interface but cannot be neglected for the $InP/In_{0.53}Ga_{0.47}As$ structure. As shown in Fig.1, this results from the difference in the locations of the SO-bands on either side of the interfaces for the two structures. Both SO-bands are located at an energy much larger than the valence band discontinuity for the $Al_{0.3}Ga_{0.7}As/GaAs$ system. For the $InP/In_{0.53}Ga_{0.47}As$ interface, the spin-orbit split-off energy is quite small (100 meV) on the InP side and is below the valence band discontinuity on the $In_{0.53}Ga_{0.47}As$ side. Neglecting the effects of the SO-bands by using the 4X4 rather than the 6X6 Burt Hamiltonian is therefore a poor approximation for the $InP/In_{0.53}Ga_{0.47}As$ heterointerface.

ACKNOWLEDGEMENT

This work was supported by the National Science Foundation under award ECS-9525942. We also acknowledge the Ohio-Cray supercomputing center for the use of their facilities.

References

[1] G. Bastard, Wave Mechanics Applied to Semiconductor Heterostructures, Wiley, New York (1988).

[2] M. G. Burt, J. Phys: Condens. Matter, 4, 6651 (1992).

[3] B. A. Foreman, Phys. Rev. B, 48, 4964 (1993).

[5] C.Y. Chao and S.L. Chuang, Phys. Rev. B, 43, 7027 (1991).

[6] C. Y. Chao and S. L. Chuang, Phys. Rev. B, 46, 4110 (1992).

[7] S. Ekbote, M. Cahay and K. Roenker, "Tunneling Properties of Holes Across Abrupt Heterostructures Using the Envelope Function Method of M. G. Burt (J. Phys: Condens. Matter 4, 6651 (1992))", submitted to **Journal of Applied Physics**, February 1999.

[8] S. L. Chuang, Phys. Rev. B, 40, 10379 (1989).

[9] D. A. Broido and L. J. Sham, Phys. Rev. B, 31, 888 (1985).

[10] S. Ekbote, M. Cahay and K. Roenker, Phys. Rev. B, 58, 16315 (1998).

[11] Due to breakdown of bulk symmetry at an heterointerface, there is an additional interface band mixing effect which couple the heavy-hole to the light-hole and split-off bands as recently pointed out by E. L. Ivchenko, A. Yu. Kaminski, and U. Rossler, Phys. Rev. B, 54, 5852 (1996) and B. A. Foreman, Phys. Rev. Letters, 81, 425 (1998). This refinement could be incorporated by a simple modification of the Hamiltonian in Eq.(1) by adding a delta-function term to the element R in Eq.(4).

[12] T. Kumar, M. Cahay, and K. Roenker, Phys. Rev. B **56**, 4836 (1997).

Table I: Luttinger-Kohn parameters and Spin-Orbit Split-Off energy used in the simulations. The values for the $Al_{0.3}Ga_{0.7}As$ and $In_{0.53}Ga_{0.47}As$ materials are found by linear interpolation.

	GaAs	InAs	InP
γ_1	6.85	20.4	4.95
γ_2	2.1	8.3	1.65
γ_3	2.9	9.1	2.35
Δ (eV)	0.34	0.38	0.1

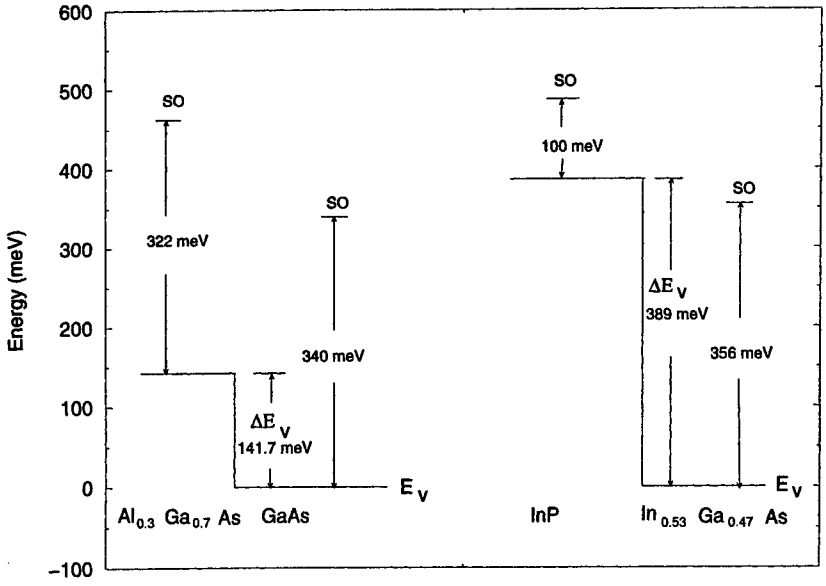


Figure 1: Illustration of the valence band discontinuity across the $Al_{0.3}Ga_{0.7}As/GaAs$ and $InP/In_{0.53}Ga_{0.47}As$ interfaces. The horizontal lines labelled "SO" are the locations of the spin-orbit split-off energy band minimum on both sides of the structure.

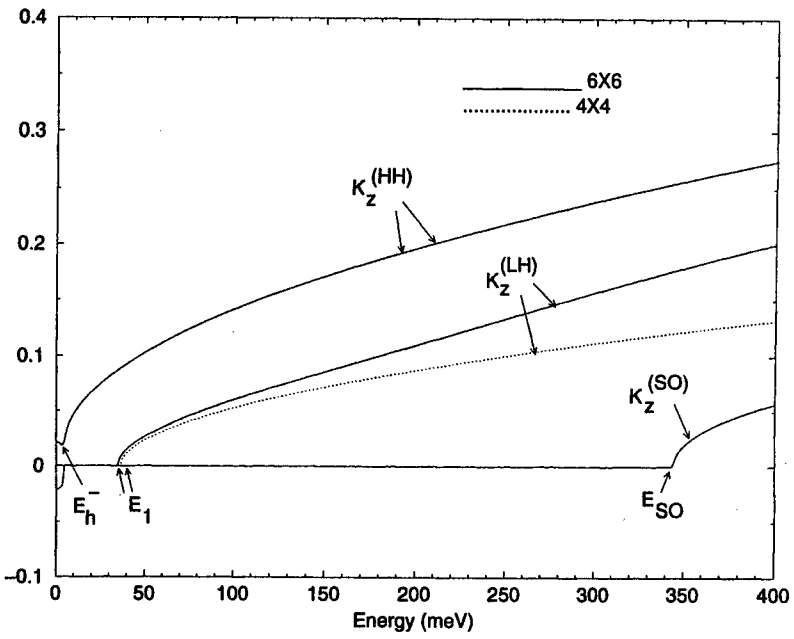


Figure 2: Real parts of the hole wavevectors in a bulk $Al_{0.3}Ga_{0.7}As$ region as a function of energy for a value of $k_\rho = 0.04\text{X}\ (2\pi/a)$ (a is 5.6533 $\AA$, the lattice constant of GaAs) and for the azimuthal angle ϕ set equal to 45°. The zero of energy is the top of the valence band in the $Al_{0.3}Ga_{0.7}As$ region of a $Al_{0.3}Ga_{0.7}As/GaAs$ interface. Energy is measured positive moving into the valence band. The full and dotted lines are the results obtained with 6X6 and 4X4 Burt Hamiltonians, respectively. The energies $E_h{}^-$, E_1, and E_{SO} are the threshold energies for free propagation in the heavy-, light-, and SO-band, respectively.

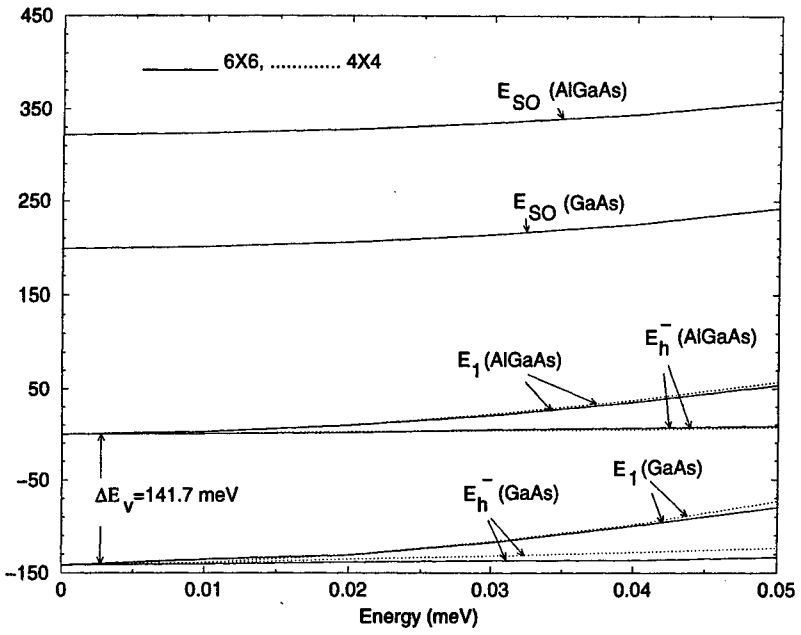


Figure 3: Dependence on the magnitude of the tranverse wave vector (k_ρ) of the energies ($E_h^-, E_h^+, E_1, E_{SO}$) thresholds in the $AlGaAs$ and $GaAs$ regions of a $Al_{0.3}Ga_{0.7}As/GaAs$ interface. The energy threshold for the $AlGaAs$ have been shifted upward in energy by an amount equal to the valence band discontinuity ($\Delta E_v = 141.7$ meV). Also shown as dotted lines are the k_ρ dependence of (E_h^-, E_h^+, E_1) when the effects of spin-orbit coupling are neglected [8, 12]. The zero of energy is the top of the valence band in the $Al_{0.3}Ga_{0.7}As$ region. Energy is measured positive moving into the valence band.

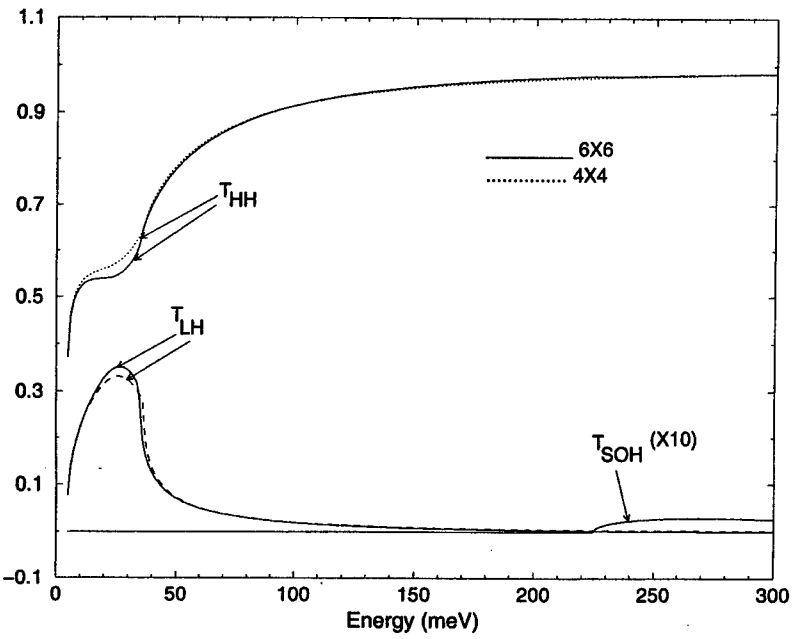


Figure 4: Transmission coefficients for a heavy-hole incident from the left of the $Al_{0.3}Ga_{0.7}As/GaAs$ interface shown in Fig.1. Energy is measured positive moving into the valence band and the zero of energy is the top of the valence band in the InP region. The results show the average of the transmission coefficients calculated with the upper and lower Hamiltonians. The full and dotted lines are the results obtained starting with the 6X6 and 4X4 Burt Hamiltonians, respectively. The in-plane wave vector is equal to $k_\rho = 0.04\ (2\pi/a)$ (where a is the lattice constant of $GaAs$) and the azimuthal angle ϕ is equal to 45°.

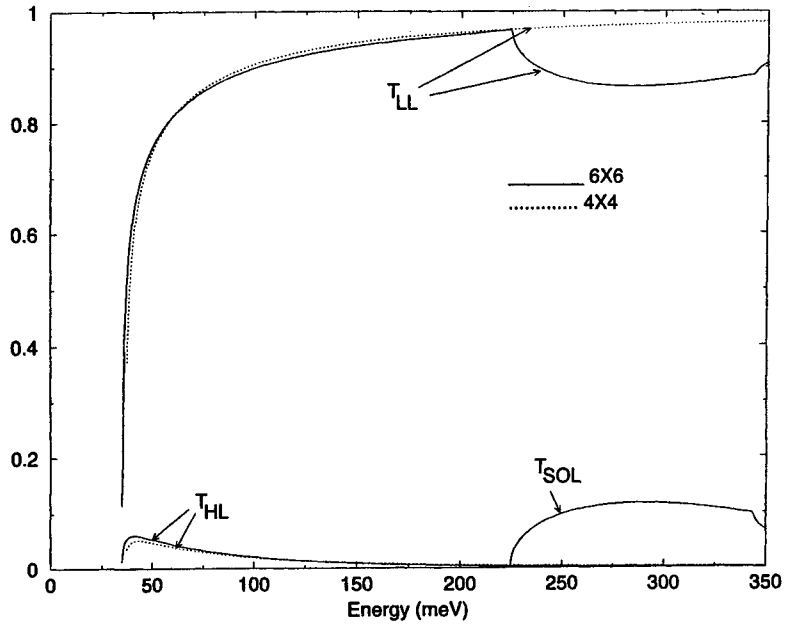


Figure 5: Same as Fig.4 for a light-hole incident from the left on the $Al_{0.3}Ga_{0.7}As/GaAs$ interface shown in Fig. 1.

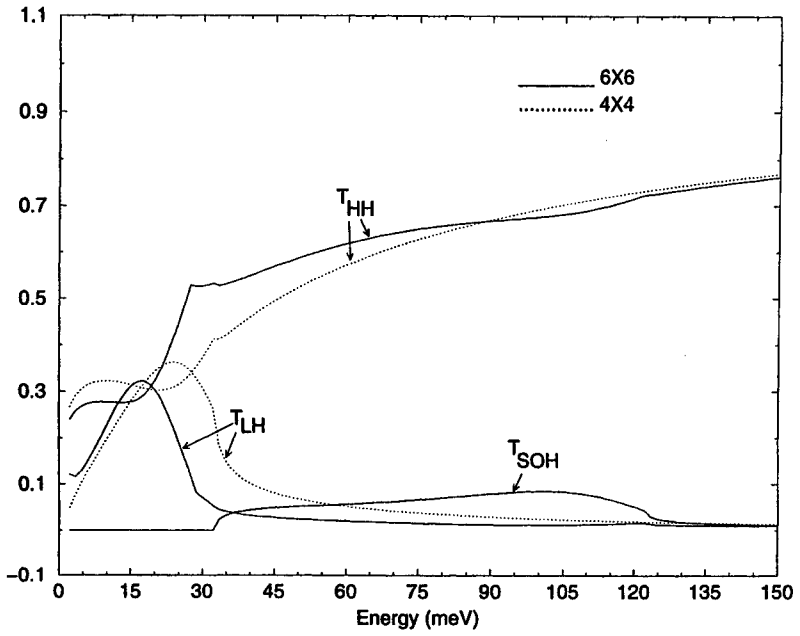


Figure 6: Transmission coefficients for a heavy-hole incident from the left of the $InP/In_{0.53}Ga_{0.47}As$ interface shown in Fig.1. Energy is measured positive moving into the valence band and the zero of energy is the top of the valence band in the InP region. The results show the average of the transmission coefficients calculated with the upper and lower Hamiltonians. The full and dotted lines are the results obtained starting with the 6X6 and 4X4 Burt Hamiltonians, respectively. The in-plane wave vector is equal to $k_\rho = 0.04\ (2\pi/a)$ (where a is the lattice constant of InP, 5.83 $\mathring{A}$) and the azimuthal angle ϕ is equal to 45°.

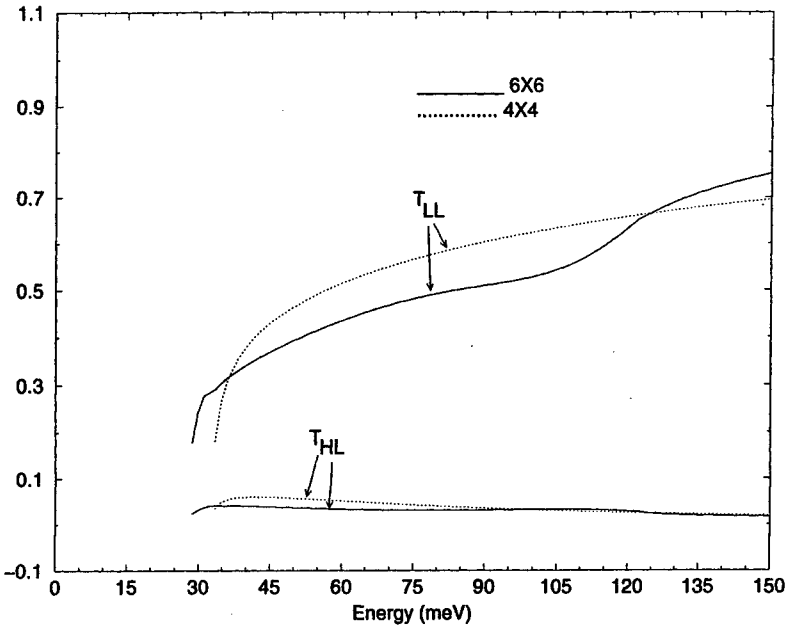


Figure 7: Same as Fig.4 for a light-hole incident from the left on the $InP/In_{0.53}Ga_{0.47}As$ interface shown in Fig. 1.

QUANTIZED CONDUCTANCE IN NARROW-CHANNEL SOI MOSFETS

J. Ahopelto, M. Prunnila and S. Eränen
VTT Microelectronics Centre, Tekniikantie 17, FIN-02015 Espoo, Finland

M. Kamp, M. Emmerling and A. Forchel
Technische Physik, Universität Würzburg, Am Hubland, D-97074 Würzburg, Germany

A. Kristensen and P. E. Lindelof
The Niels Bohr Institute, University of Copenhagen,Universitetsparken 5, DK-2100 Copenhagen, Denmark

A. Gustafsson
Solid State Physics, Lund University, Box 118, S-221 00 Lund, Sweden

ABSTRACT

Fabrication and electrical properties of narrow-channel silicon MOSFETs or silicon quantum point contacts are reported. The devices are fabricated on bonded silicon on insulator (SOI) wafers produced by Smart-Cut process. Mobility of 9000 cm^2/Vs is measured for a 60 nm-thick SOI film. Quantum point contacts fabricated from the material show quantized conductance at 4.2 K. The effective diameter of the channel constrictions of the devices are estimated to be 30-40 nm. Estimate of the dimensions is based on cross-sectional TEM analysis of oxidized silicon ridges on the same wafer with the devices.

INTRODUCTION

Most of the experimental work on 1-dimensional transport in semiconductors has been done using 3-5 compounds. These materials provide advantages such as low effective mass and well-controlled potential barriers defined by heterointerfaces. In silicon the dimensions required for the quantization of transversal modes due to the large effective mass are much smaller than in 3-5 compounds. This sets very high demands for the fabrication process of 1-dimensional silicon structures. An advantage of Si is the stable thermal oxide. The growth of the oxide can be well controlled and small structures can be fabricated by oxidation. The oxide charges are problematic and cause fluctuation and scattering in narrow channels. Although single electron phenomena and conductance quantization have been demonstrated in mesoscopic devices fabricated from silicon even at elevated temperature [1-3], the material still is a challenge for experimental work.

In this paper, the fabrication and electrical properties of a narrow-channel MOSFET or a silicon quantum point contact (SiQPC) are reported. The devices were

fabricated on bonded SOI wafers. The diameter of the channel constriction is 30-40 nm. The SOI film has a relatively high mobility and the QPC's show quantized conductance at 4.2 K.

EXPERIMENTAL

The devices were fabricated on bonded silicon on insulator (SOI) wafers. The wafers were produced by Smart-Cut process [4]. The thickness of the SOI film was 200 nm and the thickness of the buried oxide (BOX) layer 400 nm. The wafers were implanted using phosphorus to a dose of 5E14 cm^{-2}. The implantation energy was 20 keV. The areas, which were to form the active channels of the SiQPC, were protected by photoresist during implantation. The implantation was followed by oxidation in dry ambient at 1080 °C for 35 minutes. The oxidation step reduced the thickness of the SOI film to 100 nm. During the oxidation, the implanted dose was activated. The sacrificial oxide was then removed.

Mesas were selectively etched by reactive ion etching (RIE) in Cl/He plasma. The etching mask was photoresist, which was patterned by UV-lithography. The mesas contain a 3 μm-wide constriction between the current and voltage leads. The constriction was further narrowed by e-beam lithography. A 300 nm-thick PMMA layer was spun on the wafers. The PMMA layer served as etching mask for RIE. The widths of the etched constrictions ranged from 50 nm to 200 nm.

Next, the wafers were oxidized in dry ambient for 20 minutes at 1000 °C. This produced a 95 nm-thick oxide on the mesas. The purpose of this oxidation step was twofold: to reduce the size of the channels of the QPC's and to form the gate oxide. Contact windows were opened and a 300 nm-thick aluminum layer was evaporated. The Al film was patterned using UV-lithography and sintered at 400 °C. The ohmic contacts and gates were formed in a single evaporation step. The reason for the use of Al gate instead of poly-Si was to try to avoid the potential fluctuation in the channel caused by dopant segregation into the grain boundaries in poly-Si [5]. An optical micrograph of a device is shown in Fig. 1.

In addition to the QPC's, the wafers contained several test structures for the characterization of the fabrication process. These include Hall-bars, meander lines, transfer length lines (TLM), Kelvin resistors and capacitors. Structures for cross-sectional transmission electron microscopy (XTEM) analysis were also included. The XTEM samples consisted of ridges with various widths and pitches in [011] and [01-1] direction. The ridges were patterned by e-beam lithography and had widths ranging from 120 nm to 240 nm prior to the second oxidation step. The TEM samples were prepared by conventional methods of mechanical thinning, dimpling and ion milling. The images were recorded at 200 kV or 400 kV.

RESULTS

The electrical properties of the implanted and unimplanted SOI film, metallization and contacts were measured from the test structures. A sheet resistance of $R_{sqr} = 320\ \Omega$ of

the implanted areas, i.e., the current and voltage leads, was obtained. The contact resistance of Al metallization to the current and voltage leads was R_C = 25 Ω. Using the measured capacitance data, a thickness of 90 nm was obtained for the gate oxide. The thickness of the remaining SOI layer was estimated to be about 60 nm. A dielectric strength of 1E7 V/cm was measured for the gate oxide. The sheet resistance R_{sqr} of the Al metallization was 100 mΩ.

The resistivity and carrier concentration in the implanted areas can be estimated to be $\rho < 2$ mΩcm and $n > 4E19$ cm^{-3}, respectively. The profiles of the ion distribution and damage were simulated using TRIM program. The average range of phosphorus ions implanted into Si at 20 keV is 29 nm. The tail of the distribution extends to 60 nm. The maximum of the damage profile is at the depth of 20 nm, and the damage profile tails off at the depth of 60 nm. The implantation was so shallow that the damaged material was oxidized completely in the first oxidation step, and the remaining SOI layer is composed of undamaged material. The snow-plough effect was used to pile up the dopant ions into the SOI layer and to increase the final doping concentration.

The electrical properties of the unimplanted SOI material were measured from a 100 μm-wide Hall bar. The measurements were performed both as a function of temperature at fixed gate voltage and as a function of gate voltage at 10 K. At low gate voltage, the mobility increases with increasing gate voltage, passes through a maximum and starts slowly to decrease at higher voltages. The behaviour can be explained by the screening of the fixed charges in the oxide by the increasing number of electrons in the channel [6]. At high carrier concentration the scattering arising from the Si/SiO_2 interface begins to affect the mobility [6]. The maximum mobility of the 60 nm-thick SOI channel is 9000 cm^2/Vs at 10 K. Mobility and carrier density as a function of temperature at gate voltage of 5 V are shown in Fig. 2. The carrier concentration saturates to 1.3E12 cm^{-2} at temperatures below 30 K.

The cross-sectional TEM images taken after the second oxidation step from the broad areas show that the thickness of the gate oxide is 95 nm, agreeing well with the estimate obtained from the capacitance data. The thickness of the remaining SOI film after oxidation is 60 nm. In Fig. 3 is shown a cross-sectional TEM image of an originally 144 nm-wide Si ridge after the second oxidation step. The shape of the Si core is a triangle with concave sidewalls. There seems to be a tendency to form {111} crystallographic planes at the sides in the lower part of the core. High-resolution images reveal that the Si/SiO_2 interface is very sharp. A more detailed TEM study of the structures was presented elsewhere [7]. It is difficult to estimate the dimensions of the Si core of the QPC's using the TEM data obtained from the ridges. Although the narrowest QPC constrictions were 50 nm wide before oxidation, almost three times narrower than the structure shown in Fig. 3, the final size is probably not three times smaller, because the oxidation rate of small Si structures decreases with the size [8]. The effective diameter of the Si core in QPC' is probably 30-40 nm.

SiQPC's with originally 200 nm-wide and 80 nm-wide constrictions were measured at 4.2 K. The device having the 200 nm-wide constriction showed no conductance quantization. This is clear from the TEM analysis, which showed that the width of the channel after the oxidation is still of the order of 100 nm. The conductance of the SiQPC with 80 nm-wide constriction is shown in Fig. 4. At low

gate voltage no steps are seen. At gate voltage above 15 V, relatively weak but clear steps of $4(e^2/h)$ appear in the conductance curve. The appearance of the conductance steps at high gate voltage can be explained by higher mobility of electrons due to increased screening of the oxide charges in the channel at higher carrier concentration.

SUMMARY

The fabrication and transport properties of silicon MOSFETs with a narrow channel (SiQPC) are reported. The constrictions were patterned using e-beam lithography and RIE. The dimensions of the constrictions were further reduced by thermal oxidation. Devices with originally 80 nm-wide channel showed quantized conductance at 4.2 K. The diameter of the channel was estimated from XTEM analysis of Si ridges of similar size than the channels of the devices. The TEM images showed that the effective diameter of the channel is 30-40 nm.

ACKNOWLEDGEMENT

This work was partially funded by EU (Q-Switch, ESPRIT #30960) and Technology Development Centre of Finland (TEKES)

REFERENCES

1. H. Ishikuro and T. Hiramoto, Appl. Phys. Lett., 71, 3691 (1997).
2. L. Zhuang, L. Guo, and S. Y. Chou, Appl. Phys. Lett., 72, 1205 (1998).
3. Y. Nakajima, Y. Takahashi, S. Horiguchi, K. Idawate, H. Namatsu, K. Kurihara and M. Tabe, Jpn. J. Appl. Phys., 34, 1309 (1995).
4. M. Bruel, MRS Bulletin, 23, 35 (1998).
5. A. C. Irvine, Z. A. K. Durrani, and H. Ahmed, Appl. Phys. Lett., 73, 1113 (1998).
6. T. Ando, A. B. Fowler, and F. Stern, Rev. Mod. Phys., 54, 437 (1982).
7. A. Gustafsson, J. Ahopelto, M. Kamp, M. Emmerling and A. Forchel, in Proceedings of Microsc. Semicond. Mater. Conf., Oxford 22-25 March 1999.
8. H. I. Liu, D. K. Biegelsen, F. A. Ponce, N. M. Johnson, and R. F. W. Pease, Appl. Phys. Lett., 64, 1383 (1994)

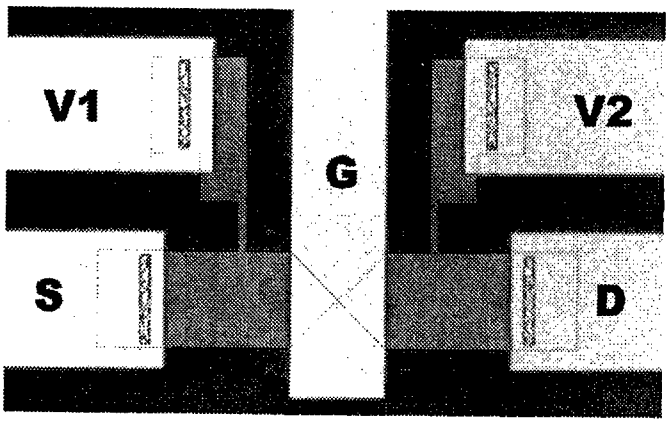


Fig. 1. Optical micrograph of a SiQPC showing the current and voltage leads. The width of the current leads is 100 μm. The channel constriction can be seen under the aluminum gate.

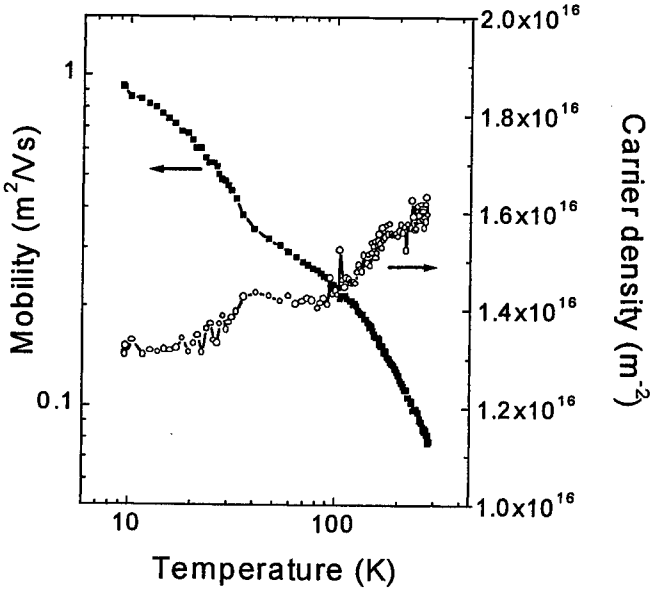


Fig. 2. Mobility and carrier density measured as a function of temperature from a 100 μm wide Hall bar. The thickness of the SOI film is 60 nm.

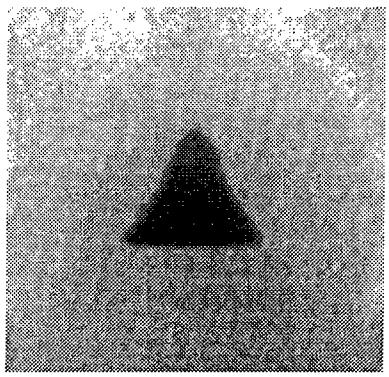


Fig. 3. Cross-sectional TEM image of an oxidized Si ridge. The width of the ridge was 140 nm before oxidation. The effective diameter of the Si core after oxidation is about 40 nm.

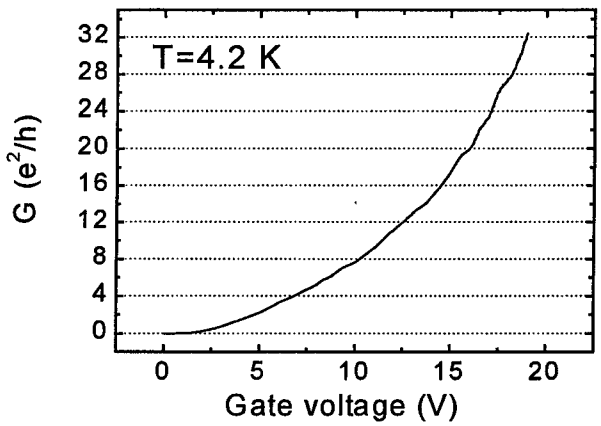


Fig. 4. Conductance of a SiQPC as a function of gate voltage measured at 4.2 K. The effective diameter of the channel is estimated to be 30-40 nm.

FAULT RATES IN NANOCHIP DEVICES

S. Spagocci, T. Fountain
University College London
Gower Street, London WC1E 6BT, England

ABSTRACT

This paper addresses the problem of estimating nanochip fault rates, taking intrinsic fault rates and fault-tolerant techniques into account. We considered single-electron device (SED) and quantum cellular automata (QCA) gates. After an analysis of the various fault sources, we surveyed the various space, time and information-redundant strategies available. For logic chips a new space-redundant technique, called cascaded general modular redundancy (CGMR), was proposed. For memory chips the use of error-correcting codes was proposed instead. Both SED and QCA-based chips, containing ~ 10^{11} gates and working at ~ 1 GHz, were considered. Our results suggest that a mean time between failures of ~ 1 y can be guaranteed for logic chips, with a redundancy level of a few tens at worse, either in space or in time. For memory chips, a mean time between failures of ~ 1 y can be guaranteed with a redundancy level of ~ 10 at worse, both in space and in time. This, however, requires carefully tuning the devices' operating conditions and design solutions.

INTRODUCTION

As pointed out in a previous paper [1], the proposed introduction of nanometer-scale components should make it possible to conceive chips containing up to 10^{12} logic gates. This would be particularly interesting for the implementation of parallel systems on a single chip. For such an assembly to work, the introduction of fault-tolerant techniques seems inevitable. The huge number of devices makes the chip unreliable, even if the devices are highly reliable in themselves.

We first considered single-electron devices, of which the electron pump [2] is a prototype. The electron pump is an array of metallic islands, separated by nanometer-scale junctions, through which an electron is made to tunnel sequentially. Logic gates based on the electron pump have been proposed [3], see Figs. (1) and (2). At high frequencies, the main fault source arises from pumping the electron too fast, so that the desired tunneling process is missed [4-6].

We also considered quantum cellular automata [7]. A QCA cell is a square array of four quantum dots, occupied by two electrons. The cell has two stable states, which are taken to mean 0 and 1. Due to electrostatic repulsion, each cell interacts with its neighbors. QCA logic gates based on this principle have been proposed [8], see Figs. (3) and (4). The main fault source arises from thermal excitation [9], which may create a kink in a row of previously aligned cells, thus giving a wrong answer.

In the previously cited work, we analyzed fault rates in SED and QCA-based devices. Extrapolation of the reported electron pump fault rates [4-6] to the nanometer scale led us

to predict intrinsic fault rates per clock cycle of ~ 10^{-6}, ~ 10^{-8} and ~ 10^{-10}, for designs based on the 5, 7 and 9-stage electron pump, respectively, and room temperature operation [1]. Similarly, we predicted intrinsic QCA fault rates per clock cycle of ~ 10^{-4} and ~ 10^{-19}, for devices operated at room and liquid Nitrogen temperature (77 K), respectively [1].

We found that "perfect" reliability can be guaranteed for SED and QCA systems of ~ 10^{11} gates working at ~ 1 GHz. This was achieved through the use of a space-redundant technique named cascaded triple modular redundancy (CTMR) [1], see Figs. (6) and (7). The resulting redundancy level is ~ 100.

The work of Ref. [1] has now been extended by surveying the various space, time and information-redundant strategies available [10] and making a distinction between logic and memory chips. We required our fault-tolerant solutions to guarantee a mean time between failures of ~ 1 y at ~ 1 GHz, with a redundancy level ≤ 100 in space and/or ≤ 10 in time. The proposed techniques and their implications in terms of space and time redundancy are presented in this paper.

1 TWO CHIP MODELS

Somewhat artificially, we assume that memory and logic functions can be implemented in separate units, which we call "chips" for terminological simplicity.

For reasons which will be made clear later, a logic chip will be considered as an aggregate of N_t interconnected logic gates, partitioned into clusters. Each cluster consists of N_g logic gates. Each gate has a faulting probability per clock cycle $P_{f;g}$, with $P_{f;g} << 1$. By a suitable partitioning process, see Fig. (5), we can obtain a linear chain of functional units, each one having a variable number of inputs and outputs.

We further assume that whenever an error occurs within a unit, it will emerge at one or more of its outputs and that errors in the various gates and at various times are statistically independent. The fact that logic gates have a certain degree of intrinsic tolerance to a faulty input can be taken into account by multiplying the gate failing probability per clock cycle by a factor, which turns out to be of ~ 1. Since we deal with order-of-magnitude estimations, such a correction will be ignored in the following. The above-mentioned assumption has the consequence that we only need to worry about one input and one output for each functional unit. Our final model for a chip, then, will simply be that of a linear chain of functional units, each one having one input and one output. Each functional unit is in turn a cluster of N_g logic gates, having a faulting probability per clock cycle $P_{f;g}$.

We assume the system to have a "perfect" clock, which is generated with micrometer-scale technology. We further assume that each cluster generates an answer (or answers) every clock cycle. This implicitly assumes perfect pipelining, which is not always a feasible solution.

Memory chips will be modeled as an array of independent 1-bit memory cells, organized into N_b—bit words. As for logic chips, we suppose that each gate has a faulting

probability per clock cycle $P_{f,g}$, with $P_{f,g} << 1$. It can be shown that the overall faulting probability per clock cycle of a memory cell is $3 \bullet P_{f,g}$.

2 SPACE-REDUNDANT TECHNIQUES

In space-redundant techniques [10], each potentially faulty unit is replaced by a number of replicated units so that, by majority voting or other means, faults can be masked to a certain extent. In particular, a line of distinction has to be drawn between permanent and transient faults [10]. A number of space-redundant techniques are available for dealing with permanent faults [11-17]. Such techniques are collectively known as general modular redundancy (GMR) [13] and reconfiguration [17].

The basic idea behind GMR is that the place of a potentially faulty unit is taken by a number of on-line units, among which some kind of a voting process is performed. Whenever an on-line unit is faulty, a spare unit is switched in to replace it. Should spare units run out, the system exhibits graceful degradation until the number of working on-line units falls below a certain level.

In reconfiguration strategies, which can be applied to processor arrays, whenever a processor is faulty its links to the other processors are reconfigured, so as to bypass it. Spare units are required, of course.

As we will see in the next sections, the errors we consider are of a transient nature. To our knowledge, the only available space-redundant techniques for dealing with transient faults are triple modular redundancy (TMR) [10,18,19], see Fig. (6), and its generalization, N-modular redundancy (NMR) [10]. In NMR, the place of each potentially faulty unit is taken by a block of N identical units and majority voting is performed among them. N has to be odd, of course. This works well provided one is dealing with binary units, under the assumption that a fault can only flip the unit's answer and the voting circuitry is perfectly reliable. If the voting circuitry is not perfectly reliable, the formalism has to be suitably modified. It has to be noticed that NMR and TMR are particular cases of GMR, in which there are no spare units and majority voting is performed.

Since a NMR unit performs majority voting, it cannot tolerate $\frac{1}{2} \bullet (N+1)$ or more faults. In the limiting case in which the intrinsic failing probability per clock cycle for an element, P_f, is small, the probability per calculation for the NMR unit to fail, $P_{f/nmr}$, is given by:

$$P_{f/nmr} = \binom{N}{\frac{N+1}{2}} \cdot (P_f)^{\frac{N+1}{2}} \qquad (1)$$

For the general case of an imperfect voting circuitry with failing probability per clock cycle $P_{f,v}$, we have to consider that the NMR unit gives a wrong answer if either majority voting would give a wrong answer and the voting circuit works, or majority voting would give a right answer and the voting circuitry fails. If, furthermore, we consider a cluster of N_g gates having a failing probability per clock cycle $P_{f,g}$, Eq. (1) can be given a more general

form. In particular, if $P_{f;v} << 1$:

$$P_{f/nmr} = \binom{N}{\frac{N+1}{2}} \cdot (N_g \cdot P_{f;g})^{\frac{N+1}{2}} + P_{f;v} \qquad (2)$$

In a previous work, we introduced a generalization of TMR, named cascaded modular redundancy (CTMR) [1]. According to CTMR, the potentially faulty units are first clustered in a suitable way and triple modular redundancy is applied to the clusters. The clusters are then suitably clustered, as well, and triple modular redundancy is applied to each cluster. The process is iterated for a number of steps, as in Fig. (7).

Here we propose a generalization of GMR (and NMR in particular), named cascaded general modular redundancy (CGMR), based on the same principles as CTMR. Generalizing Eq. (2), we suppose that:

$$P_{f/gmr} = \alpha \cdot (N_g \cdot P_{f;g})^{\beta} + P_{f;v} \qquad (3)$$

where β is the minimum number of faulty units giving an error in the CGMR output and α is a combinatorial factor.

According to the model of section 1, the chip's failing probability per calculation turns out to be proportional to $(N_g)^{\beta-1}$. In fact, it can be expressed as $N_t \bullet (N_g)^{-1} \bullet P_{f/gmr}$, where $P_{f/gmr}$ is given by the first addendum of Eq. (3) and N_t is the total number of gates in the chip. A consequence of this is that at each CGMR stage the chip's failing probability per calculation is minimized if cluster size is kept as small as possible. Eq. (3), however, shows that below a certain cluster size $P_{f;v}$ starts to dominate. We then require that, in Eq. (3):

$$\alpha \cdot (N_g \cdot P_{f;g})^{\beta} \leq \frac{N_v}{\eta} \cdot P_{f;g} \qquad (4)$$

where $\eta \approx 10$ and $P_{f;v} = N_v \bullet P_{f;g}$. It follows than that, at any stage, the clusters must have a maximum size given by the following expression:

$$N_{\max} = \sqrt[\beta]{\frac{N_v}{\alpha \cdot \eta \cdot (P_{f;g})^{\beta-1}}} \qquad (5)$$

We can now calculate the faulting probability per calculation of a cluster after i CGMR stages:

$$P_{f/gmr}(i) = \frac{N_t}{(N_{\max})^i} \cdot N_v \cdot P_{f;g} \qquad (6)$$

where, using Eq. (3), we have neglected the first addendum. The function defined by

Eq. (6) is seen to be monotonically decreasing with i. One therefore needs as many CGMR stages as possible. The iteration process cannot go on indefinitely. The maximum number of stages is defined by the condition:

$$\frac{N_t}{(N_{\max})^i} = 1 \tag{7}$$

Using Eq. (7) in conjunction with Eq. (5), we are now able to define the maximum number of CGMR stages:

$$i_{\max} = [-\beta \cdot \frac{Log(N_t)}{Log(\alpha \cdot \eta \cdot (N_v)^{-1} \cdot (P_{f;g})^{\beta-1})}] + 1 \tag{8}$$

where [.] is the integer part function. We then obtain an expression for the chip's overall failing probability per calculation. Namely:

$$P_{f/gmr} = N_v \cdot P_{f;g} \tag{9}$$

In space-redundant techniques applied to transient faults (which is the case of interest here), we are concerned with cascaded N-modular redundancy (CNMR). The problem is, then, choosing a suitable N.

Eq. (9) shows that the chip's overall failing probability per calculation only depends on N through N_v. A TMR voting unit can be implemented in the following way:

$$MV(x,y,z) = xy + xz + yz \tag{10}$$

where x,y,z are Boolean variables and MV(.) is the majority voting function. A NMR unit can be similarly implemented by summing over all the possible ½•(N+1)-ples of variables. As a consequence, N_v is seen to increase monotonically with N and, according to Eq. (9), the same holds for the chip's overall failing probability per calculation.

On the other hand, under the hypothesis that $P_{f;g} << 1$, the maximum number of CGMR levels has the following asymptotic value:

$$i_{\max} = [-\frac{Log(N_t)}{Log(P_{f;g})}] + 1 \tag{11}$$

which is nearly reached for N = 3 (CTMR). Therefore if for N = 3 the asymptotic value of Eq. (11) is reached and/or the redundancy level, as described by Eq. (14), is satisfactory, CTMR is the best solution.

If needed, it is then possible to apply NMR to the chip's output, using a voting circuitry much more reliable than the chip's gates (micron-scale technology, in practice). The system's failing probability per calculation can then be computed.

In particular:

$$P_{f/nmr} = \binom{N}{\frac{N+1}{2}} \cdot (N_v \cdot P_{f;g})^{\frac{N+1}{2}} \tag{12}$$

Furthermore, cluster size and the number of nanometer-scale CNMR levels are given by Eqs. (5) and (8), respectively, where:

$$\alpha = \binom{N}{\frac{N+1}{2}}$$
$$\beta = \frac{N+1}{2} \tag{13}$$

An expression like that of Eq. (12), with N_t in place of N_v, describes the chip's failing probability per calculation for NMR with micrometer-scale circuitry, when no redundancy at the nanometer scale is used. This could seem a straightforward solution for providing fault protection in a nanochip. Unfortunately, the condition $N_t \bullet P_{f;g} << 1$ has to be satisfied, thus limiting the applicability of the technique to gate failing probabilities $P_{f;g} << (N_t)^{-1}$.

Anyway, under the hypothesis that M-modular redundancy is used at the nanometer-scale level and N-modular redundancy is used at the micron-scale level, the time redundancy level is ≈ 1 (since $N_g >> 1$, in fact, the number of clock cycles taken by an error to reach the unit's output is on average much greater than the number of clock cycles taken to process data in the voter) and space redundancy is given by:

$$r_s = M^{i_{max}} \cdot N \tag{14}$$

where i_{max} is defined by Eq. (8).

3 TIME-REDUNDANT TECHNIQUES

In time-redundant techniques [10] processor instructions are suitably repeated, so as to achieve fault tolerance. In particular one can either mask errors [20] or detect them and restart processor operation from the previous state (backward error recovery [21]). Instructions can be repeated at any level, from single-bit level to software (software redundancy [10]). It would be difficult, at this stage of development, to give any sensible estimations on the effects of software redundancy. Therefore, we will only consider instructions at the single-bit level. Any software instruction is finally translated into bit exchanges within the processor. Our approach then can implicitly give indications on the possible effectiveness of software-redundant strategies.

An application of error-masking is suggested in Ref. [20] in the form of a voting unit

accumulating results, so as to perform TMR in the time domain. We propose to extend such a technique to CNMR. A voter unit, able to accumulate input data over N+1 clock cycles (through a shift register) and then perform voting upon them (driven by a counter), is proposed in Fig. (8). If Fig. (7) is read as a time-diagram, we have an idea of how to implement CNMR in the time domain. The clock frequency of a unit at level i has to be de-multiplied by a factor $(N+1)^i$ with respect to the master clock frequency. Note that in Fig. (8) the counter is assumed to be perfect. This can most easily implemented by supplying suitable signals generated from the master clock.

The same results as those given for CNMR in the space domain apply, except that the roles of space and time redundancies are exchanged. Micrometer-level redundancy can be added, if needed. In particular, cluster size and the number of CNMR levels are given by Eqs. (5) and (8), respectively, where α and β are defined by Eq. (13). The failing probability per calculation is given by Eqs. (9) and (12), where $N_v \approx 9$ for CTMR. Finally, space redundancy is ≈ 1 and time redundancy is given by an expression like Eq. (14).

In order to perform backward error recovery (BER), we propose the scheme shown in Fig. (9). The outputs of N copies of suitable functional units (clusters of N_g gates, as suggested in section 1) are compared through a logical OR between all the possible terms of the form $x_i \oplus x_j$. A disagreement signal from any of the N-ples of replicated units causes the system to step back to the previous state. For duplication, the task of implementing an error-detection function is straightforward. In fact, we can simply define:

$$ED(x,y) = x \oplus y \tag{15}$$

For triplication, on the other hand, Eq. (15) generalizes to:

$$ED(x,y,z) = x \oplus y + x \oplus z + y \oplus z \tag{16}$$

Eqs. (15) and (16) can be easily generalized, but we won't give a general formula here. An arrangement like that of Fig. (9) is able to detect faults occurring in the units, unless all the N units fail. The fault rate per calculation for N replicated N_g-gate units is then:

$$P_{f\,lber} = (N_g \cdot P_{f;g})^N + P_{f;v} \tag{17}$$

Once again, we can cascade the BER units and apply the CGMR formalism of section 2. Analogously to section 2, duplicated units should usually be the most effective solution.

One further micron-scale level can be added, if necessary. More specifically, cluster size and the number of BER levels are given by Eqs. (5) and (8), respectively, where:

$$\alpha = 1$$
$$\beta = N \tag{18}$$

Furthermore, the failing probability per calculation is given by Eqs. (9) and (12), where $N_v = 5$ for duplication. If BER has to make any sense, the intrinsic probability per

calculation for a fault to occur anywhere in the chip must be << 1, because otherwise there would be no point in repeating processor operation. In other words, we must have $P_{f;g} << (N_t)^{-1}$. Time redundancy is then ≈ 1. On the other hand, space redundancy is given by Eq. (14).

It is interesting to notice that BER, although usually defined as a time-redundant technique, in our cascaded version implies a non-negligible amount of space redundancy. Alternatively, the comparison process can be performed by accumulating results in time. An arrangement similar to the TMR unit of Fig. (8) has to be employed. In this case, we have $N_v \approx 13$ and the roles of space and time redundancies are exchanged.

4 INFORMATION-REDUNDANT TECHNIQUES

In information-redundant strategies [10] the information stored in a chip is made redundant through the use of error correcting codes [22]. In an error correcting code, suitable parity check bits are added to the information bits one wants to protect, so that errors can be located and/or corrected. An error-correcting code is characterized by the maximum number of errors it can detect and/or correct and its redundancy, i.e. the ratio between the total number of bits in a word and the number of information bits.

What has just been said suggests that error-correcting codes can be applied to memory chips, for which the above-mentioned clustering process would not be feasible. We will adopt the model suggested in section 1 for a memory chip. Namely, we will consider it as an array of independent memory cells, organized into memory words. We assume that every memory cell is refreshed at each clock cycle, with a finite probability of failure. We then suppose that a certain error-correcting code has the capability to correct N_e errors. The data word is written to the memory and stays there for N_s clock cycles. Once a bit error has been generated, the memory cell's feedback loop makes it permanent.

If the memory cell's fault rate per clock cycle, $P_{f;m}$, satisfies the relationship $P_{f;m} << 1$, we can neglect the process through which a bit error can be flipped back to its correct value. The probability that a N_b-bit memory word (where N_b includes the contribution of check bits) is corrupted by a number of errors ≥ N_e+1, after being stored for N_s clock cycles, is then given by:

$$P_{f/ecc} = \binom{N_b}{N_e+1} \cdot (N_s \cdot P_{f;m})^{N_e+1} \qquad (19)$$

where, as underlined in section 1, it can be shown that $P_{f;m} = 3 \bullet P_{f;g}$. Eq. (19) requires that $N_s \bullet P_{f;m} << 1$, thus limiting the applicability of this technique to failing probabilities such that $P_{f;m} << (N_s)^{-1}$. Whenever possible, it would be advisable to choose N_s as the number of clock cycles corresponding to the mean time between failures we want to guarantee. Otherwise a storage time has to be chosen and periodic correcting and re-encoding operations have to be performed. In an array of ~ 10^{11} logic gates (and ~ 10^{10} memory cells), one has $N_d \approx 10^{10} \bullet (N_b)^{-1}$ data words. Then the storage time (in clock cycles) N_s cannot be ≤ N_d, since this is the minimum number of clock cycles between two correcting

and re-encoding operations on the same data word, if those operations are performed sequentially. This is a further constraint on the applicability of Eq. (19).

The space redundancy level depends on the chosen code. On the other hand, time redundancy can be a potentially serious problem. However, if encoding and decoding are performed through a lookup table operation [22] the problem can be overcome. More specifically, when a data word has to be written to memory it is first fed to a pre-computed lookup table, which in turn produces an encoded input. The encoded input in then fed to the memory and stored. When a data word has to be read from memory, the encoded form of it is first corrected by replacing it with the nearest neighbor in terms of Hamming distance [22], then it is fed to a pre-computed lookup table, which provides decoding. The lookup tables and correcting circuitry have to be much more reliable (e.g. built with micrometer-scale technology) than the memory they are meant to protect.

For memory-intensive operations, time redundancy is given by:

$$r_t = 2.5 + 5 \cdot N_c \tag{20}$$

where N_C is the number of data word correction and re-encoding operations per computation, under the hypothesis that access to both the lookup tables and memory and Hamming error correction take the same amount of time.

There are many different kinds of error-correcting codes. We suggest the use of two quite different codes. Hamming codes [23] are characterized by a low redundancy (1.5 for an 8-bit information word) and a low error-correcting capability (1 error). Reed-Muller codes [22], on the other hand, are characterized by quite a high redundancy (16 for an 8-bit information word) and a high error-correcting capability (31 errors for an 8-bit information word).

The choice of an 8-bit information word for both the Hamming and the Reed-Muller code requires some explanation. Our encoding/decoding approach implies a lookup table dimension of 2^{Nib}, where N_{ib} is information word size. If we assume a ratio of ~ 10^4 between the typical areas of our devices and the conventional micrometer-scale devices (see section 6), we find that the lookup table cannot contain more than ~ 10^6 memory cells, if its area has to be at worst of the same order as the area occupied by the nanoscale devices. This limits information word size to less than 20 bits. Keeping code redundancy into account, both the Hamming and the Reed-Muller codes require 8-bit information words. Any longer information word can be split into N_{bl} smaller blocks, which are separately encoded and decoded. The overall failure probability for a storage time of N_s clock cycles is then:

$$P_{f\,ecc} = N_{bl} \cdot \binom{N_b}{N_e + 1} \cdot (N_s \cdot P_{f;m})^{N_e+1} \tag{21}$$

so that a negligible price is paid (in order-of-magnitude terms) for information word sizes bigger than the chosen standard size.

5 FAULT RATES IN NANOCHIPS

As pointed out in the previous sections, logic chips require the use of either space or time-redundant strategies (see sections 2 and 3). On the other hand, error-correcting codes are suitable for memory chips (see section 4). We required a mean time between failures of ~ 1 y at ~ 1 GHz for ~ 10^{11} gates, with a redundancy level $\leq$ 100 in space and/or $\leq$ 10 in time (see section 1).

We present here the results obtained for both SED and QCA-based chips. In the rest of the section, by n-junction pump we mean a gate whose design is based on the n-junction electron pump [1], operated at room temperature. Furthermore, by r_s and r_t we mean space and time redundancy, respectively.

5.1 LOGIC CHIPS

We list here the alternative solutions found for logic chips. In the list that follows, the expression "x(n)+1(m) stages" is used to describe a CGMR arrangement consisting of x cascaded stages, with n-fold replication (so, for example, n = 3 describes TMR), plus one stage with micrometer-scale voting circuitry and m-fold replication. When a 0 is used instead of x(n) (1(m), respectively), we mean that the proposed system has only micrometer-scale stages (nanometer-scale stages, respectively). The figures have been obtained by referring to the appropriate formulae of sections 2 and 3.

SED-based chips:

- 9-junction pump, CNMR in the space domain, 3(3)+1(3) stages, $r_s = 81$, $r_t = 1$
- 5-junction pump, BER in the space domain, 4(2)+1(4) stages, $r_s = 64$, $r_t = 1$
- 7-junction pump, BER in the space domain, 3(2)+1(3) stages, $r_s = 24$, $r_t = 1$
- 9-junction pump, BER in the space domain, 3(2)+1(2) stages, $r_s = 16$, $r_t = 1$

QCA-based chips:

- operated at 77 K, CNMR in the space domain, 3(2)+0 stages, $r_s = 8$, $r_t = 1$
- operated at 77 K, CNMR in the space domain, 0+1(5) stages, $r_s = 5$, $r_t = 1$
- operated at 77 K, BER in the space domain, 2(2)+0 stages, $r_s = 4$, $r_t = 1$
- operated at 77 K, CNMR in the time domain, 0+1(5) stages, $r_s = 1$, $r_t = 6$
- operated at 77 K, BER in the time domain, 2(2)+0 stages, $r_s = 1$, $r_t = 9$

5.2 MEMORY CHIPS

We list here the alternative solutions found for memory chips. The figures have been obtained by referring to the appropriate formulae of section 4. For Reed-Muller codes, a storage time of ~ 10^8 clock cycles has been used. Since this is the minimum allowable storage time for 10^{11} gates (see section 4), we have to correct and re-encode a memory word every two clock cycles. Therefore, $N_c = 1$ in Eq. (20). For Hamming codes we assume $N_c = 0$. The results are quoted for a 16-bit information word. As shown in section 4, the information word has to be split into two independent 8-bit blocks.

SED-based chips:

- 9-junction pump, Reed-Muller code, $r_s = 16$, $r_t = 7.5$

QCA-based chips:

- operated at 77K, Hamming code, $r_s = 1.5$, $r_t = 2.5$
- operated at 77K, Reed-Muller code, $r_s = 16$, $r_t = 7.5$

6 CONCLUSIONS

In this work, we addressed the problem of estimating nanochip fault rates. We considered SED and QCA-based logic gates and surveyed the various space, time and information-redundant strategies available. We proposed a new fault-tolerant technique, named cascaded general modular redundancy (CGMR) and we were able to adapt other standard techniques to our requirements. By using the figures for SED and QCA intrinsic fault rates given in Ref. [1], we were able to propose a number of fault-tolerant solutions. In particular, we had to distinguish between logic and memory chips. We found that a mean time between failures of ~ 1 y at ~ 1 GHz can be guaranteed (and in some cases vastly exceeded) for logic chips, with a redundancy level of a few tens at worse, either in space or in time. For memory chips, a mean time between failures of ~ 1 y at ~ 1 GHz can be guaranteed (and in some cases vastly exceeded) with a redundancy level of ~ 10 at worse, both in space and in time. However, a careful tuning of the devices' operating conditions and design solutions is required. For both logic and memory chips, QCA-based devices can work with lower redundancy levels than SED-based chips. However, they cannot be operated at room temperature.

The intrinsic error rates we analyzed are of a transient nature. Impurities and dislocations, however, could cause permanents faults, which have not yet been considered in our analysis. The fact that the typical dimensions of the devices we considered are ~ 10 nm, so that their area is ~ 10^4 times smaller than present-day devices [1] suggests that single crystal errors will have more significant effects than in microcircuitry. On the other hand, the level of redundancy required by the transient gate fault rates might provide protection against permanent faults, as well. The effects of cosmic rays and natural radioactivity have to be assessed, too. Once again, the level of redundancy required by the intrinsic fault rates might provide protection against cosmic rays and natural radioactivity, too.

As pointed out in Ref. [1], despite the somewhat high level of redundancy we have to provide, the linear dimensions of the nanochips considered in this paper should be of ~ 1 cm and power dissipation should be of ~ 1 W, which seems quite realistic. This is also an a fortiori justification for the choice of our space and time redundancy constraints. However, it is not the purpose of our work to give detailed design solutions. Throughout the paper, a number of simplifying assumption have been made, mainly based on the fact that the intrinsic failing probabilities for both SED and QCA-based gates are very small. These assumptions will be checked through numerical simulations.

ACNOWLEDGEMENT

This paper and associated research were funded as part of the DARPA ULTRA program. Grant number N00014-96-1-0850. Principal investigator: T J Fountain.

REFERENCES

[1] S. Spagocci and T. Fountain, in Proceedings of ECS 98-19, Quantum Confinement V: Nanostructures, M. Cahay, D.J. Lockwood, J.P. Leburton and S. Bandyopadhyay, Eds., pp 582-596, The Electrochemical Society, Pennington, NJ (1999).
[2] H. Pothier, P. Lafarge, C. Urbina, D. Esteve and M.H. Devoret, Europhys. Lett., **17**, 249 (1992).
[3] M.G. Ancona, J. Appl. Phys., **79**, 526 (1996).
[4] H.D. Jensen and J.M. Martinis, Phys. Rev. B, **46**, 13407 (1992).
[5] J.M. Martinis, M. Nahum and H.D. Jensen, Phys. Rev. Lett., **72**, 904 (1994).
[6] M.W. Keller, J.M. Martinis, N.M. Zimmermann and A.H. Steinbach, Appl. Phys. Lett., **69**, 1804 (1996).
[7] C.S. Lent, P.D. Tougaw, W. Porod and G.H. Bernstein, Nanotechnology, **4**, 49 (1993).
[8] P.D. Tougaw and C.S. Lent, J. Appl. Phys., **75**, 1818 (1994).
[9] C.S. Lent, P.D. Tougaw and W. Porod, in PhysComp '94: Proceedings of the Workshop on Physics and Computing, pp. 1-9, IEEE Computer Society Press, Los Alamitos, CA (1994).
[10] P.G. Depledge, IEE Proc. A, **128**, n. 4, 257 (1981).
[11] F.P. Matur, IEEE Trans. Comp., **C 20**, 1376 (1971).
[12] F.P Matur and P.T. de Sousa, IEEE Trans. Rel., **R 24**, n. 2, 108 (1975).
[13] F.P Matur and P.T. de Sousa, IEEE Trans. Rel., **R 24**, n. 5, 296 (1975).
[14] J. Losq, IEEE Trans. Comp., **C 25**, n. 6, 569 (1976).
[15] F.P Matur and P.T. de Sousa, IEEE Trans. Comp., **C 27**, n. 7, 624 (1978).
[16] H.Y. Lo, L.P. Ju and C.C. Su, IEE Proc. G, **137**, n. 1, 1 (1990).
[17] F. Distante, M.G. Sami and R. Stefanelli, in: V. Cantoni, L. Lombardi, M. Mosconi, M. Savini and A. Setti, Eds., Proc. CAMP 1995, pp. 340-349, IEEE Computer Society Press, Los Alamitos, CA (1995).
[18] J.F. Wakerly, Proc. IEEE, **64**, n. 6. 889 (1976).
[19] K.W. Philp and N.D. Deans, Microelectron. Reliab., **37**, n. 4, 581 (1996).
[20] M.G. Ancona, Superlattices and Nanostructures, **20**, n.4, 461 (1996).
[21] H. Schepers, in: J. Vytopil, Ed., Formal Techniques in Real-Time and Fault-Tolerant Systems, pp. 3-31, Kluwer Academic Publishers, Boston, MA (1993).
[22] S. Roman, Introduction to Coding and Information Theory, Springer-Verlag, New York, NY (1997).
[23] R.W. Hamming, Bell Syst. Tech. J., **26**, n. 2, 147 (1950).

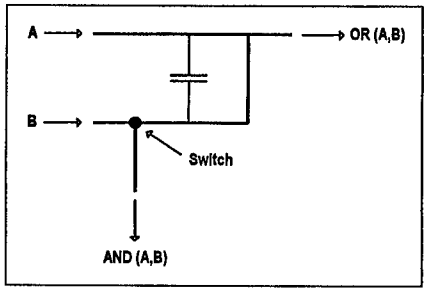


Fig. 1 An AND/OR gate, based on single-electron switching. Any electron appearing at input A is driven to the OR (A,B) output. Any electron appearing at input B is either switched to the AND (A,B) output or to the OR (A,B) output, depending on the presence or absence of the electron coming from input A. Driving happens through the electron pump mechanism. Electron pumps in the circuit are represented as thick lines.

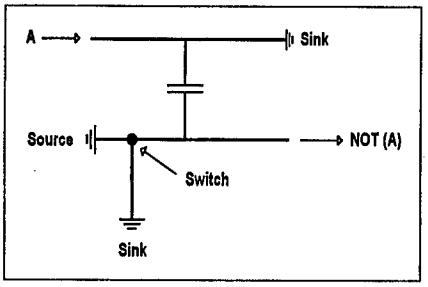


Fig. 2 A NOT gate, based on single electron switching. Any electron appearing at input A is driven to a sink. One electron per clock cycle is taken from a source and either switched to a sink or to the NOT (A) output, depending on the presence or absence of the electron coming from input A. Electrons are driven through the electron pump mechanism. Electron pumps in the circuit are schematized as thick lines.

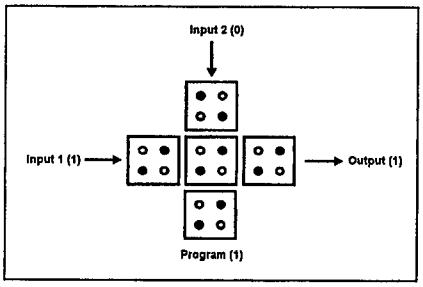


Fig. 3 A programmable AND/OR gate, based on QCAs. The central cell performs majority voting among the two input cells and the control (program) cell. Depending upon whether the control cell is set to 0 or to 1, the device works as an AND gate or as an OR gate. In the example shown the control cell is set to 1, so that we have an OR gate. Quantum dots are represented as circles. Filled circles indicate that a quantum dot is filled with an electron.

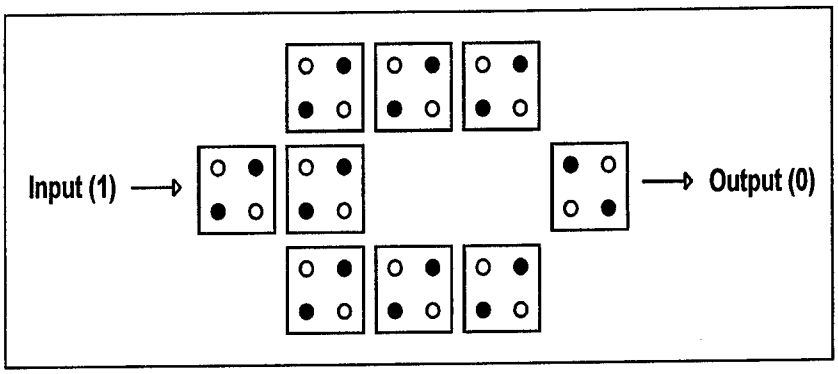


Fig. 4 A NOT gate, based on QCAs. The input line extends one cell beyond the beginning of the two circuit branches. The input signal is propagated unaltered through the branches, due to electrostatic repulsion. The two branches then converge onto the output line. In this case there is diagonal alignment, so that electrostatic repulsion causes the input signal to be inverted. Quantum dots are represented as circles. Filled circles indicate that a quantum dot is filled with an electron.

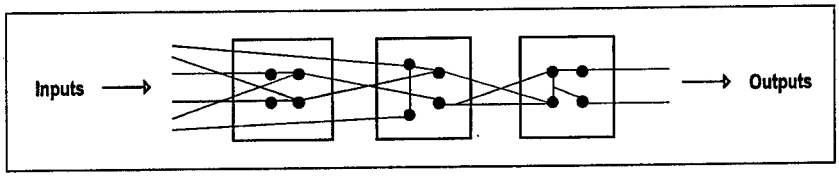


Fig. 5 A model for a logic chip. A logic chip is represented here as a set of interconnected gates. The set is suitably partitioned, so that it can be considered as a linear array of functional units. The functional units have a variable number of inputs and outputs. Gates are represented by filled circles, functional units by squares.

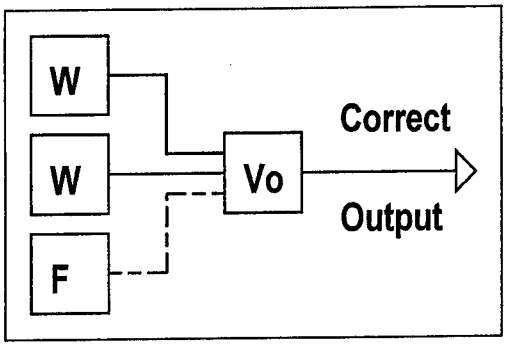


Fig. 6 A TMR unit. Three copies of the potentially faulty devices send their output to a unit, which performs majority voting among them. The answer is taken to be the correct output. W = working device, F = failing device, Vo = voting circuit. Wrong outputs are marked with a dashed line.

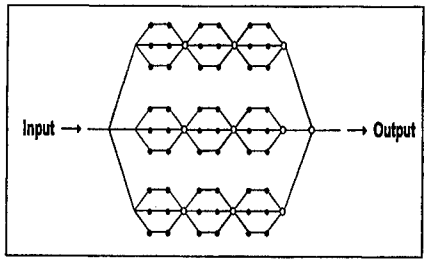


Fig. 7 A 2-stage CTMR arrangement. A linear array of six gates is partitioned into clusters of two gates. In the 1st stage, each cluster is tripled and majority voting is performed on each triplet. In the 2nd stage, the linear chain thus obtained is in turn tripled and majority voting is performed on the triplet. Gates are represented by filled circles, voting units by empty circles. The reasons behind the clustering process are explained in the text.

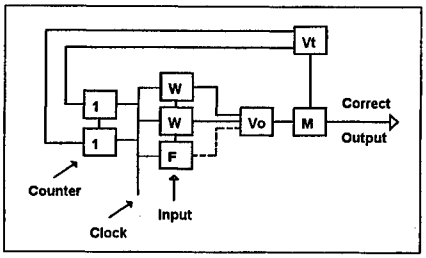


Fig. 8 A voting unit for time domain TMR. The input stream is accumulated in the shift register. The three stages of the shift register send their output to a majority voting unit. The answer of the voting unit is sent to a memory cell. A veto unit (an AND gate) prevents the memory cell from storing the input data coming from the voter unless the counter (as in the picture) gives a "11" output. This happens every four clock cycles. W = data coming from a working device, F = data coming from a failing device, Vo = voting circuit, Vt = veto unit, M = memory cell. Wrong outputs are marked with a dashed line.

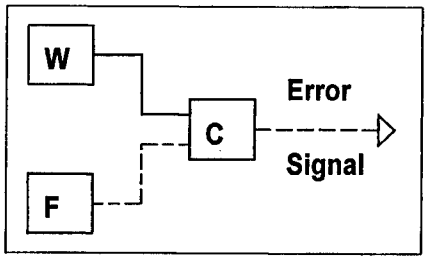


Fig. 9 A BER unit with duplication. Two copies of the potentially faulty devices send their output to a comparator (an XOR gate). The comparator detects any disagreement between the two outputs and emits an error signal. If the error signal in any of the units in the system is 1, the system steps back to its previous state. W = working device, F = failing device, C = comparator. Wrong outputs are marked with a dashed line.

The anomalous level shift due to local electric modes in confined systems

Slava V. Rotkin
Ioffe Physico-Technical Institute
of Russian Academy of Sciences
26 Polytehnicheskaya St.
St.Petersburg 194021, Russia

ABSTRACT

The shift of the electron energy level due to the coupling with the surface electromagnetic mode of the cluster is studied. The energy shift is shown to depend on the cluster size and to be much larger than the standard Lamb shift due to the delocalized electromagnetic modes. The angular momentum theory is developed for the calculation of the high-frequency response of the cluster and applied, within the spherical approach, for the computation of the energy shift in the fullerene as an example.

The zero fluctuation of the electromagnetic vacuum are well known to manifest itself as the Casimir force between close surfaces of polarizable substance, as the Van-der-Waals interaction, as the origin of the radiative lifetime and the shift of the energy levels of the charge carrier in the system placed in some cavity. The paper considers the shift of the electron levels in the field of the zero-fluctuations of the modes connected with the cluster, the cavity or the quantum box.

The most simple manifestation of the influence of the zero-fluctuation modes is the energy level shift (Lamb shift) which is the difference between the electron levels of the different symmetry those are to interact with the electromagnetic field in different degree. We raise an issue of the value of the level shift (LS) in a confined system (0D object). Its distinguishing feature is the confinement of the electromagnetic field in the volume of the charge carrier motion.

Let us consider LS of the charge carrier semiclassically following the book [1]. The frequency of oscillations of the external field (of zero fluctuations) is much higher than the inverse period of the electron orbit. Therefore, the adiabatic approximation will be used. The estimated value of LS results from the short fast deflections of the electron from its original orbit in the high-frequency field of the electromagnetic wave of the zero-fluctuation. The shift is given by the second order (see diagram in Fig.1) perturbation theory as

$$\overline{\Delta H} = \langle H(r+\delta) - H(r) \rangle = \left\langle \nabla H \cdot \vec{\delta} + \frac{1}{2}\nabla^2 H\, \vec{\delta}\cdot\vec{\delta} + \ldots \right\rangle = \frac{1}{4}\nabla^2 H\, \overline{\delta^2} + o(\overline{\delta^2}) \quad (1)$$

where $H(r)$ is the unperturbed Hamiltonian and $H(r+\delta)$ is the Hamiltonian with account for the electron deflection. The classical charge deflects from its path, acted upon by the force $e\vec{\mathcal{E}}$. Let us express all fluctuation fields $\vec{\mathcal{E}}$ in terms of the eigen modes related to the specific system (cluster or quantum box). Within the linear response theory (see Appendix A), the electron deflection reads as:

$$\overline{\delta^2} = 2\sum_\alpha \delta_\alpha^2 = 2\frac{e^2}{m^2}\sum_\alpha \mathcal{E}_\alpha^2 \left(\frac{1}{2\omega_\alpha(\omega_\alpha+\omega_o)}\right)^2 \quad (2)$$

here e and m are the electron charge and mass, ω_o is the atomic frequency. The multiplier 2 accounts for two polarisations of the light. It is easy to check that the higher the frequency of the mode, the larger the partial shift due to this mode. Hence, the local modes of the maximal frequency, those are plasmons, are of the most importance in expression (2).

The amplitude of the electric field $\vec{\mathcal{E}}_\alpha$ of the fixed mode with the quantum numbers α is related to its zero-oscillation frequency $\mathcal{E}_\alpha^2 \propto \hbar\omega_\alpha$. For example, for surface plasmons of the fullerene cluster it was calculated in [2]: $\mathcal{E}_L^2 = \hbar\omega_L \pi(L+1/2)/R^3$. The LS due to the electromagnetic modes of a free space (3D vacuum) follows from Eq.(2) when one substitutes the wave vector $\mathbf{k}$ instead of α. We change the sum into the integral. This results (in 3D-space) in well-known formula:

$$\overline{\delta^2} = \frac{e^2\hbar}{2\pi m^2 c^3}\ln\frac{\omega_{\max}}{\omega_{\min}} = \frac{\alpha^3}{2\pi}a_B^2 \ln\frac{\omega_{\max}}{\omega_{\min}} \quad (3)$$

where the wave vector of the electron, which is non-relativistic one, limits the integration region from above: $\omega_{\max} \sim mc^2/\hbar$, while atomic frequency gives the lower limit: $\omega_{\min} \sim \omega_o$. The mean deflection is less than the Bohr radius $a_B \simeq 0.53$ Å in α^3 times, where $\alpha \simeq 1/137$ is the fine constant. As a result the LS is quite small and does not affect the spectrum essentially.

This is not true if one considers the local modes related to some system. Let us calculate the surface modes of the metallic sphere of the radius R. It was shown that the plasmon modes in clusters and other nanoscale 0D-quantum confined systems (with imposed central symmetry) can be reproduced with the high accuracy by the classic hydrodynamics of the charged liquid on the surface of the spherical box. Therefore, the solution for the modes of the metal sphere gives the plasmon frequencies. The equation system to solve is in Appendix B. The frequency of the mode is proportional to the multipole index of the mode L

$$\omega_L = \sqrt{\frac{L(L+1)}{2L+1}\frac{N e^2}{m R^3}} \tag{4}$$

and in contraction limit the dependence is a square root: $\omega_L \propto \sqrt{(L+1/2)/R}$. Here N is the number of valence electrons. The local modes donate to the LS and the term in the mean squared deflection, additional to Eq.(3), reads as

$$\overline{\delta^2} = \frac{\pi e^2 \hbar}{m^2}\sqrt{2}\left(\frac{mR}{Ne^2}\right)^{3/2} \sum_{L=1}^{L_{\max}} \sqrt{L+\frac{1}{2}}$$

$$\simeq \frac{\pi 2^{3/2}}{3}\left(\frac{R}{Na_B}\right)^{3/2} a_B^2 \left(L_{\max}+\frac{1}{2}\right)^{3/2} \tag{5}$$

where $L_{\max}$ is the maximal allowed multipole index defined by the box radius.

This results in the anomalous large LS comparing with the LS related to the delocalized photon modes. The ratio of these shifts, as illustrated by the example of C_{60}, can amount about 1000. Evidently, the ratio the larger, the less the radius of the system. At the cluster size 100 times larger than C_{60} ($R \simeq 3.6$ Å), the shift related to the confined modes becomes of the same order than the standard LS.

ACKNOWLEDGEMENT

This work was partially supported by RFBR grants no. 96-15-96348 and 99-02-18170.

References

[1] A.B.Migdal, Qualitative methods in quantum theory, Moskow: Nauka, 1975 (Russian).

[2] V.V.Rotkin, PhD thesis, Ioffe Institute, St.Petersburg 1997 (Russian).

[3] V.V.Rotkin, R.A.Suris, Mol. Materials, v.4, 87-94, 1994. V.V.Rotkin, R.A.Suris, Sov.-Solid State Physics, **36**, 12, 1899-1905, 1994.

[4] D.A.Varshalovich, A.N.Moskalev, V.K.Khersonskii, Quantum theory of the angular momentum. Leningrad: Nauka, 1975 (Russian).

Appendix A: On the linear response of the electron

The electron trembling in the high-frequency field $\mathcal{E}_L$ of the plasma oscillator $|\alpha\rangle$ can be treated semiclassically and its deflection δ is described by Newton law:

$$m\partial_t^2\delta + m\omega_o^2\delta = -e\mathcal{E}, \tag{6}$$

here e is the electron charge and m is the electron mass which is supposed to be isotropic within the cluster.

For the Fourier component of the external field which is proportional to $e^{-i\omega t}$ we get the polarizability of the carrier in the form

$$\frac{e^2}{m(\omega^2-\omega_o^2)} \to \frac{e^2}{2m\omega(\omega+\omega_o)}.$$

Here we use the fact that the frequency dependence can be decomposed into two terms

$$\frac{1}{\omega^2-\omega_o^2} = \frac{1}{2\omega}\left(\frac{1}{\omega+\omega_o}+\frac{1}{\omega-\omega_o}\right)$$

where the last term corresponds to the absorption of the photon and should be omitted for the zero fluctuation field.

The total deflection is given by the sum of this expression over all α (the integral over $\mathbf{k}$ for 3D photons).

Appendix B: On the spherical surface plasmons

One of the examples of 0D system, which plasmon can be described within the classical approach, is the fullerene, the sixty-carbon-atom ball of the high symmetry. The C_{60} electron structure symmetry reflects (i) the local triangular symmetry of graphite-like lattice distorted by (ii) the global homology of the curved closed surface. The first was shown to be of small importance for the plasmon. The global symmetry — SO(3) spherical topology of the fullerene — is quantitatively captured within the quantum mechanical model of Spherical Shell Quantum Well [3]. Then the classical hydrodynamics of the charged liquid on the surface of the sphere describes the response of 240 valence electrons of the cluster.

The equation system to solve reads as follows:

$$\begin{cases} \partial_t j = -\dfrac{ne^2}{m}\nabla\varphi \\ \partial_t\sigma + \nabla j = 0 \end{cases}, \tag{7}$$

here $n = 240/4\pi R^2$ is the valence electron density for C_{60}. φ is the acting electrical potential. σ is the surface density fluctuation defining the lateral current density, j, on the surface of the sphere of radius R. ∇ is the 2D nabla operator along the surface. The solution is given in complete spherical harmonics $P_{L}(r)Y_{L,M}(\Omega)$. The use of Gauss–Ostrogradskii theorem $(2L+1)\,\varphi_{LM}/R = 4\pi\sigma_{LM}$ allows one to relate the potential and the density fluctuation.

The plasmon energy corresponds to so-called bubble diagram in the secondary quantization formalism. Let us consider the space integrals in this matrix element (Fig.2). The typical integral in the vertex of the diagram is $\langle LM|\lambda\mu|\Lambda M\rangle$. Any spherical diagram with two legs can be rewritten [4] into the closed diagram, which depicts the 3j (or 6j and higher symmetry) symbol, bearing no dependence on co-ordinates, and into the straight line, which denotes the angular momentum delta–function, representing the angular momentum conservation through the process. The same argument works for the level shift considered above. That is why the angular momentum subspaces are treated separately in this paper.

The solution of Eq.(7) is the surface mode of the spherical symmetry with the frequency:

$$\omega^2 = \frac{ne^2}{m}\frac{4\pi R}{2L+1}\frac{L(L+1)}{R^2} \to \frac{2\pi ne^2}{m}\frac{L+1/2}{R}, \tag{8}$$

which goes to the 2D–plasmon frequency when $L = kR \to \infty$ (the contraction limit).

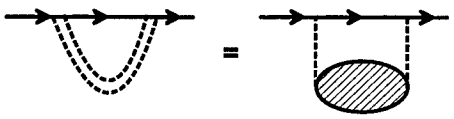


Figure 1: The diagram related to the level shift considered in the paper. The main contribution comes from the plasmon mode which is depicted as the shaded mass operator in the right.

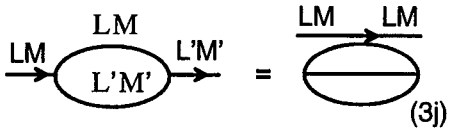


Figure 2: The angular momentum diagram [4] shows that the matrix element is equivalent to the product of the 3j–symbol and the delta–function of the incoming and outgoing angular moments.

Quantum Dots and Mesoscopic Systems

QUANTUM CHAOTIC TRANSPORT IN MESOSCOPIC ANTIDOT ARRAYS

Tsuneya ANDO and Seiji URYU

Institute for Solid State Physics, University of Tokyo
7-22-1 Roppongi, Minato-ku, Tokyo 106-8666, Japan

A review is given of quantum effects and roles of chaos in transport in antidot lattices mainly from a theoretical point of view. The topics include diffusive orbits combined with a magnetic focusing effect as the origin of the commensurability peaks, semiclassical quantization of periodic orbits as the origin of the Aharonov-Bohm type oscillation superimposed, and quantum oscillation of localization effects.

I. INTRODUCTION

The two-dimensional (2D) system modulated by a periodic strong repulsive potential is called an antidot lattice. The transport in this system is ballistic, i.e., electrons are scattered from the antidot potential itself rather than from impurities. Various interesting phenomena have been observed in magnetic fields. The purpose of this paper is to give a brief review on transport properties of antidot lattices in the presence of a magnetic field mainly from a theoretical point of view.

In section 2 antidot lattices are introduced along with commensurability peaks in the magnetoresistivity. In section 3 the origin of the commensurability peaks is discussed with emphasis on the roles of classical chaotic motion. In section 4 the close connection between quantum oscillation superimposed on the commensurability peaks and semiclassical quantization of periodic orbits is discussed. In section 6 localization effects playing an important role and varying in an oscillatory manner as a function of a magnetic field are discussed. A brief summary is given in section 6.

II. ANTIDOT LATTICES

Figure 1 shows an illustration of the potential of a square antidot lattice. The antidot lattice is characterized by the period a and the diameter d of each antidot. We have typically $d \gtrsim 1000$ Å, which is larger than the Fermi wavelength of the 2D electron system, $\lambda_F \sim 500$ Å, for a typical electron concentration less than 5×10^{11} cm^{-2} in a GaAs/AlGaAs single heterostructure. Correspondingly, the period of the antidot is usually $a \gtrsim 2000$ Å. This means that the antidot lattice is in the boundary region between quantum and semiclassical regimes. The classical electron motion is known to be fully chaotic.

The model antidot potential for a square antidot, used frequently and used also in this paper, is given by $U(\mathbf{r})=U_0F(\mathbf{r}-\mathbf{R})$ within a Wigner-Seitz cell, where U_0 is a potential maximum located at point $\mathbf{r}=\mathbf{R}$ and

$$F(\mathbf{r}) = \left|\cos\left(\frac{\pi x}{a}\right)\cos\left(\frac{\pi y}{a}\right)\right|^{2\beta}. \tag{2.1}$$

The parameter β characterizes its steepness. The antidot diameter can be defined as $d/2=|\mathbf{r}|$ with $U(\mathbf{r})=E_F$, where E_F is the Fermi energy and $\mathbf{r}$ is chosen on a line

connecting two nearest-neighbor points. A self-consistent calculation in quantum wires fabricated at GaAs/AlGaAs heterostructures suggests that the potential is nearly parabolic for a wire with small width and consists of a flat central region and a parabolic increase near the edge for a wider wire [1,2]. The width of the region where the potential increases from the bottom to the Fermi energy is of the same order as the Fermi wavelength for typical electron concentrations. This leads to roughly $\beta \sim 1$ for $d/a \sim 0.5$, $\beta \sim 2$ for $d/a \sim 0.4$, and $\beta \sim 4$ for $d/a \sim 0.3$ in the case $d \sim 1000$ Å. A similar potential can be chosen for a triangular lattice [3,4]. We sometimes use the following potential also:

$$U(\mathbf{r}) = E_{\mathrm{F}} \left(\frac{d/2+\Delta-r}{\Delta} \right)^2 \theta(d/2+\Delta-r), \tag{2.2}$$

where r is the distance from the center and $\theta(t)$ is the step function defined by $\theta(t)=1$ for $t>0$ and 0 for $t<0$. The parameter Δ describes the steepness of the antidot potential (typically $\Delta/a \sim 0.24$ for $d/a=0.5$).

In experiments performed in a square antidot lattice [5], prominent peaks were observed in the diagonal resistivity ρ_{xx} in weak magnetic fields. They are called commensurability peaks. At certain magnetic fields electrons can move on the commensurate classical orbit encircling a specific number of antidots (pinned orbits). The magnetoresistance was expected to increase at this magnetic field [5].

A classical simulation showed that the change in the volume of the pinned orbits in the phase space is not enough to cause the commensurability oscillation [6]. The importance of the "runaway" orbit, which skips regularly from an antidot to its neighboring antidot in the same direction, was also proposed [7]. Experiments on rectangular and/or disordered antidots [8–12] and numerical simulations [10–14] provided pieces of evidence showing the importance of such orbits. A better way of understanding the origin of the commensurability peaks is through diffusive orbits and magnetic focusing as discussed below.

III. COMMENSURABILITY PEAKS

Consider first the limit of the small aspect ratio $d/a \ll 1$. In this case, the electron loses its previous memory of the direction of the velocity when it collides with an antidot, and therefore successive scattering with antidots can be generally regarded as independent of each other [15]. This means that antidots are nothing but independent scatterers.

In magnetic fields, transport is possible through the migration of the center of the cyclotron motion and therefore the conductivity σ_{xx} vanishes in the absence of scattering. When the cyclotron diameter is smaller than the period, i.e., $2R_c < a$ where R_c is the cyclotron radius, the scattering of an electron from an antidot cannot give rise to diffusion or conduction because the electron is trapped by the antidot.

Scattering from antidots starts to contribute to the conductivity when $2R_c > a-d$. The migration of the center of the cyclotron orbit occurs most frequently due to successive scattering from nearest-neighbor antidots at the magnetic field corresponding to $2R_c=a$ as shown in Fig. 2. At this field the measure of such orbits becomes maximum in the phase space due to a magnetic focusing effect. In fact, an electron emitted from an antidot is focused onto a neighboring antidot. This leads

to an increase in the phase-space volume of the orbits contributing to the increase of the diffusion coefficient at $2R_c \approx a$.

The orbit corresponding to $2R_c = a$ can be denoted as $(n_x, n_y) = (\pm 1, 0)$ or $(0, \pm 1)$, where the line segment connecting the point (n_x, n_y) and the origin constitutes the diameter of the circle. With a further decrease in the magnetic field, successive scattering with next nearest-neighbor antidots becomes possible and the conductivity has a peak around $2R_c = \sqrt{2}a$ corresponding to $(\pm 1, \pm 1)$. This contribution becomes less prominent, however, because the orbit passes through the position of a nearest-neighbor antidot. The next peak arises from $(\pm 2, 0)$ or $(0, \pm 2)$ and $(\pm 2, \pm 1)$ or $(\pm 1, \pm 2)$, which lie close to each other. The latter contribution should be larger because its measure is twice as large as that of the former and therefore the peak occurs around $2R_c \sim \sqrt{5}a$. This peak should be weaker, however, as these orbits also pass through the position of other antidots. The next prominent peak is given by $(\pm 2, \pm 2)$, $(\pm 3, 0)$, $(0, \pm 3)$, $(\pm 3, \pm 1)$, and $(\pm 1, \pm 3)$. Actually, the peak is at $2R_c \approx 3a$, because the orbits $(\pm 3, 0)$ and $(0, \pm 3)$ are not disturbed by other antidots.

In this way we can explain most of the commensurability peaks observed experimentally. The reason why the peak positions can also be explained by pinned orbits is that the orbits specified by (n_x, n_y) correspond approximately to certain pinned orbits by a slight shift in the position of the guiding center.

When the diameter d is no longer negligible in comparison with the period a, the fundamental commensurability peak in σ_{xx} deviates from the condition $2R_c = a$. A simple consideration shows that the measure of the cyclotron orbit starting at an antidot and colliding with a neighboring antidot has a maximum at $2R_c = a + fd$ with $f \sim 0.3$ being a constant weakly dependent on d/a. This means that the commensurability peak is shifted to the weak-field side roughly in proportion to d/a [16].

For a nonnegligible d/a, the correlation among successive scattering from antidots becomes important. In fact, it manifests itself most directly in the Hall conductivity. It tends to enhance the left circular motion of electrons in the weak-field region $2R_c \gtrsim a$ and reduce it in the high-field region $2R_c \lesssim a$. This leads to an enhancement of $|\sigma_{xy}|$ for $2R_c \gtrsim a$ and a reduction for $2R_c \lesssim a$, giving rise to a steplike structure around $2R_c \approx a$.

With the increase of d/a, the measure of the diffusive orbits increases and the diagonal conductivity becomes larger and comparable to σ_{xy} (numerical calculations show that $\sigma_{xx} \sim |\sigma_{xy}|$ around $d/a \sim 0.5$ [15]). Therefore, the commensurability peaks in the resistivity become different from those in σ_{xx}.

Numerical simulations performed recently [15,17] show that the peak in σ_{xx} is broadened considerably with the increase of d/a and at the same time shifted to the lower magnetic field side. A step structure corresponding to the first derivative of σ_{xx} with the magnetic field appears in σ_{xy}. Interestingly, however, the commensurability peak in the resistivity ρ_{xx} remains around $2R_c = a$ independent of d/a. For $d/a \geq 0.5$, the structures in σ_{xx} and σ_{xy} disappear almost completely and ρ_{xx} does not show a clear commensurability peak.

IV. QUANTIZED PERIODIC ORBITS

A fine Aharonov-Bohm (AB) type oscillation was observed superimposed on commensurability peaks of the magnetoresistance [18,19]. The period is roughly given by the magnetic flux quantum $\Phi_0 = ch/e$.

The density of states in classically chaotic systems is given semiclassically in the so-called periodic orbit theory [20-22]. According to the trace formula, the density of states is given by the sum of the classical contribution and the quantum correction. The latter is determined by semiclassically quantized energy levels associated with each periodic orbit and the former is proportional to the classical phase-space volume at an energy.

The density of states has been shown to be correlated well with the semiclassical energy levels [23,24]. The same is true for the resistivity as shown in Fig. 3 [25]. A semiclassical expression can be obtained for the conductivity tensor [23,26,27], but has proved to be unsuccessful for the parameter range corresponding to the experiments mentioned above [23]. As discussed in the previous section, the diffusive orbits have a dominant contribution to the transport in the magnetic-field region near the commensurability peak. These orbits are perturbed by the presence of quantized periodic orbits, which is likely to lead to a quantum oscillation. The semiclassical expression for the conductivity does not take into account such effects.

Quite recently, a clear correlation between the disappearance of a periodic orbit encircling an antidot and that of the AB type oscillation was demonstrated [28]. Figure 4 shows the boundary of the existence of the periodic orbit encircling an antidot for a model potential given by Eq. (2.2). The insets in the right hand side of the figure show the periodic orbit (solid line) for $d/a = 0.6$ and 0.677. With the increase of d/a it merges into another orbit (dotted line), which is unstable and has a longer trajectory, and disappears. It contains the boundary in the case of $\Delta/a = 0.18$ (steeper) and 0.36 (softer) as well. The critical aspect ratio becomes smaller with the increase of Δ/a, i.e., as the antidot potential becomes broader.

Figure 5 shows the calculated results of the magnetoresistance for various values of the aspect ratio. Short vertical lines indicate the magnetic fields where the quantized levels of a periodic orbit encircling an antidot cross the Fermi energy. Solid lines mean stable orbits and dotted ones unstable. The AB type oscillation changes as a function of the magnetic field in an irregular manner, but the dependence on the field is, on the whole, in good agreement with that of the position of quantized levels of the periodic orbit. The oscillation disappears or becomes unrecognizable near the field corresponding to $2R_c = a$ for large aspect ratio $d/a = 0.7$. This field corresponds to the disappearance of the periodic orbit. In fact, the periodic orbit is absent in the hatched region.

V. LOCALIZATION OSCILLATION

5.1 Experiments

A kind of Altshuler-Aronov-Spivak [29] (AAS) oscillation characterized by the period given by half of the flux quantum has been observed in antidot lattices [30,31]. The amplitude of the oscillation turned out to be much larger in triangular lattices [31]. A numerical study has demonstrated that the observation presents a clear indication that real antidot lattices have a sizable amount of disorder in the antidot potential itself [3,4]. In fact, in the absence of disorder in the antidot potential, the conductance exhibits only irregular oscillations depending sensitively on parameters such as the Fermi wavelength, the aspect ratio, the steepness of the potential, etc. A regular AAS oscillation appears only when the mean free path is much smaller than the antidot period, corresponding to the usual AAS oscillation in metallic diffusive systems. An introduction of small but sizable fluctuations in

the antidot diameter lying in the range $0.035 \lesssim d_f/a \lesssim 0.07$ for $d/a \sim 0.5$ destroys irregular oscillations and leads to a regular AAS oscillation, where d_f is the root mean square fluctuation of d. Actual systems are likely to have this amount of disorder, although the exact estimation is difficult.

Quite recently, a behavior suggesting a strong localization was observed at lower temperatures [32]. The resistivity increases considerably with decreasing temperature at low magnetic fields, while it increases at high magnetic fields. At a critical magnetic field, $B_c \approx 0.47$ T, the resistivity remains almost independent of the temperature and is nearly equal to h/e^2. It was shown that the resistivity for $B < B_c$ exhibits a temperature dependence consistent with variable range hopping at low temperatures. Further, the diagonal conductivity also shows a temperature dependence reminiscent of variable range hopping for $B > B_c$. The localization length estimated from the fitting to variable range hopping turns out to be close to the lattice constant of the hexagonal lattice, showing that electrons may become completely confined in each "quantum dot" surrounded by six antidots.

Another interesting feature of the results is the fine quantum oscillation. At lower magnetic fields ($B < B_c$) the period is determined by half of the flux quantum per unit cell and by the flux quantum at higher magnetic fields ($B > B_c$). This leads to the conclusion that the localization length oscillates with a period given by half of the flux quantum at $B < B_c$ and by the flux quantum at $B > B_c$. The origin of the AAS oscillation is known to be quantum interferences of a path encircling an antidot with its time-reversal path in the weak localization regime. The AAS oscillation of the conductance alone does not mean the oscillation of the localization length itself.

5.2 Thouless Number Method

In order to study localization effects in antidot lattices, conventional Thouless-number method [33,34] was used recently [35,36]. This method is known to be useful also in magnetic fields [37]. According to a scaling argument [38], the Thouless number $g(L)$ is a dimensionless conductance defined by the ratio of the strength of effective coupling $V(L)$ and energy difference $W(L)$ of two systems with size L when the systems are combined.

The effective coupling strength is estimated from a geometric average of the curvature of energy bands $\overline{\partial^2 E/\partial k^2}$ for periodic systems having a unit cell with size L and the energy difference is determined from the average energy spacing given by $D(E)^{-1}$ where $D(E)$ is the density of states at energy E. We then have

$$g(L) = \frac{V(L)}{W(L)} = \overline{\frac{\partial^2 E}{\partial k^2}} D(E). \tag{5.1}$$

An S matrix method [39,40] is ideal for this study because calculations in large-size systems are possible. The inverse localization length α is determined by fitting the results to

$$g(L) = g(0) \exp(-\alpha L), \tag{5.2}$$

with $L = 2na$, where a is a lattice constant.

We use a model potential similar to that given by Eq. (2.1) for a square lattice with $a/\lambda_F = 3.77$. This corresponds to the electron concentration $n_s = 2.2 \times 10^{11}$ cm^{-2} for $a = 2000$ Å which is comparable to $n_s = 1.8 \times 10^{11}$ cm^{-2} in the experiments

[32]. We shall introduce a disorder in the antidot potential, i.e., fluctuations in the diameter, and use the mean free path $\Lambda/a=4$ which is consistent with a real system with a high mobility (but still much smaller) where the mean free path is much larger than the lattice constant.

5.3 Numerical Results

Figure 6 shows some examples of the calculated Thouless number g as a function of a magnetic field in hexagonal antidot lattices with size 4×2 ($L=4a$). They show an AAS oscillation with the period $\Phi_0/2$ as a function of the total magnetic flux passing through a unit cell given by $\Phi=\sqrt{3}Ba^2/2$, where B is the strength of the magnetic field. The amplitude of the oscillation Δg normalized by the Thouless number at zero magnetic field g_0 is about $\Delta g/g_0\sim0.19$ almost independent of d_f. This is consistent with the results $\Delta g/g_0\sim0.15$ calculated for similar systems in a different method, i.e., through a direct calculation of the conductance from the transmission probability [3,4].

Figure 7 shows the magnetic-field dependence of the Thouless number and the inverse localization length for $d/a=0.7$ and $d_f/a=0.035$. The Thouless number for each system size oscillates with the period of about $\Phi_0/2$ like an AAS oscillation. The localization length also exhibits a clear oscillation with the same period in good qualitative agreement with experiments [32]. The localization length oscillates in the range between $\sim 20a$ and $\sim 70a$.

For $d/a=0.8$ and $d_f/a=0.035$, the localization effect is enhanced considerably and the AAS oscillation of the localization length is reduced significantly. In fact, the localization length varies only in the range between $\sim 8a$ and $\sim 10a$ and the tendency corresponding to a negative magnetoresistance that the localization effect becomes weaker with the increase of the magnetic field can be more clearly identified.

5.4 Quantum Oscillation

The localization depends strongly on the symmetry of the system. In usual systems in the absence of a magnetic field, the Hamiltonian is chosen as a real symmetric matrix and the corresponding wavefunction is real except for an unimportant phase factor. In this orthogonal case the effective coupling $V(L)$ is given by a real number and an effective dimension of $V(L)$ is given by $\eta=1$. In the presence of a magnetic field, the Hamiltonian is given by a complex unitary matrix and the corresponding wavefunction becomes complex. In this unitary case, $V(L)$ is given by a complex number and consequently $\eta=2$. In the presence of a strong spin-orbit interaction in the absence of a magnetic field, states are always doubly degenerate (Kramers degeneracy) and $V(L)$ is given by a quarternion number. In this symplectic case we have $\eta=4$. This η is the exponent characterizing level repulsion effects in the random-matrix theory [41].

The localization effect becomes weaker with the increase of η. In fact, the localization length in quasi-one-dimensional systems is known to be approximately given by $N_c\eta\Lambda$ [42–44], where N_c is the number of channels and Λ is the mean free path. The AAS oscillation of the conductivity is closely related to the fact that the system belongs to an orthogonal ensemble for $\Phi=n\Phi_0/2$ with an integer n and to a unitary ensemble in other cases.

The amplitude of localization-length oscillation for strong localization is much smaller than that for weaker localization shown in Fig. 7. This is consistent with the fact that the AAS oscillation requires interferences between the paths encircling

an antidot in different directions. With the increase in the localization effect the probability amplitude for an electron to circle around an antidot is reduced.

According to our results on hexagonal antidot lattices with $d_f/a = 0.035$, the oscillation amplitude $\Delta\alpha$ of the inverse localization length normalized by that at zero magnetic field α_0 is $\Delta\alpha/\alpha_0 \sim 0.35$ for $d/a = 0.7$. This is in reasonable agreement with experimental results $\Delta\alpha/\alpha_0 \sim 0.20$ [32] mentioned above. However, the absolute magnitude of the localization length obtained in the present calculation is $\alpha_0^{-1} \sim 20a$, which is much larger than $\alpha_0^{-1} \sim a$ estimated experimentally.

VI. SUMMARY AND CONCLUSION

A review of magnetotransport in antidot lattices mainly from a theoretical point of view has been given. The commensurability peaks appearing in the magnetoresistivity can be understood quite well in terms of an enhancement in the measure of diffusive orbits contributing to the diffusion coefficient due to a magnetic focusing effect. The Aharonov-Bohm type oscillation superimposed on the commensurability peak is understood in terms of semiclassical quantization of periodic orbits encircling an antidot. It has also been shown that realistic antidot lattices have a large amount of disorder in the potential, which accounts for the appearance of the Altshuler-Aronov-Spivak oscillation. The disorder in the antidot potential gives rise to the localization of electron wave functions and the localization length oscillates as a function of a magnetic field with the period determined by the half of the magnetic flux quantum.

ACKNOWLEDGMENTS

This work is supported in part by the Japan Society for the Promotion of Science ("Research for the Future" Program JSPS-RFTF96P00103). One of the authors (S.U.) has been supported by Research Fellowships of the Japan Society for the Promotion of Science for Young Scientists. Some numerical calculations were performed on FACOM VPP500 in Supercomputer Center, Institute for Solid State Physics, University of Tokyo.

REFERENCES

[1] A. Kumar, S.E. Laux, and F. Stern, Phys. Rev. B **42**, 5166 (1990).
[2] T. Suzuki and T. Ando, J. Phys. Soc. Jpn. **62**, 2986 (1993); Physica B **201**, 345 (1994);
[3] T. Nakanishi and T. Ando, Phys. Rev. B **54**, 8021 (1996)
[4] T. Nakanishi and T. Ando, Physica B **227**, 127 (1996)
[5] D. Weiss, M.L. Roukes, A. Menschig, P. Grambow, K. von Klitzing, and G. Weimann, Phys. Rev. Lett. **66**, 2790 (1991)
[6] R. Fleischmann, T. Geisel, and R. Ketzmerick, Phys. Rev. Lett. **68**, 1367 (1992)
[7] E.M. Baskin, G.M. Gusev, Z.D. Kvon, A.G. Pogosov, and M.V. Entin, JETP Lett. **55**, 678 (1992)
[8] K. Ensslin, S. Sasa, T. Deruelle, and P.M. Petroff, Surf. Sci. **263**, 319 (1992)
[9] J. Takahara, A. Nomura, K. Gamo, S. Takaoka, K. Murase, and H. Ahmed, Jpn. J. Appl. Phys. **34**, 4325 (1995)
[10] K. Tsukagoshi, S. Wakayama, K. Oto, S. Takaoka, K. Murase, and K. Gamo, Phys. Rev. B **52**, 8344 (1995)

[11] K. Tsukagoshi, M. Haraguchi, K. Oto, S. Takaoka, K. Murase, and K. Gamo, Jpn. J. Appl. Phys. **34**, 4335 (1995)
[12] K. Tsukagoshi, M. Haraguchi, S. Takaoka, and K. Murase, J. Phys. Soc. Jpn. **65**, 811 (1996)
[13] T. Nagao, J. Phys. Soc. Jpn. **64**, 4097 (1995)
[14] T. Nagao, J. Phys. Soc. Jpn. **65**, 2606 (1996)
[15] S. Ishizaka and T. Ando, Phys. Rev. B **56**, 15195 (1997).
[16] T. Ando, S. Uryu, and S. Ishizaka, Jpn. J. Appl. Phys. **38**, 308 (1999).
[17] S. Ishizaka and T. Ando, Solid State Electron. **42**, 1147 (1998).
[18] F. Nihey and K. Nakamura, Physica B **184**, 398 (1993)
[19] D. Weiss, K. Richter, A. Menschig, R. Bergmann, H. Schweizer K. von Klitzing, and G. Weimann, Phys. Rev. Lett. **70**, 4118 (1993)
[20] M.C. Gutzwiller, J. Math. Phys. **8**, 1979 (1967); **10**, 1004 (1969); **11**, 1791 (1970); **12**, 343 (1971)
[21] M.C. Gutzwiller, *Path Integrals*, edited by G.J. Papadopoulos and J.T. Devrees (Plenum, New York, 1978), p. 163
[22] M.C. Gutzwiller, *Chaos in Classical and Quantum Mechanics* (Springer, New York, 1990)
[23] S. Ishizaka, F. Nihey, K. Nakamura, J. Sone, and T. Ando, Jpn. J. Appl. Phys. **34**, 4317 (1995)
[24] S. Uryu and T. Ando, Physica B **227**, 138 (1996)
[25] S. Uryu, Doctor Thesis (University of Tokyo, 1998).
[26] M. Wilkinson, J. Phys. A **20**, 2415 (1987)
[27] G. Hackenbroich and F. von Oppen, Europhys. Lett. **29**, 151 (1995)
[28] S. Uryu and T. Ando, Physica B **256-258**, 388 (1998).
[29] B.L. Altshuler, A.G. Aronov, and B.Z. Spivak, JETP Lett. **33**, 1255 (1981)
[30] G.M. Gusev, Z.D. Kvon, L.V. Litvin, Yu.V. Nastaushev, A.K. Kalagin, and A.I. Toropov, JETP Lett. **55**, 123 (1992)
[31] F. Nihey, S.W. Hwang, and K. Nakamura, Phys. Rev. B **51**, 4649 (1995)
[32] F. Nihey, M.A. Kastner, and K. Nakamura, Phys. Rev. B **55**, 4085 (1997)
[33] J. T. Edwards and D. J. Thouless, J. Phys. C: Solid State Phys. **5**, 807 (1972).
[34] D. C. Licciardello and D. J. Thouless, J. Phys. C: Solid State Phys. **8**, 4157 (1975).
[35] S. Uryu and T. Ando, Physica B **249-251**, 308 (1998).
[36] S. Uryu and T. Ando, Phys. Rev. B **58**, 10583 (1998).
[37] T. Ando, J. Phys. Soc. Jpn. **52**, 1740 (1983); **53**, 3101 (1984); **53**, 3126 (1984).
[38] E. Abrahams, P. W. Anderson, D. C. Licciardello, and T. V. Ramakrishnan, Phys. Rev. Lett. **42**, 673 (1979).
[39] S. Uryu and T. Ando, Jpn. J. Appl. Phys. **34**, 4295 (1995)
[40] S. Uryu and T. Ando, Phys. Rev. B **53**, 13613 (1996)
[41] F. J. Dyson, J. Math. Phys. **3**, 140 (1962).
[42] O. N. Dorokhov, Pis'ma Zh. Eksp. Teor. Fiz. **85**, 1040 (1983) [Sov. Phys. JETP **58**, 606 (1983)].
[43] K. Muttalib, J. L. Pichard, and A. D. Stone, Phys. Rev. Lett. **65**, 1812 (1990).
[44] H. Tamura and T. Ando, Physica B **184**, 355 (1993).

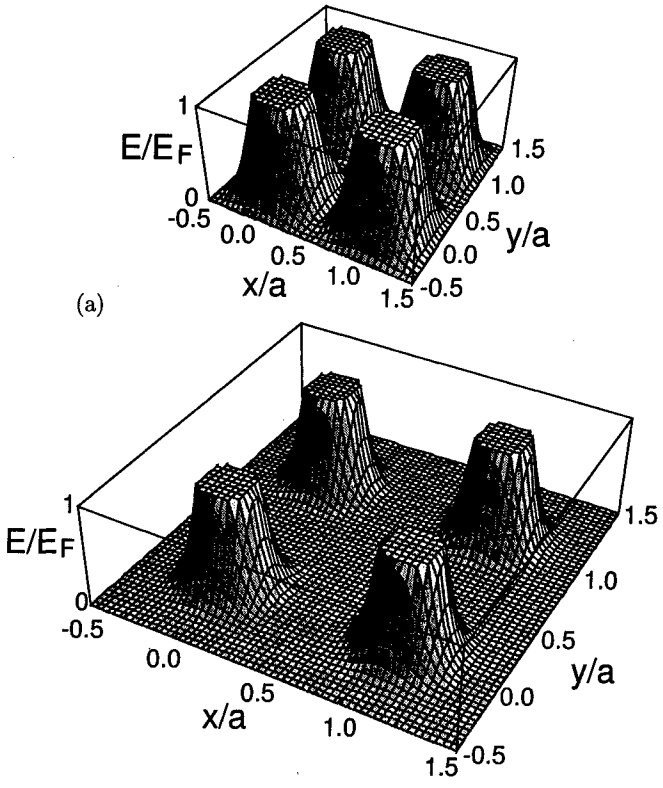


Fig. 1 A model antidot potential in a square lattice. (a) $d/a=0.5$ and $\beta=1$. (b) $d/a=0.3$ and $\beta=4$. The potential is cut off at the Fermi energy

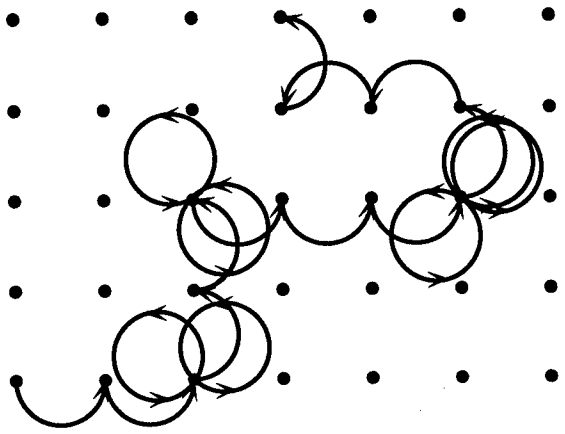


Fig. 2 A schematic illustration of the electron orbit at $2R_C \approx a$. Because of a magnetic focusing an electron has a large probability of successive scattering at neighboring antidots and a large diffusion constant.

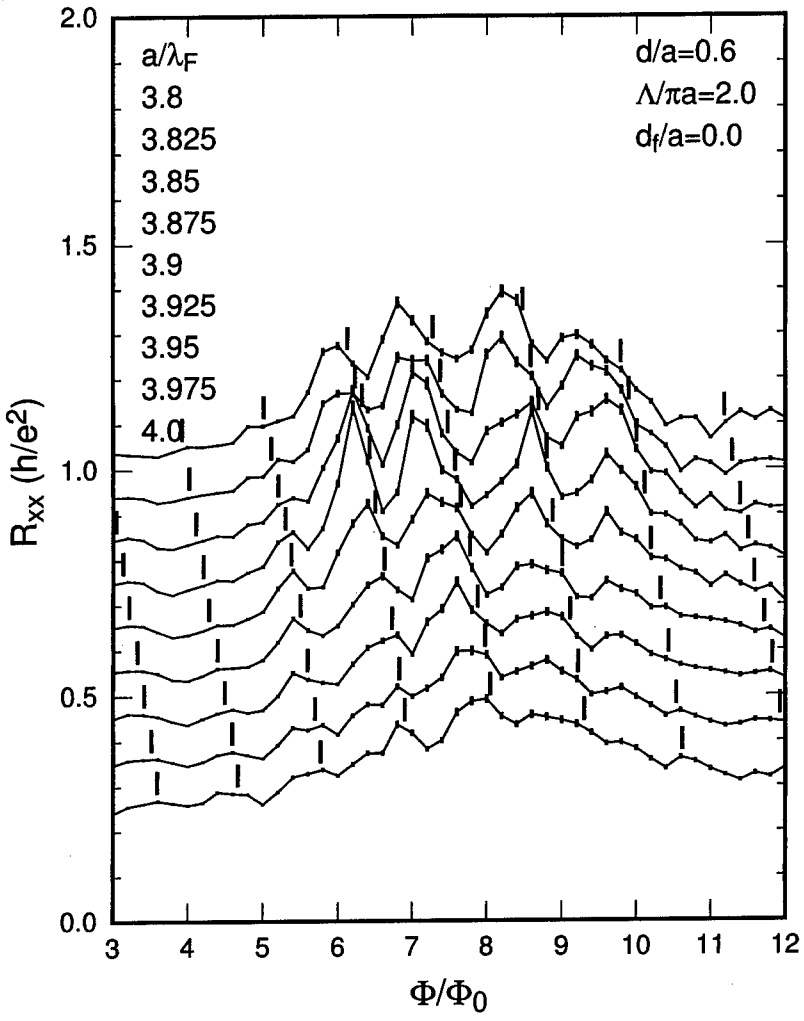


Fig. 3 Diagonal resistance as a function of the magnetic field for $d/a = 0.6$ and the mean free path $\Lambda/\pi a = 2$. After [25].

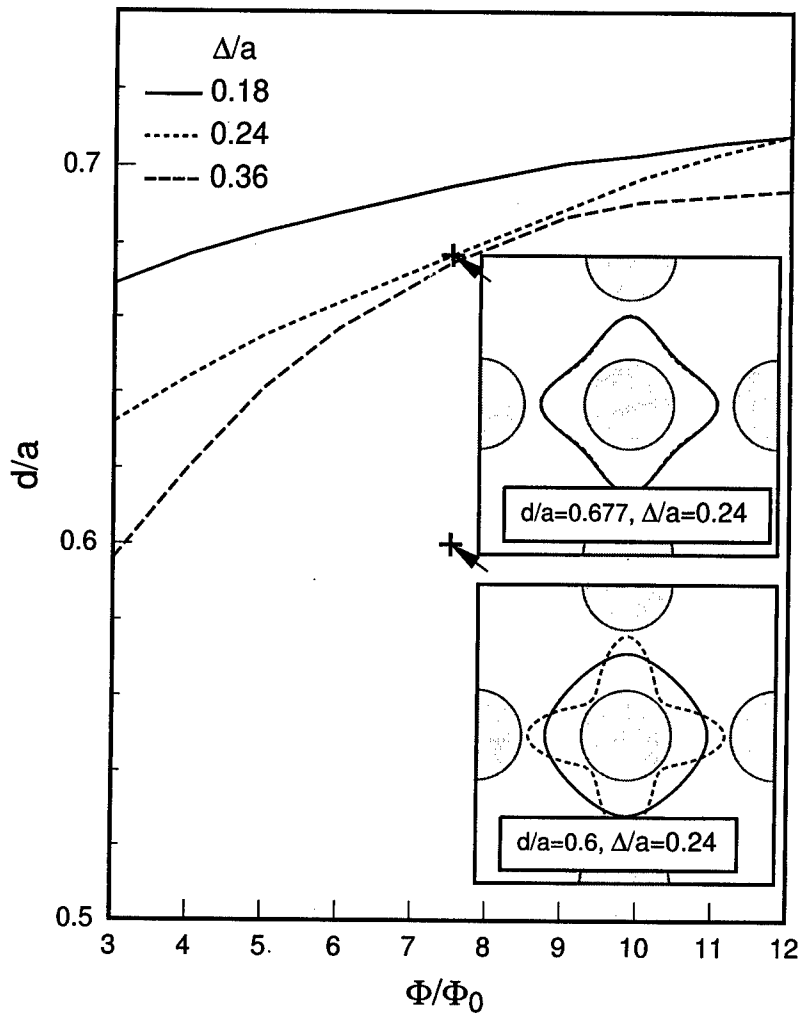


Fig. 4 Critical values of the aspect ratio at which the periodic orbit encircling an antidot disappears. $\Delta/a=0.18$ (solid line), 0.24 (dotted line, realistic), and 0.36 (dashed line). The right upper and lower insets show the periodic orbit (solid line) giving the AB type oscillation and the other (dotted line) that is unstable. These orbits merge and disappear when the aspect ratio approaches a critical value. After [28].

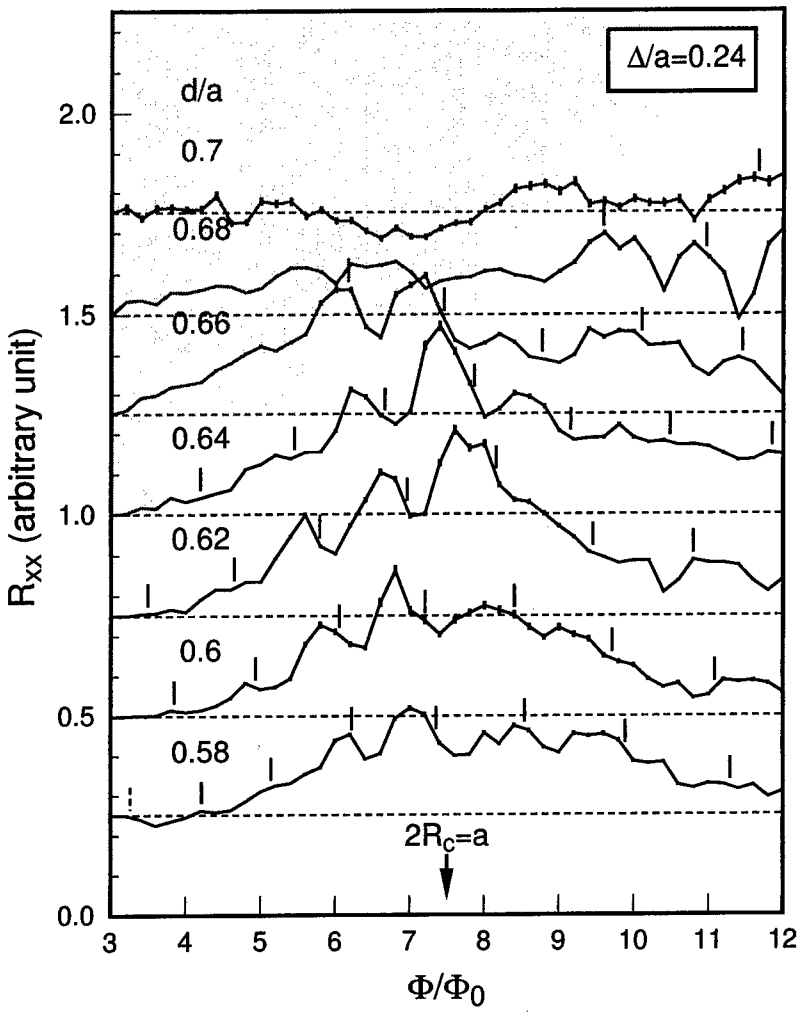


Fig. 5 Calculated resistance as a function of the total flux Φ passing through a unit cell divided by the flux quantum Φ_0 for varying Fermi wavelength. Short vertical lines represent semiclassically quantized energy levels associated with the periodic orbit encircling an antidot (solid and dotted lines for stable and unstable orbits, respectively). After [28].

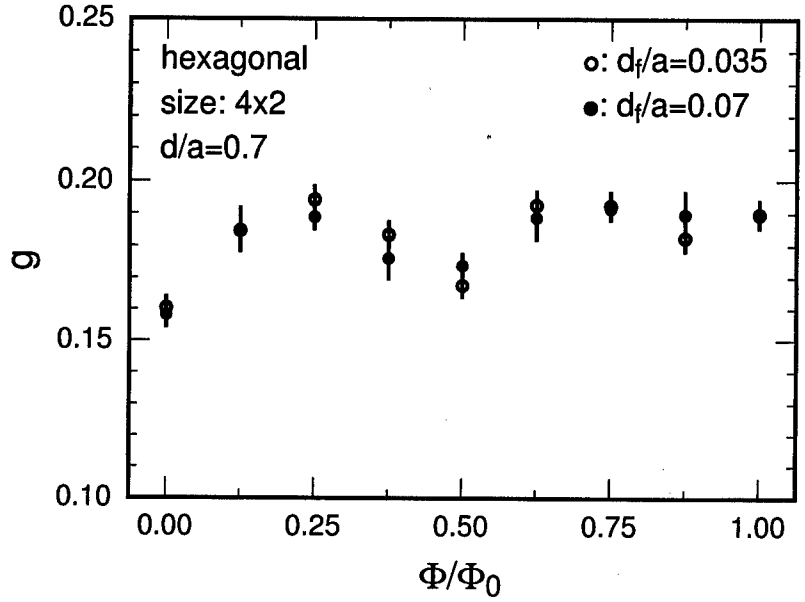


Fig. 6 Calculated Thouless numbers as a function of a magnetic field in hexagonal antidot lattices with $d/a=0.7$ and the $4a\times 2a$. After [36].

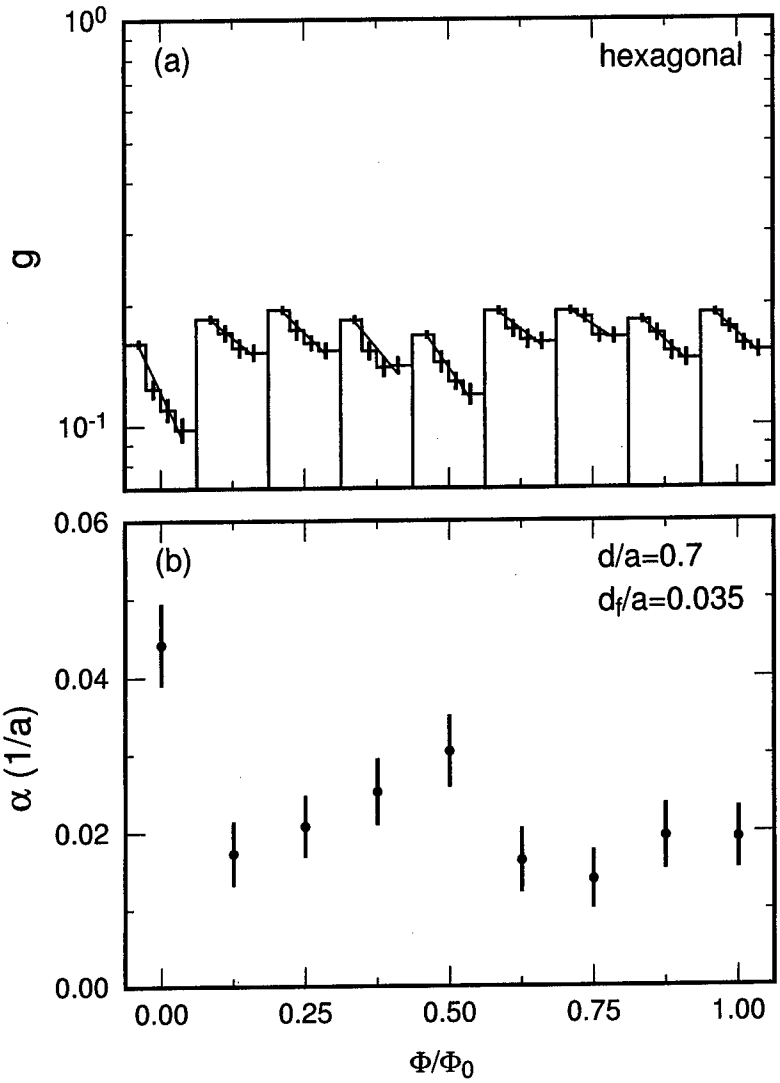


Fig. 7 Magnetic field dependence of (a) the Thouless number and (b) the inverse localization length in a hexagonal lattice with $d/a=0.7$ and $d_f/a=0.035$. After [36].

Spin effects in artificial molecules

Satyadev Nagaraja and Jean-Pierre Leburton
Beckman Institute for Advanced Science & Technology,
and
Department of Electrical & Computer Engineering,
University of Illinois at Urbana-Champaign, Urbana, IL 61801

Abstract

We study electronic properties and spin polarization in coupled quantum dot systems. We model the system using three-dimensional coupled Schrödinger and Poisson equations including many-body effects under the Local Spin Density Approximation within the density functional theory. We show that both electrostatic and quantum mechanical coupling between the two quantum dots play a role in its charging properties, in accordance with experimental observations of Waugh *et al.*. We show that when the inter-dot coupling is weak the lowest energy state is a spin polarized one, in accordance with Hund's rules. When the coupling is increased however, coherent *bonding* and *anti-bonding* states are formed which results in a termination of spin polarization. Furthermore, we find that a for strong inter-dot coupling the indirect exchange-mechanism induces ferromagnetic-like state.

I INTRODUCTION

In recent years attention has focussed on arrays of quantum dots coupled through tunnel junctions [1, 2, 3]. Their appeal stems form the many physical features they share with molecules. In artificial molecules, electron states can couple to form covalent states that are delocalized over the entire array making possible for an occupying electron to tunnel between the various dots without being localized to any [4, 5]. These *bonding states* have lower energy than the constituent dot states by an amount that is equivalent to the binding energy of the molecule. Hence a two-dot system may be compared to a diatomic molecule. Such artificial molecular systems have the advantage that the number of electrons in each dot may be varied by changing an external bias. This is equilvalent to realizing diamtomic molecules of different constituent atoms. Different molecular can be realized by varying the size of the dots, simultaneously or independently, and their number of electrons.

In the present work, we focus on a system of two similar dots whose dimensions are such that the electron-electron interaction energy is comparable to the single-particle energy level spacing, ΔE . The number of electrons in the dot, N, is restricted to very low values, a situation comparable to a light molecule such as H-H or Be-Be. We investigate the electronic properties of the coupled-dot system by solving self-consistently the Schrödinger and Poisson equations on a three dimensional (3D) grid. The electron spin has been considered explicitly under the Local Spin Density Approximation (LSDA) in the density functional theory. [6] From our investigations we find that in the weak tunneling regime, charging of the two dots can occur simultaneously, but as N increases this simultaneous charging is terminated because of the increase in the Coulomb repulsion energy. We also find that for eight electrons in the double-dot — a situation similar to a Be-Be molecule — the ground state of the system is spin polarized in the weak tunneling regime while it is unpolarized in the strong tunneling regime.

II Dot Structures

The layered structure, shown in Fig. 1a, consists of an inverted GaAs/$Al_{0.3}Ga_{0.7}As$ heterostructure which confines the electrons to a 2D gas at the interface. In our model, the simulated structure consists of a 22.5-nm layer of undoped $Al_{0.3}Ga_{0.7}As$ followed by a 125-nm layer of undoped GaAs and finally an 18 nm GaAs cap layer. The cap layer is uniformly doped to 5×10^{18} cm^{-3} so that the conduction band edge is just above the Fermi level at the GaAs-cap layer–undoped GaAs boundary. The inverted heterostructure is grown on a GaAs substrate and charge control is achieved by varying the voltage on the back gate, V_{back} . We assume a negligible voltage drop across the substrate, hence we apply V_{back} directly to the bottom of the $Al_{0.3}Ga_{0.7}As$ layer. The two dots are defined by energizing the ten metallic gates

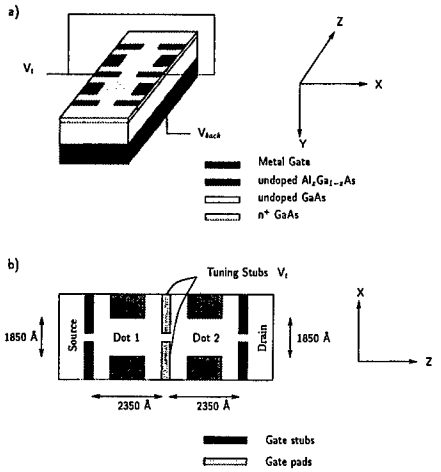


Figure 1: The double dot system a) layer structure of the double dot b) schematic representation along the $x - z$ plane. The gate stub voltage = -1.2 V; gate pad voltage = -0.40 V.

shown in Fig. 1b, while the dot coupling is modulated by applying the voltage, V_t, on the tuning gates. Electron charging of the two dots is possible by tunnel injection from the adjacent two-dimensional regions through the 35-nm opening between the opposite stubs.

III Model

We solve the single-particle effective-mass Schrödinger and Poisson equations self-consistently in the entire dot structure. The 3D Schrödinger equation is solved in the central double-dot region.

Hence the implementation of a spin-dependent scheme for the electronic structure of artificial molecules involves solution of the Schrödinger equation twice — once for each of the spins, up (↑) and down (↓). Under the spin-dependent LSDA the Hamiltonian $H^{\uparrow(\downarrow)}$ for the spin ↑ (↓) electrons reads

$$\hat{H}^{\uparrow(\downarrow)} = -\frac{\hbar^2}{2}\nabla\left[\frac{1}{m^*(\mathbf{r})}\nabla\right] + E_c(\mathbf{r}) + \mu_{xc}^{\uparrow(\downarrow)}[n] \qquad (1)$$

where $m^*(\mathbf{r})$ is the position dependent effective mass of the electron in the different materials, $E_c(\mathbf{r}) = \phi(\mathbf{r}) + \Delta E_{os}$, is the conduction band edge, where $\phi(\mathbf{r})$ is the

electrostatic potential, ΔE_{os} is the conduction band offset.

The respective Hamiltonians are identical in all respects except for the exchange-correlation potential, $\mu_{xc}^{\uparrow(\downarrow)}$, which as parametrized by Ceperley and Alder [7] is given by,

$$\mu_{xc}^{\uparrow(\downarrow)} = \frac{d(n\epsilon_{xc}[n,\zeta])}{dn^{\uparrow(\downarrow)}} \tag{2}$$

where $\epsilon_{xc}[n,\zeta]$ is the exchange-correlation energy as a function of the total electron density $n(\mathbf{r})$ $(= n^{\uparrow}(\mathbf{r}) + n^{\downarrow}(\mathbf{r}))$ and the fractional spin polarization $\zeta = (n^{\uparrow} - n^{\downarrow})/n$. [8]

The 3D Poisson equation for the electrostatic potential $\phi(\mathbf{r})$ reads:

$$\nabla[\epsilon(\mathbf{r})\nabla\phi(\mathbf{r})] = -\rho(\mathbf{r}) \tag{3}$$

where, the charge density $\rho(\mathbf{r})$ is given by $e[p(\mathbf{r}) - n(\mathbf{r}) + N_D^+(\mathbf{r}) - N_A^-(\mathbf{r})]$. Here, $\epsilon(\mathbf{r})$ is the permittivity of the material and is a function of the $y-$coordinate only throughout this work, $p(\mathbf{r})$ is the hole concentration, $n(\mathbf{r})$, the total electron concentration and $N_D^+(\mathbf{r})$ and $N_A^-(\mathbf{r})$ are the ionized donor and acceptor concentrations, respectively. $N_D^+(\mathbf{r})$ is relevant only in the region outside the quantum dot — the dot region itself being undoped or very slightly $p-$doped — and is a function of the position of the Fermi level with respect to the conduction band. $N_A^-(\mathbf{r})$ is neglected as we have only $n-$type regions in our structure. The hole density $p(\mathbf{r})$ is also neglected. At equilibrium the electron concentrations for each spin in the dot are calculated from the wavefunctions obtained from the respective Schrödinger equations, i.e. $n^{\uparrow(\downarrow)}(\mathbf{r}) = \sum_i \mid \psi_i^{\uparrow(\downarrow)}(\mathbf{r}) \mid^2$, while for the region outside the dot a Thomas-Fermi distribution is used, i.e. the electron density is locally a function of the position of the Fermi level with respect to the conduction band edge as opposed to those in the dot which are calculated from the occupation of the quantized $0D$ eigenstates. The relevant expressions for $n(\mathbf{r})$ and N_D^+ may be found in Reference [9].

The various gate voltages – V_{back} , V_t and those on the metallic pads and stubs – determine the boundary conditions for the Poisson equation. Specifically, Dirichlet conditions are imposed on the top and bottom surfaces of the dot structure by defining the potential $\phi(\mathbf{r})$ to be $\phi_m(\mathbf{r})+V_{ext}$, where $\phi_m(\mathbf{r})$ denotes the Fermi level pinning at the semiconductor surface and V_{ext} the external gate potential. For the lateral surfaces (xy plane in Fig. 1) vanishing electric fields are assumed. This is justified by the fact that these lateral boundary surfaces are far enough from the dot for the electric fields to have vanished.

Solution of the Schrödinger and Poisson equations proceeds by solving the Schrödinger for both spins, calculating the respective electron densities and exchange correlation potentials, solving the Poisson equation to determine the potential $\phi(\mathbf{r})$ and repeating the sequence until the convergence criterion is satisfied [10]. This method has been used successfully to investigate spin dependent

effects in QDs such as Hund's rules in shell filling [11, 12].

Single-electron Charging

The determination of N_{eq}, the number of electrons in the dot at equilibrium is done by using Slater's transition rule: [13]

$$E_T(N+1) - E_T(N) = \int_0^1 \epsilon_{LAO}(n)dn \simeq \epsilon_{LAO}(\frac{1}{2}) \quad (4)$$

where $E_T(N)$ is the total energy of the dot for N electrons and ϵ_{LAO} is the lowest-available-orbital occupied by 0.5 electron. The above equation gives the addition energy, i.e. the energy required to add an electron to a dot containing N electrons in terms of a transition state which is defined as a state containing $N+0.5$ electrons. From eq. 4 it is seen that if $\epsilon_{LAO}(\frac{1}{2})$ is positive $N_{eq} = N$ otherwise $N_{eq} = N + 1$. The $N \rightarrow N + 1$ transition points are determined by populating the system with $N + 0.5$ electrons and varying V_{back} until $\epsilon_{LAO}(\frac{1}{2})$ becomes negative. It should be noted that the approximation made in Equation (4) is valid only if ϵ_{LAO} varies linearly with N. Calculations of Fonseca *et al.* [12] have established the validity of the approximation in self-assembled quantum dots.

IV Results

Figure 2 shows the schematic of the lowest four states with their wavefunctions in the double dot for V_t =-0.67V and V_t =-0.60V. For both values of V_t the ground state in the individual dots is $1s$ type, and form a degenerate pair. However, the first excited states, which are p_x- and p_z-like, are degenerate for weak coupling, i.e. V_t =-0.67V, whereas for strong coupling (V_t =-0.60V), the p_z-like states couple to form symmetric (bonding) and anti-symmetric (anti-bonding) states which are lower in energy than the p_x-like states as seen in Fig. 2. This re-ordering of the states has an important bearing on the spin-polarization of the double-dot system, as shall be fully explained later.

Figure 3a shows the *Coulomb staircase* indicating the variation of the number of electrons in the dot with V_{back} at V_t = -0.67V. For V_{back} =0.9769V, $\epsilon_{LAO}(0.5)$ is just negative, implying that the dot can accept one electron in the lowermost 1s state. At this point no distinction is made as to whether Dot 1 or Dot 2 or both are occupied since, in our model, the two dots are identical from the electrostatic and quantum mechanical points of view. The dots are decoupled quantum mechanically since the leakage of the $1s$ wavefunctions into the adjacent dot is negligible, and electrostatically since the distance between the two electron distributions is large, and the resulting Coulomb repulsion, screened by the high dielectric constant of GaAs (ϵ_{GaAs}=13.2), is negligible, or at least weak enough to be overcome by less than 0.1mV change in V_{back} (which is the minimum increment in V_{back} considered

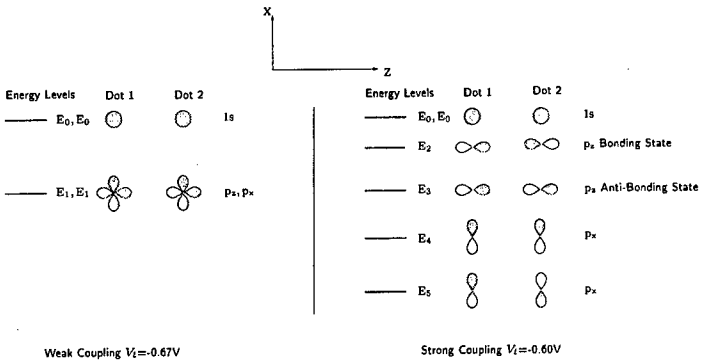


Figure 2: Schematic representation of the lowest six states in the empty double dot in the weak (V_t =-0.67V) and the strong (V_t =-0.60V) inter-dot coupling regimes. In the former the p_z- and p_x- like states are shown together since they are degenerate within each dot and are decoupled from the corresponding states in the other dot. The reordering of these single-particle states due to increased inter-dot coupling is also seen. The shaded areas denote the positive portion of the wavefunctions.

in this work). Thus both dots can be charged simultaneously with an electron each, resulting in N jumping from zero to two. Also, the orientation of the individual spins of the two electrons is arbitrary; we choose both electrons to be $\uparrow$. This simultaneous (double) charging persists as long as the two dots are isolated. However, as V_{back} is increased to 0.9804V, i.e. when the next charge degeneracy point occurs, even though Dots 1 and 2 are identical in all respects, only one of them can be charged (with a $\downarrow$ electron) but not both. This is due to the fact that charging, say, Dot 1 first increases the total Coulomb repulsion experienced by the incoming electron to Dot 2. Hence electrostatic coupling is established between the dots prior to any appreciable quantum mechanical coupling. Overcoming this repulsion requires a 0.1mV increment in V_{back} resulting in the termination of double charging, and is evident as a narrow step for N=3. At V_{back} =0.9805V, Dot 2 also can be charged with a $\downarrow$ electron increasing N to 4. At this point the double-dot is spin unpolarized and the $1s$ ground states of both the dots are completely filled with two electrons ($\uparrow \downarrow$) each.

The next available state for occupation are the p_z- and p_x-states in each of the dots which are above the ground state by $\simeq$ 1meV. These states are almost degenerate; the slight splitting of the states caused by the non-isotropicity of the two-dimensional parabolic confining potential in the $x-z$ plane is very small ($\simeq$

10^{-6}eV). Though either of the two states could be occupied we choose to occupy the p_z-state since it slightly lower in energy than the p_x-state by $\simeq 10^{-6}$eV. Even though the leakage of the p_z-state into the inter-dot barrier is greater than that of the $1s-$state, it is still not coupled to the corresponding p_z-state of the adjacent dot to form a bonding state. Consequently, charging of the two p_z-states proceeds in the same manner as done for the $N = 2$ to $N = 3$ and $N = 3$ to $N = 4$ electrons. The charging of the dot with the fifth electron occurs at V_{back} =0.9832V, where we choose to occupy the p_z-state of Dot 1 with an $\uparrow$ electron. Subsequent occupation of the p_z-state of Dot 2 with an $\uparrow$ electron ($N = 5$ to $N = 6$ transition) occurs at V_{back} = 0.9833V, the 0.1mV increment in V_{back} being required to overcome the Coulomb repulsion due the fifth electron. It must be noted that the sixth electron occupying p_z-state in Dot 2 is also of $\uparrow$ spin, which makes the double-dot spin polarized. This configuration is energetically favorable due to the attractive nature of the exchange interaction between the two $\uparrow$ electrons in the p_z-states of Dots 1 and 2. The unpolarized configuration, where the sixth electron (in p_z-state of Dot 2) is of spin $\downarrow$ is less favorable and occurs at a slightly higher value V_{back} (0.98335V) (dashed curve in Fig. 3a). Likewise, occupying the p_x-state of Dot 1 with a spin $\uparrow$ electron, thereby increasing N to 7, occurs at a lower voltage than occupying p_x-state of Dot 1 with a $\downarrow$ electron or completely filling the p_z-state of Dot 1. This is a demonstration of the familiar Hund's rule whose applicability has been reported in single quantum dots. [14, 11] Similarly the eighth electron of $\uparrow$ spin occupies the p_x-state of Dot 2 at V_{back} = 0.9848V, requiring a 0.1mV increment in V_{back} after p_x-state in Dot 1 has been occupied. As before, this 0.1mV increase in V_{back} is required to overcome the Coulomb repulsion due to the p_x-electron in Dot 1. The double-dot at this state is spin polarized with 6 $\uparrow$ and 2 $\downarrow$ electrons. The ninth through twelfth electrons (of $\downarrow$ spins) now complete the partially occupied p_x- and p_z-states in Dots 1 and 2, at V_{back} = 0.9868V, 0.9870V, 0.9881V, and 0.9883V, thereby reverting the double-dot to a zero spin state. A feature that is conspicous over the $N = 9$ to $N = 12$ range is the increasing interaction between the electrons occupying similar single-particle states in the two dots, as evident in the 0.2mV increment in V_{back} for $N = 9 \rightarrow N = 10$ ($\downarrow$ electrons in the p_z-states of Dots 1 and 2) and $N = 11 \rightarrow N = 12$ transitions , compared to the 0.1mV increment for the $N = 5 \rightarrow N = 6$ and $N = 7 \rightarrow N = 8$ transitions. This is a consequence of increasing leakage of the wavefunctions into the adjacent dot and the centre of the charge distributions in the two dots moving towards each other.

Experimental investigations of Waugh *et al* [3] on arrays of two and three coupled dots confirm our findings. At very low values of the interdot tunneling conductance , G_{dd}, *double charging* effect is observed, but as G_{dd} is increased it is terminated (Figure 2 in Ref. [5]). This is manifested as a splitting of each conductance peak in two (for a double dot) with the separation between them being proportional to the interaction energy δ and increasing with G_{dd}. Another

feature that is clear in their results (Figures 2a, 2b and 2c in Ref. [5]) is that even for a fixed G_{dd} the splitting of peak pair increases for larger N. From our investigations we attribute this behavior to the increased electrostatic interaction between the two dots as N increases, as explained in connection with the charging of $N = 3$ and $N = 4$ electrons. However, as G_{dd} is increased quantum mechanical coupling also contributes to the increased splitting as shall be explained below in relation with Fig. 3b. For instance, in Fig. 2a of Ref. [5], the splitting of the peak is barely discernible about the gate voltage of -1.07 V , but is more pronounced at -1.05 – -1.04 V.

Figure 3b shows the Coulomb staircase diagram for V_t = -0.60V: the interdot coupling is stronger than in the previous situation (V_t = -0.67V), which enhances the leakage of the $1s-$states into the interdot barrier, thereby increasing quantum mechanical as well as electrostatic couplings between the dots. The increase in electrostatic coupling between the dots (quantum mechanical coupling, although present is still negligible for $s-$states), expectedly, terminates double charging and charging proceeds sequentially from $N = 1$ (V_{back} =0.9752V) to $N = 2$ (V_{back} =0.9754V). The increase in inter-dot electrostatic interaction is evident from the 0.2mV increment required to charge Dot 2 with a $\downarrow$ electron after Dot 1 has been charged with a $\uparrow$ electron. This increment in V_{back} ,as observed from Fig. 3a, is more than the increment required to overcome the interaction between the third and fourth electrons that go to complete the $1s-$states in Dots 1 and 2 for weak coupling (V_t =-0.67V). The $N = 2 \rightarrow N = 3$ and the $N = 3 \rightarrow N = 4$ transitions occur at V_{back} =0.7586V and V_{back} =0.9788V, respectively. In each dot the p_z-states which are the lowest available for occupation, couple strongly to form symmetric and anti-symmetric states akin to *bonding* and *anti-bonding* states in molecules. As a consequence of the strong inter-dot coupling the double-dot appears as a single dot about twice as long along $z-$direction as along $x-$direction for p_z- and higher states. This leads to a reordering of electron states in the eigen-energy spectrum, as states with increasing n_z (number of nodes along $z-$direction) closer and below the p_x-state. Thus, the fifth through eighth electrons occupy sequentially the p_z- bonding and anti-bonding states. This is to be contrasted with the partial filling of p_x- and p_z-states, for V_t =-0.67V, by the fifth through the eighth electrons which create a spin polarized state with a net polarization $S = 2\hbar$. It is thus clear that an increase in the inter-dot coupling drives the double-dot from a spin polarized to an unpolarized state. Also the Coulomb staircase steps assume a more uniform width for $N > 4$ as charging proceeds similar to a single QD.

A complete transformation of the two-dot system into a single large dot requires a de-energizing of the tuning gates, i.e. V_t =0V, a case that has not been considered in this work. However from the cases considered so far, it can be extrapolated that the separation of the peaks would be maximum and equal to e/C_T, where C_T is the capacitance of the single large dot. This corresponds to the case

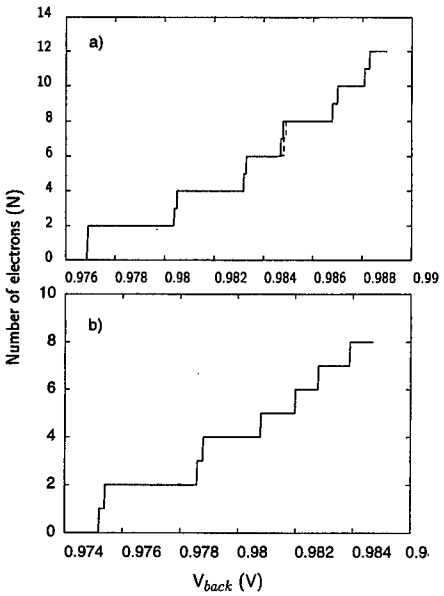


Figure 3: Coulomb staircase diagram for a) V_t = -0.67 V. The transitions that do not follow Hund's rules are shown in dashed lines. b) V_t = -0.60 V.

in Fig. 2d in the work of Waugh *et al.* [3]

Figure 4 shows the variation of the spin ↑ and ↓ electron densities at the $GaAs/Al_{0.27}Ga_{0.73}As$ interface for V_t =-0.60V, along the $z-$direction for $N = 3, 5$ and 8. Fig. 4a shows the spin densities for $N = 3$, a spin polarized state with two ↑ and one ↓ electrons. The two ↑ electrons occupy the $1s-$sates in Dots 1 and 2, respectively, while the ↓ electron occupies the $1s-$state in Dot 1. Consequently, the two electron densities have a $1s$ type distribution in the two dots. The electron densities in the interdot barrier region ($z \simeq$6000 Å) is small as the coupling of the $1s$ states is weak for this value of V_t . However, as N increases the stronger electron-electron interaction induces a lowering of the barrier, an increase in the leakage of the wavefunctions, and an increase in the electron densities, in the barrier. This is seen in Fig. 4b for $N = 5$; the dot is still spin polarized with 3 ↑ and two ↓ electrons. The two ↓ and two ↑ electrons occupy the $1s-$states of Dot 1 and 2, respectively, while the third ↓ electron, occupies the p_z-bonding state that gives the jagged profile to the ↓ electron concentration as seen in the figure. Figure 4c shows the spin densities for $N = 8$. This is a spin unpolarized state with four ↑

	V_t \ N	1	2	3	4	5	6	7	8	9	10	11	12
Spin ($\hbar$)	-0.67V	$\frac{1}{2}$	1	$\frac{1}{2}$	0	$\frac{1}{2}$	1	$\frac{3}{2}$	2	$\frac{3}{2}$	1	$\frac{1}{2}$	0
	-0.60V	$\frac{1}{2}$	0	$\frac{1}{2}$	0	$\frac{1}{2}$	0	$\frac{1}{2}$	0	$\frac{1}{2}$	0	$\frac{1}{2}$	0

Table 1: Variation of the total electron spin S in the double dot with N for V_t = -0.67V (solid line) V_t = -0.60V (dashed line).

and four $\downarrow$ electrons. These electrons fill completely the two $1s-$states in Dots A and B and the p_z-state. Hence, the two ($\uparrow$ and $\downarrow$) distributions look identical.

It also seen in Fig. 4 that the peak electron densities decrease with increasing N. This apparent anomaly is caused by an expansion of the dot, mainly in the $x-z-$plane since the confinement is weakest there. As a result, while the maximum values of the electron densities decrease with N the width of the distribution increases as apparent in Fig. 4. The increase in the widths would be more pronounced at about 400Å away from the $GaAs/Al_{0.27}Ga_{0.73}As$ interface where the electron wavefunction has its maximum in the $y-$direction.

The variation of interdot coupling by varying V_t is comparable to the vibration of a diatomic molecule. Weak coupling (a large negative V_t) is comparable to the situation wherein the distance between the atoms is large, and strong coupling when the distance is a minimum. Thus by varying V_t the level crossing as a function of separation between the artificial atoms in the molecule can be studied. From the Coulomb staircase diagrams of Figs. 3a and 3b and the ensuing discussions it is seen that a lowering of the inter-dot barrier results in a reordering of the single-particle levels, thereby transforming the double-dot (for $N = 8$) from a spin polarized to an unpolarized state. The variation of total spin with the number of electrons in the dot in the weak (V_t = -0.67V) and strong (V_t = -0.60V) coupling regimes is illustrated in Table 1. For weak coupling the total spin of the dot increases in steps of $\hbar/2$ between $N = 5$ and $N = 8$ as the p_x- and p_z-states in Dots 1 and 2 get charged with an electron each of $\uparrow$ spin, which is an illustration of the familiar Hund's rule in atomic shell filling. For strong coupling such a spin polarization of the dot is precluded by a lifting of degeneracy of the p_x- and p_z-states, and the total spin is never greater than $\hbar/2$. We would like to draw attention to the fact that for V_t = -0.67V the total spin is seen to be $\hbar$ for $N = 2$ (Table 1). This, however, does not imply that the double dot is spin polarized, but rather that since the dots are electrostatically decoupled the spins of the two electrons are not correlated in any way. Though in reality there may be a weak interaction between the two electrons, such an interaction is not observable within the resolution of our model, and our choice of the two electrons being of parallel spin is incidental.

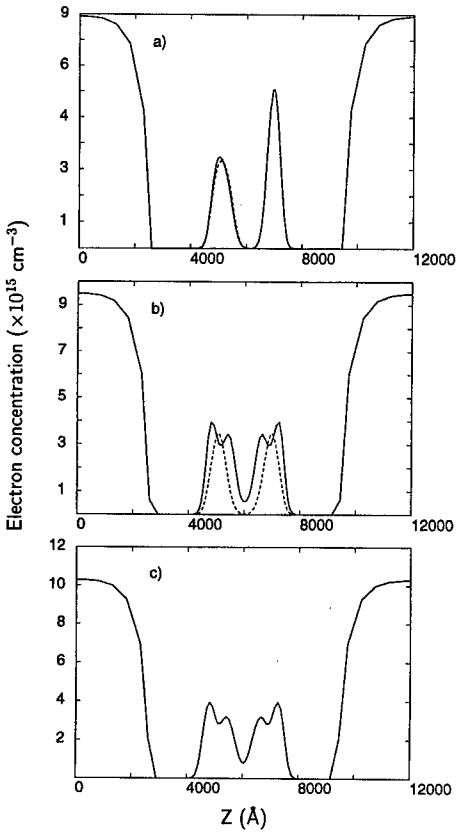


Figure 4: Variation of electron spin ↑ (solid) and the ↓ (dashed) electron densities at the $GaAs/Al_{0.27}Ga_{0.73}As$ interface along the length of the double dot for a) N = 3 , V_{back} = 0.9786 V b) N = 5, V_{back} = 0.9808 V and c) N = 8, V_{back} = 0.9839 V . Resolution of spin is confined to the dot region only, i.e. 3000 Å $\leq z \leq$ 9000 Å . The tuning voltage V_t = -0.60 V.

Spin polarization can also be obtained for $N = 3$ by driving the double dot from weak to strong coupling regimes. The polarization, however, is created by the indirect-exchange as distinguished from Hund's rule in the previous case. It is well known that indirect exchange is the underlying physical reason for the strong magnetization seen in ferromagnetic materials [15]. Their role in quantum dots

systems, has not been reported so far. A potentially useful feature in quantum dots is the ability to switch between ferromagnetic and non-magnetic states by simply varying the voltage on the tuning gates. For example, for V_t =-0.43V and V_{back} =0.9723 there are two electrons in the double-dot, one in each dot occupying the $1s-$state, in a spin singlet configuration. Upon increasing V_t to -0.41V, N increases to 3, with the third electron occupying the p_z-bonding state delocalized over both the dots. Furthermore, the exchange interaction between the delocalized (p_z) electron and the $1s-$electrons alligns the spins of the $1s-$ electrons parallel to that of the delocalized one. This is only possible because the separation between the $s-$ and p_z-states is small enough to be overcome by the attractive exchange interaction. The total spin thus jumps from 0 to $3/2\hbar$. This represented in Table 2.

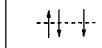
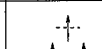
V_t	N=3	Spin, S
-0.43V		$\frac{1}{2}\hbar$
-0.41V		$\frac{3}{2}\hbar$

Table 2: Variation of the total electron spin S in the double dot with N for V_t = -0.67V (solid line) V_t = -0.60V (dashed line).

V Conclusions

We have investigated the electronic properties of a double-dot system by considering a spin dependent model under the Local Spin Density Approximation (LSDA). We observe that an increase in the inter-dot interaction caused by an increase in the coupling strength leads to a splitting of the conductance peaks. We also observe that for a fixed interdot coupling strength, an increase in the number of electrons in the system leads to an increase in the separation between the split peaks due to an increase in electrostatic coupling; these are in good agreement with experiments. Furthermore, we have realized the 'vibrational' state of the double-dot system by varying the inter-dot coupling strength. For an eight electron system, we observe that in the weak inter-dot tunneling regime the system prefers a spin polarized ground state with four electrons occupying degenerate single particle states; but as the tunneling strength increases the reordering of energy levels removes the

degeneracy and the system switches to a spin unpolarized state. For still greater coupling strengths, when $N = 3$, the indirect exchange mechanism between the electrons in each dot and that delocalized over the entire double-dot leads to the formation of a ferromagnetic state.

VI Acknowledgement

This work is supported by NSF Grant No. ECS 95-09751. One of us (S.N.) would like to acknowledge support from the Beckman Institute Research Assistantship program.

References

[1] G. W. Bryant. *Phys. Rev. B*, **48**:8024, 1993.

[2] R. H. Blick, D. Pfannkuche, R. J. Haug, K. v. Klitzing, and K. Eberl. *Phys. Rev. Lett.*, **80**:4032, 1998.

[3] F.R. Waugh, M. J. Berry, D. J. Mar, R. M. Westervelt, K. L. Campman, and A. C. Gossard. *Phys. Rev. Lett.*, **75**(4):705, 1995.

[4] L. Kouwenhoven. *Science*, **268**:1440, 9 June 1995.

[5] R. H. Blick, R. J. Haug, J. Weis, D. Pfannkuche, K. v. Klitzing, and K. Eberl. *Phys. Rev. B*, **53**:7899, 1996.

[6] R. O. Jones and O. Gunnarsson. *Rev. Mod. Phys.*, **61**(3):689–746, 1989.

[7] J. P. Perdew and Z. Zunger. *Phys. Rev. B*, **23**:5048, 1981.

[8] R. G. Parr and W. Yang. *Density Functional Theory of Atoms and Molecules.* Oxford University Press, New York, 1989.

[9] S. M. Sze. *Physics of Semiconductor Devices.* John-Wiley & Sons, Inc., New York, second edition, 1981.

[10] D. Jovanovic and J. P. Leburton. *Phys. Rev. B*, **49**:7474, 1994.

[11] I. H. Lee, V. Rao, R. M. Martin, and J. P. Leburton. *Phys. Rev. B*, **57**(12):9035, 1998.

[12] L. R. C. Fonseca, J. L. Jimenez, J. P. Leburton, and R. M. Martin. *Phys. Rev. B*, **57**:4017, 1998.

[13] J. C. Slater. *Quantum Theory of Molecules and Solids.* McGraw-Hill, New York, 1963.

[14] S. Tarucha, D. G. Austing, T. Honda, R. J. van der Hage, and L. P. Kouwenhoven. *Phys. Rev. Lett.*, **77**:3613, 1996.

[15] C. Zener. *Phys. Rev.*, **82**(3):403, 1951.

MICROWAVE SPECTROSCOPY OF A SINGLE QUANTUM DOT IN THE FEW ELECTRON LIMIT

H. Qin[1], F. Simmel[1], A. Holleitner[1], R.H. Blick[1], and J.P. Kotthaus[1]
W. Wegscheider[2] and M. Bichler[2]
[1] Center for Nanoscience and Sektion Physik, Ludwig-Maximilians-Universität,
Geschwister-Scholl-Platz 1, 80539 München, Germany
[2] Walter-Schottky-Institut der Technischen Universität München,
Am Coulombwall, 85748 München, Germany

ABSTRACT

A small dot containing only about 20 electrons is realized in a two-dimensional electron gas (2DEG) of an *AlGaAs/GaAs* heterostructure and studied by combining microwave and dc transport spectroscopy. Under irradiation with microwaves at around *40 GHz* we find clear photon-assisted tunneling (PAT) through this artificial atom. Measurement of the dc current reveals that the electron transport strongly depends on the bias across the dot. Furthermore, we observe the PAT sidebands of an excited state in the nonlinear regime of Coulomb blockade. With a more subtle two-source measurement technique we confirm the results from the dc measurement.

INTRODUCTION

Spectroscopy on quantum dots is commonly performed by straight forward tunneling measurements or by microwave spectroscopy (1-4). In the nonadiabatic regime where the photon energy hf is much larger than the thermal energy k_BT, electrons can absorb or emit energy quanta. The resulting effect is known as photon-assisted tunneling (PAT). In quantum dots, PAT through the discrete levels provides a tool for spectroscopy of these artificial atoms or molecules (5, 6). Within the existing literature, PAT through the quantum dot is usually studied by measuring the dc tunneling current. However, only in the linear regime it was possible so far to resolve the PAT-induced sidebands.

Here, we will present a detailed study of spectroscopy on a quantum dot by combining dc and microwave spectroscopy. Starting off from common dc and microwave spectroscopy on the dot, we also employ a new two microwave source setup. This setup allows us to study photon-induced transport through the ground state as well as through excited states of a single dot in the few electron limit. Especially the nonlinear regime becomes accessible with this more sensitive method.

EXPERIMENTS

Patterned split gates are adopted to selectively deplete the two dimensional electron gas (2DEG) to form a laterally confined quantum dot. The split gates are fabricated on the surface of an *AlGaAs/GaAs* heterostructure using electron-beam-lithography (EBL). The 2DEG is located about *50 nm* below the surface of the heterostructure. The carrier density is found to be $2\times10^{11}\ cm^{-2}$ and the mobility to be $80\ m^2/Vs$ at *4.2 K*. The dot has a radius about *70 nm* and a charging energy of *2.7 meV*. A simple model calculation gives an estimated number of 20 electrons populating the dot. By tuning one of the gate voltages, the potential of the dot can be varied. The conversion factor of this gate voltage to the energy scale is about *0.15 eV/V*. The electron temperature was found to be on the order of *140 mK*.

Without microwave radiation, the dc conductance is studied in the linear and nonlinear regimes. We apply two methods to study the transport properties under microwave radiation: The first one – the classical microwave spectroscopy – is to determine the dc tunneling current through the dot in dependence of the radiation of a single microwave source. As an alternative in this work, we apply a more intricate method in order to detect the ac tunneling current under the radiation of two microwave sources. The two sources have a slight frequency offset, $\delta f=f_2-f_1<< f_1, f_2$, leading to an effective modulation of the radiation with δf. Since this approach is based on lock-in techniques, we obtain a much more sensitive method of spectroscopy and are thus able to resolve PAT signatures even in the nonlinear regime.

RESULTS

The conductance peaks in the linear regime result from resonant tunneling through the ground state. In the nonlinear regime, transport is determined by not only ground states but also excited states (see Fig. 1 (a)), depending on the energetic difference between the Fermi levels of the drain and source contacts. We find that the dot has different excited states (marked by ε^*) in the region of positive and negative drain/source biases. The energy difference between the excited state and the ground state are *390 μeV* and *276 μeV*, respectively. This large difference results from the electronic structure of this small dot, i.e. electron-electron interactions are crucial. In the following, we assume that the excited states in the dot couple with different strengths to the source/drain leads. Close to zero drain/source bias, the dot has a two-fold electronic structure, as we will see in the PAT signatures. Especially, it should be noted that in the region of negative bias the tunneling through the excited state is much stronger than that through the ground state. This feature may play an important role for the electron transport under microwave radiation.

Applying microwaves and measuring the dc current, we find a well pronounced PAT at *36.16 GHz*, as is presented in Fig. 2. Under small negative drain/source bias, a side band on the right, located *1.8hf* away from the main peak and an inverted left side band at

hf from the main peak are found. The inverted sideband results from the so-called pumping effect (see level diagram b in Fig. 3). With increasing the drain/source bias the pumping current is gradually reduced. The right sideband is attributed to the PAT-induced resonant tunneling via the excited state.

As obtained from the normal conductance measurement, the excited state with negative drain/source bias is located *276 μeV* above the ground state. This is in coincidence with the distance between the main peak and the right side band *(1.8hf)*. In the linear regime eletron tunneling through the excited state is forbidden due to Coulomb blockade. However, under microwave irradiation, the electron in the ground state can absorb photons and is able to escape to the leads. In our case, since $hf<\varepsilon^*-\varepsilon<2hf$, the tunneling through the excited state is realized by a 2-photon absorption process (see diagram a in Fig. 3). With positive drain/source biases, the left and the right tunneling barriers are similar, compared to asymmetric case under negative drain/source biases. In this case, electron pumping is much weaker than resonant tunneling and PAT. The only resolved sideband on the right is located *hf* away from the main peak (see diagram c in Fig. 3). On the left side of the main peak the sideband (as shown in diagram d in Fig. 3) is not resolvable. With larger drain/source biases, none of the sidebands are resolved. The inset of Fig. 2 shows that the position of the sidebands are independent with the microwave power, which is a crucial test for PAT.

With the above understanding of electron transport through this small quantum dot, we apply our two-source spectroscopy method to obtain a better resolution. The two cw microwave sources have a frequency offset of $\delta f=f_2-f_1=2.1\ kHz<<36.16\ GHz$. Under the radiation of the two sources, we are able to determine both amplitude and phase of the resulting ac-tunneling current at the offset frequency. Here, we will only discuss the amplitude behavior in comparison to the classically measured conductance signatures. Fig. 1 (b) shows the amplitude in the whole range of drain/source bias.

Let us first focus on the amplitude behavior in the linear regime: At positive drain/source bias, the resulting amplitude is shown in Fig. 4 (a). The two amplitude peaks correspond to the left and the right photon sideband respectively, as shown in Fig. 3 (c) and (d). The peak distance is constant at *2hf* when the drain/source is very small compared to the level spacing ($\varepsilon^*-\varepsilon$) and the photon energy *hf*. With negative drain/source bias, we can see clearly the pumping or PAT through the ground state and the PAT-induced resonant tunneling through the excited state (Fig. 4 (b)). The different states are marked by **P**, **G**, and **E** in the figure. The pumping (**P**) and excited (**E**) states are separated by a transition point (amplitude = 0), at which the inverted pumping current eliminates the resonant tunneling through the ground state and the excited state. At small drain/source bias, pumping is strong and PAT through the ground state is suppressed. With increasing drain/source bias, PAT through the ground state overwhelms the pumping. Hence, only in a small critical range of negative drain/source bias the electron pumping signal is well pronounced.

In the nonlinear regime with positive drain/source bias, both, the left and the right sidebands are resolved (Fig. 1 (b)). The distance between them is correlated to the drain/source bias. Furthermore, PAT through the excited state is also well resolved which is found at a constant energy difference to the left PAT sideband. Under negative

drain/source bias, only the left sideband of PAT through the ground state is observed. PAT through the excited state is also observed in this region. The amplitude in the nonlinear regime reveals the same excited states as the ones obtained from dc conductance measurements. This two-source method has the advantage to resolve PAT in either the linear and the nonlinear regime.

CONCLUSIONS

We presented transport and microwave spectroscopy measurements on a small quantum dot with only a few electrons. The electronic structure of the dot is characterized by common dc conductance measurements without microwave radiation. The different excited states of the dot are clearly probed, by varying the coupling of the tunneling barriers to the drain/source contacts. In the linear regime with negative drain/source bias we find strong electron pumping , because of the asymmetry of the tunneling barriers. Resonant tunneling through the excited state is also enabled by the 2-photon absorption of the electron in the ground state. The two-source method enables us to probe PAT through the ground state and the excited state even in the nonlinear regime.

ACKNOWLEDGEMENT

We like to thank D.W. van der Weide and S. Manus for helpful discussion. This work was funded in part by the Volkswagen-Stiftung, the Deutsche Forschungsgemeinschaft (DFG) and the Defense Advanced Research Projects Agency (DARPA).

REFERENCES

1. L.P. Kouwenhoven, C.M. Marcus, P.L. McEuen, S. Tarucha. R.M Westervelt, and N.S. Wingreen, in Mesoscopic Electron Transport, edited by L.L. Sohn, L.P. Kouwenhoven and G. Schön, series E, **345**, pp. 105-214, Kluwer Dordrecht, Netherlands (1997).

2. R.H. Blick, R.J. Haug, D.W. van der Weide, K. von Klitzing, K. Eberl, Appl. Phys. Lett. **67**, 3924 (1995); T.H. Oosterkamp, T. Fujisawa, W.G. van der Wiel, K. Ishibashi, R.V. Hijman, S. Tarucha and L.P. Kouwenhoven, Nature **395**, 873 (1998).

3. C. Bruder and H. Schoeller, Phys. Rev. Lett. **72**, 1076 (1994).

4. Q. Sun and T. Lin, J. Phys. Condens. Matter **9**, 4875 (1997).

5. C.A. Stafford and N.S. Wingreen, Phys. Rev. Lett. **76**, 1916 (1996).

6. R.H. Blick, D.W. van der Weide, R.J. Haug, and K. Eberl, Phys. Rev. Lett. **81**, 689 (1998).

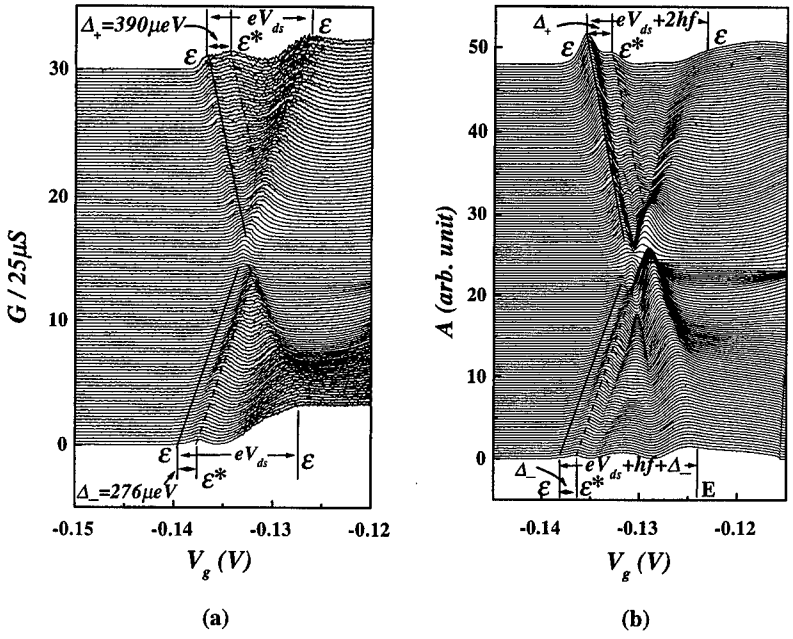


Fig. 1, (a), dc conductance of the dot: The curves are measured under different drain/source biases. From the uppermost to the lowermost, the drain/source bias varies from *1.61 mV* to *-1.61mV* in steps of *26.8 μV*. ε^* and ε represent excited states and ground states. Δ_+ and Δ_- represent the energies of different excited states of the dot with positive and negative drain/source bias, respectively. (b) The amplitude of the detected ac tunneling current under radiation of the two-source setup (see text for details). The frequencies are *36.159997900 GHz* and *36.16 GHz* respectively. From the uppermost curve to the lowermost one, the drain/source bias varies from *1.61 mV* to *-1.61mV* in steps of *21.4 μV*. The notation **E** represents the PAT-induced resonant tunneling through the excited state (see text for details) and the other notations are similar to those in (a). The solid line and the dashed line trace out ground states and excited states, respectively.

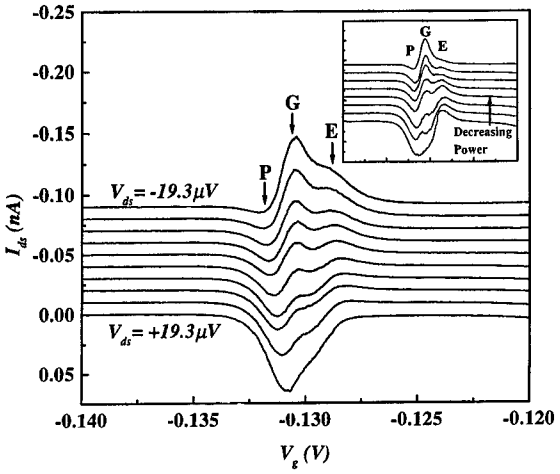


Fig. 2, Transport properties in the linear regime under the radiation of one microwave source: The different curves are with different drain/source biases. From the uppermost curve to the lowest one, the drain/source bias increases from *-19.3 μV* to *19.3 μV* in steps of *4.3 μV*. The notation **P**, **G** and **E** indicate the inverted pumping current, the resonant tunneling through the ground state and the PAT-induced resonant tunneling through the excited state, respectively. The inset shows the power dependence of the transport through the dot.

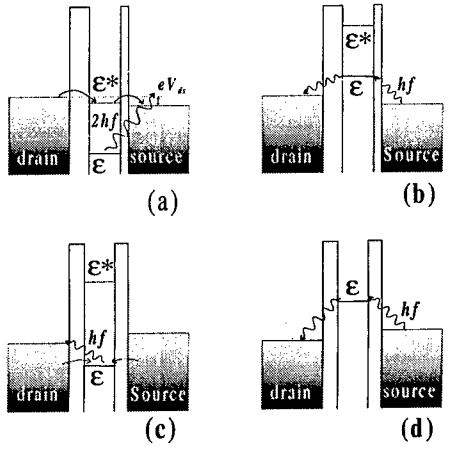


Fig. 3, The level diagrams of the dot under microwave radiation: Diagrams (a) and (b) are under small negative drain/source bias, diagrams (c) and (d) are under small positive bias.

(a) PAT-induced resonances. (b) Electron pumping. (c) The right sideband of the resonant tunneling through the ground state. (d) Left sideband of the resonant tunneling through the ground state.

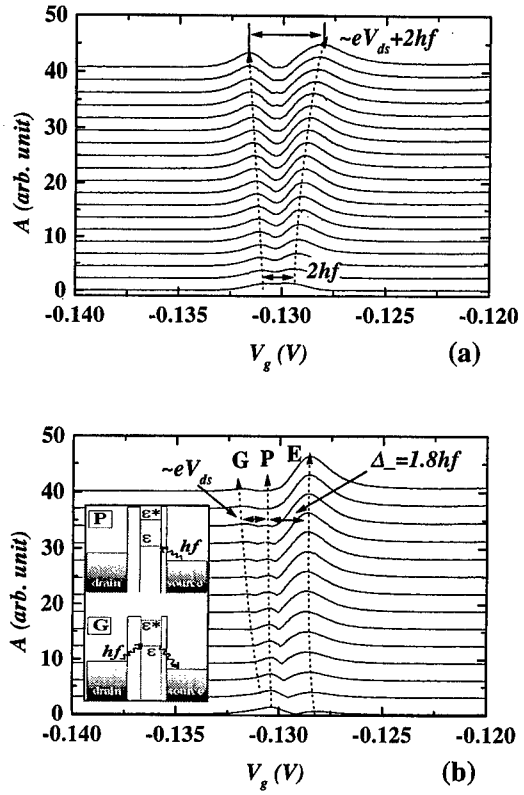


Fig. 4, Amplitude behavior in the linear regime: (a) With small positive drain/source bias, two peaks are found corresponding to the right and left sidebands discussed in Fig. 3 (c) and (d). From the uppermost curve to the lowermost curve, the drain/source bias varies from *308.5 μV* to *19.3 μV* in steps of *16.1 μV*. (b) Under small negative drain/source bias, the left sideband, pumping and the PAT-induced resonance are resolved. From the uppermost curve to the lowermost curve, the drain/source bias varies from *-222 μV* to *-13 μV* in steps of *16.1 μV*.

Magnetic properties of self-assembled Fe quantum dashes

L. Menon[†], M. Zheng[††], H. Zeng[††], D. J. Sellmyer[††] and S. Bandyopadhyay[†*]
[†]Department of Electrical Engineering and
Center for Materials Research and Analysis
[††]Department of Physics and Center for Materials Research and Analysis
University of Nebraska
Lincoln, Nebraska 68588, USA

Abstract

Regimented two-dimensional arrays of iron (α-Fe) quantum dashes have been synthesized by electrodepositing elemental Fe into self-ordered nanopores in an anodized alumite film. The Fe dashes in the pores have the shape of rotational ellipsoids ("American football") whose major and minor axes dimensions can be varied by appropriate processing control. In this work, we have experimentally investigated the time dependent magnetization properties of these dashes as a function of their transverse dimension (minor axis). We show that there is a trade-off between the magnetic viscosity and the inter-particle interaction causing spontaneous demagnetization. Consequently, there must exist an optimum particle diameter (for a fixed areal particle density) to achieve the most stable magnetization.

1 Introduction

There is significant current interest in developing high-density, high-speed magnetic recording media for data storage and memory applications. Self-assembled arrays of magnetic nanoparticles, produced by electrodepositing ferromagnetic elements into self-ordered nanopores in an alumite film, have emerged as a strong candidate for magnetic recording media with storage density exceeding 100 Gbits/inch^2. The stability of the stored data (or equivalently the "non-volatility") in such systems is determined by two somewhat related quantities: the *magnetic viscosity* and the *interparticle interaction parameter*. The viscosity is a measure of the energy barriers that need to be crossed for demagnetization (when a demagnetizing field is applied) and hence is a measure of the resistance offered to demagnetization. A lower viscosity corresponds to a stiffer resistance. The interaction parameter, on the other hand, is a measure of inter-particle magnetostatic interaction. If this quantity is negative, then the interaction tends to destabilize the magnetization. Hence the interaction parameter is a measure of the vulnerability to spontaneous demagnetization. We have studied the magnetic viscosity and the interaction parameter as a function of the transverse size of the magnetic nanoparticles which have the shapes of rotational ellipsoids (hence the name "quantum dashes"). Their average transverse size (minor axis) is on the order of 10 nm and can be varied by 2-4 nm. We find that while the viscosity decreases as we increase the particle size (while keeping the

*Corresponding author: e-mail – bandy@quantum1.unl.edu

areal density fixed), the interaction parameter increases. Hence there is a trade-off between the two parameters and there must exist an optimum particle size (for a given areal density) to achieve the longest storage times.

This paper is organized as follows. We first describe the synthesis of the quantum dash arrays followed by a discussion of magnetic viscosity and inter-particle interaction. The final section is our conclusion.

2 Synthesis: self-assembly of ferromagnetic quantum dashes

Electrodeposition of ferromagnetic elements (Fe, Ni, Co., etc.) into self-ordered pores in an alumite film has long been used as a technique for producing quantum dash arrays that are useful in magnetic recording [2, 3, 4, 5]. There are two basic steps in the synthesis. The first step is to produce an alumite film with an ordered arrangement of nanopores. This is achieved by a two-step anodization process: first, a 99.999% pure aluminum foil (0.1 mm thickness) is anodized for several hours in an appropriate acid (typically sulfuric or oxalic). This is followed by stripping off the resulting alumina film with an appropriate stripper, and then re-anodizing for a short duration (few minutes) in the same acid. The alumina film that forms on the surface of the foil after the second anodization step has a virtually periodic arrangement of nanopores with hexagonal close-packed ordering [7, 8]. A raw AFM image of an arrangement of pores is shown in Fig. 1. The average diameter of the pore depends strongly on the acid used, with sulfuric acid yielding the smallest diameter pores [6]. The second step is to fill the pores with a ferromagnetic element by ac electrodeposition. For this purpose, the foil with the porous film (termed "alumite" in magnetic recording literature) is placed in a suitable non-cyanide aqueous electrolyte containing ions of the ferromagnetic metal. An alternating signal of 10 V rms amplitude and 250 Hz frequency is imposed between the aluminum foil and a platinum counter-electrode (the frequency is important since the magnetization properties seem to depend on it; the optimal frequency is around 250 Hz. [9]). Because alumite conducts preferentially in only one direction (the cathodic direction), it is called a "valve metal oxide". Metal ions are reduced to zero-valent metal within the pores during the cathodic half-cycles of the imposed ac signal, but are not re-oxidized during the anodic half cycles. Selective deposition of the metals occurs only within the pores since they offer the least impedance path for the current to flow. Once the metal is electrodeposited, the pores are sealed by a 10-minute immersion in boiling water which covers the surface with a layer of $Al(OH)_3$. This prevents or retards surface oxidation (rusting) of the Fe particles.

We routinely produce Fe quantum dashes in thin alumite films by the above described process. For the present study, we carried out the anodization in sulfuric acid which yields a pore diameter of 12±1 nm (five times smaller than what we get with oxalic acid anodization). For depositing α-Fe in the pores, we used $FeSO_4{:}7H_2O$ and H_3BO_3 in distilled water. The presence of electrodeposited material in the pores has been verified in the past by energy dispersive analysis of x-ray [10]. cross-section TEM [10] and by variable angle spectroscopic ellipsometry [11]. The last two techniques also yield information about the shapes of the Fe quantum dashes. They appear to resemble rotational ellipsoids (somewhat like an American football).

In order to vary the transverse dimension (minor axis) of the quantum dashes, we widen the pores after anodization by soaking them in sulfuric acid for various durations. This is done prior to electrodeposition of the metal. The width of the pores increases with the soaking duration, albeit sub-linearly.

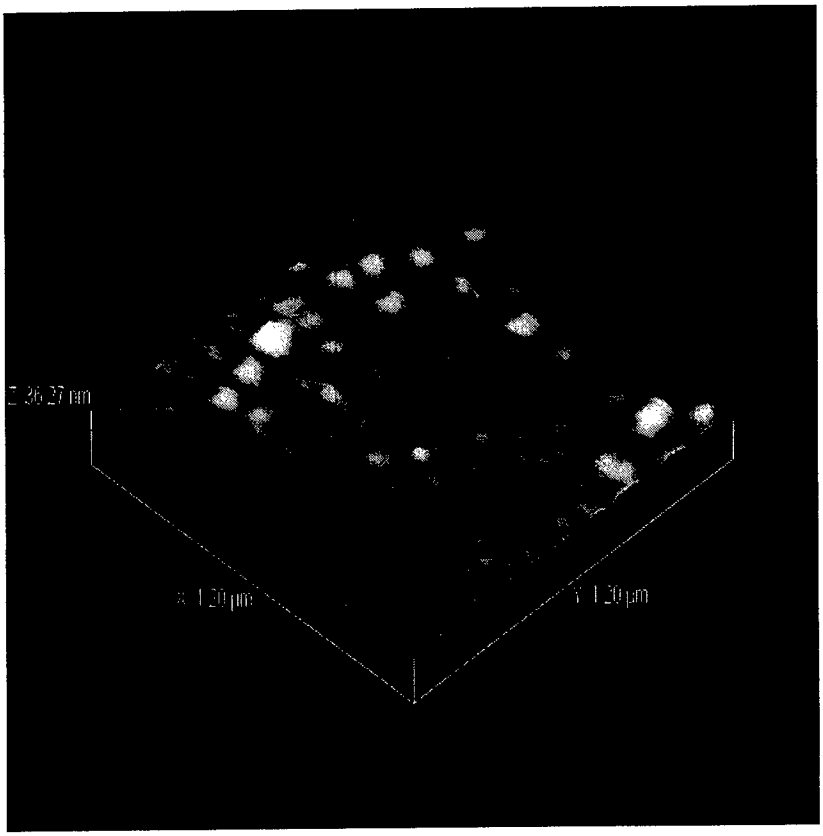


Figure 1: Atomic force micrograph of pore morphologies produced in our laboratory using anodization in oxalic acid. The average pore diameter is 52 nm with a 5% standard deviation.

In the past, nanosized elemental ferromagnets (typically nanowire arrays) were also produced by a number of other techniques such as growth on self-organized NaCl (110) gratings [12], sputtering on nanoporous alumina membranes [13, 14], etc. These techniques do not yield arrays with long range order and probably not with sufficiently high aspect ratio (eccentricity). As a result, their magnetic properties are inferior. For ferromagnetic nanoparticles containing but a *single domain*, the aspect ratio is important since theoretically the magnetic coercivity should increase with increasing aspect ratio [15, 16, 17] or so-called "shape anisotropy" (magneto-crystalline anisotropy also plays a role). Ref. [14] reports a room-temperature "absolute maximum" coercivity of 1390 Oe in Fe while ref. [3] reports a maximum coercivity of 2050 Oe - all in the direction perpendicular to the plane of the film. The larger coercivity in ref. [3] is probably a result of a higher aspect ratio. We, on the other hand, have observed a peak room- temperature coercivity in excess of 2900 Oe in Fe electrodeposited in 10-nm pores produced by anodization in sulfuric acid. The coercivity is highly anisotropic and is always higher in the direction perpendicular to the alumite film. It climbs to more than 4000 Oe at a temperature of 5 K. We have also observed a coercivity of 2400 Oe in cobalt quantum dashes and close to 1000 Oe in nickel quantum dashes. To our knowledge, these are the highest coercivities reported in such systems.

The purpose of this paper is however not to discuss static magnetic properties of quantum dashes such as coercivity. They will be discussed in another forthcoming publication. Instead, we wish to discuss here the time-dependent properties and magnetic interaction between the particles which determines spontaneous demagnetization. Both play a crucial role in magnetic data storage (recording) applications [18].

3 Magnetic viscosity

When a demagnetizing field is applied to a system of magnetized nanoparticles, the magnetization decays with time. The time dependence is governed by the magnetic reversal mechanisms operative and the distributions of energy barriers that have to be crossed for magnetic relaxation. This problem has received significant attention and has been studied in a diverse array of magnetic materials including rocks [19], permanent magnetic alloys [20] and spin-glass alloys [21]. Numerous theoretical models have been proposed to explain the temporal behavior of magnetization decay and invoke various models for magnetic reversal. Two commonly accepted models for magnetic reversal are the so-called symmetric and non-symmetric fanning models [17] which are certainly not operative in our systems because our experimentally observed coercivities exceed the theoertical maximum coercivities predicted by these two models. A more likely scenario is coherent or incoherent (curling) rotation of the magnetization [23]. However, because the particles are acicular, other mechanisms have also been proposed [22]. Furthermore, since the transverse dimension of the nanoparticles is of the order of the magnetic coherence length [24], entirely new mechanisms, hitherto unsuspected, may also be operative [25].

When a demagnetizing field H is applied to a magnetized specimen, the magnetization M decays with time t according to a semi-emperical relation [26]

$$M(H,t) = A(H) - S(H)f(t) \tag{1}$$

where $A(H)$ is a time-independent constant, $S(H)$ is the *magnetic viscosity*, and $f(t)$ is a function of time. All of these quantities depend on the magnetic reversal mechanism(s). If there are various relaxation mechanisms operative at the same time, each characterized by

Table 1: Interaction parameter α versus pore widening time

Pore widening time (minutes)	α
0	-0.46
5	-0.62
10	-1.08
15	-0.9
20	-1.2
30	-1.1

a single time constant, then the function f depends on the nature of the distribution of the time constants. For a flat-topped distribution, the following relation holds in the interval $0 << t << \infty$ [27]

$$M(H,t) = A(H) - S(H)lnt \tag{2}$$

In our samples, we always find Equation (2) to hold indicating that there are multiple time constants associated with magnetic reversal and that they have a flat distribution. Note from Equation (2) that the magnetic viscosity $S(H)$ is a measure of the resistance to demagnetization. The lower the viscosity, the slower is the demagnetization, or equivalently, stiffer is the resistance to demagnetization.

In Fig. 2, we show the magnetic viscosity $S(H)$ as a function of the demagnetizing field H for various "average transverse dimension of the particles" (minor axis dimension). As mentioned before, the average minor axis of the particles is varied by increasing the pore diameter through soaking in phosphoric acid. This is done after anodization but prior to electrodeposition. Since ascertaining the actual average minor axis dimension would require extensive cross-section transmission electron microscopy (a difficult, time-consuming and expensive propostion), we instead show $S(H)$ versus H as a function of the pore widening time (or soaking time in H_3PO_4).

In Fig. 2, we see that there is a critical transverse dimension corresponding to a 5-minute soak which results in the highest viscosity. The existence of this maximum was unexpected. Beyond this maximum, the viscosity decreases with increasing transverse dimension. The non-monotonic dependence of particle diameter may shed some light on the major magnetic reversal mechanisms. This matter will be discussed in a future publication. However, from an engineering view point, it is obvious that a larger particle size is preferable since the viscosity is lower. Note that the pore widening process does not affect the *areal density* of pores. Instead, it widens the pores at the expense of decreasing the separation between nearest neighbor pore walls. This however adversely affects the inter-particle interaction as we show in the next section.

4 Inter-particle interaction

In high density arrays, closely spaced magnetic particles interact magnetostatically. Wohlfarth [1] showed that for single-domain particles with uniaxial anisotropy and without inter-particle interaction, the d.c. demagnetization remanence magnetization $M_d(H)$, the isothermal remanence magnetization $M_r(H)$, and the saturation remanence magnetization M_r after

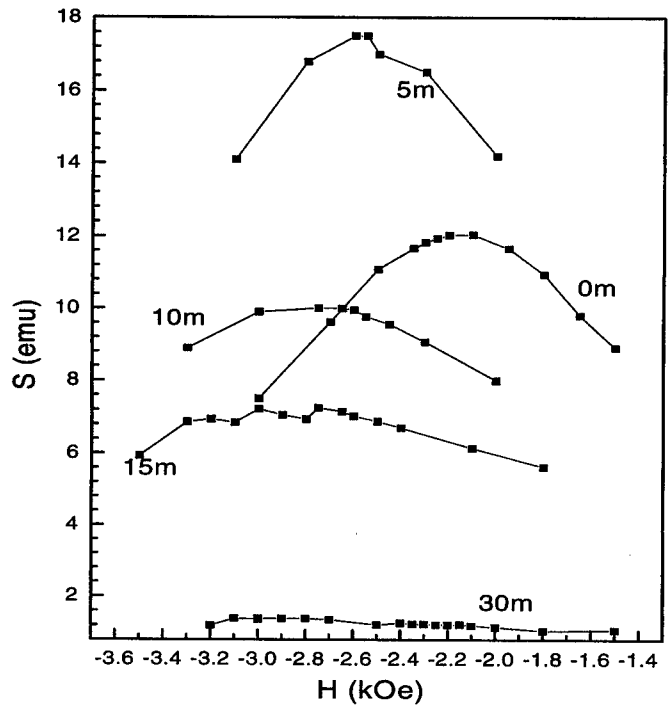


Figure 2: Room-temperature magnetic viscosity as a function of the demagnetizing field for various pore widening durations.

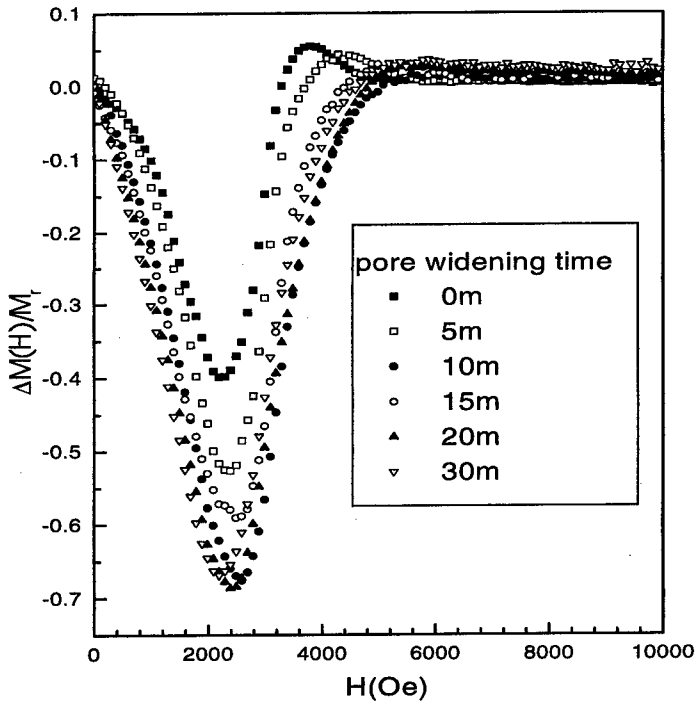


Figure 3: Room-temperature inter-particle interaction versus the demagnetizing field.

the sample is saturated at a saturation field H_s, obey the relation

$$\Delta M(H) = \frac{M_d(H)}{M_r} - 1 + 2\frac{M_r(H)}{M_r} = 0 \tag{3}$$

Henkel [28] suggested that $\Delta M(H)$ is a measure of the inter-particle interaction. Furthermore, a dimensionless quantity α is defined as

$$\alpha = 2\int_0^\infty \frac{\Delta M}{M_r} d\left(\frac{H}{H_s}\right) \tag{4}$$

If $\alpha > 0$, then the inter-particle interaction stabilizes the magnetized state and resists demagnetization, while if $\alpha < 0$, then the interaction favors demagnetization.

In Fig. 3, we plot $\Delta M/M_r$ versus the demagnetizing field H for various average transverse dimensions of the particles (or, equivalently, various pore widening times). This quantity is always negative indicating that the interparticle interaction tends to demagnetize the samples (the slight positive incursions around 4000 Oe may be an experimental artifact associated with too rapid a demagnetization cycle; all our measurements are carried out with an alternating gradient force magnetometer). The curves peak at around the coercive field. The quantity α is proportional to the area under the curves and are given in Table I.

As expected, the magnitude of α (or the strength of inter-particle interaction) decreases with decreasing pore widening time. This is *not* a particle size effect, but rather an inter-particle *separation* effect. As the pores are widened, the separation between nearest neighbor pore walls decreases since the pore density is a constant and is not affected by the pore widening process. As the particle walls approach each other, the interaction increases which hastens spontaneous demagnetization. This is the penalty incurred in increasing the pore size.

5 Conclusion

In this paper, we have demonstrated that increasing the transverse dimension (minor axis) of the magnetic quantum dashes (while at the same time reducing the separation between their walls) decreases the magnetic viscosity but also increases the interaction parameter α. Thus there is a trade-off between the two parameters. The optimum choice of the particle diameter will depend on the specific application; our contribution is to point out the existence of this trade-off in alumite films used for magentic recording.

Acknowldegement: This work was supported by the US Army Research Office under grant DAAG-55-98-1-0015, the National Science Foundation under grant DMR-96-23992, and the Center for Materials Research and Analysis constituted under the Nebraska Research Initiative (State of Nebraska). H. Zeng was supported by an IBM fellowship. Tha authors gratefully ackowledge discussions with Prof. Roger Kirby.

References

[1] E. P. Wohlfarth, *J. Appl. Phys.*, **29**, 595 (1958).

[2] S. Kawai and R. Ueda, *J. Electrochem. Soc.*, **122**, 32 (1975).

[3] D. AlMawlawi, N. Coombs and M. Moskovitz, *J. Appl. Phys.*, **70**, 4421 (1991).

[4] G. Zangari and D. N. Lambeth, *IEEE Trans. Magn.*, **33**, 3010 (1997).

[5] J. E. Wegrowe, D. Kelly, A. Fromck, S. E. Gilbert and J-Ph Ansermet, *Phys. Rev. Lett.*, **82**, 3681 (1999).

[6] C. R. Martin, *Science*, **266**, 1961 (1994).

[7] H. Masuda and K. Fukuda, *Science*, **268** 1466 (1995).

[8] H. Masuda and M. Satoh, *Jpn. J. Appl. Phys.*, **35**, L126 (1996).

[9] S. Bandyopadhyay, L. Menon, N. Kouklin, H. Zeng and D. J. Sellmyer, *J. Elect. Mat.*, **28**, 515 (1999).

[10] S. Bandyopadhyay, A. E. Miller, H-C Chang, G. Banerjee, V. Yuzhakov, D-F Yue, R. E. Ricker. S. Jones, J. A. Eastman, E. Baugher and M. Chandrasekhar, *Nanotechnology*, **7**, 360 (1996).

[11] A. Balandin, S. Bandyopadhyay, P. G. Snyder, S. Stefanovich, A. Varfolomeev, D. Zaretsky, G. Banerjee and A. E. Miller, 1997 *Phys. Low Dim. Struct.*, **11/12**, 155.

[12] A. Sugawara, D. Streblechenko, M. McCartney and M. R. Scheinfein, *IEEE Trans. Magn.*, **34**, 1081 (1998).

[13] K. Liu and C. L. Chien, *IEEE Trans. Magn.*, **34**, 1021 (1998)

[14] J. L. Weston. A. Butera, V. R. Inturi, J. D. Jarratt, T. J. Klemmer and J. A. Bernard, *IEEE Trans. Magn.*, **33**, 3628 (1997).

[15] E. C. Stoner and E. P. Wohlfarth, *Trans. Royal Soc. (London)*, **A240**, 599 (1948).

[16] C. Kittel, *Revs. Modern. Phys.*, **25**, 1 (1949).

[17] I. S. Jacobs and C. P. Bean, *Phys. Rev.*, **100**, 1060 (1955).

[18] R. M. Kloepper, B. Finkelstein and D. P. Braunstein, *IEEE Trans. Magn.*, **20**, 1081 (1984).

[19] See, for example, D. J. Dunlop, *Rev. Geophys. Space. Phys.*, **11**, 855 (1973).

[20] See, for example, P. Gaunt, *Phil. Mag.*, **34**, 775 (1976).

[21] See, for example, C. N. Guy, *J. Phys.: Met. Phys.*, **7**, 1505 (1977).

[22] J. E. Knowles, *J. Magn. Mag. Mat.*, **61**, 121 (1986).

[23] R. Skomski and J. M. D. Coey, *Permanent Magnetism* (Institute of Physics, Bristol, 1999).

[24] A. Aharoni, *Introduction to the Theory of Ferromagnetism* (Oxford University Press, Oxford, 1996).

[25] R. Skomski, private communication.

[26] E. P. Wohlfarth, *J. Phys.: Met. Phys.*, **14**, L155 (1984); R. W. Chantrell, A. Lyberatos and E. P. Wohlfarth, *J. Phys.: Met. Phys.*, **16**, L145 (1986)

[27] E. Kneller, *Ferromagnetismus* (Springer-Verlag, Berlin, 1962).

[28] D. Henkel, *Phys. Stat. Sol.*, **7**, 919 (1964).

Quantum Well Infrared Photodetectors

DEVELOPMENT OF SIMULTANEOUS MULTICOLOR QUANTUM WELL INFRARED PHOTODETECTOR FOCAL PLANE ARRAYS

Walter R. Dyer
Ballistic Missile Defense Organization
7100 Defense Pentagon
Washington, DC

ABSTRACT

Infrared (IR) focal plane arrays (FPAs) are essential to many missions in ballistic missile defense (BMD). Some BMD sensor functions can be performed with single-color FPAs, while others require simultaneous measurements in two to four IR bands. To meet these needs, the Ballistic Missile Defense Organization (BMDO) sponsors development of multi-color IR FPAs, including quantum well infrared photodetectors (QWIPs). Thus far, the QWIP effort has been successful in producing high format, two-color QWIP FPAs, which now exist in the LWIR/LWIR and MWIR/LWIR bands. Readout integrated circuits, optimized for QWIPs, have also been built under BMDO sponsorship and integrated with the QWIP arrays. BMDO expects to sponsor work on three- and four-color FPAs in the future. This paper describes the need for simultaneous multicolor FPAs in BMD. This is followed by a description of BMDO's multicolor QWIP work.

Key Words: quantum well infrared photodetectors (QWIPs), ballistic missile defense (BMD), focal plane arrays (FPAs), multi-color QWIP, temperature estimation.

I. FOCAL PLANE ARRAYS AND BALLISTIC MISSILE DEFENSE

Focal plane arrays (FPAs) are used in ballistic missile defense for surveillance, target detection, target tracking, and discrimination. These functions are performed from satellites, aircraft, ships, fixed locations or interceptors. In interceptors, FPAs can also provide the line of sight measurements needed for target intercept. The temperatures of most advanced BMD targets require FPA wavelengths in the MWIR, LWIR, or VLWIR bands. Important FPA characteristics for future BMD FPAs will include large format (512x512 or higher), high sensitivity ($D^*>2(10^{11})$ cm-$Hz^{1/2}$ / W), low 1/f noise, good uniformity (>90% uncompensated), and high operability (>99 %). Low cost FPAs will also be required. The cost of a complete FPA with the above properties should not exceed $10,000.

1.1 Multicolor FPAs

An important requirement for future BMD missions is multicolor FPAs. Although many BMD functions can be accomplished using only one color, multicolor FPAs offer better performance in many cases, and some functions can be performed only with multicolor. Surveillance, target detection, and target tracking can be done using single-color FPAs if the targets are easy to identify. However, when the target and/or background are uncertain, or may change during an engagement, single-color design involves compromises that can degrade overall mission capability. Two or more spectral bands (colors) can greatly improve overall performance in such cases. For example, when a sensor must track a ballistic missile through booster burnout, much better detection and tracking will result if two colors are used—one before and one after burnout. Discrimination of targets from decoys and debris is greatly enhanced by using multicolor FPAs. While the irradiance measured by a single-color sensor is a useful discriminant, estimation of thermal characteristics requires two to four colors. The maximum number of simultaneous colors needed for future BMD missions appears to be four. It is desirable that each of the four colors be easily and quickly variable by changing a bias voltage. This will permit simultaneous measurements in four bands optimized to target detection and background rejection, which is preferable to hyperspectral FPAs with many narrow bands.

1.2 Two-Color Temperature Estimation

Ignoring optical losses and spectral filtering, the power measured by a seeker of aperture area S m^2 in wavelength band (λ_1, λ_2) meters from a gray body of emissivity ε, area A m^2, and temperature T°K, at a range of r meters is

$$P(T,\lambda_1,\lambda_2) = \varepsilon \frac{SA}{r^2} \int_{\lambda_1}^{\lambda_2} \frac{2hc^2\lambda^{-5}}{e^{\frac{ch}{\lambda kT}} - 1} d\lambda \qquad Watts \qquad [1]$$

where c=2.988x10^8 m/sec is the speed of light, h=6.625x10^{-34} J sec is Plank's constant and k=1.381x10^{-23} J/K is Boltzman's constant. It is not possible to accurately estimate the target's temperature T using only one wavelength band (λ_1, λ_2), because ε, A, r and T are all unknown. However, if measurements are made simultaneously in two wavelength bands (λ_1, λ_2), (λ_3, λ_4), their ratio R cancels ε, A, S, and r, and can be used to estimate T. The ratio R is plotted in figure 1 for two sets of wavebands. The ratio R is a monotonic function of T, which allows T to be found uniquely for every R. Also note from figure 1 that the slope dR/dT is larger for the more separated wavebands. Hence, temperature estimation errors will be smallest when the wavebands are separated as much as practical, consistent with maximizing signal to noise ratio in both bands.

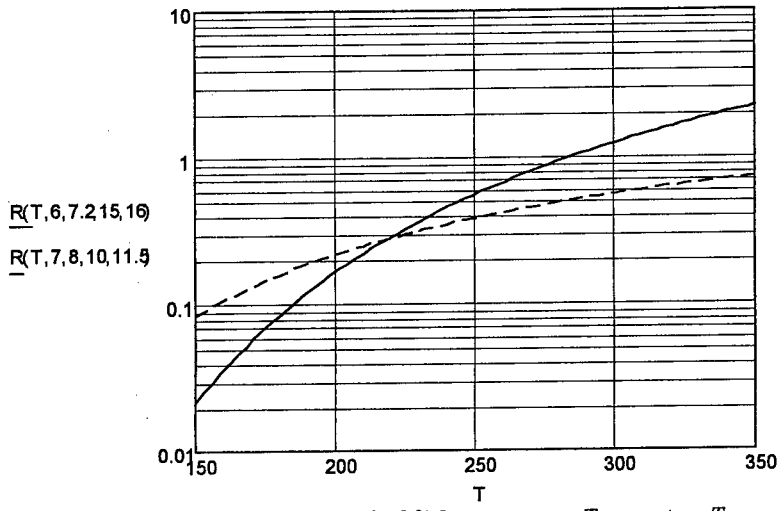


Figure 1. Ratio Of Measurements v Temperature T

1.3 Three-Color Temperature Estimation with Earthshine

While solar scattering can usually be ignored at wavelengths longer than 6 μm, temperature estimation generally will be complicated by earthshine reflected from targets at MWIR-VLWIR wavelengths. In this case, the measured irradiance is

$$P(T,\lambda_1,\lambda_2) = P_{tgt}(T,\lambda_1,\lambda_2) + \alpha P_E(\lambda_1,\lambda_2) \qquad [2]$$

where α accounts for the view factor of the reflected earthshine and the subscripts *tgt* and E denote IR emitted from the target and earthshine reflected from the target respectively. Equation [2] contains three unknowns, $P_{tgt}(T, \lambda_1, \lambda_2)$, $P_E(\lambda_1, \lambda_2)$, and α, but it is also a function of ε, A, and r, because the terms have forms similar to equation [1]. To make a temperature estimate, three measurements, $P(T, \lambda_1, \lambda_2)$, $P(T, \lambda_3, \lambda_4)$, $P(T, \lambda_5, \lambda_6)$ of the target are needed. In addition, three estimates $P_E(\lambda_1, \lambda_2)$, $P_E(\lambda_3, \lambda_4)$, $P_E(\lambda_5, \lambda_6)$ are made by looking directly at the earth or by measuring the earthshine reflected from a reference sphere near the target, with the same sensor used for the target measurements. With the P_E terms estimated, multiply $P(T,\lambda_3,\lambda_4)$ by the ratio of earthshine measurements $P_E(\lambda_1,\lambda_2)/P_E(\lambda_3,\lambda_4)$ and subtract the result from $P(T,\lambda_1,\lambda_2)$. The result is

$$D(T,\lambda_1,\lambda_2,\lambda_3,\lambda_4) = P(T,\lambda_3,\lambda_4)\left[\frac{P(T,\lambda_1,\lambda_2)}{P(T,\lambda_3,\lambda_4)} - \frac{P_E(\lambda_1,\lambda_2)}{P_E(\lambda_3,\lambda_4)}\right] \qquad [3]$$

After calculating $D(T,\lambda_1,\lambda_2,\lambda_5,\lambda_6)$ the same way, form the ratio U, defined as

$$U(T,\lambda_1,\lambda_2,\lambda_3,\lambda_4,\lambda_5,\lambda_6) = D(\lambda_1,\lambda_2,\lambda_3,\lambda_4)/D(\lambda_1,\lambda_2,\lambda_5,\lambda_6)$$

$$= \frac{P(T,\lambda_3,\lambda_4)}{P(T,\lambda_5,\lambda_6)} \times \left[\frac{\dfrac{P(T,\lambda_1,\lambda_2)}{P(T,\lambda_3,\lambda_4)} - \dfrac{P_E(\lambda_1,\lambda_2)}{P_E(\lambda_3,\lambda_4)}}{\dfrac{P(T,\lambda_1,\lambda_2)}{P(T,\lambda_5,\lambda_6)} - \dfrac{P_E(\lambda_1,\lambda_2)}{P_E(\lambda_5,\lambda_6)}} \right] \qquad [4]$$

Each term of U is a ratio of irradiance measurements, and hence is independent of ε, A, and r. Plots of U vs T are shown in figure 2 for two sets of three bands. U is a monotonic function of T, and hence it provides a unique estimate of T for each value of U. As in the no-earthshine case, errors are reduced when the wavebands are separated as much as practical. Comparison of figures 1 and 2 indicates that earthshine causes a reduction in the accuracy of the temperature estimates since the slopes of the dU/dT curves are smaller that those of the dR/dT curves.

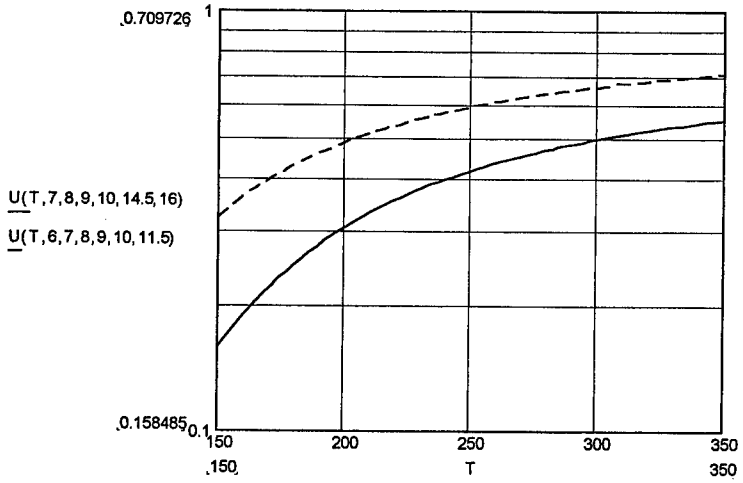


Figure 2. Ratio U vs Temperature T

Measured exoatmospheric data indicates that the accuracies of the earthshine ratio terms of [4] are maximized if one of the detector colors is chosen in a band where the earth's atmosphere partially blocks earthshine. There are three blocking bands in the MWIR-VLWIR region that can be used: the water band (5.5 μm – 7.5 μm), the ozone band (9.4 μm – 9.9 μm), and the CO_2 band (14 μm –16 μm). While none of these bands blocks earthshine totally, the CO_2 band offers the best combination of spectral width and earthshine blocking. The ozone band is narrow, and the lower portion of the water band should be avoided due to solar scattering. Best accuracy results when the color in the

blocking band is between the other two colors. This makes QWIPs attractive because they can easily cover the CO_2 band and beyond.

If the targets of interest are not very reflective, it may be possible to ignore earthshine and use a two-color FPA with both colors in located separate earthshine blocking bands. The range of expected target temperatures and reflectivities determines the benefits of this approach, but it has the advantage of relative simplicity, and in some cases better accuracy. One of the blocking bands should be the CO_2 band due to its wide spectrum and good blocking characteristics. The solid curve of figure 1 represents the potential of this method. Comparison with figure 2 shows that the two-band approximation has larger slope and therefore may provide greater accuracy than the three-band method. After T has been estimated, target's emissivity-area product, εA, can also be estimated if an estimate of range r is available.

1.4 Four-Color Temperature Estimation of Non-gray Targets

The above two- and three-color developments assume a graybody target. If the target is non-gray (i.e., ε varies with λ), simultaneous measurements in four or more bands are needed. Spitzberg (3) has shown that graybody emissivity is coordinated well enough with wavelength that four uniformly spaced wavelength bands allow fairly good temperature estimation of non-gray targets between 5 μm and 25 μm. Best results are obtained when $\varepsilon(\lambda)$ is expanded in an orthogonal series, and more bands improve the estimates somewhat. As in the graybody case, target's emissivity-area product, εA, can also be estimated if an estimate of range is available.

II. BMDO DEVELOPMENT OF MULTICOLOR QWIPS

The Ballistic Missile Defense Organization's (BMDO) development in multicolor FPAs has followed parallel paths in Mercury Cadmium Telluride (MCT) and Quantum Well Infrared Photodetectors (QWIPs). Both technologies have experienced some problems in developing FPAs with the desired LWIR wavelength bands, sensitivity, uniformity, and operability, but as more colors were added, QWIPs enjoyed somewhat better success than MCT. This is due in part to band gap engineering methods available to QWIPs through well-established techniques for doping and well depth control. In addition, multicolor QWIP array production is facilitated by the relative ease of changing wavelength by changing layer thickness and material composition in the molecular beam epitaxy (MBE) growth process. Two-, three- and four-color arrays can be produced by MBE, growing single color QWIPs on top of each other, separated by highly doped contact layers. This allows spatial pixel co-registration and nearly identical fill factors for each color. The peak spectral response of each layer is set by controlling the quantum well thickness and barrier composition.

Another reason for QWIP's success in multicolor arrays is their spectral response, which has relatively narrow full width at half maximum (10-20% of peak wavelength). While this is often cited a drawback in terms of conversion efficiency, it is beneficial in multicolor FPA manufacture because it eliminates the need for the first detection layer to

absorb all in-band photons to keep them from being detected by the second. This allows the ordering of the spectral stacks to be chosen for best array performance without concern for cross coupling.

One problem in developing multicolor QWIP FPAs is the design of multicolor gratings to couple IR radiation into the wells. As more colors are added, the difficulty of designing gratings increases because conventional grating designs have peak coupling at a single wavelength. Multi peak gratings are attained at the expense of reduced the coupling efficiency at each of the multicolor QWIP wavelengths.

Lockheed-Martin (L-M) and the Jet Propulsion Laboratory (JPL) are currently developing multicolor QWIPs for BMDO, under contracts executed by the Air Force Research Laboratory. Both contractors have successfully produced two-color FPAs and are beginning designs for three-color FPAs.

2.1 Lockheed-Martin QWIPs (1)

L-M has developed and built two-color FPAs in the MWIR/LWIR LWIR (4.7 μm and 8.6 μm) and LWIR/LWIR (8.6 μm and 11.2 μm) for BMDO. The format of these FPAs is 256x256, with 40 μm pitch. The FPAs are designed to be background limited relative to an uncooled optics background when operated at 40 K. The arrays are grown using MBE on GaAs substrates. Each stack consists of 20 periods per color of GaAs for LW and InGaAs for MW with AlGaAs barriers in the bound to quasi-bound (BQB) design. Each pixel has three indium bump connections and advanced interconnect architecture derived from MIMIC processing. It consists of vias etched through the detector that connect to buried ohmic contact layers. With the vias, the fill factor is 85%, which is expected to increase in the future. Spectral response of the MW and LW material is shown in figure 3, and a plot of detector current versus voltage for several operating temperatures is shown in figure 4 for each wave band of the two-color LWIR FPA.

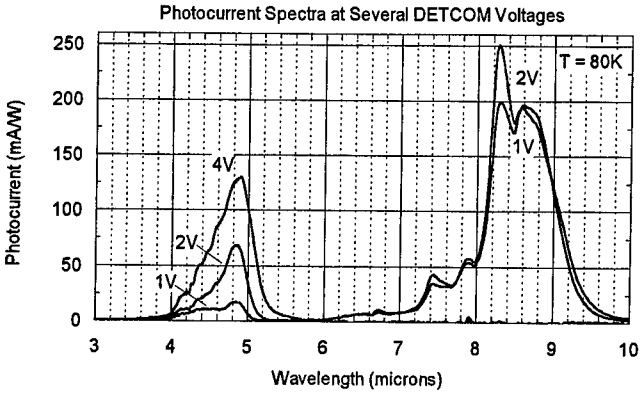


Figure 3. Spectral Response of L-M MWIR and LWIR Material

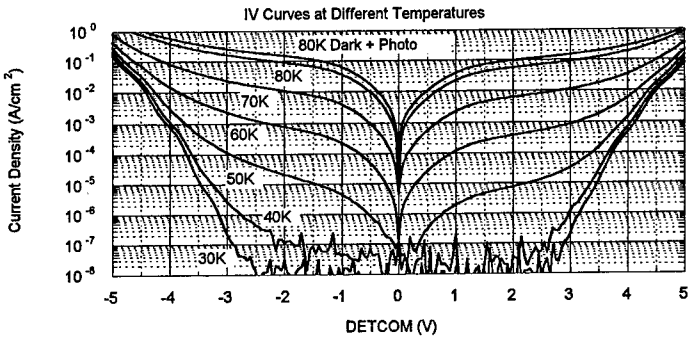


Figure 4. Current vs Bias Voltage for L-M Two-Color LWIR FPA

In addition to two-color QWIP pixel arrays, L-M has also designed and built read-out integrated circuits (ROICs) optimized for QWIP FPAs. The ROICs take advantage of QWIP's relatively high bias voltage (1-3 volts) and high detector impedance (R_0A>50,000 Ω–cm^2) to permit simple direct injection (DI). The DI ROIC frees real estate for separate charge collection, and isolates signal processing and signal transfer circuitry in each unit cell for both colors. The ROIC allows simultaneous integration of both colors, and can perform on-FPA windowing and image reversal. It has selectable gain charge wells in each unit cell and variable integration time for maximum sensitivity and high dynamic range. The responsivity of each spectral band can be controlled separately by varying its detector bias. It has a 100 Hz frame rate and consumes less than 70 mW of power.

In single-color QWIPs, the gratings required to couple infrared light into the wells are designed to have maximum coupling at the peak wavelength of the QWIP. This becomes a problem with multicolor arrays due to the difficulty of producing dual peak response gratings. L-M uses a two-dimensional waffle pattern grating, consisting of repeated rectangles with each dimension of the rectangles corresponding to one of the colors of the FPA. Best results were obtained when the arrays were oriented at 45° with respect to the pixel sides.

Grating-coupled relative spectral response for the two-color LWIR FPA is shown in figure 5. The conditions for this data were T=40K, system f/2, background T=300K, frame rate=30 Hz, integration time=10 ms. Noise equivalent differential temperature (NEDT), operating in the simultaneous integration mode, was 16 mK and 23 mK for the 8.6 μm and 11.2 μm bands, respectively. The FPA has 6.9% cross coupling due to the 11.2 μm detection of 8.6 μm light. This caused by the 11.2 μm QW material's responsivity at 8.6 μm, with gradual response roll-off (tail) at the lower wavelengths characteristic of the BQB design. The cross coupling will be reduced in future designs.

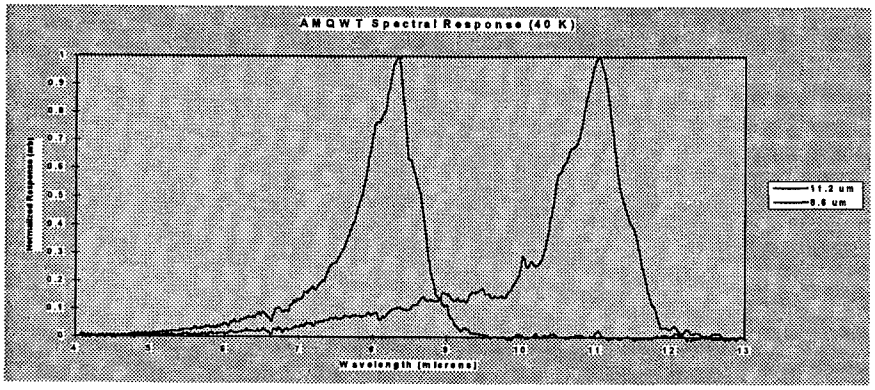


Figure 5. Relative Spectral Response of L-M Two-Color LWIR FPA

Two LWIR/LWIR FPAs were built by L-M. The uncompensated uniformity of both was above 88%. The operability of the first FPA was 98.92% for the 8.6 μm band, and 99.95% for the 11.2 μm band. For the second FPA, the corresponding operability was 97.58% and 98.21%. These are good values for a first attempt and should improve with future builds. Preliminary tests on MWIR/LWIR FPAs built by L-M, operating at 55K, showed NEDT of 27 mK and 43 mK for the 4.7 μm and 8.6 μm bands respectively. The 43 mK was higher than expected and was attributed to camera electronics noise. Operability of the MWIR/LWIR FPA was 99.78% and 98.87% respectively. This is expected to improve in future builds to greater than 99.95%, experienced by L-M in building 640x480 LWIR QWIP FPAs.

2.2 Jet Propulsion Lab QWIPs (2)

JPL has produced an optimized, simultaneous two color 640x243, LWIR/VLWIR QWIP FPA by making even rows detect LWIR and odd rows detect in a 640x486 format. The device consists of a 30 period stack of VLWIR QWIP structure and a second 18-period stack of LWIR QWIP structure separated by a heavily doped 0.5 μm thick intermediate GaAs contact layer. An advantage of this FPA is that it allows optimized gratings for both wavelengths. Disadvantages are that its spatial registration is not as good as for stacked arrays and the single pixel readout does not allow full fill factor.

The VLWIR stack was designed to have a bound-to-quasibound intersubband absorption peak at 14.5 μm, since the dark current of this stack dominates the LWIR portion. The LWIR stack has a bound-to-continuum intersubband absorption peak at 8.5 μm, because its photocurrent plus dark current are relatively small compared to the VLWIR portion of the device. The entire dual band structure was sandwiched between 0.5 μm GaAs n-doped contact layers. To obtain approximately equal total currents from the LWIR and WLWIR MQW stacks, the total current (dark current + photocurrent) of each stack was independently controlled in the design of the position of the upper state, well doping densities, and the number of periods in each MQW stack.

JPL's LWIR/VLWIR dualband QWIP was processed into an interlaced-readable dualband FPA with odd rows for one color and the even rows for the other. It was mated to a currently available single-color 640x486 CMOS readout multiplexer. This achieved simultaneous two-color data containing two readout cells per detector unit cell readout without a special dualband readout multiplexer. The disadvantage of less than full fill factor for both wavelength bands can be eliminated by fabricating (n+1) terminals (e.g., three terminals for dualband) per pixel and hybridizing with a multicolor readout having n readout cells per detector pitch, where n is the number of bands.

Test detectors were back illuminated through a 45° polished facet. The dark current and responsivity measured is shown in figures 6, 7, and 8. The responsivity of the LWIR detector peaks at 8.4 μm and its peak responsivity (R_p) is 509 mA/W at bias V_B = -2 V. The spectral width and the cutoff wavelength of the LWIR detector is $\Delta\lambda/\lambda$ = 16% and λ_c = 9.1 μm respectively. The responsivity of the VLWIR detector peaks at 14.4 μm and its R_p is 382 mA/W at a bias of V_B = -2.0 V. The spectral width and the cutoff wavelength of the VLWIR detector are $\Delta\lambda/\lambda$ = 10% and λ_c = 15 μm respectively. The measured absolute peak responsivities of both LWIR and VLWIR detectors are small, up to about V_B = -0.5 V. Beyond that, they increases almost linearly with bias, reaching R_P = 0.3 A/W (at V_B = -2V) and 1 A/W (at V_B = -3V) respectively. The peak quantum efficiency of the LWIR and VLWIR detectors were 6.4% and 11.6% respectively at operating bias V_B=-2 V indicated in figure 8 for a 45° double pass.

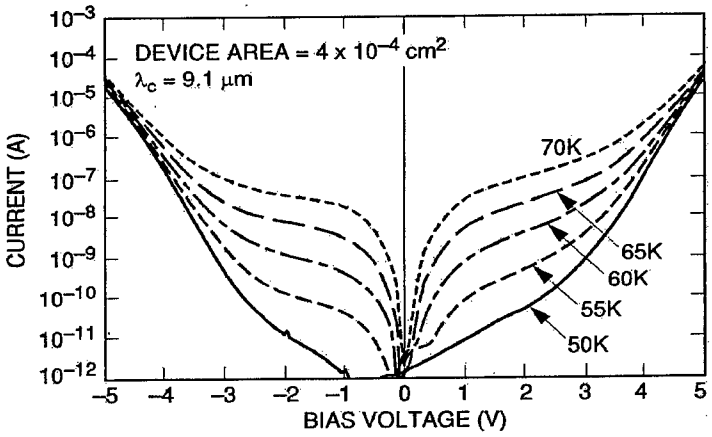


Figure 6. Dark current vs. voltage of JPL LWIR detector. Device area is $4x10^{-4}$ cm^2.

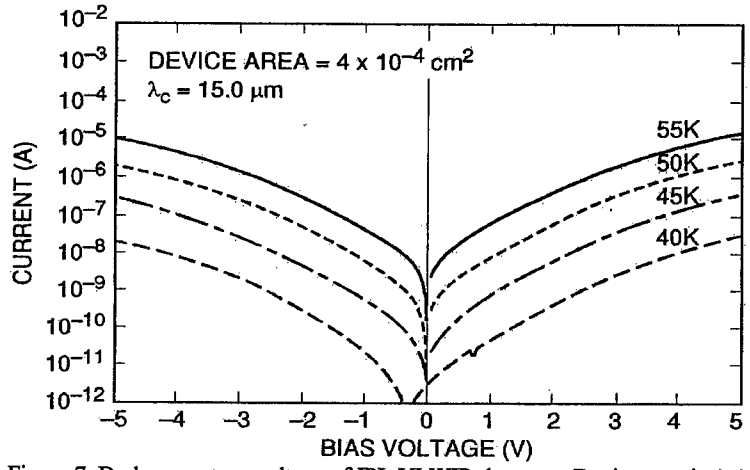


Figure 7. Dark current vs. voltage of JPL VLWIR detector. Device area is $4x10^{-4}$ cm^2.

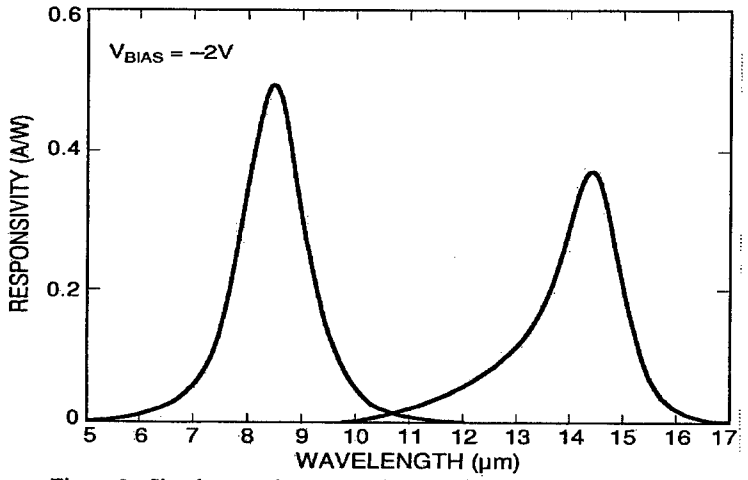


Figure 8. Simultaneously measured responsivity of JPL dualband QWIP

Two different 2-D periodic gratings were designed to independently couple the 8-9 and 14-15 μm radiation into detector pixels in even and odd rows of the FPAs. The top 0.7 μm thick GaAs cap layer was used to fabricate the light coupling 2-D periodic gratings for 8-9 μm detector pixels. The light coupling 2-D periodic gratings of the 14-15 μm detector pixels were fabricated through the photosensitive LWIR MQW layers. The total thickness of 8-9 μm detector is limited by the grating layer thickness of the VLWIR detector.

JPL dualband FPAs were tested at a background temperature of 300 K, with f/2 cold stop, and at 30 Hz frame rate. The measured quantum efficiency of the FPA at an operating temperature of T = 40 K, bias V_B = -2 V for 300 K background was 12.9%.

This measured value is the integrated FPA quantum efficiency including the 30% substrate reflection and 85% (each color) FPA fill factor. It is a factor of 2.1 higher than the double pass quantum efficiency, which agrees with the typical 2-D periodic grating light coupling efficiencies seen in other experiments. The uncorrected non-uniformity (sigma/mean) of the quantum efficiency histogram is 2%. The mean quantum efficiency of 14-15 μm detector pixels in the FPA is 8.9%, and the uncorrected quantum efficiency non-uniformity is about 1%. This mean FPA quantum efficiency value is a factor of 1.3 lower than the 45° test detector quantum efficiency, indicating that the 2-D periodic grating light coupling is very effective in the LWIR region compared to VLWIR region.

III. SUMMARY AND CONCLUSIONS

BMDO sponsors programs in development of simultaneous multicolor QWIPs and other detectors to meet the need for multicolor FPAs in advanced BMD missions. Although no BMDO systems currently use QWIPs, their potential for sensitive, high format, very uniform, low cost multicolor IR FPAs has promoted BMDO to make technology investments in QWIPs over the past four years for advanced missions where simultaneous measurements in two to four spectral bands are beneficial. These missions include surveillance, tracking and discrimination. Accurate target temperature estimation is one area in which two- to four-color simultaneous measurements are essential. BMDO's experience in developing multicolor detectors indicates that it is easier to produce good quality multicolor QWIP FPAs than with other materials, especially at VLWIR wavelengths needed for temperature estimation in the presence of earthshine. Simultaneous two color QWIP FPAs have been produced and tested by L-M and JPL for BMDO, and both are now ready to begin development of three-color devices. The two-color QWIPs show good performance for first efforts, and improvements are expected in the future.

ACKNOWLEDGEMENTS

The author is grateful to Dr. Meimei Tidrow, Dr. Paul Le Van, Dr. Richard Spitzberg, and Mr. Jim Kiessling for their helpful comments and suggestions in the preparation of this paper.

REFERENCES

1. G.L. Milne, K.B. Reiff, M.E. West, "Lockheed Martin Multi-Spectral Quantum Well Focal Plane Arrays", 1998.
2. S. D. Gunapala, S. V. Bandara, A. Singh, J. K. Liu, S. B. Rafol, E. M. Luong, J. M. Mumolo, N. Q. Tran, J. D. Vincent, C. A. Shott, J. Long, and P. D. LeVan, "8-9 and 14-15 μm Two-color 640x486 GaAs/AlGaAs Quantum Well Infrared Photodetector (QWIP) Focal Plane Array Camera", 1998
3. Spitzberg, R.M. "Parameter Estimation for Gray and Nongray Targets: Theory and Data Analyses", Optical Engineering, July 1994.

QUANTUM WELL INFRARED PHOTODETECTORS WITH DIGITAL GRADED SUPERLATTICE BARRIER FOR LONG WAVELENGTH AND BROADBAND DETECTION

Jung-Hee Lee[a], Sheng S. Li[a], M. Z. Tidrow[b], W. K. Liu[c], and K. Bacher[c]

[a] University of Florida, Gainesville, FL
[b] Army Research Laboratory, Adelphi, MD
[c] Quantum Epitaxial Designs Inc., PA

ABSTRACT

In this paper we report two high performance quantum well infrared photodetectors (QWIPs) using digital graded superlattice barriers for long wavelength infrared (LWIR) and broadband infrared detection. The compositionally digital graded superlattice barriers (DGSLB-) of the QWIP structures were grown using digital superlattices to form a stepwise linear composition grade barrier without adjustment of the source temperature and the AlGaAs composition. The digital superlattices used five repeats of a 20 Å period for each of the five composition steps for a total thickness of 500 Å. The graded barrier layer from GaAs to $Al_{0.09}Ga_{0.91}As$ was achieved by using the GaAs and $Al_{0.15}Ga_{0.85}As$ as the constituent layer, with target Al mole fractions of x = 0.018, 0.036, 0.054, 0.072, and 0.09 for the stepwise linear graded barrier layer. The results reveal that due to the graded barrier structure, both QWIP devices show highly asymmetrical dark I-V and photo-response characteristics under positive and negative bias conditions. In the first DGSLB-QWIP, a broadband photo-response from 7 to 16 μm was obtained under positive bias condition while a normal spectral response with peak wavelength at 11 μm was obtained under negative biases. We have also studied a double-barrier (DB) DGSLB-QWIP by adding a thin (20Å) undoped $Al_{0.15}Ga_{0.85}As$ double- barrier around the InGaAs quantum well for the confinement of electron wave functions. Normal spectral response with peak wavelength at 12 μm was obtained in this device under both positive and negative bias conditions, while a very large responsivity (3 A/W at +1V and 35 K) was obtained under positive bias condition.

Key Words

quantum well infrared photodetectors (QWIPs), digital graded superlattice barrier (DGSLB), broadband (BB), double barrier (DB), LWIR, spectral responsivity, detectivity

1. INTRODUCTION

Quantum well infrared photodetectors (QWIPs) have been widely investigated for the mid-wavelength infrared (MWIR) and long-wavelength infrared (LWIR) as well as for

multi-color or broadband infrared detection in recent years.[1-3] The multi-stack structure is usually employed to obtain multi-color detection in the MWIR and LWIR atmospheric spectral bands.[2,3] Voltage tunable QWIPs with asymmetrical double- or triple- coupled quantum well structures have also been reported for multi-color infrared detection by using the quantum confined Stark effect.[4-6] The broadband infrared detection has been achieved by using a wide variety of device structures with variable well width and barrier height in the quantum well.[7-14] Levine *et al.* have reported a voltage tunable LWIR QWIP using graded barrier quantum wells to achieve large shifts in the peak detection wavelength, spectral line-width, and cutoff wavelength.[14] Duboz *et al.* have studied the effect of asymmetrical barriers on the performance of GaAs/AlGaAs QWIPs.[15] In this paper we report two novel high performance InGaAs/AlGaAs/GaAs QWIPs using digital graded superlattice barriers (DGSLB) to achieve the linear- graded band gap (or linear graded composition) across the barrier region of the QWIP. The new structures enable the broadband detection and significantly improve the responsivity under positive bias operation. This band gap engineering approach has been widely used in III-V optoelectronic devices for band gap variation and for enhancing device performance.[16-17]

2. DEVICE DESIGN AND FABRICATION

In this work, two novel InGaAs/GaAs/AlGaAs QWIP structures using digital graded superlattice barriers (DGSLB) (see Figs. 1 and 2) were grown on the semi-insulating GaAs substrates by using molecular beam epitaxy (MBE) technique. The first QWIP structure (see Fig. 1) uses the InGaAs quantum well and digital graded GaAs/AlGaAs superlattice barriers to form the DGSLB-QWIP device. The second DGSLB-QWIP structure (Fig. 2) adds a thin undoped AlGaAs double barrier on both sides of the InGaAs quantum well for electron wave function confinement. The DGSLB structure was used to achieve the linear-graded barrier (i.e., linearly graded- band gap or graded composition barrier) in these devices. The standard MBE growth of the graded layer structure usually requires pausing the growth to change and stabilize the source temperature for the desired composition profile. As a result, it requires a longer growth time and may lead to more oxygen to be incorporated into the graded layer during the growth interruption. The compositionally digital graded superlattice barriers (DGSLB) of the QWIP structures were grown using digital superlattices, which enable a stepwise linear composition grade to be formed without adjustment of the source temperature and the AlGaAs composition (i.e., using a fixed (15%) Al composition). The DGSLB structure can be obtained by using short-period superlattice structures with variable barrier/well thickness to change the Al mole fraction ratio and hence the energy band gap of the graded barrier. Adjusting the duty cycle can change the barrier/well thickness for each superlattice unit cell (5 periods, 2 nm thick). Therefore, using the DGSLB structure without changing the source temperature setting greatly simplifies the growth procedure and yields excellent wafer quality. The DGSLB layers were formed by using five superlattice unit cells in series in which the thin $GaAs/Al_{0.15}Ga_{0.85}As$ layers with a 20 Å period were repeated 5 times for each superlattice unit cell. The device structure for the broadband (BB-) DGSLB-QWIP consists of a 50 Å $In_{0.2}Ga_{0.8}As$ quantum well (Si doped to 7×10^{17} cm^{-3}) and a 500 Å $GaAs/Al_{0.15}Ga_{0.85}As$ DGSLB layer. Each superlattice unit cell in the DGSLB-layer has the combination of different barrier/well thicknesses (2.4/17.6, 4.8/15.2, 7.2/12.8, 9.6/10.4, and 12/8 Å) to obtain the target Al mole fractions of x = 0.018, 0.036, 0.054, 0.072, and 0.09 from the substrate side for the stepwise linear graded barrier layer. In the

double barrier (DB-) DGSLB- QWIP, a thin (20 Å) undoped $Al_{0.15}Ga_{0.85}As$ double barrier was grown between the DGSLB layers and the 88 Å $In_{0.2}Ga_{0.8}As$ quantum well (Si doped to 7 x 10^{17} cm^{-3}) to confine the electron wave functions and to create a resonant state (E_2) with the graded superlattice barrier. The DGSLB layer is composed of five 100 Å thick superlattice layer each with 5 periods of superlattices with (barrier/well) thicknesses of 1.6/18.4, 3.2/16.8, 4.8/15.2, 6.4/13.6, and 8/12 Å for the target Al mole fractions of x = 0.012, 0.024, 0.036, 0.048, and 0.06 in the $Al_xGa_{1-x}As$ graded barrier layer. The 5000 Å contact layers (Si doped to 2 x 10^{18} cm^{-3}) were grown at a substrate temperature of 600 °C, while the rest of the structure was grown at 510 °C to avoid indium (In) desorption from the InGaAs layers.

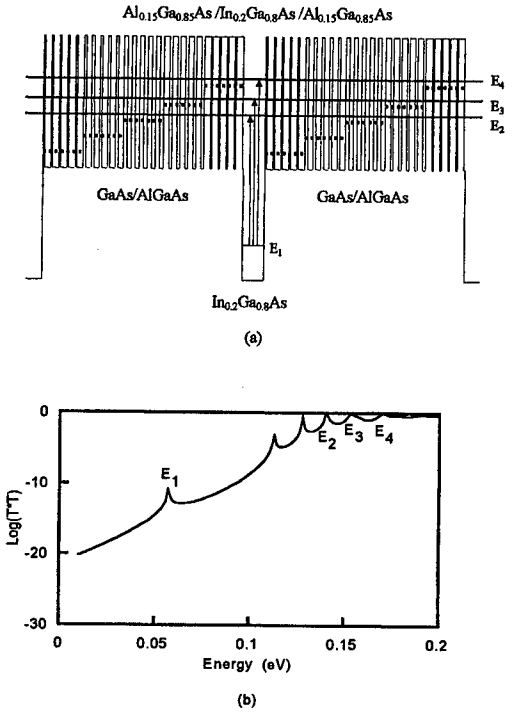


Figure 1 (a) The schematic conduction band diagram and (b) the calculated transmission coefficient versus energy at zero bias for the broadband (BB) DGSLB-QWIP.

Figure 1(a) and (b) show the schematic conduction-band diagram and the calculated transmission coefficient versus energy at zero bias using the multi-layer transfer matrix method (TMM)[18] for the broadband (BB-) DGSLB-QWIP, respectively. The dotted lines denote the effective barrier height for each superlattice unit cell (5 periods, 20 Å/period) in the DGSLB. In this calculation, the strain effect due to lattice- mismatch between the InGaAs QW and the GaAs/AlGaAs barrier and the exchange energy due to the electron-electron interaction were considered. The E_1-E_2, E_1-E_3, and E_1-E_4 transitions contribute to

the broadband detection under positive bias condition, while only transitions from the E_1 to E_4 states were observed under negative bias because the photo-generated carriers need to surmount the abrupt side of the barrier layers. Under positive bias condition, the effective barrier will decrease gradually with increasing bias to the lowest superlattice barrier height and then the bound states aligned by the DGSLB at zero bias will be the pseudo-continuum states over the DGSLB. Thus, the broadband response can be achieved by the bound-to- pseudo-continuum (BTPC) state transitions under positive bias condition. On the contrary, the effective barrier height for the photo-excited electron transport will be at its maximum under negative bias condition and the slope of the DGSLB will be much steeper than under positive biases. Thus, the capture probability of the photo-excited electrons due to the bound-to-bound (BTB) transitions will be increased and normal spectral response is expected under negative bias condition.

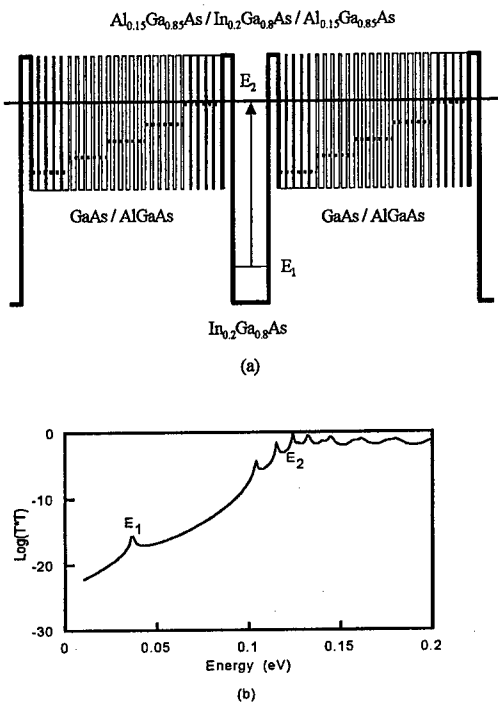


Figure 2 (a) The schematic conduction-band diagram and (b) the calculated transmission coefficient versus energy at zero bias for the double barrier (DB) DGSLB-QWIP.

Figure 2(a) and (b) show the schematic conduction-band diagram and the calculated transmission coefficient versus energy at zero bias for the double barrier (DB) DGSLB-QWIP device. The broadband response was not observed in this device because of the wave function for the peak wavelength detection is strongly confined by the thin $Al_{0.15}Ga_{0.85}As$ double-barrier and resonantly coupled to the wave functions of the E_2 state in the DGSLB region. Thus, normal spectral response with identical peak detection

wavelength (at 12 μm) due to the E_1 to E_2 state transitions was obtained under both negative and positive biases for this device.

In order to characterize the device performance, test mesa structures with active area of 216x216 μm^2 were fabricated by using standard photolithography and wet chemical etching procedure. The AuGe/Ag/Au film was deposited by E-beam evaporation on the top and periphery of the mesa structure for ohmic contacts and annealed at 450 °C for 2 minutes. The test devices were polished to 45° facet on the GaAs substrates for back illumination. The devices were mounted on TO-8 can for dark I-V and photoresponse measurements.

3. RESULTS AND DISCUSSION

We have performed the dark current-voltage (I-V) and spectral response measurements on both DGSLB-QWIPs under negative and positive bias conditions. Excellent results were obtained in the photoresponse measurements on these devices. A very broadband photo-response (λ_p = 7 ~ 16 μm) under positive bias condition and a normal spectral response with voltage tunable peak wavelength under negative bias condition were obtained for the BB- DGSLB-QWIP device. Normal spectral response was observed in the DB- DGSLB-QWIP with peak detection wavelength at 12 μm. Due to the asymmetrical graded barrier structure, a very large responsivity (R_i = 3 A/W at 12 μm, 1V and 35K) was obtained in this device under positive bias condition. Results of the dark current and spectral photoresponse measurements on both devices are discussed next.

3.1 DARK I-V CHARACTERISTICS

Figure 3(a) and (b) show the dark current density as a function of applied bias voltage for the BB- and DB- DGSLB QWIPs measured at different temperatures (T = 35, 50, 60, and 77K), respectively. The 300K background window currents with a field of view (FOV) of 180° were also given in Fig. 3(a) and 3(b).

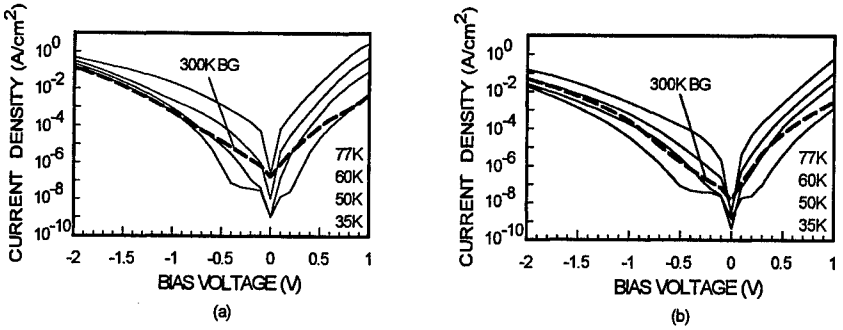


Figure 3 The dark current density versus bias voltage for (a) the BB- DGSLB QWIP and (b) the DB- DGSLB QWIP. The dashed line is the 300 K background photocurrent.

As expected in the asymmetrical quantum well structure, the dark currents and photoresponse are also highly asymmetrical under positive and negative bias conditions, which is attributed to the different effective barrier profiles under negative and positive biases, as explained previously. In both devices we have observed a much higher dark current and photo-response under positive bias condition. This is due to the barrier lowering of the DGSLB and the electron launching under positive bias condition. The BB- DGSLB QWIP device is under background limited performance (BLIP) between –1V and +0.75V at T = 35K and the BLIP temperature was 55K while the DB- DGSLB-QWIP is under BLIP between –2V and +0.35V at T =50K.

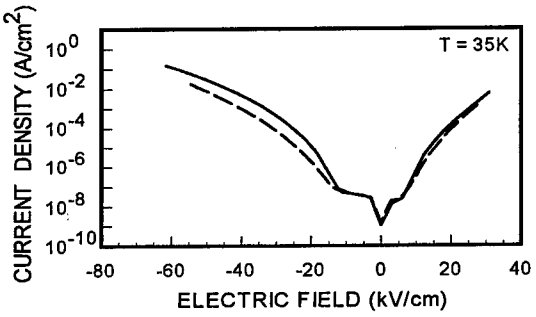


Figure 4 A comparison of the dark current density versus the electric field for the BB- DGSLB-QWIP (solid line) and the DB- DGSLB QWIP (dashed line).

Figure 4 shows a comparison of the dark current density as a function of the electric field at T = 35K for these two QWIP devices. Although the DB- DGSLB-QWIP exhibits a longer peak wavelength (12 μm peak) than the BB- DGSLB-QWIP (11 μm peak) under negative biases, the dark current density of the DB- DGSLB-QWIP is slightly lower than that of the BB- DGSLB-QWIP due to the use of a thin undoped $Al_{0.15}Ga_{0.85}As$ double-barrier around the InGaAs quantum well which tends to reduce the carrier transport probability under dark condition.

3.2 Spectral Responsivity and Detectivity

The spectral response was measured at T = 35K for both DGSLB-QWIPs by using a 1/8 monochromater, a calibrated blackbody IR source (T = 1273K), and a closed cycle liquid helium cryostat at 200 Hz chopped frequency. The spectral responsivity can be calculated by

$$R_i = \frac{I_p}{P_{in}}, \tag{1}$$

where I_p is the photocurrent output (A), and P_{in} is the input IR radiation power (W), which can be expressed as

$$I_p = \frac{V_p}{R_f}, \tag{2}$$

$$P_{in} = A_d H_{in}, \tag{3}$$

where V_p is the photovoltage of the photodetector, R_f is the gain of the transimpedance amplifier (TIA), A_d is the photodetector area (cm^2), and H_{in} is the input irradiance (W/cm^2), which is given by

$$H_{in} = \frac{V_{pyro} T_w T_d}{R_p A_p}, \tag{4}$$

where V_{pyro} is the photovoltage of the pyroelectric detector, T_w is the transmissivity of the entrance window of the cryogenic system, T_d is the transmissivity of the photodetector, R_p is the responsivity of the pyroelectric detector (V/W), and A_p is the active area of the pyroelectric detector (cm^2), respectively. The pyroelectric detector is used to calibrate the input power of the infrared radiation from the blackbody IR source onto the photodetector.

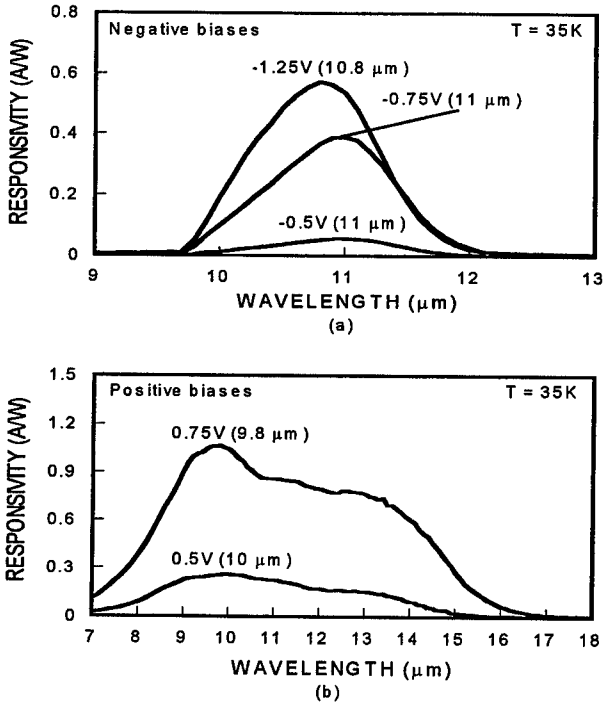


Figure 5 The spectral responsivity of the BB- DGSLB QWIP device at T = 35K: (a) at negative bias and (b) at positive bias condition.

Figure 5(a) and (b) show the spectral responsivity of the BB- DGSLB-QWIP at T= 35K under (a) negative and (b) positive bias conditions. The peak wavelength was blue-shifted from 11 μm to 10.8 μm between –0.75V and –1.25V under negative bias condition. The absolute responsivity increases with the applied bias due to the increase in photoconductive gain with increasing bias. The peak responsivities at λ_p = 10.8 μm and 9.8 μm were found to be 0.57 A/W and 1.07 A/W at V_b = -1.25V and +0.75V, respectively. It is noted that a very broad spectral bandwidth was obtained under positive bias condition in this device. The full-width half-maximum (FWHM) spectral bandwidth of this device at V_b = -1.25V was found to be $\Delta\lambda/\lambda_p$ = 13 % while FWHM spectral bandwidths at V_b = +0.75V and +0.5V were found to be $\Delta\lambda/\lambda_p$ = 62 % and 54%, respectively. This broadband detection feature was attributed to the formation of pseudo-continuum states by the overlapping of E_2, E_3, and E_4 wave functions, which enables the broadband detection from the E_1 to the E_2, E_3, and E_4 states under positive bias condition.

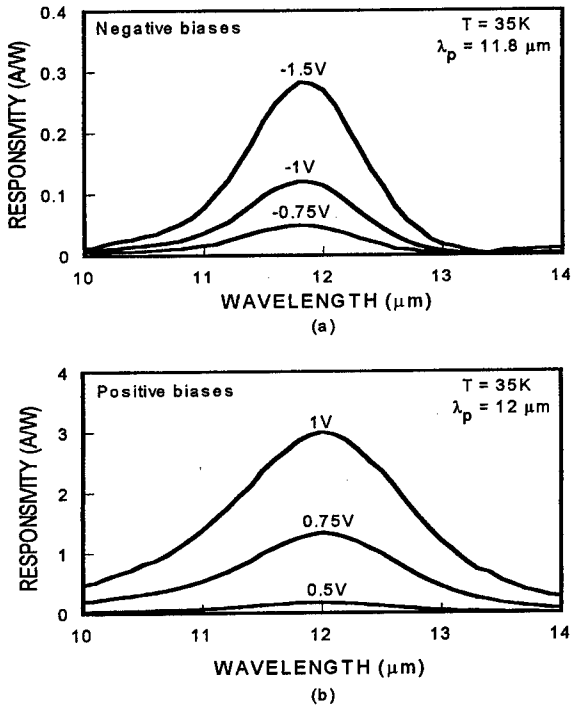


Figure 6 The spectral responsivity of the DB- DGSLB QWIP at T = 35K: (a) at negative and (b) at positive bias condition.

Figure 6(a) and (b) show the spectral responsivity of the DB- DGSLB-QWIP at T= 35K under (a) negative and (b) positive bias conditions. The maximum peak responsivity at λ_p = 11.8 μm was found to be 0.28 A/W at V_b = -1.5V and T = 35K. However, the spectral responsivity was dramatically increased under positive bias condition due to the graded barrier lowering and electron launching effect. The peak responsivity at V_b = +1V was 3 A/W at λ_p = 12 μm and T = 35K. The FWHM spectral bandwidth at V_b = -1.5V and +1V were $\Delta\lambda/\lambda_p$ = 11 % and 17%, respectively. A slightly broader spectral bandwidth detection was obtained under positive bias condition. The peak detection wavelength for this device was attributed to the E_1-E_2 state transitions.

The detectivity of both QWIPs was calculated from the results of the responsivity and dark current measurements. Under background limited performance (BLIP) condition, it is well known that the BLIP detectivity is independent of the photoconductive gain and dark current, and it can be expressed as

$$D^*_{BLIP} = \frac{\lambda}{2hc}\left(\frac{\eta g}{Q_b}\right), \tag{5}$$

where λ is the wavelength; h is the Plank constant; c is the velocity of light; ηg is the product of the quantum efficiency (η) and the photoconductive gain (g), and can be deduced from the measured spectral responsivity; Q_b is the incident photon flux density from the background for a given spectral bandwidth at peak wavelength, which can be calculated from

$$Q_b = \int_0^{\lambda_c} \frac{2\pi c}{\lambda^4} \frac{1}{e^{hc/\lambda kT_b} - 1} d\lambda, \tag{6}$$

where λ_c is the cutoff wavelength, k is the Boltzmann constant, and T_b is the background temperature. In the first DGSLB-QWIP, the BLIP detectivity (D^*_{BLIP}) at V_b = -0.75V and 0.75V were found to be 7.2 x 10^9 cm $Hz^{1/2}$/W at λ_p = 11 μm and 1.3 x 10^{10} cm $Hz^{1/2}$/W at λ_p = 9.8 μm, respectively. The BLIP detectivity (D^*_{BLIP}) at V_b = -1.5V and +1V for the DB DGSLB-QWIP were found to be 5.8 x 10^9 cm $Hz^{1/2}$/W at λ_p = 11.8 μm and 1.9 x 10^{10} cm $Hz^{1/2}$/W at λ_p = 12 μm, respectively.

4. CONCLUSIONS

In this paper, we have demonstrated a novel broadband (BB-) InGaAs/AlGaAs/GaAs quantum well infrared photodetector using digital graded superlattice barrier (BB-DGSLB QWIP) and a double-barrier (DB) InGaAs/AlGaAs/GaAs/AlGaAs DB- DGSLB-QWIP for long-wavelength infrared (LWIR) and broadband detection. For the BB-DGSLB QWIP, the peak responsivity at λ_p = 9.8 μm was found to be 1.07 A/W at V_b = +0.75V and T = 35K, with a corresponding BLIP detectivity (D^*_{BLIP}) of 1.3 x 10^{10} cm $Hz^{1/2}$/W. A very broad spectral response bandwidth covering the wavelength from 7 μm to 16 μm was obtained under positive bias condition in this device. The full-width half-maximum (FWHM) spectral bandwidth at V_b = +0.75V and +0.5V were found to be

$\Delta\lambda/\lambda_p$ = 62 % and 54%, respectively, for this device. As for the DB- DGSLB QWIP device, a very large spectral responsivity and BLIP detectivity (D^*_{BLIP}) (i.e., R_i = 3 A/W and D^*_{BLIP} = 1.9 x 10^{10} cm $Hz^{1/2}$/W) were obtained at V_b = +1V and λ_p = 12 μm. The dark current density of the DB- DGSLB-QWIP was found to be slightly lower than that of the BB- DGSLB- QWIP due to the use of a thin undoped $Al_{0.15}Ga_{0.85}As$ double-barrier around the InGaAs quantum well in this device. Excellent device performance was obtained for both QWIPs, which was attributed to the use of digital graded superlattice barriers (DGSLB) to form the linear-graded barrier layer in both device structures, enabling these DGSLB QWIPs to achieve broadband detection, high peak responsivity and wavelength tunability by the applied bias.

ACKNOWLEDGEMENT

This work was partially supported by BMDO/TO (ARL) and by U.S. Army Research Office (UF) under grant No. DAAG55-98-1-0325.

REFERENCES

1. B. F. Levine, *J. Appl. Phys.*, **74,** R1, (1993).
2. J. C. Chiang, Sheng S. Li, and A. Singh, *Appl. Phys. Lett.*, **71**(24), pp. 3546-3548, 14 October, (1996).
3. M. Z. Tidrow, Xudong Jiang, Sheng S. Li, and K. Bacher, *Appl. Phys. Lett.*, **74**(9), pp. 1335-1337, 1 March, (1999).
4. Jung-Chi Chiang, Sheng S. Li, M. Z. Tidrow, P. Ho, M. Tsai, and C. P. Lee, *Appl. Phys. Lett.*, **69**(16), pp. 2412-2414, 14 October, (1996).
5. H. Schneider, K. Kheng, M. Ramsteiner, J. D. Ralston, F. Fuchs, and P. Koidl, *Appl. Phys. Lett.*, **60**(12), pp. 1471-1473, 23 March, (1992).
6. A. Brandel, A. Fraenkel, E. Finkman, G. Bahir, G. Livescu, and M. T. Asom, *Semicond. Sci. Technol.*, **8**, S412-S416, (1993).
7. Sheng S. Li, J. Chu, J. C. Chiang, J. H. Lee, and A. Singh, *Proc. of SPIE,* **vol. 3629**, pp. 138-146, (1999).
8. J. Chu, Sheng S. Li, and A Singh, *IEEE J. of Quantum Electronics*, **vol. 35**(3), pp. 312-319, March 1, (1999).
9. J. Chu, Sheng S. Li, and A Singh, *Appl. Phys. Lett.*, **73**(23), pp. 3414-3416, 7 December, (1998).
10. S. V. Bandara, S. D. Gunapala, J. K. Liu, E. M. Luong, J. M. Mumolo, W. Hong, D. K. Sengupta, and M. J. Mckelvey, *Appl. Phys. Lett.*, **72**(19), pp. 2427-2429, 11 May, (1998).
11. L. C. Lenchyshyn, H. C. Liu, M. Buchanan, and Z. R. Wasilewski, *J. Appl. Phys.*, **79**(6), 15 March, (1996).
12. B. F. Levine, G. Hasnain, C. G. Bethea, and Naresh Chand, *Appl. Phys. Lett.*, **54**(26), pp. 2704-2706, 26 June, (1989).
13. Y. Zhang, N. Baruch and W. I. Wang, *Eletronics letters*, **vol. 29**(2), pp. 213-214, 21 January, (1993).
14. B. F. Levine, C. G. Bethea, V. O. Shen, and R. J. Malik, *Appl. Phys. Lett.*, **57**(4), pp. 383-385, 23 July, (1990).

15. J. Y. Duboz, L. Saminadayar, and J. M. Gerard, *J. Appl. Phys.*, **78**(4), 15 August, (1995).
16. Wei Gao, Paul R. Berger, George J. Zydzik, Henry M. O'Bryan, Deborah L. Sivco, and Alfred Y. Cho, *IEEE Transaction of Electronic Devices*, **vol. 44**(12), pp. 2174-2179, December 12, (1997).
17. D. H. Lee, Sheng S. Li, N. J. Sauer, and T. Y. Chang, *Appl. Phys. Lett.*, **54**(19), pp. 1863-1865, 8 May, (1989).
18. A. K. Ghatak, K. Thyagarajan, and M. R. Shenoy, *IEEE J. of Quantum Electronics*, **vol. 24**, pp. 1524-1531, March 1, (1988).

VERY-LONG-WAVELENGTH QUANTUM WELL INFRARED PHOTODETECTORS

Meimei Z. Tidrow[a], Xudong Jiang[b], Sheng S. Li[b], Junhee Moon[b] and W. K. Liu[c]

[a] U.S. Army Research Laboratory, Adelphi, MD 20783-1197
[b] University of Florida, Gainesville, FL 32611
[c] Quantum Epitaxial Designs, Inc., Bethelehem, PA 18015

ABSTRACT

In this paper we report recent developments of quantum well infrared photodetector (QWIPs) for very long wavelength infrared (VLWIR) applications. The previous work on VLWIR QWIPs is reviewed. Specific issues concerning device physics, such as the influence of doping density, temperature, and detector structure on the peak detection wavelength, detectivity, dark current, and dynamic resistance of the VLWIR QWIP are discussed. Issues concerning detector design and device performance of the VLWIR QWIP are also addressed. Finally, a VLWIR QWIP has been designed, fabricated and characterized. The structure of this detector consists of 20 repeats of a 80 Å $In_{0.04}Ga_{0.96}As$ quantum well with doping density of 2×10^{17} cm^{-3} and a 500 Å $Al_{0.09}Ga_{0.91}As$ barrier. The detection peak wavelength is at 14.7 μm, while the cut-on and cut-off wavelengths are at 12.7 and 16.3 μm, respectively, at 2 V bias and 40 K.

Key Words

Quantum well infrared photodetectors (QWIPs), very long wavelength infrared (VLWIR) detection, spectral responsivity, multi-color QWIPs.

1. INTRODUCTION

Intersubband transitions in III-V semiconductor heterostructures have been widely investigated for quantum well infrared photodetectors (QWIPs) applications [1]. Due to its material growth maturity, large array uniformity and detection wavelength flexibility, high performance and large format (640×480) GaAs/AlGaAs QWIP focal plane arrays (FPAs) have been successfully demonstrated, which challenge other infrared detector systems such as HgCdTe, PtSi, InSb, and Si:Ge for the mid-wavelength infrared (MWIR) and long-wavelength infrared (LWIR) detection. Most of the QWIP research works have been focused on the spectral regions of MWIR (3-5 μm) and LWIR (8-12 μm) bands during the past decade. Various QWIP structures have been developed to meet different application requirements. In addition, several light-coupling and grating techniques have

been developed to increase the absorption quantum efficiency of QWIPs in the mid- and long- wavelength infrared atmospheric spectral windows [2, 3].

In this paper, we will emphasize on the very long wavelength IR (VLWIR) detectors. The VLWIR detectors are of great interest for many applications such as measuring vertical temperature profiles of the atmosphere, studying the composition, structure, and the energy balance of molecular clouds and stars. It is especially important in strategic and space applications to detect far away targets with a cold background. These applications have placed stringent requirements on the performance of IR detectors and arrays such as high detectivity, low dark current, high uniformity, radiation hardness, and low power dissipation. The current state of the art HgCdTe (MCT) based IR detectors have not met all these requirements, and QWIPs provide a useful alternative for VLWIR applications.

Recent works on the VLWIR QWIPs fabricated from GaAs/AlGaAs material systems have been reported by several researchers with peak detection wavelengths ranging from 15 μm to 26.9 μm [4,5,6,7,8,9]. Table I summarizes the key device parameters, peak detection wavelengths, and detectivity of these QWIPs.

Table I Main results of works on VLWIR QWIPs reported in the literature.

Ref	Well width	Barrier thickness	$N_D(cm^{-3})$	$\lambda_p(\mu m)$	$D^*(cm\ Hz^{1/2}/W)$
4	72 Å GaAs	600 Å $Al_{0.13}Ga_{0.87}As$	2.5×10^{17}	17.5	
	72 Å GaAs	600 Å $Al_{0.135}Ga_{0.865}As$	2.5×10^{17}	16.8	
	72 Å GaAs	600 Å $Al_{0.14}Ga_{0.86}As$	2.5×10^{17}	16.5	
	72 Å GaAs	600 Å $Al_{0.145}Ga_{0.855}As$	2.5×10^{17}	15.9	
	66 Å GaAs	600 Å $Al_{0.145}Ga_{0.855}As$	2.5×10^{17}	15.6	
	66 Å GaAs	600 Å $Al_{0.15}Ga_{0.85}As$	2.5×10^{17}	15.3	
	66 Å GaAs	600 Å $Al_{0.155}Ga_{0.845}As$	2.5×10^{17}	15.0	3×10^{12} (40 K)
5	70 Å GaAs	500 Å $Al_{0.1}Ga_{0.9}As$	3×10^{17}	16.6	2×10^{12} (20 K)
6	80 Å $In_{0.15}Ga_{0.85}As$	500 Å GaAs	5×10^{17}	15.3	8×10^{9} (10 K)
	85 Å $In_{0.15}Ga_{0.85}As$	500 Å GaAs	1×10^{17}	17.8	9.7×10^{10} (10 K)
7	60 Å GaAs	500 Å $Al_{0.15}Ga_{0.85}As$	8×10^{17}	15	2×10^{11} (30 K)
8	118 Å GaAs	400 Å $Al_{0.07}Ga_{0.93}As$	1.5×10^{17}	26.9	2.5×10^{9} (4.2 K)
9	p-type superlattice	p-type superlattice		19.2	2.58×10^{7} (20 K)
	35 Å $In_{0.27}Ga_{0.73}As$	32 Å $Al_{0.15}Ga_{0.85}As$			

Major effort on VLWIR QWIP development has been made at Jet Propulsion Laboratory (JPL) for space applications. A 128 × 128 pixel QWIP FPA with a 15 μm cutoff wavelength has been demonstrated by JPL with an NEDT of 30 mK at 45 K with 300 K background and *f*/2.3 optics [10]. This initial array gives excellent images with a 99.9 % operability and a 2.4 % uncorrected responsivity nonuniformity. Comparing the array results from both the MCT detector and GaAs QWIP at 15 μm, QWIP has higher operability and uniformity due to the mature GaAs MBE growth and processing technology.

2. DESIGN CONSIDERATIONS OF VLWIR QWIPs

Several issues need to be considered when designing a VLWIR QWIP. In a VLWIR scenario, the temperature of the target is usually cold and the energy density of the blackbody radiation is small. This means that a higher response is needed from the detector. In order to tailor the peak detection wavelength of a QWIP to the VLWIR spectral region, the barrier height needs to be lowered and the well width needs to be increased with respect to MWIR (3-5 μm) and LWIR (8-12 μm) QWIPs. For QWIPs operating in the LWIR region, the typical well width is about 40 Å to 45 Å, and the aluminum mole fraction in the barrier is about 25% to 30%. While for VLWIR QWIPs, the well width is usually larger than 60 Å, and the aluminum mole fraction in the barrier is less than 15% in order to achieve lower barrier energy and longer peak detection wavelength. The lower energy barrier and wider well width will result in a smaller activation energy, which means a higher thermionic emission of electrons from the quantum wells. In order to reduce the thermionic mission, which is the dominant mechanism of dark current in a VLWIR QWIP, the doping density in the well needs to be lower than that of a LWIR QWIP. In a LWIR QWIP, typical doping density is usually 0.5 to 1×10^{18} cm^{-3}, whereas in a VLWIR QWIP the doping density is about 2 to 3×10^{17} cm^{-3}. A balance between the responsivity and the dark current needs to be considered when choosing the doping density. The corresponding D^* will also be affected. In general, under the same operating temperature, the longer the detector cutoff wavelength, the smaller the D^* value. The electron density in the quantum well of a QWIP is usually very high, and hence the exchange energy plays an important role in the intersubband transition energy. This is especially true for a VLWIR QWIP in which the exchange energy greatly affects the detection peak wavelength due to the low barrier energy. We shall discuss each of these effects in detail next.

2.1 Blackbody Radiation

The blackbody radiation spectral density decreases very rapidly when the target temperature decreases. Figure 1 shows the blackbody spectral density calculated under different temperatures using the blackbody spectral density formula

$$W(\lambda)=\frac{2\pi c^2 h}{\lambda^5}\frac{1}{\exp(hc/\lambda k_b T_B)-1} \tag{1}$$

where c, h, k_b and T_B are the light speed in vacuum, Planck constant, Boltzmann constant, and the background temperature, respectively. As can be seen in Fig.1, when the target temperature changes from 300 K to 200 K, the peak wavelength will shift from 10 μm to 15 μm, and the spectral density will also decrease. For example, the maximum spectral density at 200 K is only 13% of the maximum density at 300 K. In order to efficiently detect the radiation from a target at 200 K, a 15 μm detector with higher responsivity, or lower dark current is highly desirable to maintain the same sensitivity as a 10 μm detector for a 300 K target.

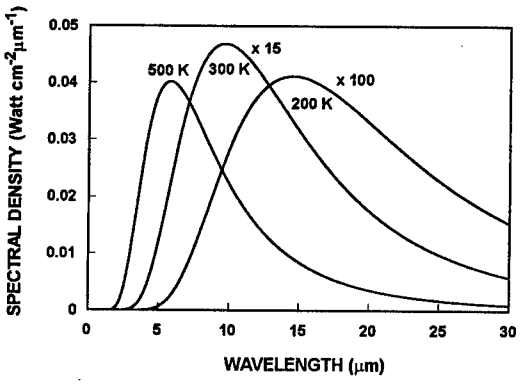


Figure 1. Blackbody spectral density at 200, 300, and 500 K.

2.2 Dark Current and Dynamic Resistance

The dark current I_d of a QWIP can be expressed as [11]

$$I_d = \frac{e m_w^* A}{\pi \hbar^2 L_p} \frac{\mu F}{\sqrt{1+(\mu F / v_s)^2}} \int_{E_1}^{\infty} f(E) T(E,F) dE \qquad (2)$$

where e is the electronic charge, m_w^* is the electron effective mass in the well, A is the device area, L_p is the QWIP period length, μ is the electron mobility, F is the electric field inside the QWIP, v_s is the electron saturation velocity, $f(E)$ is the Fermi-Dirac distribution function, and $T(E,F)$ is the bias-dependent tunneling current transmission coefficient for a single barrier. When the thermionic emission is dominant, the dark current can be expressed as

$$I_d = \frac{e^2 m_w^* A}{\pi \hbar^2} \frac{\mu F^2}{\sqrt{1+(\mu F / v_s)^2}} \frac{L_b}{L_w} \exp\left\{-\frac{(E_b - eF L_w - E_F - E_1)}{k_b T}\right\} \qquad (3)$$

The dynamic impedance Z of a single period QWIP is defined as

$$Z = \frac{dV}{d I_d} \qquad (4)$$

where V is the voltage drop across one period of the QWIP. In our calculations, the electron mobility and saturation velocity are taken as 2000 cm^2 -V^{-1}s^{-1} and 2×10^6 cm/s, respectively. Figure 2 shows the calculated dark current versus bias for the 15.5 μm and 9.2 μm QWIPs at T=40 K and 60 K, respectively. The device structure for the 15.5 μm QWIP uses a 66 Å GaAs well and a 600 Å $Al_{0.15}Ga_{0.85}As$ barrier with a doping density of 2.5×10^{17} cm^{-3}. The device structure for the 9.2 μm QWIP uses a 66 Å GaAs well with a doping density of 5×10^{17} cm^{-3} and a 600 Å $Al_{0.25}Ga_{0.75}As$ barrier. As can be seen from

this figure, the dark current of the 9.2 μm QWIP is several orders of magnitude lower than that of the VLWIR QWIP under same bias and temperature condition. As a result, a large difference in the dynamic resistance of these two detectors is expected, as shown in figure 3. Therefore, in order for the 15.5 μm QWIP to have the same performance as the 9.2 μm QWIP, a lower operating temperature is required.

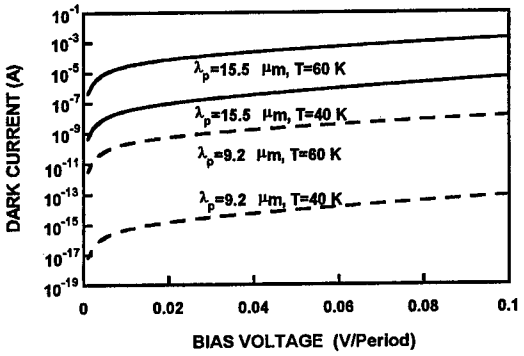


Figure 2. Calculated dark current versus bias for two QWIPs with peak wavelengths at 9.2μm and 15.5 μm, respectively.

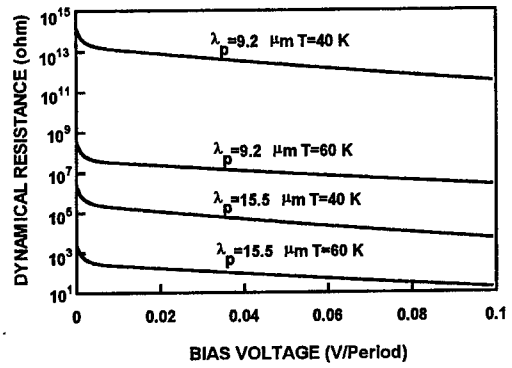


Figure 3. Calculated dynamic resistances for two QWIPs with peak wavelengths at 9.23 μm and 15.54 μm, respectively.

2.3 Detectivity

In a VLWIR QWIP the main dark current conduction mechanism is due to the thermionic emission across the barrier of quantum well. In general, over a wide range of temperatures and cutoff wavelengths, the detectivity can be expressed as [1]

$$D^* = D_0^* \exp(hc/2\lambda_c k_b T) \quad (5)$$

where λ_c is the cutoff wavelength.

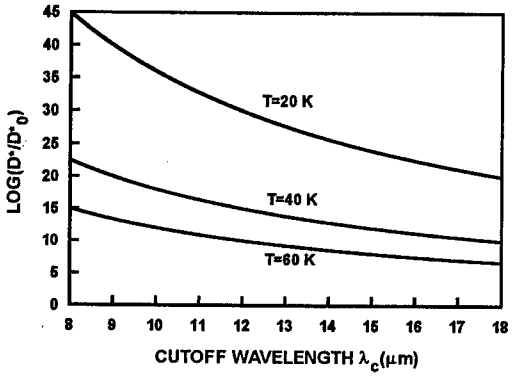


Figure 4. Variation of normalized detectivity with cutoff wavelength in the very long wavelength infrared (VLWIR) region.

As shown in figure 4, the detectivity decreases with increasing cutoff wavelength and temperature. This is due to the fact that with the increase of cutoff wavelength and temperature, the dark current and hence the dark current noise will increase significantly with increasing cutoff wavelength and temperature due to the nature of thermionic emission, while the responsivity remains unchanged over a wide range of temperatures. Therefore, we come to the conclusion that in order to keep the same D^* when extending to longer wavelength, a lower operating temperature is needed.

2.4 Peak Wavelength Shift due to Exchange Interaction

When designing a QWIP, the energy states are obtained from the Schrödinger equation by taking into account the potential at the heterojunction caused by the energy band offset of the quantum well and barrier materials. The peak detection wavelength of a VLWIR QWIP can be calculated by using the transfer matrix method (TMM) [12]. West [13] has calculated the Coulomb interaction (repulsive) of the electrons in the quantum well and found that it is very small, which is canceled out with the dynamic electron plasma interaction. However, the experimental data he observed was about 6 meV higher than the calculated value for several QWIP structures. Taking into account the exchange interaction, excellent agreement between the theory and the experiment can be obtained [14]. For a VLWIR QWIP, the transition energy is relatively small and the influence of exchange energy becomes very significant. The exchange energy can be expressed as [14]

$$E_{exch} = -\frac{e^2}{2\varepsilon}\int_0^{k_f}\frac{d^2k'}{(2\pi)^2}\int dz\int dz'\frac{e^{-|k-k'||z-z'|}}{|k-k'|}\left|\phi_1(z')\right|^2\left|\phi_1(z)\right|^2 \quad (6)$$

where $k_f=(2\pi\sigma)^{1/2}$, σ is the two-dimensional electron density in the quantum well, ε is the dielectric constant, k and k' are the in- plane wave vectors of electrons. Under normal doping condition, the exchange energy will lower the ground state subband energy by 5 to 10 meV and shifts the absorption peak to shorter wavelength.

As mentioned previously, in order to design a QWIP with peak detection wavelength in the VLWIR region, the barrier height should be lowered than that of the LWIR QWIP, and the well width should be increased with a lower doping density. As an example, let us consider the design of a VLWIR QWIP with a GaAs well width of L_w and doping density of $N_D = 2.5\times10^{17}$ cm^{-3} and a 600 Å $Al_{0.15}Ga_{0.85}As$ barrier. Figure 5 shows the calculated variation of peak detection wavelength with well width L_w; the dashed line is the result without considering the exchange energy, while the solid line is the result of taking into account the exchange energy. The result agrees well with the experiment (e.g., at L_w=66 Å, the calculated peak wavelength is 15.54 μm and the measured value is 15.3 μm [4]). The reason for the transition peak wavelength to decrease with increasing well width is that: in this system the transition occurs between the bound state and the continuum state, and increasing well width has little effect on the excited continuum state energy. On the contrary, the decrease in the bound state energy will result in the decrease of the transition peak wavelength (blue shift) for a bound to bound state transition QWIP. As can be seen from this figure that the exchange energy plays an important role on the peak detection wavelength in a VLWIR QWIP. Therefore, special attention should be paid to the doping density while designing the VLWIR QWIP.

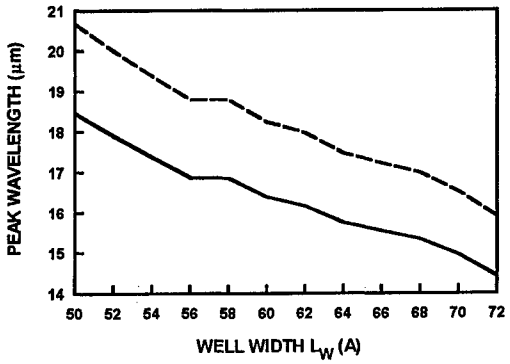


Figure 5 Variation of peak wavelength with well width in a GaAs/$Al_{0.15}Ga_{0.85}As$ VLWIR QWIP. The dashed line is without considering the exchange energy, while the solid line is taking into account the exchange energy. L_w is the well width, and the barrier thickness is 600 Å.

3. VLWIR QWIP in a Multicolor QWIP Stack

As the infrared (IR) detector technology continues to advance, there is a growing demand for multi-color IR detectors for advanced sensing and imaging systems. IR detectors with more than two colors are highly desirable for temperature registration, chemical analysis, and target discrimination and identification. Using multiple stacks of QWIPs with intermediate contact layers, the capability of multicolor detection simultaneously, or sequentially by tuning the bias voltage has been demonstrated [15,16]. When a VLWIR stack is incorporated in a multi-color QWIP, special attention has to be paid in the design. As can be seen from figure 3, the dynamic resistance of the λ_p=15.54 μm QWIP is much smaller than that of the λ_p=9.23 μm QWIP under the same bias condition. This means that the dark current, and hence the operating temperature of a multi-stack, multi-color QWIP will be limited by the longer wavelength QWIP stack. If operating temperature is the primary requirement, reducing the VLWIR dark current should be the main consideration when designing the detector. A low dynamic resistance also means a low voltage drop on this stack. When the multi-stack QWIP is used under voltage tunable mode, careful selection of period number, doping density and barrier width is necessary in order to realize the voltage tunability with a reasonable bias.

4. A 14.7 μm VLWIR QWIP

In this section we discuss the design, fabrication, characterization, and performance of a VLWIR QWIP. The QWIP structure is composed of 20 periods 80 Å $In_{0.04}Ga_{0.96}As$ well with doping density of 2×10^{17} cm^{-3} and a 500 Å $Al_{0.09}Ga_{0.91}As$ barrier. The schematic conduction band diagram of this QWIP is shown in figure 6. This structure is similar to those listed in table I with some unique features. First, a small amount of indium is added in the GaAs well region. This gives a smaller effective mass of electron, and therefore a higher absorption in the quantum well. Using aluminum free GaAs as a barrier has the advantage of having smaller defect center in the barrier which tends to reduce the dark current. However, electrons in the heavily doped GaAs contact layer can also tunnel into the quantum wells without any potential barrier, therefore causes an increase in dark current. In this design, a small amount of Al is added in the GaAs barrier to reduce the device dark current.

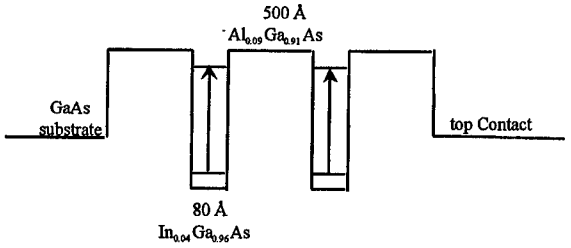


Figure 6. Schematic conduction band diagram of a 14.7 μm bound to bound state transition GaAs/AlGaAs QWIP.

The detector was designed with a peak wavelength at 14.5 μm. Theoretical calculation shows that the peak wavelength of this QWIP is at 16.1 μm without considering the exchange energy and 14.67 μm after taking into account the exchange energy. The detector is designed to use the bound to bound state intersubband transition for IR detection and for reducing the device dark current. Figure 7 shows the dark current density versus bias voltage with temperature as a parameter (40 to 60 K) for this device, along with the 300 K window current. The thermal activation energy due to thermionic emission can be determined from figure 7 using Arrehnius plot. Figure 8 shows the variation of activation energy with bias at 40 K. As can be seen from figure 8 that the activation energy versus bias voltage follows a straight line, as expected from Eq.(3). From this figure the thermal activation energy at zero bias was found to be 72.1 meV, in excellent agreement with the 75.5 meV calculated from the E_b-E_1-E_F. The spectral responsivity of this QWIP at 77 K under ±2V is shown in figure 9. The responsivity peak was found to be at 14.7 μm, which is in excellent agreement with the calculated value when the exchange energy is taken into account. Figure 10 shows the variation of peak responsivity with bias at 40 K. As can be seen from this figure, the responsivity remains zero at very low bias voltages and increases rapidly for $|V_b| > \pm 0.5$ V, which is the characteristics of the bound to bound state transition.

The detectivity can be expressed as

$$D_\lambda^* = R_i \sqrt{\frac{A_d \Delta f}{4eI_d g}} \tag{7}$$

where R_i is the responsivity, A_d is the device area, Δf is the band width, e is the electron charge, I_d is the dark current, g is the noise gain, which can be obtained by [17]

$$g(V) = \frac{I_d R_0}{\frac{kT}{e} N^2 \exp(\frac{\Delta E}{kT})} \tag{8}$$

where R_0 is the dynamic resistance at zero bias, N is the period number, k is the Boltzmann constant, ΔE is the barrier lowering, which is given by

$$\Delta E = e \sqrt{\frac{eV_b}{4l_t \pi \varepsilon_0 \varepsilon_r}} \tag{9}$$

where V_b is the bias voltage across one period, l_t is one period length, ε_0 is the free space permittivity, and ε_r is the dielectric constant.

The D^* of this device was calculated at 40 K, 2 V bias using Eqs. (7) - (9) and the measured responsivity and device dark current. The result yields a D^* of 1.12×10^{10} cm-$Hz^{1/2}W^{-1}$. This D* value is reasonably good for a VLWIR QWIP with cutoff wavelength

at 16.3 μm. New VLWIR QWIP structures are currently being studied to further improve the device performance.

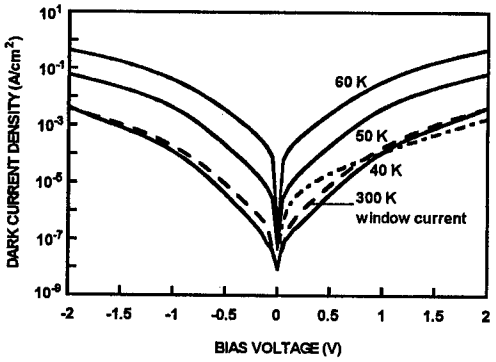


Figure 7. Measured dark current density versus bias voltage for the 14.7 μm VLWIR QWIP. The dash-dotted line is the calculated dark current density at 40 K obtained from Eq.(3).

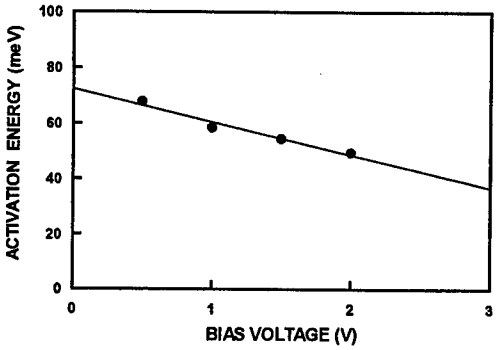


Figure 8. Activation energy versus bias voltage for the 14.7 μm VLWIR QWIP.

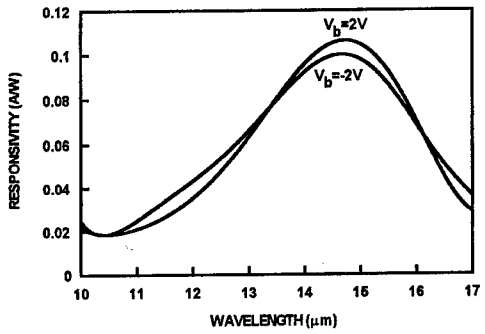


Figure 9. The spectral responsivity of the 14.7 μm VLWIR QWIP at $V_b = \pm 2V$ bias and 40K

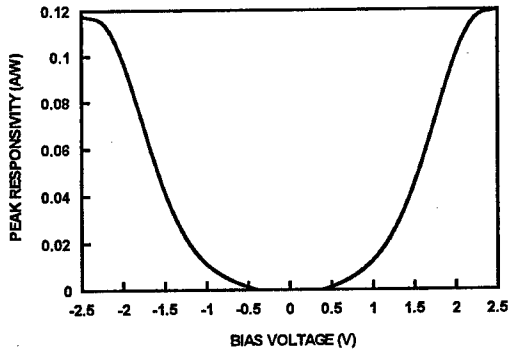


Figure 10. Variation of peak responsivity versus bias at 40 K for the 14.7 μm VLWIR QWIP.

6. CONCLUSIONS

In this paper the latest development in VLWIR QWIPs has been discussed. We have investigated the design requirement, underling fundamental device physics, multi-color QWIP including a VLWIR stack and several ways of reducing the dark current. We have also designed, fabricated, and characterized a VLWIR QWIP with cutoff wavelength at 16.3 μm. The device shows promising performance and improvement is under way with new device structures.

ACKNOWLEDGEMENT

This work was partially supported by BMDO/TO (ARL) and by US Army Research Office (UF) under grant no. DAAG55-98-1-0325.

REFERENCES

1. B.F. Levine, J. Appl. Phys., **74**, R1, (1993).
2. S.D. Gunapala and K.M.S.V. Bandara, Thin Films, **21**, 113 (1995).
3. Sheng S. Li, Journal of the Chinese Institute of Electrical Engineering, **2**, 37 (1995).
4. G. Sarusi, S.D. Gunapala, J.S. Park and B.F. Levine, J. Appl. Phys., **76**, 6001 (1994).
5. B.F. Levine, A. Zussman, J.M. Kuo and J. De Jong, J. Appl. Phys., **71**, 5130 (1992).
6. S.D. Gunapala, K.M.S.V. Bandara, B.F. Levine, G. Sarusi, D.L. Sivco and A.Y. Cho, Appl. Phys. Lett., **64**, 2288 (1994).
7. C.Y. Lee, M.Z. Tidrow, K.K. Choi, W.H. Chang, L.F. Eastman, F.J. Towner and J.S. Ahearn, J. Appl. Phys., **75**, 4731 (1994).
8. A.G.U. Perera, W.Z. Shen, S.G. Matsik, H.C. Liu, M. Buchanan and W.J. Schaff, Appl. Phys. Lett., **72**, 1596 (1998).
9. J. Chu, Sheng S. Li, A. Singh and P. Ho, Appl. Phys. Lett., **72**, 1664 (1998).
10. S. D. Gunapala, J. S. Park, G. Sarusi, T. L. Lin, J. K. Liu, P. D. Maker, R. E. A. Muller, C. A. Shott, and T. Hoelter, IEEE Trans. Electron. Devices **44,** 45 (1997).
11. B.F. Levine, C.G. Bethea, G. Hasnain, V.O. Shen, E. Pelve, R.R. Abbott and S.J. Hsieh, Appl. Phys. Lett., **56**, 851 (1990).
12. M.O. Vassell, Johnson Lee and H.F. Lockwood, J. Appl. Phys., **54**, 5206 (1983).
13. Lawrence West, "Spectroscopy of GaAs Quantum Wells", Ph. D. Thesis, July 1985.
14. K.M.S.V. Bandara, D.D. Coon, Byungsung O, Y.F. Lin and M.H. Francombe, Appl. Phys. Lett., **53**, 1931 (1988).
15. J.C. Chiang, Sheng S. Li, M.Z. Tidrow, P. Ho, M. Tsai and C.P. Lee, Appl. Phys. Lett., **69**, 2412 (1996).
16. M.Z. Tidrow, J.C. Chiang, Sheng S. Li and K.Bacher, Appl. Phys. Lett., **70**, 859 (1997).
17. D.C. Wang, G. Bosman and S.S. Li, Appl. Phys. Lett., **68**, 2532 (1997).

TWO-COLOR MW/LW QWIP FPA & COMMERCIAL ONE-COLOR LW QWIP FPA

M. Sundaram, T. Faska, M. Taylor, R. Williams, A. Reisinger, and S. Wang
Advanced Technology Division, Sanders, A Lockheed-Martin Co.
65 Spit Brook Road, Nashua, NH 03060

ABSTRACT

We report the performance of the first two-color MW/LW QWIP FPA with pixel registration and simultaneous integration. The 256x256 FPA features a 8.5 μm LW QWIP stacked on a 5.0 μm MW QWIP (both QWIPs realized in the InGaAs/GaAs/AlGaAs material system) and 3 bumps/pixel to permit each QWIP to be separately biased and the two photocurrents to be simultaneously integrated. We also report on the detailed performance of our 320x256 one-color LW GaAs/AlGaAs QWIP FPA, a device that has matured enough to enter commercial production.

INTRODUCTION

Simultaneous imaging in multiple infrared spectral bands is expected to provide or enhance clutter rejection, camouflage detection, false alarm reduction, decoy discrimination, countermeasures resistance, target ID enhancement, and absolute graybody target temperature measurement. Current multi-sensor systems require spinning filter wheels and/or cumbersome optics precisely aligned to split and direct the incoming infrared light to two or more 1-color staring focal plane arrays (FPAs), both of which add to the cost, weight, performance, and reliability risk of the systems. A single staring FPA that provides simultaneous and spatially-registered imagery in multiple infrared bands is an attractive alternative that promises to mitigate such problems. Neither moving parts nor extra aligned optics are needed. Thanks to advances in material and fabrication technologies such FPAs can be made today. We report on one such FPA: the first 2-color midwave/longwave infrared (MW/LW) FPA in 256x256 format with pixel-registered and simultaneous imagery in the two atmospheric windows (3-5.5 μm, and 8-13 μm), realized using quantum well infrared photodetectors (QWIPs).

Certain properties unique to the QWIP make it a natural choice for multi-color FPAs. Its sharp spectral response ($\Delta\lambda/\lambda \sim 10\%$) and tailorable peak ($\lambda_{Peak} \sim 3$ - 18 μm) mean that several detectors can be grown stacked on top of each other without the need for filters to prevent spectral crosstalk. One or more of the detectors can be an interband p-i-n diode for near infrared detection. Besides, the quantum wells can be realized in the InGaAs/GaAs/AlGaAs system, a material system that has reached growth and fabrication maturity to a point where it is used in several commercial state-of-the-art GaAs foundries around the world today devoted to the production of high-speed and high-frequency MIMIC chips.

The physics and technology of QWIPs have been thoroughly reviewed in the literature (1). One-color LW QWIP FPAs with formats as large as 640x480 have been made by several groups (2). A 2-color LW/LW QWIP FPA with pixel-registered and simultaneous imagery at 8.6 μm and 11.2 μm was recently reported by our group (2). We have since applied this architecture to MW/LW and MW/MW dualband combinations. Fabrication and performance details of the 2-color MW/LW QWIP FPA are provided in this paper.

QWIP FPA technology has also advanced enough that 1-color LW and MW FPAs can be consistently and reproducibly made, a requirement for commercialization. We conclude this paper with a performance summary of the one-color 320x256 LW FPA, a device that we now commercially produce and that we believe to represent the state-of-the-art of 1-color QWIP FPA technology in the market today.

EXPERIMENTAL

Architectures of a 1-color and 2-color FPA are shown in Figs. 1 and 2. The 1-color FPA has 1 In bump/pixel which is bonded to a bump connected to the source of an input switching FET in the corresponding unit cell of a matching Si readout integrated circuit (ROIC) array. A layer (called Detcom in Fig. 1) common to all the pixels serves as the other contact to the FPA and is connected to the ROIC via bumps at the array boundaries. The ROIC applies a bias across the FPA by separately adjusting Detcom and VG; the photocurrent from each pixel is fed into an integrating capacitor in the corresponding ROIC unit cell; this integrated charge is sampled and read out to generate the image.

The 2-color FPA architecture (Fig. 2) uses 3 In bumps/pixel to put two vertically stacked QWIPs (grown in series) in parallel electrically. Detcom, VGRed, VGBlue are adjusted to separately bias the Red and Blue QWIPs; the Red and Blue photocurrents are fed to two separate integrating capacitors in each unit cell which are then read out to generate the two simultaneous images. The vertical stacking of the detectors (together with the small contact geometries) ensures exact spatial registration of the two images. Such an architecture is readily extended to larger format arrays and to at least 4 simultaneous colors (the number of colors being limited by the maximum number of In bumps and contact vias that can reside on each pixel). Note that this architecture calls for complete electrical isolation between pixels: the Red photocurrent flows from the top contact and the Blue photocurrent from the bottom contact. Also note that while in the 1-color architecture Detcom is common to all pixels, in the 2-color architecture Detcom is common only to the 2 colors in each pixel: it is the middle contact layer and is more appropriately called Pixelcom.

The 2-color detector material features a LW (hereafter called Red) QWIP stack on top of a MW (hereafter called Blue) QWIP stack with three ohmic contact layers (the first below the Blue stack, the second between the Blue and Red stacks, and the third above the Red stack) grown by molecular beam epitaxy (MBE). The Red stack is an 8.5 μm QWIP realized with quantum wells of GaAs sandwiched between AlGaAs barriers; the Blue stack is a 5.0 μm QWIP realized with deeper wells of strained InGaAs sandwiched between AlGaAs barriers; the contact layers consist of doped GaAs. Two etch stop layers sandwiching a 1 μm layer of undoped GaAs are grown between the substrate and the

device layers (their purpose is explained in the process description below). QWIP designs similar to the ones used here have been extensively reviewed in the literature (1). Following growth, each wafer is xrayed and the (004) xray rocking curve analyzed (in conjunction with the MBE growth parameters) to precisely yield the thickness and composition of every layer in the device structure to ensure compliance with design tolerances. The 1-color detector material is similarly grown and characterized, the only difference being that there is a single 8.6 μm QWIP stack with top and bottom ohmic contact layers, and a single etch stop layer between the substrate and device layers.

FPA fabrication is carried out in a wafer-level process using stepper lithography and reactive ion etching (RIE) for all etching steps. The 1-color FPA is processed as follows: grating metal is first defined and a grating pattern etched into the top layer (the grating is necessary to diffract the normally incident light and cause it to be absorbed by the quantum wells), followed by etching of the pixel mesas using ohmic metal as a mask (this metal serves as both pixel electrical contact as well as grating reflector). Ohmic metal is then evaporated to contact the bottom contact layer at the FPA boundaries. All ohmic contacts are annealed. An array of In bumps (on top of each pixel and at the FPA boundaries) is then evaporated.

The wafer is diced to separate the FPAs; individual die are selected and hybridized (i.e. In bump-bonded) to matching Si ROIC die. Each hybrid is wicked with epoxy, epoxy-cured, and thinned to have the entire GaAs substrate removed through a combination of chemical-mechanical polishing and RIE (the etch stop layer aids in complete removal of any residual substrate at this step). Substrate removal eliminates thermal mismatch between the GaAs-based detector and the Si ROIC, improves optical coupling (and therefore quantum efficiency), and cuts pixel-pixel optical crosstalk. The result of all the processing is a ~ 5 μm thick epitaxial membrane glued to the Si ROIC. The hybrid is then packaged and wire-bonded in a 68-pin LCC (with a calibrated temperature sensor) for imaging. Illumination is through the bottom ohmic contact (Detcom) layer. One die from each wafer is selected and hybridized to a fanout for direct electrical and optical measurements. The 320x256 FPA has 28 μm x 28 μm pixels on a 30 μm x 30 μm pitch (i.e. fill factor ~ 87%). There are 30 FPAs on a 3-inch wafer. The control and precision of the fabrication process are readily seen in the image of a typical pixel shown in Fig. 3.

The 2-color FPA process is similar to the 1-color process, along with the extra steps required to create and contact via holes to the middle and bottom ohmic contact layers in each pixel, and to run metal lines (on an insulating layer to prevent shorting) from the two vias to the pixel top. The trenches between the pixels are etched deep enough (to the top etch stop layer) to achieve complete electrical isolation between pixels. The bottom etch stop aids in substrate removal from the backside. The 1 μm thick GaAs layer between the two etch stops serves to physically hold the array together (in addition to the In bumps and the epoxy); this layer is thin enough that complete optical isolation between the pixels is secured. The 256x256 FPA has a 40 μm x 40 μm pitch; each pixel has two 9 μm x 9 μm via cutouts on a 38 μm x 38 μm frame, resulting in ~ 80% fill factor for the top (Red) QWIP and ~ 85% fill factor for the bottom (Blue) QWIP. There are 16 FPAs on a 3-inch wafer. Fig. 4 shows the top view of a 2-color pixel prior to In bump deposition: the narrow trenches (between pixels), small vias, and vertical sidewalls testify to the advanced degree of process control.

The grating to couple light to the two spectral bands in the 2-color FPA was selected after a careful optimization of all grating parameters (pitch, duty cycle, polarity, orientation, depth, and choice of metal) in control experiments on corresponding 1-color arrays. The optimum choice turned out to be one where the Blue QWIP absorbs both light polarizations whereas the Red QWIP absorbs light of only one polarization. Of course, it is possible to make the FPA polarization insensitive in both bands at the expense of slightly less quantum efficiency in the Blue band.

RESULTS

Electrical and optical measurements are performed on every working pixel wired out from the FPA-fanout hybrids. Radiometric and noise measurements are done in a calibrated setup with f/2 or f/4 optics and a HP33655 dynamic signal analyzer. IV curves are measured with a HP4145B parameter analyzer. Spectra are measured in a FTIR spectrometer with 4 cm^{-1} resolution, 10^9 V/A transimpedance gain, and at various biases from -5V to +5V. All measurements (IV, responsivity, spectrals, etc.) showed a tight uniformity (sigma/mean < 4%). Imaging with the FPA-ROIC hybrids indicate even tighter uniformity (sigma/mean < 3%) in response and dark current, proof of the excellent uniformity in the growth and fabrication of GaAs-based QWIPs. Imaging response and noise equivalent temperature difference (NETD) measurements are done in a calibrated setup with f/2 or f/3 optics and a Sterling cycle cooler (with temperature control down to 65K) as also in a pour-fill LN2 dewar. Both the bias and integration time (Tint) are experimentally adjusted for optimum FPA operation. Electrical and optical data presented below are from a median pixel; imagery is from a typical FPA.

2-Color MW/LW QWIP FPA

The spectral response of the 2-color MW/LW array is graphed in Fig. 5. It shows detection in two distinct and separate bands peaked at 5.2 μm and 8.5 μm. Spectral crosstalk is minimal. The fringes in the Red band result from Fabry Perot resonances of the diffracted light waves in the pixel cavity due to the partial (to ~ 25 μm) thinning of the array in this case. Complete thinning removes these fringes.

The 800K blackbody responsivity R_{BB} approaches ~ 10 mA/W for the Blue QWIP and ~ 14 mA/W for the Red QWIP (Fig. 6). As stated earlier, the Red QWIP detects light of only one polarization; a grating optimized for the Red QWIP alone would double the observed maximum R_{BB} to 28 mA/W, a value routinely observed in 1-color LW QWIP FPAs. The 10 mA/W responsivity for the Blue QWIP is the highest ever measured for a MW QWIP FPA.

The bias in Fig. 6 and the following plots is measured with respect to the middle contact (i.e. for the Red QWIP the bias is the voltage applied to the top contact; for the Blue QWIP it is the voltage applied to the bottom contact, the middle contact being grounded in each case). The ROIC is designed to apply a negative bias (as defined above) across each color. A typical operating bias of -2V will therefore secure R_{BB} ~ 7 mA/W

and 9 mA/W for the Blue and Red bands, respectively. The similar response in the two bands allows for balanced operation with the same bias across the two QWIPs, an attractive feature from the point of view of ROIC operation.

The bias dependence of the peak responsivities is shown in Fig. 7. From noise measurements at 77K the quantum efficiency and photoconductive gain of the Red QWIP are calculated to maximize at 2% and 1.0, respectively. Peak and blackbody detectivities $D^* = 1x10^{10}$ Jones and $1x10^9$ Jones were obtained at this temperature. The Blue QWIP has no measurable noise at 77K (total noise dominated by system noise), so its quantum efficiency, gain, and detectivities could not be gauged. IV curves (Fig. 8) show the ~ 20 times lower current at -2V bias for the Blue QWIP compared to the Red QWIP, the difference being almost entirely due to the higher dark current of the Red QWIP at 77K.

The first imaging FPAs feature > 97% pixel operability, NETD better than 35 mK (f/3 optics, 295K background, and 60 Hz frame rate), and excellent uniformity (sigma/mean < 4%) in both colors. While falling short of the > 99.5% operability and NETD < 20 mK routinely obtained in 1-color LW QWIP FPAs, these numbers are excellent for a first attempt. We anticipate that improvements in processing and material and grating designs will boost performance to 1-color levels.

The 2-color FPA is typically operated at 60 - 70K with a bias between -1V and -2V and an integration time Tint ~ 4 ms (the two charge wells in the ROIC are differently sized to allow the same Tint for both colors for truly simultaneous integration). The temperature of operation is limited by the Red QWIP; the Blue QWIP is observed to image cleanly up to ~ 110K (the Red QWIP charge wells are saturated with dark current by then). Typical imagery is shown in Fig. 9. As stated earlier, the images are simultaneous and pixel-registered (i.e. exact temporal and spatial registration). Note the additional information inherent in imagery from such an FPA. Target spectral features unique to either the MW or LW band are strikingly seen.

Having demonstrated the feasibility of the 2-color FPA, our current efforts are aimed at improving the process to increase operability and uniformity, optimizing material and optical coupling designs to boost response and operating temperature, and making medium format (640x512) 2-color arrays. We believe substantial progress can be achieved in all these areas.

Commercial 1-Color LW QWIP FPA

The performance of our commercial 320x256 1-color LW QWIP FPA is graphed in Figs. 10 - 16. At a typical operating bias of -3V (the voltage applied to the top/grating contact with respect to the bottom/Detcom contact) the spectrum peaks at 8.6 μm (Fig. 10) with a 500K blackbody responsivity of 30 mA/W (Fig. 11), a peak responsivity of 325 mA/W (Fig. 12), a quantum efficiency of 15% (Fig. 13), and a photoconductive gain of 0.3 (Fig. 14). A peak detectivity D^* of $1.5x10^{10}$ Jones is achieved at 80K (Fig. 15), limited by the shot noise of the dark current (Fig. 16) at 80K. Cooling freezes out the dark current (dominated by thermionic emission at T > 40K) exponentially, with a corresponding increase in D^*. In fact, the FPAs are usually operated at slightly colder

temperatures, between 65K and 77K. These results are typically and consistently obtained and represent the best performance today with GaAs/AlGaAs quantum wells and a simple 2D period grating coupler. Further improvements in response in this material system have to come from improved optical coupling. Recent experiments in our laboratory (to be reported in a future paper) indicate that the quantum efficiency can be at least doubled by optimizing the grating design. With further process modifications, we believe that a quantum efficiency of 50% can be achieved in a LW QWIP FPA.

In the imaging arrays, a pixel operability (defined as every pixel that responds from 50% to 150% of the median FPA response) of > 99.5% is routinely obtained. Quite a number of the FPAs have operability in excess of 99.95%. The uncorrected response and dark current are extremely uniform with sigma/mean < 2%, testifying to the high uniformity in material growth and processing. In imaging radiometric measurements, the FPAs show a noise equivalent temperature difference (NETD) < 20 mK when operated at 65K with bias between -1V and -3V and Tint between 4 ms and 10 ms in a system with f/2 optics, 295K background, and 100 Hz frame rate. This NETD includes both temporal and spatial noise; its low value is proof of the sensitivity and uniformity of the FPA. An image from one such commercial FPA operating at a temperature of 78K in a pour-fill LN2 dewar is shown in Fig. 17. Note the high image quality even at this relatively high temperature of operation.

The CMOS ROIC (ISC 9705) features a $22x10^6$ electron charge well, a maximum full frame rate of 100 Hz with one output (346 Hz with 4 outputs), adjustable and dynamically movable windowing (32x8, 64x8, or 128x8 at 15.6 KHz frame rate), selectable integration mode (snapshot/integrate and read), RS-170 or PAL output, and dissipates 30 mW using one output (80 mW using 4 outputs).

CONCLUSIONS

In summary, we have demonstrated a 2-color QWIP FPA with simultaneous and pixel-registered imaging in the MW and LW atmospheric transmission windows. High (> 97%) operability and a balanced peak responsivity ~ 100 mA/W have been achieved in both colors. We anticipate improvements in both these parameters in the near future. Our 2-color FPA architecture is robust enough to be readily extended to other 2-color combinations (LW/LW, MW/W, NIR/MW, etc.), larger FPA formats, and to at least 4 simultaneous colors.

We have also shown that 1-color LW QWIP FPAs can be consistently and reproducibly made with proper control of the MBE growth and processing. A quantum efficiency of 15% and operating temperature between 65 - 77K are readily achieved for a 8.6 μm FPA. Further improvements in quantum efficiency are imminent with both different material systems and better optical coupling designs.

ACKNOWLEDGMENTS

It is a pleasure to thank R. Yanka, K. Nichols, L. Mohnkern, D. Burrows, K. Zabierek, R. Olson, D. Walker, S. Wade, S. Duvall, R. Cook, J. Roussis, C. Cooke, and M. Winn for their technical expertise, and P. Uppal and J. Ahearn of Sanders and A. Goldberg of the Army Research Laboratory for technical discussions. We also thank G. Milne, R. Martin, and K. Reiff of Lockheed Martin Electonics & Missiles, Orlando, for their superb 2-color ROIC design and for technical discussions. Finally, we acknowledge the strong support of D. Hayden and J. Winterberger of Eglin Airforce Base, W. Dyer of the Ballistic Missile Defense Organization, and A. Penkacik of Sanders which was crucial to the success of the 2-color effort. This work was supported by Sanders IR&D funds and by the Fedlabs MDSS program.

REFERENCES

1. For a comprehensive review of the physics and technology of QWIPs and 1-color QWIP FPAs, see B. F. Levine, J. Appl. Phys., 74, R1 (1993); *and references therein.*
2. M. Sundaram *et al.*, in Proceedings of the IRIS Specialty Group Meeting on Detectors, NIST, Boulder, CO (August 12-13, 1998).

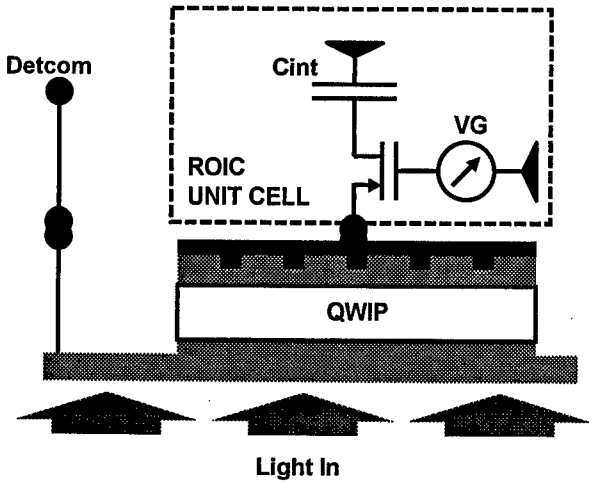


Fig. 1: One-color FPA architecture showing a QWIP pixel bumped to a Si ROIC unit cell. A grating diffracts and couples normally incident light to the quantum wells.

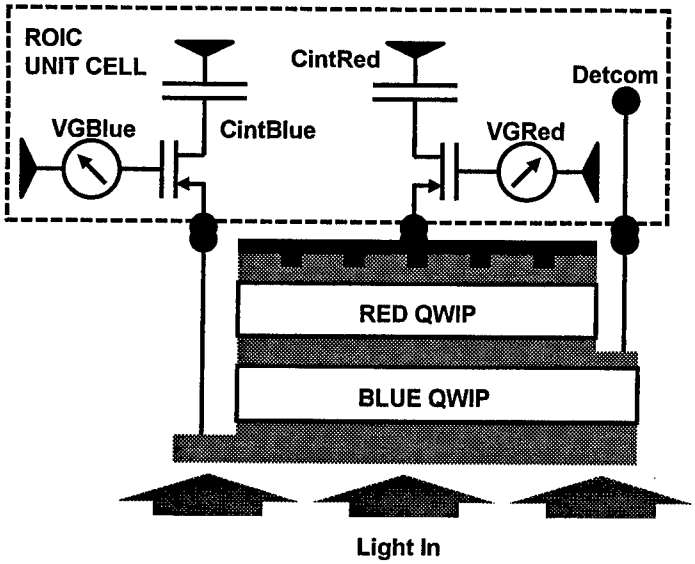


Fig. 2: Two-color FPA architecture showing a 2-color pixel with stacked QWIPs bumped (via 3 In bumps) to a 2-color ROIC unit cell. Each pixel is electrically and optically isolated from its neighbors.

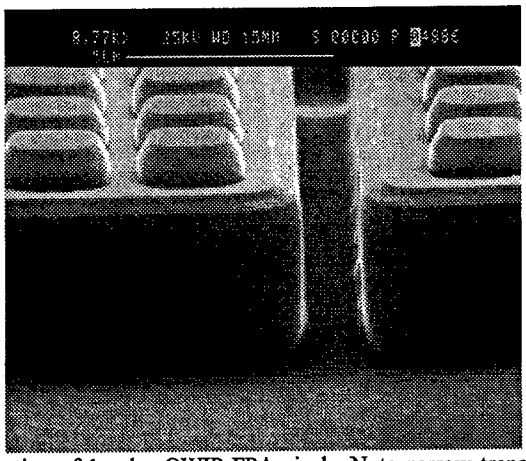


Fig. 3: Cross-section of 1-color QWIP FPA pixel. Note narrow trench, vertical walls, and high fill-factor.

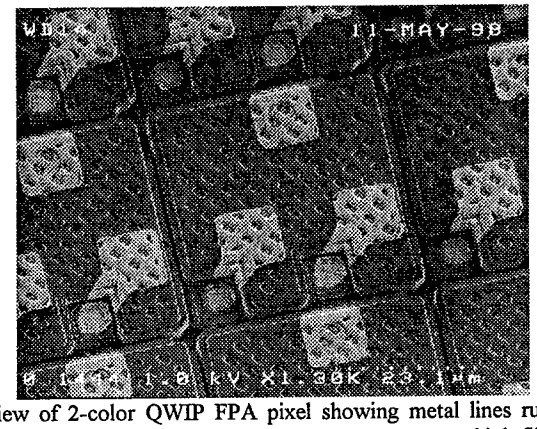


Fig. 4: Top view of 2-color QWIP FPA pixel showing metal lines running from vias (etched to middle and bottom contact layers) to pixel top. Note high fill factor for both colors due to small via sizes within a pixel and the narrow trenches between pixels.

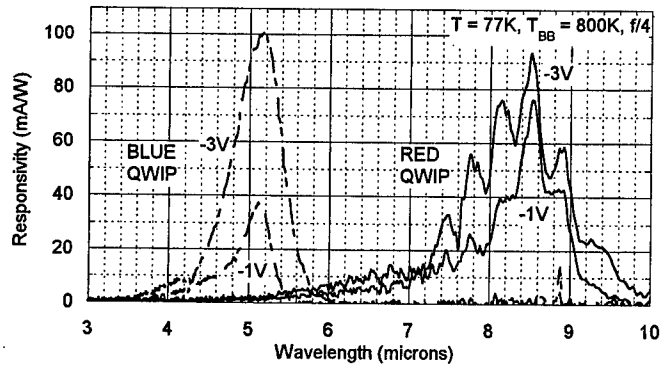


Fig. 5: Spectral response of 2-color MW/LW QWIP FPA at two biases. The fringes in the LW spectrum are due to pixel cavity resonances in this partially thinned array.

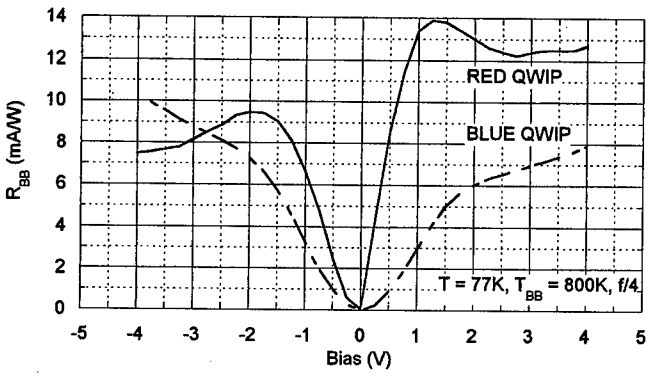


Fig. 6: 800K blackbody responsivity for the 2-color MW/LW QWIP FPA. Bias is the voltage applied to the top contact for the Red QWIP and the bottom contact for the Blue QWIP with the middle contact (Detcom) held to ground in both cases.

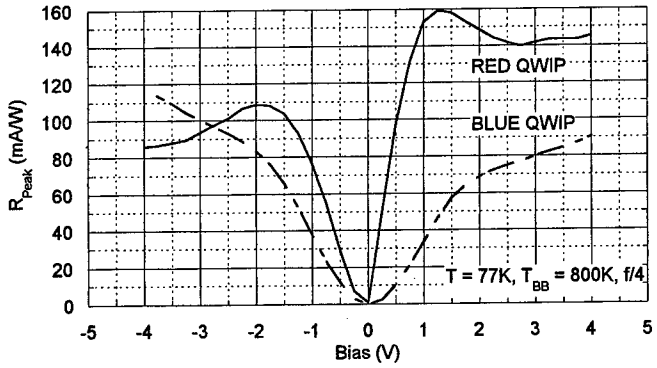


Fig. 7: Bias dependence of the peak responsivity in the 2-color MW/LW QWIP FPA.

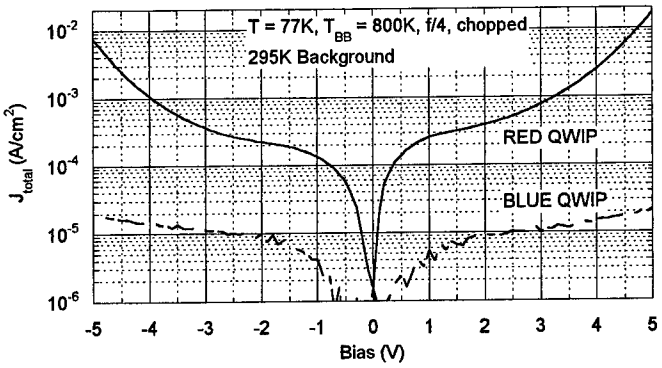


Fig. 8: IV curves for the 2-color MW/LW QWIP FPA. At 77K the Blue QWIP has negligible dark current.



Fig. 9: Simultaneous images in MW (left) and LW (right) showing spectral differences of a filter and a soldering iron in the two bands. The FPA is operated at T = 65K with bias = -1V, Tint = 4 ms, and frame rate = 60 Hz in an f/3 system with 295K background.

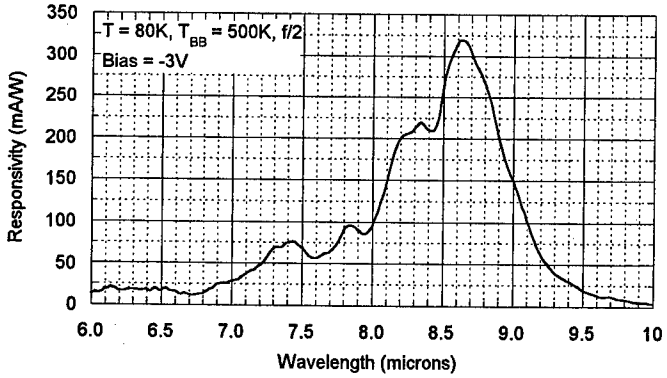


Fig. 10: Spectral response of a typical 320x256 1-color LW QWIP FPA at -3V bias. The FPA has 28 μm x 28 μm pixels on a 30 μm x 30 μm pitch.

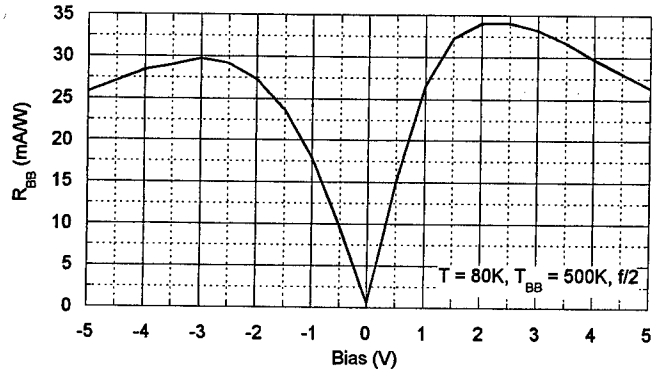


Fig. 11: Bias dependence of the 500K blackbody responsivity of the 320x256 LW FPA.

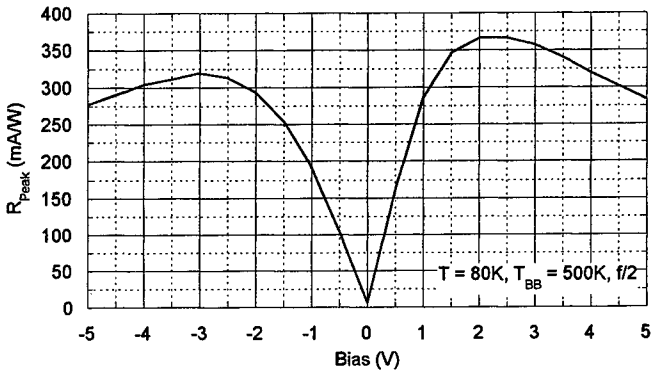


Fig. 12: Bias dependence of the peak responsivity of the 320x256 LW FPA.

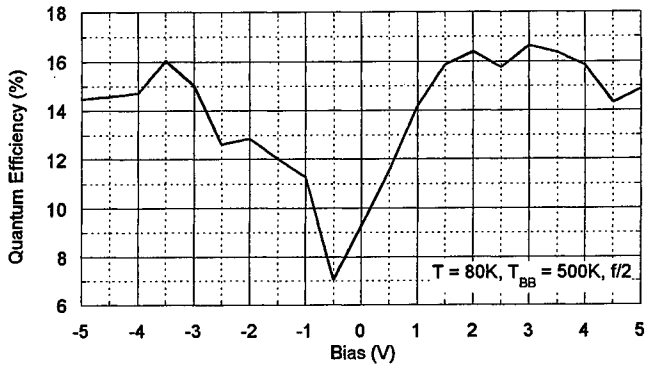


Fig. 13: Quantum efficiency of the 320x256 LW FPA. A maximum efficiency of ~ 15% is typical for a GaAs/AlGaAs LW QWIP with a simple periodic grating coupler.

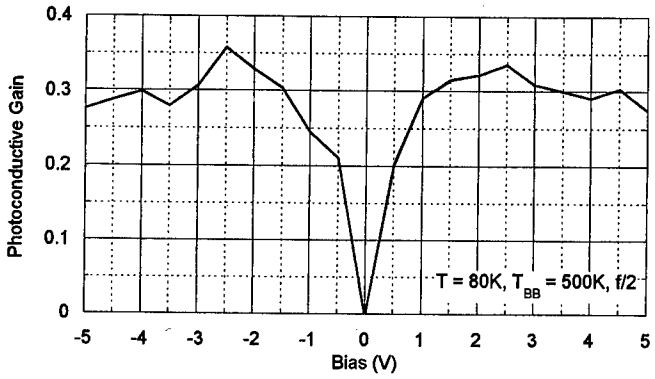


Fig. 14: Photoconductive gain is ~ 0.3 at an operating bias of -3V.

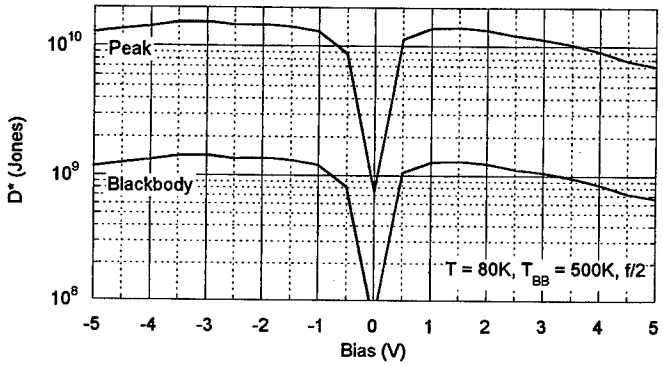


Fig. 15: Detectivity D* at 80K is limited by the shot noise due to the QWIP dark current. D* increases exponentially with cooling.

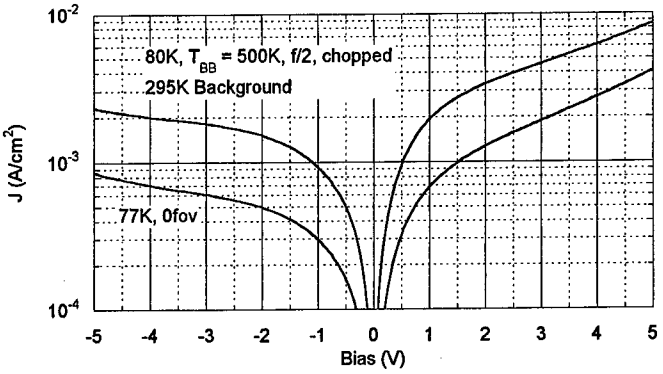


Fig. 16: Typical IV curves for the 320x256 LW QWIP FPA at 80K. The dark current drops exponentially on cooling below 80K.

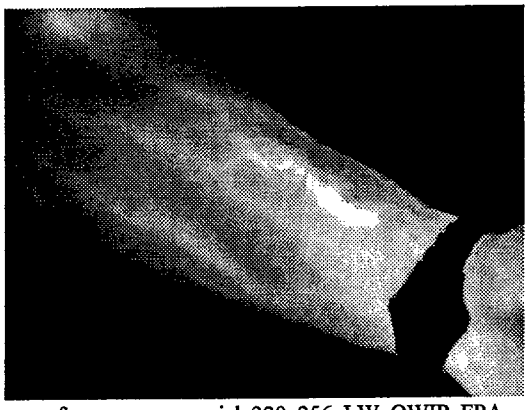


Fig. 17: 8.6 μm image from a commercial 320x256 LW QWIP FPA. The array is operated with bias = -1V, Tint ~ 10 ms, and frame rate = 100 Hz in an f/2 camera system with 295K background. The FPA is at ~ 78K in a pour-fill LN2 dewar!

The Strong Blue-Shifted Photoluminescence from Amorphous Silicon-Nitride (a-SiN_x:H) Layers Prepared by PECVD Method

Zingway Pei, Y.R. Chung, H.L. Hsiao and H.L. Hwang
Dept. of Electrical Engineering, Tsing Hua University, Sec 2, Kuang Fu Rd 101, Hsin-Chu, 30043,Taiwan R.O.C.

Abstract

In this study, the a-SiNx: H thin films were produced by the plasma enhanced chemical vapor deposition (PECVD) method. The photoluminescence at room temperature with the different SiH_4/N_2 gas flow ratio was investigated in this work. The peaks of photoluminescence spectra were demonstrated obvious blue-shifted from the 830 nm to the 430 nm with increasing the nitrogen flow rate. Further annealing the sample at 700°C for 10 min, the peaks have evidenced red-shifted about 50 nm. The X-ray photoelectron spectra (XPS) were applied to determine the configuration of the a-SiNx: H thin films. The peak of Si 2p binding energy shift from 99.7 eV toward the 102 eV. The silicon clusters and multi-phase existing in the thin films were suggested from the random bonding model. Further from the blue-shifted of the PL emission and the red-shifted of the annealing results. The optical emission may come from the alloy phase of the silicon embedded a-SiNx:H thin films.

INTRODUCTION

The light emission from silicon have recently become the subject of intense scientific and technique interest due to the promise of silicon-based light source in the opto-electronic applications and the compatible with standard ULSI silicon processing technology (1-2). The research efforts were focused on the porous silicon due to the ease to fabrication and observation to the silicon nano-phase formation (2). Unfortunately, the inherent properties of thermal instability and the using of chemical solution make porous silicon were not realized in the applications. Therefore, research interesting was focused on the silicon-rich dielectric thin films due to the possibility of the formation of embedded silicon clusters and adjustable photoluminescence (3-4). However, as a result of the high energy-gap and the low dielectric constant, the light emission devices usually need ultra-thin films that enhance the difficulty in fabrication (5). Therefore, the amorphous silicon-nitride (a-SiNx:H) thin film was the another candidate for the silicon-based luminescent material. The photoluminescence from a-SiNx: H thin film was observed by I.G.Austin et al. (6) and attributed to the luminescence from band-tail states. Six emission bands were observed and described as the defect luminescence by C.H.Mo et.al. (7) and reference therein. Few works on the origin of photoluminescence from a-SiNx:H films make the mechanisms of photoluminescence from such films still unknown. Therefore, the fundamental physics of light emission from a-SiNx:H thin films should be the first priority issue to make silicon nitride based opto-electronic applications realized. As a consequence, the a-SiNx:H thin films were fabricated in this study using the flow rate of reaction gas as the parameters. The light emissions from (a-SiNx) thin films were investigated in the room temperature in this study. The blue-shifted photoluminescence were found has simple relation to the growth conditions. The molecular bonding and chemical configuration also investigated in this study by the infrared spectra and x-ray

photoelectron spectra analysis to explore the reasons of blue-shifted photoluminescence.

EXPERIMENT

The hydrogenated amorphous silicon nitride (a-SiN_x: H) thin films were deposited on an n-type (100) silicon substrate by the plasma enhanced chemical vapor (PECVD) technique. After the standard clean procedures, the substrate was loaded to the reacting chamber. The substrate was subject to the 30 minutes in situ hydrogen plasma passivation and cleaning before growth. The reacting gases are the mixing of 5% argon diluted silane (5% Ar+SiH_4) and nitrogen (N_2). The substrate temperature was fixed at 300°C and the RF (13.56 MHz) power density was 200mW/cm^2. Moreover, the flow ratio of Γ = [SiH_4]/([N_2]+ [SiH_4]) was varying as the deposition parameters. The photoluminescence (PL) was used to study the emission of the samples and the fourier-transformed infrared spectroscopy (FTIR) was used to identify the vibration species in the samples. The local bonding configuration and the compositions were identified through the x-ray photoelectron spectroscopy (XPS). The room temperature photoluminescence was measured by using the 325 nm (3.81 eV) line excitation of a He-Cd laser with power of 1 mw focused to a spot of 100um. The emitted lighted was collected by a 50 mm f/1.4 lens in the direction normal to the illuminated surface, and focused on a SPEX 500M monochromator equipped with a thermal electrically cooled GaAs photo multiplier tube (PMT) and standard lock-in technique was used as the spectral analysis. The XPS analysis was carried out using Mg Kα (hν -1253.6 eV) X-ray source. The kinetic energy of the photoelectrons were determined using a spherical capacitor analyzer (SCA) at a constant pass energy mode. The thermal annealing was carried by using AG model 610i at temperature from 400°C to 700°C for 5min to 20 min.

EXPERIMENTAL RESULTS

Reflectance Studies of a-SiNx

The thickness, optical gap, and refractive index as fitted from the reflectance spectra measured by the "n & k method."(8) are indicated in the Table 1. The corresponding x value determined from the XPS results corrected with the sensitivity factor proposed by Wagner (9) also shown in the Table 1. From the table 1, the Γ = 0.125 sample has lower optical gap (2.4 eV) , higher refractive index (2.566) which far away from the standard Si_3N_4 thin film as shown in the last column of the Table(10). However, these two value are fully consistent with the lower x value of 0.5 and belong to highly silicon excess region will be discussed in the XPS analysis. Moreover, all the samples investigated in our studies are all belonged to silicon excess and the x value located between 0.5 to 0.90 was shown in the Table 1.

Photoluminescence

The studies of photoluminescence (PL) were carried at room temperature on the sample without any annealing. The peaks of photoluminescence are varying from the 830 nm to the 430 nm with increasing the $[SiH_4]/([N_2]+[SiH_4])$ gas flow ratio which denoted Γ from 0.125 to 0.8. The obvious blue-shifted of the PL peaks from infrared to the blue optical emissions are demonstrated in the Fig. 1. As indicated in the figure, the emission peak of 430nm has the highest intensity. The emission peaked at 470nm also shown in the figure appeared in the $\Gamma = 0.125$ sample. The emission intensity decreases with the increase of the emission wavelength until the 830nm emission that the intensity was about one-twenty of the blue emission peak.

In order to understand the optical properties of thin films after thermal treatment. Thin films are subjected to 10 minutes rapid thermal annealing for temperature varying from 400°C to 800°C. The photoluminescence spectra of sample $\Gamma=0.636$ after thermal annealing are shown in the Fig.2 . As indicated in the figure 2, the peak position was only slightly red shifted and increased from 585nm to 603nm. The relation between the PL intensity and the annealing temperature are sketched in the Fig. 3. The PL peak intensity was first slightly increased with the increased of the annealing temperature till 600°C. Then the intensity was rapidly increased with the increased of annealing temperature from 600 to 700°C and saturated. The PL intensity under 800°C annealing was about 10 times of the sample without thermal annealing. The peak position of photoluminescence emission from other Γ value samples also sketched in the Fig. 4. For $\Gamma = 0.636$ and 0.8, the peak position exhibit slightly red shifted with increase the annealing temperature. However, for the $\Gamma = 0.43$ and 0.33, the peak position exhibit clear red shifted from red to infrared emission.

Fourier Transformed Infrared Spectra (FTIR) Study

The detailed molecular bonding configuration of deposited films was clarified through the FTIR technique to investigate the molecular species incorporated in the a-SiNx: H thin films. The infrared absorption spectra obtained from Fourier-transform infrared spectra (FTIR) technique illustrate three major absorption peaks as indicated in the Fig. 4. First absorption peaks were located at 830 cm^{-1} to 860 cm^{-1} which are the Si-N stretching vibration mode for all samples as indicated in the figure and a vertical line along 849 cm^{-1} was used as the guided line to the eye. The second region was weak absorption at 2000-2300 cm^{-1} and attributed to the Si-H stretching mode. The third region was the more weak absorption at 3340-3350 cm^{-1} and comes from the N-H stretching mode (11). The lacks of 890 cm-1 and 845 cm-1 peaks at IR spectra were represented that the incorporation of polysilane $(SiH_2)_n$ into the thin films during deposition were not detectable (12). As a results the Si-N bonding was the dominated species in the thin films. The Si-H bonding was not detected in the $\Gamma=0.8$ sample and become clear in the $\Gamma=0.2$ sample. The reasons are the reaction gas is nitrogen (N_2) instead ammonia (NH_3) that introduced less quantity of hydrogen species. As a result, the quantity of Si-H bonding were less except the low Γ value samples. The N-H_2 bonding appeared at 1150 cm^{-1} and N-H stretching mode only detected in the high Γ value indicated that most hydrogen were bond to the nitrogen instead silicon. However, in the low Γ value

samples, the most hydrogen were bond to the silicon instead nitrogen. The Si-O-Si stretching mode was not found in all samples that indicated the oxygen was not involved in molecular bonding of the thin films. The FTIR spectra for sample $\Gamma = 0.636$ after thermal annealing also sketched in the Fig. 6(a). The Si-N bonding exhibit no evidence changed in the position and intensity. However, the intensity of S-H bonding demonstrated clear diminish with the increase of the annealing temperature was the indication of hydrogen escape from the films were sketched in the Fig. 6 (b).

X-Ray Photoelectron Spectra (XPS)

The position of Si-N stretching mode from FTIR spectra was exhibited no clear correlation to the growth conditions. Therefore, the FTIR spectra were not enough to explore the chemical structure between silicon and nitrogen. In order to comprehend the relation between the photoluminescence and microstructure of the samples, the x-ray photoelectron spectra (XPS) were applying to determine the configuration of the a-SiNx thin films. The core level binding energies were referenced to the N 1s peak at 397.5 eV.

The Si 2p core-level binding energy spectra for samples from a-Si to the $\Gamma = 0.8$ sample were illustrated in Figure 7. The lowest spectrum was the Si 2p binding energy of typical a-Si located at 99.7 eV in the sample deposited in the same technique as other samples except no nitrogen introduced during the deposition. The Si 2p binding energy was exhibited clear shifted from 100.98 eV to 102.39 eV for the $\Gamma = 0.125$ to the $\Gamma = 0.80$ sample. The vertical line along 99.7 eV was used as the guided line to determine the a-Si phase. Concerning the chemical structure of amorphous silicon nitride (a-SiNx:H) thin films, two models have been proposed. One model is the random bonding model by Phillip (13) another is the stoichiometric statistical model (SSM) by Temkin (14). The SSM model was explained that the silicon 2p line is an overlapping of two peaks corresponding to the a-Si and a-Si_3N_4 phase, with a fixed energy separation of 2.4 eV and with the an intensity ratio which is a monotonic function of x. According to the XPS spectra of our results, the Si 2p line was exhibited broadens and shifted in position with monotonic function of x. that could not explain by the simple SSM model (15). Therefore, according to the random bonding model consider the a-SiNx network as a statistical distribution of the [Si-(Si_nN_{4-n}) ($0 \leqq n \leqq 4$)] components. From the model, Si 2p line could be described as a superposition of five component (Si^0,Si^{1+}, Si^{2+},Si^{3+}, and Si^{4+}) peaks. These five peaks corresponding to Si atoms in which zero, one, two, three or all four Si-Si bonds have been replaced by Si-N bonds and each components has energy separation estimated to 0.78 eV (16). Therefore, in our XPS results, the broaden of the Si 2p binding energy peak could be represent as the alloy phase of five [Si-(Si_nN_{4-n}) ($0 \leqq n \leqq 4$)] structure components. The most clear alloy phase that including all five phase was the $\Gamma = 0.125$ sample, the Si 2p line exhibit strong overlap to the a-Si 2p line which contain amorphous Si-Si_4 phase in the a-SiNx thin film according to the random bonding model. The overlapping to the a-Si 2p line was not detectable for $\Gamma = 0.636$ sample and higher. The full width at half maximum (FWHM) of the Si 2p line was sketched in the Fig. 8. Two distinct trend appeared in the figure, first are FWHM increase with the Γ value until $\Gamma = 0.43$ then decline. The reason for the two trends could be suggested to the formation of silicon phase (Si-Si_4) in the films. In the low Γ value, the Si-Si_4 phase contribution to the Si 2p line that caused line broadening until Γ value increase to 0.43.

Then the broadening decreased as a result of no detectable Si-Si_4 phase demonstrated in the figure 7. As a result, the silicon clusters could possibly formed during deposition and embedded in the thin films of low Γ value. Consequently, the size and quantity of silicon clusters may be too small and few to detect in the samples of Γ value higher than 0.43. The FWHM of a-Si and Si_3N_4 are 1.12 eV and 1.62 eV respectively (16).

DISCUSSION

The red shifted of PL emission in the silicon based dielectric films was proposed to the reconstruction of the silicon clusters and the neighbor silicon atoms during thermal annealing (17). In our thin films, for the Γ value lower than 0.43, the quantity of excess silicon were higher to allow the silicon clusters grow. However, the a-SiNx networks also performed reconstruction simultaneously. As a consequence, the mechanism of red shifted of photoluminescence was not simply described as the emission from silicon clusters with size increasing. The Si-H vibration mode indicated in the figure 6(b) exhibit clear dependence to the increase of photoluminescence intensity sketched in the figure 3. The dependence is, for temperature increase from as-deposited to 600°C, the intensity of Si-H vibration mode exhibit slightly decrease that consist the photoluminescence intensity sketched in the figure 3. After 600°C annealing, the intensity of Si-H vibration in the IR spectra of the 700°C annealing sample was exhibited extensively decrease that also consistent to the photoluminescence spectra in the figure3. As a result, the increase in the photoluminescence intensity was attributed to the escaped of hydrogen and the reconstruction of amorphous silicon nitride network in our a-SiNx thin films.

Usually, two mechanisms were suggested to explain the origin of the light emission of the silicon–based materials. One is the defect luminescence model and the other is the quantum confinement model. The density of defects such as $\equiv$Si-Si$\equiv$, $=N^{\cdot}$, $\equiv Si^{0}$, and $\equiv Si^{\cdot}$ are much higher than stoichiometric silicon nitride in our plasma deposited a-SiNx thin films and exist in the gap of gap of a-SiNx (7). The optical emission of 3.1, 2.2, 2.3, and 1.9 eV are investigated belong to the recombination of defect levels (18). Referring to our a-SiNx thin films, the adjustable blue-shifted photoluminescence with decrease the SiH_4 gas flow seems not belong to the separated defect emissions because of monotonic shift in the position. However, we do not exclude the possibility of contribution from defect luminescence in our films that could possibly covered by other mechanisms in the photoluminescence spectra.

The quantum confinement model proposed that the silicon clusters may exist in the silicon-based material and the optical emission are size dependent and the strong wave function overlap. Therefore, as the size of the silicon cluster decrease, the photon energy of the emission light will increase to a higher value used named blue-shifted (19). Moreover, the decrease in cluster size will also enhance the intensity of optical emission (20). The phenomenon of blue shifted photoluminescence and the increase of the photoluminescence intensity are seems could be described by size dependent luminescence in quantum confinement model (21). However, from the XPS spectra, the Si-Si_4 bonding phase was not detectable in the samples of Γ value large than 0.43. This finding restricted us to describe the mechanism of blue-shifted photoluminescence to the

simple size dependent model of silicon clusters. In order to described the blue shifted photoluminescence from a-SiNx, the Si 2p binding energy position and photoluminescence peaks versus the gas flow Γ value are sketched in the Fig 9. This two line were exhibited the same trend along the gas flow ratio Γ. As mentioned above, the chemical structure are the superposition of five [Si-(Si_nN_{4-n}) ($0 \leqq n \leqq 4$)] components. For such a reason, not only Si-Si_4 bonding phase, other components were contributed to the photoluminescence according to the figure 9. The luminescent phenomenon could be described as follow. Firstly, in the low Γ value, Si-Si_4 bonding phase was appeared and the silicon clusters contribute substantially part of the photoluminescence. Secondly, with the increased of Γ value, Si-Si_4 bonding phase gradually disappear that the contribution of Si-Si_4 bonding phase diminish. Finally, for the Γ value larger than 0.43, the other silicon nitride phase component were dominated and the peak of photoluminescence shifted to the higher energy level. For such a reason, the luminescence from alloy phase of a-SiNx thin films was suggested to describe the blue-shifted photoluminescence.

CONCLUSIONS

In conclusions, an intense, blue-shifted photoluminescence at room temperature was observed from plasma enhanced chemical-vapor-deposited hydrogenated amorphous silicon – rich silicon nitride (a-SiNx: H, $0<x<1.33$) thin films in the range from 430 nm (blue emission) to 830 nm (infrared emission). The photoluminescence intensity was enhanced 10 times for the sample under rapid-thermal-annealing up to 700°C for 10 minutes. Only higher silicon contained samples demonstrated obvious red-shifted in PL peak position after thermal annealing. The silicon bonding phase (Si-Si_4) were observed in the low Γ value sample from the core level bonding information form x-ray photoelectron spectra analysis. The mechanisms of blue-shifted photoluminescence were suggested come from the alloy phase of five Si-N bonding configuration. However, the contribution of emission from silicon clusters and the defect levels were not excluded.

ACKNOWLEDGEMENT

The financial support by the Nation Science Council of the Republic of China (Contract No. NSC 87-2215-E-007-031) and the assistance by the Materials Research Center at the National Tsing Hua University are gratefully acknowledged.

REFERENCES

1. K.D. Hirschman, L.Tsybeskov, S.P Duttagupta and P.M Fauchet, NATURE, Vol **384**, 338(1996)
2. R.T Collins, P.M Fauchet and M.A.Tischler, PHYSICS TODAY, **Jan**. 24(1997)
3. H.Z.Song, X.M,Bao, N.S,Li and X.L.Wu, Appl.Phys.Lett. **72**(3),356(1998)
4. J.F.Tong, H.L.Hsiao and H.L.Hwang, Appl.Phys.Lett. **74**(16),2316(1999)

5. G.G.Qin, A.P.Li, B.R.Zhang and B.C. Li, J.Appl.Phys. **78**(3),2006(1995)
6. I.G.Austin, W.A.Jackson, T.M.Searle and P.K.Bhat, PHILOSOPHICAL MAGAZINE B, **52**(3), 271(1985)
7. C. Mo, L.Zhang, C. Xie and T. Wang, J.Appl.Phys. **73**(10), 5185(1993)
8. A.R. Forouhi, and I. Bloomer, Phys. Rev. B**34**, 7018(1986), *ibid.* **38**,1865(1988)
9. C.D.Wagner, L.E.Davis, M.V. Zeller, J.A.Taylor, R.H. Baymond,and H.Gale, Surf. Interface Anal. **3**,211(1981)
10. A.Iqbal, W.B.Jackson, C.C.Tsai, J.W.Allen and C.W. Bates, Jr., J.Appl.Phys. **61**,2947(1987)
11. .D.V.Tsu, G.Lucovsky, and M. Mantani, Phys. Rev. **B 33**, 7069 (1986)
12. W.S.Liao,C.H.Lin and S.C. Lee, Appl.Phys.Lett. **65**, 2229(1994)
13. H.R. Phillip, J. Non-Cryst. Solids **8/10**, 627 (1972)
14. R.J. Temkin, J. Non-Cryst. Solids **17**, 215 (1975)
15. G.M. Ingo, N. Zacchetti, D. della Sala, C. Coluzza, J. Vac. Sci.Technol. **A 7** (5) 3048(1989)
16. A. Simunek, G. Wiech, J. Non-Cryst. Solids **192 &193**, 161(1995)
17. C.S. Yang, C.J. Lin, P.Y. Kuei, S.F. Horng, C. C. H. Hsu, M.C. Liaw, Applied Surface Science **113/114**, 116(1997)
18. J. Robertson and M.J.Powell, Appl.Phys.Lett. **44**, 415 (1984)
19. A. Zunger and L.W. Wang, Appl. Surf. Sci. **102**, 350(1996)
20. T.Takagahara, K. Takeda, phys. Rev B46, 15578(1992)
21. C.Delerue, G. Allan and M. Lannoo, Light emission in silicon: From physics to Devices, p254, ACADEMIC PRESS, San Diego (1998)

Table 1. The estimated x values, film thickness, refractive index, and optical band gap of α-SiN_x:H thin films prepared at various $\Gamma=[SiH_4]/([N_2]+[SiH_4])$ gas phase compositions.

Sample (Γ =)	0.125	0.33	0.636	0.73	0.8	Si_3N_4
x value	0.47	0.56	0.78	0.87	0.91	1.33
Thickness (nm)	162	167	237	245	261	
Refractive index	2.566	2.294	1.923	1.925	1.885	1.8
Optical band gap (eV)	2.4	2.77	3.64	3.83	4.09	5.0

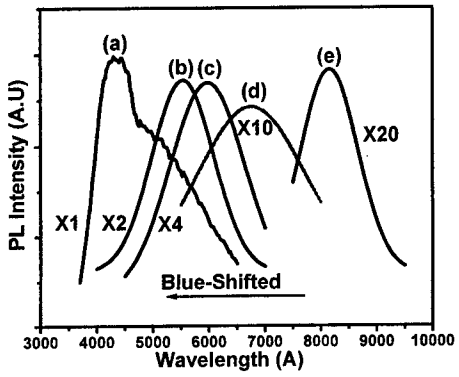


Figure 1. The photo-luminescence of different Γ value shows strong blue-shifted. (a) Γ = 0.8 (b) Γ = 0.73 (c) Γ =0.636 (d) Γ =0.2 and (e) Γ =0.125.

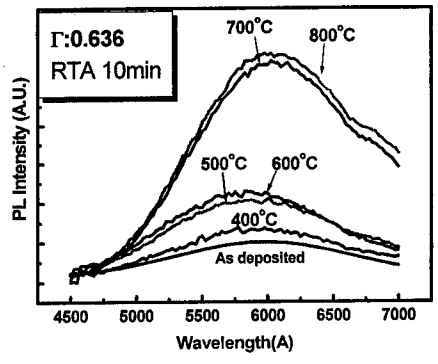


Figure 2. The photo-luminescence of Γ = 0.636 sample under 10 min. RTA annealing for different temperature including as-deposited, 400°C, 500 °C, 600 °C, 700 °C and 800 °C.

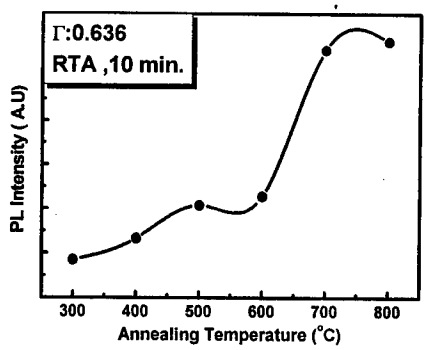


Figure 3. The PL intensity of Γ =0.636 sample after different temperature annealing.

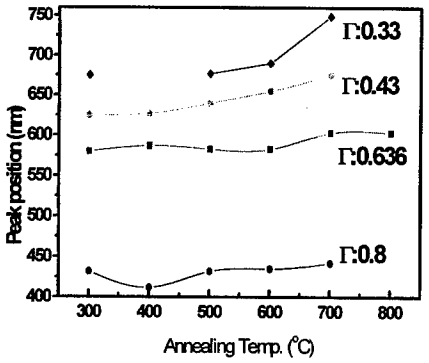


Figure 4. The PL peak position of Γ = 0.33, 0.43, 0.636 and 0.8 samples after different temperature annealing.

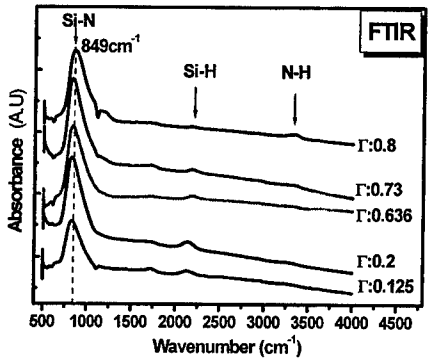


Figure 5. FTIR measurement of different Γ value. The Si-N bonding was clear for all samples and Si-H bonding only observable for low Γ samples. The N-H bonding only appeared in the Γ = 0.8 sample.

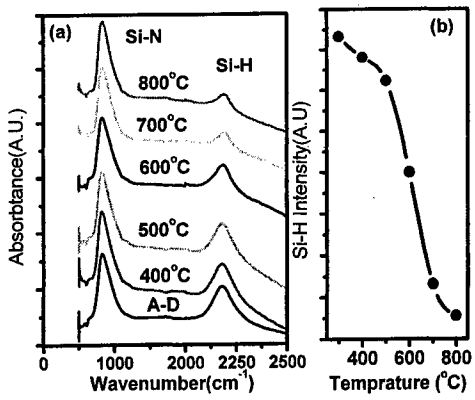


Figure 6. (a) the infrared spectra of Γ = 0.636 samples after different temperature 10 minutes RTA annealing. The A-D stands for as-deposited. (b) The intensity of Si-H vibration mode along with the anneal temperature.

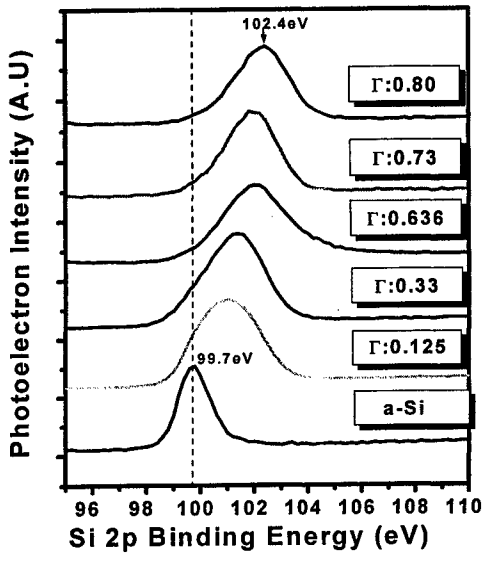


Figure 7. The X-ray photo-electron study on the different Γ value sample. The Si 2p binding energy was used to investigate the microstructure. The a0si was used as the reference as shown in the figure. The Si 2p peak was shifted to higher energy from Γ = 0.125 to 0.8.

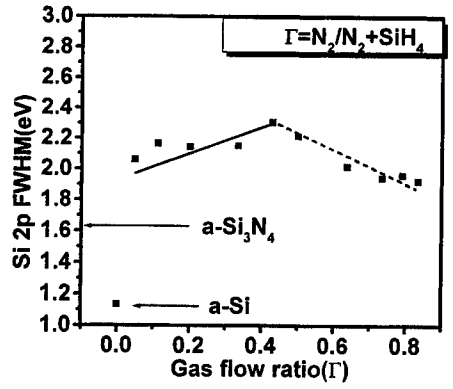


Figure 8. The full width at half maximum of Si 2p binding energy was shown in the figure. The FWHM shows two trends as indicated in the figure.

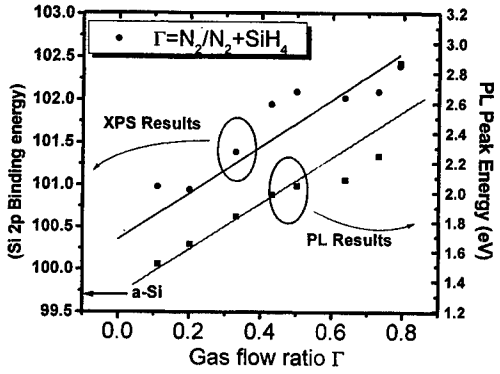


Figure 9. The relation of the Si 2p binding energy position and the PL emission peak position shows the same trend as indicated in the figure.

CHARACTERISTICS OF PHOTOVOLTAIC WAVELENGTH-TUNABLE SUPERLATTICE INFRARED PHOTODETECTOR

C. C. Chen, M. C. Hsu, and C.H. Kuan
Department of Electrical Engineering
National Taiwan University
1, Roosevelt Rd. Sec.4, Taipei, Taiwan, R.O.C. 10617

S. Y. Wang, and C. P. Lee
Department of Electronics Engineering
National Chiao Tung University
1001 Ta Hsueh Road, Hsinchu, Taiwan, R.O.C. 30050

ABSTRACT

A simple wavelength-tunable infrared photodetector containing a superlattice and a single current blocking layer sandwiched by two heavily doped contact layers was investigated. The switch of detection wavelength is realized by the current blocking layer that serves as an energy filter. Under low bias, the conduction by the photo-excited carriers in the second miniband minimum is suppressed, and is primarily due to the carriers in the second miniband maximum. While bias increased, those suppressed carriers can tunnel through the current blocking layer and contribute to the photocurrent. The measured peak detectivity of this detector is 2.6×10^{9} $cmHz^{0.5}/W$ (9.7 μm) at -0.6V and is 1.1×10^{10} $cmHz^{0.5}/W$ (6.7 μm) at -0.1V at 45K. In addition, it can be operated in photovoltaic mode. These show that the superlattice is a flexible structure for an infrared detector.

I. INTRODUCTION

The multi-wavelength detection is useful in remote temperature probing. Radiation from an object depends on the temperature and the emissivity of the object, and the distance away from the object. Thus a single-wavelength infrared photodetector is not enough in determining the temperature of the object when the distance to it is not fixed. With two-wavelength detector that can detect infrared radiation in the two atmosphere windows (3-5 μm and 8-12 μm) respectively, it is possible to determine the temperature of an object regardless of the distance between the detector and the object. Some efforts were made

to achieve multi-wavelength detection, including multi-stack [1] quantum wells, coupled quantum wells [2], and other designs [3]. However, the superlattice structure is an alternatively promising structure for infrared detection due to its flexibility in miniband engineering. Here a simple design containing a 15-period superlattice and one current blocking layer is proposed so that the wavelength is tunable by external bias. In addition, photovoltaic detection can be achieved and this makes it useful in some applications.

In the following, we will show the design and characteristics of our superlattice infrared photodetector, and a simple model was proposed to explain the mechanism of the change of the spectral responsivity with bias level.

II. DESIGN PRINCIPLES AND SAMPLE DISCRIPTION

1.Design Principle

The superlattice structure is known to have two absorption peaks due to transitions from the first miniband minimum to the second miniband maximum and the first miniband maximum to the second miniband minimum. Both absorption peaks can contribute to the photocurrent. It is intuitive that the superlattice structure can be used as a multi-wavelength detector, if some wavelength switching mechanism is incorporated. To reach the purpose, we introduce a current blocking layer to tune the wavelength, which in addition serves to reduce the dark current. In this paper, the current blocking layer is designed to be slightly higher than the second miniband minimum to prevent from the conduction of the photo-excited carriers in the miniband minimum at low bias level. Thus the long wavelength responsivity is suppressed at low bias. On the other hand, both the photo-excited carriers in the second miniband minimum and maximum can tunnel or pass through the blocking layer and contribute to the photocurrent. Therefore, the detection wavelength is tunable by applied bias.

2.Sample structure.

The structure, grown by molecular beam epitaxy on semi-insulating GaAs substrate, contains a 500nm heavily doped GaAs contact layer, a 150nm $Al_{0.23}Ga_{0.77}As$ current blocking layer, a 15-period GaAs/$Al_{0.27}Ga_{0.73}As$ superlattice, and a 400nm heavily doped top contact layer. The contact layer is doped with 1×10^{18} cm^{-3} of Si. Each period of the superlattice consists of 6.5nm GaAs well doped with $5\times10^{17}cm^{-3}$ and 3.5nm undoped $Al_{0.27}Ga_{0.73}As$ barrier. The parameters given above is the nominal values, the actual sample parameter may be slightly different. In the following discussions, some parameters were adjusted to fit the experiment results.

The band structure of the superlattice calculated by Kronig-Penney model with one band k.p and effective mass approximation. The first miniband extends from 52.2meV to 63.1meV, and the second one does from 185.7meV to 251.7meV. The height of current blocking layer is designed to be 7meV above the second miniband minimum.

3. Mesa diode fabrication

The device was fabricated into a 200×400 $(\mu m)^2$ mesa diode by standard photolithography, chemical wet etching, evaporation and lift-off processes. Top and bottom contacts were made by evaporating 100nm Ni/Ge/Au and 200nm Au. After evaporation and lift-off, thermal annealing at 390℃ was performed to make omic contact with the n+ contact layer in the semiconductor. Finally, a 45° facet on the substrate was polished to allow infrared light back illuminating onto the detector [4].

III. EXPERIMENT RESULT

1.FTIR absorption measurement

The inter-subband transition of the superlattice structure is analyzed by measuring the infrared absorbance. Since the superlattice has 15 periods, there are respective 15 discrete states in the first and second minibands. The absorption coefficient for transitions between the two minibands is given by [5]

$$\alpha=\frac{2\hbar\omega}{(2\pi)^3 I}\int_{k_x,k_y} dk_x dk_y \sum_{k_z}\frac{2\pi}{\hbar}\left|\left\langle 1\left|(e/m^*)\vec{A}\cdot\vec{p}\right|\right\rangle\right|^2 [f(E_1)-f(E_2)]\cdot\delta(E_2-E_1-\hbar\omega). \quad (1)$$

where I is the incoming light intensity, A is the vector potential of the incident light, and p is the momentum operator. $f(E_1)$ and $f(E_2)$ are the Fermi-Dirac distribution functions for the ground and excited miniband, respectively. The index k_x and k_y are the in-plane wavenumber, and k_z is the quantum number for the energy quantization in the direction normal to the epitaxial plane. In our 15-period superlattice, kz is the index for the 15 states in each miniband.

When parabolic in-plane dispersion is assumed, the integration over k_x and k_y can be performed analytically and the equation becomes [5]

$$\alpha=\frac{e^2 kT}{\varepsilon_0 c\hbar^2\pi m^*\omega}\sum_{kz}\left|\left\langle 1\left|\vec{A}\cdot\vec{p}\right|2\right\rangle\right|^2 \ln\left[\frac{1+\exp([E_f-E_1]/kT)}{1+\exp([E_f-E_2]/kT}\right]\left(\frac{\Gamma/\pi}{(E_2-E_1-\hbar\omega)+\Gamma^2}\right)\cdot \quad (2)$$

The delta function is replaced by Lorentzian function to model the broadening effect.

From the equation above, there are several factors that can affect the absorption line shape. Among them are the temperature, impurity doping, oscillator strength, and the location of the miniband energies. The oscillation strength is largest for the fist miniband minimum to the second miniband maximum transition and smallest for the fist miniband maximum to the second miniband minimum transition [6]. The Fermi level depends on the temperature and impurity doping, and it affects the occupation of the states in the first miniband.

The measured and calculated absorption coefficient at 80K together with spectral responsivity at –0.5V at 25K is shown in Fig. 1. The shape of absorption coefficient does not change much, except a little broadening at higher temperature, which agrees with the calculation of absorption coefficient when the doping level is high. This is because the ratio of the electron occupation in the maximum and minimum of the first miniband does not change much with temperature in the highly doping condition. In this case, the absorption line shape is mainly dominated by the oscillation strength which is greatest for transition from the first miniband maximum to the second miniband minimum. Thus, the long wavelength absorption peak is larger and is consistent with the peak observed in Fig. 1.

2.Dark current

Dark current at various temperatures (with 77K cold shield) and background photocurrent of the detector at 25K are shown in Fig. 2. The voltage polarity is defined as positive if higher potential is applied on the top contact. A strong asymmetry in the I-V characteristic is observed in the figure. It can be attributed to the migration of the Si dopants into the blocking layer from the bottom contact. This assists the electron tunneling process at the positive bias. The temperature range with background limited operation of the detector is below 55K when the detector is bias at –0.6V, and 65K at –0.2V. For the operation with background limited performance in the bias range between 0V and -0.6V, the detector should be cooled below 55K.

3.Noise

Figure 3 shows the current noise power spectral density of the detector at 77K at negative bias region. The measurement was performed with sample immersed in 77K liquid nitrogen and is shielded to prevent from illumination of the room temperature infrared radiation. The current noise power spectral density matches well with the shot noise performance 2eI. It may be attributed to the thermally assisted tunneling process of the electrons through the edge tip of the blocking layer.

4.Responsivity and Detectivity

The spectral responsivity was measured at various temperatures and various biases by FTIR. The observed spectral responsivity shows little temperature dependence, and the representative one at 25K is shown in Fig. 4. It is clear that at zero bias, the detection wavelength is mainly at 6.9 μm. While negative bias increases in magnitude, another peak at 9.7 μm rises, and becomes 2.3 times larger than the 6.9 μm peak at –0.6V. Therefore, the ratio of responsivity at 6.9 μm and 9.7 μm can be tuned by varying external bias.

The absolute value of spectral responsivity can be calibrated by the blackbody responsivity (R_{BB}) with the following relation

$$R_{BB}(800K) = \frac{R_P \int_0^\infty \overline{R}(\lambda) W(\lambda,800K) d\lambda}{\int_0^\infty W(\lambda,800K) d\lambda} \qquad (3)$$

Where W(λ,T) is the radiance of the blackbody source at temperature T, $\overline{R}(\lambda)$ is the relative spectral responsivity normalized by the peak responsivity.

The measured blackbody (at 800K) responsivity of the detector is 12mA/W at –0.6V at temperatures below 65K and the peak responsivity at 9.7 μm is 35.6mA/W. The detectivity is a figure of merit of detector, and is expressed as

$$D_p^* = \frac{\sqrt{A_d \Delta f}}{NEP} = \frac{\sqrt{A_d \Delta f}}{i_{rms}} R_p \qquad (4)$$

where A_d is the area of the detector, Δf is the band width of measurement, *NEP* is the noise equivalent power, R_p is the peak responsivity and i_{rms} is the current noise of the detector. The current noise matches well with the shot noise of dark current at 77K. Thus the peak detectivity is estimate with the assumption that the current noise is also shot noise at other temperatures. The peak detectivity is hence 2.6×10^9 cmHz$^{0.5}$/W (9.7 μm) at -0.6V and 1.1×10^{10} cmHz$^{0.5}$/W (6.7 μm) at –0.1V at 45K. In contrast to the well-understood quantum well infrared photo-detectors, the performance of the superlattice detector could be improved by optimization which is not carried out yet.

IV. ANALYSIS AND DISCUSSION

The electrons in a superlattice with energy located in the resonant tunneling states can tunnel through the entire superlattice without reflection. However, when the current blocking layer is introduced in the structure, the current blocking layer could reflect electrons in the resonant tunneling states. The amount of electrons that can tunnel through the current blocking layer and collected by the contact depends on the height, length and shape of the current blocking layer. The height and length of the current blocking layer is predetermined in the crystal growth phase, and can not be changed electrically. However, the shape can be easily changed by external bias.

In order to understand the bias dependence of the resonant tunneling states of the superlattice and spectral responsivity, the transfer matrix method was used to calculate the transmission versus energy of electrons in the superlattice miniband through the current blocking layer under zero and negative bias. For comparison, the electron transmission for the superlattice only is shown in the dot line of Fig. 5. At thermal equilibrium with zero bias, the Fermi level equals everywhere inside the detector, and the current blocking layer tilted up as shown in the left of Fig. 5(a). The transmission under this situation is almost zero for the electrons with energy lower than 225meV. This is consistent with the disappearance of lower energy peak in the spectral responsivity. The photocurrent is composed of the electrons with energy around 230meV to 250meV. Thus photovoltaic operation is achieved by the transmission of photo-excited carriers through the current blocking layer. With the bias of -60meV, the transmission of electrons is shown in Fig. 5(b). It is clear that photo-excited electrons in the second miniband can tunnel trough the current blocking layer, and this agrees with the measured spectral responsivity at high bias region.

In this paper, the current blocking layer is designed to be 7meV above the second mini band minimum. And the observed spectral responsivity shown in Fig. 4 indicates that there is one peak at 6.9 μ m (corresponding to carriers excited from the first miniband minimum to the second miniband maximum) at 50, 0, and –100mV. Anther peak at 9.7 μ m (corresponding to carriers excited from the first miniband maximum to the second miniband minimum) in the spectral responsivity rises much faster than the 6.9 μ m peak as the negative bias increases in magnitude. This can be attributed to the fact that the transmission of the electrons in the second miniband minimum is more sensitive to the blocking layer than electrons in the second miniband maximum.

V. CONCLUSION

Our detector utilizes the characteristics of superlattice miniband and one current blocking layer serves as an energy filter for the photo-excited carriers. The energy filter can be tuned by external bias. Therefor the spectral responsivity can be tuned simply by controlling the voltage applied to the detector. The switching voltage is about 150mV in our detector. Whereas the external bias needed to switch detection wavelength in other multi-color detector such as multi-stack quantum well infrared detectors is an order larger than our superlattice detector. Besides, the observed photovoltaic operation has the merit of extremely small dark current and thus makes it useful when the FPA readout circuit is limited by storage capacitors.

In summery, the spectral responsivity of the superlattice infrared detector can be tuned at low bias level and it can be operated in photovoltaic mode. This shows that superlattice could be a flexible structure in designing infrared photodetectors.

VI. ACKNOWLEDGEMENT

This project is supported by National Science Council in Taiwan with contract number of NSC 88-2215-E-002-022.

References

[1] A. Kock, E. Gornik, G.Abstrieter, and etc, Appl. Phys. Lett. 60, 2011 (1992).

I. Grave, A. Shakouri, N. Kuse, and A. Yariv, Appl. Phys. Leet. 60,2060(1992).

[2] K. K. Choi, The Physics of Quantum Well Infrared Photodetectors, 385.

[3] B. F. Leivine, C.G. Bethea, B. O. Shen, and R. J. Malik, Appl. Phys. Lett. 57, 383(1990).

K. K. Choi, The Physics of Quantum Well Infrared Photodetectors, 382.

[4] Hasnain, G., B. F. Levine, C. G. Bethea, R. A. Logan, and J. Walker, Appl. Phys. Lett. 54, 515(1989).

[5] H. C. Liu, B. F. Levine, and J. Y. Andersson, Quantum Well Intersubband Transition Physics and Devices, 291.

[6] Manasreh, M. O., Semiconductor Quantum wells and Superlattices for Long-Wavelength Infrared Detectors, 158.

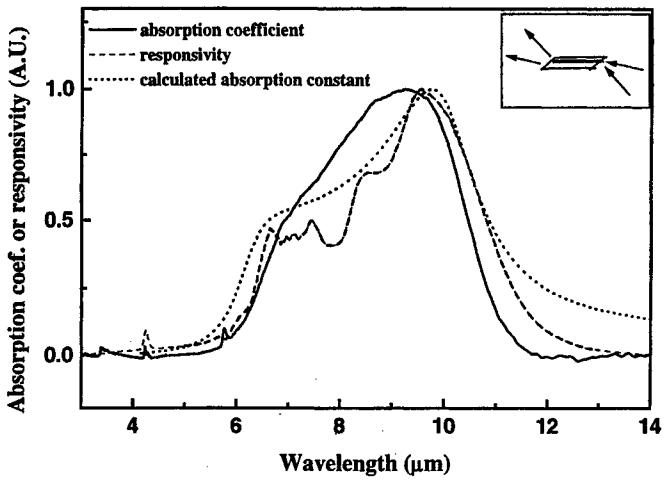


Fig. 1. The solid line and dash line shows the measured absorption coefficient at 80K and the measured spectral responsivity at 25K at –0.6V respectively. The dot line is the calculated absorption coefficient. Sample geometry for absorption coefficient measurement is shown in the inset.

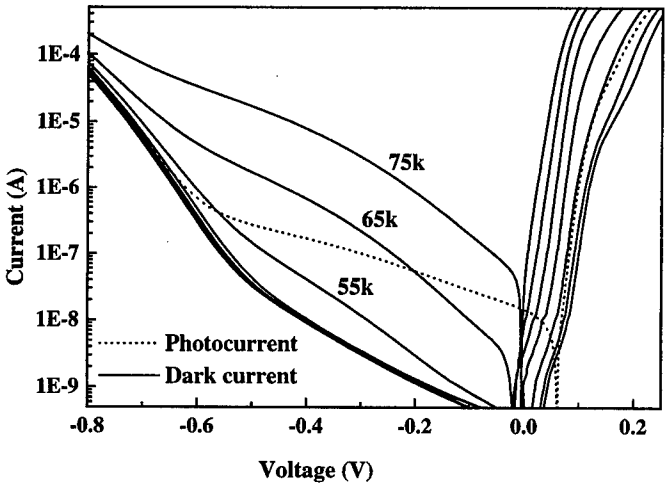


Fig. 2. Dark current versus bias at various temperatures and photocurrent at 25K. For the operation with background limited performance in the bias range between 0V and -0.6V, the detector should be cooled below 55K.

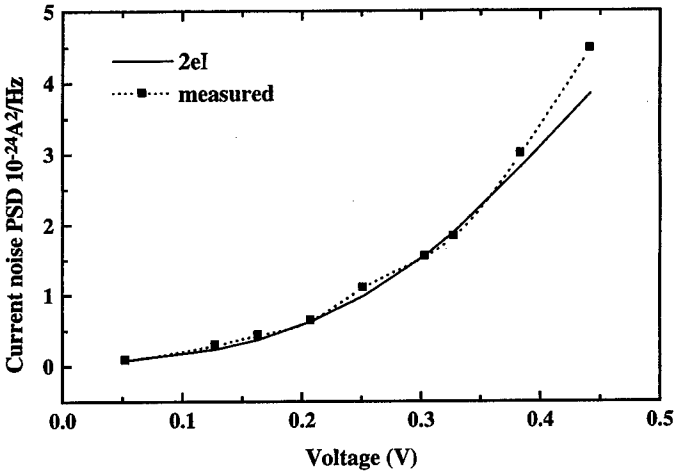


Fig. 3. Current noise power spectral density (PSD) measured with sample immersed in 77K liquid nitrogen. The sample was shielded to prevent from the illumination of room temperature infrared radiation. The measured current noise PSD is consistent with the shot noise PSD of dark current.

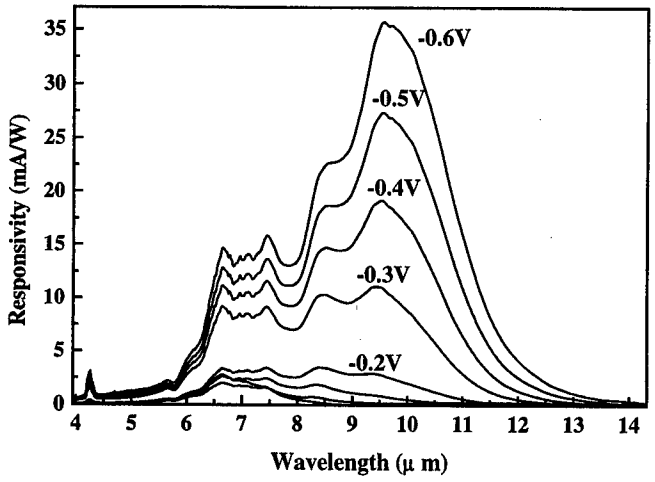


Fig. 4. Spectral responsivity of the detector at 25K at various bias level. At low bias level, the main detection wavelength is 6.7μm. While bias increases in magnitude, the detection wavelength at 9.7μm rises and becomes larger than the short wavelength peak.

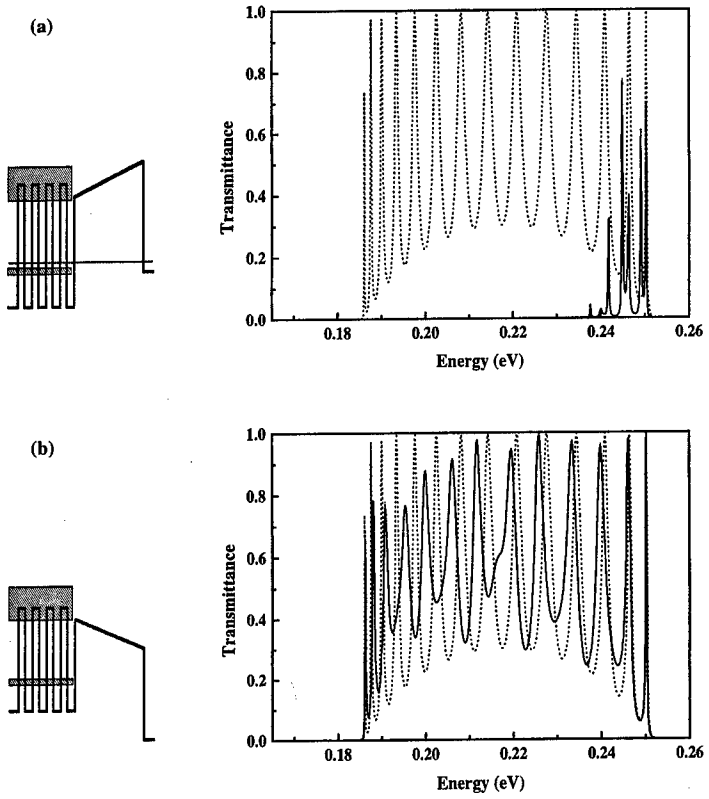


Fig. 5. Solid line is the calculated transmittance for the potential profile shown in the left, and dot line is the calculated transmittance for the superlattice without current blocking layer.

AUTHOR INDEX

Ahopelto, J., 176, 348
Al-Shahry, M., 252
Ando, T., 377
Arakawa, Y., 172
Bacher, K., 436
Balandin, A., 325
Balooch, M., 261
Bandyopadhyay,S., 413
Baribeau, J.-M., 45
Basmaji, P., 105, 181
Belolipetski, A., 189
Bichler, M., 406
Blick, R.H., 406
Bostedt, C., 261
Cahay, M.M., 333
Chaplik, A.V., 246
Chen, C.C., 485
Cheyssac, P., 216
Christen, J., 201
Christensen, D.H., 118
Chung, Y.R., 474
Csutak, S., 149
Dalba, G., 10
Daldosso, N., 10
Degoli, E., 62
Delage, A., 45
Deppe, D.G., 149
De Silvestri, S., 216
Devreese, J.T., 160
Dovidenko, K., 294
Dyer, W.R., 425
Ekbote, S., 333
Emmerling, M., 348
Eränen, S., 348
Faska, T., 459
Fauchet, P.M., 21
Fischer, P., 201
Fomin, V.M., 160
Forchel, A., 348
Fornasini, P., 10
Fountain, T.J., 354
Franco, N., 261
Fujiwara, A., 302
Galzerani, J., 105, 181
Gelloz, B., 27
Goussev, A., 189
Grimaldi, M., 10
Grisenti, R., 10
Gustafsson, A., 348
Hiramatsu, K., 201
Holleitner, A., 406
Hsiao, H.L., 474
Hsu, M.C., 485
Huffaker, D.L., 149
Hwang, H.L., 474
Iwase, M., 3, 240
Izumi, T., 3, 240
Janz, S., 45
Jiang, X., 447
Kamp, M., 201, 348
Khan, S.U.M., 252
Kikuchi, R., 266
Klimin, S.N., 160
Kofman, R., 216
Koshida, N., 27, 35
Koskenvaara, H., 176
Kotthaus, J.P., 406
Koyama, H., 21
Kristensen, A., 348
Kuan, C.H., 485
Kurihara, K., 302
Lafontaine, H., 45
Leburton, J.P., 160, 392
Lee, C.P., 485
Lee, J.-H., 436
Lewis, R.A., 130
Li, S.S., 436, 447
Lindelof, P.E, 348
Lipsanen, H., 176
Liu, W.K., 436, 447
Lockwood, D.J., 45
Lofgren, C., 294

Magarill, L.I., 246
Maka, T., 78
Markes, M.E., 189
Masunda-Jindo, K., 266
Masumoto, Y., 35
Matsumoto, T., 35
McCaffrey, J.P., 45
Menon, L., 413
Menon, M., 266
Moisa, S., 45
Möller, T., 261
Moon, J., 447
Morisaki, H., 3, 240
Moshegov, N., 105, 181
Müller, M., 78
Nagaraja, S., 392
Nagase, M., 302
Nakashima, H., 201
Namatsy, H., 302
Nisoli, M., 216
Nozaki, S., 3, 240
Ono, Y., 302
Ossicini, S., 62
Park, G., 149
Pei, Z., 474
Potemski, M., 96
Provencio, P.P., 225
Prunnila, M., 348
Pusep, Yu.A., 105, 181
Qin, H., 406
Rasulova, G.K., 137
Reisinger, A., 459
Rocca, F., 10
Roenker, K.P., 333
Romanov, S., 78
Rotkin, S.V., 369
Rowell, N.L, 45
Sadowski, M.L., 96
Samara, G., 225
Sato, K., 240
Sellmyer, D., 413
Shchekin, O., 149
Show, Y., 3, 240
Silva, M.T.O., 105
Simmel, F., 406
Sopanen, M., 176
Sotomayor Torres, C.M., 78
Spaggoci, S., 354
Stagira, S., 216
Stella, A., 216
Subbaswamy, K. R., 266
Sugiyama, Y., 240
Sundaram, M., 459
Takahashi, M., 35
Takahashi, Y., 302
Taylor, M., 459
Terminello, L., 261
Tidrow, M., 436, 447
Tognini, P., 216
Toivonen, J., 176
Toriumi, Y., 35
Toropov, A.I., 181
Tsu, R., 294
Uryu, S., 377
van Buuren, T., 261
Xu, D.-X., 45
Wang, K.L., 325
Wang, S., 459
Wang, S. Y., 485
Wegscheider, W., 406
Wilcoxon, J.P., 225
Williams, P.F., 189
Williams, R., 459
Worthington, J.C., 252
Yamada, T., 283
Yamazaki, K., 302
Zacharias, M., 201
Zanelatto, G., 181
Zeng, H., 413
Zentel, R., 78
Zhang, C., 130
Zheng, M., 413

SUBJECT INDEX

adatom chain, 283
Aharanov-Bohm oscillations, 377
amorphous silicon cluster, 240
amorphous Silicon Nitride, 474
anodic oxidation, 27
anodically oxidized porous Si, 3
anomalous level shift, 369
antibonding states, 392
antidot arrays, 377
artificial atom, 406
artificial molecule, 392
blue shift, 225, 261
Bragg reflection, 118
broadband detection, 436
Burt-Foreman formalism, 333
Casimir force, 369
coherent bonding states, 392
Coulomb blockade, 302, 406
Coulomb crystals, 189
Coulomb degeneracy, 246
Coulomb trapping potential, 96
coupled quantum dots, 392
current blocking layer, 485
dark current, 447
defect density, 294
detectivity, 447
dielectric continuum model, 160
disk shaped quantum dots, 160
dislocations, 266, 294
double barrier, 436
edge emitting device, 149
electroluminescence, 3,21,27,201,294
electron-electron scattering, 176
electron spin resonance, 240
emission killer center, 3
epitaxy, 294
error correcting code, 354
exciton-phonon coupling, 118
external quantum efficiency, 27
Fabry-Perot resonator, 35
Fe quantum dashes, 413
few electron limit, 406
focal plane arrays, 425,459
GaAs/AlAs superlattices, 105
Gallium Nitride, 325
Ge quantum dots, 216
Ge nanocluster, 261
graded superlattice, 436
Heterojunction Field Effect
Transistor, 325
Hund's rules, 392
InAs/GaAs disks, 160
infrared photodetector, 436
InGaN/GaN light-emitting
diode, 201
interdot coupling, 392
interface mode, 181
Lamb shift, 369
linear muffin-tin-orbital method, 62
liquid chromotography, 225
local spin density approximation, 392
logic chip, 354
long wavelength detection, 436
Luttinger-Kohn Hamiltonian, 333
magnetic focusing effect, 377
magnetic viscosity, 413
magneto-exciton, 246
metallic nanoparticle, 216
microwave spectroscopy, 406
MOS_2 nanoparticle, 225
multicolor photodetector, 425, 447
nanochip fault tolerance, 354
nanocrystal, 261
nanocrystalline n-TiO_2, 252
nanotube, 246
negative differential conductance, 137
nonlinear refractive index, 35
one-color QWIP, 459
oxidized porous silicon, 21
pattern dependent oxidation, 302
Pauli blocking, 176
P_b-center, 3

phonon assisted tunneling, 406
photoelectrochemical splitting, 252
photoluminescence, 3,21,78,201,240,474
photon localization, 78
photonic crystal, 78
photovoltaic infrared
photodetector, 485
piezo-doped HFET, 325
plasmon-LO phonon excitation, 105
polarization memory, 21
porous silicon, 10,27,35,254
porous silicon based devices, 21
quantized conductance, 348
quantum cellular automata, 354
quantum chaotic transport, 377
quantum computer, 96
quantum confinement, 10,225,261,325
quantum dot, 176,406
quantum dot laser, 149
quantum point contact, 348
quantum well, 436
quantum well infrared
photodetector, 425,447
Rabi splitting, 118
Raman scattering, 96,181
Raman scattering spectroscopy, 45
random bonding model, 474
rare earth ion, 78
resonantly distributed
quantum wells, 118
Self-assembled quantum
dots, 160,181
self-assembly, 189
self-organization, 216
self-organized stressor, 176
semiconductor-atomic-superlattice, 294
semiconductor-molecular-
superlattice, 294
Si clusters, 474
Si dangling bond, 62,254
Si quantum well, 62
Si nanocrystal, 21,240
Si single-electron transistor, 302,354
Si/CO-superlattice, 294
SiGe/Si superlattices, 45
Silicon on Insulator (SOI), 294
Si/SiO_2 superlattice, 62
SOI MOSFETs, 348
spectral responsitivity, 436,447
spin-orbit split-off band, 333
spontaneous demagnetization, 413
spontaneous emission, 78,149
stacking faults, 280
surface emitting laser, 118
TEM analysis, 348
thermionic cooling, 130
TiO_2 coated opals, 78
tight-binding method, 266,283
total electron yield, 10
two-color QWIP, 459
two-dimensional electron gas, 406
Van der Waals bonding, 283
Wannier-Mott exciton, 246
waveguide photodetector, 45
weakly coupled superlattices, 137
zero phonon peak, 160